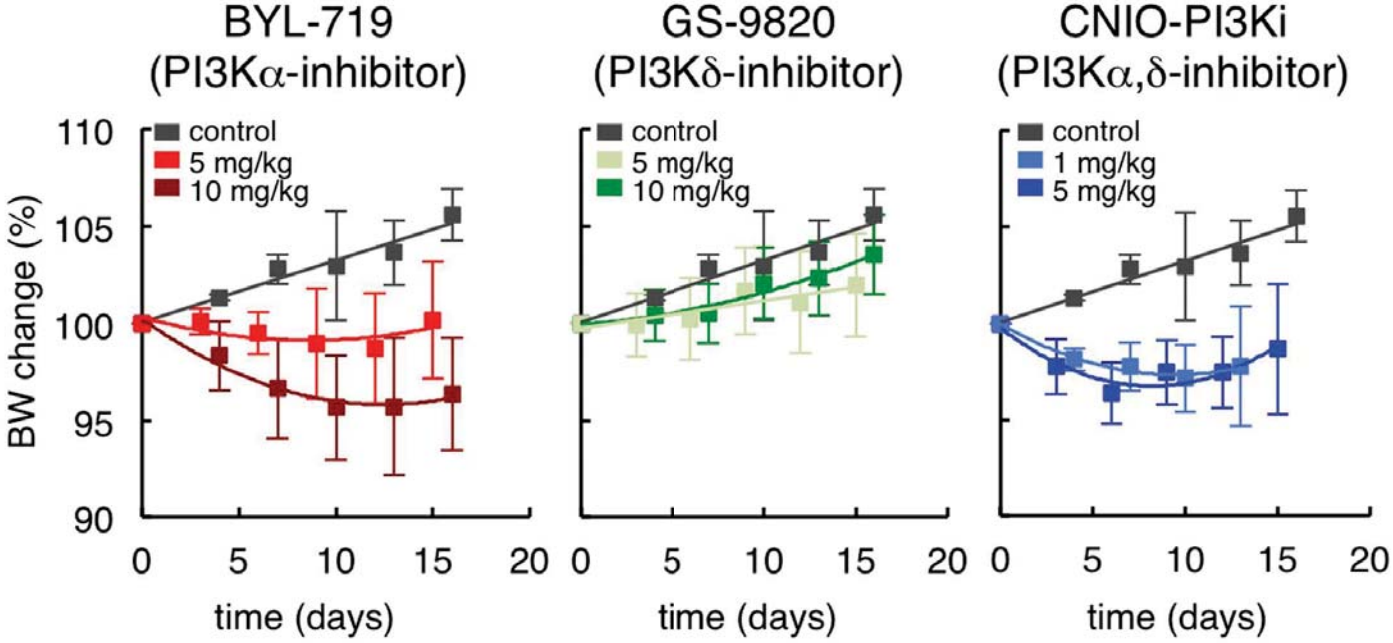

Special Collection on Cancer Therapeutics

Differential effects of PI3K inhibitors on obesity in ob/ob mice, see Lopez-Guadamillas et al. - " PI3Kα inhibition reduces obesity in mice."

Cancer Therapeutics | AGING

Editorial and Publishing Office Aging
6666 E. Quaker St., Suite 1B,
Orchard Park, NY 14127
Phone: 1-800-922-0957
Fax: 1-716-508-8254
e-Fax: 1-716-608-1380

Submission
Please submit your manuscript on-line at http://aging.msubmit.net

Editorial
For editorial inquiries, please call us or email editors@impactaging.com

Production
For questions related to preparation of your article for publication, please call us or email krasnova@impactaging.com

Indexing
If you have questions about the indexing status of your paper, please email kurenova@impactaging.com

Billing/Payments
If you have questions about billing/invoicing or would like to make a payment, please call us or email payment@impactaging.com

External & Legal Affairs
If you have questions about post publication promotion, Altmetric, video interviews or social media, please email RyanJamesJessup@impactjournals.com

Printing
Each issue or paper can be printed on demand. To make a printing request, please call us or email printing@impactjournals.com

Publisher's Office
Aging is published by Impact Journals, LLC
To contact the Publisher's Office, please email: publisher@impactjournals.com, visit www.impactjournals.com, or call 1-800-922-0957

Aging (ISSN: 1945 - 4589) is published twice a month by Impact Journals, LLC.
6666 East Quaker St., Suite 1B, Orchard Park, NY 14127

Abstracted and/or indexed in: PubMed/Medline (abbreviated as "Aging (Albany NY)"), PubMed Central (abbreviated as "Aging (Albany NY)"), Web of Science/Science Citation Index Expanded (abbreviated as Aging-US) & listed in the Cell Biology-SCIE and Geriatrics & Gerontology category, Scopus /Rank Q1(the highest rank) (abbreviated as Aging) - Aging and Cell Biology category, Biological Abstracts, BIOSIS Previews, EMBASE, META (Chan Zuckerberg Initiative), Dimensions (Digital Science's).

This publication and all its content, unless otherwise noted, is licensed under CC-BY 3.0 Creative Commons Attribution License.
Impact Journals, LLC meets Wellcome Trust Publisher requirements.
IMPACT JOURNALS is a registered trademark of Impact Journals, LLC.

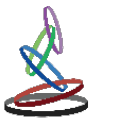

EDITORIAL BOARD

EDITORS-IN-CHIEF

Jan Vijg - Albert Einstein College of Medicine, Bronx, NY, USA

David A. Sinclair - Harvard Medical School, Boston, MA, USA

Vera Gorbunova - University of Rochester, Rochester, NY, USA

Judith Campisi - The Buck Institute for Research on Aging, Novato, CA, USA

Mikhail V. Blagosklonny - Roswell Park Cancer Institute, Buffalo, NY, USA

EDITORIAL BOARD

Frederick Alt - Harvard Medical School, Boston, MA, USA

Vladimir Anisimov - Petrov Institute of Oncology, St.Petersburg, Russia

Johan Auwerx - Ecole Polytechnique Federale de Lausanne, Switzerland

Andrzej Bartke - Southern Illinois University, Springfield, IL, USA

Nir Barzilai - Albert Einstein College of Medicine, Bronx, NY, USA

Elizabeth H. Blackburn - University of California, San Francisco, CA, USA

Maria Blasco - Spanish National Cancer Center, Madrid, Spain

Vilhelm A. Bohr - National Institute on Aging, NIH, Baltimore, MD, USA

William M. Bonner - National Cancer Institute, NIH, Bethesda, MD, USA

Robert M. Brosh, Jr. - National Institute on Aging, NIH, Baltimore, MD, USA

Anne Brunet - Stanford University, Stanford, CA, USA

Rafael de Caba - NIA, NIH, Baltimore, MD, USA

Ronald A. DePinho - Dana-Farber Cancer Institute, Boston, MA, USA

Jan van Deursen - Mayo Clinic, Rochester, MN, USA

Lawrence A. Donehower - Baylor College of Medicine, Houston, TX, USA

Caleb E. Finch - University of Southern California, Los Angeles, CA, USA

Toren Finkel - National Institutes of Health, Bethesda, MD, USA

Luigi Fontana - Washington University, St. Louis, MO, USA

Claudio Franceschi - University of Bologna, Bologna, Italy

David Gems - Inst. of Healthy Ageing, Univ. College London, UK

Myriam Gorospe - National Institute on Aging, NIH, Baltimore, MD, USA

Leonard Guarente - MIT, Cambridge, MA, USA

Andrei Gudkov - Roswell Park Cancer Institute, Buffalo, NY, USA

Michael Hall - University of Basel, Basel, Switzerland

Philip Hanawalt - Stanford University, CA, USA

Nissim Hay - University of Illinois at Chicago, Chicago, IL, USA

EDITORIAL BOARD

Siegfried Hekimi - McGill University, Montreal, Canada

Stephen L. Helfand - Brown University, Providence, RI, USA

Jan H.J. Hoeijmakers - Erasmus MC, Rotterdam, The Netherlands

John 0. Holloszy - Washington University, St. Louis, MO, USA

Stephen P. Jackson - University of Cambridge, Cambridge, UK

Heinrich Jasper - The Buck Institute for Research on Aging, Novato, CA, USA

Pankaj Kapahi - The Buck Institute for Research on Aging, Novato, CA, USA

Jan Karlseder - The Salk Institute, La Jolla, CA, USA

Cynthia Kenyon - University of California San Francisco, San Francisco, CA, USA

James L. Kirkland - Mayo Clinic, Rochester, MN, USA

Guido Kroemer - INSERM, Paris, France

Titia de Lange - Rockefeller University, New York, NY, USA

Arnold Levine - The Institute for Advanced Study, Princeton, NJ, USA

Michael P. Lisanti - University of Salford, Salford, UK

Lawrence A. Loeb - University of Washington, Seattle, WA, USA

Valter Longo - University of Southern California, Los Angeles, CA, USA

Gerry Melino - University of Rome, Rome, Italy

Simon Melov - The Buck Institute for Research on Aging, Novato, CA, USA

Alexey Moskalev - Komi Science Center of RAS, Syktyvkar, Russia

Masashi Narita - University of Cambridge, Cambridge, UK

Andre Nussenzweig - National Cancer Institute, NIH, Bethesda, MD, USA

William C. Orr - Southern Methodist University, Dallas, TX, USA

Daniel S. Peeper - The Netherlands Cancer Institute, Amsterdam, The Netherlands

Thomas Rando - Stanford University School of Medicine, Stanford, CA, USA

Michael Ristow - Swiss Federal Institute of Technology, Zurich, Switzerland

Igor B. Roninson - Ordway Research Institute, Albany, NY, USA

Michael R. Rose - University of California, Irvine, CA, USA

K Lenhard Rudolph - Hannover Medical School, Hannover, Germany

Paolo Sassone-Corsi - University of California, Irvine, CA, USA

John Sedivy - Brown University, Providence, RI, USA

Manuel Serrano - Spanish National Cancer Research Center, Madrid, Spain

Gerald S. Shadel - Yale University School of Medicine, New Haven, CT, USA

Norman E. Sharpless - University of North Carolina, Chapel Hill, NC, USA

Vladimir P. Skulachev - Moscow State University, Moscow, Russia

Sally Temple - NY Neural Stem Cell Institute, Albany, NY, USA

George Thomas - University of Cincinnati, Cincinnati, OH, USA

Jonathan L. Tilly - Massachusetts General Hospital, Boston, MA, USA

John Tower - University of Southern California, LA, CA, USA

Eric Verdin - University of California, San Francisco, CA, USA

Thomas von Zglinicki - Newcastle University, Newcastle, UK

Alex Zhavoronkov - Insilico Medicine, Baltimore, MD, USA

Table of Contents

Physiological frailty index (PFI): quantitative in-life estimate of individual biological age in mice 1

Originally published in Volume 9, Issue 3 pp 615—626

Delivery of sFIT-1 engineered MSCs in combination with a continuous low-dose doxorubicin treatment prevents growth of liver cancer 13

Originally published Volume 8, Issue 12 pp 3520—3534

RelA NF-κB subunit activation as a therapeutic target in diffuse large B-cell lymphoma 28

Originally published Volume 8, Issue 12 pp 3321—3340

Discovery of piperlongumine as a potential novel lead for the development of senolytic agents 48

Originally published Volume 8, Issue 11 pp 2915—2926

PI3Kα inhibition reduces obesity in mice 60

Originally published Volume 8, Issue 11 pp 2747—2753

Mitophagy-driven mitochondrial rejuvenation regulates stem cell fate 67

Originally published Volume 8, Issue 7 pp 1330—1352

Potential targeted therapeutic approaches in liposarcoma 90

Originally published Volume 8, Issue 4 pp 569—570

Apoptosis as anticancer mechanism: function and dysfunction of its modulators and targeted therapeutic strategies 92

Originally published Volume 8, Issue 4 pp 603—619

Fasting plus tyrosine kinase inhibitors in cancer 109

Originally published Volume 7, Issue 12 pp 1026—1027

A novel autosomal recessive TERT T1129P mutation in a dyskeratosis congenita family leads to cellular senescence and loss of CD34+ hematopoietic stem cells not reversible by mTOR-inhibition 111

Originally published Volume 7, Issue 11 pp 911—927

The p53 tumor suppressor protein protects against chemotherapeutic stress and apoptosis in human medulloblastoma cells . 128

Originally published Volume 7, Issue 10 pp 854—867

Kinase overexpressing cancers responsive to drug withdrawal 142

Originally published Volume 7, Issue 10 pp 752—753

Sonic Hedgehog in SCLC 144

Originally published Volume 7, Issue 9 pp 605—606

ARF: connecting senescence and innate immunity for clearance 146

Originally published Volume 7, Issue 9 pp 613—615

Targeting of non-oncogene addiction 149

Originally published Volume 7, Issue 8 pp 525—526

Caloric restriction induces heat shock response and inhibits B16F10 cell tumorigenesis both in vitro and in vivo 151

Originally published Volume 7, Issue 4 pp 233—240

Clearance of senescent hepatocytes in a neoplastic-prone microenvironment delays the emergence of hepatocellular carcinoma 158

Originally published Volume 6, Issue 1 pp 26—34

Therapeutic and space radiation exposure of mouse brain causes impaired DNA repair response and premature senescence by chronic oxidant production 167

Originally published Volume 5, Issue 8 pp 607—622

Rapamycin extends lifespan and delays tumorigenesis in heterozygous p53+/- mice 183

Originally published Volume 4, Issue 10 pp 709—714

Reversing the aging stromal phenotype prevents carcinoma initiation 189

Originally published Volume 3, Issue 4 pp 407—416

miR-150-5p suppresses tumor progression by targeting VEGFA in colorectal cancer 199

Originaly published Volume 10, Issue 11 pp 3421-3437

Naringin targets Zeb1 to suppress osteosarcoma cell proliferation and metastasis 216
Originaly published Volume 10, Issue 12 pp 4141-4151
Long noncoding RNA B3GALT5-AS1 suppresses colon cancer liver metastasis via repressing microRNA-203 227
Originaly published Volume 10, Issue 12 pp 3662-3682
A four-methylated mRNA signature-based risk score system predicts survival in patients with hepatocellular carcinoma 248
Originaly published Volume 11, Issue 1 pp 160-173
MicroRNA-141 suppresses growth and metastatic potential of head and neck squamous cell carcinoma 262
Originaly published Volume 11, Issue 3 pp 921-932

Priority Research Paper

Physiological frailty index (PFI): quantitative in-life estimate of individual biological age in mice

Marina P. Antoch[1], Michelle Wrobel[1,2], Karen K. Kuropatwinski[1], Ilya Gitlin[3], Katerina I. Leonova[3], Ilia Toshkov[2], Anatoli S. Gleiberman[2], Alan D. Hutson[4], Olga B. Chernova[2], Andrei V. Gudkov[3]

[1]Department of Pharmacology and Therapeutics, Roswell Park Cancer Institute, Buffalo, NY 14263, USA
[2]Everon Biosciences, Inc., Buffalo, NY 14203, USA
[3]Department of Cell Stress Biology, Roswell Park Cancer Institute, Buffalo, NY 14263, USA
[4]Biostatistics and Bioinformatics, Roswell Park Cancer Institute, Buffalo, NY 14263, USA

Correspondence to: Marina P. Antoch; **email:** marina.antoch@roswellpark.org
Keywords: aging, high fat diet, obesity, rapamycin, rapatar, chronological age DOI: 10.18632/aging.101206
Received: January 12, 2017 **Accepted:** March 11, 2017 **Published:** March 19, 2017

ABSTRACT

The development of healthspan-extending pharmaceuticals requires quantitative estimation of age-related progressive physiological decline. In humans, individual health status can be quantitatively assessed by means of a *frailty index* (FI), a parameter which reflects the scale of accumulation of age-related deficits. However, adaptation of this methodology to animal models is a challenging task since it includes multiple subjective parameters. Here we report a development of a quantitative non-invasive procedure to estimate biological age of an individual animal by creating *physiological frailty index* (PFI). We demonstrated the dynamics of PFI increase during chronological aging of male and female NIH Swiss mice. We also demonstrated acceleration of growth of PFI in animals placed on a high fat diet, reflecting aging acceleration by obesity and provide a tool for its quantitative assessment. Additionally, we showed that PFI could reveal anti-aging effect of mTOR inhibitor rapatar (bioavailable formulation of rapamycin) prior to registration of its effects on longevity. PFI revealed substantial sex-related differences in normal chronological aging and in the efficacy of detrimental (high fat diet) or beneficial (rapatar) aging modulatory factors. Together, these data introduce PFI as a reliable, non-invasive, quantitative tool suitable for testing potential anti-aging pharmaceuticals in pre-clinical studies.

INTRODUCTION

Mammalian aging is characterized by a gradual decline of numerous health parameters with multiple biochemical, physiological and behavioral manifest-tations [1]. These include reduced muscle strength, bone degeneration, osteoporosis, an increase in systemic inflammation, vascular calcification, hair loss, cataracts, cognitive decline, etc. [2]. Several animal models including *C.elegans,* yeast, *Drosophila* and rodents (rats and mice) have been successfully used over the last several decades to address mechanistic aspects of aging and development of age- related diseases. In most of these studies the major metric parameter for assessing pro-/anti-aging effect of genetic, nutritional or pharmacological manipulation has been the animals' lifespan.

While being informative, longevity by itself however, cannot provide an assessment of the animal's health status, which, like in humans, can significantly decline at older ages and therefore reduce the quality of life. This concern is particularly relevant to research focused on developing the "healthspan"-extending pharma-ceuticals , efficacy of which may not be necessarily translated in increased longevity but rather in prolongation of healthy life and require quantitative objective assessment. Clinical studies in humans measure age-related declines in performance by quan-

tifying the frailty index (FI), which reflects accumulation of health deficits during chronological aging [3].

Since numerous studies have shown that many age-associated changes that occur in humans are also present in aged mice, FI was recently introduced as a measure of mouse aging to pre-clinical models [4]. However, standardized and comprehensive approaches for FI measurements, which will address changes in a broad spectrum of physiological functions, are still missing. Here we describe development of an alternative scoring system, based on a selected set of non-invasive quantitative and physiological parameters, which could be repetitively used in the same animal over the course of its entire lifespan. We refer to this set of parameters as physiological frailty index (PFI). We show that similar to results of human studies older mice have much greater PFI reflecting age-related accumulation of deficits. We also validated our approach of PFI by testing detrimental (feeding high fat diet, HFD) and beneficial (treatment with mTOR inhibitor rapamycin) factors on animals' longevity and healthspan and revealed significant sex-dependent differences, thus emphasizing the importance of including both male and female animals in pre-clinical studies. The results of our study provide a feasible tool applicable for pre-clinical studies to test the efficacy of anti-aging pharmaceuticals.

RESULTS

Choosing informative parameters for creating PFI

To select which physiological parameters to choose for creating reliable FI we used several criteria. First, we wanted them to be diverse to reflect the status of different health-related physiological systems. Second, we wanted them to be objective and quantitative and not to involve any visual scoring. Finally, we wanted them to be minimally invasive so they can be applied in longitudinal studies. Based on these considerations, we selected 29 variables reflective of physical fitness (body weight and grip strength), cardiovascular system (systolic, diastolic and mean blood pressure, heart rate, tail blood flow and tail blood volume), total blood cell composition (white and red blood cell counts and differentials), plasma concentration of CXCL1/KC, triglycerides and glucose. All variables were measured in male and female NIH Swiss mice of different chronological ages (CA) of 26, 52, 78 and 104 weeks in a cross-sectional study. Next, using one-way ANOVA analysis, we identified those variables that demonstrate statistically significant changes during aging (p-value <0.05). Out of total of 29 parameters, 16 and 18 qualified these criteria in males and females respectively. These parameters and corresponding mean values for each age group are summarized in Tables 1 and 2. Interestingly, the two lists have only partial overlap pointing to sex-specific differences in the process of aging.

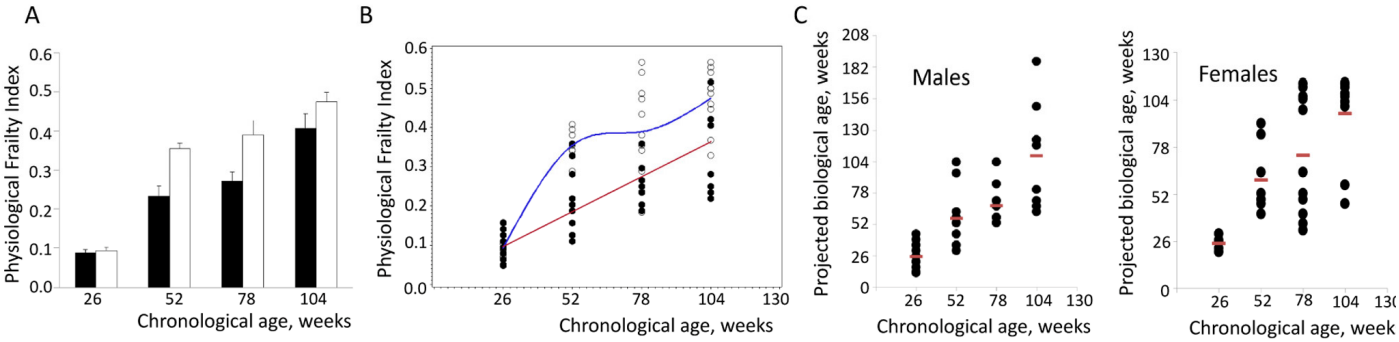

Figure 1. Assessment of individual biological age of NIH Swiss mice. (**A**) Age-related increase in PFI in male (closed bars) and female (open bars) NIH Swiss mice (n=10-12/group). PFI indices were measured as described using 16 or 18 parameters for males and females respectively. Data is presented as mean ±SEM. One-way ANOVA detects significant effect of age on FI value ($p<0.001$ for both sexes). (**B**) PFI values for individual male (closed circles) and female (open circles) mice. A cubic regression performed on this set of data generated the best fitting model as: PFI=0.00684+0.0034XBA for males (red line) and PFI=-0.67372+0.04277XCA-0.00057899XCA^2+0.00000263XCA^3 for females (blue line). All regression coefficients presented were significantly different from 0 at the 0.05 alpha-level. (**C**) Projected biological age of individual mice calculated from the PFI values using the fitting model predictions.

Quantification of PFI in chronologically aged male and female NIH/Swiss mice

To quantitatively evaluate age-dependent accumulation of health deficits, male and female NIH Swiss mice were allowed to age in the animal facility under normal husbandry conditions. Separate groups of male and female mice were tested for their overall health status at the ages of 26, 52, 78, and 104 weeks as described in Materials and Methods section. PFI was created using the 26-week old mice as a reference so that deviation of each parameter from the mean value was calculated. As shown in Fig.1A, PFI demonstrates gradual increase with age in both males and females; however, dynamics of this process was different. Consistent with previous studies, both in mice and humans [5], females show a more rapid accumulation of health deficits than males and average PFI values were higher compared to the males of the corresponding age.

Although average value of PFI showed highly statistically significant increase with age, within each age-matched group it demonstrated considerable individual variability (Fig. 1B). This is consistent with widely accepted concept originated from human and animal model studies stating that chronological age (CA, the actual age from the date of birth) and biological age (BA, reflecting individual's health status) are different [6-8]. To test whether PFI value can be used as a predictor of an individual animal's BA, polynomial regression of order 3 was fit to the data using a stepwise regression approach.

The best fitting models were given as:

PFI=0.00684+0.0034XBA for males and
FI=-0.67372+0.04277XCA-0.00057899XCA^2
+0.00000263 XCA^3 for females.

Next, we used these equations to calculate BA of each individual animal based on its PFI. Fig. 1C presents results of this analysis showing high degree of variability of estimated BA within the group of chronologically age-matched male and female mice. Overall these data indicate that our scoring system allows for an unbiased and reliable quantitation of age-related accumulation of deficits. They also suggest that PFI may be used as a tool for evaluating health status of an individual animal and determining its BA. This tool may be applied for quantitative assessment of the effects of various environmental, nutritional and pharmacological interventions on healthspan.

Sex-dependent effect of high fat diet on PFI and longevity

To validate our approach for assessing animal's BA, we subjected them to two treatments known to cause detrimental (feeding high fat diet, HFD) or beneficial (administration of rapamycin) effects on health and longevity. Fifty two week old male and female NIH Swiss mice were randomly assigned to four groups. Group 1 remained on regular chow and drinking water; group 2 remained on regular chow but started receiving rapamycin in drinking water. Group 3 started receiving HFD in combination with normal drinking water and group 4 was fed HFD in combination with rapamycin.

Table 1. Physiological parameters used to create PFI in male NIH Swiss mice. Data is presented as mean ±SEM.

Age, weeks	GS, g	Dia	Mean	Flow	NE (K/μl)	LY (K/μl)	MO (K/μl)	KC (pg/ml)
26	76.96±3.42	79.28±3.98	88.93±3.49	15.81±2.17	1.45±0.12	3.24±0.30	0.19±0.02	595.9±57.22
52	72.17±3.42	76.95±2.24	85.63±2.17	22.07±1.56	1.02±0.17	2.52±0.30	0.217±0.02	905.07±234.12
78	78.74±4.14	72.70±4.16	84.17+4.36	15.86±1.7	2.65±0.56	4.32±0.77	0.309±0.10	372.10±39.58
104	49.92±3.15	88.75±3.33	97.81±3.34	21.04±1.6	0.55±0.14	2.25±0.82	0.271±0.08	705.93±94.94

Table 1. (continued)

Age, weeks	NE %	MO %	RBC (M/μl)	HB (g/dl)	HCT %	MCV(fl)	MCH (Pg)	MCHC (g/dl)
26	24.16+4.04	3.02+0.30	8.91+0.41	13.09+0.69	39.60+2.20	44.27+0.72	14.66+0.23	32.90+0.29
52	26.01+2.09	6.03+0.57	7.97+0.46	11.83+0.73	37.85+2.37	47.34+0.69	14.81+0.21	31.28+0.30
78	34.18+2.12	3.83+0.48	9.94+0.59	15.23+0.87	49.20+2.60	49.71+0.98	15.33+0.22	30.91+0.27
104	18.10+3.16	8.78+1.41	6.6+0.63	9.50+0.97	34.01+3.23	51.73+1.00	14.33+0.0.16	27.77+0.45

GS – grip strength; Dia – diastolic pressure; Mean – mean pressure; NE – neutrophils; LY – lymphocytes; MO – monocytes; RBC – red blood cells count; HB – hemoglobin; HCT – hematocrit; MCV – mean corpuscular volume; MCH – mean corpuscular hemoglobin; MCHC – mean corpuscular hemoglobin concentration

It is well established that HFD-induced obesity has a detrimental effect on health increasing the risk of diabetes, heart disease, high blood pressure and cancer [9]. As shown in Fig. 2A, feeding HFD results in significant increase in body weight in both males and females (40% and 30% for males and females respectively). Nevertheless, effect on longevity was very different. Whereas feeding HFD reduced lifespan of male NIH Swiss mice from 121.1±9.2 to 91.5±5.9 weeks (p=0.008, Kaplan-Meier log-rank test), it had no effect on longevity of female mice (109.6 ±6.9 and 104.9±7.7 weeks for mice fed regular or high fat chow respectively; Fig. 2B). This result is consistent with previous studies showing that female mice are protected against HFD-induced metabolic changes by maintaining an anti-inflammatory environment in the intra-abdominal adipose tissue, whereas HFD-fed male mice develop adipose tissue inflammation, glucose intolerance, hyperinsulinemia, and islet hypertrophy [10].

To further test whether reduction in lifespan in males correlates with an increase in accumulation of health deficits, after 26 weeks of feeding HFD (at the age of 78 weeks) we created PFI for each individual animal.

Consistent with longevity data, feeding HFD significantly increased PFI in male but not in female mice (Fig. 2C). These data indicate that HFD-induced obesity produces stronger damaging effect in male mice affecting both their longevity and health status and that our approach can reliably detect overall health decline in a quantitative manner.

Chronic treatment with rapamycin increases the lifespan of female NIH Swiss mice without affecting their health status

To further validate our method, we decided to test whether we can reliably measure the beneficial effects of lifespan increasing approaches on animals' health. For this we chose to use rapamycin, which has been shown to extend lifespan of inbred and genetically heterogeneous mice [11, 12] as well as of mice that develop syndrome of premature aging [13]. Several studies performed in cancer-prone animal models suggest that rapamycin extends lifespan by delaying tumor development and progression [11, 14, 15]. In our previous work, we successfully used nanoformulated water soluble rapamycin (rapatar), which can be admi-

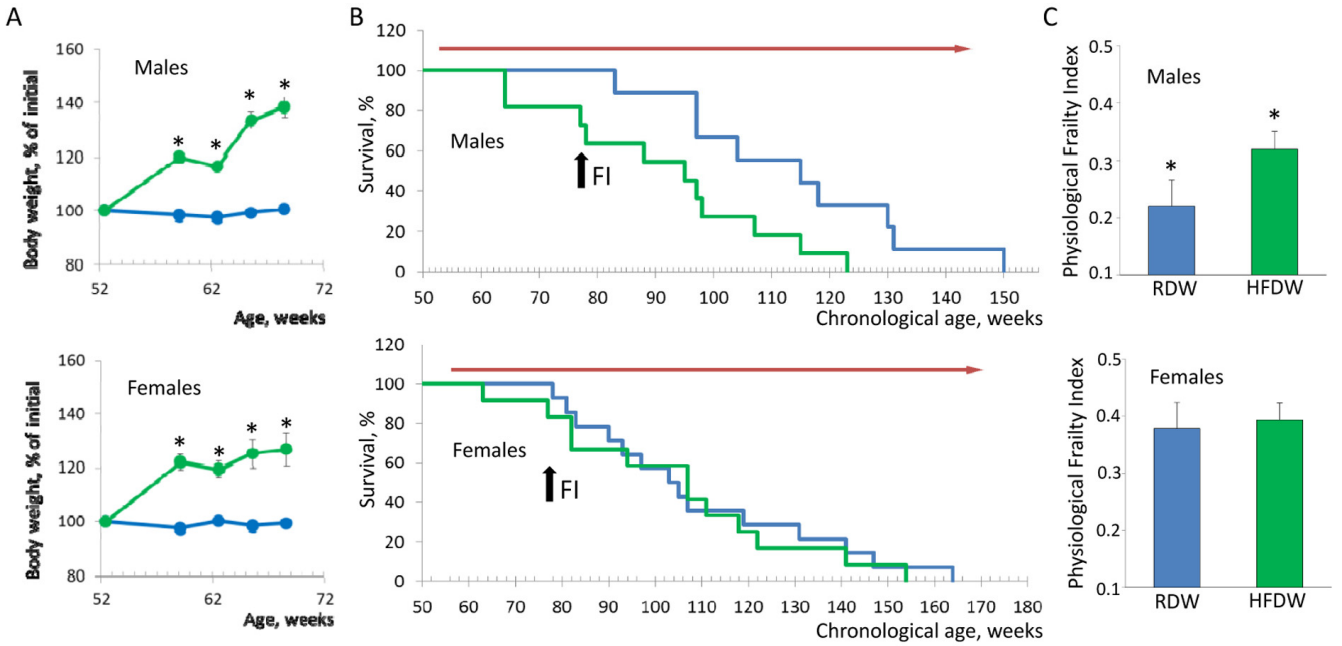

Figure 2. Sex-specific effects of HFD on lifespan and health of NIH Swiss mice. (**A**) HFD-induced body weight gain in male and female mice. Feeding HFD results in 40% and 30% increase in body weight in males and females respectively (p<0.001, Student's t-test). Since mortality is usually preceded by rapid weight loss, data is shown for the initial period of treatment before the first case of death in each group was recorded. Blue line – regular diet; green line – HFD. (**B**) Feeding HFD reduces lifespan of male mice from 121.1±9.2 to 91.5±5.9 weeks (p=0.008, Kaplan-Meier log-rank test) but had no effect on longevity of female mice (109.6 ±6.9 and 104.9±7.7 weeks for mice fed regular or high fat chow respectively). Blue line – regular diet; green – HFD. Red arrow indicates the period of time when mice received HFD. Black arrow indicates time when PFI was measured (at the age of 78 weeks). (**C**) PFI created at 78 weeks of age using 16 or 18 parameters for male and female mice respectively. Feeding HFD significantly increases PFI of male (p=0.019, Student's t-test) but not female mice. RDW - regular diet in combination with water (group 1), HFDW – HFD in combination with water (group 3).

nistered with drinking water and demonstrated high bioavailability [14]. In concurrence with the previous study, chronic administration of rapatar did not cause any toxicity as both male and female mice in control and experimental groups maintained similar body weight (Fig. 3A). However, there was a significant difference in the effect of rapamycin on longevity between the sexes. Chronic rapamycin treatment had no effect on longevity of male mice (mean survival 113.91+6.98 and 100.8+6.96 weeks for control and rapamycin-treated mice respectively) whereas in females, it increased lifespan from 110.09+7.12 to 131.23+8.29 weeks (p=0.05, Kaplan-Meier log-rank test; Fig. 3B). Surprisingly, this effect was not translated into improved health status between the groups as monitored by PFI (Fig. 3C). Thus, our data provides an additional support for the concept that chronological and biological aging may not be intrinsically identical and that other factors besides time may affect the pace ofage-dependent functional decline.

Rapamycin alleviates detrimental effect of high fat diet on male mice longevity and healthspan

Our data show that HFD-induced obesity shortens lifespan and deteriorates health status of NIH Swiss male mice (Fig. 1). It has been previously demonstrated that in rodents HFD-induced obesity increases activation of mTOR pathway in liver and skeletal muscle [16]. Therefore, we hypothesize that treatment with rapamycin can ameliorate detrimental effects of HFD. Comparison of the dynamics of body weight change showed that chronic treatment with rapamycin did not affect HFD-induced obesity in male mice but did prevent it in females (Fig. 4A). Longevity was not affected in mice of both sexes (Fig. 4B) constituting 91.45±5.87 and 100.55±6.26 weeks for male (p=0.26) and 105.01±7.74 and 110.50±7.58 weeks for female mice (p=0.6). Strikingly, rapamycin administration significantly alleviated detrimental effects of HFD in male mice as judged by a significant decrease in PFI

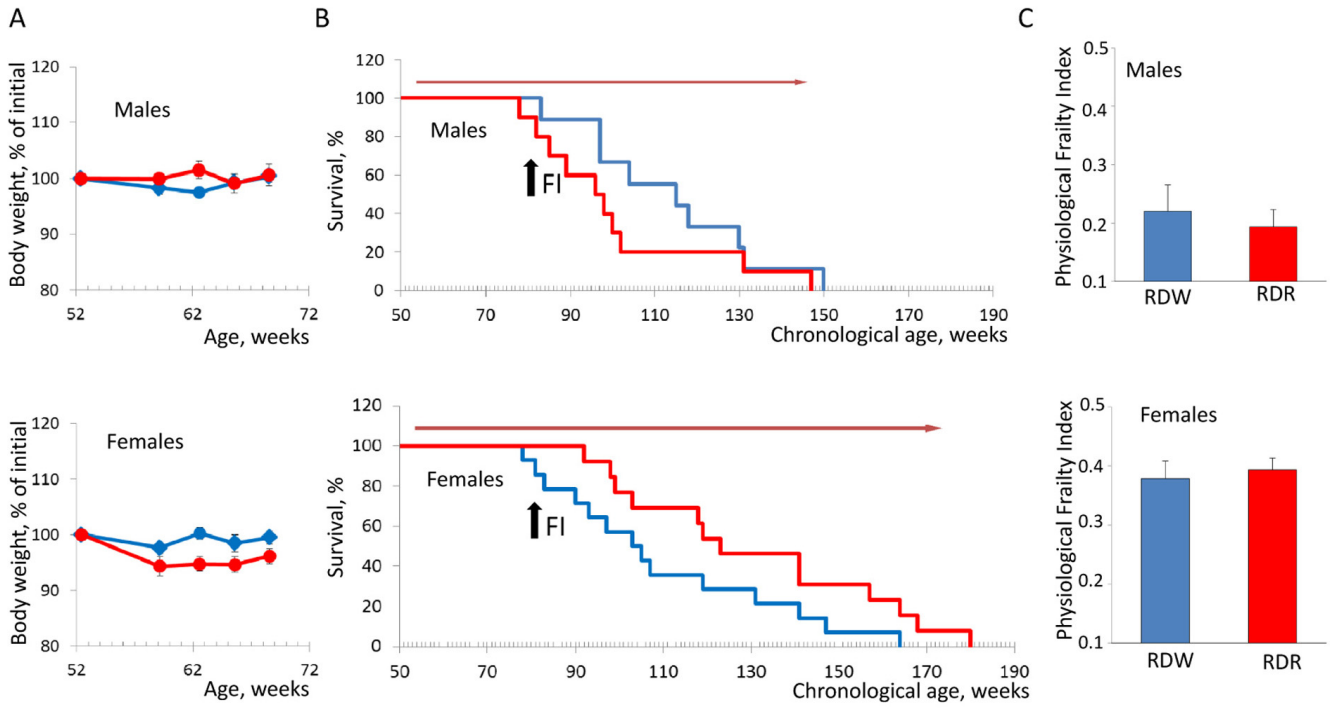

Figure 3. Sex-specific effects of rapamycin on lifespan and health of NIH Swiss mice. (**A**) Animals receiving rapamycin in drinking water maintain their body weights comparable to control mice. Blue line – normal drinking water; red line – water with rapamycin. (**B**) Kaplan-Meier survival curves for mice fed regular chow in combination with normal drinking water (blue line) or rapamycin (red line). Chronic administration of rapamycin has no effect on longevity of male mice (mean survival is 113.91±6.98 and 100.8±6.96 weeks for control and rapamycin-treated mice respectively. In females, rapamycin administration increases lifespan from 110.09±7.12 to 131.23±8.29 weeks (p=0.05, Kaplan-Meier log-rank test). Red arrow indicates the period of time when mice received rapamycin. Black arrow indicates time when PFI was measured. (**C**) PFI created at described above. No effect of rapamycin on health status was detected in male and female mice fed regular chow. RDW – regular diet in combination with normal drinking water (group1); RDR – regular diet in combination with rapamycin (group 2).

(Fig. 4C). Thus, whereas chronic treatment with rapamycin had no effect on lifespan and health status of male mice under standard diet conditions, it did prevent development of HFD-induced decline in health.

Table 2. Physiological parameters used to create PFI in female NIH Swiss mice. Data is presented as mean +SEM

Age, weeks	BW, g	GS, g	Dia	Flow	WBC (K/μl)	NE (K/μl)	NE %	LY %	MO %
26	26.61±0.31	76.96±3.42	79.28±3.98	15.81±2.17	5.19±0.27	0.86±0.07	16.56±0.96	77.82±0.81	4.90±0.37
52	32.20±1.15	72.17±3.42	76.95±2.24	22.07±1.56	4.41±0.46	1.28±0.14	30.50±4.22	61.90±4.27	7.06±0.66
78	37.17±1.86	78.74±4.14	72.70±4.16	15.86±1.7	7.47±0.91	2.57±0.42	34.23±3.36	59.59±3.90	4.01±0.29
104	35.71±1.17	49.92±3.15	88.75±3.33	21.04±1.6	6.55±2.32	1.57±0.50	22.86±3.69	63.99±4.12	7.90±0.83

Table 2. (continued)

Age, weeks	EO%	RBC (M/μl)	HB (g/dl)	HCT %	MCV(fl)	MCH (Pg)	MCHC (g/dl)	PLT	MPV
26	0.11±0.02	9.86±0.25	14.95±0.19	49.05±2.13	49.47±1.34	14.72±0.15	30.15±0.86	1134.53±28.53	4.83±0.04
52	0.50±0.1	11.21±0.27	16.33±0.31	61.13±1.43	54.65±1.16	14.60±0.31	26.75±0.37	706.00±97.92	4.76±0.11
78	1.70±0.58	10.11±0.42	15.39±0.76	49.12±2.45	48.44±0.77	15.16±0.20	31.35±0.19	1285.09±134.26	5.26±0.09
104	3.95±0.67	9.63±1.07	9.50±0.97	33.49±3.65	48.15±1.05	13.83±0.30	28.72±0.22	876.25±96.58	5.57±0.19

WBC – white blood cells, NE – neutrophils; LY – lymphocytes; MO – monocytes; EO – eosinophils; RBC – red blood cells count; HB – hemoglobin; HCT – hematocrit; MCV – mean corpuscular volume; MCH – mean corpuscular hemoglobin; MCHC – mean corpuscular

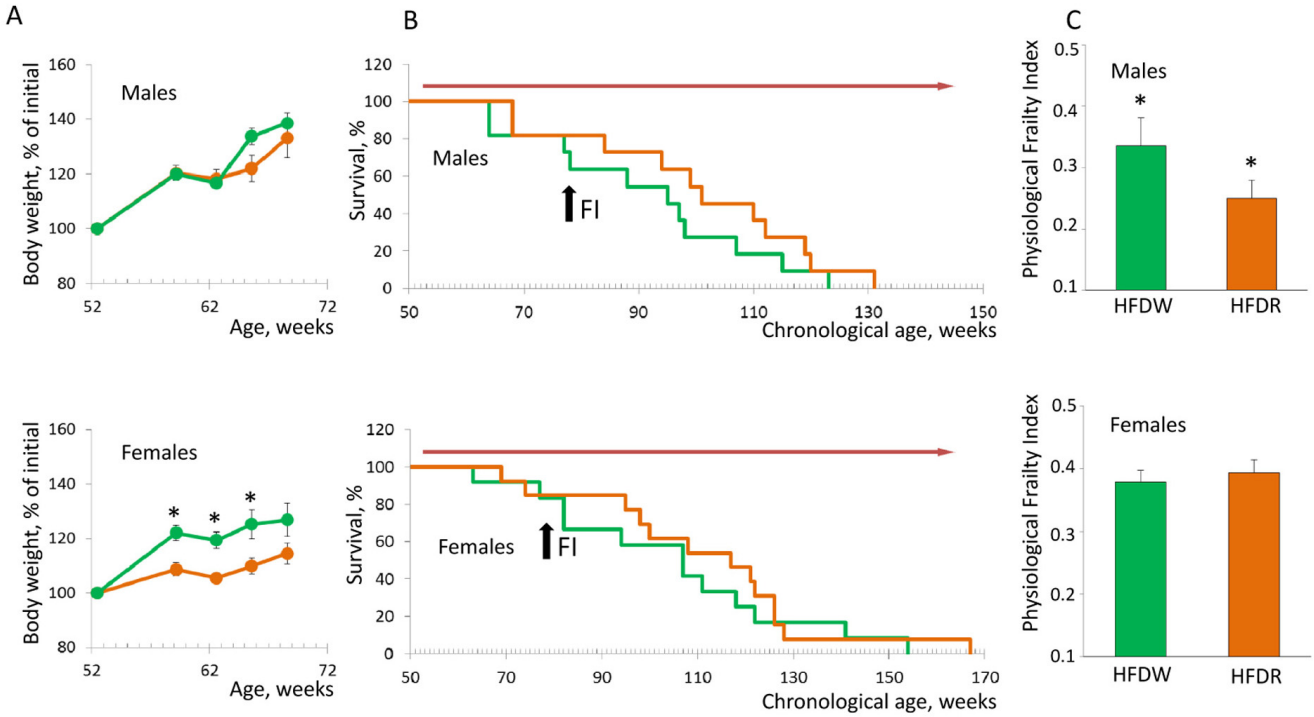

Figure 4. Chronic treatment with rapamycin ameliorates HFD-induced health decline in male mice. (**A**) Rapamycin prevents HFD-induced weight gain in female but not in male mice (p<0.01, Student's t-test). Green – HFD given with normal water, orange – HFD given in combination with rapamycin. (**B**) Kaplan-Meier survival curves for mice fed HFD in combination with normal drinking water (green line) or rapamycin (orange line). Chronic administration of rapamycin has no effect on longevity of both male (mean survival is 91.5±5.9 and 100.5±6.26 weeks) and female mice (mean survival is 104.9±7.7 and 110.5±7.6 weeks for control and rapamycin-treated mice respectively). Red arrow indicates the period of time when mice received rapamycin. Black arrow indicates time when PFI was measured. (**C**) PFI created at 78 weeks of age using 16 or 18 parameters for male and female mice respectively. Chronic administration of rapamycin ameliorates detrimental effect of HFD and brings the PFI values down to the normal range characteristic for this age (p=0.014, Student's t-test). HFDW – high-fat diet in combination with regular drinking water (group 3), HFDR – high-fat diet in combination with rapamycin (group 4).

To further illustrate the complex effects of diet and rapamycin on animal's health, we calculated projected biological age of each 78 week old male and female mouse based on their PFI. Results of this analysis are presented in Fig. 5. Similar to our data for chronologically aged mice, we observed a significant individual variability within each experimental group of age-matched animals. The data showed that feeding HFD increases mean BA of male mice by 34 weeks (from 62.7±13.3 to 96.4±8.8 weeks; p=0.03, Student's t-test; Fig. 5A). Chronic treatment with rapamycin improves animals' health status and reduces their BA to values characteristic for control group (from 96.4±8.8 to 71.5±9.6 weeks (p=0.04, Student's t-test; Fig. 5B). No difference between groups was detected in female mice, in which BA was very close to their CA in all groups. Slight reduction of BA in rapamycin treated group from 71.8±7.8 to 62.6±7.0 weeks was not statistically significant (p=0.3 Student's t-test).

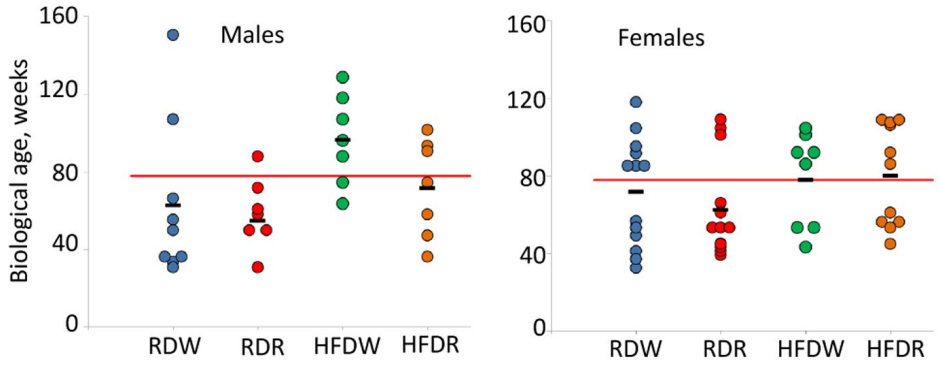

Figure 5. Sex-specific effects of detrimental (HFD) and beneficial (rapamycin) factors on BA of NIH Swiss mice. Feeding HFD accelerates aging of NIH Swiss male mice whereas rapamycin counteracts this process. Projected biological age of individual mice (shown by circles) and mean BA for the group (black marker) were calculated from the corresponding FI value using the fitting model predictions. Red line designates chronological age of all mice at the time of testing (78 weeks). Data show that projected BA of all mice that received HFD (green circles) is significantly higher that their actual chronological age and mean BA age for control group on regular diet (62.7±13.3 and 96.4±8.8 weeks for RDW and HFDW groups respectively (p=0.03, Student's t-test). Chronic administration of rapamycin reduces BA of males fed HFD to values characteristic for control group (from 96.4±8.8 to 71.5±9.6 weeks; p=0.04, Student's t-test). No difference between groups was detected in female mice, in which BA was very close to their CA. Slight reduction in BA in rapamycin treated group from 71.8±7.8 to 62.6±7.0 weeks was not statistically significant (p=0.3 Student's t-test).

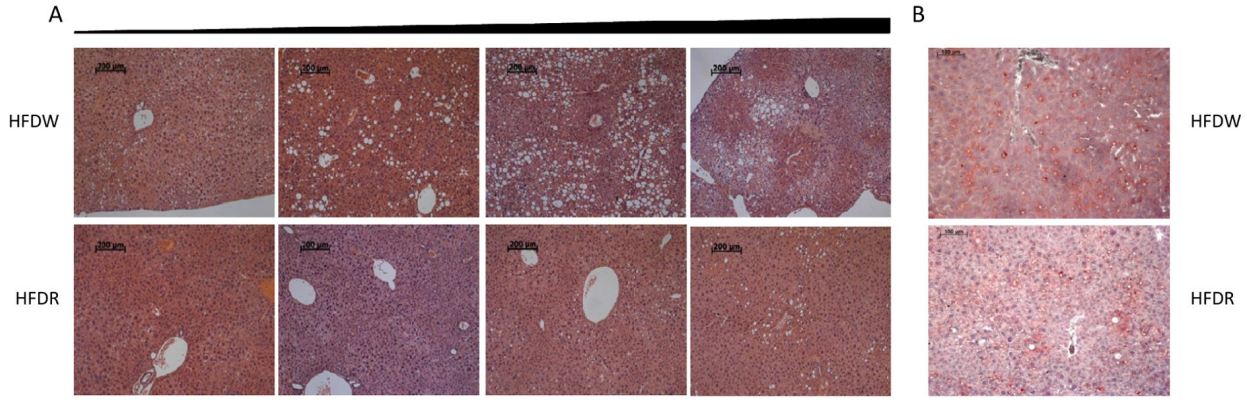

Figure 6. Rapamycin prevents development of HFD-induced hepatic steatosis in male mice. (**A**) H&E staining of representative liver sections graded from the least affected (left) to the worst affected (right) within each group. (**B**) Representative oil-red O stained sections of livers. HFDW – mice fed with HFD; HFDR – mice received HFD in combination with rapamycin.

To confirm the preventive role of rapamycin in the development of diet-induced obesity, at completion of the experiment we performed hematoxylin-eosin and Oil Red O staining of livers of male mice fed HFD in combination with either normal water or rapamycin. Fig. 6A shows examples of H&E staining that were graded from the best to the worst within each group demonstrating larger and more lipid droplet accumulation in liver parenchyma in high-fat diet group and significant improvement of hepatic steatosis by rapamycin administration. These conclusions were consistent with the results of the Oil Red O staining (Fig. 6B). Taken together, these data suggest that our approach for frailty assessment allows for reliable and quantitative evaluation of animal's health status both during normal aging process as well as after various interventions.

DISCUSSION

Aging is characterized by accumulation of deficits and increased frailty, which in turn increases vulnerability of an older organism to various stressors. In clinical gerontology two major tools were developed to evaluate frailty in elderly: the phenotype model and FI (reviewed in [17]). The phenotype model describes frailty as a phenotype that can be scored using 5 criteria of patient's physical performance [18]. In contrast, FI represents cumulative score of a degree of deviation that multiple behavioral, physical and physiological parameters developed with age compared to normal values characteristic to healthy young individuals [3]. Since FI was introduced to human gerontology, it was used in many epidemiological and clinical studies to evaluate the risk of adverse health events in elderly. These include a decline in overall activity, reduced muscle strength, bone degeneration, osteoporosis, an increase in inflammation, vascular calcification, hair loss, cataracts, cognitive decline, etc.

The strategy of estimating FI as a measurement of health status has been also applied to the mouse models [19, 20]. However, the majority of frailty assessment tools use multiple observational approaches such as recording and scoring of visible pathologies (eye inflammation or cataracts, high respiratory rate, visible tumors, alopecia, dermatitis, distended abdomen etc.), or behavioral signs (circling behavior, reduced or excessive grooming, etc.). Although informative, this approach has some significant limitations and researcher bias. First, these parameters are subjective by nature and require scoring by several independent raters in consistent manner [21-23]. Secondly, many health problems start a lot earlier than could be detected by their visual manifestation. Therefore, the goal of our study was to develop a reliable, quantitative scoring system, physiological frailty index (PFI) that would be based on non-invasive quantitative measurements of various physiological parameters, which could be repetitively used in the same animal during the course of its entire lifespan and would represent its overall health status.

Several previous studies suggest that the more diverse variables are used for creating the FI, more reliable FI value is [24]. At the same time to optimize the robustness of the procedure in order to make it applicable to a large number of animals, we were inclined to minimize the number of variables. This rationale was supported by several previous studies, which reported good correlation between FI calculated with 8 and 31 items [24]. Therefore, after measuring 29 diverse physiological parameters including physical (body weight and grip strength), blood cell composition, metabolic, and immune, we selected those that show statistically significant change with age. These parameters were used to create PFI of individual mice of different chronological age. The observed gradual increase in mean PFI values with age suggests that our approach can reliably detect the scale of age-dependent health deterioration in a quantitative manner.

Interestingly, the dynamics of deficit accumulation appeared to be very gender-specific. Thus, in male NIH Swiss mice increase in PFI can be approximated by linear function suggesting that health deficits are evenly accumulated with age. In females the dynamics of increase in PFI is more complicated with sharp increase observed between 26 and 52 weeks of age followed by a period of almost no change (between 52 and 78 weeks) and a second increase after 78 weeks. This is an important observation that has to be considered in both pre-clinical and clinical studies. First, it points to fundamental sex-related differences in the process of aging and consequently, has to be taken into account when developing strategies for treatment of aging and age-related diseases. Second, our data provide an additional explanation for numerous examples of sexual dimorphism in response to life-extending genetic or pharmacological interventions. Although clear mechanistic details of this phenomenon are still not understood, most of the previous reports linked it to interactions of the interventions with sex hormones, sex differences in immune function or in distribution of adipose tissue and accordingly differences in the effects of its secretory activity (reviewed in [25]). Our results suggest that in addition to basic gender differences, females' response to treatments may vary depending on the age at which it is applied. Thus, based on observed sex-related differences in the pattern of deficits accumulation, the lack of effects of both detrimental and beneficial interventions on the health status of

female mice may be explained by the fact that treatments started at 52 weeks of age (beginning of "no-change" period in females) and the FI was measured at the end of this phase (78 weeks).

Our results in the experiment with chronic rapamycin treatment showing an increase in lifespan of female NIH Swiss mice without improvement in their health, underscores the importance of using health status as the major metrics in development of anti-aging therapeutics. These data are consistent with previous observations made in different model systems demonstrating that increase in longevity is not necessarily accompanied by improved health status. Such as, caloric restriction extends lifespan in *Drosophila* without improving their cognitive function [26]. Long-lived calorie-restricted mice and IGF-1 knockout mice develop multiple health deficits [27, 28]. Recent work in *C. elegans,* which measured simultaneously worms' longevity and health status, demonstrated that four different long-lived mutants that were used in the study increased the proportion of time spent in a frail state [29]. Altogether, we suggest that our approach allows for unbiased and reliable assessment of healthspan by quantitation of age-related accumulation of deficits during chronological aging than may serve as a valuable tool in a variety of pre-clinical aging studies. Importantly, experimental validation of this approach demonstrated its ability to quantitatively evaluate detrimental effect of HFD on animal's health as well as the ability of rapamycin to mitigate it, thereby providing an alternative age-accelerated model for testing the effects of various environmental, nutritional and pharmacological interventions on healthspan.

MATERIALS AND METHODS

Animals

Male and female Cr:NIH(S) Mice (NIH Swiss) mice were purchased from Charles River at the age of 6-8 weeks and were allowed to age at the RPCI Animal Facility. During this time mice were housed 1-3 per cage and were fed ad lib with standard chow (Tekland Global 18% Pretein Rodent Diet). To quantitatively evaluate age-dependent decline in animals' health, FI was created for individual male and female mouse at 26, 52, 78 and 104 weeks of age as described below using cross-sectional experimental design (10-14 mice per group). In a separate experiment, male and female mice (9-14 per group) were randomly assigned to four groups. Group 1 remained on regular chow and drinking water; group 2 remained on regular chow but started receiving rapamycin in drinking water. Group 3 started receiving high fat diet (Harlan Laboratories, TD.03584, 35% Lard Diet) in combination with normal drinking water and group 4 received HFD in combination with rapamycin. Rapamycin was delivered in the form of Rapatar (polymeric formulation developed by Everon Biosciences as previously described [14] at a concentration of 125 mg/L (corresponds to 2.5 mg/L rapamycin). Based on the assumption that mice drink 3-5ml water per day, we estimated that in average each animal received 7.5-12.5 µg rapamycin daily. To preserve rapamycin stability in was delivered in non-acidified water in light-protected water bottles, which were replaced twice/week. When mice were 78 weeks of age FI was created for each individual animal as described below. Mice remained on their designated feeding/water schedules for the rest of the experiments and their longevity was recorded. Data for males and females were analyzed separately. All animal studies were conducted in accordance with the regulations of the Committee on Animal Care and Use at Roswell Park Cancer Institute.

Grip strength measurement

Fore limb grip strength measurements were performed using Animal Grip Strength System (San Diego Instruments). Five measurements were recorded for each individual animal and the average value was assigned.

Non-invasive measurement of hemodynamic parameters

Non-invasive measurement of hemodynamic parameters was performed using CODA apparatus (Kent Scientific) according to manufacturer's protocol. Mice were placed into cylinder-shaped restraint devices and allowed to acclimate for 5 min on a heating platform before blood pressure measurements begin. Body temperature was continuously monitored by observation of animal behavior, tail blood volume and an infrared thermo-meter. Recorded hemodynamic parameters include systolic, diastolic and mean blood pressure, heart rate, tail blood flow and tail blood volume.

Blood samples collection

To evaluate age-dependent changes in blood composition, blood samples were collected using the least invasive method that does not require anesthesia or restraining. Twenty µl of blood was collected from a single submandibular vein bleed into EDTA-treated Vacutainer tubes (BD) and used for whole blood cell counts and glucose measurements. Another 75ul of blood was collected into Li-Heparin treated plasma separator tubes; plasma was purified by centrifugation at 5000 x g for 5 min and used for measuring con-

centration of circulating pro-inflammatory cytokines and triglycerides.

Whole blood cell counts, blood chemistry and inflammatory cytokines

Whole blood cell analysis was performed in 20 µl of blood using Hemavet 950 Analyzer (Drew Scientific). The following parameters were measured: while blood cell counts (WBC), neutrophil (NE), lymphocyte (LY), monocyte (MO) and eosinophil (EO) counts and percentage, red blood cell (RBC) counts, hemoglobin (Hb), hematocrit (HCT), mean corpuscular volume (MCV), mean corpuscular hemoglobin (MCH), mean corpuscular hemoglobin concentration (MCHC), red cell distribution width (RDW), platelet (PLT) counts and mean platelet volume (MPV). Plasma concentration of chemokine (C-X-C motif) ligand 1(CXCL1/KC) was measured using ELISA kit (R&D) according to manufacturer's protocol. Plasma concentration of triglycerides was measured using triglyceride quantification Kit (Abcam) according to manufacturer's protocol. In both assays reactions were run in duplicates and concentrations were calculated from a calibration curve generated for each experiment. Glucose concentration was measured using AlphaTRAK 2 Blood Glucose Monitoring Kit (Abbott Laboratories).

Creating physiological Frailty Index

Frailty Index was created for each individual mouse as previously described [20] using 26 week-old group as a "young mouse" reference. For each parameter mean value and standard deviation were calculated. Animals differing in more than one standard deviation (STDEV) from mean value in any single parameter were excluded from the reference group. Value for each parameter measured for mice of older ages (52, 78 and 104 weeks) was compared with corresponding value for the reference group and assigned a score. Values that differ less than 1 STDEV were assigned the score of 0 (no deficit, within the range of the reference group). Values that were different for one STDEV were scored as 0.25 (minimal deficit). Values that differ from the corresponding values in the reference group by 2 STDEV were scored as 0.5 and those that differ by 3 STDEV were scored as 0.75. If the value is above 3 STDEV it was scored as 1 (extreme deficit). The number of deficits the individual mouse is expressed was calculated as a ratio of total number of parameters measured and was referred to as Physiological Frailty Index (PFI).

Histological evaluation

After completion of the experiment mouse livers were fixed in 10% neutral formalin for 24 h. For morphological observations samples were transferred to 70% ethanol and processed in an automated processor (Leica ASP 300) and embedded in paraffin using LEICA EG 1150H embedding unit according to manufacturer's protocols. Five micron sections were obtained using rotary microtome (LEICA RM 2235) and stained with hematoxylin and eosin (H&E). Neutral lipids were revealed by Oil Red O staining according to standard protocol on 12 micron cryo-sections prepared from formalin-fixed material using CM1900 cryostat. Histopathological examination was performed using Zeiss AxioImager A1 with Axiocam MRc digital camera.

Statistics

Survival curves were generated using Kaplan-Meier estimators and compared using the log-rank test. Continuous data are expressed as mean $\pm$ SEM. Statistical analyses were performed using one or two-way ANOVA with Tukey post hoc tests for multiple comparisons, ANOVA on ranks with Dunn's tests or Student's t-test where appropriate. P-values <0.05 were considered significant. To generate a trend line that would best describe age-dependent increase in FI, a cubic regression was fit regressing the PFI on chronological age (CA), CA^2 and CA^3. A stepwise selection procedure was then used to eliminate unnecessary terms for any or all of the higher order polynomial terms. The models were fit individually by sex.

AUTHOR CONTRIBUTIONS

Marina P. Antoch conceived the study, designed and carried out experiments, analyzed and interpreted data, generated the figures and table and wrote the manuscript; Michelle Wrobel, Karen Kuropatwinski, Ilya Gitlin and Katerina Leonova carried out experiments, analyzed and interpreted data; Ilia Toshkov and Anatoli Gleiberman performed histological evaluation of tissue sections; Alan Hutson performed statistical data analysis; Olga Chernova and Andrei Gudkov analyzed and interpreted data, and reviewed the manuscript.

ACKNOWLEDGEMENTS

We would like to thank Eugene Kononov for his excellent assistance with animal experiments. We also thank the staff of the Laboratory Animal Shared Resources at Roswell Park Cancer Institute for their veterinary and technical assistance. We are very grateful to the research team of Everon Biosciences and all members of A.V.G. laboratory for constructive discussions.

CONFLICTS OF INTEREST

O.B.C. and A.V.G. are co-founders and shareholders of Everon Biosciences.

FUNDING

This work was supported by National Cancer Institute (NCI) grant P30CA016056 involving the use of Roswell Park Cancer Institute's Laboratory Animals Shared Resource, by Roswell Park Alliance Foundation and Everon Biosciences, Inc. (M.P.A. and A.V.G.)

REFERENCES

1. López-Otín C, Blasco MA, Partridge L, Serrano M, Kroemer G. The hallmarks of aging. Cell. 2013; 153:1194–217. doi: 10.1016/j.cell.2013.05.039

2. Rodier F, Campisi J. Four faces of cellular senescence. J Cell Biol. 2011; 192:547–56. doi: 10.1083/jcb.201009094

3. Mitnitski A, Rockwood K. Aging as a process of deficit accumulation: its utility and origin. Interdiscip Top Gerontol. 2015; 40:85–98. doi: 10.1159/000364933

4. Howlett SE. Assessment of Frailty in Animal Models. Interdiscip Top Gerontol Geriatr. 2015;41:15–25.

5. Rockwood K, McMillan M, Mitnitski A, Howlett SE. A Frailty Index Based on Common Laboratory Tests in Comparison With a Clinical Frailty Index for Older Adults in Long-Term Care Facilities. J Am Med Dir Assoc. 2015; 16:842–47. doi: 10.1016/j.jamda.2015.03.027

6. Jonker MJ, Melis JP, Kuiper RV, van der Hoeven TV, Wackers PF, Robinson J, van der Horst GT, Dollé ME, Vijg J, Breit TM, Hoeijmakers JH, van Steeg H. Life spanning murine gene expression profiles in relation to chronological and pathological aging in multiple organs. Aging Cell. 2013; 12:901–09. doi: 10.1111/acel.12118

7. Melis JP, Jonker MJ, Vijg J, Hoeijmakers JH, Breit TM, van Steeg H. Aging on a different scale--chronological versus pathology-related aging. Aging (Albany NY). 2013; 5:782–88. doi: 10.18632/aging.100606

8. Mitnitski A, Collerton J, Martin-Ruiz C, Jagger C, von Zglinicki T, Rockwood K, Kirkwood TB. Age-related frailty and its association with biological markers of ageing. BMC Med. 2015; 13:161. doi: 10.1186/s12916-015-0400-x

9. Ogden CL, Carroll MD, Fryar CD, Flegal KM. Prevalence of Obesity Among Adults and Youth: united States, 2011-2014. NCHS Data Brief. 2015; 219:1–8.

10. Pettersson US, Waldén TB, Carlsson PO, Jansson L, Phillipson M. Female mice are protected against high-fat diet induced metabolic syndrome and increase the regulatory T cell population in adipose tissue. PLoS One. 2012; 7:e46057. doi: 10.1371/journal.pone.0046057

11. Anisimov VN, Zabezhinski MA, Popovich IG, Piskunova TS, Semenchenko AV, Tyndyk ML, Yurova MN, Antoch MP, Blagosklonny MV. Rapamycin extends maximal lifespan in cancer-prone mice. Am J Pathol. 2010; 176:2092–97. doi: 10.2353/ajpath.2010.091050

12. Spong A, Bartke A. Rapamycin slows aging in mice. Cell Cycle. 2012; 11:845. doi: 10.4161/cc.11.5.19607

13. Khapre RV, Kondratova AA, Patel S, Dubrovsky Y, Wrobel M, Antoch MP, Kondratov RV. BMAL1-dependent regulation of the mTOR signaling pathway delays aging. Aging (Albany NY). 2014; 6:48–57. doi: 10.18632/aging.100633

14. Comas M, Toshkov I, Kuropatwinski KK, Chernova OB, Polinsky A, Blagosklonny MV, Gudkov AV, Antoch MP. New nanoformulation of rapamycin Rapatar extends lifespan in homozygous p53-/- mice by delaying carcinogenesis. Aging (Albany NY). 2012; 4:715–22. doi: 10.18632/aging.100496

15. Komarova EA, Antoch MP, Novototskaya LR, Chernova OB, Paszkiewicz G, Leontieva OV, Blagosklonny MV, Gudkov AV. Rapamycin extends lifespan and delays tumorigenesis in heterozygous p53+/- mice. Aging (Albany NY). 2012; 4:709–14. doi: 10.18632/aging.100498

16. Khamzina L, Veilleux A, Bergeron S, Marette A. Increased activation of the mammalian target of rapamycin pathway in liver and skeletal muscle of obese rats: possible involvement in obesity-linked insulin resistance. Endocrinology. 2005; 146:1473–81. doi: 10.1210/en.2004-0921

17. Kane AE, Hilmer SN, Mach J, Mitchell SJ, de Cabo R, Howlett SE. Animal models of frailty: current applications in clinical research. Clin Interv Aging. 2016; 11:1519–29. doi: 10.2147/CIA.S105714

18. Fried LP, Tangen CM, Walston J, Newman AB, Hirsch C, Gottdiener J, Seeman T, Tracy R, Kop WJ, Burke G, McBurnie MA, and Cardiovascular Health Study Collaborative Research Group. Frailty in older adults: evidence for a phenotype. J Gerontol A Biol Sci Med Sci. 2001; 56:M146–56. doi: 10.1093/gerona/56.3.M146

19. Liu H, Graber TG, Ferguson-Stegall L, Thompson LV. Clinically relevant frailty index for mice. J Gerontol A Biol Sci Med Sci. 2014; 69:1485–91. doi: 10.1093/gerona/glt188

20. Parks RJ, Fares E, Macdonald JK, Ernst MC, Sinal CJ, Rockwood K, Howlett SE. A procedure for creating a frailty index based on deficit accumulation in aging mice. J Gerontol A Biol Sci Med Sci. 2012; 67:217–27. doi: 10.1093/gerona/glr193

21. Feridooni HA, Sun MH, Rockwood K, Howlett SE. Reliability of a Frailty Index Based on the Clinical Assessment of Health Deficits in Male C57BL/6J Mice. J Gerontol A Biol Sci Med Sci. 2015; 70:686–93. doi: 10.1093/gerona/glu161

22. Howlett SE, Rockwood K. Factors that influence reliability of the mouse clinical frailty index. J Gerontol A Biol Sci Med Sci. 2015; 70:696. doi: 10.1093/gerona/glv045

23. Kane AE, Hilmer SN, Huizer-Pajkos A, Mach J, Nines D, Boyer D, Gavin K, Mitchell SJ, de Cabo R. Factors that Impact on Interrater Reliability of the Mouse Clinical Frailty Index. J Gerontol A Biol Sci Med Sci. 2015; 70:694–95. doi: 10.1093/gerona/glv032

24. Whitehead JC, Hildebrand BA, Sun M, Rockwood MR, Rose RA, Rockwood K, Howlett SE. A clinical frailty index in aging mice: comparisons with frailty index data in humans. J Gerontol A Biol Sci Med Sci. 2014; 69:621–32. doi: 10.1093/gerona/glt136

25. Austad SN, Bartke A. Sex Differences in Longevity and in Responses to Anti-Aging Interventions: A Mini-Review. Gerontology. 2015; 62:40–46. doi: 10.1159/000381472

26. Burger JM, Buechel SD, Kawecki TJ. Dietary restriction affects lifespan but not cognitive aging in Drosophila melanogaster. Aging Cell. 2010; 9:327–35. doi: 10.1111/j.1474-9726.2010.00560.x

27. Longo VD, Finch CE. Evolutionary medicine: from dwarf model systems to healthy centenarians? Science. 2003; 299:1342–46. doi: 10.1126/science.1077991

28. Partridge L, Gems D, Withers DJ. Sex and death: what is the connection? Cell. 2005; 120:461–72. doi: 10.1016/j.cell.2005.01.026

29. Bansal A, Zhu LJ, Yen K, Tissenbaum HA. Uncoupling lifespan and healthspan in Caenorhabditis elegans longevity mutants. Proc Natl Acad Sci USA. 2015; 112:E277–86. doi: 10.1073/pnas.1412192112

Research Paper

Delivery of sFIT-1 engineered MSCs in combination with a continuous low-dose doxorubicin treatment prevents growth of liver cancer

Jian Niu[1], Yue Wang[1], Ji Wang[1], Bin Liu[1], Xin Hu[2]

[1]General Surgery of the Hospital Affiliated Hospital of Xuzhou Medical University, Digestive Disease Research Laboratory of Xuzhou Medical University, Xuzhou, Jiangsu 221002, PR China
[2]The University of Texas Graduate School of Biomedical Sciences at Houston, MD Anderson Cancer Center, Houston, TX 77030, USA

Correspondence to: Jian Niu; **email:** njnj_001@163.com DOI: 10.18632/aging.101146
Keywords: liver cancer, gene therapy, mesenchymal stem cells, vascular endothelial growth factor, soluble Fms-like tyrosine kinase-1 (sFlt1)
Received: November 7, 2016 **Accepted:** December 12, 2016 **Published:** December 28, 2016

ABSTRACT

One important process in liver cancer growth and progression is angiogenesis. Vascular endothelial growth factor (VEGF) has the significant role in liver cancer angiogenesis. sFlt1 (soluble Fms-like tyrosine kinase-1) is the promising inhibitor of VEGF and can be used as the new method of inhibiting angiogenesis. MSCs (Mesenchymal stem cells) can infiltrate into tumor tissue and function as the efficient transgene delivery mediator. Here, we engineered murine MSCs to express sFlt1 and examined the anti-tumor effect of MSC- sFlt1 in combination with continues low-dose doxorubicin treatment. We found that this combination therapy significantly inhibited liver cancer cells proliferation. Above all, HepG2 xenografts treated with this combination therapy went into remission. It is of note that this inhibition effect was not p53 binding and by increasing caspase8. This study suggests that this combination treatment has novel therapeutic potential for liver cancer because of significantly inhibiting cancer cells growth and anti-angiogenesis in vitro and in vivo.

INTRODUCTION

Despite aggressive treatment with operation and combination with chemotherapy, the prognosis of liver cancer remains poor. Most liver cancers are of rich blood supply and there is the close correlation between angiogenesis and tumor progression [1−2]. Recently, anti-angiogenesis has been proved to be the hopeful strategy for liver cancer treatment [3−4].

VEGF is the significant angiogenic factor and plays its roles by interacting with its receptors including Flt-1 (Fms-like tyrosine kinase-1) and Flk-1 /KDR (fetal liver kinase-1/kinase insert domain containing receptor). sFlt1 is a spliced form of the Flt1 receptor and it comes from the Flt1 transmembrane domain. sFlt1 binds to VEGF as a part of the full-length receptor and this binding blocks signal transduction. Importantly, Flt1 protein is expressed in liver cancer cells [5-8].

Reports have shown that transferring of sFlt1 into tumor can inhibit tumor angiogenesis and growth [9−10]. MSCs can be engineered to express genes and are known to infiltrate into tumor tissues [11-14]. Therefore, MSCs may provide an avenue for sFlt1 delivery in liver cancer.

Doxorubicin leads to DNA damage and cell apoptosis in a lot of cancer cells .Doxorubicin has also the distinct antitumor effect for liver cancer cells. In this study, we used the treatment of continuous low-dose doxorubicin combination with MSC.sFlt1 to demonstrate the additive inhibition of liver cancer cells growth and anti-angiogenesis in vitro and in vivo.

RESULTS

sFlt1 is expressed by MSCs and released into the culture media

To measure transient expression of sFlt1 in MSCs, 24 hours after adv-sFlT1 transduction into MSCs, sFlt1 protein (100.0±18.7mg7/ml) was found from cell

culture supernatant and the expression of sFlt1 was detected for more than 7 days (Figure 1).

Endothelial cells are sensitive to low dose doxorubicin treatment

Since most endothelial cell assays utilize HUVEC (human umbilical vein endothelial cells) [15], we tested the sensitivity of HUVEC cells to doxorubicin which is widely used in liver cancer chemotherapy. Our data suggested that HUVEC cells proliferation were significantly more inhibited at low-dose doxorubicin (0.02μM) than HepG2 cells (Figure 2).

Combination treatment had more inhibitory effect on HUVEC cells functions

To prove that sFlt1 engineered MSCs can inhibit the growth of HUVEC cells, we investigated the effect of sFlt1 and/or low-dose doxorubicin on HUVEC cells functions in vitro. The results showed single-agent sFlt1(concentrated conditioned medium) or low concentration doxorubicin inhibited the migration and proliferation of HUVEC cells. Interestingly, the combination therapy exerted a significant enhanced inhibitory effect on HUVEC cells proliferation and migration (Figure 3).

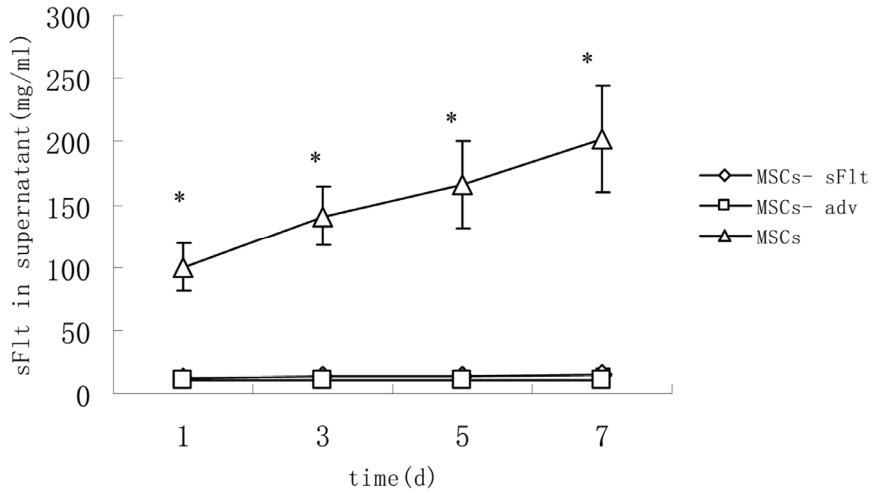

Figure 1. The content of sFlt1 in supernatant increased significantly in MSCs-sFlt1 group as compared with day-matched MSCs-adv group or MSCs group. Data from 3 independent experiments are shown. *P<0.05 versus MSC-sFlt1 group.

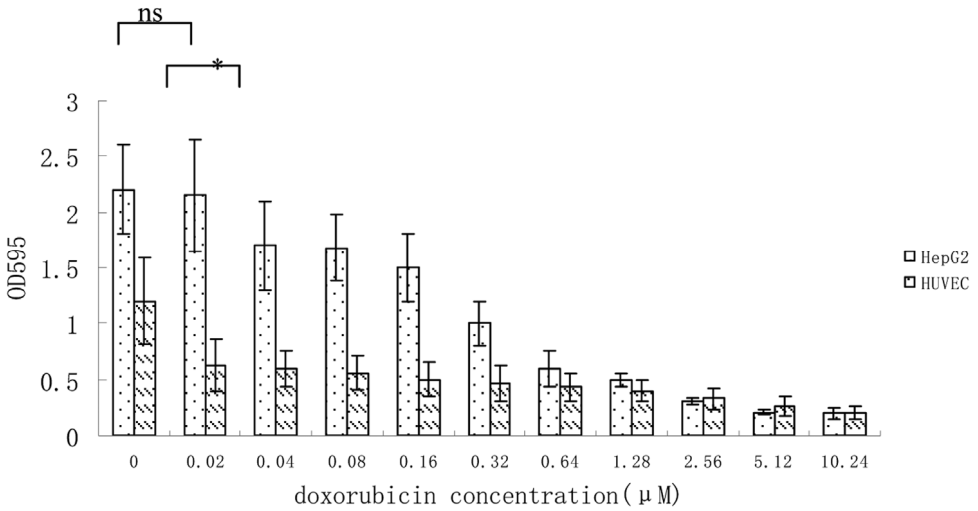

Figure 2. Growth inhibition of HUVEC and HepG2 cells at different concentration of oxorubicin. Data from 3 independent experiments are shown. *p < 0.05, n.s. not significant, vs 0.02μM.

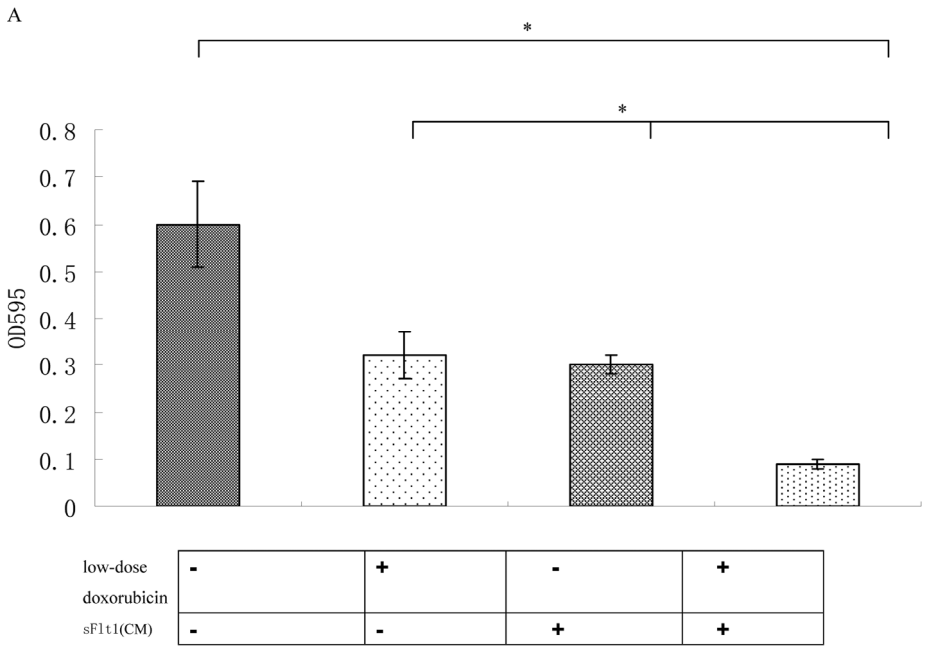

Figure 3. (**A**) The combination therapy enhanced the proliferation inhibition of HUVECs cells in vitro.

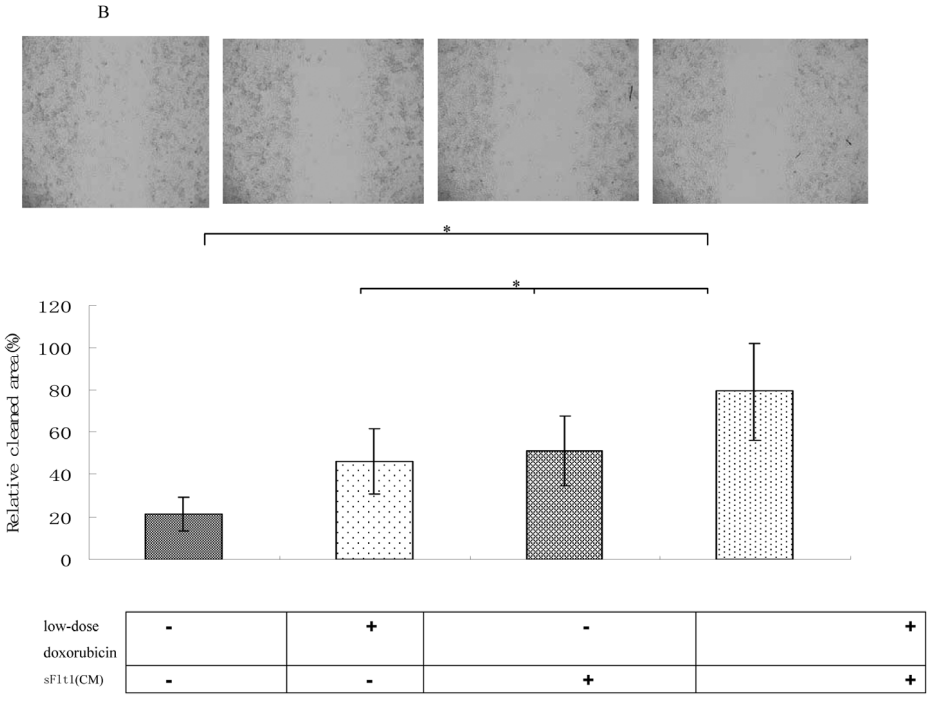

Figure 3. (**B**) Wound healing assays were performed. The amount of migrating cells of sFlt1 (1.5 ml of concentrated conditioned medium) plus low-dose doxorubicin group were much lower than control. Magnification, 200×. Picture of one representative experiment of 3 is shown. Data from 3 independent experiments are shown. *$p < 0.05$, vs sFlt1 plus low-dose doxorubicin group.

Combination therapy of doxorubicin and sFlt1 leads to additive apoptosis induction

Because low-dose doxorubicin (0.02μM) alone was not efficient to inhibit HepG2 cells, we began to test sFlt1 -based treatment utilizing combination with low-dose doxorubicin. We treated HepG2 cells with sFlt1 (1.0 ml of concentrated conditioned medium) plus 0.02 μM doxorubicin for 48h before we measured cell apoptosis. This combination therapy resulted in 37±0.6% apoptosis as compared with 2.6±0.4% (sFlt1 group) and 10.5± 0.4% (low-dose doxorubicin group). Apoptosis could be inhibited by zVAD (carbobenzoxy-valyl-alanyl-aspartyl- [O-methyl] -fluoromethylketone), showing that apoptosis was correlate with caspase (Figure 4A).

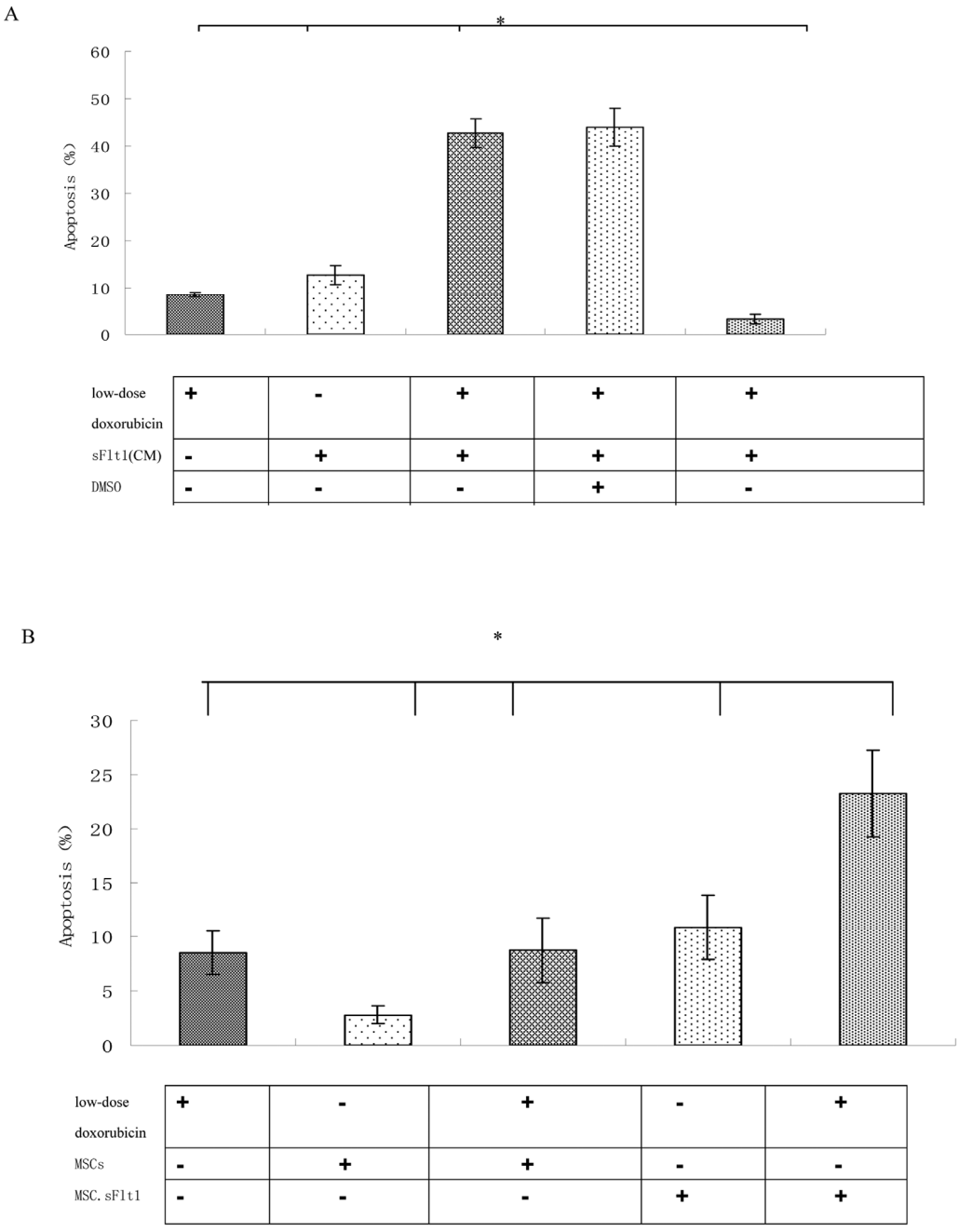

Figure 4. HepG2 cells can be sensitized to low-dose doxorubicin inducing by MSC. sFlt1. (**A**) Apoptosis measurement was conducted after the combination treatment. Addition of zVAD to the HepG2 cells before combination treatment can inhibit apoptosis. (**B**) Mixing HepG2 cells with MSC.sFlt1 (in a ratio of 10:1) plus 0.02μM doxorubicin treated for 48 h showed significantly increased apoptosis as compared with other group. Data from 3 independent experiments are shown. *$p < 0.05$, vs sFlt1 plus low-dose doxorubicin group.

One important step for clinical use of sFlt1 is effective delivery and sufficient bioavailability in carcinoma. The carcinoma-infiltrating properties of MSCs could be used to deliver sFlt1. We had to determine whether MSCs could effectively deliver sFlt1. To test this in vitro, we mixed MSC.sFlt1 with HepG2 cells for 48 h. This gave rise to apoptosis levels significantly (Figure 4B).

Combined therapy of MSC.sFlt1 plus continuous low-dose doxorubicin is efficacious and safe *in vivo*

We established HepG2 xenografts in immune-deficient Balb/c mice. Although the tumors in saline group, grew almost exponentially, xenografts either treated with continuous low-dose doxorubicin or MSC.sFlt1 showed

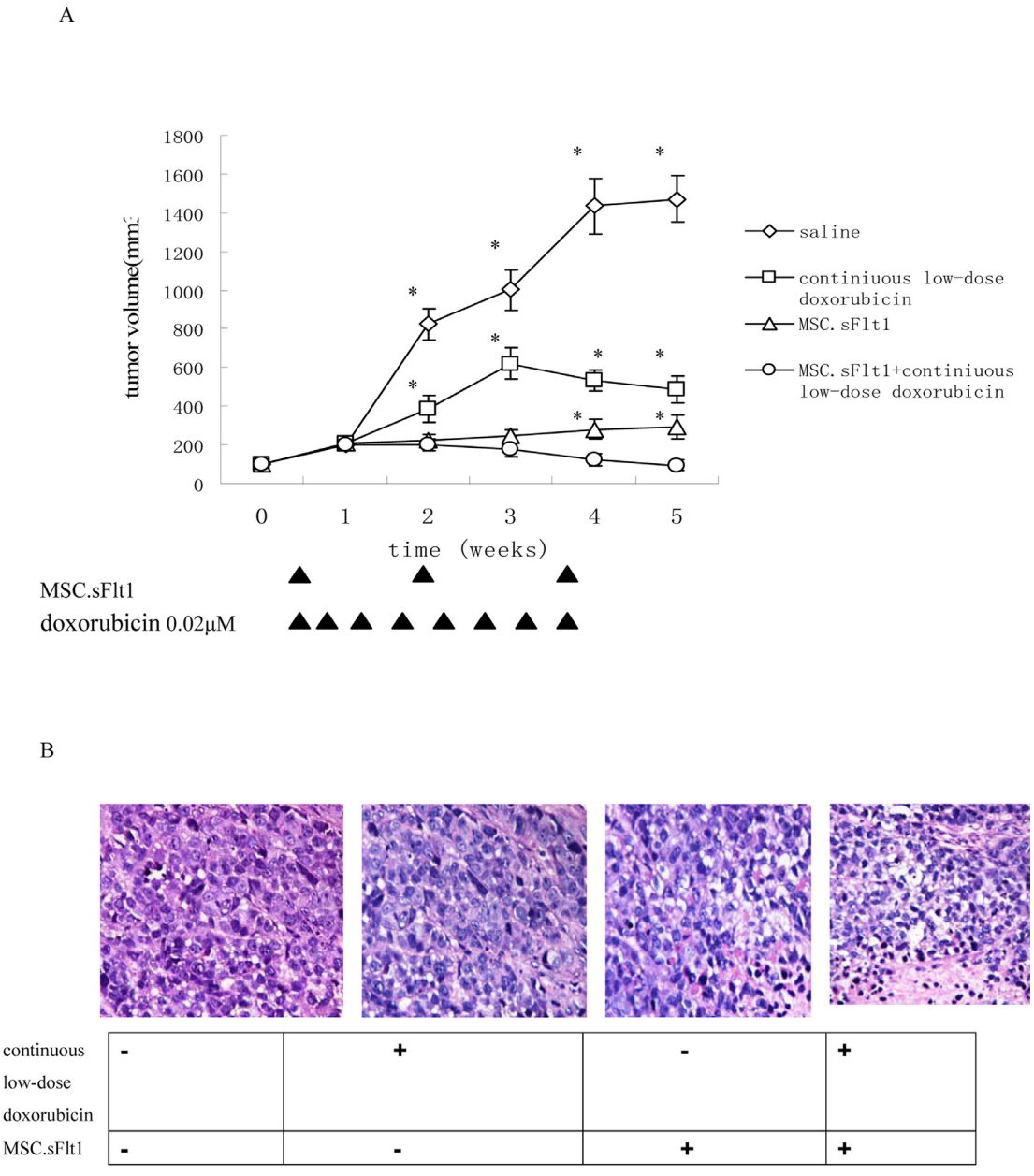

Figure 5. Treatment with continuous low-dose doxorubicin plus MSC.sFlt1 leaded to tumor remission and was safe in vivo. (**A**) Animals bearing HepG2 xenografts began treatments when tumor diameters reached 5 mm as described in "Materials and Methods." Arrows: days on which treatment was administered. Results are given as mean tumor volume of 7 mice /group. *p < 0.05 , vs MSC.sFlt1 plus continuous low-dose doxorubicin group. (**B**) HE staining was to examine general tumor tissue morphology from saline group, continuous low-dose doxorubicin group, MSC.sFlt1 group and MSC.sFlt1 plus continuous low-dose doxorubicin group. Magnification, 200×.

obvious growth inhibition. Surprisingly, xenografts treated with combination therapy went into remission (Figure 5A). Nonencapsulated tumor with cancer cells infiltration was found in sample sections of saline group by HE analysis. In contrast, MSC.sFlt1 plus continuous low-dose doxorubicin group clearly showed cellular necrosis and fibrosis instead of cancer cells (Figure 5B). Moreover, PCNA (nuclear proliferating cell nuclear antigen) protein was detected by immunohisto-chemistry. PCNA levels decreased significantly from the combination therapy group compared with other group (Figure 5C). To determine whether combination therapy inhibit tumor angiogenesis, tissue specimens were immunostained with CD31 mAb to count microvessels density (MVD). The data showed MVD was significantly lower in combination therapy group than other group (Figure 5D).

Then, we detected the safety of combination therapy on MSCs. We incubated MSCs with 0.02μM doxorubicin plus sFlt1 (concentrated conditioned medium) for 48h. MSCs were resistant to the single treatment as well as to the combination therapy by detecting apoptosis (Figure 5E).

Moreover, we detected the liver tissue of mice that had treated with combination therapy and could not detect any signs of tissue damage showing that this treatment is safe relatively (Figure 5F).

The molecular mechanism of the combination therapy is not p53 binding

To further improve sFlt1-based combination treatments, the better knowing of the molecular mechanisms is

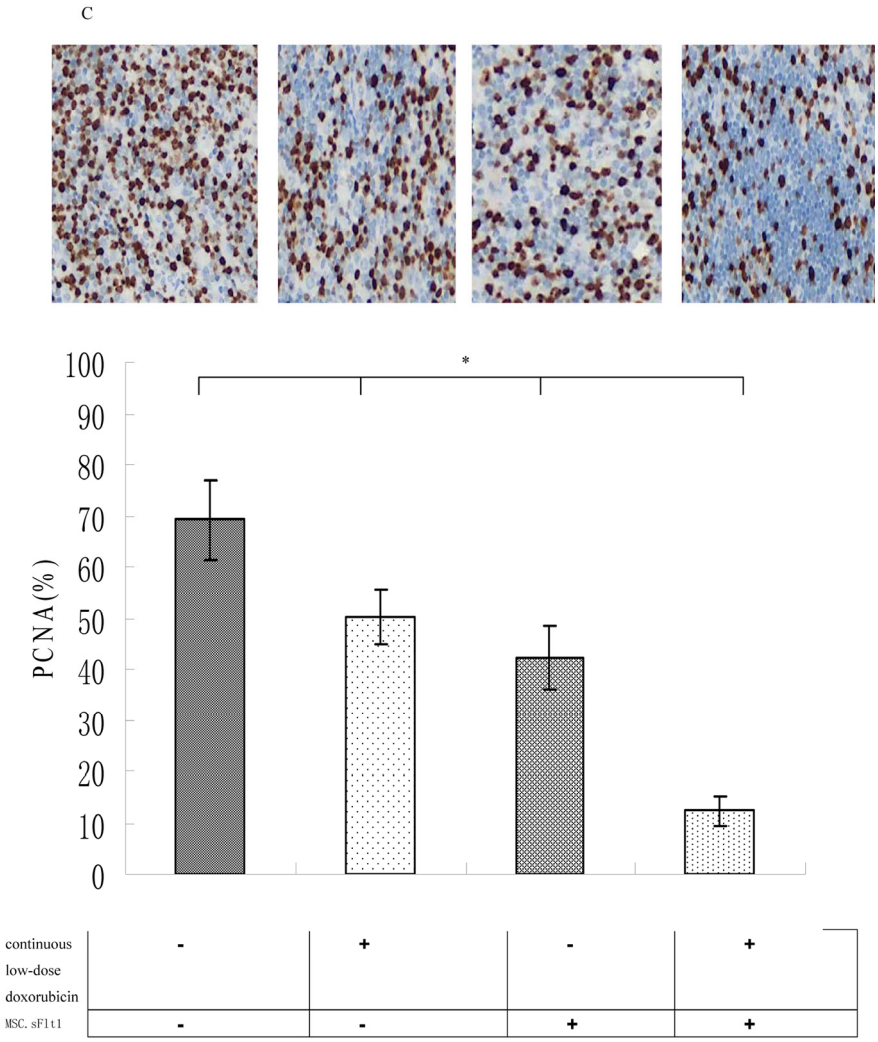

Figure 5. (**C**) Immunohistochemical detection of PCNA protein expression (brown color) of saline group, continuous low-dose doxorubicin group, MSC.sFlt1 group and MSC.sFlt1 plus continuous low-dose doxorubicin group. Combination therapy enhanced the inhibition of tumor cell proliferation in vivo. Magnification, 200×. Data from 3 independent experiments are shown. *$p < 0.05$, vs MSC.sFlt1 plus continuous low-dose doxorubicin group.

necessary. First, caspase8 was tested which is the important molecular event in the apoptosis pathway. Caspase8 activation is markedly increased in sFlt1 treated group compared to saline group. Additionally, caspase8 level increased further in sFlt1 plus low-dose doxorubicin group compared with other groups. In order to further testify that the sFlt1 sensitization effect is by caspase8, we cloned stable cell lines of caspase8 knockdown, named HepG2.shc8 (Figure 6A) .HepG2.shc8 were treated with 0.02μM doxorubicin plus sFlt1 for 48 h, then the apoptosis was measured. Results showed that the apoptosis of HepG2.shc8 was decreased, showing that caspase8 is the initiator in this process (Figure 6B). Next, we want to prove the apoptosis induced by the combination treatment is p53 independent. We found that low-dose doxorubicin plus sFlt1-triggered apoptosis reached the same level in HepG2 $p53^{-/-}$cells as in HepG2 cells. To test that combination treatment-induced apoptosis is not cell specific, we also analyzed huh7 cells, which express p53 mutation, and found that huh7 cells could exhibit increased apoptosis in response to combination treatment (Figure 6C).

DISCUSSION

As a lot of tumor growth are correlate on angiogenesis, antiangiogenic therapy shows the great promise for tumor treatment.

Recently, scientists found that blocking VEGF/VEGFR signaling pathway can inhibit tumor growth [16, 17]. As we all know, human liver cancer cells produce lots of proangiogenic factors including VEGF/ VEGFR that

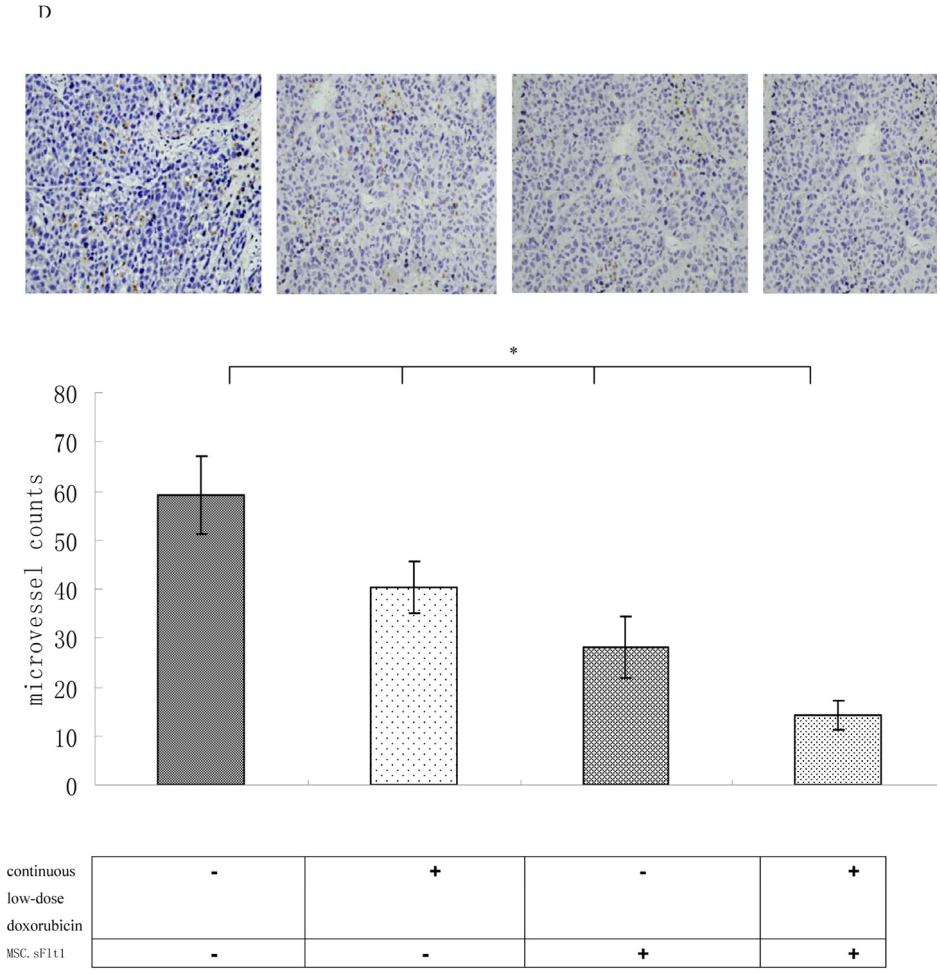

Figure 5. (**D**) Immunohistochemical analysis for MVD in HepG2 xenografts and combination therapy enhanced the inhibition of tumor angiogenesis in vivo. Magnification , 200×. *p < 0.05 , vs MSC.sFlt1 plus continuous low-dose doxorubicin group.

.

may serve as therapeutic targets. For example, some synthesized drugs in the market by targeting VEGF receptors can suppress the proliferation of liver cancer cells [18-21].

But all of these drugs have many side effects and with only moderate therapeutic activities. The possible explanation is that these drugs have the short half time or limited accessibility to liver cancer tissue.

Tumor-targeted therapy is one of the major strategies for pharmacotherapy of cancer today. sFlt1 is the potent antagonist of VEGF. sFlt1 could selectively incorporate with VEGF and inhibit VEGF activity [22, 23].

As MSCs can infiltrate into tumor tissue, they have been applied in cancer treatment [24-26]. In this study, we successfully constructed sFlt1 engineered MSCs as verified by ELISA assay (Figure 1) and explored the potential of MSC-sFlt to target tumor angiogenesis and growth.

Previous reports showed that withdrawal of neutralizing anti-VEGF antibody treatment resulted in tumor recur-

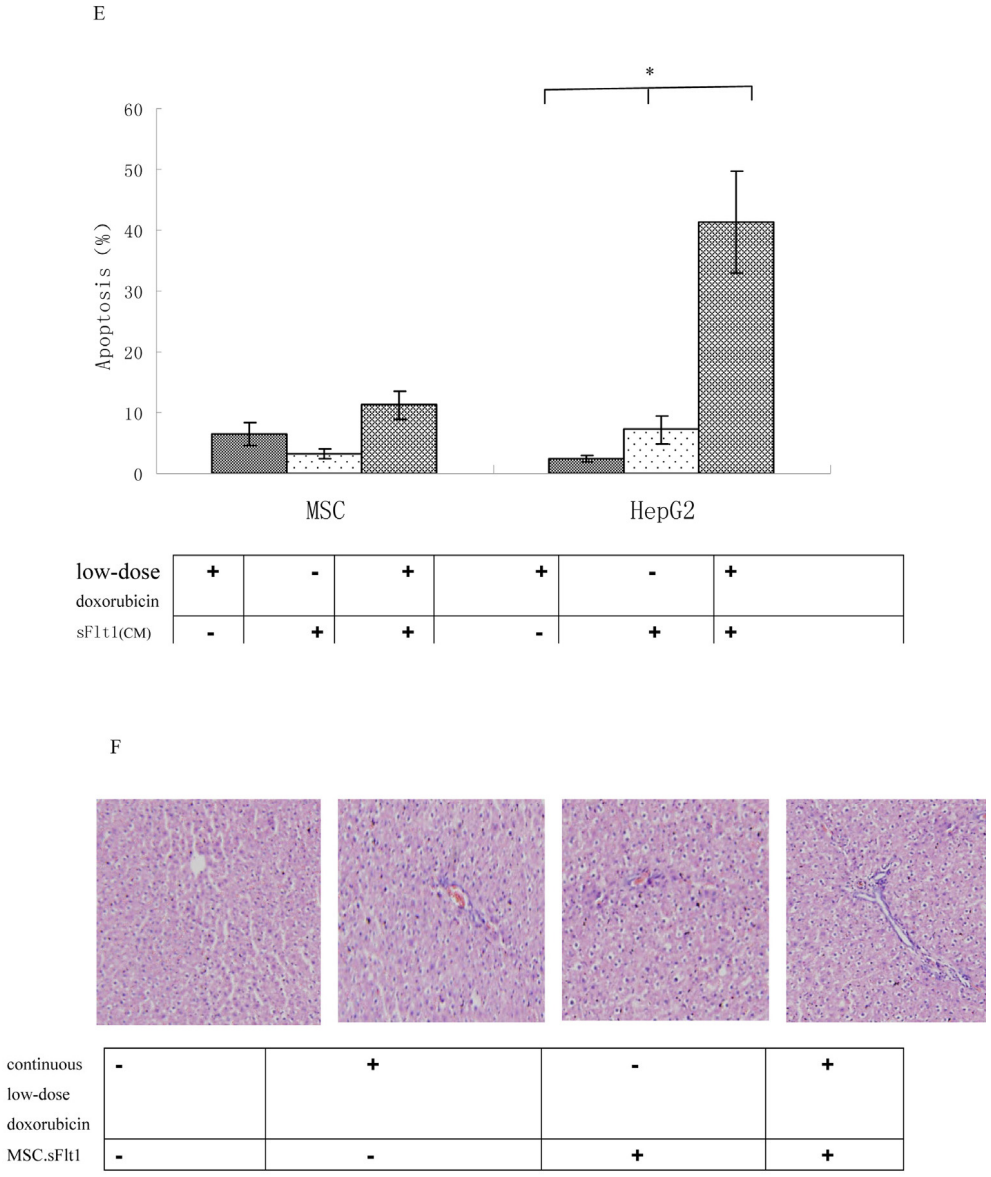

Figure 5. (**E**) Apoptosis was measured after exposure of MSCs or HepG2 cells to 0.02μM doxorubicin plus sFlt1 (1.0 ml of concentrated conditioned medium) for 48 h. *p < 0.05 , vs sFlt1 plus low-dose doxorubicin group. (**F**) HE staining of liver sections from mice treated with saline, continuous low-dose doxorubicin, MSC.sFlt1 and MSC.sFlt1plus continuous low-dose doxorubicin, respectively. Magnification, 200×.

.

rence [16-17]. These experiments proved that antiangiogenic therapy is insufficient and combination with chemotherapy is needed. Antiangiogenic-schedule chemotherapy is recommended because this kind of chemotherapy enable clinicians to give lower doses of drugs and has less side effects [27-28]. This novel strategy is explored as anti-tumor treatment effectively [29-31].

Doxorubicin has the significant anti-tumor effect for human liver cancer, either as a single agent or in combination with other cytotoxic agents [32]. Our data prove that low-dose doxorubicin inhibited HUVEC cells growth significantly more than HepG2 cell growth (Figure 2). And low dose doxorubicin plus sFlt1 can inhibit proliferation and migration of HUVEC cells more efficiently in vitro (Figure 3). Moreover, we observed the direct inhibition effect of this combination treatment on proliferation of HepG2 cells in vitro (Figure 4).

Next, we conducted animal experiments to test whether MSC.sFlt1 plus continuous low dose doxorubicin treatment can induce growth retardation or remission of xenografts with less side effects.

Our data showed that this combination treatment inhibited the growth of HepG2 xenografts in nude mice and had no toxicity as represented by liver histology examination (Figure 5). To prove whether the inhibitory

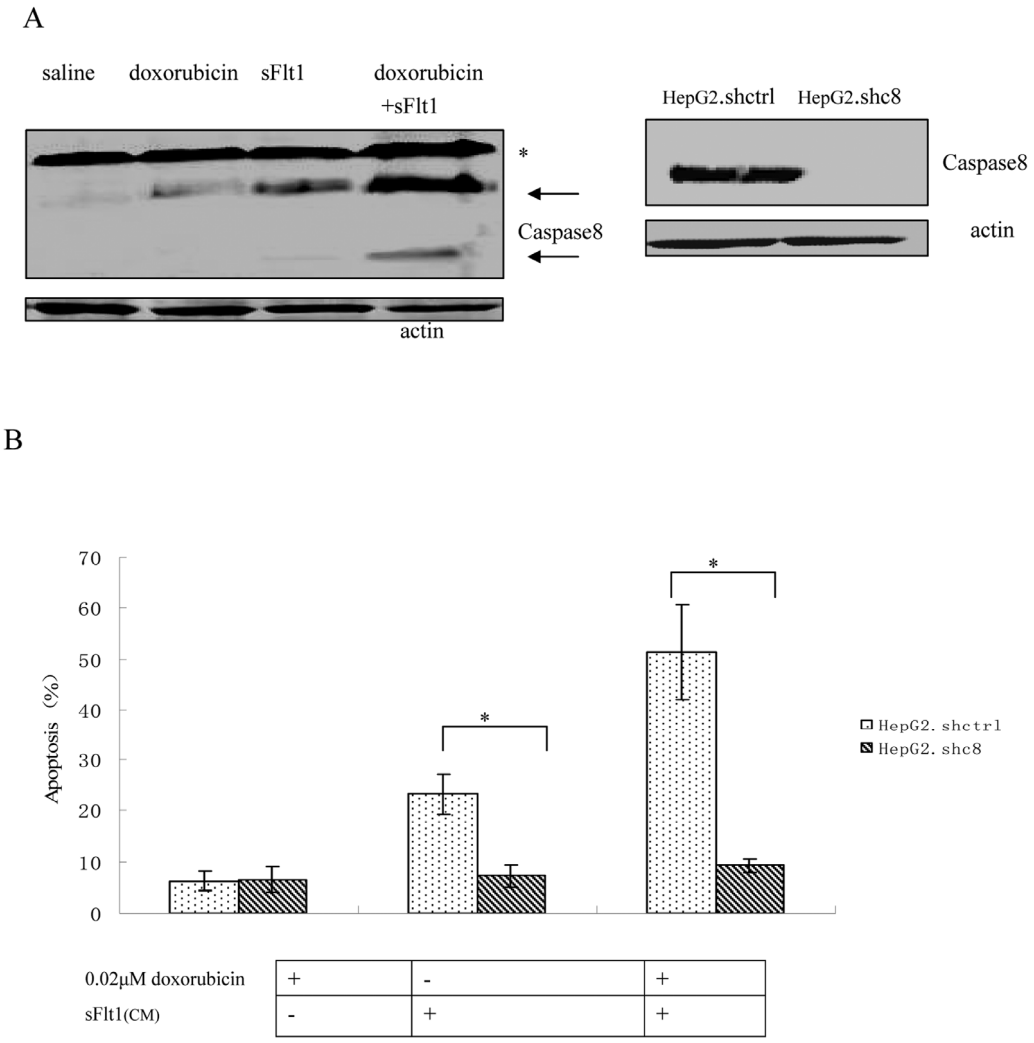

Figure 6. (**A**) Western blot of Caspase8 that HepG2 cells were either treated with saline, 0.02μM doxorubicin, sFlt1, or 0.02μM doxorubicin plus sFlt1 for 48 h. Pro-caspase bands are marked by an (*), whereas Caspase8 are labeled by arrows. (**B**)Caspase8 knockdown clone (HepG2.shc8) and control clone (HepG2.shctrl) were treated with doxorubicin plus sFlt1 before the apoptosis was measured. The apoptosis of HepG2.shc8 was decreased. *p < 0.05, vs sFlt1 plus 0.02μM doxorubicin group.

effect was related with anti-angiogenesis, we tested MVD in tumor samples and found this combination treatment led to significant decreasing in MVD compared with other group (Figure 5).The mechanisms of anti-tumor growth of MSC.sFlt1 plus continuous low dose doxorubicin includes the elevated apoptosis of cancer cells and endothelial cells (Figure 4, 5).

HepG2 cells express wild p53 but many kinds of liver cancer cells express p53 mutated and/or dysfunctional. Hence, in order to evaluate the combination treatment, we analyzed huh7 p53 mutated cells and HepG2 $p53^{-/-}$ cells. We observed the increased apoptosis following the combination treatment in both cancer cell lines. These results proved that the therapy is effective in cancer cells expressing p53 mutated and/or dysfunctional (Figure 6). Subsequently, we want to clarify the mechanism in this progress to improve the MSC. sFlt1 system. Silencing of caspase8 resulted in the apoptosis inhibition of huh7 p53 mutated cells or HepG2 $P53^{-/-}$ cells. This result showed that the inhibition of cancer cells was correlate with caspase8 (Figure 6).

In conclusion, MSC.sFlt1 plus low-dose doxorubicin therapy effectively suppressed the progression of liver cancer cells with less side effects in the mice xenograft model. The mechanism lies in its anti-angiogenesis and anti-cancer cells effect. This treatment might be more practical for clinical application and can be of the development of the targeted therapy for liver cancer.

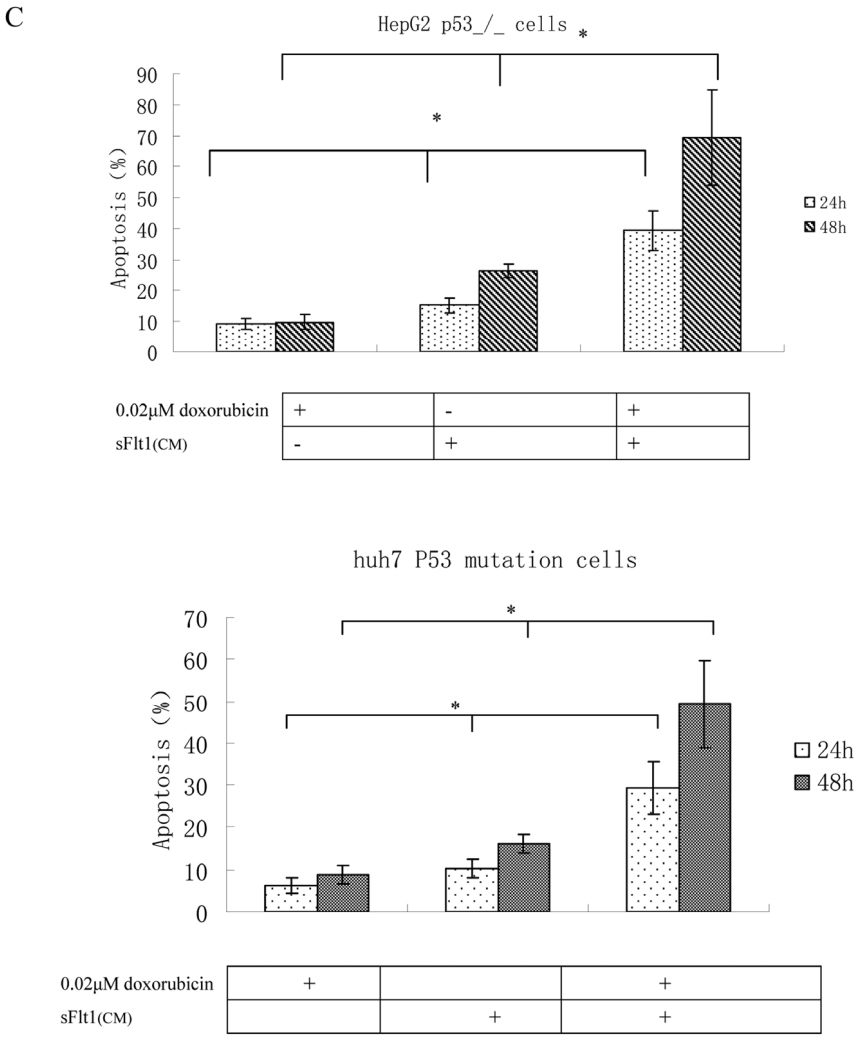

Figure 6. (**C**) Apoptosis measurements in HepG2 p53_/_ cells or huh cells after treatment with 0.02μM doxorubicin plus sFlt1 (concentrated conditioned medium) for 24h and for 48h. HepG2 p53-/-cells and huh7 cells exhibited increased apoptosis in response to combination treatment *p < 0.05 , vs sFlt1 plus low-dose doxorubicin group.

METHODS

Materials and reagents

Recombinant adenovirus (adv-sFlt) was provided by Dr. S Luo (Zhongsan University, Guangdong, China). Adv-sFlt contained the 1–3 Ig-like domains of Flt according to the sequence information from GenBank (accession No. X51602) [33]. Cell lines HepG2, huh7 and HUVEC were obtained from Chinese national human genome center (Shanghai, China). With regard to P53 status, HepG2 cells carry wild-type P53 and huh7 cells carry mutation P53 [34] . HepG2 cells were maintained in MEM and huh7 cells in DMEM containing 100U/ml of penicillin and 100 g/ml of streptomycin in a humidified chamber at 37°C in 5% CO_2. HUVEC cells were cultured in DMEM with 10% fetal bovine serum, 100 unit/ml heparin, and 75 μg/ml of endothelial cell growth supplement (ECGs; SIGMA, Saint Louis, MI) in 5% CO_2 at 37°C. MSCs from 4 to 6 week old female BALB/c nu/nu mice were prepared based on the method of Peister et al [37]. The cells were grown in Dulbecco's modified Eagle's medium (DMEM)–low glucose with 100 U/ml penicillin, 100ug/ml streptomycin and 10% fetal bovine serum. The mice bone marrow mesenchymal stem cells (BMMSCs) are generally referred to as MSCs throughout the text.

Generation of secreted MSC-sFlt1 and ELISA

The adenovirus hosting sFlt was introduced into the MSCs at a multiplicity of infection (MOI) of 100 in DMEM for 24 hours with 8μg/mL polybrene. After 24hours, the collected supernatant was concentrated by a centrifugal filter (Millipore, Schwalbach, Germany) at 4000 rpm for 30 min at 4°C.The concentrated conditioned medium (CM) was then filtered through 0.2 μm filters and stored at −80°C for further use. MSCs were infected with adv-sFlt for 24 hours, then washed twice and the culture supernatant containing secreted sFlt was examined for 7 days. sFlt1 expression was verified via ELISA using a commercial kit (Invitrogen, USA) according to the instructions provided by the manufacturer. The sFlt1 concentration in the cell supernatant samples was calculated based on the standard curve.

Cell proliferation assay

Cell proliferation were examined by MTT assay [35] . 20 ml of MTT solution (5 mg/ml in PBS) (Aqueous One Solution Assay, Promega, USA) was added to each well, and the cells were incubated for 4 h at 37°C. Then, absorbances were measured at 595 nm using a microtitre plate reader (Titertek Multiskan MCC, USA). The percentage of cell proliferation was calculated by defining the absorption of cells not treated with doxorubicin (control) as 100%. A total of three independent experiments were performed, and the means were used to depict the survival curve.

Apoptosis assay

Apoptosis was measured as previously described [36] . In brief, 3×10^4 HepG2 cells were cultured in a 24-well plate for 24h. We treated HepG2 cells with sFlt1 (1.5 ml of concentrated conditioned medium, CM) plus 0.02μM doxorubicin for 48h, then we measured cell apoptosis. Cells were collected by trypsinization and washed twice with cold 1× PBS. Then, Nicoletti buffer (Sodium citrate 0.1 % containing 0.1 % Triton X-100) and propidiumiodide (50g/ml) was added to the cell pellets. Tubes were vortexed for 10s at medium speed and left for 5 h in the dark (4°C). The fluorescence intensity was then measured in a flow cytometer (BD, USA).

Wound healing assay

3×10^4 HUVEC cells were cultured in a 24-well plate for 24 h. After a tight cell monolayer was formed, the cells were incubated with serum-free medium for 24 h and the cell monolayer was wounded with a plastic pipette tip [37] . The remaining cells were washed twice with fresh medium to remove cell debris, and further incubated with 1.5ml CM for 12h, purified recombinant human VEGF165 (R&D Systems, Minneapolis, USA) at 10 ng/ml was added to HUVEC cells, which were assayed for migratory ability. After 24h, the migrant cells at the wound front were photographed with a microscope .

Mixture of MSC-sFlt with liver cancer cells

Tumor cells were plated in six-well plates at 1×10^6 cells per well and left overnight to adhere. Then, HepG2 cells were treated with 1×10^5 MSC.sFlt1 and doxorubicin (0.02μM) for 48h (in a ratio of 10:1). Then cells were collected for apoptosis assays.

Animal studies

The animal study was performed to verify the effects of MSC.sFlt1 plus continuous low-dose doxorubicin in inhibiting the growth of liver tumors in vivo. Balb/c nu/nu mice (4-6 weeks old, 18-20 g body weight) were purchased from the experimental animal center of Shanghai, Chinese Academy of Sciences (Shanghai, China) and kept at a specific pathogen-free facility.

The nude mice were implanted subcutaneously with 1×10^6 HepG2 cells. When the tumor diameters reach 5mm, the animals were intraperitoneally injected with

doxorubicin (1 mg/kg, American Pharmaceutical Partners, USA). Doxorubicin was administered every 3 days for a total of eight dosages (continuous low-dose schedule dosage). 1×10^5 MSC.sFlt1 were delivered intravenously to the mice 24hrs after MSC transduction with adv-sFlt1. The injections with 1×10^5 MSC.sFlt1 were repeated two weeks later. Combined treatment consisted of at the beginning of 1×10^5 MSC.sFlt1 treatment, 1 mg/kg doxorubicin given once every 3 days for a total of eight times.

The animals were randomly assigned into four groups (n=12/group): (i) saline group (ii) continuous low-dose doxorubicin group (iii) MSC.sFlt1group (iV) MSC.sFlt1 plus continuous low-dose doxorubicin group. Tumor diameters were measured with a caliper and tumor volumes were calculated by using the equation $V(mm^3)=0.5\times a\times b^2$, where a=length, b=width. All procedures with animals were reviewed and approved by the Instructional Animal Care and Use Committee at Xuzhou Medical University.

The mice were sacrificed 42 days after HepG2 cells injection. The tumors were excised. A section of the tumor was fixed in paraformaldehyde (4%) and paraffin-embedded, and HE was performed. Tissue specimens were also used for immunohistochemical analyses. The animal study was repeated independently once.

Immunohistochemistry for expression of PCNA and microvessel density (MVD)

Tumor tissue sections (5 μm) were prepared for immunohistochemistry following reports [38]. Mouse anti-PCNA monoclonal antibody (1:100) (Leica Biosystems, UK) or goat anti-mouse CD31 polyclonal antibody (1:100) (Santa Cruz, USA) were used as primary antibodies. PBS instead of primary antibody was used as a negative control. The intensity of PCNA immunostaining was quantified using a computerized imaging system with 5 randomly selected fields at 200 times magnification. Staining was considered negative when the percentage of cells positive for PCNA staining was less than 10%. For MVD quantitation, 5 fields containing CD31 staining were selected and the number of CD31 positive cells in a field was quantified.

Western blot

Western blots were principally carried out as described previously [35]. In brief, the protein lysate was mixed with loading buffer, boiled for 5 mins, and loaded into sodium dodecyl sulfate-polyacrylamide gels (SDS-PAGE) with equal amounts of protein. The gel was run at 200 V for 60mins, followed by transfer to nitro-cellulose membrane (Amersham Biosciences, USA) at 100 V for 30 min at room temperature and incubation with primary antibodies. The primary antibodies include anti-caspase8 (1:100), anti-wtP53 (1:100) (Santa Cruz Biotechnology, CA).The secondary antibodies, anti-goat/rabbit/mouse immunoglobulin G (IgG)-HRP, were purchased from Zhongshan Company (Beijing, China). The protein expression levels were detected by chemiluminescence (ECL system, Amersham, UK) and quantified using Quantity One software (Bio-Rad). The expression level of the genes of interest were normalized using . -actin.

pSUPER-siRNA constructs and stable cell lines generation

The caspase8 siRNA and wtP53 siRNA hairpin oligos were designed by Ambion website (www.ambion.com) and synthesized by Shanghai SBS Genetech. Inc. (Shanghai, China). The sense strand oligo sequences were: caspase8: 5′-GGGTCATGCTCTATCAGAT-3' and wtP53: 5'-TCTGTGACTTGCACGTACTTT-3'.The synthesized siRNA specific to the caspase8 or wtP53 gene was inserted into pSUPER vector according to our previous procedures[39] , which was co-transfected with pSUPER-caspase8-siRNA or pSUPER-P53-siRNA and pEGFP vectors using Lipofectamine 2000 (Invitrogen, USA) to generate the HepG2-caspase8-siRNA or HepG2- P53-siRNA cell line. Clones that did not show a knock-down were used as controls.

Statistical analysis

The results were expressed as means ± standard error of means of at least 3 independent experiments, unless stated otherwise. Experimental values are expressed as mean value ±SD. For significance analyses, analysis of variance (ANOVA) between groups was used (SAS 6.12, SAS Institute, USA).*P<0.05 was considered significant.

Abbreviations

BCA, Bicinchoninic acid; FBS, Fetal bovine serum; PBS, Phosphate buffered saline; PVDF, Polyvinylidene difluoride; HE, Hematoxylin and eosin; MTT 3, 4,5-dimethylthiazol-2yl)-2,5-diphenyltetra-zoliumbromide; VEGF, Vascular endothelial growth factor; Flk-1 /KDR, fetal liver kinase-1/kinase insert domain containing receptor; MSCs, Mesenchymal stem cells; HUVEC, human umbilical vein endothelial cells; Zvad, carbobenzoxy -valyl- alanyl-aspartyl- [O-methyl] - fluoromethylketone; PCNA, nuclear proliferating cell nuclear antigen; MVD, microvessels density; CM,

concentrated conditioned medium; sFlt1,soluble Fms-like tyrosine kinase-1.

AUTHOR CONTRIBUTIONS

Jian Niu made critical intellectual contributions that formed the central concept of this study and were involved in the writing process of the manuscript. Wang Yue, Wang-ji, Liu bin, Xin Hu did part of the experiments and collected data.

CONFLICTS OF INTEREST

No conflicts of interest, financial or otherwise, are declared by the authors.

FUNDING

This study was supported by grants from of the National Science Foundation of China (30801125) and Jiangsu province natural science foundation of China（BK20161176）. No support has been received from any company and the author has no financial conflict of benefits.

REFERENCES

1. Marshall A, Alexander G. Vascular invasion leaves its mark in hepatocellular carcinoma. J Hepatol. 2011; 55:1174–75. doi: 10.1016/j.jhep.2011.05.005

2. Kaseb AO, Hanbali A, Cotant M, Hassan MM, Wollner I, Philip PA. Vascular endothelial growth factor in the management of hepatocellular carcinoma: a review of literature. Cancer. 2009; 115:4895–906. doi: 10.1002/cncr.24537

3. Cao Y. Future options of anti-angiogenic cancer therapy. Chin J Cancer. 2016; 35:21. doi: 10.1186/s40880-016-0084-4

4. Vasudev NS, Reynolds AR. Anti-angiogenic therapy for cancer: current progress, unresolved questions and future directions. Angiogenesis. 2014; 17:471–94. doi: 10.1007/s10456-014-9420-y

5. Peng S, Wang Y, Peng H, Chen D, Shen S, Peng B, Chen M, Lencioni R, Kuang M. Autocrine vascular endothelial growth factor signaling promotes cell proliferation and modulates sorafenib treatment efficacy in hepatocellular carcinoma. Hepatology. 2014; 60:1264–77. doi: 10.1002/hep.27236

6. Sia D, Alsinet C, Newell P, Villanueva A. VEGF signaling in cancer treatment. Curr Pharm Des. 2014; 20:2834–42. doi: 10.2174/13816128113199990590

7. Waidmann O, Trojan J. Novel drugs in clinical development for hepatocellular carcinoma. Expert Opin Investig Drugs. 2015; 24:1075–82. doi: 10.1517/13543784.2015.1058776

8. Li T, Zhu Y, Qin CY, Yang Z, Fang A, Xu S, Ren W. Expression and prognostic significance of vascular endothelial growth factor receptor 1 in hepatocellular carcinoma. J Clin Pathol. 2012; 65:808–14. doi: 10.1136/jclinpath-2012-200721

9. Farnia P, Ghanavi J, Bahrami A, Bandehpour M, Kazemi B, Velayati AA. Increased production of soluble vascular endothelial growth factors receptor-1 in CHO-cell line by using new combination of chitosan-protein lipid nanoparticles. Int J Clin Exp Med. 2015; 8:1526–33.

10. Zhu H, Li Z, Mao S, Ma B, Zhou S, Deng L, Liu T, Cui D, Zhao Y, He J, Yi C, Huang Y. Antitumor effect of sFlt-1 gene therapy system mediated by Bifidobacterium Infantis on Lewis lung cancer in mice. Cancer Gene Ther. 2011; 18:884–96. doi: 10.1038/cgt.2011.57

11. Zhou YL, Li YM, He WT. Application of Mesenchymal Stem Cells in the Targeted Gene Therapy for Gastric Cancer. Curr Stem Cell Res Ther. 2016; 11:434–39. doi: 10.2174/1574888X10666151026113818

12. Rhee KJ, Lee JI, Eom YW. Mesenchymal Stem Cell-Mediated Effects of Tumor Support or Suppression. Int J Mol Sci. 2015; 16:30015–33. doi: 10.3390/ijms161226215

13. Bhere D, Shah K. Stem Cell-Based Therapies for Cancer. Adv Cancer Res. 2015; 127:159–89. doi: 10.1016/bs.acr.2015.04.012

14. Shah K. Mesenchymal stem cells engineered for cancer therapy. Adv Drug Deliv Rev. 2012; 64:739–48. doi: 10.1016/j.addr.2011.06.010

15. Liu J, Li J, Su C, Huang B, Luo S. Soluble Fms-like tyrosine kinase-1 expression inhibits the growth of multiple myeloma in nude mice. Acta Biochim Biophys Sin (Shanghai). 2007; 39:499–506. doi: 10.1111/j.1745-7270.2007.00310.x

16. Niu J, Qian H, Han Z. siRNA-mediated type 1 insulin-like growth factor receptor silencing induces chemosensitization of a human liver cancer cell line with mutant P53. Cell Biol Int. 2006; 10:1016–19.

17. Peister A, Mellad JA, Larson BL, Hall BM, Gibson LF, Prockop DJ. Adult stem cells from bone marrow (MSCs) isolated from different strains of inbred mice vary in surface epitopes, rates of proliferation, and differentiation potential. Blood. 2004; 103:1662–68. doi: 10.1182/blood-2003-09-3070

18. Mohr A, Büneker C, Gough RP, Zwacka RM. MnSOD protects colorectal cancer cells from TRAIL-induced apoptosis by inhibition of Smac/DIABLO release. Oncogene. 2008; 27:763–74.

doi: 10.1038/sj.onc.1210673

19. Wang Y-H, Dong Y-Y, Wang W-M, Xie X-Y, Wang Z-M, Chen R-X, Chen J, Gao D-M, Cui J-F, Ren Z-G. Vascular endothelial cells facilitated HCC invasion and metastasis through the Akt and NF-κB pathways induced by paracrine cytokines. J Exp Clin Cancer Res. 2013; 32:51. doi: 10.1186/1756-9966-32-51

20. Niu J, Yue W, Song Y, Zhang Y, Qi X, Wang Z, Liu B, Shen H, Hu X. Prevention of acute liver allograft rejection by IL-10-engineered mesenchymal stem cells. Clin Exp Immunol. 2014; 176:473–84. doi: 10.1111/cei.12283

21. Zhou J-R, Yu L, Mai Z, Blackburn GL. Combined inhibition of estrogen-dependent human breast carcinoma by soy and tea bioactive components in mice. Int J Cancer. 2004; 108:8–14. doi: 10.1002/ijc.11549

22. Niu J. Xiangnong-Li, Zeguang-Han. siRNA mediated the type 1 insulin-like growth factor receptor and Epidermal Growth Factor Receptor silencing induces chemosensitization of liver cancer cells. J Cancer Res Clin Oncol. 2008; 26:703–08.

23. Zhu B, Lin N, Zhang M, Zhu Y, Cheng H, Chen S, Ling Y, Pan W, Xu R. Activated hepatic stellate cells promote angiogenesis via interleukin-8 in hepatocellular carcinoma. J Transl Med. 2015; 13:365. doi: 10.1186/s12967-015-0730-7

24. Tsai AC, Pan SL, Liao CH, Guh JH, Wang SW, Sun HL, Liu YN, Chen CC, Shen CC, Chang YL, Teng CM. Moscatilin, a bibenzyl derivative from the India orchid Dendrobrium loddigesii, suppresses tumor angiogenesis and growth in vitro and in vivo. Cancer Lett. 2010; 292:163–70. doi: 10.1016/j.canlet.2009.11.020

25. Barral M, Raballand A, Dohan A, Soyer P, Pocard M, Bonnin P. Preclinical Assessment of the Efficacy of Anti-Angiogenic Therapies in Hepatocellular Carcinoma. Ultrasound Med Biol. 2016; 42:438–46. doi: 10.1016/j.ultrasmedbio.2015.10.012

26. Zhang Z, Zhang H, Peng T, Li D, Xu J. Melittin suppresses cathepsin S-induced invasion and angiogenesis via blocking of the VEGF-A/VEGFR-2/MEK1/ERK1/2 pathway in human hepatocellular carcinoma. Oncol Lett. 2016; 11:610–18.

27. Ye ZL, Huang Y, Li LF, Zhu HL, Gao HX, Liu H, Lv SQ, Xu ZH, Zheng LN, Liu T, Zhang JL, Jin HJ, Qian QJ. Argonaute 2 promotes angiogenesis via the PTEN/VEGF signaling pathway in human hepatocellular carcinoma. Acta Pharmacol Sin. 2015; 36:1237–45. doi: 10.1038/aps.2015.18

28. Liu L, Yu H, Huang X, Tan H, Li S, Luo Y, Zhang L, Jiang S, Jia H, Xiong Y, Zhang R, Huang Y, Chu CC, Tian W. A novel engineered VEGF blocker with an excellent pharmacokinetic profile and robust anti-tumor activity. BMC Cancer. 2015; 15:170. doi: 10.1186/s12885-015-1140-1

29. Torimura T, Iwamoto H, Nakamura T, Abe M, Ikezono Y, Wada F, Sakaue T, Masuda H, Hashimoto O, Koga H, Ueno T, Yano H. Antiangiogenic and Antitumor Activities of Aflibercept, a Soluble VEGF Receptor-1 and -2, in a Mouse Model of Hepatocellular Carcinoma. Neoplasia. 2016; 18:413–24. doi: 10.1016/j.neo.2016.05.001

30. Farnia P, Ghanavi J, Bahrami A, Bandehpour M, Kazemi B, Velayati AA. Increased production of soluble vascular endothelial growth factors receptor-1 in CHO-cell line by using new combination of chitosan-protein lipid nanoparticles. Int J Clin Exp Med. 2015; 8:1526–33.

31. Goi T, Nakazawa T, Hirono Y, Yamaguchi A. The anti-tumor effect is enhanced by simultaneously targeting VEGF and PROK1 in colorectal cancer. Oncotarget. 2015; 6:6053–61. doi: 10.18632/oncotarget.3474

32. Maleki M, Ghanbarvand F, Reza Behvarz M, Ejtemaei M, Ghadirkhomi E. Comparison of mesenchymal stem cell markers in multiple human adult stem cells. Int J Stem Cells. 2014; 7:118–26. doi: 10.15283/ijsc.2014.7.2.118

33. Zhou YL, Li YM, He WT. Application of Mesenchymal Stem Cells in the Targeted Gene Therapy for Gastric Cancer. Curr Stem Cell Res Ther. 2016; 11:434–39. doi: 10.2174/1574888X10666151026113818

34. Bhere D, Shah K. Stem Cell-Based Therapies for Cancer. Adv Cancer Res. 2015; 127:159–89. doi: 10.1016/bs.acr.2015.04.012

35. Rico MJ, Perroud HA, Mainetti LE, Rozados VR, Scharovsky OG. Comparative effectiveness of two metronomic chemotherapy schedules-our experience in the preclinical field. Cancer Invest. 2014; 32:92–98. doi: 10.3109/07357907.2013.877480

36. Albertsson P, Lennernäs B, Norrby K. Dose effects of continuous vinblastine chemotherapy on mammalian angiogenesis mediated by VEGF-A. Acta Oncol. 2008; 47:293–300. doi: 10.1080/02841860701558781

37. Rico MJ, Perroud HA, Mainetti LE, Rozados VR, Scharovsky OG. Comparative effectiveness of two metronomic chemotherapy schedules-our experience in the preclinical field. Cancer Invest. 2014; 32:92–98. doi: 10.3109/07357907.2013.877480

38. Tseng JC, Granot T, DiGiacomo V, Levin B, Meruelo D. Enhanced specific delivery and targeting of oncolytic Sindbis viral vectors by modulating vascular leakiness

in tumor. Cancer Gene Ther. 2010; 17:244–55. doi: 10.1038/cgt.2009.70

39. Al-Abbasi FA, Alghamdi EA, Baghdadi MA, Alamoudi AJ, El-Halawany AM, El-Bassossy HM, Aseeri AH, Al-Abd AM. Gingerol Synergizes the Cytotoxic Effects of Doxorubicin against Liver Cancer Cells and Protects from Its Vascular Toxicity. Molecules. 2016; 21:580–91. doi: 10.3390/molecules21070886

Research Paper

RelA NF-κB subunit activation as a therapeutic target in diffuse large B-cell lymphoma

Mingzhi Zhang[1,2*], Zijun Y. Xu-Monette[2*], Ling Li[1*], Ganiraju C. Manyam[3], Carlo Visco[4], Alexandar Tzankov[5], Jing Wang[3], Santiago Montes-Moreno[6], Karen Dybkaer[7], April Chiu[8], Attilio Orazi[9], Youli Zu[10], Govind Bhagat[11], Kristy L. Richards[12], Eric D. Hsi[13], William W.L. Choi[14], J. Han van Krieken[15], Jooryung Huh[16], Maurilio Ponzoni[17], Andrés J.M. Ferreri[17], Michael B. Møller[18], Ben M. Parsons[19], Jane N. Winter[20], Miguel A. Piris[6], L. Jeffrey Medeiros[2], Lan V. Pham[2], Ken H. Young[2,21]

[1]Department of Oncology, The First Affiliated Hospital Zhengzhou University, Zhengzhou, Henan, China;
[2]Department of Hematopathology, The University of Texas MD Anderson Cancer Center, Houston, TX 77030, USA
[3]Department of Bioinformatics and Computational Biology, The University of Texas MD Anderson Cancer Center, Houston, TX 77030, USA
[4]San Bortolo Hospital, Vicenza, Italy
[5]University Hospital, Basel, Switzerland
[6]Hospital Universitario Marques de Valdecilla, Santander, Spain
[7]Aalborg University Hospital, Aalborg, Denmark
[8]Memorial Sloan-Kettering Cancer Center, New York, NY 10065, USA
[9]Weill Medical College of Cornell University, New York, NY 10065, USA
[10]The Methodist Hospital, Houston, TX 77030, USA
[11]Columbia University Medical Center and New York Presbyterian Hospital, New York, NY 10032, USA
[12]University of North Carolina School of Medicine, Chapel Hill, NC 27514, USA
[13]Cleveland Clinic, Cleveland, OH 44195, USA
[14]University of Hong Kong Li Ka Shing Faculty of Medicine, Hong Kong, China
[15]Radboud University Nijmegen Medical Centre, Nijmegen, the Netherlands
[16]Asan Medical Center, Ulsan University College of Medicine, Seoul, Korea
[17]San Raffaele H. Scientific Institute, Milan, Italy
[18]Odense University Hospital, Odense, Denmark
[19]Gundersen Medical Foundation, La Crosse, WI 54601, USA
[20]Feinberg School of Medicine, Northwestern University, Chicago, IL 60611, USA
[21]The University of Texas School of Medicine, Graduate School of Biomedical Sciences, Houston, TX 77030, USA
[*]Equal contribution

Correspondence to: Mingzhi Zhang; Ken H. Young; **email:** mingzhi_zhang@126.com, khyoung@mdanderson.org
Keywords: NF-κB; p65; diffuse large B-cell lymphoma; TP53, GCB, gene expression profiling, proteasome inhibitor
Received: October 29, 2016 **Accepted:** November 11, 2016 **Published:** December 8,2016
DOI:10.18632/aging.101121

ABSTRACT

It has been well established that nuclear factor kappa-B (NF-κB) activation is important for tumor cell growth and survival. RelA/p65 and p50 are the most common NF-κB subunits and involved in the classical NF-κB pathway. However, the prognostic and biological significance of RelA/p65 is equivocal in the field. In this study, we assessed RelA/p65 nuclear expression by immunohistochemistry in 487 patients with *de novo* diffuse large

B-cell lymphoma (DLBCL), and studied the effects of molecular and pharmacological inhibition of NF-κB on cell viability. We found RelA/p65 nuclear expression, without associations with other apparent genetic or phenotypic abnormalities, had unfavorable prognostic impact in patients with stage I/II DLBCL. Gene expressionprofiling analysis suggested immune dysregulation and antiapoptosis may be relevant for the poorer prognosis associated with p65 hyperactivation in germinal center B-cell–like (GCB) DLBCL and in activated B-cell–like (ABC) DLBCL, respectively. We knocked down individual NF-κB subunits in representative DLBCL cells in vitro, and found targeting p65 was more effective than targeting other NF-κB subunits in inhibiting cell growth and survival. In summary, RelA/p65 nuclear overexpression correlates with significant poor survival in early-stage DLBCL patients, and therapeutic targeting RelA/p65 is effective in inhibiting proliferation and survival of DLBCL with NF-κB hyperactivation.

INTRODUCTION

Diffuse large B-cell lymphoma (DLBCL), the most common form of aggressive non-Hodgkin lymphoma, accounts for nearly 40% of non-Hodgkin lymphomas [1]. Although most cases of DLBCL are curable with the standard immunochemotherapy regimen, rituximab plus cyclophosphamide, hydroxydaunomycin, vincristine, and prednisone (R-CHOP), 30-40% of patients have drug-resistant disease or recurrence [2]. DLBCL is a highly heterogeneous disease. Based on gene expression profiling (GEP), DLBCL can be classified into two molecular subtypes: germinal center B-cell–like (GCB) and activated B-cell–like (ABC) DLBCL [3]. The ABC subtype of DLBCL typically exhibits constitutive activation of the nuclear factor-kappaB (NF-κB) pathway [4, 5] and patients have inferior clinical outcomes compared with patients with GCB-DLBCL [6, 7]. Recent studies have shown that NF-κB expression is not limited to ABC-DLBCL but also can occur in GCB-DLBCL [8-10].

The NF-κB/Rel family contains five transcription factors: RelA (p65), NF-κB1 (p50; p105), NF-κB2 (p52; p100), RelB, and c-Rel. Only RelA/p65, RelB, and c-Rel had transactivation domains [11]. NF-κB activity is controlled by inhibitors of NF-κB (such as IκBα which inhibits p65/p50 dimers) that keep NF-κB inactive in the cytoplasm. Constitutive activation of NF-κB in ABC-DLBCL is caused by chronic activation of B-cell-receptor (BCR) signaling and elevated IκB kinase (IKK) activities which phosphorylate IκBα. As a result, IκBα is degraded releasing homo- or hetero-dimers of NF-κB to enter the nucleus where NF-κB activates gene transcription [4, 12-14]. *In vivo* the most abundant NF-κB dimers are p50/p65 heterodimers which are ubiquitously expressed in mammalian tissue [11, 15-17], consistent with the highest level of nuclear p50/p65 in DLBCL samples among all NF-κB subunits by our previous studies [10, 18]. Detection of p65/p50 nuclear expression in tumor cells has been considered as homodimers with distinct DNA-binding modes and functions [19-21].

NF-κB activation suppresses apoptosis and promotes tumor cell survival and proliferation, leading to treatment resistance. Different NF-κB subunits had distinct and overlapping functions [22-24]. In addition, transcriptional and functional crosstalk between antiapoptotic NF-κB and proapoptotic p53 (an essential tumor suppressor) plays a critical role in determining the fate of tumor cells [25, 26]. The p65 subunit of NF-κB and p53 counteract each other's function in regulating cell proliferation, metabolism and apoptosis [25, 27-29]. p65 increases MDM2 levels, which decrease the stabilization of p53 and cell death induced by cytotoxic chemotherapy [25]. However, cooperation between p65 and p53 has been also reported [30-33], making interactions between p65/NF-κB and p53 much more complicated. Both p53 and p65 were unexpectedly found necessary for either p53 or NF-κB-directed gene transcription under replicational stress or atypical and classical stimuli for NF-κB. Induced p65 in stimulated cancer cells by pro-inflammatory tumor necrosis factor α (TNF-α) binds to p53 and the p65/p53 complex transcriptionally activates NF-κB target genes (*survivin/BIRC5*, *BCL2*, *BCL-XL*, and *FASL*) [32]. Moreover, p65 and p53 co-regulate induction of proinflammatory genes in monocytes and macrophages [33].

Despite the well-established role of NF-κB signaling in lymphoma pathogenesis and treatment resistance, conflicting results on the prognostic significance of NF-κB and RelA/p65 expression (as a surrogate marker of NF-κB activation) in DLBCL have been reported by previous clinical studies [8, 9, 34-36]. To help clarify the prognostic effect of RelA/p65 nuclear expression, in this study we evaluated nuclear expression of RelA/p65 by immunohistochemistry (IHC) in a large cohort of DLBCL treated with R-CHOP, and studied the prognostic effects and gene expression profiles associated

with p65 nuclear expression. Moreover, we inactivated individual NF-κB subunits in vitro and investigated their differential effects on proliferation and apoptosis of DLBCL cells which highlighted the important therapeutic value of RelA/p65.

RESULTS

p65 hyperactivation has significant adverse impact in early-stage DLBCL

p65 expression was evaluable in 487 DLBCL patients, including 287 men and 200 women. GCB/ABC ratio was close to 1 (243 GCB and 239 ABC). The median age of the patients in the study group was 63 years, and 58% of the study cohort had elderly age (≥60). Immunohistochemical results showed that 58% of DLBCL samples had p65 nuclear expression indicative of p65 activation at various levels (Fig. 1A) with a mean level of 14%. p65 nuclear expression was not specific for ABC-DLBCL. In fact, the GCB-DLBCL group had a slightly higher mean level of p65 nuclear expression (16.1%) than the ABC-DLBC group (12.6%) (Fig. 1A). Table 1 showed the clinical and pathological features of the study cohort.

Low levels (10-40%) of p65 nuclear expression did not have significant prognostic impact in DLBCL (Fig. 1B). However, high p65 nuclear expression ($p65^{high}$, ≥50% tumor cells with p65 positive nuclei) correlated with significantly shorter PFS and OS durations in patients with stage I/II DLBCL and in patients with an International Prognostic Index score (IPI) ≤2 (Fig. 1B, Fig. 2A). In contrast, in patients with stage III/IV DLBCL or an IPI >2, p65 expression was not prognostic. $p65^{high}$ patients with stage I/II DLBCL had similar survival rates compared with $p65^{high}$ patients with stage III/IV DLBCL (Fig. 2B).

When analyzed individually in GCB and ABC subtypes, in GCB-DLBCL only, the $p65^{high}$ group frequently had large (≥ 5cm) tumors (65% *vs.* 37%, $P = 0.011$) (Table 1), and significantly decreased PFS ($P = 0.04$, Fig. 2C) and OS ($P = 0.015$) rates than other patients ($p65^{low}$ group, IHC <50%). However, the unfavorable prognostic effect manifested in GCB-DLBCL was limited in stage I/II (Fig. 1C) and minimal in stage III/IV GCB-DLBCL ($P = 0.95$ for PFS and $P = 0.60$ for OS); also, in stage I/II ABC-DLBCL patients, $p65^{high}$ expression also significantly correlated with worse PFS (Fig. 1C).

p65 nuclear expression correlates with p50 nuclear expression in DLBCL

We found high p65 nuclear expression was significantly associated with $p50^{+}$ and $p50^{high}$ nuclear expression in overall DLBCL, GCB-DLBCL, and ABC-DLBCL (Table 1), suggesting the predominance of p65/p50 dimer activation via the canonical NF-κB pathway [9]. Significant association with c-Rel^{+} nuclear expression was also found in overall DLBCL and GCB-DLBCL (p50/c-Rel is another dimer activated via the canonical pathway [37, 38]). No significant association was observed between $p65^{high}$ and $RelB^{+}$. $p65^{high}$ showed significant association with $p52^{+}$ in overall DLBCL but not in either GCB or ABC subset.

Nuclear expression of p50, p52, and c-Rel did not show further prognostic effects among the $p65^{high}$ patients. We did not observe associations of $p65^{high}$ with any other adverse biomarkers such as *TP53* mutations, *MYC*/*BCL2* translocation, and Myc/Bcl-2 over-expression which may confound the prognostic effects [39-42]. In contrast, in the GCB but not the ABC subgroup, $p65^{high}$ compared with $p65^{low}$ patients less frequently had Bcl-2 overexpression (18% *vs.* 40%, $P = 0.036$).

p65 hyperactivation has significant adverse impact in patients with wild-type *TP53*

Cases of DLBCL with wild-type *TP53* (*WT-TP53*) had significantly lower levels of *RELA* mRNA ($P = 0.018$, Fig. 1D) and a trend toward lower nuclear p65 levels ($P = 0.11$) than those with mutated *TP53* (*MUT-TP53*), suggesting that wild-type p53 suppressed *RELA* NF-κB expression. Conversely, p65 antagonized p53 function as suggested by survival analysis: in *WT-TP53* DLBCL, patients with $p65^{high}$ expression correlated with significantly decreased PFS ($P = 0.0076$, Fig. 2C) and OS ($P = 0.0082$) rates than patients with $p65^{low}$ tumors, independent of GCB and ABC cell-of-origin. However, when subdivided cohorts by disease stages, we found the prognostic impact was only significant in patients with stage I/II disease ($P < 0.0001$ for PFS, $P = 0.0004$ for OS). Also in *MUT-TP53* patients with stage I/II DLBCL, positive p65 nuclear expression was associated with significant poorer survival; in contrast, opposite trends were observed in *MUT-TP53* patients with stage III/IV DLBCL (Fig. 1E).

Multivariate survival analysis

Multivariate survival analysis (Cox regression) for high p65 nuclear expression with adjustments for clinical variables confirmed that $p65^{high}$ was an independent adverse prognostic factor in patients with GCB-DLBCL and in patients with *WT-TP53* DLBCL, but not in the overall study group, the ABC-DLBCL subgroup, or the *MUT-TP53* DLBCL subgroup (Table 2).

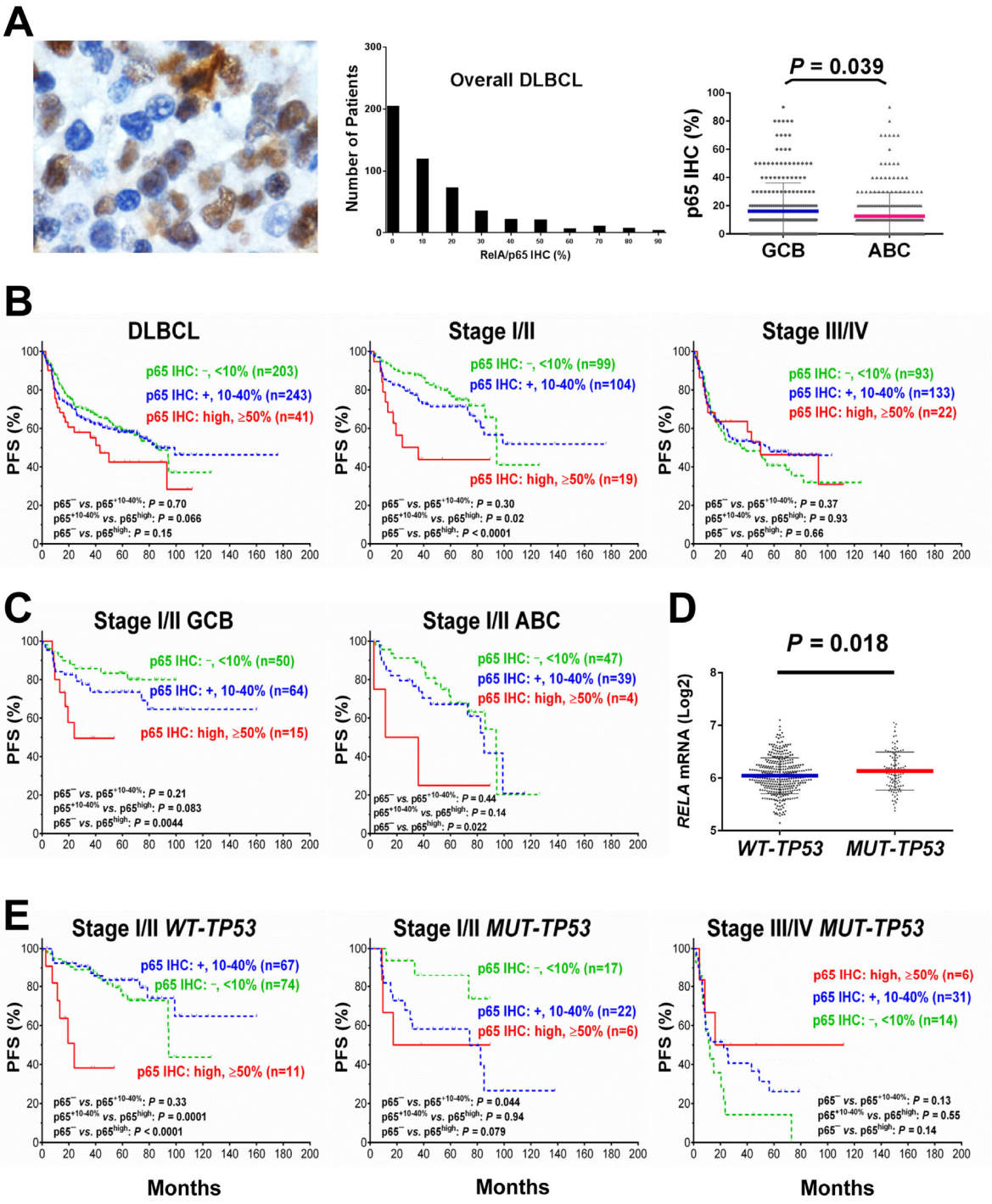

Figure 1. Nuclear expression of p65 and its effect on progression-free survival (PFS) in diffuse large B-cell lymphoma (DLBCL) (**A**) Representative immunohistochemical analysis (IHC) and histograms for p65 nuclear expression in DLBCL. The mean expression of nuclear p65 was significantly higher in the germinal center B-cell–like (GCB) subtype than in the activated B-cell–like (ABC) subtype. (**B**) In overall DLBCL, high p65 nuclear expression ($p65^{high}$, ≥50% nuclear expression) was associated with a trend towards worse PFS. In patients with stage I/II DLBCL, $p65^{high}$ correlated with significantly shorter PFS. In patients with stage III/IV DLBCL, $p65^{high}$ did not show signficant prognostic impact. (**C**) $p65^{high}$ correlate with significantly shorter PFS in patients with stage I/II DLBCL independent of GCB/ABC subtypes. (**D**) *TP53* mutation status was significantly associated with higher *RELA* mRNA expression. (**E**) In patients with stage I/II DLBCL, $p65^{high}$ correlate with significantly shorter PFS independent of *TP53* mutation status although more significant in patients with wild-type *TP*53 (*WT-TP53*). In patients with mutated *TP53* (*MUT-TP53*) and stage III/IV DLBCL, $p65^{high}$ was associated with a trend of better PFS.

Table 1. Clinical characteristics of 487 patients with *de novo* diffuse large B-cell lymphoma (DLBCL).

	DLBCL			GCB-DLBCL			ABC-DLBCL			*WT-TP53*			*MUT-TP53*		
	$p65^{high}$	$p65^{low}$	*P*	$p65^{high}$	$p65^{low}$	*P*	$p65^{high}$	$p65^{low}$	*P*	$p65^{high}$	$p65^{low}$	*P*	$p65^{high}$	$p65^{low}$	*P*
Characteristics	N (%)	N (%)		N (%)	N (%)		N (%)	N (%)		N (%)	N (%)		N (%)	N (%)	
Patients	41	446		28	215		13	226		26	312		12	84	
Age (years)															
<60	21 (51)	183 (41)	0.21	16 (57)	106 (49)	0.44	5 (39)	74 (33)	0.67	13 (50)	124 (40)	0.31	7 (58)	30 (36)	0.13
≥60	20 (49)	263 (59)		12 (43)	109 (51)		8 (61)	152 (67)		13 (50)	188 (60)		5 (42)	54 (64)	
Gender															
Female	8 (20)	192 (43)	**0.003**	6 (21)	95 (44)	**0.022**	2 (15)	95 (42)	0.057	6 (30)	130 (42)	0.063	2 (17)	38 (45)	0.06
Male	33 (80)	254 (57)		22 (79)	120 (56)		11 (85)	131 (58)		20 (70)	182 (58)		10 (83)	46 (55)	
Stage															
I/II	19 (46)	203 (47)	0.90	15 (54)	114 (56)	0.84	4 (31)	86 (39)	0.54	11 (42)	141 (48)	0.60	6 (50)	39 (46)	0.82
III/IV	22 (54)	226 (53)		13 (46)	91 (45)		9 (69)	133 (61)		15 (58)	155 (52)		6 (50)	45 (54)	
B-symptoms															
No	25 (61)	272 (64)	0.67	18 (64)	141 (70)	0.55	7 (54)	127 (59)	0.73	16 (61)	196 (66)	0.61	7 (58)	54 (68)	0.53
Yes	16 (39)	151 (36)		10 (36)	61 (30)		6 (46)	89 (41)		10 (39)	99 (34)		5 (42)	26 (33)	
LDH levels															
Normal	14 (34)	161 (40)	0.51	8 (29)	86 (44)	0.12	6 (46)	74 (36)	0.44	10 (39)	121 (43)	0.65	3 (25)	28 (36)	0.46
Elevated	27 (66)	247 (60)		20 (71)	109 (56)		7 (54)	134 (64)		16 (61)	160 (57)		9 (75)	50 (64)	
Extranodal sites (n)															
0–1	35 (85)	327 (77)	0.22	23 (82)	160 (80)	0.75	12 (92)	163 (74)	0.15	21 (81)	231 (79)	0.79	11 (92)	64 (78)	0.27
≥2	6 (15)	98 (23)		5 (18)	41 (20)		1 (8)	56 (26)		5 (19)	63 (21)		1 (8)	18 (22)	
Performance status															
0–1	34 (87)	329 (83)	0.53	23 (85)	158 (86)	0.87	11 (92)	166 (80)	0.33	22 (85)	231 (85)	0.93	10 (91)	69 (90)	0.89
≥2	5 (13)	66 (17)		4 (15)	25 (14)		1 (8)	41 (20)		4 (15)	40 (15)		1 (9)	8 (10)	
Size of largest tumor															
<5cm	14 (44)	192 (58)	0.11	8 (35)	97 (63)	**0.011**	6 (67)	93 (54)	0.47	8 (38)	146 (62)	**0.035**	5 (50)	33 (49)	0.96
≥5cm	18 (56)	137 (42)		15 (65)	58 (37)		3 (33)	78 (46)		13 (62)	91 (38)		5 (50)	34 (51)	
IPI risk group															
0–2	29 (71)	284 (62)	0.25	21 (75)	164 (71)	0.82	8 (61)	118 (54)	0.78	17 (65)	189 (63)	1.0	10 (83)	47 (57)	0.12
3-5	12 (29)	162 (38)		7 (25)	60 (29)		5 (39)	102 (46)		9 (35)	109 (37)		2 (17)	43 (35)	
Therapy response															
CR	29 (71)	343 (77)	0.37	17 (61)	166 (77)	0.057	12 (92)	172 (76)	0.18	17 (65)	257 (82)	**0.034**	9 (75)	49 (58)	0.27
Non-CR	12 (29)	103 (23)		11 (39)	49 (23)		1 (8)	22 (24)		9 (35)	55 (18)		3 (25)	35 (42)	
Primary origin															
Extranodal	20 (49)	149 (34)	0.058	14 (50)	68 (32)	0.063	6 (46)	79 (36)	0.44	14 (54)	102 (33)	**0.035**	4 (33)	26 (32)	0.91
Nodal	21 (51)	289 (66)		14 (50)	143 (68)		7 (54)	143 (64)		12 (46)	204 (67)		8 (67)	56 (68)	

Cell-of-origin															
GCB	28 (68)	215 (49)	**0.022**	-	-	-	-	-	-	18 (69)	143 (46)	**0.039**	9 (75)	49 (58)	0.35
ABC	13 (32)	226 (51)		-	-		-	-		8 (31)	165 (54)		3 (25)	35 (42)	
p50 nuclear expression															
<20%	15 (40)	278 (67)	**0.002**	12 (46)	149 (74)	**0.005**	3 (27)	129 (60)	**0.05**	9 (41)	188 (65)	**0.037**	6 (50)	57 (71)	0.18
≥20%	22 (60)	138 (33)		14 (54)	52 (26)		8 (73)	85 (40)		13 (59)	102 (35)		6 (50)	23 (29)	
p52 nuclear expression															
–	21 (55)	300 (71)	**0.043**	14 (54)	142 (71)	0.11	7 (58)	157 (72)	0.33	14 (58)	208 (71)	0.25	5 (46)	59 (74)	0.078
+	17 (45)	120 (29)		12 (46)	58 (29)		5 (42)	61 (28)		10 (42)	86 (29)		6 (54)	21 (26)	
c-Rel nuclear expression															
–	17 (46)	297 (72)	**0.002**	11 (44)	147 (74)	**0.004**	6 (50)	150 (70)	0.20	9 (41)	207 (73)	**0.003**	7 (58)	55 (67)	0.53
+	20 (54)	117 (28)		14 (56)	52 (26)		6 (50)	64 (30)		13 (59)	78 (27)		5 (42)	27 (33)	
Bcl-2 expression															
<70%	27 (66)	229 (52)	0.10	23 (82)	127 (60)	**0.036**	4 (31)	99 (44)	0.40	17 (65)	164 (53)	0.31	7 (58)	40 (48)	0.55
≥70%	14 (34)	208 (48)		5 (18)	83 (40)		9 (69)	125 (56)		9 (35)	143 (47)		5 (42)	44 (52)	

Abbreviations: $p65^{high}$, high levels of nuclear p65; $p65^{low}$, low levels of p65 nuclear expression; LDH, lactate dehydrogenase; IPI, international prognostic index; CR, complete remission; PR, partial response; GCB, germinal center B-cell–like; ABC, activated B-cell–like; *WT-TP53*, wild-type *TP53*; *MUT-TP53*, mutated *TP53*. Some of the clinicopathologic data were not available. Percentages are calculated among cases with specific data available. Significant *P* values in bold.

Table 2. Multivariate analysis of clinicopathologic parameters for survival of patients with diffuse large B-cell lymphoma (DLBCL) treated with R-CHOP.

	Overall survival			Progression-free survival		
	HR	95% CI	*P*	HR	95% CI	*P*
DLBCL (*n* = 497)						
IPI > 2	2.41	1.70–3.42	**< 0.001**	2.29	1.64–3.19	**< 0.001**
Female sex	1.03	0.72–1.49	0.86	0.99	0.70–1.41	0.98
Tumor size ≥ 5	1.28	0.91–1.81	0.16	1.23	0.89–1.71	0.21
B-symptoms	1.35	0.94–1.94	0.099	1.31	0.93–1.85	0.12
$p65^{high}$	1.56	0.91–2.68	0.11	1.44	0.85–2.42	0.18
GCB-DLBCL (*n* = 243)						
IPI > 2	2.47	1.40–4.38	**0.002**	2.39	1.39–4.09	**0.002**
Female sex	1.00	0.55–1.82	1.00	0.98	0.56–1.71	0.95
Tumor size ≥ 5	1.30	0.88–1.91	0.19	1.40	0.82–2.40	0.22
B-symptoms	1.44	0.80–2.58	0.22	1.34	0.77–2.33	0.31
$p65^{high}$	2.30	1.14–4.62	**0.02**	2.01	1.06–3.82	**0.034**
***WT-TP53* DLBCL (*n* = 338)**						
IPI > 2	2.54	1.66–3.88	**< 0.001**	2.33	1.57–3.46	**< 0.001**
Female sex	0.98	0.63–1.53	0.92	0.99	0.65–1.51	0.96
Tumor size ≥ 5	1.20	0.79–1.84	0.39	1.09	0.73–1.63	0.18
B-symptoms	1.59	1.04–2.43	**0.034**	1.57	1.05–2.33	**0.028**
$p65^{high}$	1.91	1.04–3.52	**0.037**	1.94	1.08–3.48	**0.026**

Abbreviations: R-CHOP, rituximab with cyclophosphamide, doxorubicin, vincristine, and prednisone; HR, hazard ratio; CI, confidence interval; IPI, International Prognostic Index; $p65^{high}$, high levels of nuclear p65; GCB, germinal center B-cell–like; ABC, activated B-cell–like; WT-TP53, wild-type TP53. *Significant P values in bold.

GEP analysis suggests different signaling pathways activated in GCB- and ABC-DLBCL

To gain insight into the molecular mechanisms underlying the prognostic effects of p65 hyperactivation in DLBCL, we compared gene expression profiles of $p65^{high}$ and $p65^{low}$ tumors. $p65^{high}$ patients showed GEP signatures compared with other DLBCL including $p65^{-}$ DLBCL patients (IHC <10%), stronger in GCB-DLBCL than in ABC-DLBCL subset (Fig. 3A, Fig. 4, Tables 3-4).

In line with the unfavorable prognosis of patients with $p65^{high}$ DLBCL, GEP analysis found that *JUN* and *PTPRD* (involved in cell cycle progression) were upregulated (1.43-fold and 1.31-fold respectively) whereas pro-apoptotic *NOXA*/*PMAIP1* and *BTG3* which negatively regulates proliferation and cell cycle progression were downregulated (1.62-fold and 1.45-fold, respectively) in $p65^{high}$ DLBCL compared with $p65^{low}$ DLBCL. *RBMS1* which transactivates *MYC* was upregulated (1.48-fold) in $p65^{high}$ compared with $p65^{low}$ GCB-DLBCL (Table 3). Paradoxically, antiapoptotic

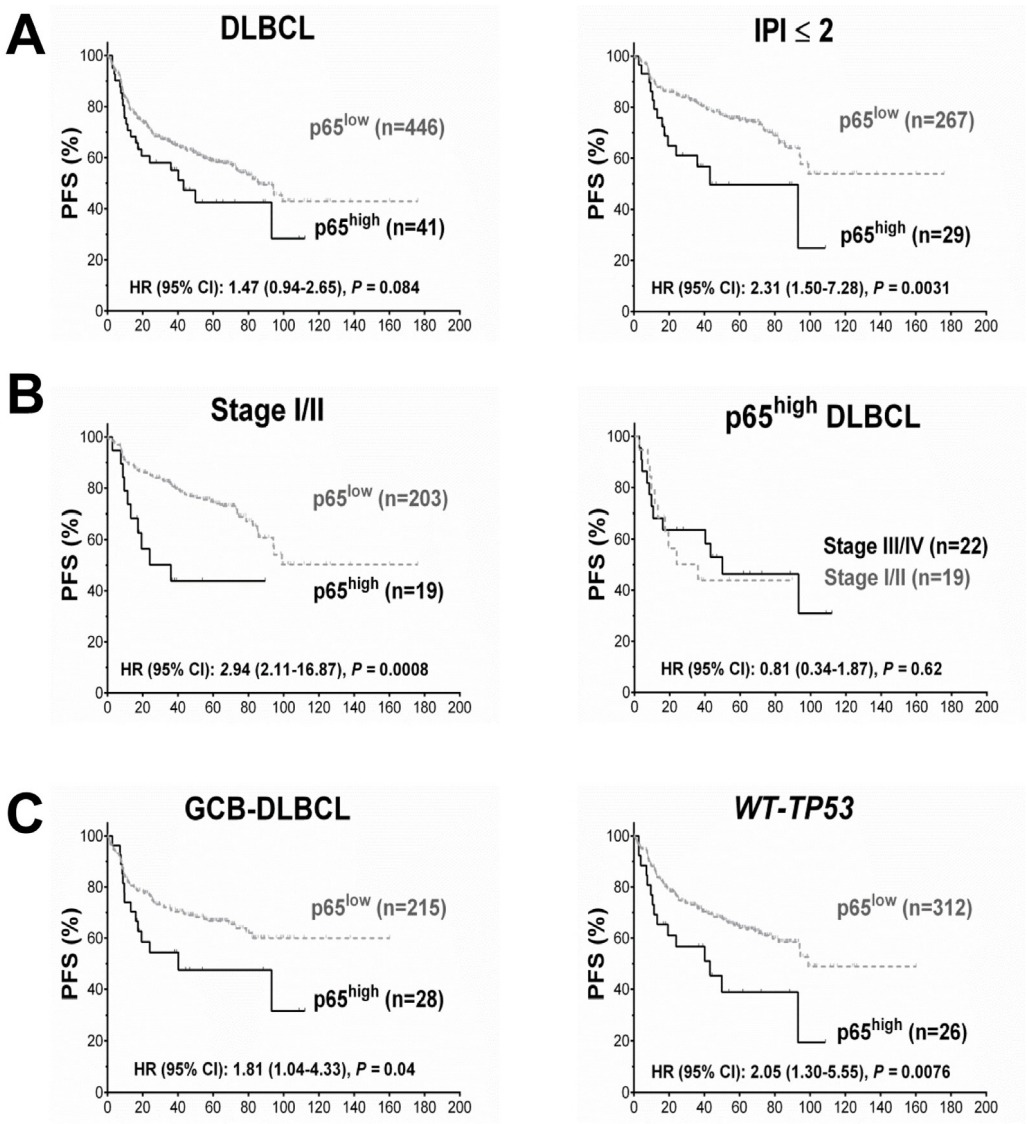

Figure 2. Prognosis for p65 hyperactivation in diffuse large B-cell lymphoma (DLBCL). (**A**) In overall DLBCL, high p65 nuclear expression ($p65^{high}$, ≥50% nuclear expression) was associated with unfavorable progression-free survival (PFS). The adverse prognostic impact was significant in patients with an international prognostic index score (IPI) ≤2. (**B**) In patients with stage I/II DLBCL, $p65^{high}$ correlated with significantly poorer PFS. Among $p65^{high}$ DLBCL patients, disease stages did not show further prognostic impact. (**C**) $p65^{high}$ correlated with significantly poorer PFS in patients with GCB-DLBCL and patients with wild-type *TP*53 (*WT-TP53*).

BIRC6, *MCM10* (involved in the initiation of eukaryotic genome replication), *CARS* (cysteinyl-tRNA synthetase) and *PA2G4* (involved in growth regulation) were downregulated in p65^{high} patients, and *TENC1* (which inhibits AKT1 signaling) was upregulated in p65^{high} DLBCL.

When analyzed in GCB and ABC subtypes individually, we found such paradoxical association was limited in the GCB subset. *RNF130* involved in apoptosis showed 1.81-fold upregulation in p65^{high} GCB-DLBCL patients. In contrast, in p65^{high} ABC-DLBCL, antiapoptotic *BIRC5* and *BCL2L2* were significantly upregulated whereas pro-apoptotic *NOXA*/*PMAIP1* was significantly downregulated (Fig. 3B-C), in addition to the proliferative signatures (such as upregulation of genes involved in replication, transcription, translation, and metabolism) in ABC-DLBCL (Table 3).

Table 3. Differentially expressed (canonical activation) genes between p65^{high} *vs.* p65^{low} patients with diffuse large B-cell lymphoma (DLBCL).

	p65^{high} vs. p65^{low}		
Functional categories	In overall DLBCL (FDR <0.30)	In GCB-DLBCL (FDR <0.05)	In ABC-DLBCL (FDR <0.20)
Signaling, ion channels	***TNFRSF1A*** ↑ ***FYN*** ↑ ***LCP2*** ↑ ***PTPRD*** ↑ ***GTPBP2*** ↑ ***PROCR*** ↑ ***TENC1*** ↑ ***ITPR3*** ↑ ***TEK*** ↑ ***CACNA2D1*** ↑ ***AGTRAP*** ↑ *LPAR3* ↓	***MT1X*** ↑ ***MT1G*** ↑ ***SERPING1*** ↑ ***PSEN1*** ↑	***ARHGEF2*** ↑ ***FGFBP1*** ↑ ***EPHA1*** ↑ ***MS4A3*** ↑
Immune responses, inflammation		***CD163*** ↑ ***FCER1G*** ↑ ***CYBB*** ↑ ***GRN*** ↑ ***CD84*** ↑ ***LILRB1*** ↑	***DEFB4*** ↑
Cell cycle, DNA metabolism, transcription and translation regulation	***JUN*** ↑ ***MLLT10*** ↑ ***GATAD2A*** ↑ ***HOXD10*** ↑ ***NFRKB*** ↑ *ZWINT* ↓ *MCM10* ↓ *HMGB1* ↓ *PPP2CA* ↓*UHRF1* ↓ *BTG3* ↓ *ZNF254* ↓ *CARS* ↓ *PA2G4* ↓ *SERBP1* ↓	***RBMS1*** ↑ ***ANKRD11*** ↑ ***FAM89B*** ↑	***ESRP1*** ↑ ***DPPA4*** ↑
Apoptosis	*PMAIP1* ↓ *BIRC6* ↓	***RNF130*** ↑	
Metabolism	***SULT1A1*** ↑ ***SPTLC2*** ↑ ***SLC25A16*** ↑ ***SLC9A9*** ↑	***GLUL*** ↑ ***SERINC1*** ↑ ***CAT*** ↑ ***SLC9A9*** ↑	***S100A16*** ↑ ***SLC9A5*** ↑
Transport, trafficking, protein folding, chaperone	***CPNE8*** ↑ ***DNAJC5*** ↑ ***RHD*** ↑ ***AGFG2*** ↑	***SLC8A1*** ↑ ***NPC2*** ↑ ***VAMP5*** ↑ ***DNAJC5*** ↑	
Cell adhesion, cytoskeleton, collagen, matrix	***SH3D19*** ↑ ***ITGA6*** ↑ ***MYLK*** ↑ ***COL6A1*** ↑ ***UTRN*** ↑ ***FMOD*** ↑		***CCDC151*** ↑ ***KRT13*** ↑ ***ANTXR2*** ↑ ***COL17A1*** ↑
Degradation, ubiquitination	***RNASE1*** ↑	***SCARB2*** ↑ ***CTSB*** ↑ ***UBA7*** ↑	***PSMB1*** ↑
IncRNA genes, unknown	***NCRNA00185*** ↑ ***C19orf6*** ↑ ***PLEKHO2*** ↑ ***FAM124A*** ↑	***MT1P2*** ↑ ***ZDHHC20*** ↑ ***PLEKHO2*** ↑	*FAM105B* ↓ ***CG030*** ↑ ***NCRNA00185*** ↑ ***IQCG*** ↑

Abbreviations: p65^{high}, p65 immunohistochemistry results: ≥50% nuclear expression; p65^{low}, p65 immunohistochemistry results: <50% nuclear expression; GCB, germinal center B-cell–like; ABC, activated B-cell–like; FDR, false discovery rate.
*Upregulated genes in bold.

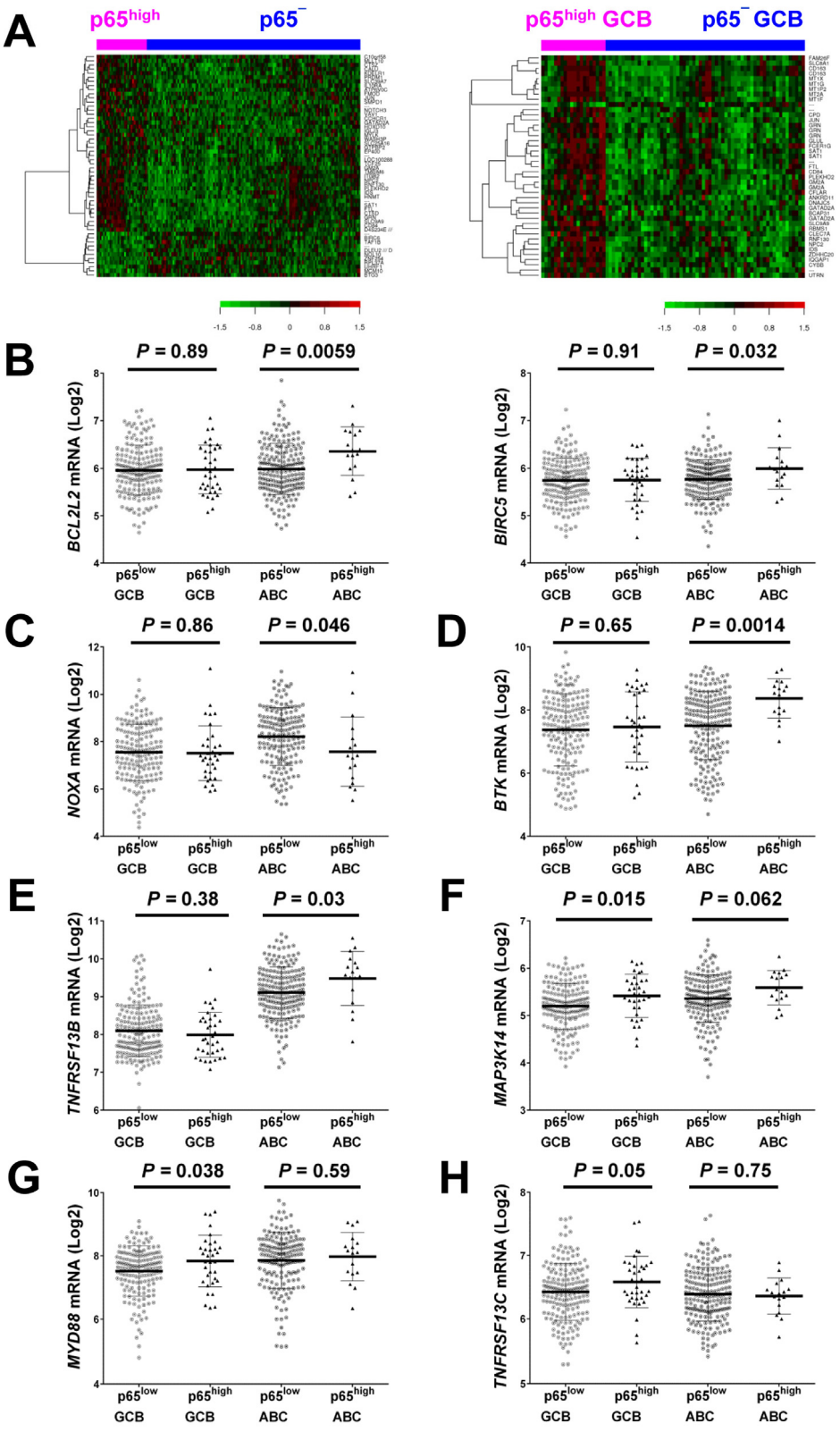

Figure 3. Gene expression profiling analysis. (**A**) Heatmaps for comparisons between DLBCL patients with p65^{high} expression (IHC≥50%) and those without p65 nuclear expression (IHC <10%) in the overall and GCB-DLBCL cohorts (FDR <0.15 and FDR <0.05, respectively). (**B**) *BIRC5/survivin* and *BCL2L2* were significantly upregulated in p65^{high} ABC-DLBCL. (**C**) *NOXA*/*PMAIP1* was significantly downregulated in p65^{high} ABC-DLBCL. (**D**-**E**) *BTK* and *TNFRSF13B* were significantly upregulated in the p65^{high} group in ABC-DLBCL but not in GCB-DLBCL. (**F**-**H**) *MAP3K14/NIK*, *MYD88*, and *TNFRSF13C* were significantly upregulated in the p65^{high} group in GCB-DLBCL but not in ABC-DLBCL.

GEP suggested that in GCB-DLBCL, instead of antiapoptotic mechanisms, dysregulations in immune responses and tumor microenvironment may be relevant for the poor prognosis associated with $p65^{high}$. Such immune signatures included *FCER1G* (Fc fragment of IgE high affinity I receptor for gamma subunit), 2.21-fold upregulation, *CYBB* (critical component of phagocytes generating superoxide), 1.77-fold upregulation, granulin gene *GRN*, 1.63-fold up-regulation, *LILRB1* (a MHC class I receptor resulting in immunosuppression), 1.49-fold upregulation, *CD163* (an antigen exclusively expressed in monocytes and macrophages), 2.46-fold upregulation, and *CD84* (an adhesion molecule involved in regulating receptor-mediated signaling in immune cells), 1.55-fold up-regulation. In the GEP comparison in overall DLBCL, a few immune-related genes were also found up- or down-regulated in $p65^{high}$ DLBCL compared with $p65^{low}$ DLBCL, including upregulation of *LCP2* (lymphocyte cytosolic protein 2, involved in T cell receptor signaling, 1.27-fold) and *TEK* (anti-inflammatory, 1.21-fold), and downregulation of *UHRF1* (an epigenetic regulator promoting proliferation of immunosuppressive Treg cell, 1.48-fold down-regulation) [43] in $p65^{high}$ DLBCL (Table 3).

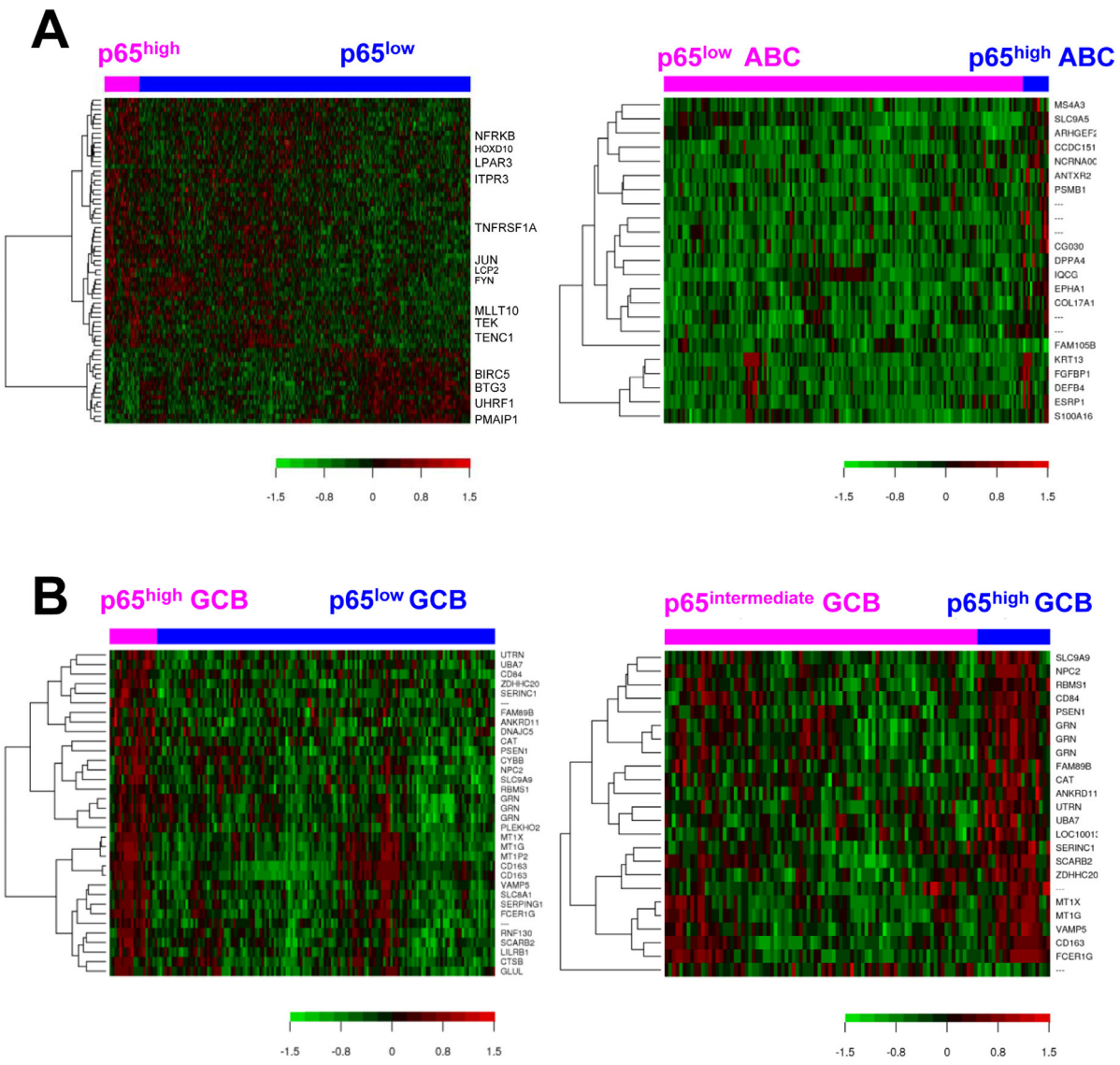

Figure 4. Gene expression analysis for p65 hyperactivation in diffuse large B-cell lymphoma (DLBCL). (**A**) Heatmaps for gene differentially expressed between $p65^{high}$ (IHC ≥50%) and $p65^{low}$ (IHC <50%) patients in DLBCL overall and in ABC-DLBCL (false discovery rate <0.30 and <0.20, respectively). (**B**) Heatmaps for genes differentially expressed between $p65^{high}$ (IHC ≥50%) and $p65^{low}$ (IHC <50%) patients and between $p65^{high}$ (IHC ≥50%) and $p65^{intermediate}$ (IHC 10-40%) patients with germinal center B-cell–like DLBCL (false discovery rate <0.05 and <0.20, respectively).

Table 4. Differentially expressed genes between p65^{high} *vs.* p65^{-} patients with diffuse large B-cell lymphoma (DLBCL) in the overall cohort and in the germinal-center-B-cell-like subgroup.

Functional categories	**p65^{high} vs. p65^{-} DLBCL** (FDR <0.15)	**p65^{high} GCB vs. p65^{-} GCB** (FDR <0.05)
Signaling, ion channels	***IL10RA*** ↑ ***GPS2*** /// ***D4S234E*** ↑ ***NOTCH3*** ↑ ***VAV1*** ↑	***FAM26F*** ↑ ***MT1X*** ↑ ***MT1G*** ↑ ***MT2A*** ↑ ***MT1F*** ↑ ***CFLAR*** ↑ ***CLEC7A*** ↑
Immune responses, inflammation	***GRN*** ↑	***CD163*** ↑ ***GRN*** ↑ ***FCER1G*** ↑ ***CD84*** ↑ ***CYBB*** ↑
Cell cycle, DNA metabolism, transcription and translation regulation	***JUN*** ↑ ***PRDM1*** ↑ ***GATAD2A*** ↑ ***TCF25*** ↑ ***MLLT10*** ↑ ***EP400*** ↑ ***HOXD10*** ↑ *TAF1B* ↓ *ZNF254* ↓ *RPL37A* ↓ *UHRF1* ↓ *MCM10* ↓ *BTG3* ↓	***JUN*** ↑ ***GATAD2A*** ↑ ***RBMS1*** ↑
Apoptosis	***TMBIM6*** ↑ ***RNF130*** ↑ *BIRC6* ↓	***RNF130*** ↑
Metabolism, redox regulation	***SLC9A9*** ↑ ***ATP6V0C*** ↑ ***SLC25A16*** ↑ ***SAT1*** ↑ ***SMPD1*** ↑ ***C10orf58*** ↑ ***HNMT*** ↑ ***GTPBP2*** ↑	***CPD*** ↑ ***GLUL*** ↑ ***SAT1*** ↑ ***FTL*** ↑ ***ANKRD11*** ↑ ***SLC9A9*** ↑
Transport, trafficking, protein folding, modification	***NPC2*** ↑ ***WASH3P*** ↑ ***FTL*** ↑ ***GM2A*** ↑ ***KDELR1*** ↑ ***SLC39A7*** ↑ ***CTSD*** ↑ ***CALU*** ↑	***SLC8A1*** ↑ ***GM2A*** ↑ ***DNAJC5*** ↑ ***BCAP31*** ↑ ***NPC2*** ↑
Cell adhesion, cytoskeleton, collagen, extracellular matrix	***ITGB2*** ↑ ***MYLK*** ↑ ***CD84*** ↑ ***FMOD*** ↑	***IQGAP1*** ↑ ***UTRN*** ↑
Degradation	***CTSZ*** ↑ ***IDS*** ↑	***IDS*** ↑
IncRNA genes, other function	***PLEKHO2*** ↑ ***LOC100288142*** /// ***NBPF1*** /// ***NBPF10*** ↑ ***CCHCR1*** ↑ ***IGLJ3*** ↑ *DLEU2* /// *DLEU2L* ↓ *NOL10* ↓	***MT1P2*** ↑ ***PLEKHO2*** ↑ ***ZDHHC20*** ↑

Abbreviations: p65^{high}, high p65 nuclear expression (immunohistochemistry results: ≥50%); p65^{-}, negative p65 nuclear expression (immunohistochemistry results: <10%); FDR, false discovery rate. *Upregulated genes in bold.

These data indicated that the antiapoptotic and pro-proliferation function of p65 was primarily activated in ABC-DLBCL, whereas immune dysregulation might be more relevant for the significantly adverse impact of p65 hyperactivation in GCB-DLBCL. We further analyzed the expression of p65-activating upstream signals in GCB- and ABC-DLBCL. *TNFRSF1A* encoding a TNF-α receptor which can activate NF-κB by degrading inhibitory IkBα (canonical activation), was upregulated in the overall p65^{high} group than in the overall p65^{low} group (P = 0.0001). *LPAR3* which encodes a receptor for lyso-phosphatidic acid/LPA was downregulated in p65^{high} DLBCL. In the ABC-DLBCL subset only, *PSMB1*, which encodes a 20S core beta subunit of the proteasome B-type family, was upregulated in p65^{high} compared with p65^{low} patients (suggesting canonical activation of NF-kB). Bruton tyrosine kinase gene BTK which plays an important role in BCR signaling activation (canonical activation), and *TNFRSF13B* which encodes the tumor necrosis factor receptor for APRIL and BAFF were significantly upregulated in p65^{high} ABC-DLBCL but not in p65^{high} GCB-DLBCL (Fig. 3D-E). In comparison, in GCB-DLBCL but not in ABC-DLBCL, *TNFRSF13C* which encodes the receptor specific for BAFF (non-canonical activation), *MYD88* which encodes an adapter protein essential for the Toll-like receptor (TLR) and interleukin-1 receptor signaling pathways, and *MAP3K14*/*NIK* which is involved in non-canonical activation of NF-κB were significantly upregulated in the p65^{high} compared with p65^{low} group (Fig. 3F-H).

Targeting NF-κB in DLBCL cells

Molecular inhibition of constitutive NF-κB activation in DLBCL cell lines

First, we examined whether specific inhibition of NF-κB was sufficient to block cell survival by over-expressing a super repressor mutant form of IκBα

(pCMV-IκBαM) in a representative DLBCL cell line, MS, that has been previously shown to have constitutive NF-κB activation [44]. IκBαM binds to NF-κB subunits but cannot be phosphorylated on the basis of alanine substitution for serines 32 and 36, acting as a dominant negative (DN) and thereby preventing the NF-κB subunits from translocating into the nucleus. Transient transfection (70-80 efficiency and 75% viability) of a DLBCL-MS cell line with the DN-IκBαM leads to the induction of IκBα protein level while suppressing constitutive NF-κB activation (Fig. 5A). In addition, cells over-expressing the DN-IκBαM are prone to apoptosis as demonstrated by Annexin V binding assays (Fig. 5B). This result suggests that constitutive NF-κB

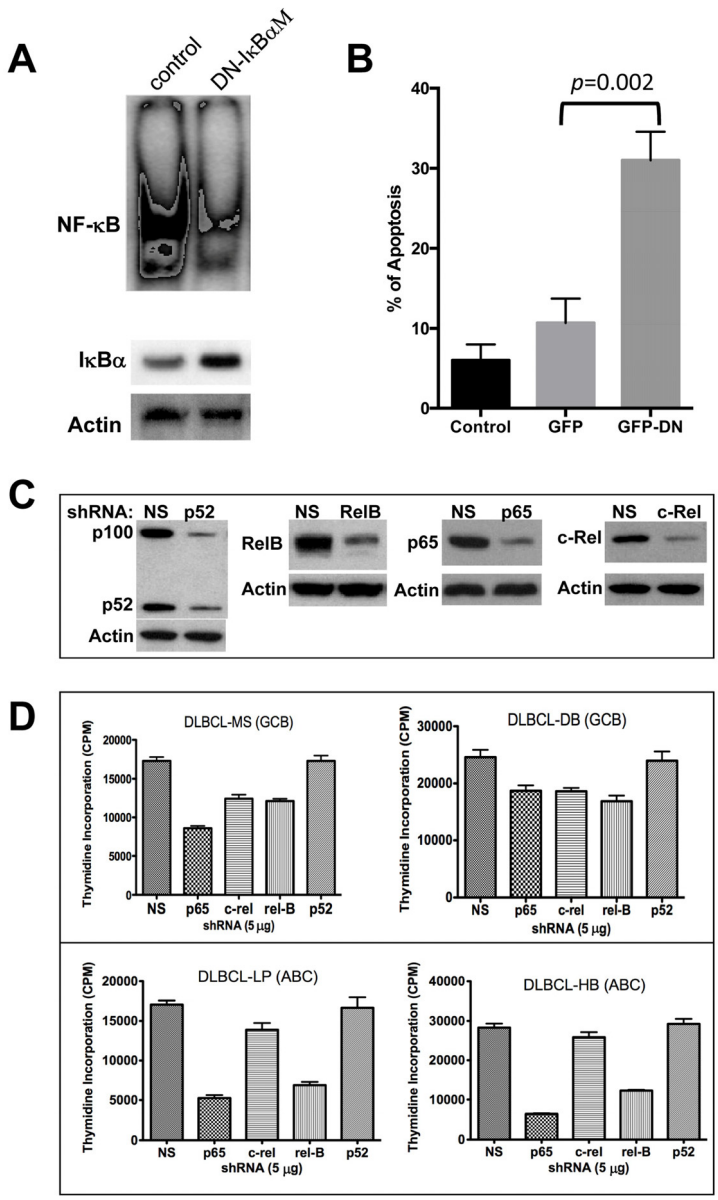

Figure 5. Molecular targeting of NF-κB in diffuse large B-cell lymphoma (DLBCL) cell lines. (**A**) DLBCL-MS cells were transfected with empty control vector or a pCMV-IκBαM vector for 24 hrs. Nuclear extracts (10 μg) were analyzed for NF-κB expression by EMSA. Cytoplasmic extracts were assessed for IκBα and actin protein expression by Western blotting. (**B**) Transfected cells from part **A** were also assessed for apoptosis after 24 hours of incubation using annexin V assays. (**C**) MS cells were transfected with plasmids expressing the p52, RelB, p65, c-Rel, or a non-specific (NS) shRNA. Forty-eight hours post-transfection, proteins were extracted and analyzed for NF-κB component inhibition by Western blot. (**D**) Indicated DLBCL cell lines were transfected with the validated green fluorescent protein (GFP)-plasmid–based shRNA for each of the NF-κB subunits. After 16 hours, GFP–positive cells were sorted and assessed using proliferation assays. Data represent two independent experiments with triplicate samples. **Abbreviations**: GCB, germinal center B-cell–like; ABC, activated B-cell–like, DN, dominant negative.

activation is required for the survival of this cell line. To determine the functional significance of each NF-κB subunit on growth and survival regulation in DLBCL, we used specific validated shRNAs to selectively silence each NF-κB component individually in four representative DLBCL cell lines (two GCB-DLBCLs, two ABC-DLBCLs). These validated shRNAs inhibited endogenous NF-κB by more than 70% (Fig. 5C). Except for p52, downregulation of p65, c-Rel, and RelB protein expression with individual shRNAs inhibited DLBCL cell growth (thymidine incorporation assay), and inhibition of p65 was most effective (Fig. 5D), particularly in cell lines with mutated p53 (MS, LP and HB).

Pharmacological targeting of constitutive NF-κB activation in DLBCL cells

To evaluate the effects of pharmacological inhibition of NF-κB activation on transcription activities of NF-κB subunits and DLBCL cell growth and survival, we selected the proteasome inhibitor bortezomib (BZ), and the small molecule NF-κB inhibitor BAY 11-7082 (BAY-11) that selectively inhibits the phosphorylation and degradation of IκBα [45-47] in MS (GCB-DLBCL) cells.

To ascertain whether BZ or BAY-11 has an effect on constitutive NF-κB activation in DLBCL cells, we performed EMSA with nuclear extracts purified from BZ- or BAY-11-treated GCB-DLBCL cell line (MS). After BZ or BAY-11 treatment, NF-κB DNA-binding activity (Fig. 6A) and the level of phosphorylated-IκBα (Fig. 6B) gradually declined in a dose-dependent manner in the MS DLBCL cell line. Confocal microscopy analysis also demonstrated that BZ or BAY-11 treatment inhibits the nuclear accumulation of p50 and p65 NF-κB subunits, leading to DNA fragmentation, indicative of cells undergoing apoptosis (Fig. 6C). Next, we evaluated the effects of BZ or BAY-11 on DLBCL cell viability using *in vitro* proliferation assays in four representative DLBCL cell lines

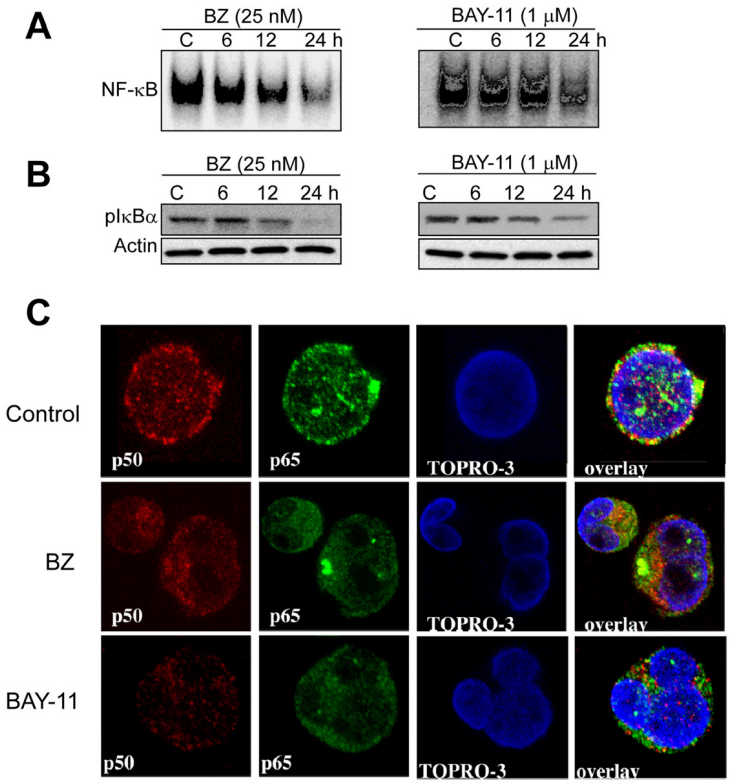

Figure 6. Pharmacological inhibition of constitutive NF-κB activation in DLBCL cells. (**A-B**) DLBCL cells (MS) were cultured in the presence of bortezomib (BZ, 25 nM) or BAY-11 (1 μM) for the indicated time points (hours). Nuclear extracts were purified and subjected to EMSA analyzed for NF-κB DNA binding activity; cytoplasmic extracts were subjected to immunobloting for pIκBa and actin. (**C**) DLBCL-MS cells cultured in the presence of bortezomib (BZ, 25 nM) or BAY-11 (1 μM) for 24 hours and then analyzed for p50 (red) and p65 (green) protein expression by confocal microscopy analysis. Topro-3 (blue) serves as a nuclear staining marker.

(two ABC, two GCB). Both BZ and BAY-11 inhibited cell proliferation in the representative DLBC cell lines in a dose-dependent manner (Fig. 7A). BZ and BAY-11 inhibit NF-κB by different mechanisms, as we

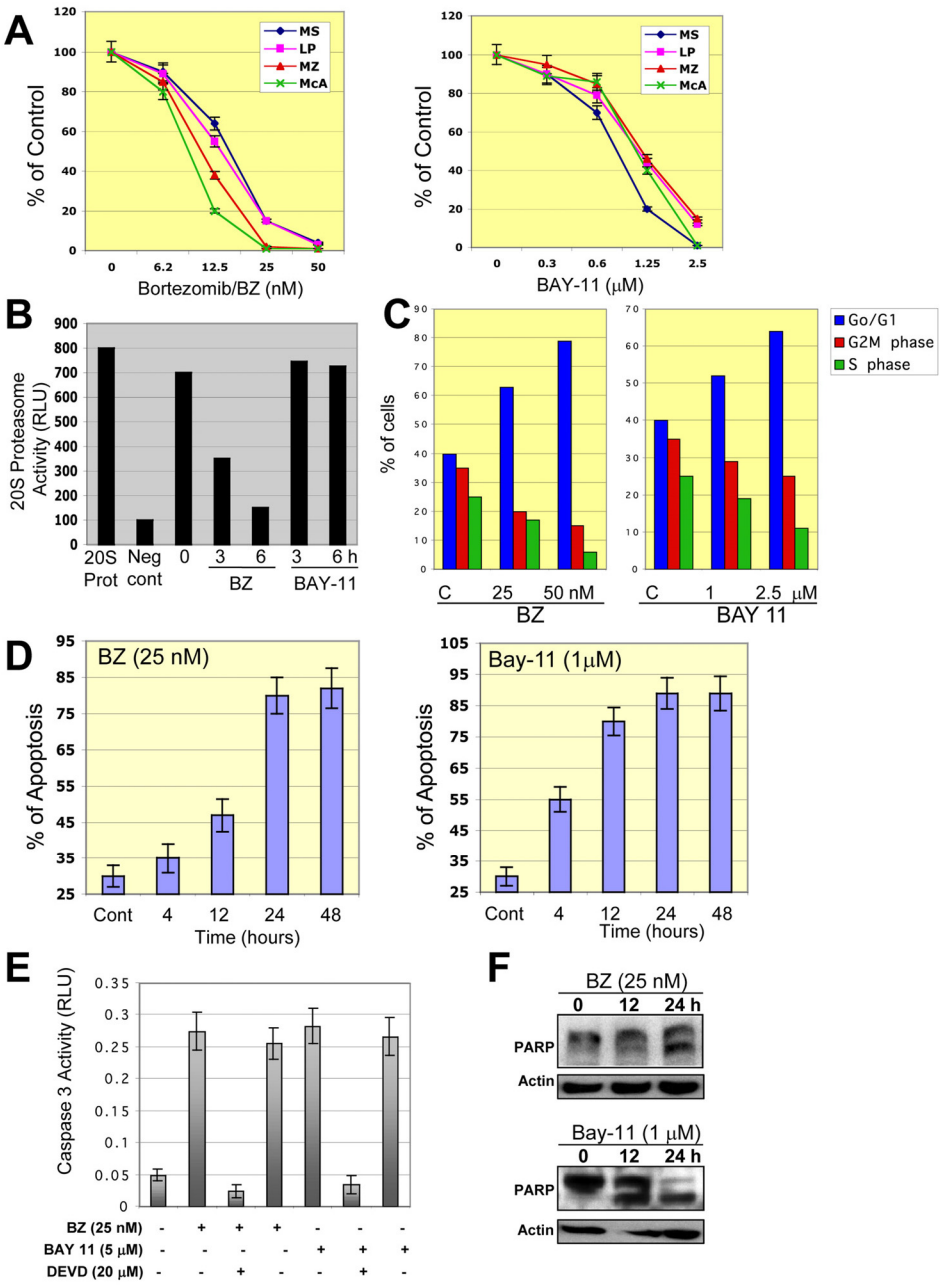

Figure 7. Inhibition of NF-κB in DLBCL cells leads to cell growth inhibition, G0/G1 cell cycle arrest, and apoptosis. (**A**) Representative ABC- and GCB-DLBCL cell lines were treated with bortezomib (BZ) or BAY-11 for 48 hours and cell proliferation was measured using 3H-thymidine incorporation assays. The percentages of growth inhibition of treated cells relative to untreated (control cells) were plotted. The data shown are the means and ranges of triplicate cultures from three independent experiments. (**B**) DLBCL-MS cells were cultured in the absence or presence of bortezomib (BZ) or BAY-11 and subjected to a 20S proteasome assay. Purified 20S proteasome was used as a positive control. **Abbreviations**: RLU, relative light unit; 20S pro, 20S proteasome, Neg Cont., negative control. (**C**) DLBCL-MS cells were cultured in the absence or presence of BZ (50 nM) or BAY-11 (1 μM) and analyzed for cell cycle profile. The percentages of cells in G0/G1, S, and G2M phases are shown. (**D**) DLBCL-MS cells were cultured in the absence or presence of BZ (50 nM) or BAY-11 (1 μM) for the indicated time points and then analyzed for apoptosis using annexin V assays. (**E**) DLBCL-MS cells were cultured in the presence of BZ (50 nM) or BAY-11 (1 μM) and in some cases with the caspase 3 inhibitor DEVD or the caspse 1 inhibitor VAD. Caspase 3 activity was measured after 24 hours of treatments. Caspase 3 activity was observed after 12 hours of treatment. **Abbreviations**: RLU, relative light units. (**F**) DLBCL-MS cells were cultured in the presence of BZ (50 nM) or BAY-11 (1 μM) for the indicated time points and cell extracts were subjected to Western blotting for a known caspase substrate, poly-(ADP-ribose) polymerase (PARP) cleavage.

analyzed the cell lysates from BZ-treated and BAY-11-treated DLBCL-MS cells to a 20S proteasome proteolysis assay, and found proteasome activity was substantially inhibited (>50%) after 3 hours of BZ treatment, whereas BAY-11 treatment did not affect proteasome activity in a similar time points (Fig. 7B). To determine whether the cell growth inhibition effects of BZ and BAY-11 involve their activity in the cell cycle regulation, we analyzed the cell cycle profile. As shown in Fig. 7C, in a representative DLBCL cell line (MS), both BZ-and BAY-11-treated DLBCL cells accumulated in the G0/G1 phase of the cell cycle, while cells in G2M and S phases were decreased. In addition, BZ or BAY-11 treatments in MS DLBCL cell line resulting in cells undergoing apoptosis in a time-dependent manner (Fig. 7D). To verify that these cells had actually undergone apoptosis, we measured the generation of caspase 3 activities. DLBCL cells treated with BZ or BAY-11 activated caspase 3 activity after 12 hours of treatment, which can be block with a caspase 3 inhibitor (DVED) but not with a caspase 1 inhibitor (VAD) (Fig. 7E). In addition, a known caspase substrate, poly-(ADP-ribose) polymerase (PARP), was cleaved after BZ or BAY-11 treatment (Fig. 7F). These experiments provide additional and interesting insights into the putative role of NF-κB in DLBCL cell proliferation and viability maintenance.

DISCUSSION

In this study we studied the significance of RelA/p65 NF-κB in DLBCL by two ways. In the first part of this study, we evaluated the prognostic significance of RelA/p65 nuclear expression in a large cohort of *de novo* DLBCL treated with R-CHOP (n = 487). Although p65 nuclear expression may not be a strong prognostic marker in overall DLBCL, we found p65 hyperactivation (IHC ≥50%) had significant adverse impact on survival of patients with stage I/II DLBCL independent of cell-of-origin and *TP53* mutation status, even though it was not associated with apparent genetic or phenotypic abnormalities, such as *TP53* mutations, *MYC*/*BCL2* translocation, and Myc/Bcl-2 overexpression.

The adverse prognostic significance of p65 hyperactivation was also seen in the GCB-DLBCL subtype overall and in the subset with wild-type *TP53*, but not in the subsets with strong unfavorable factors including advanced stages, *TP53* mutations, and ABC cell-of-origin. In addition, lower levels (10-40%) of p65 nuclear expression did not have significant prognostic impact in DLBCL. This limited significance of p65 expression in DLBCL may reflect different signaling transductions pathways activating p65, different p65 NF-κB dimers, and complicated p65 functions influenced by other factors including p53 in different stimulatory signals. For example, NF-κB p65 activation induced by cytotoxic stimuli promotes apoptosis in mouse embryo fibroblasts, which contrasts with the prosurvival function of p65 induced by inflammatory cytokines [30]. In various cancer cell lines, p65 and p53 formed p65/p53 complex and bound to DNA targets; the function of p65 and fate of tumor cells are significantly affected by p53 and stress levels [32]. Others have shown that there is transcriptional and functional crosstalk between NF-κB and p53. p53 can negatively regulate NF-κB activation by regulating *IKK1* expression [29] and suppressing glycolysis [28]; NF-κB and p53 antagonize each other's function in apoptosis, proliferation and tumor invasion that appears to depend on cellular context. Overall the results in this study suggested that p65 and wild-type p53 counter-acted each other in DLBCL, and that the inhibition of p53 tumor suppressor function by p65 hyperactivation had a significant adverse impact on clinical outcomes.

GEP suggested that BCR, TNF, TLR, and mitogen-activated protein kinase signaling pathways were all implicated in p65 hyperactivation in DLBCL. These upstream pathways were activated preferably in ABC-DLBCL or GCB-DLBCL, and correspondingly, resulting in different downstream pathways in ABC and GCB subtypes. In ABC-DLBCL, $p65^{high}$ GEP signatures were featured by proliferation and anti-apoptosis, whereas in GCB-DLBCL in which subgroup p65 hyperactivation showed significant adverse prognostic impact, $p65^{high}$ expression was accompanied with upregulation of some pro-apoptosis genes as well as many immune genes. Upregulation of *LILRB1* and *CD163* in $p65^{high}$ patients suggested immune suppression and dysregulation, which may contribute to the associated poor prognosis.

In the second part of this study, we tested whether NF-κB p65 subunit in particular is a potential molecular target by the proteasome inhibitor bortezomib and the small molecule NF-κB inhibitor BAY-11 *in vitro*. Previous studies have shown that proteasome inhibitors have better antitumor efficacy in patients with ABC-DLBCL than in patients with GCB-DLBCL, probably due to higher p65 expression in the ABC subtype [45, 48, 52]. Consistently, our GEP analysis also found the proteasome gene *PSMB1* was upregulated in ABC-DLBCL. Our *in vitro* experiments found that these anti-NF-κB agents can effectively inhibit p65 protein expression and DNA binding activity, leading to cell cycle arrest, decreased cell proliferation, and apoptosis induction in both GCB and ABC types of p65-overexpressing DLBCL cell lines. Intriguingly, representative DLBCL cell lines with mutated p53 are more sensitive to p65 shRNA targeting approach as compared to a cell line with wild-type p53, opposite the

prognostic effects observed in the DLBCL study cohort. These findings may suggested that although p65 subunit only manifested prognostic significance in certain DLBCL subsets due to the complexity of NF-κB dimers and activating mechanisms, *in vitro* experiments nonetheless demonstrated that NF-κB overexpressing DLBCL cells were addictive to NF-κB and vulnerable for NF-κB inhibitors. This vulnerability of DLBCL cells was also apparent in the context of mutated p53; p65 may have an important role in the oncogenic activities of mutated p53 in DLBCL. Importantly, *in vitro* p65 subunit stood out as a critical factor in controlling cell growth and survival and showed the most sensitivity to molecular and pharmacological inhibition of NF-κB activation. Therefore, our current study in both patient samples and DLBCL cell lines provided additional insights into the putative roles of NF-κB p65 in immune regulation, DLBCL cell proliferation, and viability maintenance, and the utility of p65 as a biomarker to stratify DLBCL patients to receive alternative therapeutic regimens including agents targeting NF-κB [52]. However, these findings warrant further investigation and validation in more representative DLBCL cell lines as well as primary DLBCL cells.

In summary, we provide clinical and experimental data that RelA/p65 NF-κB has prognostic and therapeutic value in DLBCL. High p65 nuclear expression is a significant adverse biomarker in patients with early-stage (I/II) DLBCL. Pharmacological p65 inactivation effectively inhibited cell growth and survival in both GCB-DLBCL and ABC-DLBCL cell lines with p65 hyperactivation.

METHODS

Patients

The study cohort included 487 patients with *de novo* DLBCL treated with R-CHOP, as part of the International DLBCL R-CHOP Consortium Program. All patients were diagnosed as DLBCL between 2001 and 2012 according to the World Health Organization classification criteria, and did not have a history of low-grade B-cell lymphoma, primary mediastinal, cutaneous, central nervous system DLBCL, or human immunodeficiency virus infection. Informed consent was obtained from all patients. This study was conducted in accordance with the Helsinki Declaration and was approved by the Institutional Review Boards of all participating centers. GCB/ABC subtype classification by GEP or immuno-histochemistry algorithms [49], and *TP53* mutation detection using p53 AmpliChip [39] have been described previously. Overall survival (OS) was calculated from the date of diagnosis to the date of death from any cause or the date of last follow-up for censored patients. Progression-free survival (PFS) was calculated from the date of diagnosis to the date of disease progression, recurrence, or patient death from any cause. Survival analysis was performed using the Kaplan-Meier method and the log-rank (Mantel-Cox) test. The clinical features of DLBCL patients with high or low levels of p65 at the time of presentation were compared using the chi-square test. Univariate survival analysis was performed using the GraphPad Prism 6 (GraphPad Software, San Diego, CA). Multivariate survival analysis was performed using the Cox regression model and SPSS software (version 19.0; IBM Corporation, Armonk, NY). *P* values ≤0.05 were considered statistically significant.

Immunohistochemical staining

Immunohistochemistry for p65 and other NF-κB subunits using specific antibodies (Abcam, Cambridge, MA) was performed on tissue microarrays of formalin-fixed, paraffin-embedded lymphoma samples using methods described previously [10, 49]. The immuno-histochemical stains were assessed in 10% increments by three pathologists blinded to the clinical outcomes. Disagreements about the percentage of positive cells were resolved by joint review at a multi-headed microscope.

Gene expression profiling

GEP was performed using the Affymetrix GeneChip Human Genome U133 Plus 2.0 array (Santa Clara, CA) and CEL files were deposited in the NCBI Gene Expression Omnibus repository (GSE#31312) [49]. GEP were available for 444 DLBCL patients of this study cohort with high or low levels of p65 nuclear expression. The *P* values for differential expression obtained via multiple *t*-tests were corrected for false discovery rates using the beta-uniform mixture method.

In vitro studies

Cell lines

Human DLBCL cell lines MS (mutated *TP53*) and DB (wild-type for p53) (GCB subtype), as well as LP (mutated *TP53*) and HB (mutated *TP53*) (ABC subtype) were previously characterized and described [44, 50]. The DLBCL cells were cultured in Roswell Park Memorial Institute medium (Life Technologies, Carlsbad, CA) containing 15% fetal calf serum and 1% penicillin/streptomycin (HyClone Laboratories, Logan, UT).

Antibodies and small hairpin RNA plasmids

The following primary antibodies were used: p50, p65, c-Rel and p52 (Millipore, Billerica, MA), and RelB

(Santa Cruz Biotechnology, Santa Cruz, CA). The SureSilencing small hairpin RNA (shRNA) green fluorescent protein (GFP)–based plasmids for the NF-κB subunits p52, p65, c-Rel, and RelB were purchased from SuperArray Biosciences (Frederick, MD). pCMV-IκBαM and control vectors were purchased from Clontech Laboratories (Mountain View, CA).

Transfection

Transfection experiments in DLBCL cells with validated green fluorescent protein (GFP)-shRNAs were performed *in vitro* in representative transfectable DLBCL cells, using the Neon transfection system from Invitrogen (Life Technologies Corporation, Grand Island, NY) as described previously [44], and were repeated at least twice to verify reproducible experimental results. Twenty-four hours after transfection, GFP^+ cells were sorted by a fluorescence-activated cell sorter (FACS) flow cytometer and plated. Cell proliferation was measured 96 hours after sorting by thymidine incorporation assays, while some cells were lysed for Western blot analysis for NF-κB subunit inhibition. A set of four shRNA plasmids for each NF-κB subunit was tested and the optimal (>75%) gene knock-down shRNA plasmid was selected.

Therapeutic NF-κB inhibition experiment

DLBCL cells were treated with increasing doses of bortezomib (0–50 nM), or organic compounds BAY 11-7082/BAY-11 (1μM) for 6-48 hours and subjected to cell proliferation assays, electromobility gel shift assay (EMSA), immunofluorescence, apoptosis detection assay, and cell cycle analysis according to the manufacturer's instructions or procedures as previously described [51]. Data are representative of three independent experiments.

Thymidine incorporation assays

In vitro thymidine incorporation proliferation assays were performed as described previously [1]. Briefly, cells were plated (in triplicate) at 4.0×10^4 cells/well in 200 μl of RPMI 1640 with 10% FCS and the indicated reagents in a 96-well plate and incubated in 5% CO_2 at 37°C. After 72 h, each well was pulsed with 0.5 μCi/10 μl of [^{3}H]thymidine (Amersham, Arlington Heights, IL) for 16 h. Cells were harvested and the radioactivity was measured.

CONFLICTS OF INTEREST

KHY receives research support from Roche Molecular System, Gilead Sciences Pharmaceutical, Seattle Genetics, Dai Sanyo Pharmaceutical, Adaptive Biotechnology, Incyte Pharmaceutical, and HTG Molecular Diagnostics. EDH is a Consultant for HTG Molecular Diagnostics. BMP joins speakers Burea for Celgene and Amgen, and a Consultant for Celgene.

FUNDING

The work was supported by the National Cancer Institute/National Institutes of Health (R01CA138688, R01CA187415, and 1RC1CA146299 to KHY). This work was also partially supported by NSFC (81570203 to MZ and 81570204 to LL), the National Cancer Institute and National Institutes of Health grants P50CA136411 and P50CA142509, and by MD Anderson's Cancer Center Support Grant CA016672. MZ is the recipient of professorship award. KHY is also supported by The University of Texas MD Anderson Cancer Center Institutional Research and Development Fund, an Institutional Research Grant Award, an MD Anderson Cancer Center Lymphoma Specialized Programs on Research Excellence (SPORE) Research Development Program Award, an MD Anderson Cancer Center Myeloma SPORE Research Development Program Award, a Gundersen Lutheran Medical Foundation Award, the University Cancer Foundation via the Sister institution network Fund at The University of Texas MD Anderson Cancer Cancer and is partially supported by grants from the National Cancer Institute/National Institutes of Health (P50CA136411 and P50CA142509).

REFERENCES

1. Abramson JS, Shipp MA. Advances in the biology and therapy of diffuse large B-cell lymphoma: moving toward a molecularly targeted approach. Blood. 2005; 106:1164–74. doi: 10.1182/blood-2005-02-0687

2. Sehn LH, Donaldson J, Chhanabhai M, Fitzgerald C, Gill K, Klasa R, MacPherson N, O'Reilly S, Spinelli JJ, Sutherland J, Wilson KS, Gascoyne RD, Connors JM. Introduction of combined CHOP plus rituximab therapy dramatically improved outcome of diffuse large B-cell lymphoma in British Columbia. J Clin Oncol. 2005; 23:5027–33. doi: 10.1200/JCO.2005.09.137

3. Alizadeh AA, Eisen MB, Davis RE, Ma C, Lossos IS, Rosenwald A, Boldrick JC, Sabet H, Tran T, Yu X, Powell JI, Yang L, Marti GE, et al. Distinct types of diffuse large B-cell lymphoma identified by gene expression profiling. Nature. 2000; 403:503–11. doi: 10.1038/35000501

4. Davis RE, Brown KD, Siebenlist U, Staudt LM. Constitutive nuclear factor kappaB activity is required for survival of activated B cell-like diffuse large B cell

lymphoma cells. J Exp Med. 2001; 194:1861–74. doi: 10.1084/jem.194.12.1861

5. Kloo B, Nagel D, Pfeifer M, Grau M, Düwel M, Vincendeau M, Dörken B, Lenz P, Lenz G, Krappmann D. Critical role of PI3K signaling for NF-kappaB-dependent survival in a subset of activated B-cell-like diffuse large B-cell lymphoma cells. Proc Natl Acad Sci USA. 2011; 108:272–77. doi: 10.1073/pnas.1008969108

6. Roschewski M, Staudt LM, Wilson WH. Diffuse large B-cell lymphoma-treatment approaches in the molecular era. Nat Rev Clin Oncol. 2014; 11:12–23. doi: 10.1038/nrclinonc.2013.197

7. Ben-Neriah Y, Karin M. Inflammation meets cancer, with NF-κB as the matchmaker. Nat Immunol. 2011; 12:715–23. doi: 10.1038/ni.2060

8. Odqvist L, Montes-Moreno S, Sánchez-Pacheco RE, Young KH, Martín-Sánchez E, Cereceda L, Sánchez-Verde L, Pajares R, Mollejo M, Fresno MF, Mazorra F, Ruíz-Marcellán C, Sánchez-Beato M, Piris MA. NFκB expression is a feature of both activated B-cell-like and germinal center B-cell-like subtypes of diffuse large B-cell lymphoma. Mod Pathol. 2014; 27:1331–37. doi: 10.1038/modpathol.2014.34

9. Espinosa I, Briones J, Bordes R, Brunet S, Martino R, Sureda A, Sierra J, Prat J. Activation of the NF-kappaB signalling pathway in diffuse large B-cell lymphoma: clinical implications. Histopathology. 2008; 53:441–49. doi: 10.1111/j.1365-2559.2008.03139.x

10. Ok CY, Xu-Monette ZY, Li L, Manyam GC, Montes-Moreno S, Tzankov A, Visco C, Dybkær K, Routbort MJ, Zhang L, Chiu A, Orazi A, Zu Y, et al. Evaluation of NF-κB subunit expression and signaling pathway activation demonstrates that p52 expression confers better outcome in germinal center B-cell-like diffuse large B-cell lymphoma in association with CD30 and BCL2 functions. Mod Pathol. 2015; 28:1202–13. doi: 10.1038/modpathol.2015.76

11. Oeckinghaus A, Ghosh S. The NF-kappaB family of transcription factors and its regulation. Cold Spring Harb Perspect Biol. 2009; 1:a000034. doi: 10.1101/cshperspect.a000034

12. Davis RE, Ngo VN, Lenz G, Tolar P, Young RM, Romesser PB, Kohlhammer H, Lamy L, Zhao H, Yang Y, Xu W, Shaffer AL, Wright G, et al. Chronic active B-cell-receptor signalling in diffuse large B-cell lymphoma. Nature. 2010; 463:88–92. doi: 10.1038/nature08638

13. Wan F, Lenardo MJ. The nuclear signaling of NF-kappaB: current knowledge, new insights, and future perspectives. Cell Res. 2010; 20:24–33. doi: 10.1038/cr.2009.137

14. Scheidereit C. IkappaB kinase complexes: gateways to NF-kappaB activation and transcription. Oncogene. 2006; 25:6685–705. doi: 10.1038/sj.onc.1209934

15. Chen FE, Huang DB, Chen YQ, Ghosh G. Crystal structure of p50/p65 heterodimer of transcription factor NF-kappaB bound to DNA. Nature. 1998; 391:410–13. doi: 10.1038/34356

16. Schmidt-Ullrich R, Mémet S, Lilienbaum A, Feuillard J, Raphaël M, Israel A. NF-kappaB activity in transgenic mice: developmental regulation and tissue specificity. Development. 1996; 122:2117–28.

17. Geymayer S, Doppler W. Activation of NF-kappaB p50/p65 is regulated in the developing mammary gland and inhibits STAT5-mediated beta-casein gene expression. FASEB J. 2000; 14:1159–70.

18. Li L, Xu-Monette ZY, Ok CY, Tzankov A, Manyam GC, Sun R, Visco C, Zhang M, Montes-Moreno S, Dybkaer K, Chiu A, Orazi A, Zu Y, et al. Prognostic impact of c-Rel nuclear expression and REL amplification and crosstalk between c-Rel and the p53 pathway in diffuse large B-cell lymphoma. Oncotarget. 2015; 6:23157–80. doi: 10.18632/oncotarget.4319

19. Ganchi PA, Sun SC, Greene WC, Ballard DW. A novel NF-kappa B complex containing p65 homodimers: implications for transcriptional control at the level of subunit dimerization. Mol Cell Biol. 1993; 13:7826–35. doi: 10.1128/MCB.13.12.7826

20. Chen YQ, Sengchanthalangsy LL, Hackett A, Ghosh G. NF-kappaB p65 (RelA) homodimer uses distinct mechanisms to recognize DNA targets. Structure. 2000; 8:419–28. doi: 10.1016/S0969-2126(00)00123-4

21. Tsui R, Kearns JD, Lynch C, Vu D, Ngo KA, Basak S, Ghosh G, Hoffmann A. IκBβ enhances the generation of the low-affinity NFκB/RelA homodimer. Nat Commun. 2015; 6:7068. doi: 10.1038/ncomms8068

22. Kim HJ, Hawke N, Baldwin AS. NF-kappaB and IKK as therapeutic targets in cancer. Cell Death Differ. 2006; 13:738–47. doi: 10.1038/sj.cdd.4401877

23. Baldwin AS. Control of oncogenesis and cancer therapy resistance by the transcription factor NF-kappaB. J Clin Invest. 2001; 107:241–46. doi: 10.1172/JCI11991

24. Gasparini C, Celeghini C, Monasta L, Zauli G. NF-kappaB pathways in hematological malignancies. Cellular and molecular life sciences. Cell Mol Life Sci. 2014; 71:2083–102. doi: 10.1007/s00018-013-1545-4

25. Tergaonkar V, Pando M, Vafa O, Wahl G, Verma I. p53 stabilization is decreased upon NFkappaB activation: a role for NFkappaB in acquisition of resistance to chemotherapy. Cancer Cell. 2002; 1:493–503.

doi: 10.1016/S1535-6108(02)00068-5

26. Ak P, Levine AJ. p53 and NF-κB: different strategies for responding to stress lead to a functional antagonism. FASEB J. 2010; 24:3643–52. doi: 10.1096/fj.10-160549

27. Huang WC, Ju TK, Hung MC, Chen CC. Phosphorylation of CBP by IKKalpha promotes cell growth by switching the binding preference of CBP from p53 to NF-kappaB. Mol Cell. 2007; 26:75–87. doi: 10.1016/j.molcel.2007.02.019

28. Kawauchi K, Araki K, Tobiume K, Tanaka N. p53 regulates glucose metabolism through an IKK-NF-kappaB pathway and inhibits cell transformation. Nat Cell Biol. 2008; 10:611–18. doi: 10.1038/ncb1724

29. Gu L, Zhu N, Findley HW, Woods WG, Zhou M. Identification and characterization of the IKKalpha promoter: positive and negative regulation by ETS-1 and p53, respectively. J Biol Chem. 2004; 279:52141–49. doi: 10.1074/jbc.M407915200

30. Campbell KJ, Rocha S, Perkins ND. Active repression of antiapoptotic gene expression by RelA(p65) NF-kappa B. Mol Cell. 2004; 13:853–65. doi: 10.1016/S1097-2765(04)00131-5

31. Bohuslav J, Chen LF, Kwon H, Mu Y, Greene WC. p53 induces NF-kappaB activation by an IkappaB kinase-independent mechanism involving phosphorylation of p65 by ribosomal S6 kinase 1. J Biol Chem. 2004; 279:26115–25. doi: 10.1074/jbc.M313509200

32. Schneider G, Henrich A, Greiner G, Wolf V, Lovas A, Wieczorek M, Wagner T, Reichardt S, von Werder A, Schmid RM, Weih F, Heinzel T, Saur D, Krämer OH. Cross talk between stimulated NF-kappaB and the tumor suppressor p53. Oncogene. 2010; 29:2795–806. doi: 10.1038/onc.2010.46

33. Lowe JM, Menendez D, Bushel PR, Shatz M, Kirk EL, Troester MA, Garantziotis S, Fessler MB, Resnick MA. p53 and NF-κB coregulate proinflammatory gene responses in human macrophages. Cancer Res. 2014; 74:2182–92. doi: 10.1158/0008-5472.CAN-13-1070

34. Zhao Q, Fu W, Jiang H, Du J, Zhang C, Xi H, Zhou F, Li R, Hou J. Clinicopathological implications of nuclear factor κB signal pathway activation in diffuse large B-cell lymphoma. Hum Pathol. 2015; 46:524–31. doi: 10.1016/j.humpath.2014.06.032

35. Bavi P, Uddin S, Bu R, Ahmed M, Abubaker J, Balde V, Qadri Z, Ajarim D, Al-Dayel F, Hussain AR, Al-Kuraya KS. The biological and clinical impact of inhibition of NF-κB-initiated apoptosis in diffuse large B cell lymphoma (DLBCL). J Pathol. 2011; 224:355–66. doi: 10.1002/path.2864

36. Hu CR, Wang JH, Wang R, Sun Q, Chen LB. Both FOXP1 and p65 expression are adverse risk factors in diffuse large B-cell lymphoma: a retrospective study in China. Acta Histochem. 2013; 115:137–43. doi: 10.1016/j.acthis.2012.06.001

37. Shaffer AL 3rd, Young RM, Staudt LM. Pathogenesis of human B cell lymphomas. Annu Rev Immunol. 2012; 30:565–610. doi: 10.1146/annurev-immunol-020711-075027

38. Staudt LM. Oncogenic activation of NF-kappaB. Cold Spring Harb Perspect Biol. 2010; 2:a000109. doi: 10.1101/cshperspect.a000109

39. Xu-Monette ZY, Wu L, Visco C, Tai YC, Tzankov A, Liu WM, Montes-Moreno S, Dybkaer K, Chiu A, Orazi A, Zu Y, Bhagat G, Richards KL, et al. Mutational profile and prognostic significance of TP53 in diffuse large B-cell lymphoma patients treated with R-CHOP: report from an International DLBCL Rituximab-CHOP Consortium Program Study. Blood. 2012; 120:3986–96. doi: 10.1182/blood-2012-05-433334

40. Hu S, Xu-Monette ZY, Tzankov A, Green T, Wu L, Balasubramanyam A, Liu WM, Visco C, Li Y, Miranda RN, Montes-Moreno S, Dybkaer K, Chiu A, et al. MYC/BCL2 protein coexpression contributes to the inferior survival of activated B-cell subtype of diffuse large B-cell lymphoma and demonstrates high-risk gene expression signatures: a report from The International DLBCL Rituximab-CHOP Consortium Program. Blood. 2013; 121:4021–31. doi: 10.1182/blood-2012-10-460063

41. Tzankov A, Xu-Monette ZY, Gerhard M, Visco C, Dirnhofer S, Gisin N, Dybkaer K, Orazi A, Bhagat G, Richards KL, Hsi ED, Choi WW, van Krieken JH, et al. Rearrangements of MYC gene facilitate risk stratification in diffuse large B-cell lymphoma patients treated with rituximab-CHOP. Mod Pathol. 2014; 27:958–71. doi: 10.1038/modpathol.2013.214

42. Xu-Monette ZY, Dabaja BS, Wang X, Tu M, Manyam GC, Tzankov A, Xia Y, Zhang L, Sun R, Visco C, Dybkaer K, Yin L, Chiu A, et al. Clinical features, tumor biology, and prognosis associated with MYC rearrangement and Myc overexpression in diffuse large B-cell lymphoma patients treated with rituximab-CHOP. Mod Pathol. 2015; 28:1555–73. doi: 10.1038/modpathol.2015.118

43. Obata Y, Furusawa Y, Endo TA, Sharif J, Takahashi D, Atarashi K, Nakayama M, Onawa S, Fujimura Y, Takahashi M, Ikawa T, Otsubo T, Kawamura YI, et al. The epigenetic regulator Uhrf1 facilitates the proliferation and maturation of colonic regulatory T cells. Nat Immunol. 2014; 15:571–79. doi: 10.1038/ni.2886

44. Pham LV, Fu L, Tamayo AT, Bueso-Ramos C, Drakos E, Vega F, Medeiros LJ, Ford RJ. Constitutive BR3 receptor signaling in diffuse, large B-cell lymphomas stabilizes nuclear factor-κB-inducing kinase while activating both canonical and alternative nuclear factor-κB pathways. Blood. 2011; 117:200–10. doi: 10.1182/blood-2010-06-290437

45. Dunleavy K, Pittaluga S, Czuczman MS, Dave SS, Wright G, Grant N, Shovlin M, Jaffe ES, Janik JE, Staudt LM, Wilson WH. Differential efficacy of bortezomib plus chemotherapy within molecular subtypes of diffuse large B-cell lymphoma. Blood. 2009; 113:6069–76. doi: 10.1182/blood-2009-01-199679

46. Mori N, Yamada Y, Ikeda S, Yamasaki Y, Tsukasaki K, Tanaka Y, Tomonaga M, Yamamoto N, Fujii M. Bay 11-7082 inhibits transcription factor NF-kappaB and induces apoptosis of HTLV-I-infected T-cell lines and primary adult T-cell leukemia cells. Blood. 2002; 100:1828–34. doi: 10.1182/blood-2002-01-0151

47. Buhrmann C, Mobasheri A, Busch F, Aldinger C, Stahlmann R, Montaseri A, Shakibaei M. Curcumin modulates nuclear factor kappaB (NF-kappaB)-mediated inflammation in human tenocytes in vitro: role of the phosphatidylinositol 3-kinase/Akt pathway. J Biol Chem. 2011; 286:28556–66. doi: 10.1074/jbc.M111.256180

48. Wilson WH. Treatment strategies for aggressive lymphomas: what works? Hematology (Am Soc Hematol Educ Program). 2013; 2013:584–90. doi: 10.1182/asheducation-2013.1.584

49. Visco C, Li Y, Xu-Monette ZY, Miranda RN, Green TM, Li Y, Tzankov A, Wen W, Liu WM, Kahl BS, d'Amore ES, Montes-Moreno S, Dybkær K, et al. Comprehensive gene expression profiling and immunohistochemical studies support application of immunophenotypic algorithm for molecular subtype classification in diffuse large B-cell lymphoma: a report from the International DLBCL Rituximab-CHOP Consortium Program Study. Leukemia. 2012; 26:2103–13. doi: 10.1038/leu.2012.83

50. Pham LV, Tamayo AT, Li C, Bueso-Ramos C, Ford RJ. An epigenetic chromatin remodeling role for NFATc1 in transcriptional regulation of growth and survival genes in diffuse large B-cell lymphomas. Blood. 2010; 116:3899–906. doi: 10.1182/blood-2009-12-257378

51. Pham LV, Tamayo AT, Yoshimura LC, Lo P, Ford RJ. Inhibition of constitutive NF-kappa B activation in mantle cell lymphoma B cells leads to induction of cell cycle arrest and apoptosis. J Immunol. 2003; 171:88–95. doi: 10.4049/jimmunol.171.1.88

52. Yu L, Li L, Medeiros LJ, Young KH. NF-κB signaling pathway and its potential as a target for therapy in lymphoid neoplasms. Blood Rev. 2016S0268-960X(16)30046-7.

Research Paper

Discovery of piperlongumine as a potential novel lead for the development of senolytic agents

Yingying Wang[1,2], Jianhui Chang[1,2], Xingui Liu[1], Xuan Zhang[1], Suping Zhang[1,2], Xin Zhang[1,2], Daohong Zhou[1,2], Guangrong Zheng[1]

[1]Department of Pharmaceutical Sciences, College of Pharmacy, University of Arkansas for Medical Sciences, Little Rock, AR 72205, USA
[2]Winthrop P. Rockefeller Cancer Institute, University of Arkansas for Medical Sciences, Little Rock, AR 72205, USA

Correspondence to: Daohong Zhou, Guangrong Zheng; **email:** dzhou@uams.edu, gzheng@uams.edu
Keywords: piperlongumine, aging, senescent cells, senolytic agents, ABT-263, reactive oxygen species, synergistic effect
Received: July 13, 2016 **Accepted:** November 4, 2016 **Published:** November 19, 2016 DOI: 10.18632/aging.101100

ABSTRACT

Accumulating evidence indicates that senescent cells play an important role in many age-associated diseases. The pharmacological depletion of senescent cells (SCs) with a "senolytic agent", a small molecule that selectively kills SCs, is a potential novel therapeutic approach for these diseases. Recently, we discovered ABT-263, a potent and highly selective senolytic agent, by screening a library of rationally-selected compounds. With this screening approach, we also identified a second senolytic agent called piperlongumine (PL). PL is a natural product that is reported to have many pharmacological effects, including anti-tumor activity. We show here that PL preferentially killed senescent human WI-38 fibroblasts when senescence was induced by ionizing radiation, replicative exhaustion, or ectopic expression of the oncogene *Ras*. PL killed SCs by inducing apoptosis, and this process did not require the induction of reactive oxygen species. In addition, we found that PL synergistically killed SCs in combination with ABT-263, and initial structural modifications to PL identified analogs with improved potency and/or selectivity in inducing SC death. Overall, our studies demonstrate that PL is a novel lead for developing senolytic agents.

INTRODUCTION

Cellular senescence, an essentially irreversible arrest of cell proliferation, can be triggered when cells experience a potential risk for malignant transformation due to the activation of oncogenes and/or DNA damage [1-7]. While eliminating aged or damaged cells by inducing senescence is an effective barrier to tumorigenesis, the accumulation of senescent cells (SCs) over time compromises normal tissue function and contributes to aging and the development of age-associated diseases [6, 8, 9]. Often, SCs secrete a broad spectrum of pro-inflammatory cytokines, chemokines, growth factors, and extracellular matrix proteases, a feature collectively termed the senescence-associated secretory phenotype. These factors degrade the local tissue environment and induce inflammation in various tissues and organs if SCs are not effectively cleared by immune system [6, 8-11].

Studies have shown that the genetic clearance of SCs extends the lifespan of mice and delays the onset of several age-associated diseases in both progeroid and naturally-aged mice [12-15]. It has also been shown that rapamycin and metformin increase lifespan in mice and marmoset monkeys, by suppressing the induction of senescence [16-20]. These findings support the hypothesis that SCs play a causative role in aging and age-associated diseases [6, 21, 22] and, importantly, highlight the tremendous therapeutic potential of pharmacologically targeting SCs [23, 24]. Consistent with these findings, we have shown that ABT-263 (navitoclax), an inhibitor of the antiapoptotic Bcl-2 family proteins, acts as a potent senolytic agent to deplete SCs *in vivo* and functionally rejuvenates hematopoietic stem cells in both sublethally irradiated and naturally-aged mice [25]. Complementary studies from other labs have confirmed that the Bcl-2 protein

family is a promising molecular target for the development of senolytic drugs [26, 27]. These studies further establish the concept that the pharmacological depletion of SCs is a promising, novel approach for treating age-associated diseases [28].

ABT-263 was identified by screening a small library of structurally diverse, rationally-selected small molecules that target pathways predicted to be important for SC survival [25]. By titrating their cytotoxicity against normal human WI-38 fibroblasts and ionizing radiation (IR)-induced senescent WI-38 fibroblasts, this targeted screen also identified the promising senolytic agent piperlongumine (PL, Fig. 1A); PL is a natural product isolated from a variety of species in the genus Piper [29]. Here, we report the characterization of PL as a potential novel lead for the development of senolytic agents.

RESULTS

Piperlongumine is a potential senolytic agent

Because we identified PL as a potential senolytic agent by screening a library of rationally-selected compounds with IR-induced senescent WI-38 fibroblasts, we tested its ability to selectively kill senescent human WI-38 fibroblasts induced by different means. PL exhibited moderate selectivity in reducing the viability of IR-induced WI-38 SCs (IR-SCs) compared to non-senescent WI-38 cells (NCs) (Fig. 1B and Table 1), and PL induced cell death in a time-dependent manner (Fig. 1C). We also assessed the survival of WI-38 cells in which senescence was induced by replicative exhaustion or by ectopic expression of the oncogene *Ras* (Fig. 1B). Replicative WI-38 SCs, which were previously

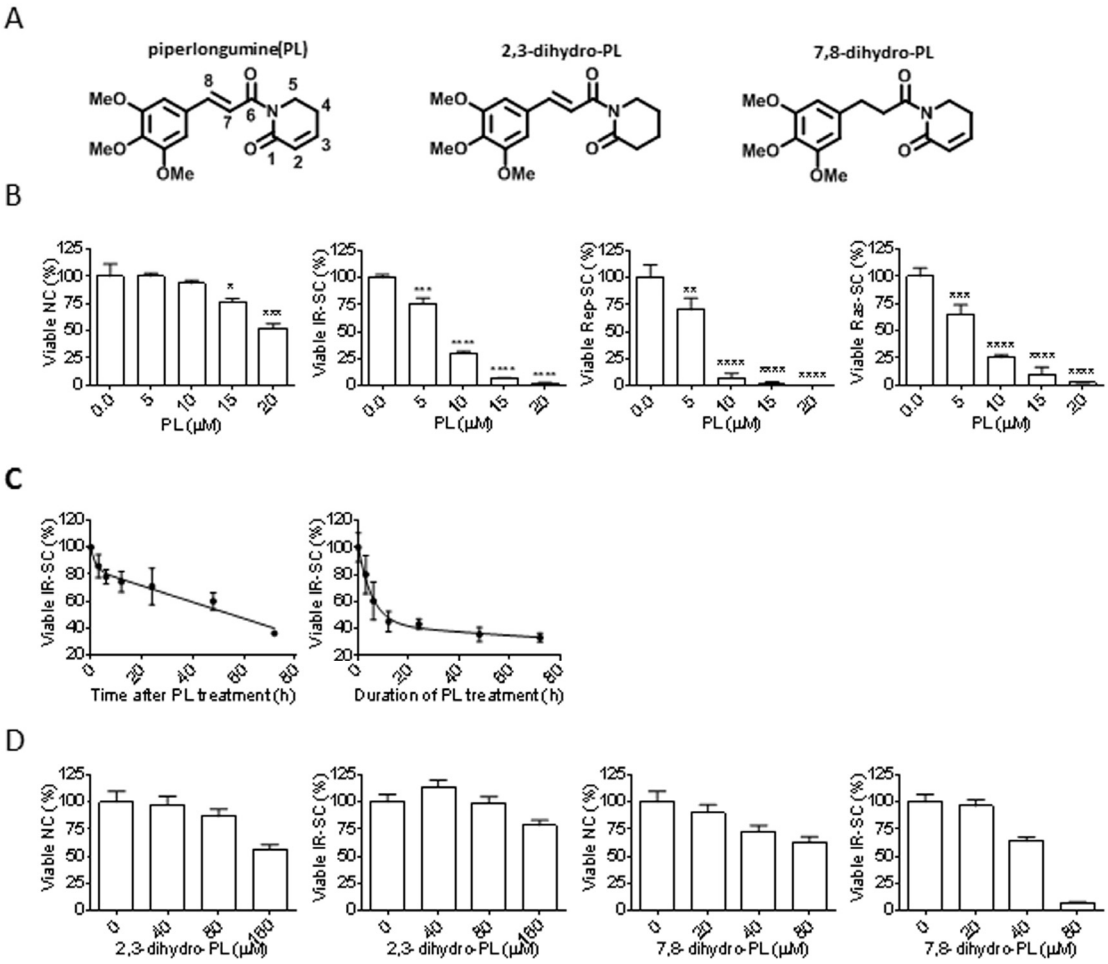

Figure 1. Senolytic activity of piperlongumine (PL). (**A**) Structures of PL, 2,3-dihydro-PL, and 7,8-dihydro-PL. (**B**) Quantification of viable WI-38 non-senescent cells (NC), IR-induced senescent cells (IR-SC), replication-exhausted senescent cells (Rep-SC), or Ras-induced senescent cells (Ras-SC) 72 h after treatment with increasing concentrations of PL (n = 3). (**C**) Quantification of viable IR-SCs over time after treatment with 10 μM PL (left) or after incubation with 10 μM PL, removal of the drug, and further culture for 72 h (right) (n = 3). (**D**) Quantification of viable WI-38 NCs and IR-SCs 72 h after treatment with increasing concentrations of 2,3-dihydro-PL or 7,8-dihydro-PL (n = 3). Data are represented as the mean ± SEM.

shown to be more resistant to ABT-263 [25], were slightly more sensitive to PL (Fig. 1B) than IR- and Ras-induced SCs. The mechanisms underlying the difference of SCs induced by different stimuli have yet to be elucidated.

Table 1. EC_{50} values and selectivity of PL in WI-38 cells

Cell types	EC_{50} (μM)	EC_{50} Ratio (NC/SC)
NC	20.28	-
IR-SC	7.97	2.54
Rep-SC	6.24	3.25
Ras-SC	7.09	2.86

Structurally, PL contains two electrophiles, the C2-C3 and C7-C8 α,β-unsaturated imides, both of which are important for the toxicity of PL in cancer cells [30]. Thus, we investigated whether the integrity of the two-electrophile system was also important for the ability of PL to kill SCs. Consistent with the findings in cancer cells, 2,3-dihydro-PL and 7,8-dihydro-PL (Figure 1A), in which the C2-C3 olefin or the C7-C8 olefin was saturated, respectively, showed little or no senolytic activity toward IR-SCs (Fig. 1D).

Piperlongumine induces apoptosis in SCs

Next, we investigated the mechanism by which PL selectively kills SCs. Because PL induces apoptosis in cancer cells [31-41], we hypothesized that the same is true for SCs. We used Annexin V and propidium iodide staining and subsequent fluorescence-activated cell sorting to detect apoptosis, respectively, in senescent WI-38 cells. PL treatment increased the number of Annexin-V-positive cells in SCs by 5.5-fold when compared to the vehicle group (Fig. 2A). To further confirm that PL killed cells by apoptosis, we treated IR-induced WI-38 SCs with the pan-caspase inhibitor Q-VD-OPh (QVD) [42] to inhibit apoptosis. Ten μM QVD, in the presence of PL, significantly reduced apoptosis and partially rescued SCs from PL-induced death (Fig. 2A, B). In addition, western blot analysis showed elevated levels of activated caspase-3 and degradation of poly(ADP-ribose) polymerase (PARP) in PL-treated IR-SCs (Fig. 2C), confirming the apoptotic cell-death mechanism. Furthermore, PL had no effect on the levels of receptor-interacting protein kinase 1 and 3 (RIP1 and RIP3), indicating that PL did not induce necroptosis in IR-SCs (Fig. 2D) [43].

Piperlongumine kills senescent cells through an ROS-independent mechanism

Initially, PL has been proposed to selectively induce cancer cell death by increasing reactive oxygen species (ROS) production, based on the observation that PL elevates cellular ROS levels in various cancer cells, but not in normal cells [31]. However, structural modifications to PL have revealed that there is no correlation between a PL analog's ability to increase ROS and its toxicity toward cancer cells, leading to the conclusion that ROS-independent mechanisms are also involved in cancer cell death [30]. We hypothesized that the same scenario is true for the PL-induced killing of SCs. We used the non-fluorescent ROS indicator dihydrorhodamine 123 (DHR 123), which can passively diffuse across membranes where it is oxidized to green fluorescent rhodamine 123 in the presence of ROS, and flow cytometry to determine if PL increased ROS in IR-SCs. Treatment with 10 μM PL for 6 or 24 h significantly elevated ROS levels in IR-SCs compared to vehicle-treated IR-SCs or non-senescent WI-38 cells with PL treatment, whereas IR-SCs have a higher baseline level of ROS (Fig. 3A). In addition, similar to the results obtained in cancer cells [31, 33-35, 41, 44-47], co-treatment with 2 mM N-acetyl-L-cysteine (NAC), an antioxidant, fully reversed PL-induced ROS elevation and cell death (Fig. 3B), suggesting that the selective induction of ROS in SCs may be the basis for the senolytic activity of PL. However, a number of small molecules, including hydrogen peroxide, parthenolide, arsenic trioxide, phenethyl isothiocyanate, auranofin [a thioredoxin reductase inhibitor], buthionine sulfoximine [a γ-glutamylcysteine synthetase inhibitor], and decyl-triphenylphosphonium, that were previously shown to kill cancer cells by inducing oxidative stress were not able to selectively kill IR-SCs [25]. This finding suggests that ROS elevation alone is insufficient to selectively kill SCs. Interestingly, it has been reported that PL can chemically react with the sulfhydryl group of methyl thioglycolate to form the product of conjugate addition at C3 [30]. Based on this, we hypothesized that NAC, rather than acting as an ROS scavenger, inactivates PL through a similar reaction in cell culture media. In support of this hypothesis, we observed that PL (10 μM) disappeared within 2 h after co-incubation with NAC (2 mM) in cell culture media under conditions mimicking a cell viability assay (Fig. 3C), forming the corresponding hetero-conjugated product, NAC-PL (Fig. 3C). NAC-PL was isolated from this reaction, and it exhibited diminished toxicity toward IR-SCs (Fig. 3C). To further investigate the role of ROS in PL-induced SC death, we treated IR-SCs with PL in the presence of a different, potent antioxidant, γ-tocotrienol (GT3, 5 μM) [48]. GT3 did not decrease PL-induced cell death in IR-SCs, although GT3 reversed the PL-induced increase in ROS (Fig. 3D). These data suggest that ROS were not involved in the SC death induced by PL.

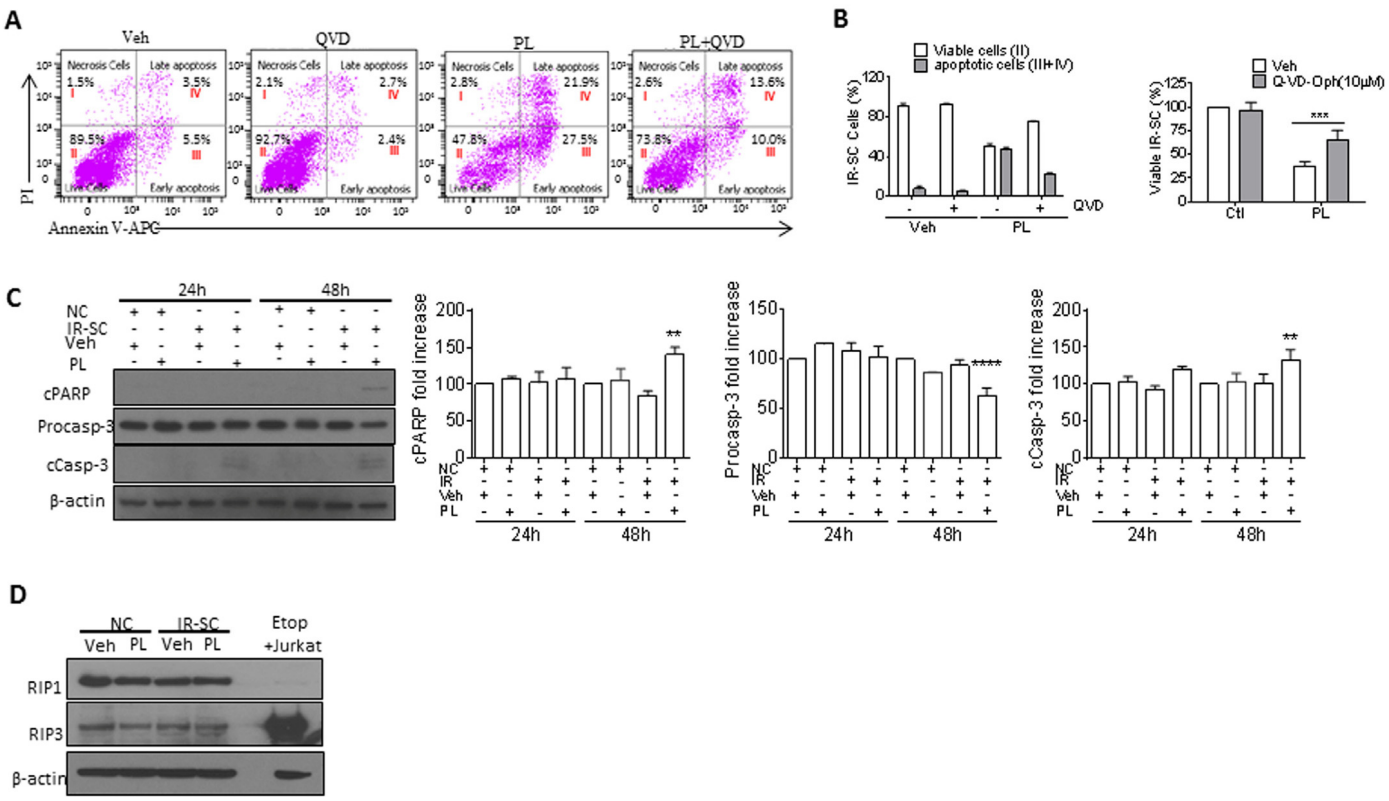

Figure 2. PL kills SCs by apoptosis. (**A**) Representative flow cytometric plots to measure apoptotic WI-38 IR-SCs at 48 h after treatment with vehicle (Veh), 10 μM PL, 10 μM Q-VD-Oph (QVD), or the combination of PL and QVD. (**B**) Quantification of the percentage of viable (gate II: PI^- Annexin V^-) and apoptotic (gates III and IV: PI^- Annexin V^+ and PI^+ Annexin V^+) (right) IR-SCs 48 h after treatment as in (**A**) (left), and quantification of the percentage of viable IR-SCs 72 h after treatment as in (**A**) (right). (**C**) Representative western blot and quantitative analysis of cleaved-poly(ADP-ribose) polymerase (cPARP), procaspase-3 (Procasp-3), cleaved caspase-3 (cCasp-3), and β-actin in NCs and WI-38 IR-SCs 24 h and 48 h after incubation with Veh or 10 μM PL. (**D**) Representative western blot analysis of RIP1, RIP3, and β-actin in WI-38 NCs and IR-SCs 24 h after incubation with Veh or 10 μM PL. A cell lysate of etoposide-treated Jurkat cells was used as a positive control. Data are represented as the mean ± SEM.

To determine if PL-based senolytic agents with increased potency/selectivity could be developed, we synthesized a series of PL analogs that have been reported as potent anti-cancer agents. No obvious correlation between ROS induction and senolytic potency was observed in these analogs. Specifically, BRD4809 [49], an abbreviated PL analog (Fig. 3E), and PL-DI [30], a PL dimer (Fig. 3F), showed unchanged or increased potency against IR-SCs, respectively, compared to PL; however, these analogs did not affect ROS levels in SCs at concentrations near their EC_{50} values for SC viability (Table 2). On the other hand, PL-FPh [30], which contains an alkenyl substituent at C2 of PL, selectively induced ROS production in IR-SCs and had increased potency and selectivity in killing these SCs when compared to PL (Fig. 3G). Finally, PL-7 [30], a PL analog with an enlarged ring, inhibited ROS production, yet retained the senolytic potency of PL toward IR-SCs (Fig. 3H). Taken together, these results further confirm that PL and its analogs kill SCs in an ROS-independent manner.

Table 2. EC_{50} values and selectivity of PL analogs in WI-38 cells

PL analogs	EC_{50} (μM)		EC_{50} ratio (NC/IR)
	NC	IR	
BRD4809	35.7	9.7	3.68
PL-DI	1.53	0.76	2.01
PL-7	12.96	8.85	1.46
PL-FPh	5.87	1.11	5.29

The synergistic senolytic effect of piperlongumine and ABT-263

PL has been tested for its synergistic anti-tumor effect in combination with TNF-related apoptosis-inducing

ligand [46], ataxia telangiectasia and Rad3-related protein inhibition [50], or a chemotherapeutic agent, such as cisplatin [33, 34], paclitaxel [34], docetaxel [51], and gemcitabine [39]. Thus, we investigated the synergistic senolytic effect of PL and ABT-263 on IR-SCs. We tested 1.25 μM ABT-263 with 5 or 10 μM PL and 10 μM PL with 0.08-1.25 μM ABT-263; the ABT-263 concentrations were selected based on our recent studies [25]. The combination of 10 μM PL with 1.25 μM ABT-263 did not induce significant toxicity in non-senescent WI-38 cells (Fig. 4A). When the combinations were applied to IR-SCs, however, we observed significant synergistic effects (Fig. 4B-C). For example, treatment of SCs with 10 μM PL or 1.25 μM ABT-263 individually resulted in cell viability of 30.4% and 25.8%, respectively. However, the combined treatment with PL and ABT-263 killed almost all IR-SCs (Fig. 4C). The coefficient of drug interaction (CDI) method [52] was then used to evaluate the effects of PL and ABT-263; Table 3 gives the CDI values for these

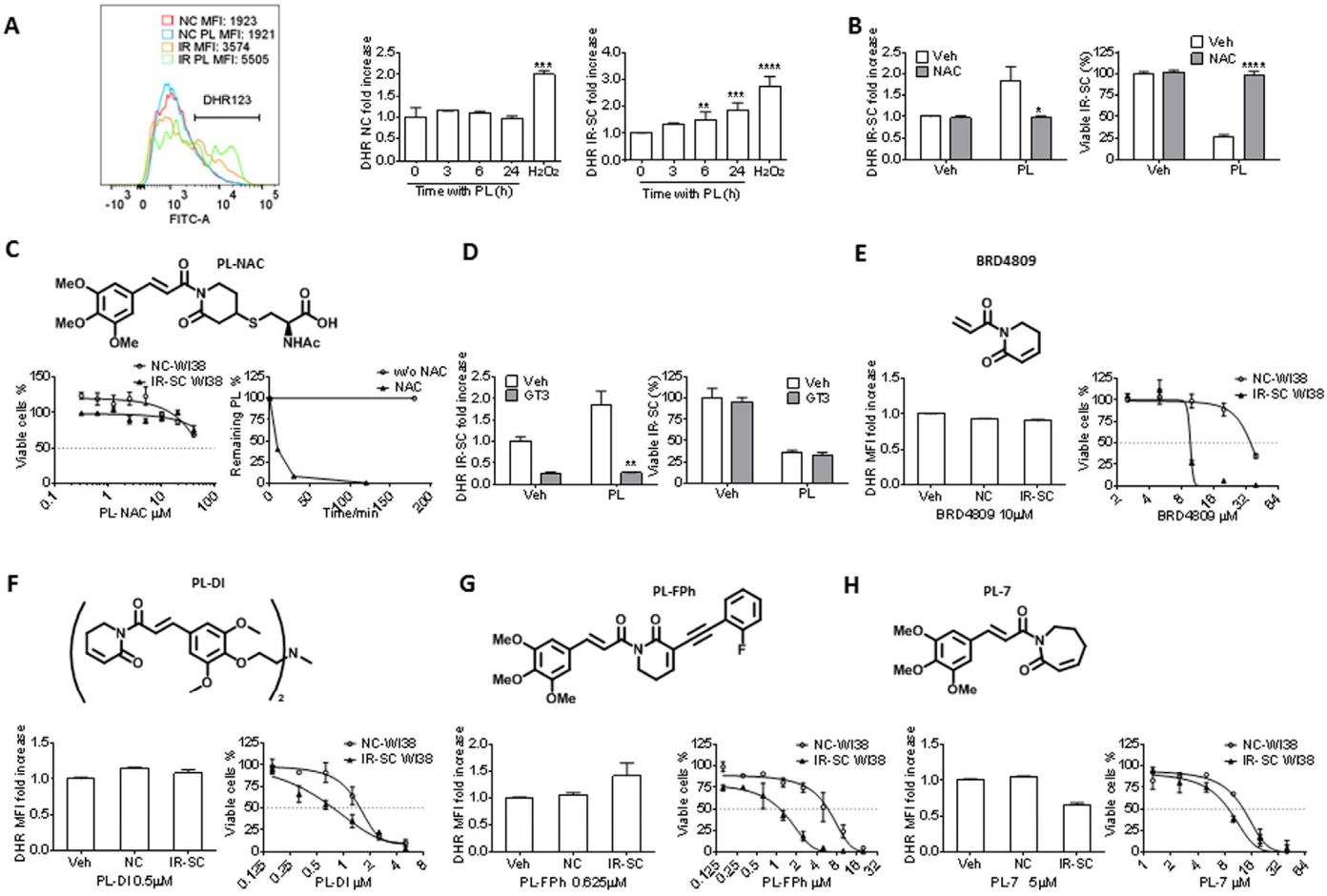

Figure 3. Effect of PL and its analogs on ROS production and senolytic activity in WI-38 IR-SCs. (**A**) Representative flow cytometric analysis of ROS production in NCs and IR-SCs 24 h after incubation with or without PL by DHR (left) (MFI, mean fluorescence intensity) and quantification of the fold increase of ROS levels in WI-38 NCs and WI-38 IR-SCs cells at the indicated times (middle and right) after incubation with 10 μM PL. As a positive control, cells were treated with 100 μM of H_2O_2 for 2 h, the H_2O_2 was removed, and cells were cultured for an additional 24 h (*n* = 3). (**B**) Quantification of the fold increase in DHR-123 MFI (left) in WI-38 IR-SCs 24 h after treatment with Veh, 10 μM PL, 2 mM NAC (pretreatment overnight), or the combination of PL and NAC, and (right) the percentage of viable WI-38 IR-SCs 72 h after treatment with Veh, 10 μM PL, 2 mM NAC (pretreatment overnight), or the combination of PL and NAC (*n* = 3). (**C**) Structure of PL-NAC and (Left) quantification of viable WI-38 NCs and WI-38 IR-SCs 72 h after treatment with increasing concentrations of PL-NAC (*n* = 3). (Right) Percentage of 10 μm PL remaining in the culture medium vs. time with or without 2mM NAC. (**D**) Left panel: quantification of the fold increase in DHR MFI (left) of WI-38 IR-SCs 24 h after treatment with Veh, 10 μM PL, 5 μM γ-tocotrienol (GT3, pretreatment overnight), or the combination of PL and GT3; and right panel: the percentage of viable WI-38 IR-SCs 72 h after treatment with Veh, 10 μM PL, 5 μM GT3 (pretreatment overnight), or the combination of PL and GT3 (*n* = 3). (**E-H**) Quantification of the fold increase in DHR-123 MFI after 24 h treatment (left) and viability of WI-38 NCs and WI-38 IR-SCs 72 h treatment (right) after they were treated with increasing concentrations or (**E**)10 μM BRD4809, (**F**) 0.5 μM PL-DI, (**G**) 0.625 μM PL-FPh, and (**H**) 5 μM PL-7 (*n* = 3). Data are represented as the mean ± SEM.

combinations. An additive effect for the combination of 10 μM PL and 0.08 μM ABT-263 (CDI = 0.99) was observed. The CDI values for the other combinations ranged from 0.02-0.41, indicating that PL and ABT-263 exerted a strong synergistic senolytic effect on IR-SCs. It is worth noting that, in our previous studies, increasing the concentration of ABT-263 from 1.25 μM to 5 μM did not increase cell killing in WI-38 SCs. PL appeared to eliminate the subpopulation of IR-SCs that was resistant to ABT-263.

Table 3. CDI values for the combination of PL and ABT-263

ABT-263 (μM)	PL (μM)	CDI
0.08	10	0.99
0.156	10	0.20
0.313	10	0.05
0.625	10	0.02
1.25	10	0.38
1.25	5	0.41

DISCUSSION

Selective depletion of SCs is a potentially novel anti-aging strategy that may prevent cancer and various human diseases associated with aging and rejuvenate the body to live a longer, healthier life. As such, several senolytic agents, including ABT-263, have been identified recently [23, 25-27], demonstrating the feasibility of pharmacologically targeting SCs. However, ABT-263 induces thrombocytopenia [53], and it remains to be determined whether ABT-263 can be used to safely treat age-related diseases, since individuals may require long-term treatment with a senolytic drug. Thus, it is necessary to identify a safer senolytic drug. In the present study, we evaluated PL as a novel senolytic agent. PL induced caspase-mediated apoptosis in SCs and effectively killed SCs induced by IR, replicative exhaustion, or ectopic expression of the oncogene *Ras*. Similar to the observations in cancer cells versus normal cells, PL elevated ROS levels in IR-SCs, but not in non-senescent WI-38 cells.

Because NAC blocks PL-induced ROS elevation in cancer cells and abolishes the anti-tumor effect of PL, it has been proposed that induction of ROS production is a key mechanism of PL-induced cancer cell apoptosis [31, 33-35, 41, 45-47]. Indeed, we showed that co-treatment of IR-SCs with PL and NAC fully reversed the senolytic effect of PL. However, we found that PL was chemically inactivated by NAC in culture media through a conjugated addition reaction between the sulfhydryl group of NAC and the C2-C3 α,β-unsaturated imide group of PL; the resulting adduct, NAC-PL, was not senolytic. Based on these findings, caution is warranted when using NAC or similar compounds that contain a nucleophilic sulfhydryl group, such as dithiothreitol [54], as an ROS scavenger to study ROS inducers such as PL. In contrast, GT3, a potent ROS scavenger that does not react with PL, effectively blocked PL-induced ROS elevation but had no inhibitory effect on PL-induced SC death. In addition, through evaluation of PL analogs, we found that there is no correlation between senolytic potency and ROS-induction in IR-SCs. These results led us to conclude that the senolytic activity of PL is ROS independent.

Unlike ABT-263, the precise mechanism of action (MOA) by which PL induces SC apoptosis remains unclear. PL modulates the activity of many cell signaling and survival pathways in cancer cells [31], and a number of studies have investigated the MOA by

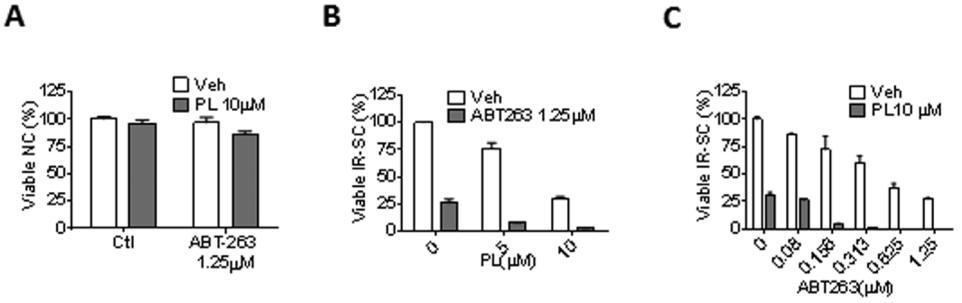

Figure 4. PL synergistically and selectively kills SCs in combination with ABT-263. (**A**) Quantification of NC viability 72 h after the cells incubation with vehicle, 1.25 μM ABT-263, 10 μM PL, or the combination of ABT-263 and PL (*n* = 3). (**B**) Quantification of WI-38 IR-SC viability 72 h after incubation with vehicle, 1.25 μM ABT-263, 5 or 10 μM PL, or the combination of ABT-263 and PL (*n* = 3-5). (**C**) Quantification of WI-38 IR-SC viability 72 h after incubation with vehicle, 10 μM PL, 0.08-1.25 μM ABT-263, or the combination of ABT-263 and PL (*n* = 3-6). Data are represented as the mean ± SEM.

which PL induces apoptosis in these cells [30, 35-40, 45, 54-69]. Data from these studies may be translatable to PL-induced SC apoptosis because SCs and cancer cells share some common pro-survival pathways [23]. In addition, mass spectrometry-based proteomic approaches using probes derived from PL could be used to identify direct molecular target(s) of PL in SCs. In this regard, novel anti-senescent protein target(s) and MOAs could be identified, making it possible to develop promising novel classes of senolytic agents. Importantly, PL appears to be safe; the maximum tolerated dose in mice is very high, and it maintains high bioavailability after oral administration [31]. Furthermore, our initial structural modifications to PL demonstrate that we can develop PL analogs with increased potency and selectivity toward SCs (Fig. 3), supporting the use of PL as a lead for further drug discovery and development.

Another potential use of PL and its derivatives is in combination with ABT-263, or other inhibitors of Bcl-2 family proteins, for a synergistic senolytic effect. Although ABT-263 is a highly specific senolytic agent, it causes transient thrombocytopenia and neutropenia in patients [70]; this results from its inhibitory effect on Bcl-xL, which is important for platelet survival [71, 72]. We showed that PL had a strong synergistic effect on the senolytic activity of ABT-263 *in vitro*, potentially reducing the dose of ABT-263 needed to effectively deplete SCs. We expect this therapeutic approach would significantly reduce ABT-263-induced thrombocytopenia, making senolytic treatment with ABT-263 safer.

Although clearance of SCs with a senolytic drug may be used to treat some age-related diseases, it is well recognized that cellular senescence is also functionally linked to many beneficial physiological processes, such as wound healing, tissue remodeling, and embryonic development [73]. Attempt to clear SCs in certain situations may produce some side effects. Therefore, we should proceed with caution to use senolytic drugs to treat age-related diseases before we have a better understanding of their risks.

MATERIALS AND METHODS

Cells, induction of senescence, and senolytic agents

Human WI-38 fibroblasts (WI-38, catalog no. CCL-75, American Type Culture Collection, Manassas, VA) were cultured in a complete cell culture medium (CM) (Dulbecco's Modified Eagle Medium supplemented with 10% Fetal Bovine Serum, FBS; catalog no. 16000044, Thermo Fisher Scientific, Waltham, MA) supplemented with 100 U/ml penicillin and 100 μg/ml streptomycin (purchased from Atlanta Biologicals, Norcross, GA) in a 37°C, humidified incubator with 5% CO_2.

Low-passage WI-38 (< 25 passages) cells were used as controls or for the induction of senescence.

Replicative senescence

To induce replicative senescence (Rep-SC), WI-38 cells were subcultured until they stopped dividing and became senescent (after approximately 38 passages for WI-38).

Ionizing radiation-induced senescence

To induce senescence with ionizing radiation (IR), WI-38 cells, roughly 70% confluent, were exposed to 15 Gy of IR in a J.L. Shepherd Model Mark I ^{137}Cesium ϒ-irradiator (J.L. Shepherd, Glendale, CA) at a dose rate of 1.080 Gy/min. Three days after irradiation, cells were passaged once at a 1:3 dilution. WI-38 cells became fully senescent 10 d after irradiation.

Ras-induced senescence

WI-38 cells were made senescent by ectopically expressing the oncogene *Ras* (Ras-SC), as previously described [25].

PL was purchased from Biovision (catalog no. 1919-10; Milpitas, CA). ABT-263 was purchased from Selleckchem (catalog no. S1001; Houston, TX). The PL analogs 2,3-dihydro-PL, 7,8-dihydro-PL, BRD4809, PL-DI, PL-FPh, and PL-7 were synthesized according to reported methods, with minor modifications [30, 49]. PL-NAC was obtained by incubating equal volume of 20 μM PL with 4 mM NAC in culture media at 37°C for 30 min, followed by extraction with methylene chloride and silica gel column purification. The structure of PL-NMR was characterized by NMR and MS: ^{1}H NMR (400 MHz, $CDCl_3$) δ 7.59 (d, J = 15.6 Hz, 1H), 7.28 (d, J = 15.6 Hz, 1H), 6.86 (br, 1H), 6.76 (s, 2H), 4.68 (s, 1H), 3.99 (m, 1H), 3.88–3.75 (m, 9H), 3.63 (m, 1H), 3.27 (m, 1H), 3.13–2.87 (m, 3H), 2.69–2.44 (m, 1H), 2.25 (m, 1H), 2.04 (s, 3H), 1.81 (m, 1H) ppm; ESI-MS *m/z* 479.2 $[M-H]^+$.

Cell viability assays

Cell viability was measured with flow cytometry, as previously described [25].

Calculation of EC_{50} values

Dose-response curves were generated for each senolytic agent, and the half-maximal effective concentrations (EC_{50} values) were calculated with GraphPad Prism 6 software.

ROS assay

Control, non-senescent WI-38 cells were plated in 24-well plates (60,000 cells/well). IR-induced WI-38 senescent cells (10 d after 15 Gy IR) were plated in 6-well plates (50,000 cells/well) and allowed to recover. Cells were incubated overnight with NAC (2 mM; catalog no. 138061, Sigma-Aldrich, St. Louis, MO) and GT3 (5 μM; isolated from annatto oil). The next day, the cells were treated with dilutions of compounds in DMSO and incubated for 24 h, or as indicated. The medium was then replaced with pre-warmed DMEM (no supplements) containing 1 μM dihydrorhodamine 123 (DHR 123, catalog no. D632, Thermo Fisher Scientific), and the cells were incubated at 37°C for 30 min. The cells were then harvested with trypsin and washed twice with PBS. Mean fluorescence intensity (MFI) was determined with a BD LSR II flow cytometer (BD Biosciences, San Jose, CA).

Apoptosis assay

WI-38 cells were pretreated with vehicle or 10 μM Q-VD-Oph (QVD, catalog no. A1901, APExBIO, Houston, TX) for 4 h. Cells were then treated with 10 μM PL for the indicated time. The cells were harvested and washed twice with Annexin V binding buffer and then stained with Alexa Fluor 647-Annexin V (1: 50, catalog no. 640912, BioLegend, San Diego, CA) and propidium iodide (PI, 10 μg/ml, catalog no. P4170, Sigma-Aldrich), according to the manufacturer's instructions (Biotium, Hayward, CA). All of the stained cells were analyzed with the BD LSR II flow cytometer.

Western blot analysis

Cells were lysed in RIPA buffer with EDTA and EGTA (catalog no. BP-115DG, Boston BioProducts, Ashland, MA), supplemented with 1% Phosphatase Inhibitor Cocktail 3 (catalog no. P0044, Sigma-Aldrich) and 1% Protease Inhibitor Cocktail (catalog no. P8340, Sigma-Aldrich). An equal amount of protein (15-30 μg/lane) from each cell extract was resolved on a 12% SDS-PAGE gel. Proteins were blotted to a NOVEX PVDF membrane (catalog no. LC2002, Life Technologies) by electrophoresis. The membranes were blocked with TBS-T blocking buffer (5% nonfat milk in 25 mM Tris-HCL, pH 7.4; 3 mM KCl; 140 mM NaCl; and 0.05% Tween) and probed with primary antibodies (at a predetermined optimal concentration) overnight at 4°C or for 1 h at room temperature. After extensive washing with TBS-T, the membranes were incubated with an appropriate peroxidase-conjugated secondary antibody (Jackson ImmunoResearch Europe, Suffolk, UK) for 1 h at room temperature. After three washes with TBS-T, the proteins of interest were detected with ECL Western Blotting Detection Reagents (catalog no. WBKLS0100, EMD Millipore, Newmarket, Suffolk, UK) and recorded with autoradiography (Pierce Biotech, Rockford, IL, USA). The primary antibodies included cleaved-Poly (ADP-ribose) polymerase (catalog no. 9541, Cell Signaling Technology, Boston, MA), Procaspase-3 (catalog no. 9662S, Cell Signaling Technology), cleaved-caspase 3 (catalog no. 9664S, Cell Signaling Technology), RIP1 (D94C12, catalog no. 3493S, Cell Signaling Technology), β-actin (catalog no. SC-1615, Santa Cruz Biotechnology, Dallas, TX), and RIP3 (catalog no. IMG-5846A, IMGENEX, San Diego, CA).

Statistical analysis

The data displayed normal variance. The data were analyzed by analysis of variance (ANOVA) with Graphpad Prism from GraphPad Software (San Diego, CA). In the event that ANOVA justified post hoc comparisons between group means, the comparisons were made with Neuman-Keuls or Tukey's multiple-comparisons test. $P < 0.05$ was considered to be significant. CDI was calculated as: CDI = AB/ (A × B). AB represents the percent of viable cells remaining after the treatment with the combined drugs, while A and B represent the percent of viable cells remaining after the treatment with each drug independently. CDI < 1 indicates a synergistic effect, CDI = 1 indicates an additive effect, and CDI > 1 indicates antagonism. CDI < 0.7 indicates that the drugs are significantly synergistic.

CONFLICTS OF INTEREST

Y.W., J.C., X.L., G.Z., and D.Z. filed a patent application for the use of PL and PL analogs as anti-aging agents. A potential royalty stream to Y.W., J.C., X.L., G.Z., and D.Z. may occur consistent with University of Arkansas for Medical Sciences policy. G.Z. is a consultant and D.Z. is a co-founder and advisor of UNITY Biotechnology that develops senolytic drugs.

FUNDING

This work was initially supported in part by grants from the National Institutes of Health (R01CA122023 and P20GM109005) and a scholarship from the Arkansas Research Alliance. The development of various PL analogs was supported by a sponsored research agreement between UNITY Biotechnology and the University of Arkansas for Medical Sciences. This manuscript was edited in the Office of Grants and Scientific Publications at the University of Arkansas for Medical Sciences.

REFERENCES

1. Braig M, Lee S, Loddenkemper C, Rudolph C, Peters AH, Schlegelberger B, Stein H, Dörken B, Jenuwein T, Schmitt CA. Oncogene-induced senescence as an initial barrier in lymphoma development. Nature. 2005; 436:660–65. doi: 10.1038/nature03841

2. Chen Z, Trotman LC, Shaffer D, Lin HK, Dotan ZA, Niki M, Koutcher JA, Scher HI, Ludwig T, Gerald W, Cordon-Cardo C, Pandolfi PP. Crucial role of p53-dependent cellular senescence in suppression of Pten-deficient tumorigenesis. Nature. 2005; 436:725–30. doi: 10.1038/nature03918

3. Campisi J, d'Adda di Fagagna F. Cellular senescence: when bad things happen to good cells. Nat Rev Mol Cell Biol. 2007; 8:729–40. doi: 10.1038/nrm2233

4. Prieur A, Peeper DS. Cellular senescence in vivo: a barrier to tumorigenesis. Curr Opin Cell Biol. 2008; 20:150–55. doi: 10.1016/j.ceb.2008.01.007

5. Kuilman T, Michaloglou C, Mooi WJ, Peeper DS. The essence of senescence. Genes Dev. 2010; 24:2463–79. doi: 10.1101/gad.1971610

6. Campisi J. Aging, cellular senescence, and cancer. Annu Rev Physiol. 2013; 75:685–705. doi: 10.1146/annurev-physiol-030212-183653

7. Aravinthan A. Cellular senescence: a hitchhiker's guide. Hum Cell. 2015; 28:51–64. doi: 10.1007/s13577-015-0110-x

8. Rodier F, Campisi J. Four faces of cellular senescence. J Cell Biol. 2011; 192:547–56. doi: 10.1083/jcb.201009094

9. Ohtani N, Takahashi A, Mann DJ, Hara E. Cellular senescence: a double-edged sword in the fight against cancer. Exp Dermatol. 2012 (Suppl 1); 21:1–4. doi: 10.1111/j.1600-0625.2012.01493.x

10. Tchkonia T, Zhu Y, van Deursen J, Campisi J, Kirkland JL. Cellular senescence and the senescent secretory phenotype: therapeutic opportunities. J Clin Invest. 2013; 123:966–72. doi: 10.1172/JCI64098

11. Salama R, Sadaie M, Hoare M, Narita M. Cellular senescence and its effector programs. Genes Dev. 2014; 28:99–114. doi: 10.1101/gad.235184.113

12. Baker DJ, Wijshake T, Tchkonia T, LeBrasseur NK, Childs BG, van de Sluis B, Kirkland JL, van Deursen JM. Clearance of p16Ink4a-positive senescent cells delays ageing-associated disorders. Nature. 2011; 479:232–36. doi: 10.1038/nature10600

13. Baker DJ, Childs BG, Durik M, Wijers ME, Sieben CJ, Zhong J, Saltness RA, Jeganathan KB, Verzosa GC, Pezeshki A, Khazaie K, Miller JD, van Deursen JM. Naturally occurring p16(Ink4a)-positive cells shorten healthy lifespan. Nature. 2016; 530:184–89. doi: 10.1038/nature16932

14. Xu M, Tchkonia T, Ding H, Ogrodnik M, Lubbers ER, Pirtskhalava T, White TA, Johnson KO, Stout MB, Mezera V, Giorgadze N, Jensen MD, LeBrasseur NK, Kirkland JL. JAK inhibition alleviates the cellular senescence-associated secretory phenotype and frailty in old age. Proc Natl Acad Sci USA. 2015; 112:E6301–10. doi: 10.1073/pnas.1515386112

15. Hall BM, Balan V, Gleiberman AS, Strom E, Krasnov P, Virtuoso LP, Rydkina E, Vujcic S, Balan K, Gitlin I, Leonova K, Polinsky A, Chernova OB, Gudkov AV. Aging of mice is associated with p16(Ink4a)- and β-galactosidase-positive macrophage accumulation that can be induced in young mice by senescent cells. Aging (Albany NY). 2016; 8:1294–315. doi: 10.18632/aging.100991

16. Johnson SC, Rabinovitch PS, Kaeberlein M. mTOR is a key modulator of ageing and age-related disease. Nature. 2013; 493:338–45. doi: 10.1038/nature11861

17. Anisimov VN. Metformin for aging and cancer prevention. Aging (Albany NY). 2010; 2:760–74. doi: 10.18632/aging.100230

18. Komarova EA, Antoch MP, Novototskaya LR, Chernova OB, Paszkiewicz G, Leontieva OV, Blagosklonny MV, Gudkov AV. Rapamycin extends lifespan and delays tumorigenesis in heterozygous p53+/- mice. Aging (Albany NY). 2012; 4:709–14. doi: 10.18632/aging.100498

19. Menendez JA, Joven J. One-carbon metabolism: an aging-cancer crossroad for the gerosuppressant metformin. Aging (Albany NY). 2012; 4:894–98. doi: 10.18632/aging.100523

20. Ross C, Salmon A, Strong R, Fernandez E, Javors M, Richardson A, Tardif S. Metabolic consequences of long-term rapamycin exposure on common marmoset monkeys (Callithrix jacchus). Aging (Albany NY). 2015; 7:964–73. doi: 10.18632/aging.100843

21. van Deursen JM. The role of senescent cells in ageing. Nature. 2014; 509:439–46. doi: 10.1038/nature13193

22. Sharpless NE, Sherr CJ. Forging a signature of in vivo senescence. Nat Rev Cancer. 2015; 15:397–408. doi: 10.1038/nrc3960

23. Zhu Y, Tchkonia T, Pirtskhalava T, Gower AC, Ding H, Giorgadze N, Palmer AK, Ikeno Y, Hubbard GB, Lenburg M, O'Hara SP, LaRusso NF, Miller JD, et al. The Achilles' heel of senescent cells: from transcriptome to senolytic drugs. Aging Cell. 2015; 14:644–58. doi: 10.1111/acel.12344

24. Kirkland JL, Tchkonia T. Clinical strategies and animal models for developing senolytic agents. Exp Gerontol. 2015; 68:19–25. doi: 10.1016/j.exger.2014.10.012

25. Chang J, Wang Y, Shao L, Laberge RM, Demaria M, Campisi J, Janakiraman K, Sharpless NE, Ding S, Feng W, Luo Y, Wang X, Aykin-Burns N, et al. Clearance of senescent cells by ABT263 rejuvenates aged hematopoietic stem cells in mice. Nat Med. 2016; 22:78–83. doi: 10.1038/nm.4010

26. Zhu Y, Tchkonia T, Fuhrmann-Stroissnigg H, Dai HM, Ling YY, Stout MB, Pirtskhalava T, Giorgadze N, Johnson KO, Giles CB, Wren JD, Niedernhofer LJ, Robbins PD, Kirkland JL. Identification of a novel senolytic agent, navitoclax, targeting the Bcl-2 family of anti-apoptotic factors. Aging Cell. 2016; 15:428–35. doi: 10.1111/acel.12445

27. Yosef R, Pilpel N, Tokarsky-Amiel R, Biran A, Ovadya Y, Cohen S, Vadai E, Dassa L, Shahar E, Condiotti R, Ben-Porath I, Krizhanovsky V. Directed elimination of senescent cells by inhibition of BCL-W and BCL-XL. Nat Commun. 2016; 7:11190. doi: 10.1038/ncomms11190

28. Geiger H. Depleting senescent cells to combat aging. Nat Med. 2016; 22:23–24. doi: 10.1038/nm.4024

29. Bezerra DP, Pessoa C, de Moraes MO, Saker-Neto N, Silveira ER, Costa-Lotufo LV. Overview of the therapeutic potential of piplartine (piperlongumine). Eur J Pharm Sci. 2013; 48:453–63. doi: 10.1016/j.ejps.2012.12.003

30. Adams DJ, Dai M, Pellegrino G, Wagner BK, Stern AM, Shamji AF, Schreiber SL. Synthesis, cellular evaluation, and mechanism of action of piperlongumine analogs. Proc Natl Acad Sci USA. 2012; 109:15115–20. doi: 10.1073/pnas.1212802109

31. Raj L, Ide T, Gurkar AU, Foley M, Schenone M, Li X, Tolliday NJ, Golub TR, Carr SA, Shamji AF, Stern AM, Mandinova A, Schreiber SL, Lee SW. Selective killing of cancer cells by a small molecule targeting the stress response to ROS. Nature. 2011; 475:231–34. doi: 10.1038/nature10167

32. Han SS, Son DJ, Yun H, Kamberos NL, Janz S. Piperlongumine inhibits proliferation and survival of Burkitt lymphoma in vitro. Leuk Res. 2013; 37:146–54. doi: 10.1016/j.leukres.2012.11.009

33. Roh JL, Kim EH, Park JY, Kim JW, Kwon M, Lee BH. Piperlongumine selectively kills cancer cells and increases cisplatin antitumor activity in head and neck cancer. Oncotarget. 2014; 5:9227–38. doi: 10.18632/oncotarget.2402

34. Gong LH, Chen XX, Wang H, Jiang QW, Pan SS, Qiu JG, Mei XL, Xue YQ, Qin WM, Zheng FY, Shi Z, Yan XJ. Piperlongumine induces apoptosis and synergizes with cisplatin or paclitaxel in human ovarian cancer cells. Oxid Med Cell Longev. 2014; 2014:906804. doi: 10.1155/2014/906804

35. Liu JM, Pan F, Li L, Liu QR, Chen Y, Xiong XX, Cheng K, Yu SB, Shi Z, Yu AC, Chen XQ. Piperlongumine selectively kills glioblastoma multiforme cells via reactive oxygen species accumulation dependent JNK and p38 activation. Biochem Biophys Res Commun. 2013; 437:87–93. doi: 10.1016/j.bbrc.2013.06.042

36. Randhawa H, Kibble K, Zeng H, Moyer MP, Reindl KM. Activation of ERK signaling and induction of colon cancer cell death by piperlongumine. Toxicol In Vitro. 2013; 27:1626–33. doi: 10.1016/j.tiv.2013.04.006

37. Ginzburg S, Golovine KV, Makhov PB, Uzzo RG, Kutikov A, Kolenko VM. Piperlongumine inhibits NF-κB activity and attenuates aggressive growth characteristics of prostate cancer cells. Prostate. 2014; 74:177–86. doi: 10.1002/pros.22739

38. Jin HO, Lee YH, Park JA, Lee HN, Kim JH, Kim JY, Kim B, Hong SE, Kim HA, Kim EK, Noh WC, Kim JI, Chang YH, et al. Piperlongumine induces cell death through ROS-mediated CHOP activation and potentiates TRAIL-induced cell death in breast cancer cells. J Cancer Res Clin Oncol. 2014; 140:2039–46. doi: 10.1007/s00432-014-1777-1

39. Wang Y, Wu X, Zhou Y, Jiang H, Pan S, Sun B. Piperlongumine Suppresses Growth and Sensitizes Pancreatic Tumors to Gemcitabine in a Xenograft Mouse Model by Modulating the NF-kappa B Pathway. Cancer Prev Res (Phila). 2016; 9:234–44. doi: 10.1158/1940-6207.CAPR-15-0306

40. Zheng J, Son DJ, Gu SM, Woo JR, Ham YW, Lee HP, Kim WJ, Jung JK, Hong JT. Piperlongumine inhibits lung tumor growth via inhibition of nuclear factor kappa B signaling pathway. Sci Rep. 2016; 6:26357. doi: 10.1038/srep26357

41. Chen SY, Liu GH, Chao WY, Shi CS, Lin CY, Lim YP, Lu CH, Lai PY, Chen HR, Lee YR. Piperlongumine Suppresses Proliferation of Human Oral Squamous Cell Carcinoma through Cell Cycle Arrest, Apoptosis and Senescence. Int J Mol Sci. 2016; 17:E616. doi: 10.3390/ijms17040616

42. Caserta TM, Smith AN, Gultice AD, Reedy MA, Brown TL. Q-VD-OPh, a broad spectrum caspase inhibitor with potent antiapoptotic properties. Apoptosis. 2003; 8:345–52. doi: 10.1023/A:1024116916932

43. Walsh CM. Grand challenges in cell death and survival: apoptosis vs. necroptosis. Front Cell Dev Biol. 2014; 2:3. doi: 10.3389/fcell.2014.00003

44. Wang Y, Wang JW, Xiao X, Shan Y, Xue B, Jiang G, He

Q, Chen J, Xu HG, Zhao RX, Werle KD, Cui R, Liang J, et al. Piperlongumine induces autophagy by targeting p38 signaling. Cell Death Dis. 2013; 4:e824. doi: 10.1038/cddis.2013.358

45. Liu QR, Liu JM, Chen Y, Xie XQ, Xiong XX, Qiu XY, Pan F, Liu D, Yu SB, Chen XQ. Piperlongumine inhibits migration of glioblastoma cells via activation of ROS-dependent p38 and JNK signaling pathways. Oxid Med Cell Longev. 2014; 2014:653732. doi: 10.1155/2014/653732

46. Li J, Sharkey CC, King MR. Piperlongumine and immune cytokine TRAIL synergize to promote tumor death. Sci Rep. 2015; 5:9987. doi: 10.1038/srep09987

47. Duan C, Zhang B, Deng C, Cao Y, Zhou F, Wu L, Chen M, Shen S, Xu G, Zhang S, Duan G, Yan H, Zou X. Piperlongumine induces gastric cancer cell apoptosis and G2/M cell cycle arrest both in vitro and in vivo. Tumour Biol. 2016; 37:10793–804. doi: 10.1007/s13277-016-4792-9

48. Cerecetto H, López GV. Antioxidants derived from vitamin E: an overview. Mini Rev Med Chem. 2007; 7:315–38. doi: 10.2174/138955707780059871

49. Boskovic ZV, Hussain MM, Adams DJ, Dai M, Schreiber SL. Synthesis of piperlogs and analysis of their effects on cells. Tetrahedron. 2013; 69:7559–67. doi: 10.1016/j.tet.2013.05.080

50. Cottini F, Hideshima T, Suzuki R, Tai YT, Bianchini G, Richardson PG, Anderson KC, Tonon G. Synthetic Lethal Approaches Exploiting DNA Damage in Aggressive Myeloma. Cancer Discov. 2015; 5:972–87. doi: 10.1158/2159-8290.CD-14-0943

51. Patel K, Chowdhury N, Doddapaneni R, Boakye CH, Godugu C, Singh M. Piperlongumine for Enhancing Oral Bioavailability and Cytotoxicity of Docetaxel in Triple-Negative Breast Cancer. J Pharm Sci. 2015; 104:4417–26. doi: 10.1002/jps.24637

52. Hao JQ, Li Q, Xu SP, Shen YX, Sun GY. Effect of lumiracoxib on proliferation and apoptosis of human nonsmall cell lung cancer cells in vitro. Chin Med J (Engl). 2008; 121:602–07.

53. Kaefer A, Yang J, Noertersheuser P, Mensing S, Humerickhouse R, Awni W, Xiong H. Mechanism-based pharmacokinetic/pharmacodynamic meta-analysis of navitoclax (ABT-263) induced thrombocytopenia. Cancer Chemother Pharmacol. 2014; 74:593–602. doi: 10.1007/s00280-014-2530-9

54. Han JG, Gupta SC, Prasad S, Aggarwal BB. Piperlongumine chemosensitizes tumor cells through interaction with cysteine 179 of IκBα kinase, leading to suppression of NF-κB-regulated gene products. Mol Cancer Ther. 2014; 13:2422–35. doi: 10.1158/1535-7163.MCT-14-0171

55. Bharadwaj U, Eckols TK, Kolosov M, Kasembeli MM, Adam A, Torres D, Zhang X, Dobrolecki LE, Wei W, Lewis MT, Dave B, Chang JC, Landis MD, et al. Drug-repositioning screening identified piperlongumine as a direct STAT3 inhibitor with potent activity against breast cancer. Oncogene. 2015; 34:1341–53. doi: 10.1038/onc.2014.72

56. Chen Y, Liu JM, Xiong XX, Qiu XY, Pan F, Liu D, Lan SJ, Jin S, Yu SB, Chen XQ. Piperlongumine selectively kills hepatocellular carcinoma cells and preferentially inhibits their invasion via ROS-ER-MAPKs-CHOP. Oncotarget. 2015; 6:6406–21. doi: 10.18632/oncotarget.3444

57. Golovine K, Makhov P, Naito S, Raiyani H, Tomaszewski J, Mehrazin R, Tulin A, Kutikov A, Uzzo RG, Kolenko VM. Piperlongumine and its analogs down-regulate expression of c-Met in renal cell carcinoma. Cancer Biol Ther. 2015; 16:743–49. doi: 10.1080/15384047.2015.1026511

58. Golovine KV, Makhov PB, Teper E, Kutikov A, Canter D, Uzzo RG, Kolenko VM. Piperlongumine induces rapid depletion of the androgen receptor in human prostate cancer cells. Prostate. 2013; 73:23–30. doi: 10.1002/pros.22535

59. Han SS, Tompkins VS, Son DJ, Kamberos NL, Stunz LL, Halwani A, Bishop GA, Janz S. Piperlongumine inhibits LMP1/MYC-dependent mouse B-lymphoma cells. Biochem Biophys Res Commun. 2013; 436:660–65. doi: 10.1016/j.bbrc.2013.06.012

60. Jarvius M, Fryknäs M, D'Arcy P, Sun C, Rickardson L, Gullbo J, Haglund C, Nygren P, Linder S, Larsson R. Piperlongumine induces inhibition of the ubiquitin-proteasome system in cancer cells. Biochem Biophys Res Commun. 2013; 431:117–23. doi: 10.1016/j.bbrc.2013.01.017

61. Kong EH, Kim YJ, Kim YJ, Cho HJ, Yu SN, Kim KY, Chang JH, Ahn SC. Piplartine induces caspase-mediated apoptosis in PC-3 human prostate cancer cells. Oncol Rep. 2008; 20:785–92.

62. Lee HN, Jin HO, Park JA, Kim JH, Kim JY, Kim B, Kim W, Hong SE, Lee YH, Chang YH, Hong SI, Hong YJ, Park IC, et al. Heme oxygenase-1 determines the differential response of breast cancer and normal cells to piperlongumine. Mol Cells. 2015; 38:327–35. doi: 10.14348/molcells.2015.2235

63. Li W, Wen C, Bai H, Wang X, Zhang X, Huang L, Yang X, Iwamoto A, Liu H. JNK signaling pathway is involved in piperlongumine-mediated apoptosis in human colorectal cancer HCT116 cells. Oncol Lett. 2015; 10:709–15.

64. Makhov P, Golovine K, Teper E, Kutikov A, Mehrazin R, Corcoran A, Tulin A, Uzzo RG, Kolenko VM. Piperlongumine promotes autophagy via inhibition of Akt/mTOR signalling and mediates cancer cell death. Br J Cancer. 2014; 110:899–907. doi: 10.1038/bjc.2013.810

65. Niu M, Shen Y, Xu X, Yao Y, Fu C, Yan Z, Wu Q, Cao J, Sang W, Zeng L, Li Z, Liu X, Xu K. Piperlongumine selectively suppresses ABC-DLBCL through inhibition of NF-κB p65 subunit nuclear import. Biochem Biophys Res Commun. 2015; 462:326–31. doi: 10.1016/j.bbrc.2015.04.136

66. Ryu J, Kim MJ, Kim TO, Huh TL, Lee SE. Piperlongumine as a potential activator of AMP-activated protein kinase in HepG2 cells. Nat Prod Res. 2014; 28:2040–43. doi: 10.1080/14786419.2014.919283

67. Shrivastava S, Jeengar MK, Thummuri D, Naidu VG. Piperlongumine inhibits growth potential of gastric cancer cells by targeting PI3K/Akt/mTOR signaling pathway. Eur J Cancer. 2014; 50:S9–9. doi: 10.1016/S0959-8049(14)70032-2

68. Shrivastava S, Kulkarni P, Thummuri D, Jeengar MK, Naidu VG, Alvala M, Redddy GB, Ramakrishna S. Piperlongumine, an alkaloid causes inhibition of PI3 K/Akt/mTOR signaling axis to induce caspase-dependent apoptosis in human triple-negative breast cancer cells. Apoptosis. 2014; 19:1148–64. doi: 10.1007/s10495-014-0991-2

69. Wang F, Mao Y, You Q, Hua D, Cai D. Piperlongumine induces apoptosis and autophagy in human lung cancer cells through inhibition of PI3K/Akt/mTOR pathway. Int J Immunopathol Pharmacol. 2015; 28:362–73. doi: 10.1177/0394632015598849

70. Rudin CM, Hann CL, Garon EB, Ribeiro de Oliveira M, Bonomi PD, Camidge DR, Chu Q, Giaccone G, Khaira D, Ramalingam SS, Ranson MR, Dive C, McKeegan EM, et al. Phase II study of single-agent navitoclax (ABT-263) and biomarker correlates in patients with relapsed small cell lung cancer. Clin Cancer Res. 2012; 18:3163–69. doi: 10.1158/1078-0432.CCR-11-3090

71. Schoenwaelder SM, Jarman KE, Gardiner EE, Hua M, Qiao J, White MJ, Josefsson EC, Alwis I, Ono A, Willcox A, Andrews RK, Mason KD, Salem HH, et al. Bcl-xL-inhibitory BH3 mimetics can induce a transient thrombocytopathy that undermines the hemostatic function of platelets. Blood. 2011; 118:1663–74. doi: 10.1182/blood-2011-04-347849

72. Vogler M, Hamali HA, Sun XM, Bampton ET, Dinsdale D, Snowden RT, Dyer MJ, Goodall AH, Cohen GM. BCL2/BCL-X(L) inhibition induces apoptosis, disrupts cellular calcium homeostasis, and prevents platelet activation. Blood. 2011; 117:7145–54. doi: 10.1182/blood-2011-03-344812

73. Lujambio A. To clear, or not to clear (senescent cells)? That is the question. BioEssays. 2016 (Suppl 1); 38:S56–64. doi: 10.1002/bies.201670910

Research Paper

PI3Kα inhibition reduces obesity in mice

Elena Lopez-Guadamillas[1], Maribel Muñoz-Martin[1], Sonia Martinez[2], Joaquin Pastor[2], Pablo J. Fernandez-Marcos[3], Manuel Serrano[1]

[1]Tumor Suppression Group, Spanish National Cancer Research Center (CNIO), Madrid E28029, Spain
[2] Experimental Therapeutics Programme, Spanish National Cancer Research Center (CNIO), Madrid E28029, Spain
[3]Bioactive Products and Metabolic Syndrome Group, Madrid Institute of Advanced Studies (IMDEA) in Food, CEI UAM+CSIC, Madrid E28049, Spain

Correspondence to: Manuel Serrano; **email:** mserrano@cnio.es
DOI: 10.18632/aging.101075
Keywords: PI3K, obesity, energy expenditure, diabetes, metabolism
Received: August 19, 2016 **Accepted:** October 18, 2016 **Published:** November 4, 2016

ABSTRACT

Partial inhibition of PI3K is one of the best-validated and evolutionary conserved manipulations to extend longevity. The best known health beneficial effects of reduced PI3K are related to metabolism and include increased energy expenditure, reduced nutrient storage, and protection from obesity. We have previously shown that a dual chemical inhibitor of the alpha and delta PI3K isoforms (CNIO-PI3Ki) reduces obesity in mice and monkeys, without evident toxic effects after long-term treatment. Here, we dissect the role of the alpha and delta PI3K isoforms by making use of selective inhibitors against PI3Kα (BYL-719 also known as alpelisib) or PI3Kδ (GS-9820 also known as acalisib). Treatment of mice with the above mentioned inhibitors indicated that BYL-719 increases energy expenditure in normal mice and efficiently reduces body weight in obese (ob/ob) mice, whereas these effects were not observed with GS-9820. Of note, the dose of BYL-719 required to reduce obesity was 10-times higher than the equivalent dose of CNIO-PI3Ki, which could suggest that simultaneous inhibition of PI3K alpha and delta is more beneficial than single inhibition of the alpha isoform. In summary, we conclude that inhibition of PI3Kα is sufficient to increase energy expenditure and reduce obesity, and suggest that concomitant PI3Kδ inhibition could play an auxiliary role.

INTRODUCTION

The first gene mutation found to extend longevity in an animal was in the age-1 gene of *Caenorhabditis elegans* [1], which was later shown to encode the catalytic p110alpha subunit of class I phosphatidylinositol-4,5-bisphosphate 3-kinase (PI3Kα) [2]. PI3Kα mediates the signaling of numerous factors, being insulin and insulin-like growth factor 1 (IGF1) of special relevance. Indeed, partial genetic reduction of the insulin and IGF1 signaling (IIS) pathways at different levels extends longevity in worms, flies and mice [3]. For example, similar to worms, heterozygous inactivation of the gene encoding PI3Kα also extends longevity in mice [4]. Despite the strong link between PI3K down-modulation and longevity, it remains unclear which of its multiple physiological consequences are responsible for the beneficial effects on health and aging. A main function of the PI3K pathway is to activate anabolism and nutrient storage and, conversely, a consistent observation in a variety of genetic mouse models with partial PI3K down-modulation is their higher energy expenditure and protection from obesity [5]. Therefore, the beneficial metabolic effects of reduced PI3K signaling could explain, at least in part, the improved healthspan and delayed aging. Furthermore, inhibition of the PI3K downstream effector mTOR by rapamycin also increases longevity [6] and reduces body weight [7].

The above-described genetic evidences make very attractive the possibility that moderate inhibition of PI3K with small chemical compounds could have beneficial health effects. Indeed, two selective inhibitors of PI3Kα, PIK75 and A66, reduce body weight in normal lean mice but present negative effects including reduced locomotor activity [8]. On the other hand, we have shown that a chemical PI3K inhibitor with good

oral bioavailability and pharmacokinetics, named CNIO-PI3Ki, can efficiently reduce adiposity in obese mice and in obese Rhesus monkeys in the absence of detectable toxicities [9]. Of note, CNIO-PI3Ki not only inhibits PI3Kα but also PI3Kδ [9]. PI3Kδ is one of the four class I PI3K isoforms [10] and is mainly involved in the regulation of immune cells [11]. Interestingly, there is a strong association between inflammation of the adipose tissue and the pathological manifestations of obesity [12]. Based on this, it is conceivable that the inhibition of PI3Kδ could also contribute to the beneficial metabolic effects of CNIO-PI3Ki.

In this report, we use selective inhibitors of PI3Kα and PI3Kδ in mice to determine their efficacy in reducing obesity and elevating energy expenditure.

RESULTS

Differential effects of PI3K inhibitors on obesity in ob/ob mice

To dissect the relative contribution of PI3Kα and PI3Kδ inhibition in the reduction of obesity, we treated obese hyperphagic ob/ob mice with a selective PI3Kα inhibitor, BYL-719 [13], or with a selective PI3Kδ inhibitor, GS-9820 (also known as CAL-120) [14]. Remarkably, BYL-719 reduced body weight after 15 days of treatment to a similar extent as CNIO-PI3Ki, whereas GS-9820 had no significant effect at the same doses as BYL-719 (Figure 1A and 1B). It should be noted that 10 mg/kg of GS-9820 is sufficient to reduce the growth of multiple myeloma xenografts in mice [15]. Interestingly, CNIO-PI3Ki at 1 mg/kg was as effective as BYL-719 at 10 mg/kg. The higher efficiency of CNIO-PI3Ki may be due to a number of reasons, such as for example a better pharmacokinetics, but it could also reflect a contribution of PI3Kδ inhibition in the reduction of obesity in the context of simultaneous PI3Kα inhibition. We conclude that inhibition of PI3Kα is sufficient to reduce obesity, but we cannot exclude an additional auxiliary benefit due to the concomitant inhibition of PI3Kδ.

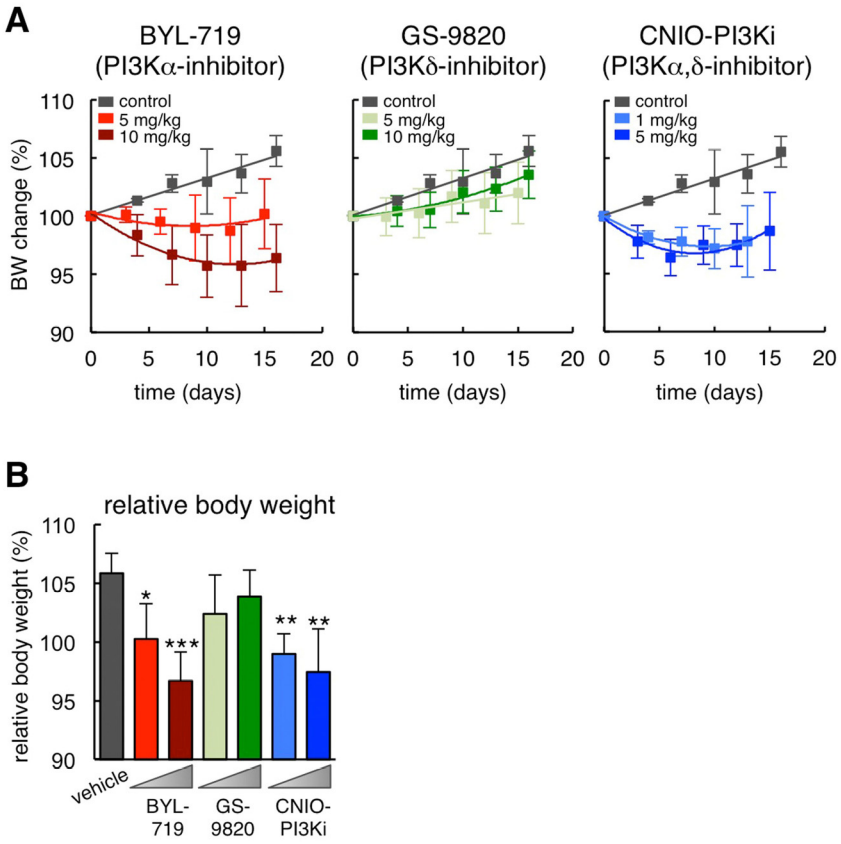

Figure 1. Differential effects of PI3K inhibitors on obesity in ob/ob mice. (**A**) Body weight change relative to day 0 during daily dosing of the indicated PI3K inhibitors (n=10 per group, ob/ob males, 20 weeks old). The vehicle treated group is the same for the three graphs. (**B**) Relative body weight change at the end of the treatment (day 15 or 16) of the same experimental groups shown in panel A. Values correspond to average ± s.d. Statistical significance was determined by the two-tailed Student's t-test relative to vehicle controls: *$p < 0.05$, ** $p < 0.01$, *** $p < 0.001$.

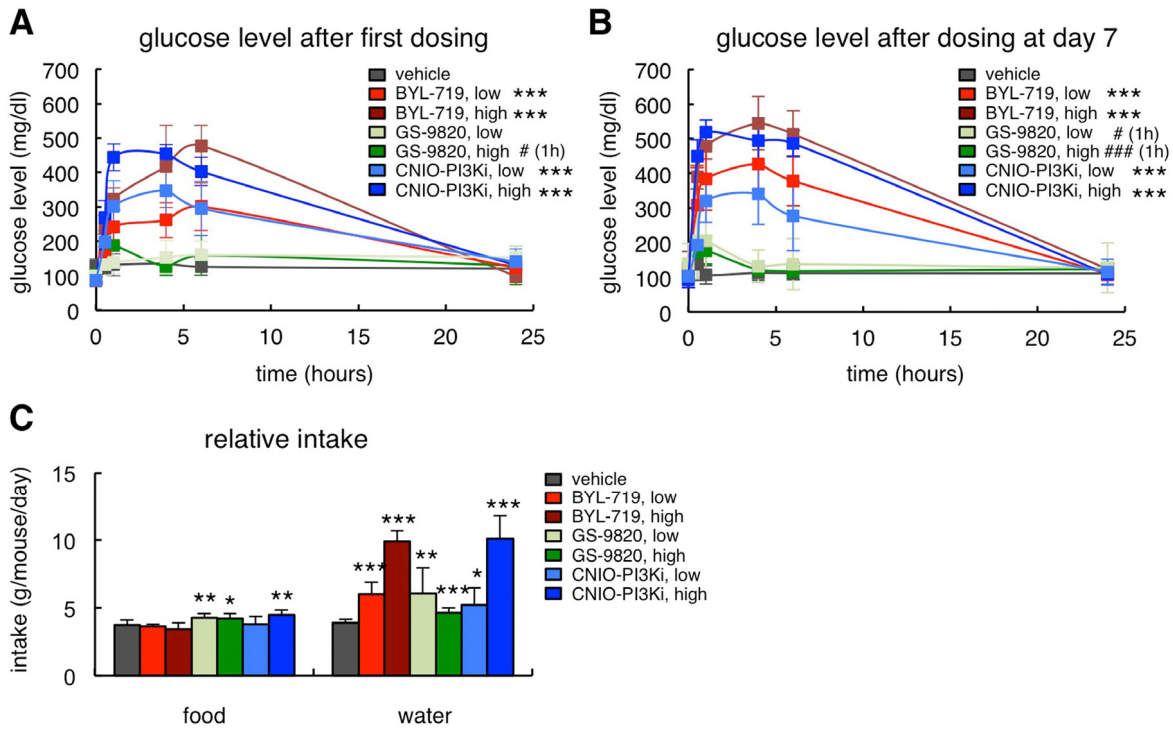

Figure 2. On-target effects of PI3Kα inhibition in ob/ob mice. (**A**) Glucose serum excursions after a single administration of vehicle, BYL-719 (5 or 10 mg/kg), GS-9820 (5 or 10 mg/kg) or CNIO-PI3Ki (1 or 5 mg/kg) by oral gavage (n=10 per group, ob/ob males, 20 weeks old). Treatments and measurements were done under ad libitum feeding. (**B**) Glucose serum excursions measured 7 days after the beginning of the treatment in the same mice as in Figure 2A. (**C**) Relative food and water intake in the same mice as in Figure 1A. The results correspond to the average daily food and water intake from days 7 to 12. Values correspond to average ± s.d. Statistical significance was determined by the two-tailed Student's t-test relative to vehicle controls: * $p < 0.05$, ** $p < 0.01$, *** $p < 0.001$. In Figures 2A and 2B, significant differences were found from 0.5 h to 6 h post-gavage, except for acalisib that is significant only at 1 h, indicated with # (1h).

On-target effects of PI3Kα inhibition in ob/ob mice

PI3Kα is involved in the signaling of insulin and, therefore, hyperglycemia is an expected on-target effect of PI3Kα inhibitors. In this regard, we have previously reported that, in lean mice, CNIO-PI3Ki at 15 mg/kg produces a moderate glycemic excursion, within physiological range (up to 150 mg/dl of serum glucose), and reversible within 8 h [9]. Obese ob/ob mice are insulin resistant and therefore their glycemic excursions were severe (up to 500 mg/dl) in the case of the two PI3Kα inhibitors, CNIO-PI3Ki and BYL-719, whereas GS-9820 had a comparatively minor effect (Figure 2A). It is important to note that the hyperglycemia produced by 1 mg/kg CNIO-PI3Ki was less severe than the one produced by 10 mg/kg BYL-719 (Figure 2A), being both treatments equally efficient in reducing obesity (Figures 1A and 1B). The hyperglycemic peaks were in all cases fully normalized after 24 h (Figure 2A). Furthermore, in mice that had been treated daily with the PI3K inhibitors for 7 days, glucose levels were also normal 24 h after the last administration of inhibitors (Figure 2B). The severe hyperglycemia produced in ob/ob mice was also reflected by their increased water intake, a compensatory response to reduce hyperglycemia (Figure 2C). Finally, we observed a modest increase in food intake in mice treated with GS-9820 or with high-dose CNIO-PI3Ki (Figure 2C).

Inhibition of insulin signaling not only affects glucose homeostasis but also lipid metabolism. Therefore, another anticipated on-target effect of PI3Kα inhibition in the white adipose tissue is a reduction in the uptake of dietary triglycerides (TG) and an increase in lipolysis that results in elevated serum free fatty acids (FFA) [16,17]. These effects are recapitulated by treatment with rapamycin, which inhibits mTOR, a key down-stream effector of PI3K [18]. In agreement with this, mice treated for 15 days with BYL-719 or CNIO-PI3Ki presented increased serum TG (Figure 3A) and FFA (Figure 3B), while GS-9820 had no detectable effect on serum lipids.

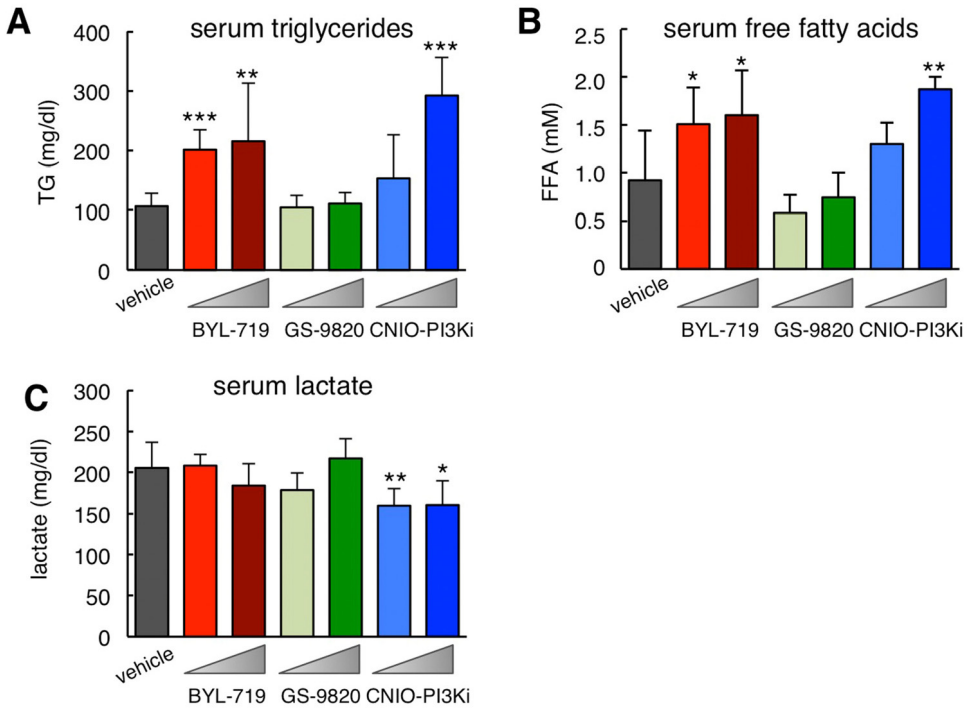

Figure 3. Biochemical serum profile of ob/ob mice after treatment with PI3K inhibitors. (**A**) Serum triglycerides (TG) in the same mice as in Figure 1A measured 3-4 hours after the last dosing at the end of the treatment (always under ad libitum feeding). (**B**) Serum free fatty acids (FFA) as in panel A. (**C**) Serum lactate as in panel A. Values correspond to average ± s.d. Statistical significance was determined by the two-tailed Student's t-test relative to vehicle controls: * $p< 0.05$, ** $p <0.01$, *** p

Partial down-modulation of PI3K has been reported to reduce serum lactate levels due to increased mitochondrial oxidative phosphorylation [19] and this effect has also been observed upon treatment with rapamycin [20]. Interestingly, mice treated for 15 days with 1 mg/kg CNIO-PI3Ki had a significant reduction in serum lactate, whereas this was not observed with BYL-719 or with GS-9820 at 10 mg/kg (Figure 3C). All together, we validate that BYL-719 and CNIO-PI3Ki are inhibiting PI3Kα *in vivo* by using a number of on-target readouts (hyperglycemia, increased serum lipids, and reduced serum lactate), whereas these effects are absent upon treatment with GS-9820.

Differential effect of PI3K inhibitors in energy expenditure

The PI3K pathway is a major inducer of anabolism and, therefore, genetic down-modulation of PI3K by PTEN or treatment of mice with CNIO-PI3Ki elevates energy expenditure [19,21]. We used lean wild-type mice to test the effect of a single dose (15 mg/kg) of each of the three PI3K inhibitors on energy expenditure. Interestingly, BYL-719, but not GS-9820, elevated energy expenditure during 7 h after oral administration in a similar way as CNIO-PI3Ki (Figure 4A). No changes in locomotor activity were observed in any of the treated mice (Figure 4B). Normal locomotor activity suggests the absence of severe toxic effects, and also excludes the possibility that increased physical activity could be the underlying reason for the increased energy expenditure. We conclude that PI3Kα, but not PI3Kδ, regulates energy expenditure in mice.

DISCUSSION

Previous work by us has shown that a dual PI3Kα and PI3Kδ inhibitor, namely CNIO-PI3Ki, reduces obesity and elevates energy expenditure in mice. Here, we have used selective inhibitors of PI3Kα and PI3Kδ and we have concluded that PI3Kα is the main isoform responsible for these beneficial metabolic effects. These observations are in agreement with the reported protection against aging-associated obesity of mice with reduced expression of PI3Kα [4]. It should be noted that CNIO-PI3Ki seems more efficient that BYL-719 in reducing obesity. Although the differential efficacy of the two inhibitors can have several explanations, one possibility is that PI3Kδ inhibition, although not sufficient by itself, contributes to reduce obesity in the context of simultaneous PI3Kα inhibition.

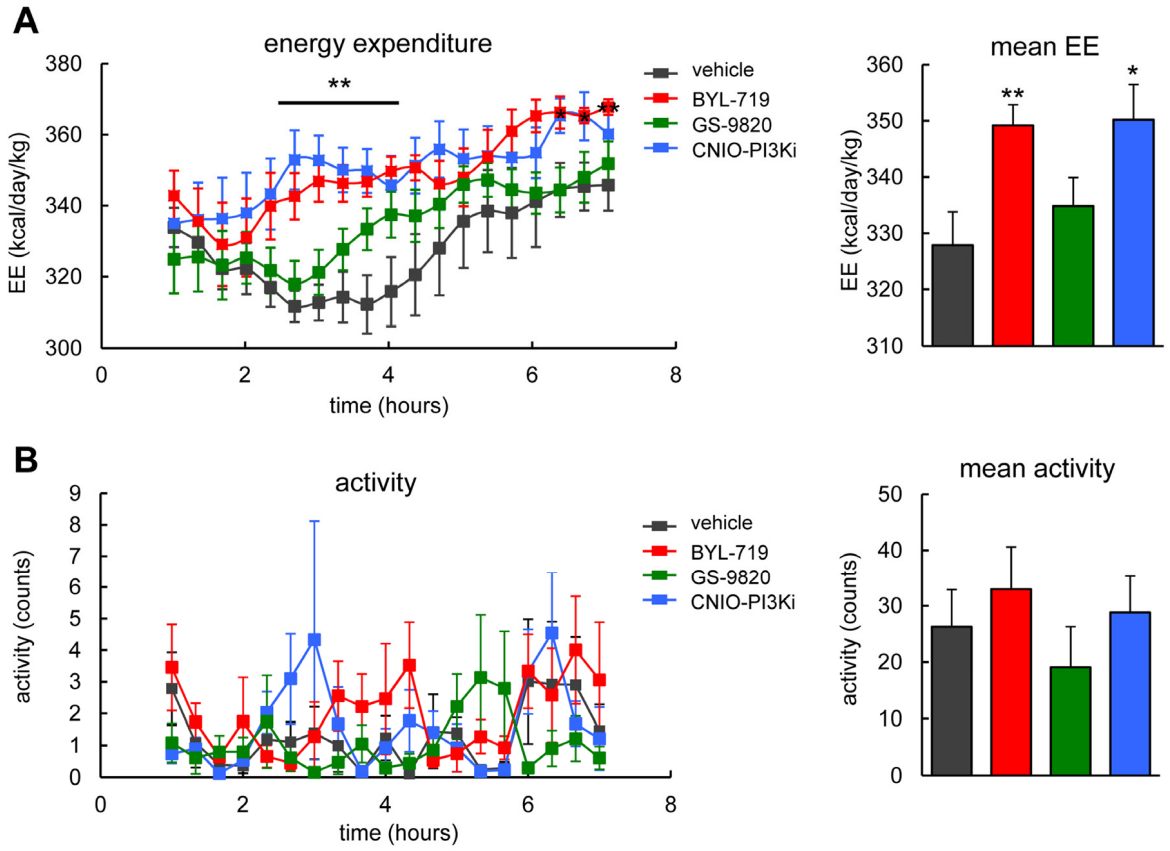

Figure 4. Energy expenditure and activity of wild-type mice after treatment with PI3K inhibitors. (**A**) *Left*, energy expenditure (EE). *Right*, mean EE. Calorimetry of male WT mice, under ad libitum feeding, after a single oral dose of 15 mg/kg of the indicated PI3K inhibitors (n=7-8 per group, C57BL6 males, 20 weeks old). The line and asterisks indicate that CNIO-PI3Ki and BYL-719 are significantly different relative to vehicle at these time points. (**B**) *Left*, activity. *Right*, mean activity. Activity was measured in the same mice as in panel A. Values correspond to average ± s.e.m. Statistical significance was determined by the two-tailed Student's t-test relative to vehicle controls: * $p < 0.05$, ** $p < 0.01$.

In addition, we have validated some on-target effects of PI3Kα inhibition produced as a consequence of reduced insulin signaling, including elevated levels of serum glucose, and serum lipids. In contrast, PI3Kδ inhibition by GS-9820 did not produce any of these effects even administered at a dose that was shown to have anti-tumoral effectiveness [15], thereby confirming its minor role in insulin signaling. The most dramatic on-target effect of PI3Kα inhibition was hyperglycemia, which in the case of the ob/ob mice was severe due to their diabetic condition. However, it is important to note that in normal lean mice, the glycemia induced by PI3Kα inhibition is within physiological range [9]. In summary, we conclude that moderate pharmacological inhibition of PI3Kα is sufficient to elicit the metabolic beneficial effects of reduced PI3K signaling. Our results, however, leave open the possibility that inhibition of PI3Kδ could also contribute to these effects in the context of concomitant PI3Kα inhibition.

MATERIALS AND METHODS

Ethics statement

All animal procedures were approved by the CNIO-ISCIII Ethics Committee for Research and Animal Welfare (CEIyBA) and the Community of Madrid, and conducted in accordance to the recommendations of the Federation of European Laboratory Animal Science Associations (FELASA) and the institutional guidelines.

Mouse experimentation

Mice were housed under specific pathogen free (SPF) conditions, at 22°C, and with 12 hours dark/light cycles (light cycle from 8 am to 8 pm). Mice were fed with standard chow diet (Harlan Teklad 2018, 18% of fat-based caloric content). Ob/ob C57BL6J mice were purchased from Charles River Laboratories. Wild-type C57BL6J/Ola.Hsd mice were purchased from Harlan.

All mice used were males of 20 weeks of age. PI3K inhibitors were administered daily by oral gavage during 15 or 16 days as follows, BYL-719 (5 and 10 mg/kg) and GS-9820 (5 and 10 mg/kg), CNIO-PI3Ki (1 and 5 mg/kg), dissolved in PEG-300 (Sigma) and 10% N-methyl-2-pyrrolidone (Sigma).

Serum analyses

For glucose excursions (Figure 2 A and B), mice under ad libitum feeding were treated with a single dose of the indicated PI3K inhibitors by oral gavage (at 10:00 am) and blood was collected from the tail tip for the determination of glucose (Glucocard strips; A. Meranini). For all the other serum analyses, mice at the end of their corresponding daily treatments for 15-16 days received a final dose of treatment and were sacrificed 3-4 h later (always under ad libitum feeding). Blood was collected from post-mortem heart puncture. Serum free fatty acids were quantified by a colorimetric assay (BioVision #K612-100). Triglycerides and lactate levels were measured using the ABX PENTRA 400 clinical chemical analyzer (Horiba ABX Diagnostics).

Indirect calorimetry and activity

Indirect calorimetry was performed following standard methods using Oxylet System metabolic chambers (Panlab Harvard Apparatus). Acclimatization of mice to the measurement cages was three days prior to data recording. Mice under ad libitum feeding were treated with a single dose of 15 mg/kg for each PI3K inhibitor (BYL-719, GS-9820 and CNIO-PI3Ki) by gavage. The volumes of consumed O_2 (VO_2) and eliminated CO_2 (VCO_2) were recorded every 24 min (8 simultane-ous metabolic chambers) for the following 7 hrs. Room temperature was constantly kept at 21°C. Energy Expenditure (EE) was calculated as EE=3.815+(1.232x (VCO_2/VO_2)) x VO_2 x 1.44. Mouse activity was recorded in time intervals of 20 min during the whole measurement period.

Statistical analyses

Values are expressed as mean ± s.d. (Figures 1 to 3) or mean ± s.e.m (Figure 4). Statistical analyses were performed using unpaired two-tailed Student´s t-test and differences with P values of <0.05 were considered to be statistically significant (* p<0.05, ** p<0.01, *** p<0.001). Statistical analyses were performed using Excel or GraphPad Prism software.

AUTHOR CONTRIBUTIONS

E.L.-G. participated in the conceptual and experimental design, carried out and analyzed most of the experiments, and wrote the manuscript; M.M.-M. helped with animal experimentation; S.M. and J.P synthesized the PI3K inhibitors; P.J.F.-M. carried out the calorimetry; M.S. conceived, designed, supervised the work and wrote the manuscript. All authors discussed the results and commented on the manuscript.

ACKNOWLEDGEMENTS

We thank Cristina Pantoja for her help. We also thank Gema Iglesias for animal handling.

CONFLICTS OF INTEREST

The authors have no conflict of interests to declare.

FUNDING

E.L.-G. was recipient of a predoctoral contract from the Spanish Ministry of Education. P.J.F.-M. has been funded by the Spanish Association Against Cancer (aecc). Work in the laboratory of M.S. is funded by the CNIO and by grants from the Spanish Ministry of Economy co-funded by the European Regional Development Fund (SAF project), the European Research Council (ERC Advanced Grant), the Regional Government of Madrid co-funded by the European Social Fund (ReCaRe project), the Botin Foundation and Banco Santander (Santander Universities Global Division), the Ramon Areces Foundation, and the AXA Foundation.

REFERENCES

1. Friedman DB, Johnson TE. A mutation in the age-1 gene in Caenorhabditis elegans lengthens life and reduces hermaphrodite fertility. Genetics. 1988; 118:75–86.

2. Morris JZ, Tissenbaum HA, Ruvkun G. A phosphatidylinositol-3-OH kinase family member regulating longevity and diapause in Caenorhabditis elegans. Nature. 1996; 382:536–39. doi: 10.1038/382536a0

3. Fontana L, Partridge L, Longo VD. Extending healthy life span--from yeast to humans. Science. 2010; 328:321–26. doi: 10.1126/science.1172539

4. Foukas LC, Bilanges B, Bettedi L, Pearce W, Ali K, Sancho S, Withers DJ, Vanhaesebroeck B. Long-term p110α PI3K inactivation exerts a beneficial effect on metabolism. EMBO Mol Med. 2013; 5:563–71. doi: 10.1002/emmm.201201953

5. Ortega-Molina A, Serrano M. PTEN in cancer, metabolism, and aging. Trends Endocrinol Metab. 2013; 24:184–89. doi: 10.1016/j.tem.2012.11.002

6. Harrison DE, Strong R, Sharp ZD, Nelson JF, Astle CM, Flurkey K, Nadon NL, Wilkinson JE, Frenkel K, Carter CS, Pahor M, Javors MA, Fernandez E, Miller RA. Rapamycin fed late in life extends lifespan in genetically heterogeneous mice. Nature. 2009; 460:392–95. doi: 10.1038/nature08221

7. Leontieva OV, Paszkiewicz GM, Blagosklonny MV. Comparison of rapamycin schedules in mice on high-fat diet. Cell Cycle. 2014; 13:3350–56. doi: 10.4161/15384101.2014.970491

8. Smith GC, Ong W-K, Costa JL, Watson M, Cornish J, Grey A, Gamble GD, Dickinson M, Leung S, Rewcastle GW, Han W, Shepherd PR. Extended treatment with selective phosphatidylinositol 3-kinase and mTOR inhibitors has effects on metabolism, growth, behaviour and bone strength. FEBS J. 2013; 280:5337–49. doi: 10.1111/febs.12428

9. Ortega-Molina A, Lopez-Guadamillas E, Mattison JA, Mitchell SJ, Muñoz-Martin M, Iglesias G, Gutierrez VM, Vaughan KL, Szarowicz MD, González-García I, López M, Cebrián D, Martinez S, et al. Pharmacological inhibition of PI3K reduces adiposity and metabolic syndrome in obese mice and rhesus monkeys. Cell Metab. 2015; 21:558–70. doi: 10.1016/j.cmet.2015.02.017

10. Vanhaesebroeck B, Guillermet-Guibert J, Graupera M, Bilanges B. The emerging mechanisms of isoform-specific PI3K signalling. Nat Rev Mol Cell Biol. 2010; 11:329–41. doi: 10.1038/nrm2882

11. Hawkins PT, Stephens LR. PI3K signalling in inflammation. Biochim Biophys Acta. 2015; 1851:882–97. doi: 10.1016/j.bbalip.2014.12.006

12. Pellegrinelli V, Carobbio S, Vidal-Puig A. Adipose tissue plasticity: how fat depots respond differently to pathophysiological cues. Diabetologia. 2016; 59:1075–88. doi: 10.1007/s00125-016-3933-4

13. Furet P, Guagnano V, Fairhurst RA, Imbach-Weese P, Bruce I, Knapp M, Fritsch C, Blasco F, Blanz J, Aichholz R, Hamon J, Fabbro D, Caravatti G. Discovery of NVP-BYL719 a potent and selective phosphatidylinositol-3 kinase alpha inhibitor selected for clinical evaluation. Bioorg Med Chem Lett. 2013; 23:3741–48. doi: 10.1016/j.bmcl.2013.05.007

14. Lannutti BJ, Meadows SA, Herman SE, Kashishian A, Steiner B, Johnson AJ, Byrd JC, Tyner JW, Loriaux MM, Deininger M, Druker BJ, Puri KD, Ulrich RG, Giese NA. CAL-101, a p110δ selective phosphatidylinositol-3-kinase inhibitor for the treatment of B-cell malignancies, inhibits PI3K signaling and cellular viability. Blood. 2011; 117:591–94. doi: 10.1182/blood-2010-03-275305

15. Ikeda H, Hideshima T, Fulciniti M, Perrone G, Miura N, Yasui H, Okawa Y, Kiziltepe T, Santo L, Vallet S, Cristea D, Calabrese E, Gorgun G, et al. PI3K/p110delta is a novel therapeutic target in multiple myeloma. Blood. 2010; 116:1460–68. doi: 10.1182/blood-2009-06-222943

16. Dimitriadis G, Mitrou P, Lambadiari V, Maratou E, Raptis SA. Insulin effects in muscle and adipose tissue. Diabetes Res Clin Pract. 2011 (Suppl 1); 93:S52–59. doi: 10.1016/S0168-8227(11)70014-6

17. Frayn KN. Adipose tissue as a buffer for daily lipid flux. Diabetologia. 2002; 45:1201–10. doi: 10.1007/s00125-002-0873-y

18. Blagosklonny MV. Rapamycin-induced glucose intolerance: hunger or starvation diabetes. Cell Cycle. 2011; 10:4217–24. doi: 10.4161/cc.10.24.18595

19. Garcia-Cao I, Song MS, Hobbs RM, Laurent G, Giorgi C, de Boer VC, Anastasiou D, Ito K, Sasaki AT, Rameh L, Carracedo A, Vander Heiden MG, Cantley LC, et al. Systemic elevation of PTEN induces a tumor-suppressive metabolic state. Cell. 2012; 149:49–62. doi: 10.1016/j.cell.2012.02.030

20. Leontieva OV, Blagosklonny MV. M(o)TOR of pseudo-hypoxic state in aging: rapamycin to the rescue. Cell Cycle. 2014; 13:509–15. doi: 10.4161/cc.27973

21. Ortega-Molina A, Efeyan A, Lopez-Guadamillas E, Muñoz-Martin M, Gómez-López G, Cañamero M, Mulero F, Pastor J, Martinez S, Romanos E, Mar Gonzalez-Barroso M, Rial E, Valverde AM, et al. Pten positively regulates brown adipose function, energy expenditure, and longevity. Cell Metab. 2012; 15:382–94. doi: 10.1016/j.cmet.2012.02.001

Research Paper

Mitophagy-driven mitochondrial rejuvenation regulates stem cell fate

Alejandro Vazquez-Martin[1], Chris Van den Haute[2], Sílvia Cufí[3], Bruna Corominas-Faja[4], Elisabet Cuyàs[4], Eugeni Lopez-Bonet[5], Esther Rodriguez-Gallego[6], Salvador Fernández-Arroyo[6], Jorge Joven[6], Veerle Baekelandt[2], and Javier A. Menendez[4,7]

[1]Cancer Research Group, Latvian Biomedical Research & Study Centre, Riga, Latvia
[2]Laboratory for Neurobiology and Gene Therapy, Department of Neurosciences, Katholieke Universiteit Leuven, Leuven, Flanders, Belgium
[3]Josep Carreras Leukemia Research Institute, Stem Cell Lab, Barcelona, Spain
[4]Molecular Oncology Group, Girona Biomedical Research Institute (IDIBGI), Girona, Spain
[5]Department of Anatomical Pathology, Dr. Josep Trueta Hospital of Girona, Girona, Catalonia, Spain
[6]Unitat de Recerca Biomèdica, Hospital Universitari Sant Joan, Institut d'Investigació Sanitaria Pere Virgili (IISPV), Universitat Rovira i Virgili, Reus, Spain
[7]ProCURE (Program Against Cancer Therapeutic Resistance), Metabolism and Cancer Group, Catalan Institute of Oncology, Girona, Spain

Key words: mitophagy, mitochondria, stem cells, pluripotency, cancer, epigenetics
Received: 02/11/16; Accepted: 05/30/16; Published: 06/13/16 DOI: 10.18632/aging.100976
Correspondence to: Javier A. Menendez, PhD; Veerle Baekelandt, PhD; Alejandro Vazquez-Martin, PhD
E-mail: jmenendez@idibgi.org; veerle.baekelandt@med.kuleuven.be; jandraes@yahoo.es

Abstract: **Our understanding on how selective mitochondrial autophagy, or mitophagy, can sustain the archetypal properties of stem cells is incomplete. PTEN-induced putative kinase 1 (PINK1) plays a key role in the maintenance of mitochondrial morphology and function and in the selective degradation of damaged mitochondria by mitophagy. Here, using embryonic fibroblasts from *PINK1* gene-knockout (KO) mice, we evaluated whether mitophagy is a causal mechanism for the control of cell-fate plasticity and maintenance of pluripotency. Loss of *PINK1*-dependent mitophagy was sufficient to dramatically decrease the speed and efficiency of induced pluripotent stem cell (iPSC) reprogramming. Mitophagy-deficient iPSC colonies, which were characterized by a mixture of mature and immature mitochondria, seemed unstable, with a strong tendency to spontaneously differentiate and form heterogeneous populations of cells. Although mitophagy-deficient iPSC colonies normally expressed pluripotent markers, functional monitoring of cellular bioenergetics revealed an attenuated glycolysis in mitophagy-deficient iPSC cells. Targeted metabolomics showed a notable alteration in numerous glycolysis- and TCA-related metabolites in mitophagy-deficient iPSC cells, including a significant decrease in the intracellular levels of α-ketoglutarate -a key suppressor of the differentiation path in stem cells. Mitophagy-deficient iPSC colonies exhibited a notably reduced teratoma-initiating capacity, but fully retained their pluripotency and multi-germ layer differentiation capacity *in vivo*. *PINK1*-dependent mitophagy pathway is an important mitochondrial switch that determines the efficiency and quality of somatic reprogramming. Mitophagy-driven mitochondrial rejuvenation might contribute to the ability of iPSCs to suppress differentiation by directing bioenergetic transition and metabolome remodeling traits. These findings provide new insights into how mitophagy might influence the stem cell decisions to retain pluripotency or differentiate in tissue regeneration and aging, tumor growth, and regenerative medicine.**

INTRODUCTION

Mitochondrial autophagy, or mitophagy, is a key cellular pathway for mitochondrial quality control that functions to clear mitochondria [1-4]. Because the selective autophagosome-based mitochondrial degradation process eliminates unwanted or dysfunctional mitochondria after cell stress [5-9],

abnormal mitophagy has a deleterious impact on cell homeostasis and may lead to cell death, which causally contributes to the pathogenesis of degenerative disorders [10-16]. Although our knowledge of mitophagy in somatic cell physiology is extensive, the role of mitophagy in the physiology of stem cells, which have the unique ability to self-renew and differentiate into various cell types, is less understood. Thus, while mitophagy is believed to play a pivotal role in stem cell functions during aging, tissue regeneration, and cancer [17-24], our current understanding on how mitophagy can sustain the archetypal properties of stem cells is rudimentary.

Mitochondria appear to play crucial roles during stemness factor-mediated nuclear reprogramming of somatic cells into induced pluripotent stem cells (iPSCs), a convenient "in a dish" model that allows a comprehensive understanding of stem cell biology. Functional metamorphosis of somatic oxidative phosphorylation into glycolytic metabolism plays a causal role in enabling the reprogramming process of acquisition and maintenance of stemness to occur [25-35]. It is also apparent that the intrinsic metabolic demands that drive reprogramming to stemness involve substantial structural mitochondrial reorganization, transforming mitochondria into a cristae-poor, immature phenotype [36-45]. Paradoxically, the establishment of induced pluripotency requires a transient and early energy-demanding metabolic state characterized by increased mitochondrial oxidative phosphorylation and hyperactive mitophagy [46, 47]. Because the unique metabolic state required to achieve cell plasticity is accompanied by significant temporal changes in mitochondrial function, composition, structure, and maturation, it might appear elementary to suggest that mitophagy is a prerequisite of induced pluripotency. Nonetheless, recent studies have shed light on how interlinked processes critical for mitochondrial health, including mitochondrial fragmentation and mitochondrial fission/fusion, significantly alter the efficiency and speed of induced pluripotency [48-51], but little information is available on the role of mitophagy in the acquisition and maintenance of stemness.

PTEN-induced putative kinase 1 (*PINK1*) encodes a key mitochondrial protein that specifically identifies and commits mitochondria to degradation via selective autophagy [52-63]. Using embryonic fibroblasts from *PINK1* gene-knockout (KO) mice, we here tested the hypothesis that mitophagy is a pivotal mechanism of cell-fate plasticity by converting functionally mature mitochondrial networks into immature states and vice versa during nuclear reprogramming to stemness and commitment to differentiation, respectively. By examining the ability of mitophagy to causally modulate cell fate decisions during the entry to and exit from pluripotency, we have identified a hitherto unrecognized role of the mitophagy pathway as a critical mitochondrial switch that directs bioenergetic transition and metabolome remodeling traits to ultimately determine the efficiency and quality of nuclear reprogramming and stemness transition in somatic cells.

RESULTS

PINK1-mediated mitophagy is necessary for efficient nuclear reprogramming of somatic cells into iPSCs

Because the initial stages of reprogramming trigger a stress response involving repression of mitochondrial functions and oxidative stress [36-45, 66], we hypothesized that the critical ability of PINK1 to identify and selectively trim impaired mitochondria from the mitochondrial network might determine the efficiency of reprogramming. To test whether *PINK1*-KO mouse embryonic fibroblasts (MEFs) constitute a useful model to dissect the role of mitophagy in the establishment of induced pluripotency, we first mimicked mitochondrial damage by experimentally depolarizing mitochondria with the uncoupler carbonyl cyanide *m*-chlorophenylhydrazone (CCCP) and then monitoring loss of MitoTracker staining after mitophagy stimulation [62, 67]. Collectively, our findings show that PINK1 is necessary to efficiently drive the mitophagic digestion of damaged mitochondria (Supplemental data; supplemental Fig. 1).

We then used *PINK1*$^{-/-}$ MEFs to explore whether PINK1-mediated mitophagy might constitute part of the molecular roadmap facilitating reprogramming. To do this, we compared iPSC generation in early-passage *PINK*$^{+/+}$ and *PINK*$^{-/-}$ MEFs using a three-factor induction protocol (*Oct4*, *Sox2*, and *Klf4*, hereafter referred to as OSK). We transduced MEFs with OSK at a 1:1:1 ratio on day 0 and repeated the transduction up to four times (one infection every 12 h using the same batch of all three retroviruses), after which the regular media was replaced with standard mESC media supplemented with the knockout serum replacement (KSR). As early as 7 days after transduction, clearly recognizable flat, packed, tight colonies characteristic of ES-like cells appeared in OSK-transduced *PINK1*$^{+/+}$ MEF cultures (Fig. 1A). Conversely, OSK-transduced *PINK1*$^{-/-}$ MEFs mostly failed to display the typical compact ES cell colony morphology (Fig. 1A). Indeed, using a parallel live cell-imaging 96-well-plate-based screening assay to rapidly assess the expression of the

pluripotency-associated surface marker Ssea-1 during reprogramming, we found that the appearance of Ssea-1^{+} clusters was delayed by 3-4 days in *PINK1*$^{-/-}$ MEFs compared with *PINK1*$^{+/+}$ isogenic counterparts (data not shown). We combined the observations of ES cell-like morphological changes (e.g., defined boundaries and high nucleus-to-cytoplasm ratio within individual cells) with alkaline phosphatase (AP) activity, a commonly used pluripotency indicator, to quantify *bona fide* iPSC colonies. From 50,000 *PINK1*$^{+/+}$ MEFs transduced, 150±10 colonies were AP-positive at day 14 after transduction, resulting in an iPSC generation efficiency of 0.3% (Fig. 1A). In contrast, only 30±4 colonies were generated from an equivalent number of *PINK1*$^{-/-}$ MEFs, equivalent to an iPSC generation efficiency of 0.06% (Fig. 1A). Concerning the transduction efficiency, we did not observe any significant differences between the two groups (data not shown), thus confirming that the observed decrease in reprogramming efficiency is due to the absence of *PINK1*. These findings show that loss of PINK1-dependent mitophagy is sufficient to dramatically decrease the speed and efficiency of nuclear re-programming.

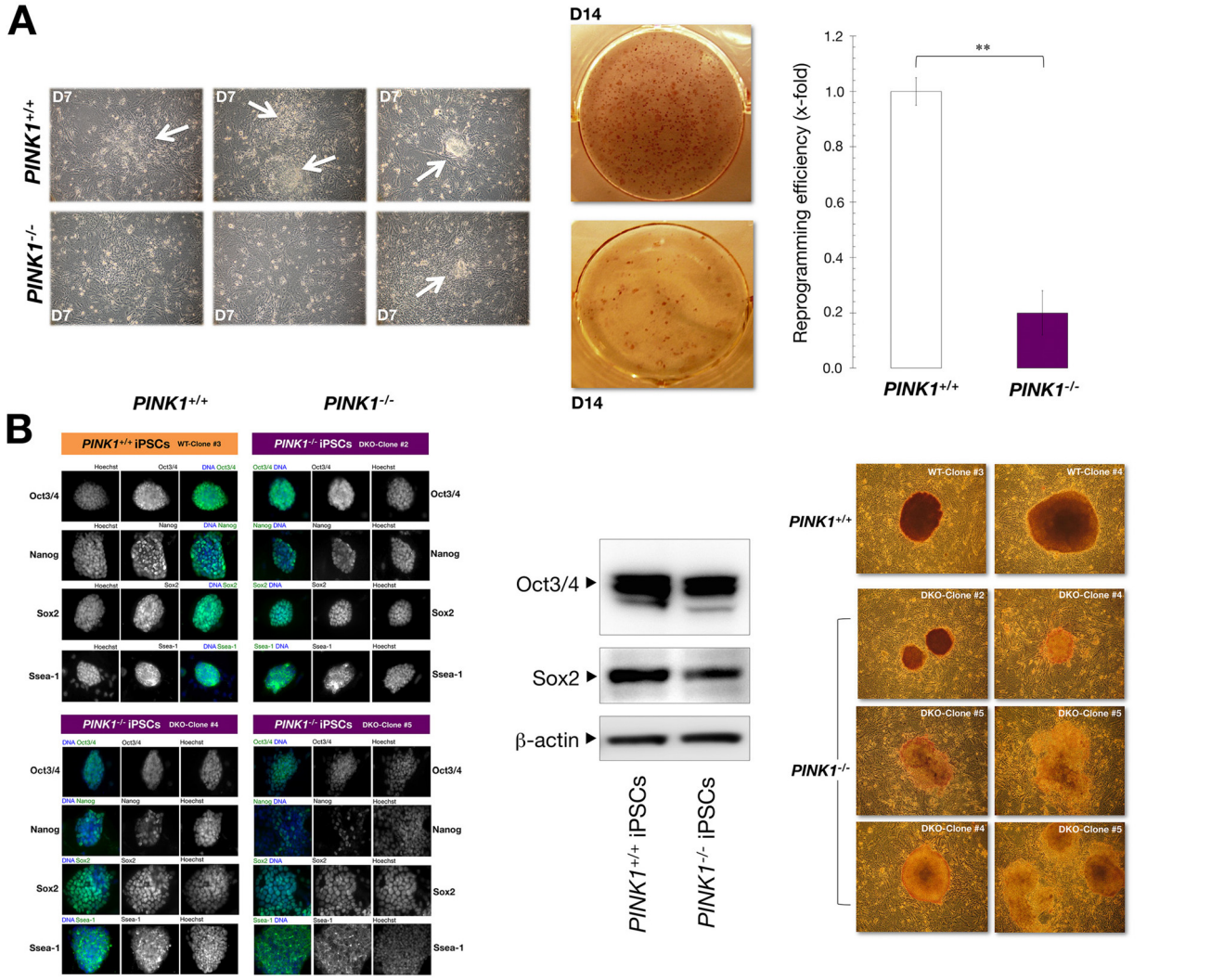

Figure 1. Mitophagy deficiency is a reprogramming barrier. (**A**) Early passage *PINK1*$^{+/+}$ and *PINK1*$^{-/-}$ MEFs were transduced with retroviral vectors encoding for Oct4, Sox2, and Klf4 and cultured in ES medium. Phase-contrast microphotographs of representative *PINK1*$^{+/+}$ and *PINK1*$^{-/-}$ MEFs at day 7 (D7) after the initial transduction with OSK are shown (white arrows indicate emerging iPSC-like colonies). Representative photographs of colonies of AP-stained OSK-transduced *PINK1*$^{+/+}$ and *PINK1*$^{-/-}$ MEFs. The number of AP^{+} colonies was counted 14 days after the initial infection and represent reprogramming efficiency relative to *PINK1*$^{+/+}$ MEFs (x-fold) (n=6 for each condition). **, P<0.01. (**B**) Individual iPSC-like colonies were randomly selected from each *PINK1* subtype, cultured on 6-well plates coated with MEF feeder layers, and stained either for AP activity (*left*) or with antibodies against Oct3/4, Nanog, Sox2, and Ssea-1 (*right*), as indicated in the "Methods" section. Nuclear staining was performed with Hoechst 33258. Panel depicts representative images of iPSC colonies that were captured using different channels for Oct3/4 (*green*), Nanog (*green*), Sox2 (*green*), Ssea-1 (*green*), or Hoechst 33258 (*blue*), as specified. Representative Western blots for Oct3/4 and Sox2 protein expression in *PINK1*$^{+/+}$- *PINK1*$^{-/-}$-iPSCs are shown (*middle*; n = 2).

Loss of PINK1-mediated mitophagy destabilizes the undifferentiated state in iPSCs

To verify that loss of PINK1-driven mitophagy dampens the reprogramming process, we picked random colonies from the previous experiment and established *PINK1*$^{+/+}$-iPSC and *PINK1*$^{-/-}$-iPSC clonal cell lines on pre-seeded MEF feeder layers, which are known to encourage induced stem cells to remain in an undifferentiated state. Immunofluorescence staining analysis of early-passage iPSCs failed to reveal major differences in the expression level of Oct3/4, Nanog, Sox2, and Ssea-1 of individual cells within *PINK1*$^{-/-}$- and *PINK1*$^{+/+}$-iPSC colonies (Fig. 1B, right). Indeed, immunoblotting procedures demonstrated a similar expression profile of the pluripotency markers Oct3/4 and Sox2 in early-passage *PINK1*$^{-/-}$- and *PINK1*$^{+/+}$-iPSCs (Fig. 1B, middle). Both early- and late-passage *PINK1*$^{+/+}$-iPSC colonies were large and well-rounded and stained strongly for AP, reflective of a high percentage of non-differentiated cells (Fig. 1B). The majority of relatively late-passage *PINK1*$^{-/-}$-iPSC colonies, however, were slightly smaller upon colony expansion, with very few showing a smooth, circular and distinct edge, and in many cases displaying irregular morphologies and undefined edges. Indeed, late-passage *PINK1*$^{-/-}$-iPSC colonies tended to rapidly lose AP activity and failed to stably retain the compact colony morphology typical of undifferentiated iPSCs [50, 68] (Fig. 1B, right).

Given that the apparent destabilization of the undifferentiated state of *PINK1*$^{-/-}$-iPSCs occurred without drastic changes in the expression of several pluripotency markers, we explored whether loss of PINK1-driven mitophagy significantly altered the well-known ability of nuclear reprogramming to transform the mitochondrial infrastructure and induce iPSC-associated bioenergetic transition and metabolome remodeling traits [30].

Mitophagy deficient-iPSCs cannot "rejuvenate" the morphological characteristics of the mitochondria network

We first confirmed that loss of *PINK1* induces a moderate mitochondrial fragmentation in MEFs [52] as well as a more prominent accumulation of mitochondrial aggregates due to impaired mitophagy (Fig. 2A). Given that cell reprogramming leads to mitochondrial structural and functional alterations described as "rejuvenation" [36-42, 44, 45, 66], we used transmission electron microscopy (TEM) to examine whether the decreased capacity of *PINK1*$^{-/-}$-iPSCs to maintain their undifferentiated state involves alterations in the morphology of the mitochondrial network. Although we could detect a small decrease in the length and area of mitochondria in *PINK1*$^{-/-}$ MEFs, together with an increase in the number of mitochondria per cell (Fig. 2B), the majority of mitochondria in both MEF populations had a similar morphology characterized by mature mitochondrial networks with tubular structures and densely-packed cristae (Fig. 2B).

PINK1$^{+/+}$-iPSC mitochondria exhibited a dramatically decreased long diameter and increased short diameter relative to *PINK1*$^{-/-}$ MEFs (Fig. 2B). Interestingly, though nuclear reprogramming of *PINK1*$^{+/+}$-iPSCs led to the acquisition of an immature mitochondrial phenotype characterized by a rounded morphology with sparse cristae, it was noteworthy that reprogramming failed to fully reset the mitochondrial morphology of *PINK1*$^{-/-}$ MEFs to a *bona fide* embryonic-like state. Con-sequently, *PINK1*$^{-/-}$ iPSCs accumulated larger, irregular mitochondria containing different inclusions and more cristae (Fig. 2B). These findings, altogether, strongly suggest that mitophagy deficient-iPSCs fail to fully rejuvenate the morphological characteristics of the mitochondrial network.

Loss of PINK1-driven mitophagy impairs the bioenergetic transition associated with nuclear reprogramming

Mitochondrial rejuvenation is a key mechanism to protect cells from reprogramming factor-induced oxidative stress and reactive oxygen species (ROS) accumulation, a well-known roadblock to re-programming [36-42, 44, 45, 66]. We therefore speculated that blockade of PINK1-driven mitophagy might lead to a detrimental accumulation of ROS during the initial stages of reprogramming (Supplemental data; supplemental Fig. 2). Only when forced expression of c-Myc, which can override the cell cycle checkpoints imposed in response to ROS accumulation [69-71], was combined with the exogenous addition of vitamin C *PINK1*$^{-/-}$ MEFs reached reprogramming efficiencies equivalent to those observed in OSK-transduced *PINK1*$^{+/+}$ MEFs in the absence of this antioxidant (Supplemental data; supplemental Fig. 2). Because the incapacity of the ROS scavenger and epigenetic regulator vitamin C [72-75] to fully bypass the reprogramming roadblock imposed by the loss of *PINK1* suggested that mitophagy-driven remodeling of the mitochondria network into an immature state might constitute a critical barrier during somatic reprogram-ming, we performed a multimodal metabolic characterization of *PINK1*$^{-/-}$ and *PINK1*$^{+/+}$ iPSCs at the level of cellular bioenergetics and intracellular metabolome.

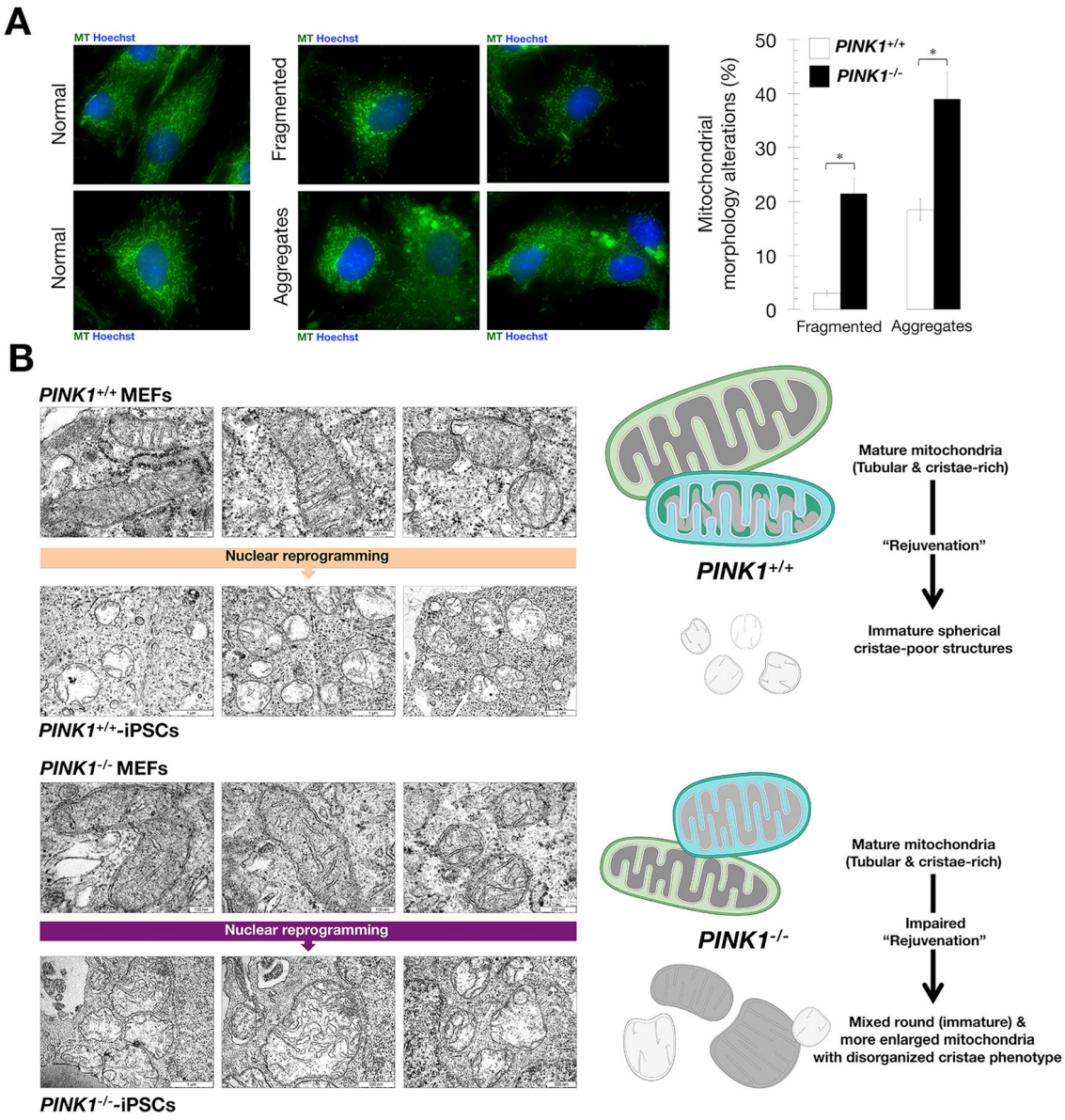

Figure 2. Mitophagy deficiency impedes the rejuvenation of mitochondria networks in iPSCs. (**A**) Loss of *PINK1* induces moderate mitochondrial fragmentation and aggregation in MEFs (MT: MitoTracker). Bar chart depicts the average percentages of cells showing fragmentation and/or aggregation (n=3). *, P<0.05. (**B**) Representative TEM images of mitochondria in all cell lines. *PINK1*$^{+/+}$ and *PINK1*$^{-/-}$ MEFs display a preponderance of tubular and cristae-rich mature mitochondria. *PINK1*$^{+/+}$ iPSCs display a preponderance of "rejuvenated" spherical cristae-poor immature mitochondria, whereas *PINK1*$^{-/-}$ iPSCs display an impaired "rejuvenation" characterized by an assortment of mitochondrial configurations including round (immature) and more enlarged mitochondria with disorganized cristae.

First, a well-validated extracellular flux technology was employed to establish functional monitoring of cellular bioenergetics in *PINK1*$^{-/-}$ and *PINK1*$^{+/+}$ iPSCs. Measurement of the extracellular acidification rate (ECAR) enabled real-time assessment of the glycolytic phenotype associated with iPSCs (Fig. 3A). Sequential supplementation of the glycolytic fuel glucose, the ATP synthase complex V mitochondrial inhibitor oligomycin, and the competitive inhibitor of glucose 2-deoxy-glucose (2-DG), dissected key parameters of glycolytic function, including glycolysis (i.e., the ECAR rate reached by iPSCs after the addition of saturating

amounts of glucose), glycolytic capacity (i.e., the maximum ECAR rate reached upon blockade of oxidative phosphorylation), and glycolytic reserve (i.e., the capability of iPSCs to respond to an energetic demand). *PINK1*$^{-/-}$-iPSCs were found to be significantly less glycolytic than *PINK1*$^{+/+}$-iPSCs (Fig. 3A), suggesting that the reduced capacity of mitophagy deficient-iPSCs to efficiently drive mitochondrial metamorphosis translate into a reduced capacity to bioenergetically transitioning from somatic cellular respiration to glycolysis during iPSC derivation [30].

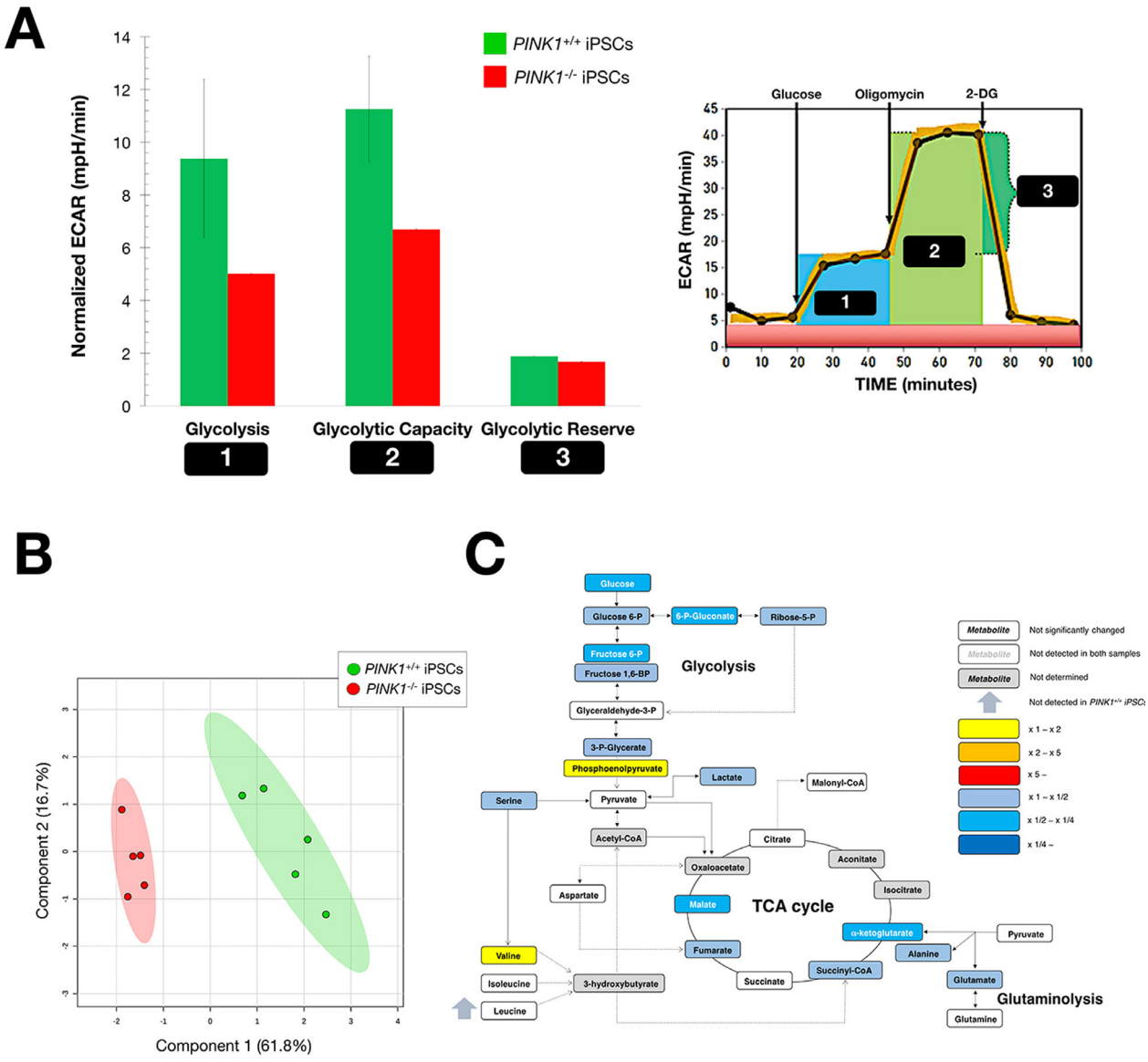

Figure 3. Mitophagy deficiency impairs the bioenergetic transition associated with nuclear reprogramming. (**A**) Calculated glycolysis (maximum rate measurement before oligomycin injection – Last rate measurement before glucose injection [1]), glycolytic capacity (maximum rate measurement after oligomycin injection – Last rate measurement before glucose injection [2]), and glycolytic reserve (glycolytic capacity – glycolysis [3]) were calculated with normalized ECAR values in *PINK1*$^{+/+}$- and *PINK1*$^{-/-}$ -iPSCs (n = 2). (**B**) Two-dimensional PLS-DA models to view the separation of the two groups (*PINK1*$^{+/+}$- and *PINK1*$^{-/-}$ -iPSCs) following GC-EI-QTOF-MS-based metabolomic profiling. (**C**) Metabolites in *PINK1*$^{+/+}$-iPSCs were extracted and quantitatively analyzed by GC-EI-QTOF-MS and compared with metabolites from *PINK*$^{-/-}$-iPSCs (n = 2). Significantly increased and decreased metabolites are shown using yellow-red and light blue-dark blue color scales, respectively.

Loss of PINK1-driven mitophagy impairs the metabolome remodeling associated with nuclear reprogramming

We utilized our recently developed targeted metabolomics platform coupling gas chromatography with quadrupole time-of-flight mass spectrometry and an electron impact source (GC-EI-QTOF-MS), which allows the simultaneous measurement of selected metabolites representative of the catabolic and anabolic status of key metabolic nodes. These metabolites include not only representatives of glycolysis and the mitochondrial tricarboxylic acid (TCA) cycle, but also other biosynthetic routes such as pentose phosphate pathway, amino acid metabolism and *de novo* fatty acid biogenesis [76, 77]. Metabolite-based clustering obtained by partial least squares-discriminant analysis (PLS-DA) model revealed a clear and significant separation between *PINK1*$^{-/-}$-iPSCs and *PINK1*$^{+/+}$-iPSCs in two-dimensional (2D) score plots (Fig. 3B). Profiling of the intracellular metabolome supported a *PINK1*$^{-/-}$ iPSCs signature distinct from the *PINK1*$^{+/+}$ iPSCs counterpart, which apparently involved a notable decrease in a majority of the measured glycolysis- and TCA-related biochemicals (Fig. 3C).

Heatmap visualization, commonly used for unsupervised clustering, likewise revealed distinct segregation of metabolites in *PINK1*$^{-/-}$-iPSCs and *PINK1*$^{+/+}$-iPSCs groups, pointing to an altered metabolic signature associated with the loss of *PINK1*-dependent mitophagy in iPSCs (Fig. 4). Unsupervised hierarchical clustering of all pairwise comparisons among individual metabolites revealed several "hot spots" of highly correlated metabolites in a correlation matrix (Fig. 4). When VIP scores ≥ 1 in the PLS-DA model were used to maximize the difference of metabolic profiles between *PINK1*$^{-/-}$- and *PINK1*$^{+/+}$-iPSCs, the TCA metabolite α-ketoglutarate was the metabolite majorly impacted in mitophagy-deficient *PINK1*$^{-/-}$-iPSCs (Fig. 5). Quantitative assessment of metabolite concentrations confirmed that *PINK1*$^{-/-}$-iPSCs significantly accumulated > 3-fold less α-ketoglutarate than *PINK1*$^{+/+}$-iPSCs (Table 1), suggesting that the reduced capacity of mitophagy deficient-iPSCs to efficiently drive mitochondrial metamorphosis during nuclear reprogramming translate into a reduced capacity to achieve the embryonic stem cell-like metabolome that characterizes generated iPSCs.

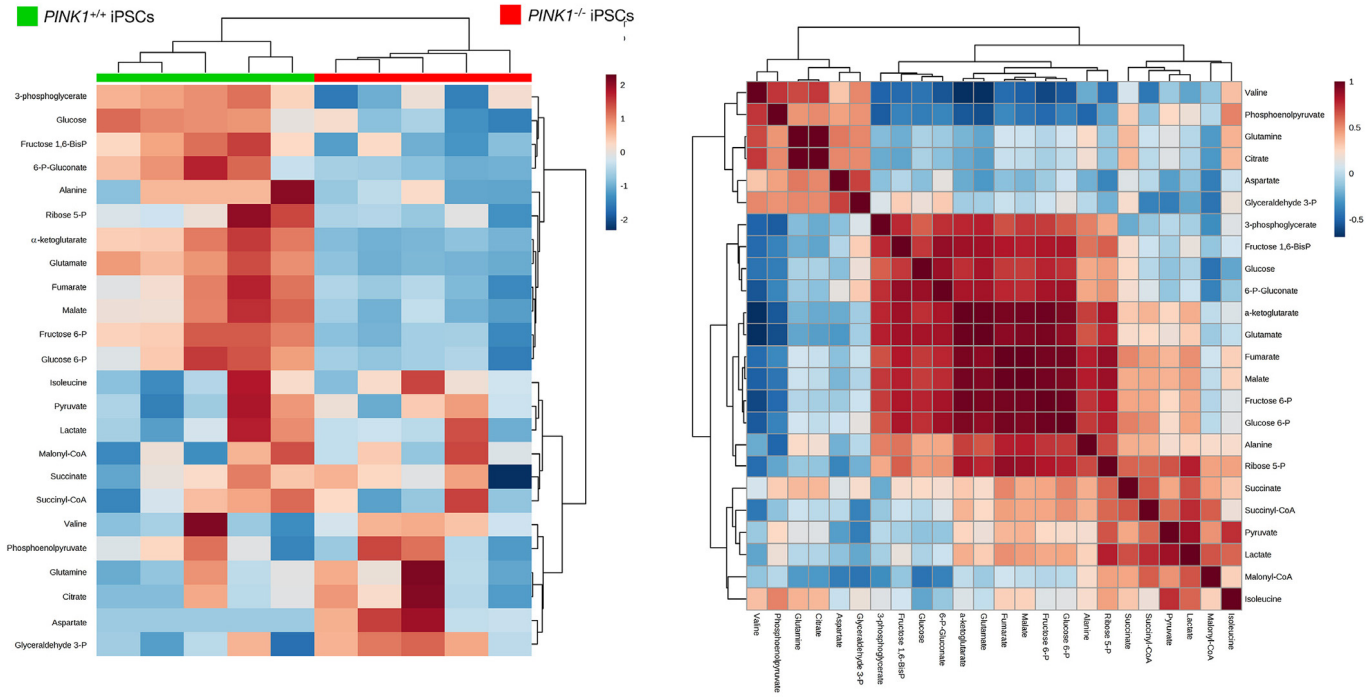

Figure 4. Mitophagy deficiency impairs the metabolome remodeling associated with nuclear reprogramming. *Left.* Heatmap to view the agglomerative hierarchical clustering of the *PINK1*$^{+/+}$- and *PINK1*$^{-/-}$ -iPSCs groups analyzed with MetaboAnalyst's data annotation tool [103]. Rows: metabolites; columns: samples; color key indicates metabolite expression value (blue: lowest; red: highest). *Right.* Heatmap of correlations between iPSCs metabolites. Each square represents the Spearman's correlation coefficient between the metabolite of the column with that of the row. Metabolite order is determined as in hierarchical clustering using the distance function 1-correlation. Self-self correlations are identified in dark brown.

Table 1. Concentration (in μM/mg protein) and fold-change of bioenergetic metabolites in *PINK1*$^{-/-}$- vs *PINK*$^{+/+}$-iPSCs cells.

Metabolite	*PINK1*$^{+/+}$ *iPSCs*	*PINK1*$^{-/-}$ *iPSCs*	Fold-change
3-phosphoglycerate*	136.079 ± 16.415	77.173 ± 15.581	-1.76
6-P-Gluconate*	11.045 ± 3.159	5.715 ± 0.397	-1.93
α-ketoglutarate*	0.364 ± 0.111	0.116 ± 0.005	-3.14
Alanine	2.435 ± 1.029	1.415 ± 0.335	-1.72
Aspartate	102.883 ± 11.692	106.727 ± 3.873	1.04
Citrate	4.533 ± 0.531	5.104 ± 1.146	1.13
Fructose 1,6-BisP*	144.329 ± 29.863	80.327 ± 20.233	-1.80
Fructose 6-P*	12.079 ± 2.511	5.499 ± 0.759	-2.20
Fumarate*	1.814 ± 0.389	1.130 ± 0.116	-1.61
Glucose*	40.668 ± 7.493	20.546 ± 6.196	-1.98
Glucose 6-P*	9.085 ± 1.600	5.877 ± 0.587	-1.55
Glutamate*	338.181 ± 2.622	322.962 ± 0.710	-1.05
Glutamine	5.122 ± 0.630	5.643 ± 1.159	1.10
Glyceraldehyde 3-P	54.602 ± 5.824	55.356 ± 7.668	1.01
Isoleucine	24.623 ± 7.773	25.745 ± 5.453	1.05
Lactate	212.007 ± 24.712	182.187 ± 18.347	-1.16
Leucine*	ULOQ	4.693 ± 1.384	-
Malate*	10.379 ± 3.172	4.824 ± 0.693	-2.15
Malonyl-CoA	24.615 ± 3.858	25.290 ± 2.881	1.03
Phosphoenolpyruvate*	0.315 ± 0.124	0.541 ± 0.134	1.72
Pyruvate	2.245 ± 0.946	2.136 ± 0.443	-1.05
Ribose 5-P*	6.136 ± 1.768	4.286 ± 0.499	-1.43
Serine*	36.239 ± 1.181	22.870 ± 0.448	-1.59
Succinate	35.714 ± 3.785	34.638 ± 5.498	-1.03
Succinyl-CoA	1.142 ± 0.296	1.044 ± 0.341	-1.09
Valine*	2.943 ± 0.001	3.856 ± 0.761	1.31

Data are expressed as mean ± SD.
* Metabolite statistically significant ($p<0.005$). ULOQ: under limit of quantitation

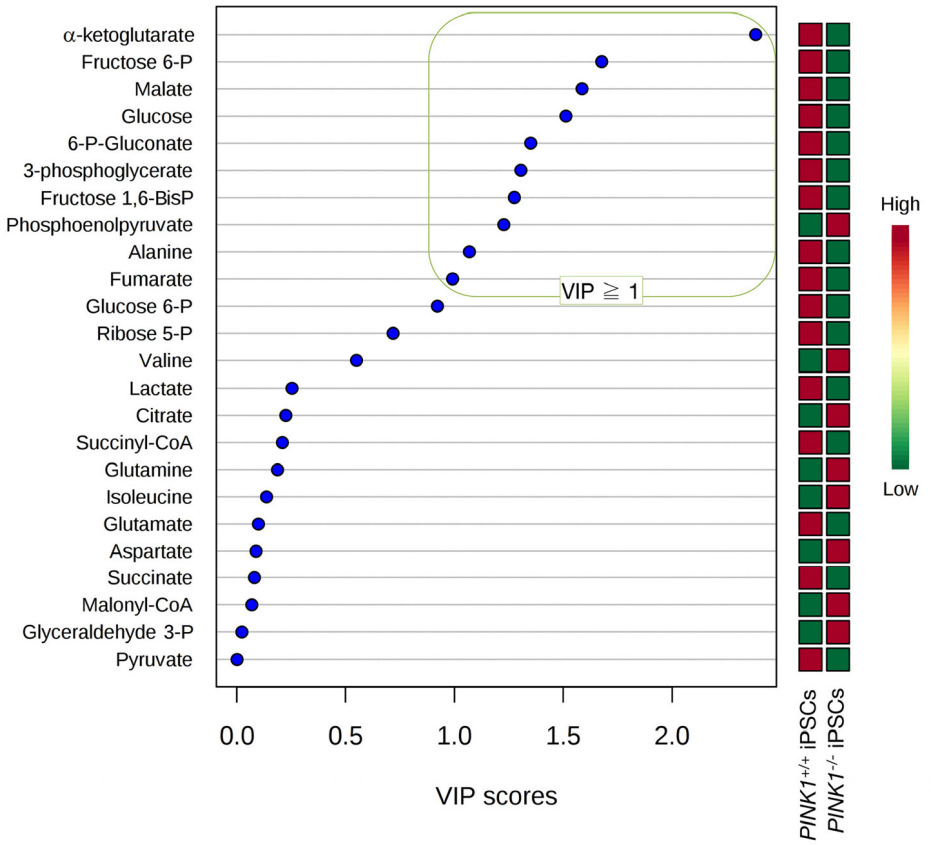

Figure 5. α-ketoglutarate is the most impacted metabolite in mitophagy deficient-iPSCs. VIP rank-score of quantified metabolites in the *PINK1*$^{+/+}$- and *PINK1*$^{-/-}$-iPSCs groups. Green box indicates metabolites that achieved VIP scores above 1.0.

Mitophagy-deficient iPSC colonies exhibit a significantly reduced teratoma-initiating capacity

The ability to derive the three germ layers generated during development, (ectoderm, mesoderm and endoderm), is the gold standard for determining whether potential iPSC candidates are fully pluripotent [78-80]. We thus examined the teratoma initiating and differentiation potential of *PINK1*$^{+/+}$- and *PINK1*$^{-/-}$-iPSCs *in vivo*. To exclude the possibility that any uncoupling of pluripotent capacity from tumorigenesis might be dose-dependent, i.e., with differentiation occurring at lower cell doses but tumors forming at higher cell doses, we injected 4- to 5-week-old athymic nude mice subcutaneously either with 5 x 10^5 undifferentiated iPSCs or with 2 x 10^6 cells, the latter being a saturating concentration to ensure the development of teratoma masses within a few weeks [64, 81]. We then analyzed efficiency, latency, and histology of teratoma composition. The rate of teratoma formation in *PINK1*$^{+/+}$-iPSCs was 100% (6/6 mice in each group) regardless of the number of cells injected (Fig. 6A). In contrast, we observed a cell number-independent reduction in the rate of teratoma formation following the injection of *PINK1*$^{-/-}$-iPSCs (60%; 4/6 mice in each group). Thus, the time required for 50% of animals to develop palpable teratomas was lengthened by 161% (from 26 to 68 days) upon injection of 5 x 10^5 *PINK1*$^{-/-}$-iPSCs, and by 166% (from 21 to 56 days) upon injection of 2 x 10^6 *PINK1*$^{-/-}$-iPSCs *in* (Fig. 6A). Indeed, injection of *PINK1*$^{-/-}$-iPSCs resulted in drastically smaller teratomas than those observed upon injection of *PINK*$^{+/+}$-iPSCs, i.e., the lesions in *PINK1*$^{-/-}$-iPSC-injected mice were 15-fold smaller in size compared to the mean teratoma size observed in the *PINK*$^{+/+}$-iPSC group (78 mm^3 versus 1166 mm^3, respectively) (Fig. 6B).

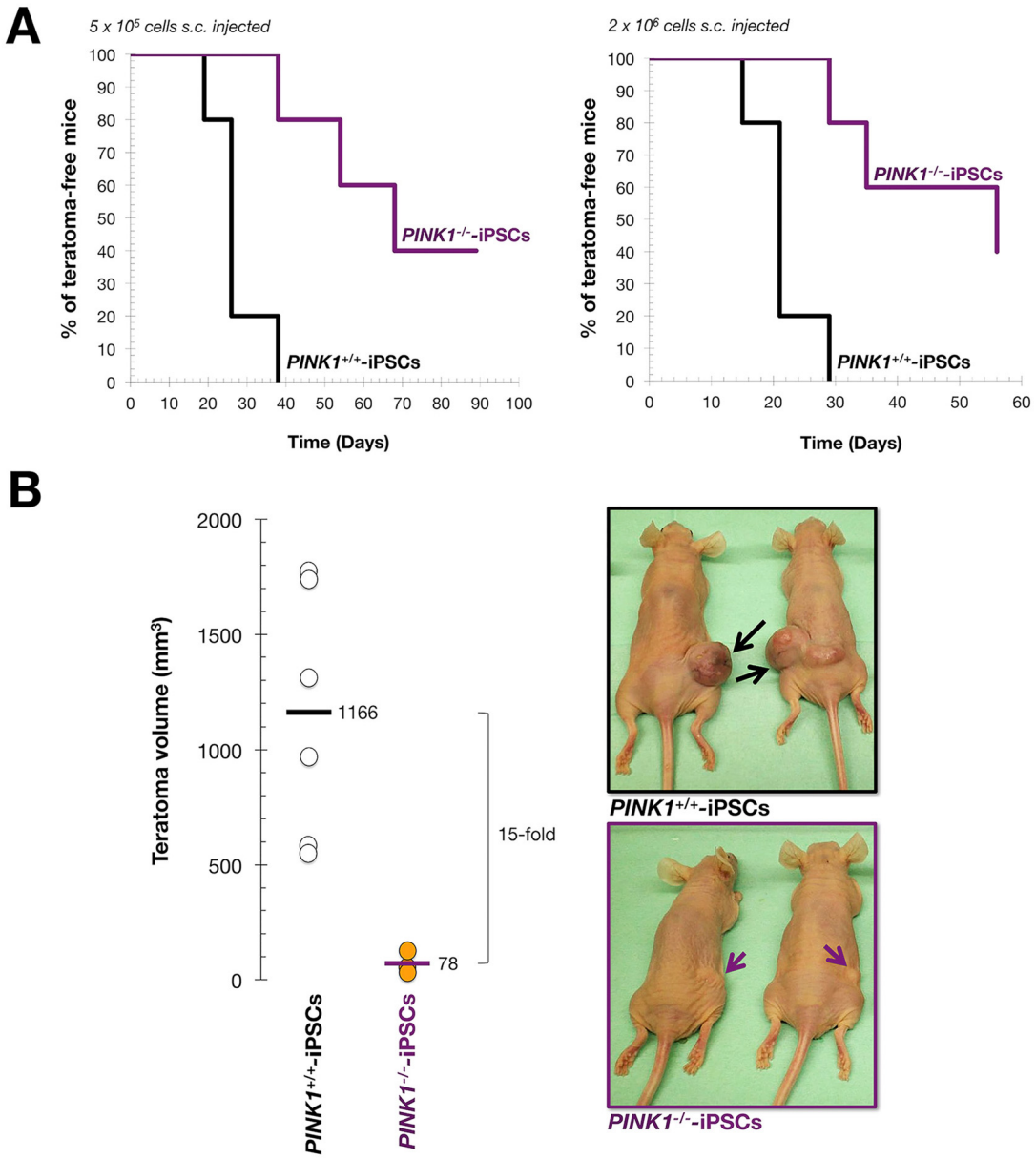

Figure 6. Mitophagy deficiency reduces tumorigenicity of iPSC colonies. Athymic mice were injected with 5 x 10^5 or 2 x 10^6 cells obtained from *PINK1*$^{+/+}$-iPSC or *PINK1*$^{-/-}$-iPSC colonies. Teratoma growth rate was calculated by measuring teratoma volume. (**A**) Kaplan-Meier plots show the percentage of mice that remained teratoma-free after subcutaneous injection of iPSCs obtained as described in Fig. 2. (**B**) Mean teratoma volumes obtained at the end of the experiment (*left*) as well as representative images of animals bearing *PINK1*$^{+/+}$-iPSC- and *PINK1*$^{-/-}$-iPSC-derived teratomas after injection with 2 x 10^6 cells (*right*). Note that teratomas formed from *PINK1*$^{+/+}$-iPSCs present a dramatically higher growth rate that those derived from *PINK1*$^{-/-}$-iPSCs.

Mitophagy-deficient iPSC colonies retain pluripotency and multi-germ layer differentiation potential

Given the above results, it might be argued that blockade of teratoma formation upon loss of PINK1-dependent mitophagy was due to the failure of *PINK1*$^{-/-}$-iPSCs to differentiate into primitive tissues representing all three germ layers. To question this, we carried out an ultrastructure analysis of teratomas from both groups of mice. Despite the lower efficiency in teratoma formation and the longer latency, tissue composition of

PINK1$^{-/-}$-teratomas was not noticeably different from equivalent *PINK*$^{+/+}$-teratomas at the histological level. Hematoxylin-eosin staining showed various tissue derivatives of the three germ layers, including neural rosettes (ectoderm), gut-like epithelial tissues (endoderm), and smooth muscle, adipocytes, bone, and cartilage (mesoderm), in both teratoma groups (Fig. 7), confirming the full pluripotency and multi-germ layer differentiation potential of the iPSCs regardless of the PINK1-mediated mitophagy status. These findings, together with the fact that *PINK1*$^{-/-}$-iPSCs normally expressed pluripotent markers confirmed that mitophagy-deficient iPSCs re-established pluripotency at the molecular and cellular level.

Although *PINK1*$^{+/+}$- and *PINK1*$^{-/-}$-iPSCs gave rise to teratomas composed of various recognizable tissue elements, we observed striking differences in the embryonal carcinoma (EC)-like component of poorly differentiated, primitive-appearing, blast-like teratocarcinoma stem cells. Accordingly, the large teratomas originating from *PINK1*$^{+/+}$-iPSCs displayed extensive areas of undifferentiated tissue, e.g., abundant embryonic-appearing neuroepithelium with a high number of mitotic figures, which were considered as malignant based on the examination by a pathologist (Fig. 7). Conversely, *PINK1*$^{-/-}$-iPSCs developed teratomas consisting almost exclusively of fully committed adult tissues, forming very small, morpho-

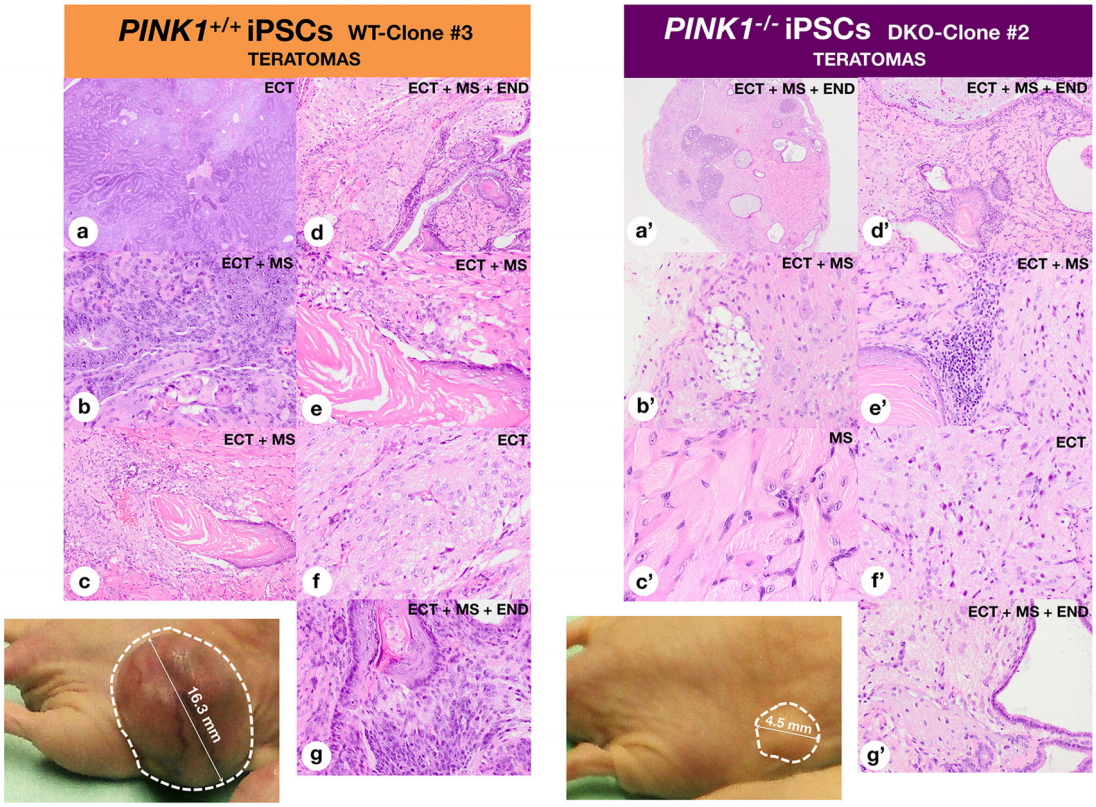

Figure 7. Mitophagy deficiency preserves the pluripotency of iPSCs. Histological analyses of *PINK1*$^{+/+}$- and *PINK1*$^{-/-}$-iPSC-derived teratomas. Representative photographs of teratomas (circled with white dotted lines) are shown. *PINK1*$^{+/+}$-iPSC-derived teratomas: (**a**) Primitive neural tissue, (**b**) Primitive neural tissue and skeletal muscle tissue, (**c**) Squamous epithelium, immature neural and glial tissue, (**d**) Mature nervous tissue, squamous keratinized epithelium, skeletal muscle tissue, mucinous glands, (**e**) Squamous keratinized epithelium, skeletal muscle tissue, (**f**) Mature nervous tissue, (**g**) Squamous keratinized epithelium, skeletal muscle tissue, respiratory epithelium. *PINK1*$^{-/-}$-iPSC-derived teratomas; (**a'**) Whole-tumor section with dark areas of primitive neuroepithelium mixed with skeletal muscle tissue and seromucinous glands, (**b'**) Mature nervous tissue, (**c'**) Skeletal muscle tissue, (**d'**) Mature nervous tissue, squamous keratinized epithelium, skeletal muscle tissue, mucinous glands, (**e'**) Mature nervous tissue, squamous keratinized epithelium, skeletal muscle tissue, (**f'**) Mature nervous tissue, (**g'**) Mature nervous tissue, mucinous glands, osteoid substance. Note that teratomas from *PINK1*$^{+/+}$-iPSCs and *PINK1*$^{-/-}$-iPSCs similarly show mixed tissues apparently derived from the three germ layers, i.e., ECT: Ectoderm, MS: Mesoderm, and END: Endoderm.

logically benign, mature, and well-differentiated cystic lesions. Using TEM, we found that the cytoplasm of the extensive undifferentiated regions in *PINK1*$^{+/+}$-iPSC-generated teratomas exhibited a simple architecture typical of embryonic-like cells in the early stages of development. Consequently, these regions were devoid of most organelles except for the presence of numerous ribosomes, a well-developed Golgi apparatus, and rough endoplasmic reticulum (Fig. 8). These regions contained few mitochondria and, when found, presented a globular shape with poorly developed cristae and electron-lucid matrix, and perinuclear localization, all indicative of functionally immature mitochondria. Conversely, teratomas from *PINK1*$^{-/-}$-iPSCs generated tissues with conspicuous and numerous mitochondria, possessing a complex morphology with well-developed cristae, denser matrix, and elongated or branched appearance (Fig. 8).

Although it might be argued that, because mitophagy-deficient iPSC colonies tended to rapidly differentiate *in vitro* and exhibited a significantly reduced teratoma-initiating capacity, the percentage of fully reprogrammed cells might be significantly lower within *PINK1*$^{-/-}$-iPSC colonies, these findings are also consistent with a more rapid differentiation of mitophagy-deficient iPSCs *in vivo*.

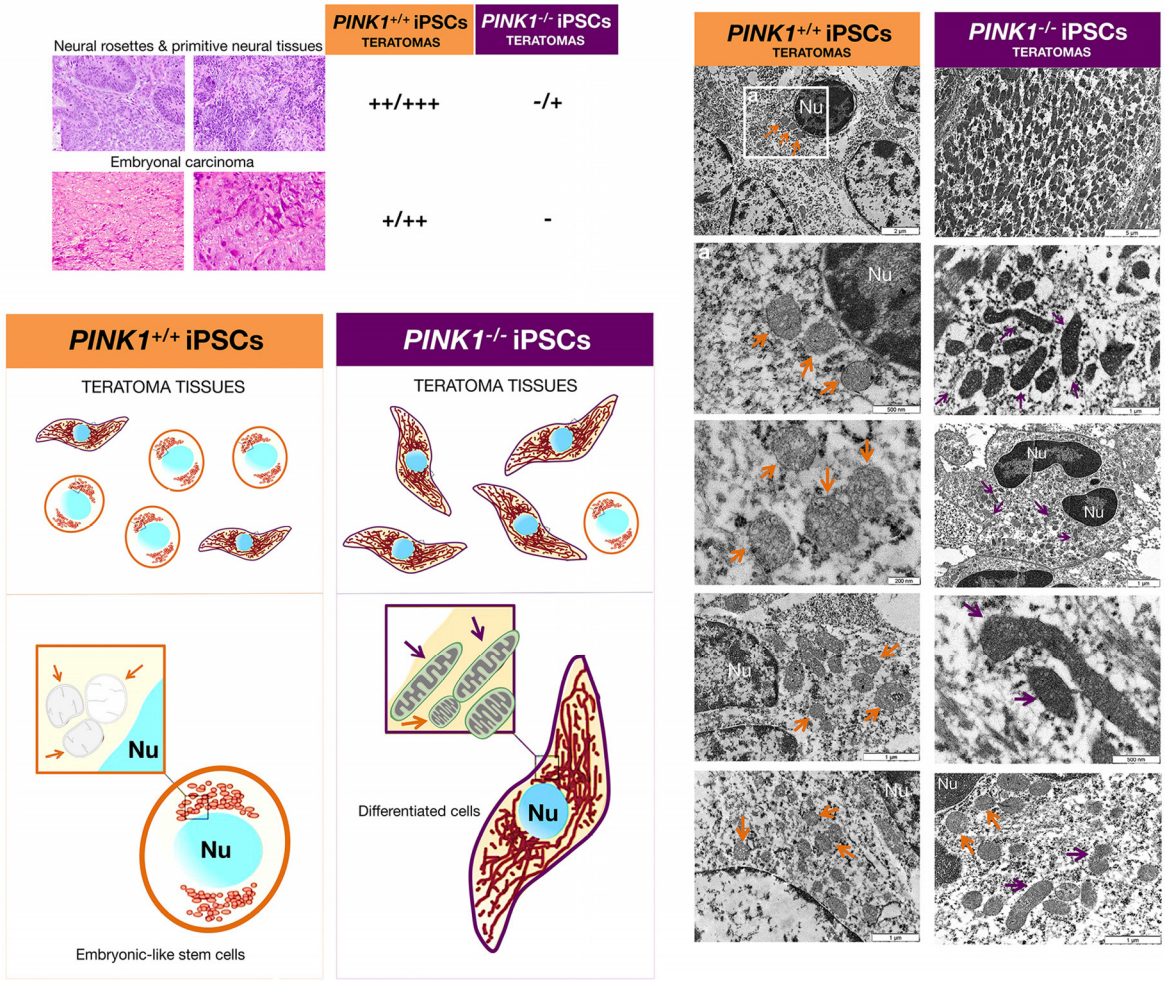

Figure 8. Mitophagy-deficient iPSC colonies are prone to direct differentiation *in vivo*. *Left.* Analyses of histopathological features associated with the malignant behavior of iPSC-derived teratomas including the presence of neural rosettes/primitive neural tissues and embryonal carcinoma. Note that small *PINK1*$^{-/-}$-iPSC-derived teratomas lack all the malignant features of iPSCs, which were highly abundant in *PINK1*$^{+/+}$-iPSC-derived teratomas. "-" means that no features are present, "+" a small number present, "++" a medium number, and "+++" a large number. *Right.* Representative TEM images of mitochondria in *PINK1*$^{+/+}$- and *PINK1*$^{-/-}$-iPSC-derived teratomas. While the mitochondria in many tissue sections from *PINK1*$^{+/+}$-iPSCs-derived teratomas were characterized by a punctate, perinuclear arrangement, an electron-lucid matrix and poorly developed cristae, mitochondria in the majority of tissue sections from *PINK1*$^{-/-}$-iPSC-derived teratomas formed more developed networks, had an electron-dense matrix and developed cristae. (Nu: Nucleus).

DISCUSSION

Here we provide the first demonstration that mitophagy is a necessary mechanism for the conversion of somatic cells to a pluripotent cell fate with maximum efficiency. Our discovery that mitophagy-driven mitochondrial rejuvenation is required for induction and maintenance of stem cell pluripotency and that the mitophagy pathway plays a critical mitochondrial switch that determines the efficiency and quality of somatic reprogramming, illustrates how mitophagy can play a pivotal role in stem cell functions during aging and tissue regeneration.

We first addressed the question of whether mitophagy is a crucial process during nuclear reprogramming. Our findings reveal that the sole loss of PINK1-dependent mitophagy was sufficient to dramatically decrease the efficiency (~80% reduction) and speed of the nuclear reprogramming process (Fig. 9). Deficiency of PINK1-regulated mitochondrial quality control constitutes a previously unrecognized barrier to reprogramming. This fact, taken together with recent studies showing that whereas activation of DRP1-driven mitochondrial fragmentation contributes to the acquisition and maintenance of stem cell pluripotency [48, 50], deficiency of mitofusins Mfn1 and Mfn2 (which co-

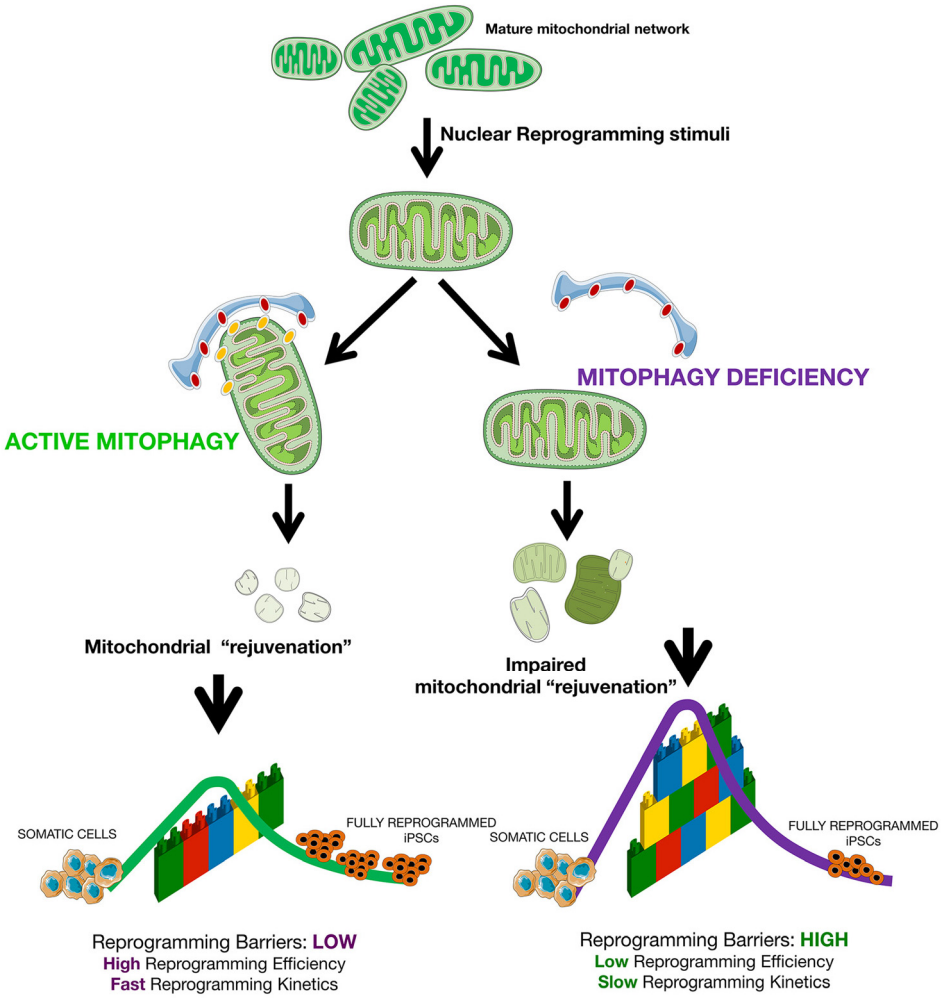

Figure 9. Mitophagy-regulated nuclear reprogramming of somatic cells into pluripotent stem cells. Mitophagy is part of the roadmap during nuclear reprogramming of somatic cells to pluripotency and, as such, its blockade is sufficient to dramatically alter the speed and efficiency of iPSC reprogramming by "elevating" the "reprogramming barriers" of the epigenetic landscape and decreasing the size of the stem cell state basin of attraction, which results in the deceleration (i.e., lower efficiency and slower kinetics) of the nuclear reprogramming process. This conceptual figure represent cells stabilized in an initial non-pluripotent, somatic attractor and how nuclear reprogramming can make cells exceed the "reprogramming barriers", represented as a wall of interlocking bricks, easier or harder in the presence or absence of PINK1-dependent mitophagy, respectively, and fall down in a final attractor of fully reprogrammed, induced pluripotent stem cell states. The cellular reprogramming process is presented as a colored line from the initial to the final cellular state.

ordinately regulate mitochondrial fusion) instead elicits mitochondrial metabolic reprogramming to pluripotency [49], bolsters the notion that the ability of mitochondrial fission/fusion and mitophagy to restructure mitochondrial dynamics is central for the control of cell-fate plasticity. Accordingly, it was reported that a restricted 2-day burst of autophagy (causing mitophagy) at the early stages of reprogramming was vital for iPSC generation [47].

We next focused on whether mitophagy is the driving mechanism for the conversion of functionally mature mitochondria to an immature state and vice versa, during reprogramming to stemness and commitment to terminal differentiation, respectively. The fact that loss of PINK1-dependent mitophagy impeded the full rejuvenation of the mitochondrial network during reprogramming indicates that mitophagy operates as a key mechanism in generating the immature mitochondrial structure commonly found in stem cells. Because a high level of mitophagy has recently been found to be a requisite for the high quality of mitochondria required for the stem cell state [82], and given that the number of AP^+ colonies during early stages of reprogramming is used as an initial indicator of successful reprogramming of cells, the fact that cells within *PINK1*$^{-/-}$ iPSC colonies appeared to inherit a mixture of mature ("old") and immature ("young") mitochondria when compared with *PINK1*$^{+/+}$-iPSCs colonies whose cells almost exclusively inherited immature mitochondria might suggest that the ratio of fully reprogrammed colonies among AP^+ colonies is significantly lower in the absence of *PINK1*-dependent mitophagy. Furthermore, because AP expression levels is a less sensitive measure to differentiate between undifferentiated and early differentiating cells, the fact that mitophagy-deficient iPSC colonies normally expressed the pluripotent markers Oct4 and Sox2 together with their strong tendency to spontaneously differentiate and form heterogeneous populations of cells strongly suggest that PINK1-dependent mitophagy might be necessary for the iPSCs to remain in undifferentiated state. Indeed, with growing evidence for remodeling of energy metabolism in cell fate decisions, the fact that functional monitoring of cellular bioenergetics revealed an attenuated glycolytic capacity in mitophagy-deficient iPSC cells strongly suggest that the mitophagy pathway is an operating mechanism of mitochondrial switching that directs bioenergetic transition from somatic oxidative in somatic cells to glycolysis in iPSCs. While mitophagy might ultimately determine the efficiency and quality of nuclear reprogramming and stemness transition in somatic cells by participating in the bioenergetic conversion for establishing functional pluripotency, it remains to be unambiguously defined whether the ultimate role of mitophagy in stem cells is to regulate the preferential, asymmetric apportion of younger mitochondria during self-renewal [82].

The main characteristics of iPSC mitochondria are their rounded morphology with condensed cristae and their poor oxidative activity due to the low membrane potential [36-45, 65]. Given that mitophagy is triggered by mild oxidative stress in a mitochondrial fission-dependent manner [83], we hypothesized that abnormal mitophagy might lead to the accumulation of "old", ROS-generating mitochondria, and this, in turn, might impair the efficiency of reprogramming. Our results showed that the mitophagy deficiency-imposed roadblock for reprogramming is bypassed, in part, by the ROS scavenger vitamin C upon the inclusion of oncogenic c-Myc, which is a key inducer of glycolytic reconfiguration [31, 84]. Interestingly, c-Myc also functions as the major contributor of reprogramming-mediated oxidative stress [38, 85]. Therefore, while it seems likely that ROS partially contribute to the lower reprogramming efficiency of *PINK1*$^{-/-}$ MEFs, other ROS-independent mitochondrial changes imposed by the loss of PINK1-driven mitophagy seem to operate as a dominant roadblock during reprogramming. Because histone demethylases have been shown to be the direct downstream effectors of vitamin C-dependent enhancement of cell reprogramming, in addition to its antioxidant activity [72-75], it is possible that mitophagy deficiency might impede reprogramming by inhibiting histone demethylation. In this regard, it was noteworthy that the iPSC metabolite majorly impacted by loss of *PINK1*-dependent mitophagy was α-ketoglutarate, a key mitochondrial metabolite that is siphoned from the TCA cycle to support rapid cell proliferation via lipid and amino acid biosynthesis that can exit also the mitochondria to function as a cofactor for dioxygenase enzymes including Jumonji-family histone demethylases, TET-family DNA hydroxylases, and prolyl hydroxylases [86-88]. Indeed, the intracellular α-ketoglutarate levels have been shown to contribute to the maintenance of cellular identity and have a mechanistic role in the transcriptional and epigenetic state of stem cells [89]. Further research, however, is needed to evaluate the precise epigenetic modifications associated with mitophagy-related changes in mitochondrial biogenesis, structure, and function, i.e., how mitophagy might drive the acquisition and maintenance of stemness by metabolically regulating the epigenetic landscape of the nuclear genome [90-92].

The fact that *PINK1*$^{-/-}$-iPSCs possessed a normal capacity to differentiate into mature tissue confirmed

that deficiency of PINK1-driven mitophagy does not interfere with the pluripotent quality of iPSCs. Because the kinetics of teratoma formation is dependent on the number of remaining pluripotent stem cells during the differentiation procedure [93-98], it might be tempting to suggest that loss of PINK1-driven mitophagy facilitates the depletion of residual undifferentiated pluripotent cells (teratocarcinoma-initiating cells) during *in vivo* teratoma formation. Moreover, because the retention of the embryonal character is considered the basis for continuous and progressive growth of malignant teratomas, loss of biological aggressiveness in *PINK1*$^{-/-}$-iPSC-derived teratomas apparently suggest that mitophagy deficiency impedes the retention of undifferentiated pluripotent stem cells by promoting their differentiation and inhibiting potential dedifferentiation of committed cells. Accordingly, the highly significant more active mitochondrial state of tissues from *PINK1*$^{-/-}$ teratomas might be indicative of rapid, most committed differentiation of otherwise pluripotent *PINK1*$^{-/-}$-iPSCs. Conversely, it might be argued that these findings reflect that the percentage of fully reprogrammed cells might be significantly lower within mitophagy-deficient *PINK1*$^{-/-}$-iPSC colonies. Forthcoming studies should evaluate whether rapidly differentiating, mitophagy-deficient heterogeneous colonies of *PINK1* KO-iPSCs might illuminate new mitochondria-centered mechanisms aimed to restore or stimulate a differentiation checkpoint capable of limiting the aberrant self-renewal of life-threatening cancer stem cells in tumor tissues.

We are beginning to dissect the roles of mitochondria in the establishment and homeostasis of stemness, which may help to uncover novel insights into our understanding of a wide variety of degenerative diseases, aging, and aging-related diseases including cancer. Although we are still far from a comprehensive understanding of the physiological functions of mitochondria in stem cells, our findings extend previous studies into the causal mechanism behind the well-recognized metabolic switch during the establishment of pluripotency, which is accompanied by significant changes in mitochondrial function, composition, structure, maturation, and signaling. Mitophagy appears to be a crucial cellular process for the conversion of functionally mature mitochondria to an immature state and vice versa during reprogramming and differentiation, respectively. In this regard, mitophagy may ensure a metabolic transition to meet the specific energetic and anabolic demands of the stemness state, e.g., mitophagy-induced repression of mitochondrial functions including mitochondrial clearance might accelerate the onset of the glycolytic metabolism [99]. Furthermore, mitophagy-driven mitochondrial rejuvenation might contribute to the ability of stem cells to suppress differentiation by orchestrating the mitochondria function as signaling organelles of diverse biological functions [100, 101], including not only bioenergetic transitions but, perhaps more importantly, metabolome remodeling traits connecting mitochondrial metabolites with epigenetics [100-102]. Further studies are warranted to determine the causal role of mitophagy-driven mitochondrial rejuvenation as part of the mechanism involved in the maintenance and asymmetric transmission of the pluripotency and differentiation fate of stem cells. Our discovery that mitophagy-controlled mitochondrial quality is a critical director of cell-fate plasticity and stem-cell fate should provide new insights into how mitophagy might influence the stem cell decisions to retain pluripotency or differentiate in tissue regeneration and aging, tumor growth, and regenerative medicine.

MATERIALS AND METHODS

PINK1-knockout mouse embryonic fibroblasts. *PINK1*-knockout mice were generated by targeted deletion of exon 1 as described [52]. Loss of Pink1 mRNA expression in primary embryonic fibroblasts (MEFs) was confirmed by quantitative RT-PCR [52].

Generation of iPSCs. Mouse primary iPSCs were created by transducing MEFs deficient for *PINK1* (*PINK1*$^{-/-}$) and wild-type (*PINK1*$^{+/+}$) counterparts with the pMXs-based retroviruses that individually encode the mouse transcription factors Oct3/4, Sox2, and Klf4 following a previously-described protocol [64, 65]. Characterization of iPSC-like colonies was carried out by analyzing pluripotent marker expression by alkaline phosphatase (AP) staining using the StemTAG™ Alkaline Phosphatase Staining and Activity Assay Kit (Cell Biolabs, Inc. Cat. No. CBA-302) and the expression of Oct3/4, Nanog, Sox2, and Ssea-1 by immunofluorescence (see below).

To generate feeder-free iPSC cultures for teratoma assays, culture plates were coated with 0.3 mg/mL Matrigel (growth factor-reduced, BD Biosciences, San Jose, CA) at 4^{o}C overnight. Unbound Matrigel was aspirated, and the cells were washed with DMEM/F12 medium. iPSCs were seeded on Matrigel-coated plates in MEF-conditioned ES cell medium supplemented with leukemia inhibitory factor (LIF) and bFGF (4 ng/mL). The medium was changed every day.

Immunofluorescence staining. High-content confocal imaging was performed in 96-well clear bottom imaging tissue culture plates (BD Biosciences) optimized for automated imaging applications. Triton®

X-100 permeabilization and blocking, primary antibody staining, secondary antibody staining using Alexa Fluor® 488 goat anti-rabbit/mouse IgG (Invitrogen, Molecular Probes, Eugene, OR) and counterstaining (Hoechst 33258; Invitrogen) were performed following BD Biosciences protocols. Images were captured in different channels for Alexa Fluor® 488 (pseudocolored green) and Hoechst 33258 (pseudocolored blue) on a BD PathwayTM 855 Bioimager System (BD Biosciences) with 20× or 40× objectives (NA 075, Olympus). Merged images were obtained according to the Recommended Assay Procedure using BD Attovision™ software.

Reactive Oxygen Species (ROS) detection. Cells were incubated for 60 min with 10 μmol/L 2',7'-dihydro-dichlorofluorescein-diacetate (H2DCF-DA) (Invitrogen, Molecular Probes) at 37˚C. Cellular green fluorescence was then measured by flow cytometry. Cell-permeant non-fluorescent H_2DCF-DA, upon cleavage of the acetate moiety by intercellular esterases and oxidation by ROS, is converted to strongly fluorescent DCF and thus reports the ROS abundance.

Immunoblotting. Equal concentration of proteins (50 μg) was loaded into a 10% SDS-polyacrylamide gel and then electrotransferred. After blocking (5% nonfat powder milk in TBS plus 0.1% TritonX100 for 1 h at room temperature), the nitrocellulose membranes were incubated for 16-20 h at 4°C with the primary antibody (Oct3/4, Abcam ab-1985, 1:600; Sox2, Abcam ab-97959, 1:1000; β-actin, Santa Cruz sc-47778; 1:500). The detection of the immune complexes after incubation with the appropriate peroxidase-conjugated secondary antibody (Cell Signaling #7074, 1:1000; Calbiochem #401215, 1:5000) was performed with the Clarity Western ECL Substrate (Bio-Rad).

Extracellular flux bioenergetic assays. Extracellular acidification rates were measured using an XF Extracellular Flux Seahorse Analyzer (Seahorse Bioscience). XFp Glycolysis Stress tests were performed in accordance with manufacturer's instructions. Each plotted value is the mean of at least 6 replicates and was normalized to Hoechst signal in each well.

Targeted metabolomics and data analysis. Measurements of bioenergetics metabolites obtained from *PINK1*$^{+/+}$-iPSC and *PINK1*$^{-/-}$-iPSC clonal cell lines were performed by employing a previously described simple and quantitative method based on gas chromatography coupled to quadrupole-time of flight mass spectrometry and an electron ionization interface (GC-EI-QTOF-MS) [76, 77].

Raw data were processed and compounds were detected and quantified using the Qualitative and Quantitative Analysis B.06.00 software (Agilent Technologies), respectively. MetaboAnalyst 3.0 (http://www.metaboanalyst.ca) was used to generate scores/loading plots, Heatmaps, and correlation maps [103].

Teratoma assays. To form teratomas, iPSCs were harvested from Matrigel-coated culture dishes and injected subcutaneously (s.c.) into the dorsal flank of female athymic nude mice (four- to five-weeks-old, 23-25g; Harlan Laboratories, France). Mice were weighed once per week. Teratomas were measured daily with electronic calipers and tumour volumes were calculated using the formula: volume (mm3) = length × width^2 × 0.5. General health of the mice in response to teratoma development (e.g., subcutaneous teratomas cause ulceration on the skin) was monitored daily by a specialized veterinarian. Teratomas were carefully dissected and removed in entirety, fixed in 10% phosphate buffered formalin (3.6% formaldehyde) for 24 hours, and paraffin-embedded. For histopathological analysis, consecutive sections (4 μm) were cut and stained with haematoxylin and eosin according to standard procedures.

The Institutional Animal Care and Use Committee (IACUC) of the Institut d'Investigació Biomèdica de Bellvitge (IDIBELL; Animal Use Protocol #6302 authorized by the Animal Experimental Commission from the Catalan Government, Barcelona, Spain) approved the experiments.

Transmission electron microscopy. Small pieces of teratomas were fixed in a 2% glutaraldehyde solution in 0.1 M cacodylate buffer, pH 7.4. Samples were then post-fixed in 1% osmium tetroxide (OsO_4) for 2 h and dehydrated through a graded series of acetone prior to impregnation in increasing concentrations of resin in acetone over a 24 h period. Semi-thin sections (500 nm) were stained with 1% toluidine blue. Ultrathin sections (70 nm) were subsequently cut using a diamond knife, double-stained with uranyl acetate and lead citrate, and examined with a transmission electron microscope (Hitachi, Tokyo, Japan).

Statistical analysis. The results are presented as the mean ± SD of at least three repeated individual experiments for each group. The analyses were performed using XLSTAT 2010 (Addinsoft™). A P-value ≤ 0.05 was considered statistically significant.

ACKNOWLEDGEMENTS

The authors would like to thank Dr. Kenneth McCreath for editorial support.

Funding

This work was supported by grants from the Ministerio de Ciencia e Innovación (Grant SAF2012-38914), Plan Nacional de I+D+I, Spain and the Agència de Gestió d'Ajuts Universitaris i de Recerca (AGAUR) (Grant 2014 SGR229), Departament d'Economia I Coneixement, Catalonia, Spain to Javier A. Menendez. And by the FP7 RTD MEFOPA HEALTH-2009-241791 and EC-FP7/2007-2013 project, HEALTH-F2-2011-278850 (INMiND) to VB.

Author contributions

A. V-M. and J.A.M conceived the idea for this project. C. VdH. and V. B. provided essential study materials. A. V-M. designed and conducted the nuclear reprogramming assays and carried out the confocal fluorescence microscopy experiments. A. V-M. and J.A.M designed and analyzed the experiments on living cells. S.C. performed all the teratoma formation assays. E. L-B. performed all the histopathological tissue analyses. E. R-G, S. F-A. and J. J. conducted and analyzed the experiments with the transmission electron microscopy. B. C-F. and E. C. participated in the nuclear reprogramming and ROS experiments. E. C. performed and analyzed the immunoblotting and cell energy phenotyping procedures. B. C-F., E. C., J.J., E. R-G, and S. F-A. designed, conducted and analyzed the metabolomic experiments. J.A.M and J. J. wrote the manuscript. We confirm that the manuscript has been read and approved by all named authors and that there are no other persons who satisfied the criteria for authorship but are not listed. We further confirm that the order of authors listed in the manuscript has been approved by all of us. Correspondence and requests for materials should be addressed to corresponding authors.

Conflict of interest statement

The authors confirm that there are no known conflicts of interest associated with this publication and there has been no significant financial support for this work that could have influenced its outcome. We further confirm that any aspect of the work covered in this manuscript that has involved experimental animals has been conducted with the ethical approval of all relevant bodies and that such approvals are acknowledged within the manuscript.

REFERENCES

1. Ding WX, Yin XM. Mitophagy: mechanisms, pathophysiological roles, and analysis. Biol Chem. 2012; 393: 547-64.

2. Kim I, Rodriguez-Enriquez S, Lemasters JJ. Selective degradation of mitochondria by mitophagy. Arch Biochem Biophys. 2007; 462: 245-53.

3. Novak I. Mitophagy: a complex mechanism of mitochondrial removal. Antioxid Redox Signal. 2012; 17: 794-802.

4. Tolkovsky AM. Mitophagy. Biochim Biophys Acta. 2009; 1793: 1508-15.

5. Ashrafi G, Schwarz TL. The pathways of mitophagy for quality control and clearance of mitochondria. Cell Death Differ. 2013; 20: 31-42.

6. Feng D, Liu L, Zhu Y, Chen Q. Molecular signaling toward mitophagy and its physiological significance. Exp Cell Res. 2013; 319: 1697-1705.

7. Gomes LC, Scorrano L. Mitochondrial morphology in mitophagy and macroautophagy. Biochim Biophys Acta. 2013; 1833: 205-12.

8. Mishra P, Chan DC. Mitochondrial dynamics and inheritance during cell division, development and disease. Nat Rev Mol Cell Biol. 2014; 15: 634-46.

9. Wei H, Liu L, Chen Q. Selective removal of mitochondria via mitophagy: distinct pathways for different mitochondrial stresses. Biochim Biophys Acta. 2015; 1853: 2784-90.

10. Dupuis L. Mitochondrial quality control in neurodegenerative diseases. Biochimie. 2014; 100: 177-83.

11. Itoh K, Nakamura K, Iijima M, Sesaki H. Mitochondrial dynamics in neurodegeneration. Trends Cell Biol. 2013; 23: 64-71.

12. Osellame LD, Duchen MR. Defective quality control mechanisms and accumulation of damaged mitochondria link Gaucher and Parkinson diseases. Autophagy. 2013; 9: 1633-35.

13. Osellame LD, Duchen MR. Quality control gone wrong: mitochondria, lysosomal storage disorders and neurodegeneration. Br J Pharmacol. 2014; 171: 1958-1972.

14. Pickrell AM, Youle RJ. The roles of PINK1, parkin, and mitochondrial fidelity in Parkinson's disease. Neuron. 2015; 85: 257-73.

15. Ryan BJ, Hoek S, Fon EA, Wade-Martins R. Mitochondrial dysfunction and mitophagy in Parkinson's: from familial to sporadic disease. Trends Biochem Sci. 2015; 40: 200-10.

16. Zhu J, Wang KZ, Chu CT. After the banquet: mitochondrial biogenesis, mitophagy, and cell survival. Autophagy. 2013; 9: 1663-76.

17. Guan JL, Simon AK, Prescott M, Menendez JA, Liu F, Wang F, Wang C, Wolvetang E, Vazquez-Martin A, Zhang J. Autophagy in stem cells. Autophagy. 2013; 9: 830-49.

18. Joshi A, Kundu M. Mitophagy in hematopoietic stem cells: the case for exploration. Autophagy. 2013; 9: 1737-49.

19. Menendez JA, Joven J. Energy metabolism and metabolic sensors in stem cells: the metabostem crossroads of aging and cancer. Adv Exp Med Biol. 2014; 824: 117-40.

20. Menendez JA, Vellon L, Oliveras-Ferraros C, Cufí S, Vazquez-Martin A. mTOR-regulated senescence and autophagy during reprogramming of somatic cells to pluripotency: a roadmap from energy metabolism to stem cell renewal and aging. Cell Cycle. 2011; 10: 3658-77.

21. Michel S, Wanet A, De Pauw A, Rommelaere G, Arnould T, Renard, P. Crosstalk between mitochondrial (dys)function and mitochondrial abundance. J Cell Physiol. 2012; 227: 2297-10.
22. Pan H, Cai N, Li M, Liu GH, Izpisua Belmonte JC. Autophagic control of cell 'stemness'. EMBO Mol Med. 2013; 5: 327-31.
23. Phadwal K, Watson AS, Simon AK. Tightrope act: autophagy in stem cell renewal, differentiation, proliferation, and aging. Cell Mol Life Sci. 2013; 70: 89-103.
24. Vessoni AT, Muotri AR, Okamoto OK. Autophagy in stem cell maintenance and differentiation. Stem Cells Dev. 2012; 21: 513-20.
25. Chen CT, Hsu SH, Wei YH. Mitochondrial bioenergetic function and metabolic plasticity in stem cell differentiation and cellular reprogramming. Biochim Biophys Acta. 2012; 1820: 571-76.
26. Folmes CD, Nelson TJ, Martinez-Fernandez A, Arrell DK, Lindor JZ, Dzeja PP, Ikeda Y, Perez-Terzic C, Terzic, A. Somatic oxidative bioenergetics transitions into pluripotency-dependent glycolysis to facilitate nuclear reprogramming. Cell Metab. 2011; 14: 264-71.
27. Folmes CD, Nelson TJ, Terzic A. Energy metabolism in nuclear reprogramming. Biomark Med. 2011; 5: 715-29.
28. Folmes CD, Dzeja PP, Nelson TJ, Terzic, A. Metabolic plasticity in stem cell homeostasis and differentiation. Cell Stem Cell. 2012; 11: 596-06.
29. Folmes CD, Nelson TJ, Dzeja PP, Terzic A. Energy metabolism plasticity enables stemness programs. Ann N Y Acad Sci. 2012; 1254: 82-89.
30. Folmes CD, Arrell DK, Zlatkovic-Lindor J, Martinez-Fernandez A, Perez-Terzic C, Nelson TJ, Terzic A. Metabolome and metaboproteome remodeling in nuclear reprogramming. Cell Cycle. 2013; 12: 2355-65.
31. Folmes CD, Martinez-Fernandez A, Faustino RS, Yamada S, Perez-Terzic C, Nelson TJ, Terzic A. Nuclear reprogramming with c-Myc potentiates glycolytic capacity of derived induced pluripotent stem cells. J Cardiovasc Transl Res. 2013; 6: 10-21.
32. Ito K, Suda T. Metabolic requirements for the maintenance of self-renewing stem cells. Nat Rev Mol Cell Biol. 2014; 15: 243-56.
33. Panopoulos AD, Yanes O, Ruiz S, Kida YS, Diep D, Tautenhahn R, Herrerías A, Batchelder EM, Plongthongkum N, Lutz M, Berggren WT, Zhang K, Evans RM, Siuzdak G, Izpisua Belmonte JC. The metabolome of induced pluripotent stem cells reveals metabolic changes occurring in somatic cell reprogramming. Cell Res. 2012; 22: 168-177.
34. Son MJ, Jeong BR, Kwon Y, Cho YS. Interference with the mitochondrial bioenergetics fuels reprogramming to pluripotency via facilitation of the glycolytic transition. Int J Biochem Cell Biol. 2013; 45: 2512-18.
35. Teslaa T, Teitell MA. Pluripotent stem cell energy metabolism: an update. EMBO J. 2015; 34: 138-53.
36. Bukowiecki R, Adjaye J, Prigione, A. Mitochondrial function in pluripotent stem cells and cellular reprogramming. Gerontology. 2014; 60: 174-82.
37. Prigione A, Adjaye J. Modulation of mitochondrial biogenesis and bioenergetic metabolism upon in vitro and in vivo differentiation of human ES and iPS cells. Int J Dev Bio. 2010; 54: 1729-41.
38. Prigione A, Adjaye J. A mitochondrial strategy for safeguarding the reprogrammed genome. Cell Regen (Lond). 2014; 3: 5.
39. Prigione A, Fauler B, Lurz R, Lehrach H, Adjaye J. The senescence-related mitochondrial/oxidative stress pathway is repressed in human induced pluripotent stem cells. Stem Cells. 2010; 28: 721-33.
40. Prigione A, Hossini AM, Lichtner B, Serin A, Fauler B, Megges M, Lurz R, Lehrach H, Makrantonaki E, Zouboulis CC, Adjaye J. Mitochondrial-associated cell death mechanisms are reset to an embryonic-like state in aged donor-derived iPS cells harboring chromosomal aberrations. PLoS One. 2011; 6: e27352.
41. Prigione A, Ruiz-Pérez MV, Bukowiecki R, Adjaye J. Metabolic restructuring and cell fate conversion. Cell Mol Life Sci. 2015; 72: 1759-77.
42. Suhr ST, Chang EA, Tjong J, Alcasid N, Perkins GA, Goissis MD, Ellisman MH, Perez GI, Cibelli JB. Mitochondrial rejuvenation after induced pluripotency. PLoS One. 2010; 5: e14095.
43. Vazquez-Martin A, Corominas-Faja B, Cufi S, Vellon L, Oliveras-Ferraros C, Menendez OJ, Joven J, Lupu R, Menendez JA. The mitochondrial H(+)-ATP synthase and the lipogenic switch: new core components of metabolic reprogramming in induced pluripotent stem (iPS) cells. Cell Cycle. 2013; 12: 207-18.
44. Wang Y, Mah N, Prigione A, Wolfrum K, Andrade-Navarro MA, Adjaye J. A transcriptional roadmap to the induction of pluripotency in somatic cells. Stem Cell Rev. 2010; 6: 282-96.
45. Xu X, Duan S, Yi F, Ocampo A, Liu GH, Izpisua Belmonte JC. Mitochondrial regulation in pluripotent stem cells. Cell Metab. 2013; 18: 325-32.
46. Kida YS, Kawamura T, Wei Z, Sogo T, Jacinto S, Shigeno A, Kushige H, Yoshihara E, Liddle C, Ecker JR, Yu RT, Atkins AR, Downes M, Evans RM. ERRs Mediate a Metabolic Switch Required for Somatic Cell Reprogramming to Pluripotency. Cell Stem Cell. 2015; 16: 547-55.
47. Wang S, Xia P, Ye B, Huang G, Liu J, Fan Z. Transient activation of autophagy via Sox2-mediated suppression of mTOR is an important early step in reprogramming to pluripotency. Cell Stem Cell. 2013; 13: 617-25.
48. Son MY, Choi H, Han YM, Cho YS. Unveiling the critical role of REX1 in the regulation of human stem cell pluripotency. Stem Cells. 2013; 31: 2374-87.
49. Son MJ, Kwon Y, Son MY, Seol B, Choi HS, Ryu SW, Choi C, Cho YS. Mitofusins deficiency elicits mitochondrial metabolic reprogramming to pluripotency. Cell Death Differ. 2015; 22: 1957-69.
50. Vazquez-Martin A, Cufi S, Corominas-Faja B, Oliveras-Ferraros C, Vellon L, Menendez JA. Mitochondrial fusion by pharmacological manipulation impedes somatic cell reprogramming to pluripotency: new insight into the role of mitophagy in cell stemness. Aging (Albany NY). 2012; 4: 393-401. doi: 10.18632/aging.100465.
51. Wang L, Ye X, Zhao Q, Zhou Z, Dan J, Zhu Y, Chen Q, Liu L. Drp1 is dispensable for mitochondria biogenesis in induction to pluripotency but required for differentiation of embryonic stem cells. Stem Cells Dev. 2014; 23: 2422-34.
52. Heeman B, Van den Haute C, Aelvoet SA, Valsecchi F, Rodenburg RJ, Reumers V, Debyser Z, Callewaert G, Koopman WJ, Willems PH, Baekelandt V. Depletion of PINK1 affects mitochondrial metabolism, calcium homeostasis and energy maintenance. J Cell Sci. 2011; 124: 1115-25.
53. Oliveras-Salvá M, Van Rompuy AS, Heeman B, Van den Haute C, Baekelandt V. Loss-of-function rodent models for parkin and PINK1. J Parkinsons Dis. 2011; 1: 229-51.

54. Chu CT. A pivotal role for PINK1 and autophagy in mitochondrial quality control: implications for Parkinson disease. Hum Mol Genet. 2010; 19: R28-R37.
55. Clark IE, Dodson MW, Jiang C, Cao JH, Huh JR, Seol JH, Yoo SJ, Hay BA, Guo M. Drosophila pink1 is required for mitochondrial function and interacts genetically with parkin. Nature. 2006; 441: 1162-66.
56. Deng H, Dodson MW, Huang H, Guo M. The Parkinson's disease genes pink1 and parkin promote mitochondrial fission and/or inhibit fusion in Drosophila. Proc Natl Acad Sci U S A. 2008; 105: 14503-508.
57. Eiyama A, Okamoto K. PINK1/Parkin-mediated mitophagy in mammalian cells. Curr Opin Cell Biol. 2015; 33: 95-101.
58. Gautier CA, Kitada T, Shen J. Loss of PINK1 causes mitochondrial functional defects and increased sensitivity to oxidative stress. Proc Natl Acad Sci U S A. 2008; 105: 11364-369.
59. Gegg ME, Cooper JM, Chau KY, Rojo M, Schapira AH, Taanman JW. Mitofusin 1 and mitofusin 2 are ubiquitinated in a PINK1/parkin-dependent manner upon induction of mitophagy. Hum Mol Genet. 2010; 19: 4861-70.
60. Geisler S, Holmström KM, Skujat D, Fiesel FC, Rothfuss OC, Kahle PJ, Springer W. PINK1/Parkin-mediated mitophagy is dependent on VDAC1 and p62/SQSTM1. Nat Cell Biol. 2010; 12: 119-31.
61. Kawajiri S, Saiki S, Sato S, Sato F, Hatano T, Eguchi H, Hattori N. PINK1 is recruited to mitochondria with parkin and associates with LC3 in mitophagy. FEBS Lett. 2010; 584: 1073-79.
62. Springer W, Kahle PJ. Regulation of PINK1-Parkin-mediated mitophagy. Autophagy. 2011; 7: 266-78.
63. Vives-Bauza C, Zhou C, Huang Y, Cui M, de Vries RL, Kim J, May J, Tocilescu MA, Liu W, Ko HS, Magrané J, Moore DJ, Dawson VL, et al. PINK1-dependent recruitment of Parkin to mitochondria in mitophagy. Proc Natl Acad Sci U S A. 2010; 107: 378-83.
64. Vazquez-Martin A, Cufi S, Lopez-Bonet E, Corominas-Faja B, Oliveras-Ferraros C, Martin-Castillo B, Menendez JA. Metformin limits the tumourigenicity of iPS cells without affecting their pluripotency. Sci Rep. 2012; 2: 964.
65. Vazquez-Martin A, Vellon L, Quirós PM, Cufí S, Ruiz de Galarreta E, Oliveras-Ferraros C, Martin AG, Martin-Castillo B, López-Otín C, Menendez JA. Activation of AMP-activated protein kinase (AMPK) provides a metabolic barrier to reprogramming somatic cells into stem cells. Cell Cycle. 2012; 11: 974-89.
66. Rehman J. Empowering self-renewal and differentiation: the role of mitochondria in stem cells. J Mol Med (Berl). 2010; 88: 981-86.
67. Rodriguez-Enriquez S, Kim I, Currin RT, Lemasters JJ. Tracker dyes to probe mitochondrial autophagy (mitophagy) in rat hepatocytes. Autophagy. 2006; 2: 39-46.
68. Jiang J, Chan YS, Loh YH, Cai J, Tong GQ, Lim CA, Robson P, Zhong S, Ng HH. A core Klf circuitry regulates self-renewal of embryonic stem cells. Nat Cell Biol. 2008; 10: 353-60.
69. Vafa O, Wade M, Kern S, Beeche M, Pandita TK, Hampton GM, Wahl GM. c-Myc can induce DNA damage, increase reactive oxygen species, and mitigate p53 function: a mechanism for oncogene-induced genetic instability. Mol Cell. 2002; 9: 1031-44.
70. Prochownik EV, Li Y. The ever expanding role for c-Myc in promoting genomic instability. Cell Cycle. 2007; 6: 1024-29.
71. Sancho P, Burgos-Ramos E, Tavera A, Bou Kheir T, Jagust P, Schoenhals M, Barneda D, Sellers K, Campos-Olivas R, Graña O, Viera CR, Yuneva M, Sainz B Jr, Heeschen C. MYC/PGC-1α Balance Determines the Metabolic Phenotype and Plasticity of Pancreatic Cancer Stem Cells. Cell Metab. 2015; 22: 590-605.
72. Chung TL, Brena RM, Kolle G, Grimmond SM, Berman BP, Laird PW, Pera MF, Wolvetang EJ. Vitamin C promotes widespread yet specific DNA demethylation of the epigenome in human embryonic stem cells. Stem Cells. 2010; 28: 1848-55.
73. Esteban MA, Wang T, Qin B, Yang J, Qin D, Cai J, Li W, Weng Z, Chen J, Ni S, Chen K, Li Y, Liu X, Xu J, et al. Vitamin C enhances the generation of mouse and human induced pluripotent stem cells. Cell Stem Cell. 2010; 6: 71-79.
74. Monfort A, Wutz A. Breathing-in epigenetic change with vitamin C. EMBO Rep. 2013; 14: 337-46.
75. Wang T, Chen K, Zeng X, Yang J, Wu Y, Shi X, Qin B, Zeng L, Esteban MA, Pan G, Pei D. The histone demethylases Jhdm1a/1b enhance somatic cell reprogramming in a vitamin-C-dependent manner. Cell Stem Cell. 2011; 9: 575-87.
76. Cuyàs E, Fernández-Arroyo S, Corominas-Faja B, Rodríguez-Gallego E, Bosch-Barrera J, Martin-Castillo B, De Llorens R, Joven J, Menendez JA. Oncometabolic mutation IDH1 R132H confers a metformin-hypersensitive phenotype. Oncotarget. 2015; 6:12279-296. doi: 10.18632/oncotarget.3733.
77. Riera-Borrull M, Rodríguez-Gallego E, Hernández-Aguilera A, Luciano F, Ras R, Cuyàs E, Camps J, Segura-Carretero A, Menendez JA, Joven J, Fernández-Arroyo S. Exploring the Process of Energy Generation in Pathophysiology by Targeted Metabolomics: Performance of a Simple and Quantitative Method. J Am Soc Mass Spectrom. 2016;27:168-77.
78. Gutierrez-Aranda I, Ramos-Mejia V, Bueno C, Munoz-Lopez M, Real PJ, Mácia A, Sanchez L, Ligero G, Garcia-Parez JL, Menendez P. Human induced pluripotent stem cells develop teratoma more efficiently and faster than human embryonic stem cells regardless the site of injection. Stem Cells. 2010; 28: 1568-70.
79. Knoepfler PS. Deconstructing stem cell tumorigenicity: a roadmap to safe regenerative medicine. Stem Cells. 2009; 27: 1050-56.
80. Müller FJ, Goldmann J, Löser P, Loring JF. A call to standardize teratoma assays used to define human pluripotent cell lines. Cell Stem Cell. 2010; 6: 412-14.
81. Menendez S, Camus S, Herreria A, Paramonov I, Morera LB, Collado M, Pekarik V, Maceda I, Edel M, Consiglio A, Sanchez A, Li H, Serrano M, Belmonte JC. Increased dosage of tumor suppressors limits the tumorigenicity of iPS cells without affecting their pluripotency. Aging Cell. 2012; 11: 41-50.
82. Katajisto P, Döhla J, Chaffer CL, Pentinmikko N, Marjanovic N, Iqbal S, Zoncu R, Chen W, Weinberg RA, Sabatini DM. Stem cells. Asymmetric apportioning of aged mitochondria between daughter cells is required for stemness. Science. 2015; 348: 340-43.
83. Frank M, Duvezin-Caubet S, Koob S, Occhipinti A, Jagasia R, Petcherski A, Ruonala MO, Priault M, Salin B, Reichert AS. Mitophagy is triggered by mild oxidative stress in a mitochondrial fission dependent manner. Biochim Biophys Acta. 2012; 1823: 2297-2310.
84. Miller DM, Thomas SD, Islam A, Muench D, Sedoris K. c-Myc and cancer metabolism. Clin Cancer Res. 2012; 18: 5546-53.
85. Ji J, Sharma V, Qi S, Guarch ME, Zhao P, Luo Z, Fan W, Wang Y, Mbabaali F, Neculai D, Esteban MA, McPherson JD, Batada NN. Antioxidant supplementation reduces genomic aberrations in human induced pluripotent stem cells. Stem Cell Reports. 2014; 2: 44-51.

86. Teperino R, Schoonjans K, Auwerx J. Histone methyl transferases and demethylases; can they link metabolism and transcription? Cell Metab. 2010;12:321-27.

87. Cascella B, Mirica LM. Kinetic analysis of iron-dependent histone demethylases: α-ketoglutarate substrate inhibition and potential relevance to the regulation of histone demethylation in cancer cells. Biochemistry. 2012;51:8699-701.

88. Salminen A, Kauppinen A, Hiltunen M, Kaarniranta K. Krebs cycle intermediates regulate DNA and histone methylation: epigenetic impact on the aging process. Ageing Res Rev. 2014;16:45-65.

89. Carey BW, Finley LW, Cross JR, Allis CD, Thompson CB. Intracellular α-ketoglutarate maintains the pluripotency of embryonic stem cells. Nature. 2015;518:413-16.

90. Minocherhomji S, Tollefsbol TO, Singh KK. Mitochondrial regulation of epigenetics and its role in human diseases. Epigenetics. 2012;7:326-34.

91. Salminen A, Kaarniranta K, Hiltunen M, Kauppinen A. Krebs cycle dysfunction shapes epigenetic landscape of chromatin: novel insights into mitochondrial regulation of aging process. Cell Signal. 2014;26:1598-1603.

92. Merkwirth C, Jovaisaite V, Durieux J, Matilainen O, Jordan SD, Quiros PM, Steffen KK, Williams EG, Mouchiroud L, Tronnes SU, Murillo V, Wolff SC, Shaw RJ, Auwerx J, Dillin A. Two Conserved Histone Demethylases Regulate Mitochondrial Stress-Induced Longevity. Cell. 2016; 165:1209-23.

93. Ben-David U, Benvenisty N. Chemical ablation of tumor-initiating human pluripotent stem cells. Nat Protoc. 2014; 9: 729-40.

94. Ben-David U, Gan QF, Golan-Lev T, Arora P, Yanuka O, Oren YS, Leikin-Frenkel A, Graf M, Garippa R, Boehringer M, Gromo G, Benvenisty N. Selective elimination of human pluripotent stem cells by an oleate synthesis inhibitor discovered in a high-throughput screen. Cell Stem Cell. 2013; 12: 167-79.

95. Chen F, Cai B, Gao Y, Yuan X, Cheng F, Wang T, Jiang M, Zhou Y, Lahn BT, Li W, Xiang AP. Suicide gene-mediated ablation of tumor-initiating mouse pluripotent stem cells. Biomaterials. 2013; 34: 1701-11.

96. Lee MO, Moon SH, Jeong HC, Yi JY, Lee TH, Shim SH, Rhee YH, Lee SH, Oh SJ, Lee MY, Han MJ, Cho YS, Chung HM, Kim KS, Cha HJ. Inhibition of pluripotent stem cell-derived teratoma formation by small molecules. Proc Natl Acad Sci U S A. 2013; 110: E3281-E3290.

97. Menendez JA. Metabolic control of cancer cell stemness: Lessons from iPS cells. Cell Cycle. 2015; 14: 3801-11.

98. Tang C, Lee AS, Volkmer JP, Sahoo D, Nag D, Mosley AR, Inlay MA, Ardehali R, Chavez SL, Pera RR, Behr B, Wu JC, Weissman IL, Drukker M. An antibody against SSEA-5 glycan on human pluripotent stem cells enables removal of teratoma-forming cells. Nat Biotechnol. 2011; 29: 829-34.

99. Ma T, Li J, Xu Y, Yu C, Xu T, Wang H, Liu K, Cao N, Nie BM, Zhu SY, Xu S, Li K, Wei WG, Wu Y, Guan KL, Ding S. Atg5-independent autophagy regulates mitochondrial clearance and is essential for iPSC reprogramming. Nat Cell Biol. 2015; 17: 1379-87.

100. Chandel NS. Evolution of Mitochondria as Signaling Organelles. Cell Metab. 2015;22:204-06.

101. Martínez-Reyes I, Diebold LP, Kong H, Schieber M, Huang H, Hensley CT, Mehta MM, Wang T, Santos JH, Woychik R, Dufour E, Spelbrink JN, Weinberg SE, Zhao Y, DeBerardinis RJ, Chandel NS. TCA Cycle and Mitochondrial Membrane Potential Are Necessary for Diverse Biological Functions. Mol Cell. 2016;61:199-209.

102. Fernández-Arroyo S, Cuyàs E, Bosch-Barrera J, Alarcón T, Joven J, Menendez JA. Activation of the methylation cycle in cells reprogrammed into a stem cell-like state. Oncoscience. 2016;2:958-67.

103. Xia J, Sinelnikov IV, Han B, Wishart DS. MetaboAnalyst 3.0--making metabolomics more meaningful. Nucleic Acids Res. 2015; 43:W251-W257.

SUPPLEMENTAL DATA

Loss of PINK1 prevents mitophagic elimination of damaged mitochondria

To test whether *PINK1*-KO mouse embryonic fibroblasts (MEFs) constitute a useful model to dissect the role of mitophagy in the establishment of induced pluripotency, we first mimicked mitochondrial damage by experimentally depolarizing mitochondria [62]. To probe PINK1-dependent autophagic digestion of mitochondria (Supplemental Fig. 1A), we tracked the intracellular distribution of MitoTracker in $PINK^{+/+}$ and $PINK^{-/-}$ MEFs upon treatment with the uncoupler carbonyl cyanide *m*-chlorophenylhydrazone (CCCP), a lipid-soluble weak acid that drastically increases proton permeability across the mitochondrial inner membranes, thus dissipating the transmembrane potential and depolarizing the mitochondria. Because MitoTracker becomes covalently bound to mitochondrial proteins after uptake and remains in mitochondria even if a mitochondrion subsequently depolarizes, loss of MitoTracker after mitophagy stimulation largely represents lysosomal digestion of mitochondrial peptide fragments or breakage of covalent bonds between MitoTracker and mitochondrial proteins [67].

When we monitored mitochondrial clearance following treatment with 20 μmol/L CCCP for 18 h (Supplemental Fig. 1B, *top panels*), no MitoTracker-labeled mitochondria were detected in 86±6% of $PINK1^{+/+}$ MEFs (Supplemental Fig. 1C). In clear contrast, mitochondria were retained in *PINK1*-deficient cells (Supplemental Fig. 1B, *bottom panels*) and mitochondrial clearance occurred solely in a very small percentage (14±7%) of $PINK1^{-/-}$ MEFs following depolarization with CCCP (Supplemental Fig. 1C).

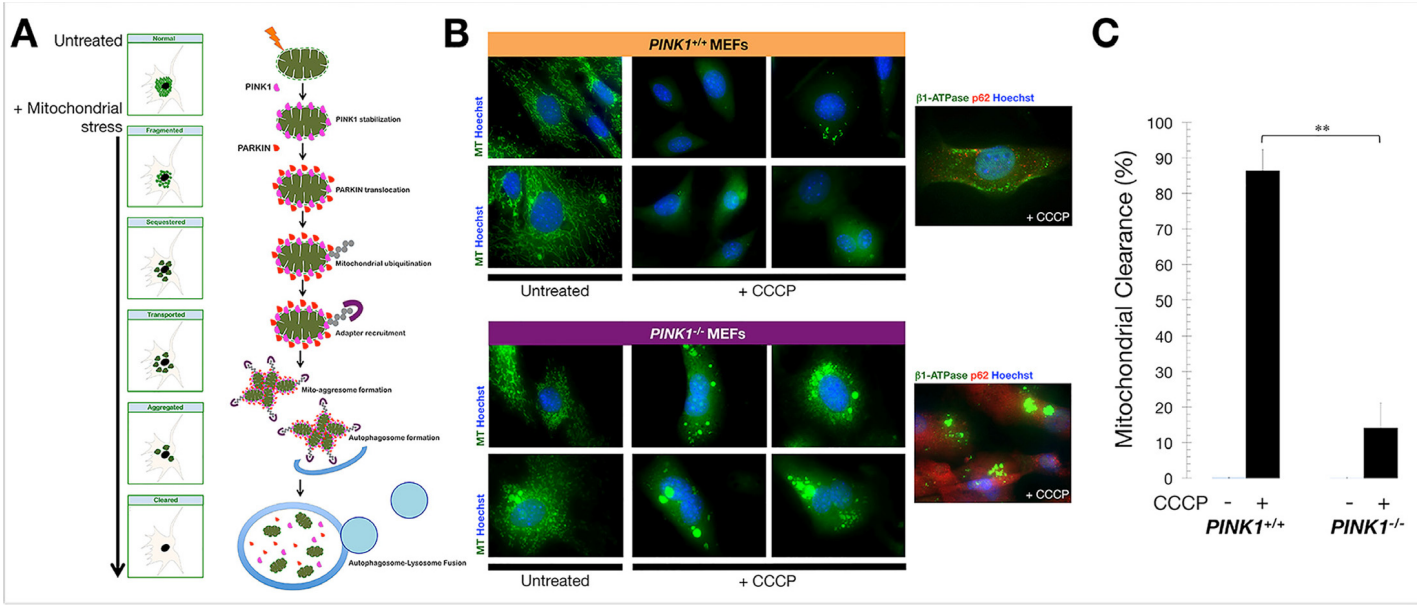

Supplemental Figure 1. PINK1 is necessary to drive mitophagy. (**A**) The schematic illustrates individual steps of the apparently sequential process of PINK1-dependent mitophagy. In response to several mitochondrial stresses, including chemical uncoupling (by CCCP treatment), mtDNA mutations, increasing ROS levels, and other yet-to-be discovered stimuli (e.g., nuclear reprogramming), PINK1 becomes stabilized on the mitochondrial outer membrane of unwanted or damaged mitochondria. Association of PINK1 with mitochondria results in the subcellular distribution and translocation of the ubiquitin ligase Parkin, which ubiquitinates specific mitochondrial surface proteins, such as mitofusins (Mfn1/2). Mitochondrial ubiquitination, in turn, results in the recruitment of adapter proteins including p62/SQSTM1 and HDAC6 that ultimately links ubiquitinated substrates to cellular transport and autophagic machineries. This transport results in the peri-nuclear clustering and formation of mito-aggresomes, which may thereby serve to restrict cellular distribution of unwanted or damaged mitochondria as well as to prepare targeted mitochondria for autophagic clearance. LC3 and autophagosomal membranes are co-recruited during transport and aggregation of targeted mitochondria and, consequently, mito-aggresomes become engulfed by the forming autophagosomes that finally fuse with lysosomes for degradation and mitochondria clearance. (**B**) $PINK1^{+/+}$ MEFs (*top*) and $PINK1^{-/-}$ MEFs (*bottom*) were preloaded with MitoTracker followed by an 18 h treatment with 20 μmol/L (μM) CCCP (MT: MitoTracker). Cells were then fixed (MitoTracker Red is retained after permeabilization) and, where shown, immunostained with an antibody against the β1-subunit of the mitochondrial F1-ATPase to visualize mitochondria or an antibody against p62. **C.** Average percentages of mitochondria-free cells from **A** (n=3). **, P<0.01.

Indeed, CCCP treatment resulted in the formation of large MitoTracker-positive aggregates in *PINK1*$^{-/-}$ MEFs, mainly in the perinuclear region, with relatively sparse cytosolic staining (Supplemental Fig. 1B, *bottom panels*). We further confirmed this mitophagy defect by immunostaining with an antibody against the β1-subunit of the mitochondrial F1-ATPase complex, which strongly labeled mitochondrial aggregates in *PINK1*$^{-/-}$ MEFs (Supplemental Fig. 1B). Similarly, staining of p62/SQSTM1, an adapter protein that binds ubiquitinated mitochondria, was readily detectable in *PINK1*$^{-/-}$ MEFs, consistent with the accumulation of mitochondria.

Mitophagy deficiency-imposed roadblock for reprogramming is partially circumvented by vitamin C.

Using 2'-7'-dichlorodihydrofluorescein diacetate (DCFH-DA) to measure ROS generation in the cytoplasm and cellular organelles such as the mitochondria, we noted a marked increase in oxidative stress in mitophagy-deficient *PINK1*$^{-/-}$ MEFs relative to mitophagy-competent *PINK1*$^{+/+}$ MEFs following treatment with CCCP (Supplemental Fig. 2A). Indeed, although an inspection of the temporal production of

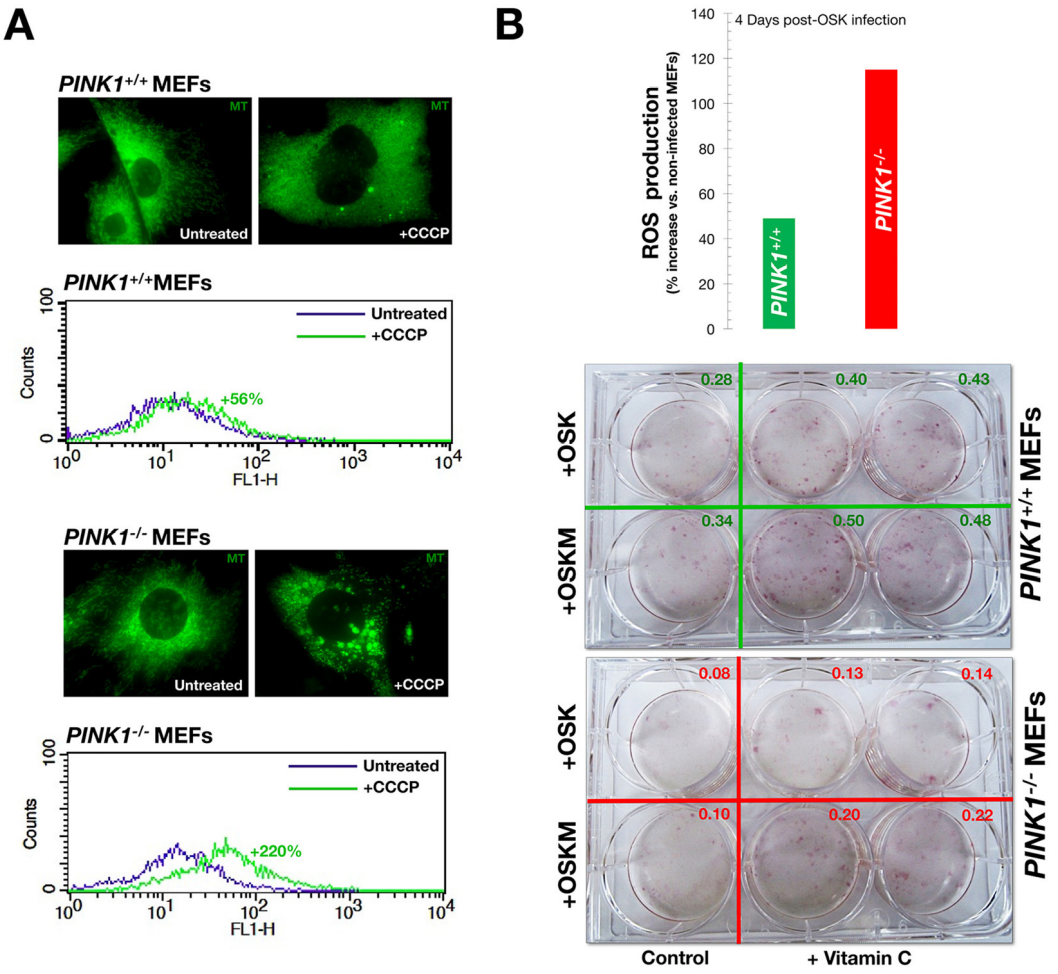

Supplemental Figure 2. Mitophagy deficiency enhances oxidative stress in response to reprogramming. **(A)** MitoTracker was used to stain mitochondria in live *PINK1*$^{+/+}$ and *PINK1*$^{-/-}$ cells after short-term (1 h) treatment with CCCP (*top*). Measurement of ROS in CCCP-treated cells (*bottom*). Untreated or CCCP-treated *PINK1*$^{+/+}$ and *PINK1*$^{-/-}$ MEFs were exposed for 60 min to H_2DCF-DA and fluorescence intensity was measured by flow cytometry. Shown are representative scatter plot histograms of DCF fluorescence. (**B**) Measurement of ROS in OSK-transduced cells (*left*). Bar charts of representative measurements of ROS levels (% increase versus baseline ROS levels in untransduced MEF populations cultured in parallel) in *PINK1*$^{+/+}$ MEFs (*top*) and *PINK1*$^{-/-}$ MEFs (*bottom*) at days indicated post-infection with OSK. **C.** Representative AP staining of OSK- and OSKM-infected untreated or treated with vitamin C (*right*). For each experimental condition, reprogramming efficiency was calculated by dividing the average count of AP-positive colonies per well by the initial number of cells plated (n=6 for each condition).

ROS during reprogramming revealed that both cell types displayed a marked burst of ROS at day 4 after OSK transduction, ROS production at this time was significantly greater in *PINK1*$^{-/-}$ MEFs compared with equivalent wild-type cells (Supplemental Fig. 2B, *top*).

A testable prediction from this observation is that inhibition or alleviation of excessive ROS production should increase the number of mitophagy-deficient cells that surpass the early reprogramming barrier imposed by abnormal mitophagy. We therefore evaluated whether the ability of vitamin C to block steady-state ROS levels in OSK-transduced *PINK1*$^{-/-}$ MEFs might lead to an increase in reprogramming efficiency. Addition of vitamin C (50 μg/mL) notably increased the reprogramming efficiency of OSK-transduced *PINK1*$^{-/-}$ MEFs (Supplemental Fig. 2B, *bottom*); however, when both cell types were supplemented with vitamin C during reprogramming, OSK-transduced *PINK1*$^{+/+}$ MEFs still generated significantly more colonies than *PINK1*$^{-/-}$ MEFs (Supplemental Fig. 2B, *bottom*).

Editorial

Potential targeted therapeutic approaches in liposarcoma

DOI: 10.18632/aging.100945

Deepika Kanojia, Manoj Garg, and H. Phillip Koeffler

Liposarcoma (LPS) is rare malignant tumor of fat cells in deep soft tissue that affects adults between the ages of 40 and 60 [1]. This tumor is extremely aggressive with high morbidity and mortality. World Health organization classifies LPS into five subtypes: well-differentiated (WDLPS)/Atypical lipomatous tumors (ALT); dedifferentiated (DDLPS); myxoid (MLPS); pleomorphic (PLPS); and mixed type LPS [2]. Most common modality of treatment is surgical removal of tumor followed by radiation and chemotherapy. The five year survival rate of LPS patients vary from 56%-100% based on different subtypes [3]. Previous genetic studies have focused either on a subset of target genes or one subtype of LPS. Till now no reports have provided a detailed genomic analysis of LPS which included all different subtypes of LPS. Therefore, recently we defined the genomic landscape of LPS using SNP array and whole exome sequencing and identified a spectrum of altered genes and pathways in different subtypes of LPS patients and cell lines [4].

WDLPS and DDLPS subtypes have a characteristic feature of amplified region of chromosome 12q13-15 containing several well-known oncogenes such as MDM2, CDK4 and HMGA2 [5]. SNP array analysis of LPS patients and cell lines identified recurrent amplification of Carboxypeptidase M (CPM) gene only in WDLPS and DDLPS subtypes. We studied in detail CPM gene in vitro and in vivo and showed its involvement in liposarcomagenesis. CPM is a membrane bound enzyme and we found it expressed on the cell surface of LPS cells suggesting it as a potential therapeutic target. Carboxypeptidase activity of CPM is known to regulate the processing of EGF [6]. We found downregulation of CPM expression leads to reduced EGFR signalling and induces apoptosis of LPS cells. Future studies are ongoing detailing further role of enzymatic activity of CPM in EGFR signaling and enhancement of tumor growth. Further, we are developing both a quantitative PCR assay and an ELISA to measure CPM activity in the serum to develop a biomarker to measure minimal residual disease which might aid in monitoring therapy. Specific and selective inhibitors of CPM are not available in the market; therefore, we are also aiming to do screening to find selective and specific small molecules to inhibit CPM enzymatic activity. We proposed CPM as potential therapeutic candidate which could be used as targeted approach to manage CPM amplified WDLPS or DDLPS patients.

Next, whole exome sequencing and targeted exome sequencing identified various known cancer related and novel genes recurrently mutated in different subtypes of LPS. MAPK, ErbB, JAK-STAT, Wnt, apoptosis, cell cycle, DNA replication and repair and axon guidance pathways were found to be potentially involved in liposarcomagenesis. We identified recurrent mutations in previously unidentified genes in LPS associated with DNA damage repair pathways. LPS tumors with DNA repair mutations could be completely dependent on other backup repair pathways for the survival which may be exploited to induce synthetic lethality as therapeutic approach in these tumors.

Interestingly, we reported for the first time multi-region genomic analysis of single LPS patient's tumor signifying intra-tumor mutational and copy number heterogeneity. The current basis for most of the personalized medicine approaches depends on the genomic landscape of a single tumor biopsy sample. Due to the frequent large size of LPS tumors compared to other solid tumors, intra-tumor heterogeneity will lead to difficulties in identifying biomarkers and therapeutic targets. Our preliminary analysis of intra-tumor heterogeneity mandates the need for future detailed studies exploring the evolution of LPS tumors leading to progression.

In summary, our recent work gave insights into global genomic spectrum of LPS cohort for development of novel therapeutic strategies and for understanding the pathogenesis this deadly disease.

REFERENCES

1. Mack TM. Cancer. 1995; 75:211-244.

2. Fletcher CDM BJ, Hogendoorn PCW, Mertens F eds. Lyon: IARC Press. 2013; (4th ed).

3. Dalal KM, et al. J Surg Oncol. 2008; 97:298-313.

4. Kanojia D, et al. Oncotarget. 2015; 6:42429-42444. doi: 10.18632/oncotarget.6464.

5. Barretina J, et al. Nat Gen. 2010;42:715-721.

6. McGwire GB and Skidgel RA. J Biol Chem. 1995; 270:17154-17158.

Deepika Kanojia: Cancer Science Institute of Singapore, National University of Singapore, Singapore

Correspondence: *Deepika Kanojia*
Email: *csidk@nus.edu.sg*
Keywords: *liposarcoma, therapeutics, exome sequencing, tumor heterogeneity, genomic landscape*

Received: April 8, 2016
Published: April 14, 2016

Review

Apoptosis as anticancer mechanism: function and dysfunction of its modulators and targeted therapeutic strategies

Giuseppa Pistritto[1], Daniela Trisciuoglio[2], Claudia Ceci[1], Alessia Garufi[2,3], and Gabriella D'Orazi[2,3]

[1]Department of Systems Medicine, University "Tor Vergata", 00133 Rome, Italy
[2]Department of Research, Advanced Diagnostics, and Technological Innovation, Regina Elena National Cancer Institute, 00158 Rome, Italy
[3]Department of Medical Oral and Biotechnological Sciences, Tumor Biology Unit, University "G. d'Annunzio", 66013 Chieti, Italy

Key words: apoptosis, defective apoptotic pathways, cancer, small molecules, miRNAs, p53
Received: 01/04/16; Accepted: 03/08/16; Published: 03/27/16 DOI: 10.18632/aging.100934
Correspondence to: Gabriella D'Orazi, MD/PhD; Giuseppa Pistritto, MD/PhD; **E-mail:** gabriella.dorazi@unich.it; pistritto@med.uniroma2.it

Copyright: Pistritto et al. This is an open-access article distributed under the terms of the Creative Commons Attribution License, which permits unrestricted use, distribution, and reproduction in any medium, provided the original author and source are credited

Abstract: Apoptosis is a form of programmed cell death that results in the orderly and efficient removal of damaged cells, such as those resulting from DNA damage or during development. Apoptosis can be triggered by signals from within the cell, such as genotoxic stress, or by extrinsic signals, such as the binding of ligands to cell surface death receptors. Deregulation in apoptotic cell death machinery is an hallmark of cancer. Apoptosis alteration is responsible not only for tumor development and progression but also for tumor resistance to therapies. Most anticancer drugs currently used in clinical oncology exploit the intact apoptotic signaling pathways to trigger cancer cell death. Thus, defects in the death pathways may result in drug resistance so limiting the efficacy of therapies. Therefore, a better understanding of the apoptotic cell death signaling pathways may improve the efficacy of cancer therapy and bypass resistance. This review will highlight the role of the fundamental regulators of apoptosis and how their deregulation, including activation of anti-apoptotic factors (i.e., Bcl-2, Bcl-xL, etc) or inactivation of pro-apoptotic factors (i.e., p53 pathway) ends up in cancer cell resistance to therapies. In addition, therapeutic strategies aimed at modulating apoptotic activity are briefly discussed.

INTRODUCTION

Apoptosis, the programmed cell death, is finely regulated at gene level resulting in the orderly and efficient removal of damaged cells such as those occurring following DNA damage or during development [1]. The machinery of apoptosis is complex and involves many signaling pathways. Apoptosis can be triggered in a cell through either the caspase-mediated extrinsic or intrinsic pathways. Both pathways converge to activate the effector apoptotic caspases resulting ultimately in morphological and biochemical cellular alterations, characteristics of apoptosis [2]. Usually, the balance between the pro-apoptotic and anti-apoptotic protein regulators is a critical key point to determine if a cell undergoes apoptosis. The induction of apoptosis as result of DNA damage in precancerous lesions can remove potentially harmful cells, thereby blocking tumor growth. Deregulation of this death process is associated with unchecked cell proliferation, development and progression of cancer and cancer resistance to drug therapies [3,4]. For that reason, deregulation of apoptosis is considered one of the hallmarks of cancer [5]. Therapeutic strategies targeting molecules involved in apoptotic resistance therefore represent a valid approach to be pursued in order to restore cancer cells sensitivity to apoptosis and overcome the ineffectiveness of the treatments [6,7]. This article focuses on the mechanisms of apoptosis, how defects along the

apoptotic pathway contribute to cancer development and drug resistance and, briefly, how apoptosis can be used as a vehicle of targeted treatment in cancer.

Morphological and biochemical changes in apoptosis

From the morphological point of view apoptotic cells show a characteristic cytoplasmic cell shrinkage, budding of plasma membrane, membrane exposure of phosphatidylserine (PS) on extracellular side, chromatin condensation and DNA fragmentation [8,9]. The plasma membrane is intact throughout the total process. The expression of PS in the outer layers of the cell membrane allows early recognition of dead cells by macrophages, resulting in phagocytosis without the release of proinflammatory cellular components [10]. At the later stage of apoptosis some of the morphological features include membrane blebbing, ultrastructural modification of cytoplasmic organelles and loss of membrane integrity [11]. Usually phagocytic cells engulf apoptotic cells before apoptotic bodies occur [12]. Apoptosis is primarily executed by a family of proteases known as the caspases (cysteinyl, aspartate-specific proteases) [13]. Caspases are central to the mechanism of apoptosis as they are both the initiators (caspase-2, -8, -9 and -10, primarily responsible for the beginning of the apoptotic pathway) and the executors (caspase-3, -6 and -7, responsible for the definite cleavage of cellular components) of cell death [14]. After being produced as inactive proteins (zymogens or pro-caspases), the initiator caspases auto-activate through auto-proteolysis, a process that is facilitated by their interaction with specific adapter molecules [15]. Once activated, the initiator caspases cleave off the executors caspases that perform critical cleavage of specific cellular substrates resulting in the final apoptotic cell death [16]. This caspases activity is responsible of the apoptotic hallmarks, such as chromatin condensation, plasma membrane asymmetry and cellular blebbing. The extensive and irreversible proteolytic activity mediated by executor caspases represents the ultimate outcome of both the extrinsic and the intrinsic apoptotic pathways (see below). Thus, both pathways converge on caspases-3, 6, or -7 that allow disruption of DNA and cellular components inducing the typical morphological changes in apoptosis [17]. Of note, caspases activity has been also extended to non-apoptotic functions such as cell differentiation/maturation suggesting that the caspase cascade may become activated independently of– or without inducing- an apoptotic cascade [18-20].

Extrinsic apoptotic pathway

The extrinsic apoptotic pathway (death receptor-dependent) is initiated by the interaction of cell surface exposed death receptors, belonging to the superfamily of tumor necrosis factor receptor (TNFR), with their respective protein TNF family ligands [21]. Death receptors are structurally defined by an intracellular protein-protein interaction domain, called the death domain (DD), which is critically involved in apoptosis-inducing signalling [22]. The more broadly characterized signaling systems of death receptor-ligands include TNFR1-TNFα, FAS (CD95, APO-1)-FasL, TRAILR1 (DR4)-TRAIL, TRAILR2 (DR5)-TRAIL. Upon death receptor stimulation by its corresponding ligand, the same receptor undergoes oligomerization and a conformational change to reveal its cytoplasmic DD to support homotypic interactions with other DD-containing proteins [21]. The role of adapter proteins (FADD/TRADD) is to sequester, at level of this protein complex, the initiator pro-caspase-8 and/or -10 resulting in the formation of the so-called death-inducing signaling complex (DISC), increasing the local concentration of pro-caspase and promoting the mutual auto-activation [23]. The activation of initiator caspases results in the processing of the downstream effector caspases-3, -6 and -7 whose activation leads to the cleavage of essential substrates for cell viability, inducing cell death (Figure 1) [17]. Some cells do not die in response to the extrinsic pathway alone and require an amplification step that is induced by caspase-8. In this situation, capase-8 targets the BH3-only protein Bid (BH3-interacting-domain death agonist) for cleavage and generate the activated fragment t-Bid; t-Bid then directly activates pro-apoptotic multi-domain proteins to induce mitochondrial outer membrane permeability (MOMP), so this co-engages the intrinsic pathway [3] (Figure 1) (see below).

Intrinsic apoptotic pathway

The intrinsic apoptotic pathway (mitochondria-dependent) is mediated by intracellular signals that converge at the mitochondrial level in response to different stress conditions (i..e, irradiation, treatment with chemotherapeutic agents, etc.) [24]. Internal stimuli such as irreparable genetic damage, hypoxia, extremely high concentrations of cytosolic Ca^{+} and severe oxidative stress are some triggers of the initiation of the intrinsic mitochondrial pathway [25]. Subsequent activation of pro-apoptotic BH3-only members of the Bcl-2 family (Bax, Bak) neutralizes the antiapoptotic proteins Bcl-2, Bcl-xL, and Mcl-1, leading to disruption of mitochondrial membrane outer membrane permeability (MOMP) so that proteins normally confined in the intermembrane space spread into the cytosol. These proteins include the so-called apopto-genic factors, such as cytochrome-*c*, which plays a

crucial role in activating the mitochondrial-dependent death in the cytosol [26]. Cytochrome-*c* binds to the cytosolic Apaf-1 (apoptosis protease activating factor-1) and triggers the formation of a complex named apoptosome, which recruits initiator pro-caspase-9 to its caspase recruitment domain (CARD), allowing auto-activation and then proteolysis. The process in turn activates downstream executor caspases-3, -6 and -7 for cleavage of cellular substrates leading to apoptotic cell death (Figure 1) [27,28].

The B-cell lymphoma 2 (Bcl-2) family proteins

The intrinsic pathway is closely regulated by the B-cell lymphoma 2 (Bcl-2) family of intracellular proteins. This proteins family regulates both pro-apoptotic and anti-apoptotic intrinsic pathways controlling the alteration of MOMP [29]. Therefore, by mediating permeabilization of the mitochondrial membrane, the Bcl-2 proteins serve as an "apoptotic switch" [30]. The Bcl-2 proteins are classified into three subgroups, one group with anti-apoptotic and two with pro-apoptotic function, depending on the composition of typical BH (Bcl-2 Homology) domains, listed from BH1 to BH4 [31,32] (Figure 2). Whereas the BH1 and BH2 domains of bcl-2 are required for dimerization with pro-apoptotic proteins, BH3 domain is crucially important to the interaction between pro-apoptotic and anti-apoptotic proteins and is contained by all family members. The amino-terminal BH4 domain is mainly found in the bcl-2 family members with death-repressing activity, but is also present in some pro-apoptotic molecules. The anti-apoptotic multi-domain group includes Bcl-2, Bcl-xL, Bcl-W, Mcl-1, A1, and Bcl-B, containing from three to four BH domains; the pro-apoptotic multi-domain group includes Bax, Bak and Bok proteins, containing three

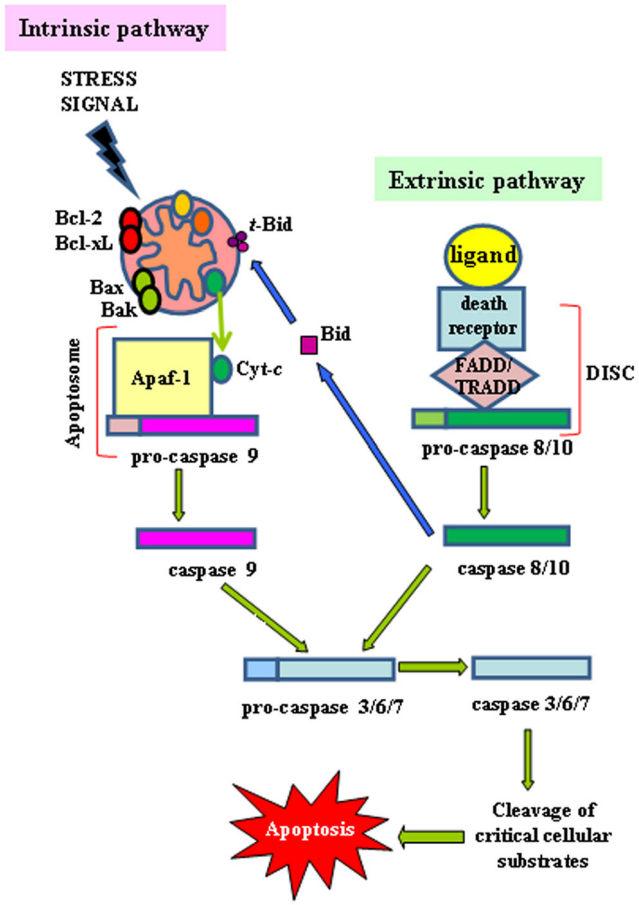

Figure 1. Intrinsic and extrinsic apoptotic pathways. The intrinsic (mitochondrial) and the extrinsic (ligands/death receptors) cell death pathways and their convergence through t-Bid are depicted (see text for details).

BH-domains (BH1, BH2 and BH3); and the pro-apoptotic BH3-only proteins group includes Bid (BH3 interacting-domain death agonist), Bim (Bcl-2-like protein 11), Bad (Bcl-2-associated death promoter), Puma (p53 upregulated modulator of apoptosis), Noxa, BMF, HRK and BIK (Figure 3) [33]. While the anti-apoptotic proteins regulate apoptosis by blocking the mitochondrial release of cytochrome-*c*, the pro-apoptotic proteins act by promoting such release.

The balance and protein-protein interactions between Bcl-2 family members is required to determine whether a cell undergoes cell survival or apoptosis. The activation of Bax (cytosolic protein that translocates into mitochondria during induction of apoptosis), and Bak (integral membrane protein located in the mitochondria and endoplasmic reticulum) involves conformational changes that trigger the formation of homo-oligomeric protein complexes that end up altering

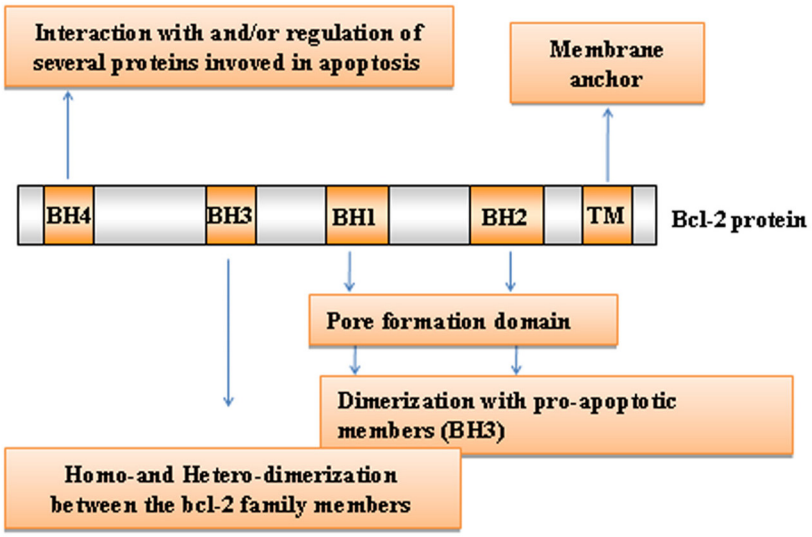

Figure 2. Bcl-2 family members domain composition and function. Typical BH (Bcl-2 Homology) domains, listed from BH1 to BH4, are shown. TM: transmembrane domain.

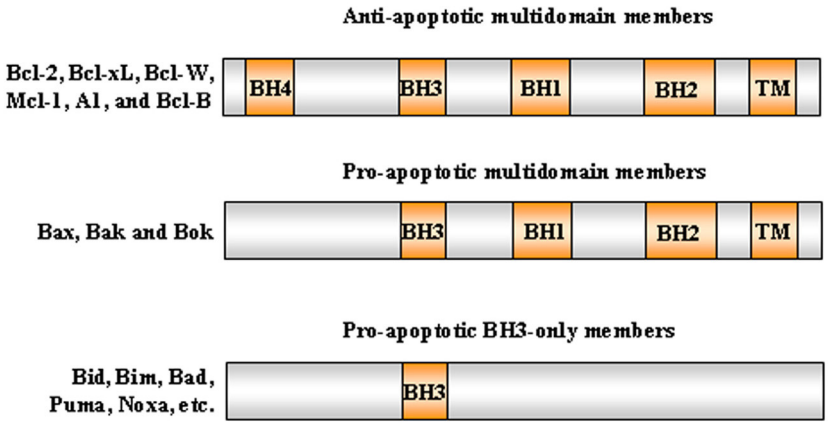

Figure 3. Bcl-2 protein subgroups. The Bcl-2 proteins are classified into three subgroups, one group with anti-apoptotic and two with pro-apoptotic function, depending on the composition of the typical BH domains, listed from BH1 to BH4. Representative members of each subfamily are shown.

the mitochondrial membrane permeability [34,35]. The pro-apoptotic BH3-only proteins act upstream of this event binding with high affinity to anti-apoptotic Bcl-2 family members thereby allowing Bax/Bak to elicit MOMP and activation of the caspase cascade [36,37]. Anti-apoptotic multidomain members of the Bcl-2 protein family not only counteract the pore-forming activity of Bax and Bak by engaging in direct inhibitory interactions, but also prevent the generation of pro-apoptotic cytosolic Ca^{2+} waves either by reducing capacity of endoplasmic reticulum (ER) Ca^{2+} storage, an effect that is antagonized by Bax and Bak or by interacting with inositol 1,4,5- trisphosphate (IP3) receptor [38,39]. Other apoptotic factors that are released from the mitochondrial intermembrane space into the cytoplasm include apoptosis inducing factor (AIF), second mitochondria-derived activator of caspase (Smac), direct IAP Binding protein with Low pI (DIABLO) and Omi/high temperature requirement protein A (HtrA2) [40].

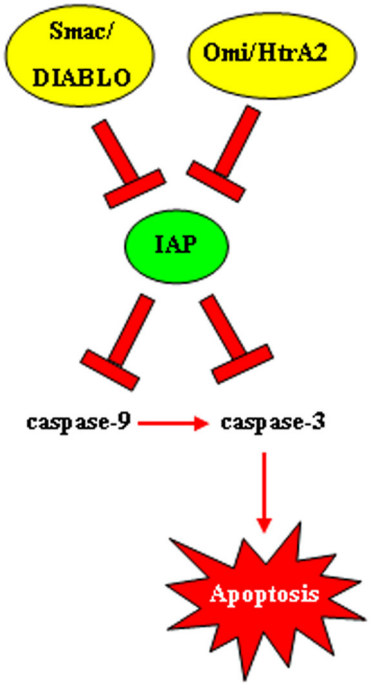

Figure 4. Function of inhibitors of apoptosis *proteins* (IAPs). IAPs are often overexpressed in cancer and they have the ability to bind and inactivate caspases 9 and 3. The activities of IAPs, on the other hand, may be suppressed by mitochondrial proteins, such as Omi/HtrA2 and Smac/DIABLO, released into the cytosol during apoptosis.

The inhibitors of apoptosis proteins (IAPs)

Considering that proteolysis is an irreversible process, strict control of caspases-mediated proteolytic cleavage is imperative to prevent inappropriate cell destruction [41]. Negative regulation of caspases function is achieved by IAP proteins family whose principal members in humans are NAIP (BIRC1), cIAP1 (BIRC2), cIAP2 (BIRC3), X-linked IAP (XIAP, BIRC4), Survivin (BIRC5), Apollon (BRUCE, BIRC6), Livin/ML-IAP (BIRC7), and IAP-like protein 2 (ILP2 – BIRC8) [42]. Their characteristic BIR (baculovirus IAP repeat) domain mediates the interaction with various proteins and gives them the ability to bind and inactivate caspases [43]. The activities of IAPs, however, may be suppressed by mitochondrial proteins, such as Omi/HtrA2 and Smac/DIABLO, released into the cytosol during apoptosis (Figure 4). These endogenous IAPs antagonists are able to bind to the BIR domain of IAPs reducing their ability to interact with caspase-3 or -9 thereby restoring their activity [44]. XIAP is the best characterized IAP so far and is generally recognized as the most potent endogenous caspase inhibitor. XIAP anti-apoptotic activity involves inhibition of active executor capsases as well as prevention of initiator caspase-9 activation [45].

Alterations of the apoptotic pathways

There are many ways through which both the extrinsic and the intrinsic apoptotic pathways may be altered, resulting in reduction of apoptosis or acquisition of apoptosis resistance. They include impaired death receptor signaling, disrupted balance between pro-apoptotic and anti-apoptotic proteins, reduced caspase function and impaired p53 function (Figure 5). Alteration of extrinsic apoptotic signaling has been associated with different types of human tumors, underscoring how the loss of activity of Fas-FasL system [46] or the aberrant expression of cytosolic components of this death receptor apoptotic pathway (i.e., FADD) [47] can contribute to the tumor transformation. Several genetic defects have been proven to contribute to the resistance of tumor cells to Fas-mediated apoptosis. Fas transcriptional silencing is a common oncogenic event in the epithelial transformation, while its mutation has been often associated with B-cell germinal center-derived lymphomas [48]. In acute myelogenous leukemia (AML) reduced or absent expression of FADD has been frequently observed, resulting in resistance to chemotherapy and poor patient prognosis [47,49]. Moreover, in several cancers including neuroblastoma, medulloblastoma, and small cell lung cancer (SCLC), absent or reduced expression of caspase-8 was reported

[50-52]. Another resistance mechanism reported in a variety of human tumors is the overexpression of anti-apoptotic protein c-Flip, recruited at the DISC level, that prevents the pro-caspase-8 auto-activation thereby rendering cell resistant to death receptor-mediated apoptosis [53-55].

As for the extrinsic pathway, alteration of some components of the intrinsic apoptotic pathway can play a fundamental role in the development of resistance to chemotherapy in different types of tumors. Disruption in the balance of anti-apoptotic and pro-apoptotic members of the Bcl-2 family results in deregulated apoptosis in the affected cells. This can be due to overexpression of one or more anti-apoptotic proteins or downregulation of one or more pro-apoptotic proteins or a combination of both. Anti-apoptotic Bcl-2 over-expression has been reported in several human cancers, including prostate cancer, diffuse large B-cell lymphoma (DLBCL), melanoma, etc. [56-58], resulting in protection of cancer cells from apoptosis or inhibition of TRAIL-induced apoptosis [59,60]. Overexpression of Bcl-xL has also been reported in colorectal cancer and Kaposi's sarcoma [61,62]. Such overexpression confers a multi-drug resistance phenotype in tumor cells and prevents them from undergoing apoptosis [63]. Thus, high expression levels of anti-apoptotic proteins Bcl-2 and Bcl-xL have been reported to correlate with cisplatin resistance and tumor recurrence in different cancers including non-small cell lung cancer (NSCLC), head and neck, ovarian, and breast [64-68]. On the other hand, mutations in the pro-apoptotic Bax gene have been reported in colorectal cancers and contribute to resistance to anticancer treatments [69]. Increased Bcl-2/Bax ratio has been reported in chronic lymphocytic leukaemia (CLL) patients. [70]. Other examples of alteration of the intrinsic pathway include reduced expression of the basic component of the apoptosome, Apaf-1, in melanomas [71,72], as result of promoter aberrant methylation. In addition, tumor cells resistance to apoptosis also occurs as a result of alteration of mediators that control the intrinsic apoptotic pathway downstream from the apoptosome formation, i.e. acting on caspase activity. In this regard, high level of IAPs expression has been found in different types of cancers, and this evidence is considered a marker of poor prognosis for patients [73,74].

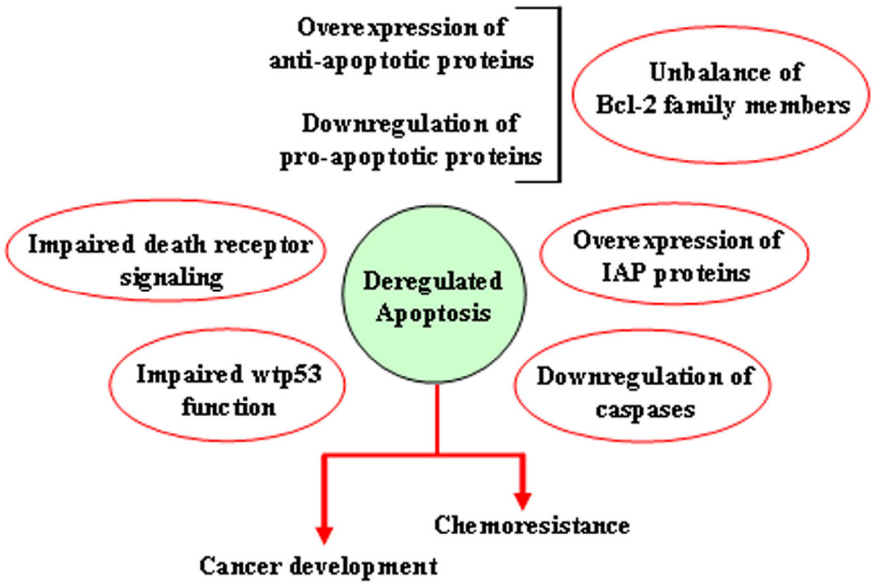

Figure 5. Mechanisms leading to deregulation of apoptosis. Schematic representation of the different ways through which both the extrinsic and the intrinsic apoptotic pathways may be altered, resulting in reduction of apoptosis or acquisition of apoptosis resistance.

Pharmacological targeting of the apoptotic pathways

Based on this evidence, restoration of apoptotic pathway by drugs targeting both apoptotic pathways constitutes a promising anticancer therapeutic approach. Regarding the extrinsic pathway, the down-regulation of c-Flip by metabolic inhibitors and the promotion of caspase-8 activation by interferon, are some examples of strategies aimed at making tumors responsive to death receptor-induced apoptosis, and more generally, to chemotherapy-induced apoptosis [55,75,76]. The therapeutic importance of inducing apoptosis through the extrinsic pathway also extends to cancer cells that do not show defects in components of that pathway. Indeed, inducing the apoptosis by stimulating the extrinsic pathway can overcome the resistance to therapeutic agents that act by causing DNA damage, as death receptor-dependent apoptosis may occur regardless of the stress response. An example of such therapeutic strategy is represented by the ligand TRAIL known to induce apoptosis in different tumor cell lines [77]. The preferential destructive effect against tumor cells and the apparent absence of systemic toxicity through TRAIL-induced apoptosis, led to the development of antibodies with agonistic activity against the TRAIL death receptors (DR4 and DR5) or soluble recombinant derivatives of TRAIL (sTRAIL) as promising chemotherapeutic agents [78]. An attractive strategy to sensitize resistant malignancies to TRAIL-induced cell death is the design of small molecules that target and promote caspase-8 activation. Through an *in silico* screening some authors successfully found a small molecule activator of caspase-8 [79]. Experimental validation performed in multiple cell lines, such as leukemic and prostate cells, revealed that CaspPro small molecule promotes caspase-8 activation, caspase-3 activation and PARP cleavage, in the presence of TRAIL, leading to cell death [79]. Owing to its different toxicity for transformed as opposed to normal cells, Apo2/TRAIL shows promise as potential cancer therapy agent [80,81].

As in the extrinsic pathway, mediators of the intrinsic pathway involved both in tumorigenesis and chemo-resistance, are targeted for therapeutic approaches. These anticancer strategies attempt to develop drug-designed inhibitors of anti-apoptotic proteins typically overexpressed in cancer cells, such as Bcl-2, Bcl-xL and IAPs [82]. Efforts to target Bcl-2 proteins involve the development of agents that disrupt Bcl-2 complexes. BH3 mimetics bind to the hydrophobic groove of antiapoptotic proteins mimicking the action of BH3-only proteins in binding to pro-survival proteins, leading to the release of BH3-only proteins from complexes and activation of BAX and BAK. So far, nearly a dozen BH3 mimetics are under investigation as Bcl-2 inhibitors in different phases of human clinical trials such as AT-101 (R-(-)-gossypol) [83,84], ABT-199 (venetoclax) [85], ABT-737 [86], ABT-263 (navitoclax, orally available derivative of ABT-737) [87,88], GX15-070 (obatoclax) [89,90] and TW37 [91]. The field of inhibitors of Bcl-2 family members is in continuous development [92,93], underscoring the importance of these molecules as potent anticancer agents. Moreover, targeting the specific BH4 domain of Bcl-2 is also emerging as a novel strategy for anticancer therapy [94]. Thus, Bcl-2, via its BH4 domain, cooperates with numerous proteins regulating different cellular pathways involved in tumor progression and chemoresistance such as hypoxia and angiogenesis [95-97]. Recently, a small molecule namely BDA-366 was discovered as a potent and effective BH4 domain antagonist, displaying remarkable anticancer activity in vitro and in vivo, thus providing the proof-of-concept of this approach [98]. Another innovative approach to inhibit Bcl-2 comes from the evidence that human bcl-2 gene contains a GC-rich sequence located in its promoter with the potential to form G-quadruplex structures [99] and functions as a transcriptional repressor element. Therefore, G-quadruplex-specific ligands can regulate the transcription of bcl-2 through stabilization of quadruplex structure [100,101].

Interestingly, it has been shown that the tumor suppressor p53, at least in part by transcription independent mechanisms, contributes to cell death induction by BH3 mimetic inhibitors of BCL-xL. In addition to mildly facilitating the ability of compounds to derepress BAX from BCL-xL, p53 also provides a death signal downstream of anti-apoptotic proteins inhibition that is independent from PUMA, as enhanced p53 can substitute for PUMA to promote BAX activation in response to BH3 mimetics [102]. It is thus of particular relevance that p53, even when expressed constitutively under conditions where it does not influence the expression of its pro-apoptotic transcription targets, enhances cell death induced by BCL-xL inhibition [102]. Such results suggest on one hand that BH3 mimetics may not totally substitute for the lack of an active p53 tumor suppressor in cancer cells; on the other hand, they imply that healthy tissues may be more harmed than anticipated when BCL-xL inhibitors are combined with chemotherapeutic agents that even mildly affect p53.

Among the therapeutic strategies targeting IAPs two approaches have being developed, that is the use of antisense oligonucleotides and of small-molecule inhibitors. The XIAP down-regulation through administration of antisense agents carried by an

adenoviral vector has been proven effective in inducing apoptosis in chemoresistant ovarian cancer cells [103] and sensitizing lung cancer cells to the radiation treatment [104]. Similarly, the inhibition of XIAP expression with specific oligomers has been shown to induce caspase-3 activity, boosting the apoptotic effect of cisplatin and TRAIL in human prostate androgen-insensitive cancer cells [105]. Moreover, preclinical studies have shown that Smac mimetics can directly trigger cancer cell death or sensitize tumor cells to various cytotoxic therapies, including conventional chemotherapy, radiotherapy, or novel agents. They promote activation of caspases by neutralizing XIAP-mediated caspase inhibition [106]. Therefore, the success of each therapeutic strategy depends mainly on the ability of the therapeutic tool to induce apoptosis either by targeting the overexpressed anti-apoptotic proteins or by stimulating the expression of the pro-apoptotic molecules.

However, it is worth to mention that the cancer genetic background may induce failure of apoptosis by drugs. In this regard, KRAS and the PI3K/AKT/mTOR pathway are frequently dysregulated in cancer and, for such reason, are the most critical targets in clinical oncology. Thus, direct targeting of KRAS has not been successful so far and, similarly, inhibition of the PI3K/AKT/mTOR pathway often results in apoptosis resistance. Using a panel of 20 human KRAS-mutant NSCLC (non-small cell lung cancer) cell lines Hata and collaborators show that most human KRAS-mutant cell lines fail to undergo marked apoptosis in response to AZD6244 (Selumetinib, a potent, selective, and ATP-uncompetitive inhibitor of MEK1/2 kinases) [107] in combination with GDC-0941 (an orally bioavailable inhibitor of class I PI3K) [108], thus suggesting that failure to induce apoptosis may limit the efficacy of combined MEK and PI3K inhibition for KRAS-mutant NSCLCs. This differential apoptotic response induced by MEKi/PI3Ki is not simply explained by variable inhibition of RAS effector pathways but results from differential ability of the MEK and PI3K pathways to modulate the BCL-2 family of apoptotic regulatory proteins [109]. Another recent study reveals that Bcl-xL upregulation is an important mechanism of apoptosis resistance in mutant KRAS cells. Concurrent induction of pro-apoptotic Noxa/Bik and antagonism of Bcl-xL have been shown to synergistically interact to overcome KRAS-mediated apoptosis resistance [110]. These findings highlight a promising therapeutic strategy to overcome apoptosis resistance in KRAS-mutant colorectal cancer cells. Moreover, Corcoran and collaborators identified, by a pooled shRNA-drug screen, a synthetic, lethal interaction of combined Bcl-xL and MEK inhibition to promote tumor regressions in KRAS mutant cancer models [111]. Therefore, a dual-targeted or multitargeted strategy may be more efficient to overcome the resistance due to cancer genetic background.

Oncosuppressor p53 and apoptosis

The tumor suppressor p53 is a transcription factor that, upon DNA damage, is activated to induce sequence-specific target genes involved in either cancer cell growth arrest or apoptosis [112]. Activation of wild-type (wt) p53 occurs in response to genotoxic stress essentially through posttranslational modifications, such as acetylation and phosphorylation, resulting in protein stabilization (by escape from proteasome-mediated degradation) and nuclear localization leading to binding to sequence-specific promoters of target genes as final outcome of its function as transcription factor [113]. The induction of apoptosis by p53 in response to cellular stress is its most conserved function and is crucial for p53 tumor suppression [114]. The apoptotic activation of p53 is central not only for preventing tumor transformation but also for efficient response to therapies aiming at tumor eradication. In response to cellular stress p53 regulates molecules involved in both the death receptor (extrinsic) and mitochondria-dependent (intrinsic) apoptotic pathways [115]. In response to multiple chemotherapeutic drugs two pro-apoptotic members of the TNFR superfamily, Fas/Apo1 and Killer/DR5, are regulated in a p53-dependent manner [116,117]. In addition to stimulating Fas transcription, activated p53 may enhance levels of Fas at the cell surface promoting trafficking of the Fas receptor from the Golgi [118]. Another membrane-bound protein that was identified as a p53 target gene is p53 apoptosis effector related PMP-22 (PERP), although the precise mechanism by which its induction occurs has not being fully elucidated [119] (Figure 6). Regarding the apoptotic function of the intrinsic pathway, p53 seems to play a pivotal role because it modulates both pro-survival and pro-apoptotic Bcl-2 family members. Indeed, a key subset of the Bcl-2 family genes are p53 targets, including *Bax*, *Noxa*, *PUMA* and *Bid* [120-122] (Figure 6). *PUMA* gene is extremely effective in inducing apoptotic cell death within few hours and, more importantly, knockout experiments in human colorectal cancer cells showed that *PUMA* is required for p53-induced apoptosis [123]. Moreover, p53 appears to promote the convergence of the intrinsic and extrinsic pathways through *Bid* regulation. Indeed, *Bid* gene has been found to be transcriptionally induced by p53 in response to γ-irradiation [124]. Interestingly, cellular chemo-sensitivity to the DNA-damaging agents doxorubicin and 5-fluorouracil appears to be critically dependent on

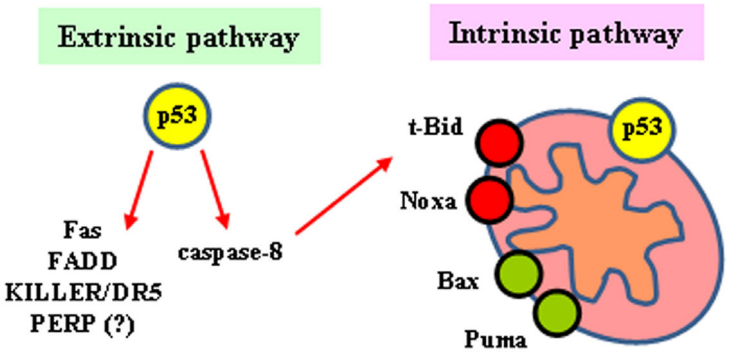

Figure 6. p53-mediated apoptosis. Role of p53 in both the extrinsic and the intrinsic pathway and their convergence through t-Bid.

the presence of wtp53 and Bid. Therefore, the induction of Bid by p53 helps to sensitize the cells to the toxic effects of chemotherapeutic drugs [124]. While the induction of some p53 target genes appears to be sufficient to initiate apoptosis, another class of p53 target genes (i.e., Apaf-1, caspase-6, and Bid) does not efficiently induce apoptosis per se but rather sensitizes cancer cells to the effects of chemotherapeutic agents, improving the apoptotic outcome [124-127]. Moreover, p53 also participates in apoptosis induction in a transcription-independent way by acting directly at mitochondria [128]; mechanistically, p53 interacts with anti-apoptotic Bcl-xL as well as pro-apoptotic Bcl-2 family proteins resulting in releasing of the pro-apoptotic effectors Bax/Bak that elicit cytochrome-*c* release and procaspase-3 activation [129].

Waking up the guardian: p53 as a druggable target

Because of its critical antitumor function, p53 is frequently targeted for inactivation and suffers disabling mutations or deletions in about 50% of all malignant tumors. The other half of human cancers express wild-type p53 protein that, however, can be inactivated by deregulation of regulatory proteins [130]. Stimulation of disabled p53 pathways has been suggested as a valuable anticancer strategy and, interestingly, activated wtp53 may target cancer cells though sparing the normal ones [131] which is an important concern in clinical studies. The p53 oncosuppressor protein is normally kept at low level because subject to negative regulation by MDM2-dependent proteasome degradation [132]; in response to genotoxic stress, however, p53 undergoes post-translational modifications that allow the protein to escape MDM2 control, accumulate, and become active [133]. The *mdm2* gene is amplified in a significant proportion of human tumor types, thereby contributing to tumor development by efficiently reducing the availability of a functional p53 protein [134]. The MDM2-negative regulation of p53 protein can be neutralized by specific protein modifications such as serine 46 (Ser46) phosphorylation [135], a key determinant in shifting the p53 pro-apoptotic transcription in response, for instance, to UV irradiation and chemotherapy [136,137]. In particular, p53-Ser46 phosphorylation by kinase HIPK2 is able to neutralize MDM2-mediated p53 inhibition rescuing p53 transcriptional activity of pro-apoptotic factors such as *p53AIP1*, *PIG3*, *Bax*, *Noxa*, *Puma* and *Killer/DR5* [138-142]. The interaction between p53 and MDM2 is a promising target in anticancer therapy [143]. To this aim, various peptidomimetic small molecules have been developed as protein-protein interaction blockers [144]. Among these is Nutlin-3, an imidazoline-based MDM2 antagonist that potentially inhibits the p53/MDM2 interaction though maintaining MDM2 E3 ligase activity [145]. The pharmacological action of Nutlin-3 is through both the transcription-dependent and -independent p53 apoptotic pathways [128,146,147]. MDM2 can also trigger, in response to low genotoxic damage, the downregulation of p53 apoptotic activator HIPK2 [148]. In agreement, the use of Nutlin-3 has been shown to mainly induce mitotic arrest rather than apoptosis [149]. Interestingly, co-treatment of cancer cells with zinc ion in the presence of Nutlin-3 can interfere with the interplay between HIPK2, p53 and MDM2 favoring HIPK2 stabilization and induction of p53 apoptotic activity through inhibition of MDM2 ligase activity [150]. In addition, p53 apoptotic activation can be achieved by zinc combination with

low-dose doxorubicin (ADR) that used alone does not achieve such effect; mechanistically, zinc supplementation reduces the p53 binding to MDM2, improving the low-dose drug-induced cytotoxic effect and cancer cell apoptosis [151]. Additionally, zinc ion restores the HIPK2/p53 apoptotic pathway that is inhibited by hypoxia [152]. Co-treatment with Nutlin-3 and Bcl-2 inhibitor ABT-737 has been shown to greatly enhance the sensitivity to apoptosis of cancer cells with high MDM2 levels [153], suggesting that the combined inhibition of MDM2 and Bcl-2 could be a multi-target-based anticancer strategy to trigger tumor death [154]. Some p53 activators as small-molecules MDM2 antagonist are in clinical trials [155] (https://clinicaltrials.gov). In contrast with the majority of the approaches that target the interaction between p53 and MDM2, a new method has been developed aimed at inhibiting the activity of the MDM2/MDM4 complexes by interfering with their heterodimerization [156]. The binding of the peptide mimicking the MDM4 C-terminus tail to MDM2 impairs MDM2-mediated p53 ubiquitination and activates p53-dependent transcription and oncosuppressive activities [156]. MDM4 (also known as HDM4, MDMX or HDMX) is a cytoplasmic protein with p53-activating function under DNA damage conditions. Particularly, MDM4 promotes mitochondrial localization of p53 phosphorylated at Ser46 through MDM4/HIPK2/p53 cytoplasmic assembly, uncovering coordinated repression of molecules with anti-apoptotic activity such as Bcl-2, release of cytochrome-*c* and apoptosis [157,158]. The existence of nuclear and cytoplasmic complexes able to stimulate the same p53 modification, that is $Ser46^{P}$, may indicate the presence of overlapping pathways to ensure the proper realization of a crucial process as the apoptosis. These findings highlight the potential therapeutic value of targeting the MDM2/MDM4 heterodimers for p53 apoptotic function.

Pharmacological reactivation of mutant (mut) p53 is an interesting field of research under continuous development aimed at designing new drugs. Some of them exploit the intrinsically unstable nature of mutp53 and therefore the possibility to stabilize the wild-type conformation thus restoring wild-type function and tumor response to therapies. Numerous findings about this subject have been shown and summarized in different reviews [159-161].

MicroRNA and apoptosis

MicroRNAs (miRNAs) are highly conserved, small noncoding RNA molecules, which post-transcriptionally regulate gene expression via inhibition of mRNA translation or inducing degradation of target mRNAs [162]. They are key regulators of many cell processes often deregulated in cancer, including apoptosis. Indeed, it is becoming clear that miRNAs might act as both anti-apoptotic and pro-apoptotic by directly targeting, respectively, pro- or anti-apoptotic mRNAs or their positive regulators [163]. The currently known apoptosis-regulating miRNAs list is expected to expand quickly and hopefully also their therapeutic use; therefore, we just highlight here some miRNAs involved in apoptosis regulation. Among the microRNAs involved in regulating the extrinsic apoptotic pathway, miR-20a, miR-21, miR-196b and miR-590 were reported as potential modulator of Fas/FasL system in different cancer types [164-167], while MiR-34a, miR-181c and miR-187 were shown to directly target TNF-α mRNA [168-170]. Among the microRNAs involved in regulating the intrinsic pathway there are the let-7 family, miR-15a, miR-16-1, miR-204, and miR-608, just to mention a few. The Let-7 family is highly conserved in sequence across animal species and is one of the first identified miRNA families. Let-7 miRNAs have been shown to negatively regulate Bcl-xL expression in human hepatocellular carcinomas and induce apoptosis in cooperation with anti-cancer drug targeting Mcl-1 [171]. Bcl-2 mRNA may be targeted by miR-204 with consequent increase in cells responsiveness to both 5-fluorouracil and oxaliplatin treatments and therefore to apoptotic cell death [172]. MiR-608 has been reported to target Bcl-xL in chordoma malignancy and lung cancer [173]. Notably, numerous miRNAs are also transcriptionally modulated by wtp53 [174] and among them is miR-34a [175,176], a member of the MiR-34 family implicated in cell death/survival signaling. MiR-34a is associated with G1 cell cycle arrest, senescence and apoptosis, thereby possessing a tumor suppressor activity. Deregulation of MiR-34a has been reported in several types of cancers [175,176]. Mutant (mut) p53 was also found to play a role in the regulation of miRNA processing. Garibaldi and collaborators demonstrate that mutp53 proteins modulate the biogenesis of several miRNAs in cancer cells directly interfering with Drosha-p72 association and promoting cell survival and cell migration [177]. They demonstrate a global impact of mutp53 on miRNA biogenesis and suggest that miRNAs are downregulated by mutp53 in order to inactivate tumor suppressive pathways. Of note they found that the endogenous wtp53 has an opposite effect on the expression of mutp53 repressed miRNAs on colon cancer cell lines confirming the contribution of mutp53 gain of oncogenic function (GOF) on miRNA repression [177]. Additional studies on a large scale would help in identifying the entire repertoire of miRNAs negatively downregulated by different mutp53 in different tumor models. According to the authors, the

characterization of the entire gene-regulatory networks governed by mutp53-miRNA cross-talks will offer a molecular basis for diagnostic and therapeutic strategies based on miRNA biology. In the meanwhile, developing strategies to block mutp53 GOF may have clinical impact in cancer treatment.

Delivery of miRNAs as synthetic miRNA mimics or antagomirs has emerged as a promising approach to treat cancer. Although different miRNAs are currently in the preclinical stage and ready to enter Phase 1 clinical trials, to date, only two miRNA therapeutics are registered for the treatment of cancers [https://clinicaltrials.gov]. The first therapeutic trial began in 2013 and is a Phase I, open-label, multicenter, dose-escalation study to investigate the safety, pharmacokinetics and pharmacodynamics of MRX34 in patients with unresectable primary liver cancer or advanced/metastatic cancer with or without liver involvement or in patients with hematologic malignancies (Mirna Therapeutics). MRX34 is based on the formulation of miR-34 mimic and the liposomal delivery technology SMARTICLES (Marina Biotech). The second one, began in early 2015, and is an early stage clinical trial of a new therapeutical approach for selected patients with malignant pleural mesothelioma or non-small cell lung cancer. The trial aims to test optimal dose of TargomiRs, an experimental medication consisting of three components, that is, miR-16-based microRNA mimic, a nanoparticle drug delivery system using nonliving bacterial minicells, and an anti-epidermal growth factor receptor antibody as a targeting moiety. The trial is being carried out in three different hospitals in Australia and the study is expected to be completed in mid 2016.

Concluding remarks

Intensive investigation in the last decades on the molecular mechanisms of apoptosis in cancer cells has led to the identification of the several molecules involved in both the intrinsic and the extrinsic apoptotic pathways. This is underscored by the extensive literature that those studies have produced in the last years. Those findings also reported how the many different alterations of key players of the apoptotic mechanisms are responsible of evasion from apoptosis and therefore of tumor development and resistance to therapies. For that reason, evasion from apoptosis is an hallmark of cancer and apoptotic proteins are interesting therapeutic targets. Therefore, this insight into the deregulation of apoptosis has focused the research attention towards the development of apoptosis-reactivating strategies, to be used in the treatment of various types of cancer, that hold great promise for the benefit of patients, although the mechanisms defining their mode of action still need to be unveiled, as recently highlighted [178]. Some molecules or therapeutic strategies are in preclinical trial, others are already in clinical trials, though underscoring the usefulness of such discoveries.

However, the study of apoptosis still presents challenges that should be addressed in future studies. They include, for instance, the study of 3-D cellular models, since most of the findings have been so far produced in 2-D cell culture systems. Knowing that the tumor is a three-dimensional entity and that the environment plays a big role in the cross-talk with cancer cells, it is likely that more physiological studying approach for the manipulation of the apoptotic machinery might give us novel insight into the mechanisms of tumor development and response to therapies. Moreover, additional studies on the development of drugs aiming at targeting, for instance, IAP proteins or mutp53 should take in consideration also the in vivo toxicity and the fact that they should selectively induce apoptosis in malignant and not in normal cells. In conclusion, there is little doubt that drugs that target the deregulated apoptotic pathways could have wide application in the treatment of cancer. The intense effort devoted lately to target the apoptotic pathway is encouraging and supportive for the development of new approaches to drug discovery and therapy.

Funding

This work was supported by AIRC Grant (IG 2015 Id.16742) to GDO.

Conflict of interest statement

The authors declare no conflict of interest.

REFERENCES

1. Fuchs Y, Steller H. Programmed cell death in animal development and disease. Cell. 2011; 147; 742–758.

2. Wong RSY. Apoptosis in cancer: from pathogenesis to treatment. JECCR. 2011; 30:87.

3. Plati J, Bucur O, Khosravi-Far R. Dysregulation of apoptotic signaling in cancer. Molecular mechanisms and therapeutic opportunities. J Cell Biochem. 2008; 104:1124-1149.

4. Fulda S. Tumor resistance to apoptosis. Int J Cancer. 2009; 124:515-515.

5. Hanahan D, Weinberg RA. Hallmarks of cancer: The next generation. Cell. 2011; 144:646-674.

6. Gimenez-Bonafe P, Tortosa A, Perez-Tomas R. Overcoming drug resistance by enhancing apoptosis of tumor cells. Curr Cancer Drug Targ. 2009; 9:320-340.

7. Fulda S. Targeting apoptosis for anticancer therapy. Sem Cancer Biol. 2015; 31:84-88.
8. Hacker G. The morphology of apoptosis. Cell Tissue Res. 2000; 301:5-17.
9. Saraste A, Pulkki K. Morphologic and biochemical hallmarks of apoptosis. Cardiovasc Res. 2000; 45:528-537.
10. Hengartner MO. Apoptosis: corralling the corpses. Cell. 2000; 104:325-328.
11. Kroemer G, El-Deiry WS, Golstein P, Peter ME, Vaux D, Vandenabeele P, Zhivotovsky B, Blagosklonny MV, Malorni W, Knight RA, Piacentini M, Nagata S, Melino G. Classification of cell death: recommendations of the Nomenclature Committee on Cell Death. Cell Death Diff. 2005; 12:1463-1467.
12. Bucur O, Nat R, Cretoiu D, Popescu LM. Phagocytosis of apoptotic cells by microglia in vitro. J Cell Mol Med. 2001; 5:438-441.
13. Li J, Yuan J. Caspases in apoptosis and beyond. Oncogene. 2008; 27:6194-6206.
14. Thomberry NA, Laxebnik Y. Caspases: enemies within. Science 1998; 281:1312-1316.
15. Nicholson DW. Caspase structure, proteolytic substrates, and function during apoptotic cell death. Cell Death Diff. 1999; 6:1028-1042.
16. Stennicke HR, Salvesen GS. Caspases - controlling intracellular signals by protease zymogen activation- Biochim Biophys Acta-Port Struct Mol Enzimol. 2000; 1477:299-306.
17. Degterev A, Boyce M, Yuan JY. A decade of caspases. Oncogene. 2003; 22:8543-8567.
18. Pistritto G, Jost M, Srinivasula SM, Baffa R, Poyet JL, Kari C, Lazebnik Y, Rodeck U, Alnemri ES. Expression and transcriptional regulation of caspase-14 in simple and complex epithelia. Cell Death Diff. 2002; 9:995-1006.
19. Pistritto G, Papaleo V, Sanchez P, Ceci C, Barbaccia ML. Divergent modulation of neuronal differentiation by caspase-2 and-9. PLoS ONE. 2012; 7:e36002.
20. Shalini S, Dorstyn L, Dawar S and Kumar S. Old, new and emerging functions of caspases. Cell Death Diff. 2015; 22: 526-39.
21. Guicciardi ME, Gores, Gregory J. Life and death by death receptors FASEB J. 2009; 23:1625-1637.
22. Fulda S, Debatin KM. Death receptor signaling in cancer therapy. Curr Med Chem Anticancer Agents. 2003; 3: 253-262.
23. Boatright KM, Salvesen GS. Mechanisms of caspase activation. Curr Opin Cell Biol. 2003; 6:725-731.
24. Green DR, Kroemer G. The pathophysiology of mitochondrial cell death. Science 2004; 305:626-629.
25. Kroemer G, Galluzzi L, Brenner C: Mitochondrial membrane permeabilisation in cell death. Physiol Rev. 2007; 87:99-163.
26. Danial NN, Korsmeyer SJ. Cell death: critical control points. Cell. 2004; 116:205-219.
27. Slee EA, Adrain C, Martin SJ. Serial killers: ordering caspase activation events in apoptosis. Cell Death Diff. 1999; 6:1067-1074.
28. Kuribayashi K, Mayes PA, El-Dery WS. What are caspases 3 and 7 doing upstream of the mitochondria? Cancer Biol Ther. 2006; 5:763-765.
29. Giam M, Huang DC, Bouillet P. BH3-only proteins and their roles in programmed cell death. Oncogene. 2008; 27:S128-36.
30. Adams JM, Cory S. The Bcl-2 apoptotic switch in cancer development and therapy. Oncogene. 2007; 26:1324-1337.
31. Danial NN. BCL-2 family proteins: Critical checkpoints of apoptotic cell death. Clin Cancer Res. 2007; 13:7254-7263.
32. Lomonosova E and G Chinnadurai. BH3-only proteins in apoptosis and beyond: an overview. Oncogene. 2009; 27:S2–S19.
33. Youle RJ, Strasser A. The BCL-2 protein family: opposing activities that mediate cell death. Nat Rev Mol Cell Biol. 2008; 9: 47-59.
34. Dewson G, Kratina T, Sim HW, Puthalakath H, Adams JM, Colman PM, Kluck RM. To trigger apoptosis, Bak exposes its BH3 domain and homodimerizes via BH3 : Groove interactions. Mol Cell. 2008; 30:369-380.
35. Bleicken St, Classen M, Padmavathi PVL, Ishikawa T, Zeth K, Steinhoff HJ, Bordignon E. Molecular details of Bax activation, oligomerization, and membrane insertion. J Biol Chem. 2010; 285: 6636-6647.
36. Gavathiotis E, Suzuki M, Davis ML, Pitter K, Bird GH, Katz SG, Tu HC, Kim H, Cheng EH, Tjandra N, Walensky LD. BAX activation is initiated at a novel interaction site. Nature. 2008; 455:1076-U6
37. Brunelle JK, Letai A. Control of mitochondrial apoptosis by the Bcl-2 family. J Cell Sci. 2009; 122:437-441.
38. Oakes SA, Scorrano L, Opferman JT, Bassik MC, Nishino M, Pozzan T, Korsmeyer SJ. Proapoptotic BAX and BAK regulate the type 1 inositol trisphosphate receptor and calcium leak from the endoplasmic reticulum. Proc Natl Acad Sci USA. 2005; 102:105-110.
39. Distelhorst CW, Bootman MD. Bcl-2 interaction with the inositol 1,4,5-trisphosphate receptor: Role in Ca2+ signaling and disease. Cell Calcium. 2011; 50:234-241.
40. Hegde R, Srinivasula SM, Zhang Z, Wassell R, Mukattash R, Cilenti L, DuBois G, Lazebnik Y, Zervos AS, Fernandes-Alnemri T, Alnemri ES. Identification of Omi/HtrA2 as a mitochondrial apoptotic serine protease that disrupts inhibitor of apoptosis protein-caspase interaction. J Biol Chem. 2002; 277: 432-438.
41. Pop C, Salvesen GS. Human caspases: activation, specificity, and regulation. J Biol Chem. 2009; 284:21777-21781.
42. Salvesen GS and Duckett CS. IAP proteins: Blocking the road to death's door. Nat Rev Mol Cell Biol. 2002; 3:401:410.
43. Berthelet J, Dubrez L. Regulation of apoptosis by inhibitors of apoptosis (IAPs). Cells. 2013; 2:163-87.
44. LaCasse EC, Mahoney DJ, Cheung HH, Plenchette S, Baird S, Korneluk RG: IAP-targeted therapies for cancer. Oncogene. 2008; 27:6252-6275.
45. Mace PD, Shirley S, Day CL. Assembling the building blocks: structure and function of inhibitor of apoptosis proteins. Cell Death Differ. 2010; 17:46-53.
46. Müschen M, Beckmann MW. CD95 ligand expression as a criterion of malignant transformation in breast cancer J Pathol. 2000; 191: 468-470.
47. Tourneur L, Buzyn A, Chiocchia G. FADD adaptor in cancer. Med Immunol. 2005; 4:1.
48. Müschen M, Rajewsky K, Krönke M, Küppers R. The origin of CD95-gene mutations in B-cell lymphoma. Trends Immunol. 2002; 23:75-80.
49. Tourneur L, Delluc S, Levy V, Valesi F, Radford-Weiss I, Legrand O, Vargftig J, Boix C, Macintyre EA, Varet B, Chiocchia G, Buzyn A. Absence or low expression of fas-associated protein with death domain in acute myeloid leukemia cells predicts resistance to chemotherapy and poor outcome. Cancer Res. 2004; 64: 8101-8108.

50. Teitz T, Wei T, Valentine MB, Vanin EF, Grenet J, Valentine VA, Behm FG, Look AT, Lahti JM, Kidd VJ. Caspase 8 is deleted or silenced preferentially in childhood neuroblastomas with amplification of MYCN. Nat Med. 2000; 6: 529-535.

51. Shivapurkar N, Toyooka S, Eby MT, Huang CX, Sathyanarayana UG, Cunningham HT, Reddy JL, Brambilla E, Takahashi T, Minna JD, Chaudhary PM, Gazdar AF. Differential inactivation of caspase-8 in lung cancers. Cancer Biol Ther. 2002; 1: 65-69.

52. Zuzak TJ, Steinhoff DF, Sutton LN, Phillips PC, Eggert A, Grotzer MA. Loss of caspase-8 mRNA expression is common in childhood primitive neuroectodermal brain tumor/medulloblastoma. Eur J Cancer. 2002; 38: 83-91.

53. Irmler M, Thome M, Hahne M, Schneider P, Hofmann K, Steiner V, Bodmer JL, Schröter M, Burns K, Mattmann C, Rimoldi D, French LE, Tschopp J. Inhibition of death receptor signals by cellular FLIP. Nature. 1997; 388:190-195.

54. Bagnoli M, Canevari S, Mezzanzanica D. Cellular FLICE-inhibitory protein (c-FLIP) signalling: A key regulator of receptor-mediated apoptosis in physiologic context and in cancer. Int J Biochem Cell Biol. 2010; 42:210–213.

55. Shirley S, Micheau O. Targeting c-FLIP in cancer. Cancer Lett. 2013; 332:141-150.

56. Gandour-Edwards R, Mack PC, Devere-White RW, Gumerlock PH. Abnormalities of apoptotic and cell cycle regulatory proteins in distinct histopathologic components of benign prostatic hyperplasia. Prost Cancer Prost Dis. 2004; 7:321-326.

57. Abramson JS, Shipp MA. Advances in the biology and therapy of diffuse large B-cell lymphoma: moving toward a molecularly targeted approach. Blood. 2005; 106:1164-1174.

58. Watanabe A, Yasuhira S, Inoue T, Kasai S, Shibazaki M, Takahashi K, Akasaka T, Masuda T, Maesawa C. BCL2 and BCLxL are key determinants of resistance to antitubulin chemotherapeutics in melanoma cells. Exp Dermatol. 2013; 22: 518-523.

59. Raffo AJ, Perlman H, Chen MW, Day ML, Streitman JS, Buttyan R. Overexpression of bcl-2 protects prostate cancer cells from apoptosis in vitro and confers resistance to androgen depletion in vivo. Cancer Res. 1995; 55:4438.

60. Fulda S, Meyer E, Debatin KM. Inhibition of TRAIL-induced apoptosis by Bcl-2 overexpression. Oncogene. 2000; 21:2283-2294.

61. Foreman KE, Wrone-Smith T, Boise LH, Thompson CB, Polverini PJ, Simonian PL, Nunez G, Nickoloff BJ. Kaposi's sarcoma tumor cells preferentially express Bcl-xL Am J Pathol. 1996; 149: 795-803.

62. Krajewska M, Moss SF, Krajewski S, Song K, Holt PR, Reed JC. Elevated expression of Bcl-X and reduced Bak in primary colorectal adenocarcinomas. Cancer Res. 1996; 56: 2422-2427.

63. Minn AJ, Rudin CM, Boise LH, Thompson CB. Expression of Bcl-xL can confer a multidrug resistance phenotype. Blood. 1995; 86:1903-1910.

64. Han JY, Hong EK, Choi BG, Park JN, Kim KW, Kang JH, Jin JY, Park SY, Hong YS, Lee KS Death receptor 5 and Bcl-2 protein expression as predictors of tumor response to gemcitabine and cisplatin in patients with advanced non-small-cell lung cancers. Med Oncol. 2003; 20:355-362.

65. Erovic BM, Pelzmann M, Grasl MCh, Pammer J, Kornek G, Brannath W, Selzer E, Thurnher D. Mcl-1, vascular endothelial growth factor-R2, and 14-3-3sigma expression might predict primary response against radiotherapy and chemotherapy in patients with locally advanced squamous cell carcinomas of the head and neck. Clin Cancer Res. 2005; 11:8632-8636.

66. Williams J, Lucas PC, Griffith KA, Choi M, Fogoros S, Hu YY, Liu JR. Expression of Bcl-xL in ovarian carcinoma is associated with chemoresistance and recurrent disease. Gynecol Oncol. 2005; 96: 287-295.

67. Michaud WA, Nichols AC, Mroz EA, Faquin WC, Clark JR, Begum S, Westra WH, Wada H, Busse PM, Ellisen LW, Rocco JW. Bcl-2 blocks cisplatin-induced apoptosis and predicts poor outcome following chemoradiation treatment in advanced oropharyngeal squamous cell carcinoma. Clin Cancer Res. 2009; 15: 1645-1654.

68. Yang D, Chen MB, Wang LQ, Yang L, Liu CY, Lu PH. Bcl-2 expression predicts sensitivity to chemotherapy in breast cancer: a systematic review and meta-analysis. JECCR 2013; 32:105.

69. Miquel C, Borrini F, Grandjouan S, Aupérin A, Viguier J, Velasco V, Duvillard P, Praz F, Sabourin JC. Role of bax mutations in apoptosis in colorectal cancers with microsatellite instability. Am J Clin Pathol. 2005; 23:562-570.

70. Pepper C, Hoy T, Bentley DP. Bcl-2/Bax ratios in chronic lymphocytic leukaemia and their correlation with in vitro apoptosis and clinical resistance. Br J Cancer. 1997; 76:935-938.

71. Soengas MS, Capodieci P, Polsky D, Mora J, Esteller M, Opitz-Araya X, McCombie R, Herman JG, Gerald WL, Lazebnik YA, Cordón-Cardó C, Lowe SW. Inactivation of the apoptosis effector Apaf-1 in malignant melanoma. Nature. 2001; 409:207-211.

72. Baldi A, Santini D, Russo P, Catricala' C, Amantea A, Picardo M, Tatangelo F, Botti G, Dragonetti E, Murace R, Tonini G, Natali PG, Baldi F, Paggi MG. Analysis of APAF-1 expression in human cutaneous melanoma progression. Exp Dermatol. 2004; 13:93-97.

73. Schimmer AD. Inhibitor of apoptosis proteins: translating basic knowledge into clinical practice. Cancer Res. 2004; 64: 7183-7190.

74. Fulda S. Inhibitor of apoptosis proteins in hematological malignancies. Leukemia. 2009; 23:467-476.

75. Fulda S, Debatin KM. IFNgamma sensitizes for apoptosis by upregulating caspase-8 expression through the Stat1 pathway. Oncogene. 2002; 21:2295-2308.

76. Subramanian K, Hirpara JL, Tucker-Kellogg L, Tucker-Kellogg G, Pervaiz S. FLIP: A flop for execution signals. Cancer Lett. 2013; 332:151-155.

77. Almasan A, Ashkenazi A. Apo2L/TRAIL: apoptosis signaling, biology, and potential for cancer therapy. Cytok Growth Fact Rev. 2003; 14:337-348.

78. Amarante-Mendes GP, Griffith TS. Therapeutic applications of TRAIL receptor agonists in cancer and beyond. Pharmacol Ther. 2015; 155:117-131.

79. Bucur O, Gaidos G, Yatawara A, Pennarum B, Rupasinghe C, Roux J, Andrei S, Guo B, Panaititu A, Pellegrini M, Mierke DF, Khosravi-Far R. A novel caspase 8 selective small molecule potentiates TRAIL-induced cell death. Sci Rep. 2015; 5:9893.

80. Ashkenazi A, Pai RC, Fong S, Leung S, Lawrence DA, Marsters SA, Blackie C, Chang L, McMurtrey AE, Hebert A, DeForge L, Koumenis IL, Lewis D, et al. Safety and antitumor activity of recombinant soluble Apo2 ligand. J Clin Invest. 1999; 104:155-162.

81. LeBlanc H, Ashkenazi A. Apo2/TRAIL and its death and decoy receptors. Cell Death Diff. 2003; 10:66-75.

82. Kang MH, Reynolds CP. Bcl-2 inhibitors: targeting mitochondrial apoptotic pathways in cancer therapy. Clin Cancer Res. 2009; 15:1126-1132.

83. Sonpavde G, Matveev V, Burke JM, Caton JR, Fleming MT, Hutson TE, Galsky MD, Berry WR, Karlov P, Holmlund JT, Wood BA, Brookes M, Leopold L. Randomized phase II trial of docetaxel plus prednisone in combination with placebo or AT-101, an oral small molecule Bcl-2 family antagonist, as first-line therapy for metastatic castration-resistant prostate cancer. Annal Oncol. 2012; 23:1803-1808.

84. Stein MN, Hussain M, Stadler WM, Liu G, Tereshchenko IV, Goodin S, Jeyamohan C, Kaufman HL, Mehnert J, Di Paola RS. A Phase II study of AT-101 to overcome Bcl-2-mediated resistance to androgen deprivation therapy in patients with newly diagnosed castration-sensitive metastatic prostate cancer. Clin Genitour Cancer. 2016; 14:22-27.

85. Souers AJ, Leverson JD, Boghaert ER, Ackler SL, Catron ND, Chen J, Dayton BD, Ding H, Enschede SH, Fairbrother WJ, Huang DCS, Hymowitz SG, Jin S, et al. ABT-199, a potent and selective BCL-2 inhibitor, achieves antitumor activity while sparing platelets. Nat Med. 2013; 19:202-208.

86. Oltersdorf T, Elmore SW, Shoemaker AR, Armstrong RC, Augeri DJ, Belli BA, Bruncko M, Deckwerth TL, Dinges J, Hajduk PJ, Joseph MK, Kitada S, Korsmeyer SJ, et al. An inhibitor of Bcl-2 family proteins induces regression of solid tumors. Nature. 2005; 435:677-681.

87. Tse C, Shoemaker AR, Adickes J, Anderson MG, Chen J, Jin S, Johnson EF, Marsh KC, Mitten MJ, Nimmer P, Roberts L, Tahir SK, Mao Y, Yang X, Zhang HC, Fesik S, Rosenberg SH, Elmore SW. ABT-263: a potent and orally bioavailable Bcl-2 family inhibitor. Cancer Res. 2008; 68:3421-3428.

88. Roberts AW, Seymour JF, Brown JR, Wierda WG, Kipps TJ, Khaw SL, Carney DA, He SZ, Huang DCS, Xiong H, Cui Y, Busman TA, McKeegan EM, et al. Substantial susceptibility of chronic lymphocytic leukemia to BCL2 inhibition: results of a phase I study of navitoclax in patients with relapsed or refractory disease. J Clin Oncol. 2012; 30:488-496.

89. Chiappori A, Williams C, Northfelt DW, Adams JW, Malik S, Edelman MJ, Rosen P, Van Echo DA, Berger MS, Haura EB. Obatoclax mesylate, a pan-bcl-2 inhibitor, in combination with docetaxel in a phase 1/2 trial in relapsed non-small-cell lung cancer. J Thorac Oncol. 2014; 9:121-125.

90. Theile D, Allendorf D, Koehler BC, Jassowicz A, Weiss J. Obatoclax as a perpetrator in drug-drug interactions and its efficacy in multidrug resistance cell lines. J Pharm Pharmacol. 2015; 67:1575-1584.

91. Zeitlin BD, Joo E, Dong Z, Warner K, Wang G, Nikolovska-Coleska Z, Wang S, Nor JE. Antiangiogenic effect of TW37, a small-molecule inhibitor of Bcl-2. Cancer Res. 2006; 66:8698-8706.

92. Tao ZF, Hasvold L, Wang L, Wang X, Petros AM, Park CH, et al. Discovery of a potent and selective Bcl-xL inhibitor with in vivo activity. ACS Med Chem Lett. 2014; 5:1088-1093.

93. Bruncko M, Wang L, Sheppard GS, Phillips DC, Tahir SK, Xue J, et al. Structure-guided design of a series of MCL-1 inhibitors with high affinity and selectivity. J Med Chem. 2015; 58:2180–2194.

94. Vervloessem T, La Rovere R, Bultynck G. Antagonizing Bcl-2's BH4 domain in cancer. Aging (Albany NY). 2015; 7:748-749. doi: 10.18632/aging.100828.

95. Trisciuoglio D, Gabellini C, Desideri M, Ragazzoni Y, De Luca T, Ziparo E, Del Bufalo D. Involvement of BH4 domain of bcl-2 in the regulation of HIF-1-mediated VEGF expression in hypoxic tumor cells. Cell Death Diff. 2011; 18:1024-1035.

96. Trisciuoglio D, De Luca T, Desideri M, Passeri D, Gabellini C, Scarpino S, Liang C, Orlandi A, Del Bufalo D. Removal of the BH4 domain from Bcl-2 protein triggers an autophagic process that impairs tumor growth. Neoplasia. 2013; 15:315-327.

97. Gabellini C, De Luca T, Trisciuoglio D, Desideri M, Di Martile M, Passeri D, Candiloro A, Biffoni M, Rizzo MG, Orlandi A, Del Bufalo D. BH4 domain of bcl-2 protein is required for its proangiogenic function under hypoxic condition. Carcinogenesis. 2013; 34:2558-2567.

98. Han B, Park D, Li R, Xie M, Owonikoko T, Zhang G, Sica GL, Ding C, Zhou J, Magis AT, Chen ZG, Shin DM, Ramalingam S, Khuri FR, Curran WJ, Deng X. Small-molecule Bcl-2 BH4 antagonist for lung cancer therapy. Cancer Cell. 2015; 27:852-863.

99. Dexheimer TS, Sun D, Hurley LH. Deconvoluting the structural and drug-recognition complexity of the G-quadruplex-forming region upstream of the bcl-2 P1 promoter. J Am Chem Soc. 2006; 128:5404-5415.

100. Lin J, Hou JQ, Xiang HD, Yan YY, Gu YC, Tan JH, Li D, Gu LQ, Ou TM, Huang ZS. Stabilization of G-quadruplex DNA by C-5-methyl-cytosine in bcl-2 promoter:implications for epigenetic regulation. Biochem Biophys Res Commun. 2013; 433:368-373.

101. Sun H, Xiang J, Shi Y, Yang Q, Guan A, Li Q, Yu L, Shang Q, Zhang H, Tang Y,Xu G. A newly identified G-quadruplex as a potential target regulating Bcl-2 expression. Biochim Biophys Acta. 2014; 1840:3052-3057.

102. Le Pen J, Laurent M, Sarosiek K, Vuillier C, Gautier F, Montessuit S, Martinou JC, Letaï A, Braun F, Juin PP. Constitutive p53 heightens mitochondrial apoptotic priming and favors cell death induction by BH3 mimetic inhibitors of BCL-xL. Cell Death Dis. 2016; 7:e2083.

103. Sasaki H, Sheng Y, Kotsuji F, Tsang BK. Down-regulation of X-linked inhibitor of apoptosis protein induces apoptosis in chemoresistant human ovarian cancer cells. Cancer Res. 2000; 60: 5659-5666.

104. Holcik M, Yeh C, Korneluk RG, Chow T. Translational upregulation of X-linked inhibitor of apoptosis (XIAP) increases resistance to radiation induced cell death. Oncogene. 2000; 19: 4174-4177.

105. Amantana A, London CA, Iversen PL, Devi GR. X-linked inhibitor of apoptosis protein inhibition induces apoptosis and enhances chemotherapy sensitivity in human prostate cancer cells. Mol Cancer Ther. 2004; 3:699-707.

106. Fulda S. Promises and challenges of Smac mimetics as cancer therapeutics. Clin Cancer Res. 2015; 21:5030-5036.

107. Davies BR, Logie A, McKay JS, Martin P, Steele S, Jenkins R, Cockerill M, Cartlidge S, Smith PD. AZD6244 (ARRY-142886), a potent inhibitor of mitogen activated protein kinase/extracellular signal-regulated kinase kinase 1/2 kinases: mechanism of action in vivo, pharmacokinetic/pharmacodynamic relationship, and potential for combination in preclinical models. Mol Cancer Ther. 2007; 6:2209-2219.

108. Folkes AJ, Ahmadi K, Alderton WK, Alix S, Baker SJ, Box G, Chuckowree IS, Clarke PA, Depledge P, Eccles SA, Friedman LS, Hayes A, Hancox TC, et al. The identification of 2-(1H-indazol-4-yl)-6-(4-methanesulfonyl-piperazin-1-ylmethyl)-4-morpholin-4-yl-thieno[3,2-d] pyrimidine (GDC-0941) as a potent, selective, orally bioavailable inhibitor of class I PI3 kinase for the treatment of cancer. J Med Chem. 2008; 51:5522–5532.

109. Hata AN, Yeo A, Faber AC, Lifshits E, Chen Z, Cheng KA, Walton Z, Sarosiek KA, Letai A, Heist RS, Mino-Kenudson M,

Wong KK, Engelman JA. Failure to induce apoptosis via BCL-2 family proteins underlies lack of efficacy of combined MEK and PI3K inhibitors for KRAS-mutant lung cancers. Cancer Res. 2014; 74:3146-3156.

110. Okamoto K, Zaanan A, Kawakami H, Huang S, Sinicrope FA. Reversal of mutant KRAS-mediated apoptosis resistance by concurrent Noxa/Bik induction and Bcl-2/Bcl-xL antagonism in colon cancer cells. Mol Cancer Res. 2015;13:659-669.

111. Corcoran RB, Cheng KA, Hata AN, Faber AC, Ebi H, Coffee EM, Greninger P, Brown RD, Godfrey JT, Cohoon TJ, Song Y, Lifshits E, Hung KE, et al. Synthetic lethal interaction of combined BCL-XL and MEK inhibition promotes tumor regressions in KRAS mutant cancer models. Cancer Cell. 2013; 23:121-128.

112. Vousden KH, Lane DP. P53 in health and disease. Nat Rev Mol Cell Biol. 2007;8:275–283.

113. Brooks CL, Gu W. Ubiquitination, phosphorylation and acetylation: the molecular basis for p53 regulation. Curr Opin Cell Biol. 2003; 15:164-171.

114. Haupt S, Berger M, Goldberg Z, Haupt Y. Apoptosis – the p53 network. J Cell Sci. 2003; 116:4077-4085.

115. Vousden KH. P53: Death Star. Cell. 2000; 103:691-694.

116. Wu GS, Burns TF, McDonald III ER, Jiang W, Meng R, Krantz ID, Kao G, Gan DD, Zhou JY, Muschel R, Hamilton SR, Spinner NB, Matkowitz S, et al. KILLER/DR5 is a DNA damage-induced p53-regulated death receptor gene. Nat Genet. 1997; 17:141-143.

117. Muller M, Wilder S, Bannasch D, Israeli D, Lehlbach K, Li-Weber M, Friedman SL, Galle PR, Stremmel W, Oren M, Krammer PH. P53 activates the CD95 (APO-1/Fas) gene in response to DNA damage by anticancer drugs. J Exp Med. 1998; 188:2033-2045.

118. Bennet M, Macdonald K, Chan SW, Luzio JP, Simari R, Weissberg. Cell surface trafficking of Fas: a rapid mechanisms of p53-mediated apoptosis. Science. 1998; 282:290-293.

119. Attardi LD, Reczek EE, Cosmas C, Demicco EG, McCurrach ME, Lowe SW, Jacks T. PERP, an apoptosi-associated target of p53, is a novel member of the PMP-22/gas3 family. Genes Dev. 2000; 14:704-718.

120. Oda E, Ohki R, Murasawa H, Nemoto J, Shibue T, Yamashita T, Tokino T, Taniguchi T, Tanaka N. Noxa, a BH3-only member of the Bcl-2 family and candidate mediator of p53-induced apoptosis. Science. 2000; 288:1053-1058.

121. Nakano K, Vousden KH. PUMA, a novel proapoptotic gene, is induced by p53. Mol Cell. 2001; 7:683-694.

122. Thornborrow EC, Patel S, Mastropietro AE, Schwartzfarb EM, Manfredi JJ. A conserved intronic response element mediates direct p53-dependent transcriptional activation of both the human and murine bax gene. Oncogene. 2002; 21:990-999.

123. Yu J, Wang Z, Kinzler KW, Vogelstein B, Zhang L. PUMA mediates the apoptotic response to p53 in colorectal cancer cells. Proc Natl Acad Sci U S A. 2003; 100:1931-1936.

124. Sax JK, Fei P, Murphy ME, Bernhard E, Korsmeyer SJ, El-Deiry WS. BID regulation by p53 contributes to chemosensitivity. Nat Cell Biol. 2002; 4: 842-849.

125. Moroni MC, Hickman ES, Denchi EL, Caprara G, Colli E, Cecconi F, Muller H, Helin K. Apaf-1 is a transcriptional target for E2F and p53. Nat Cell Biol. 2001; 3:553-558.

126. MacLachlan TK, and El-Deiry WS. Apoptotic threshold is lowered by p53 transactivation of caspase-6. Proc Natl Acad Sci. 2002; 99: 9492-9497.

127. Sax JK, El-Deiry WS. P53 downstream targets and chemosensitivity. Cell Death Diff. 2003; 10:413-417.

128. Chi SW. Structural insights into the transcription-independent apoptotic pathway of p53. BMB Rep. 2014; 47:167-172.

129. Tomita Y, Marchenko N, Erster S, Nemajerova A, Dehner A, Klein C, Pan H, Kessler H, Pancoska P, Moll UM. WT p53, but not tumor-derived mutants, bind to Bcl2 via the DNA binding domain and induce mitochondrial permeabilization. JBC 2006; 281:8600–8606.

130. Brown CJ, Lain S, Verma CS, Fersht AR, Lane DP. Awakening guardian angels: drugging the p53 pathway. Nat Rev Cancer. 2009; 9:862–873.

131. D'Orazi G, Marchetti A, Crescenzi M, Coen S, Sacchi A, Soddu S: Exogenous wt-p53 protein is active in transformed cells but not in their nontransformed counterparts: implications for cancer gene therapy without tumor targeting. J Gene Med. 2000; 2: 11–21.

132. Momand J, Wu HH, Dasgupta G. MDM2 - master regulator of the p53 tumor suppressor protein. Gene. 2000; 242:15-29.

133. Harris SL, Levine, AJ. The p53 pathway: positive and negative feedback loops. Oncogene. 2005; 24:2899-2908.

134. Momand J, Jung D, Wilczynski S, Niland J. The MDM2 gene amplification database. Nucleic Acids Res. 1998; 26:3453-3459.

135. Di Stefano V, Blandino G, Sacchi A, Soddu S, D'Orazi G. HIPK2 neutralizes MDM2 inhibition rescuing p53 transcriptional activity and apoptotic function. Oncogene. 2004; 23:5185-5192.

136. Oda K, Arakawa H, Tanaka T, Matsuda K, Tanikawa C, Mori T, Nishimori H, Tamai K, Tokino T, Nakamura Y, Taya Y. p53AIP1, a potential mediator of p53-dependent apoptosis, and its regulation by Ser-46-phosphorylated p53. Cell. 2000; 102:849-862.

137. Mayo LD, Seo YR, Jackson MW, Smith ML, Guzman JR, Korgaonkar CK, Donner DB. Phosphorylation of human p53 at serine 46 determines promoter selection and whether apoptosis is attenuated oramplified. J Biol Chem 2005; 280:25953-25959.

138. D'Orazi G, Cecchinelli B, Bruno T, Manni I, Higashimoto Y, Saito S, Gostissa M, Coen S, Marchetti A, Del Sal G, Piaggio G, Fanciulli M, Appella E, et al. Homeodomain-interacting protein kinase 2 phosphorylates p53 at Ser46 and mediates apoptosis. Nat Cell Biol. 2002; 4:11-19.

139. Di Stefano V, Rinaldo C, Sacchi A, Soddu S, D'Orazi G. Homeodomain-interacting protein kinase-2 activity and p53 phosphorylation are critical events for cisplatin-mediated apoptosis. Exp Cell Res. 2004; 293:311-320.

140. Pistritto G, Puca R, Nardinocchi L, Sacchi A, D'Orazi G. HIPK2-induced p53Ser46 phosphorylation activates the KILLER/DR5-mediated caspase-8 extrinsic apoptotic pathway. Cell Death Diff. 2007; 14:1837-1839.

141. Puca R, Nardinocchi L, Sacchi A, Rechavi G, Givol D, D'Orazi G. HIPK2 modulates p53 activity towards pro-apoptotic transcription. Mol Cancer. 2009; 8:85.

142. Garufi A, D'Orazi G. High glucose dephosphorylates serine 46 and inhibits p53 apoptotic activity. JECCR. 2014; 33:79.

143. Jin ZG, Shen JF, He JY, Hu CQ. Combination therapy with p53-MDM2 binding inhibitors for malignancies. Med Chem Res. 2015; 24:1369-1379.

144. Vassilev LT. MDM2 inhibitors for cancer therapy. Trends Mol Med. 2007; 13:23-31.

145. Vassilev LT, Vu BT, Graves B, Carvajal D, Podlaski F, Filipovic Z, Kong N, Kammlot U, Lukacs C, Klein C, Fotouhi N, Liu EA. In

vivo activation of the p53 pathway by small-molecule antagonists of MDM2. Science. 2004; 303:844-848.

146. Kojima K, Konopleva M, McQueen T, O'Brien S, Plunkett W, Andreeff M. Mdm2 inhibitor Nutlin-3a induces p53-mediated apoptosis by transcription-dependent and transcription-independent mechanisms that may overcome Atm-mediated resistance to fluodarabine in chronic lymphocytic leukemia. Blood 2006; 108:993-1000.

147. Vaseva AV and Moll UM. The mitochondrial p53 pathway. Biochim Biophys Acta. 2009; 1787: 414-420.

148. Rinaldo C, Prodosmo A, Mancini F, Iacovelli S, Sacchi A, Moretti F, Soddu Silvia. MDM2-regulated degradation of HIPK2 prevents p53Ser46 phosphorylation and DNA damage-induced apoptosis. Mol Cell. 2007; 25:739-750.

149. Rinaldo C, Prodosmo A, Siepi F, Moncada A, Sacchi A, Selivanova G, Soddu S. HIPK2 regulation by MDM2 determines tumor cell response to the p53-reactivating drugs Nutlin-3 and RITA. Cancer Res. 2009; 69:6241–6248.

150. Nardinocchi L, Puca R, Givol D, D'Orazi G. Counteracting MDM2-induced HIPK2 downregulation restores the HIPK2/p53 apoptotic signaling in cancer cells. FEBS Lett. 2010; 584:4253-4258.

151. Garufi A, Ubertini V, Mancini F, D'Orazi V, Baldari S, Moretti F, Bossi G, D'Orazi G. The beneficial effect of Zinc(II) on low-dose chemotherapeutic sensitivity involves p53 activation in wild-type p53-carrying colorectal cancer cells JECCR. 2015; 34:87.

152. Nardinocchi L, Puca R, D'Orazi G. HIF-1α antagonizes p53-mediated apoptosis by triggering HIPK2 degradation. Aging (Albany NY). 2011; 3:33-43. doi: 10.18632/aging.100254.

153. Kojima K, Konopleva M, Samudio IJ, Schober WD, Bornmann WG, Andreeff M. Concomitant inhibition of MDM2 and Bcl-2 protein function synergistically induces mitovhondrial apoptosis in AML. Cell Cycle 2006; 5:2778-2786.

154. Wade M, Rodewald LW, Espinosa JM, Wahl G. BH3 activation blocks Hdmx suppression of apoptosis and cooperates with Nutlin to induce cell death. Cell Cycle 2008; 7:1973-1982.

155. Zhao YJ, Aguilar A, Bernard D, Wang S. Small-molecule inhibitors of the MDM2-p53 protein-protein interaction (MDM2 Inhibitors) in clinical trials for cancer treatment. J Med Chem. 2015; 58:1038-1052.

156. Pellegrino M, Mancini F, Lucà R, Coletti A, Giacchè N, Manni I, Arisi I, Florenzano F, Teveroni E, Buttarelli M, Fici L, Brandi R, Bruno T, et al. Targeting the MDM2/MDM4 interaction interface as a promising approach for p53 reactivation. Cancer Res. 2015; 75:4560-4572.

157. Mancini F, Di Conza G, Pellegrino M, Rinaldo C, Prodosmo A, Giglio S, D'Agnano I, Florenzano F, Felicioni L, Buttitta F, Marchetti A, Sacchi A, Pontecorvi A, et al. MDM4 (MDMX) localizes at the mitochondria and facilitates the p53-mediated intrinsic-apoptotic pathway. EMBO J. 2009; 28:1926-1939.

158. Mancini F, Pieroni L, Monteleone V, Luca R, Fici L, Luca E, Urbani A, Xiong S, Soddu S, Masetti R, Lozano G, Pontecorvi A, Moretti F. MDM4/ HIPK2/p53 cytoplasmic assembly uncovers coordinated repression of molecules with anti-apoptotic activity during early DNA damage response. Oncogene. 2016; 35:228–240.

159. Hoe KK, Verma CS, Lane DP. Drugging the p53 pathway: understanding the route to clinical efficacy. Nat Rev Drug Discov. 2014; 13:217-236.

160. Yu X, Narayanan S, Vazquez A, Carpizo DR. Small molecule compounds targeting the p53 pathway: are we finally making progress? Apoptosis. 2014; 19:1055-1068.

161. Zawancka-Pankau, Selivanova G. Pharmacological reactivation of p53 as a strategy to treat cancer. J Intern Med. 2015; 277: 248-259.

162. Lujambio A, Lowe SW. The microcosmos of cancer. Nature. 2012; 482:347-355.

163. Lima RT, Busacca S, Almeida GM, Gaudino G, Fennell DA, Helena Vasconcelos M MicroRNA regulation of core apoptosis pathways in cancer. Eur J Cancer. 2011; 47:163-174.

164. Huang G, Nishimoto K, Zhou Z, Hughes D, Kleinerman ES. miR-20a encoded by the miR-17–92 cluster increases the metastatic potential of osteosarcoma cells by regulating Fas expression. Cancer Res. 2012; 72:908–916.

165. Wang P, Zhuang L, Zhang J, Fan J, Luo J, Chen H, Wang K, Liu L, Chen Z, Meng Z. The serum miR-21 level serves as a predictor for the chemosensitivity of advanced pancreatic cancer, and miR-21 expression confers chemoresistance by targeting FasL. Mol Oncol. 2013; 7:334–345.

166. Li Z, Huang H, Chen P, He M, Li Y, Arnovitz S, Jiang X, He C, Hyjek E, Zhang J. miR-196b directly targets both HOXA9/MEIS1 oncogenes and FAS tumour suppressor in MLL-rearranged leukaemia. Nat Commun. 2012; 2:688.

167. Shaffiey F, Cross E, Sathyanarayana P. Mir-590 is a novel STAT5 regulated oncogenic miRNA and targets FasL in acute myeloid leukemia. Blood. 2013; 122:3811–3811.

168. Guennewig B, Roos M, Dogar AM, Gebert LF, Zagalak JA, Vongrad V, Metzner KJ, Hall J. Synthetic pre-microRNAs reveal dual-strand activity of miR-34a on TNF-α. RNA. 2014; 20:61–75.

169. Zhang L, Dong L, Li Y, Hong Z, Wei W. The microRNA miR-181c controls microglia-mediated neuronal apoptosis by suppressing tumor necrosis factor. J Neuroinflamm. 2012; 9:211.

170. Rossato M, Curtale G, Tamassia N, Castellucci M, Mori L, Gasperini S, Mariotti B, De Luca M, Mirolo M, Cassatella MA. IL-10-induced microRNA-187 negatively regulates TNF-α, IL-6, and IL-12p40 production in TLR4-stimulated monocytes. Proc Natl Acad Sci USA. 2012; 109:E3101–E3110.

171. Shimizu S, Takehara T, Hikita H, Kodama T, Miyagi T, Hosui A, Tatsumi T, Ishida H, Noda T, Nagano H, Doki Y, Mori M, Hayashi N. The let-7 family of microRNAs inhibits Bcl-xL expression and potentiates sorafenib-induced apoptosis in human hepatocellular carcinoma. J Hepatol. 2010; 52:698-704.

172. Sacconi A, Biagioni F, Canu V, Mori F, Di Benedetto A, Lorenzon L, Ercolani C, Di Agostino S, Cambria AM, Germoni S, Grasso G, Blandino R, Panebianco V, et al. miR-204 targets Bcl-2 expression and enhances responsiveness of gastric cancer. Cell Death Dis. 2012; 3:e423.

173. Zhang Y, Schiff D, Park D, Abounader R. MicroRNA-608 and MicroRNA-34a regulate chordoma malignancy by targeting EGFR, Bcl-xL and MET. PloS ONE. 2014; 9:e91546.

174. Kurataka O, Takahiro O. Genetic networks lead and follow tumor development: MicroRNA regulation of cell cycle and apoptosis in the p53 pathways. Bio Med Res Intern. 2014; 2014:ID749724.

175. Raver-Shapira N, Marciano E, Meiri E, Spector Y, Rosenfeld N, Moskovits N, Bentwich Z, Oren M. Transcriptional activation of miR-34a contributes to p53-mediated apoptosis. Mol Cell. 2007; 26:731-743.

176. Chang TC, Wentzel EA, Kent OA, Ramachandran K, Mullendore M, Lee KH, Feldmann G, Yamakuchi M, Ferlito M,

Lowenstein CJ. Transactivation of miR-34a by p53 broadly influences gene expression and promotes apoptosis. Mol Cell. 2007; 26:745-752.

177. Garibaldi F, Falcone E, Trisciuoglio D, Colombo T, Lisek K, Walerych D, Del Sal G, Paci P, Bossi G, Piaggio G, Gurtner A. Mutant p53 inhibits miRNA biogenesis by interfering with the microprocessor complex. Oncogene 2016. doi: 10.1038/onc.2016. 51. [Epub ahead of print]

178. Baig S, Seevasant I, Mohamad J, Mukheem A, Huri HZ, Kamarul T. Potential of apoptotic pathway-targeted cancer thereapeutic research: Where do we stand? Cell Death Dis. 2016; 7:e2058.

Editorial

Fasting plus tyrosine kinase inhibitors in cancer

DOI: 10.18632/aging.100857

Irene Caffa, Valter D. Longo, and Alessio Nencioni

Tyrosine kinase inhibitors (TKIs), such as Tarceva (erlotinib), Iressa (gefitinib), Tykerb (lapatinib), and Gleevec (imatinib), are among the most broadly applied cancer therapeutics. By blocking the tyrosine kinase activity of mutated or overexpressed oncogenes, such as Epidermal Growth Factor Receptor (EGFR) and human epidermal growth factor receptor 2 (HER2), they interfere with signaling cascades which cancer cells are frequently "addicted" to, inducing vigorous and prolonged clinical responses in responsive patients [1]. Nevertheless, particularly in solid cancers, patients will sooner or later face relapses due to the emergence of resistant cell clones. Thus, strategies to safely increase the effectiveness of TKIs, but also reduce their toxicity are critically needed.

Studies show that cycles of prolonged fasting (PF, water only for more than two days) or of fasting-mimicking diets (FMDs) enhance the activity of chemo- and radio-therapy in preclinical cancer models [2, 3]. In addition, another advantage of administering chemotherapy during PF is that its overall tolerability appears to be increased [4]. As a result, several clinical trials are currently exploring the effects of PF/FMDs in patients undergoing chemotherapy (NCT01304251, NCT01175837, NCT00936364, NCT01175837, NCT01802346, NCT02126449).

Given this background, it is important to ask whether starvation would also be a useful approach to increase the efficacy of TKIs [5]. Results show that starvation strongly potentiates the antitumor activity of these agents both in vitro and in vivo in mice carrying human tumor xenografts. This goes along with a marked increase in the ability of TKIs to block signaling via the pro-tumorigenic mitogen-activated protein kinase (MAPK) cascade when they are administered under starvation conditions. Gene expression microarrays indicated that starvation and crizotinib (a TKI that is commonly used in advanced non-squamous non-small-cell lung cancer with EML4-ALK translocation) lead to similar changes in gene expression (primarily affecting cell cycle and DNA repair genes), whereas combining the two treatments compounds such effects by activating E2F6 (a dominant negative inhibitor of other E2F family members) and RB1, and by inhibiting the cell cycle-promoting transcription factors E2F1 and E2F4.

Overall, this work indicated that PF and FMDs, recently shown to be effective in reducing IGF-1 levels in both mice and human subjects [6], may not only be effective when coupled to standard chemotherapy or to radiotherapy, but that they may also find applications in patients receiving more modern, molecularly-targeted agents, such as TKIs, making them more effective. That being said, this study also left several questions open and opportunities for investigations. Do PF/FMDs also reduce the likelihood of secondary resistance (or delay its occurrence), thereby extending progression-free survival and overall survival? Can PF/FMDs achieve cases of advanced solid cancers cured with TKIs? Do PF/FMDs also increase the activity of commonly used anti-EGFR and anti-HER2 monoclonal antibodies, such as cetuximab or trastuzumab? Last, but not least, can PF/FMDs also increase the tolerability of TKIs, as much as they do with chemotherapeutics? Indeed, although the toxicity of TKIs is typically less severe that of chemotherapy, it can still be invalidating and lead to dose reductions or treatment discontinuations [1]. Reduced toxicity is anticipated considering the already demonstrated differential regulation of the growth of normal vs. cancer cells by PF/FMDs, which would promote entry of many normal cell types into a non-dividing and protected mode and make them less dependent on tyrosine kinase activity. Thus, if PF/FMDs helped spare healthy tissues from the toxicity of TKIs, the overall effectiveness of these agents could be strongly improved [7]. Answering these questions through preclinical and clinical studies is going to be crucial to provide a clear frame of usefulness for PF/FMDs in oncology.

REFERENCES

1. Gridelli C et al. Clini cal lung cancer. 2014; 15:173-181.

2. Lee C et al. Science Translational Medicine. 2012;4:124ra127.

3. Safdie F et al. PloS one. 2012; 7:e44603

4. Raffaghello L et al. Proceedings of the National Academy of Sciences of the United States of America. 2008;105:8215-8220.

5. Caffa I et al. Oncotarget. 2015; 6:11820-11832. DOI: 10.18632/oncotarget.3689

6. Brandhorst S et al. Cell Metab. 2015. pii: S1550-4131(15)00224-7.
7. Eichler HG et al. Nature Reviews Drug Discovery. 2010; 9:277-291.

Alessio Nencioni: Department of Internal Medicine, University of Genoa, 16132 Genoa, Italy

Correspondence: *Alessio Nencioni*
Email: *alessio.nencioni@unige.it*
Keywords: *cancer; fasting; tyrosine kinase inhibitors; MAPK signaling; molecularly, targeted therapy*
Received: July 11, 2015
Published: December 6, 2015

Research Paper

A novel autosomal recessive TERT T1129P mutation in a dyskeratosis congenita family leads to cellular senescence and loss of CD34+ hematopoietic stem cells not reversible by mTOR-inhibition

Clemens Stockklausner[1*], Simon Raffel[2, 3, 4*], Julia Klermund[5], Obul Reddy Bandapalli[1], Fabian Beier[6], Tim H. Brümmendorf[6], Friederike Bürger[7], Sven W. Sauer[7], Georg F. Hoffmann[7], Holger Lorenz[5], Laura Tagliaferri[1], Daniel Nowak[8], Wolf-Karsten Hofmann[8], Rebecca Buergermeister[1, 5], Carolin Kerber[1], Tobias Rausch[9, 10], Jan O. Korbel[10], Brian Luke[5, 11*], Andreas Trumpp[2, 3, 4*] and Andreas E. Kulozik[1*]

[1]Department of Pediatric Oncology, Hematology and Immunology, University of Heidelberg and Molecular Medicine Partnership Unit, 69120 Heidelberg, Germany
[2]Division of Stem Cells and Cancer, German Cancer Research Center (DKFZ), Im Neuenheimer Feld 280, 69120 Heidelberg, Germany
[3]Heidelberg Institute for Stem Cell Technology and Experimental Medicine (HI-STEM gGmbH), Im Neuenheimer Feld 280, 69120 Heidelberg, Germany
[4]German Cancer Consortium (DKTK), 69120 Heidelberg, Germany
[5]Zentrum für Molekulare Biologie der Universität Heidelberg (ZMBH), DKFZ-ZMBH Alliance, 69120 Heidelberg, Germany
[6]Department of Hematology, Oncology, Hemostaseology and Stem Cell Transplantation, Medical Faculty of the RWTH Aachen University, 52062 Aachen, Germany
[7]Center for Pediatric and Adolescent Medicine, Heidelberg University Hospital, Im Neuenheimer Feld 430, 69120 Heidelberg, Germany
[8]Department of Hematology and Oncology, University Hospital Mannheim, Medical Faculty Mannheim of the University of Heidelberg, 68167 Mannheim, Germany
[9]European Molecular Biology Laboratory (EMBL), Genomics Core Facility, D 69117 Heidelberg, Germany
[10]European Molecular Biology Laboratory (EMBL), Genome Biology Unit and Molecular Medicine Partnership Unit, D 69117 Heidelberg, Germany
[11]Institute of Molecular Biology gGmbH, gefördert durch die Böhringer Ingelheim Stiftung, 55128 Mainz, Germany
*Equally contributed

Key words: TERT, TERC, mTOR, rapamycin, sirolimus, senescence
Received: 09/24/15; Accepted: 10/30/15; Published: 11/06/15 DOI: 10.18632/aging.100835
Correspondence to: Andreas E. Kulozik, MD/PhD; **E-mail:** andreas.kulozik@med.uni-heidelberg.de

Copyright: Stockklausner et al. This is an open-access article distributed under the terms of the Creative Commons Attribution License, which permits unrestricted use, distribution, and reproduction in any medium, provided the original author and source are credited

Abstract: The TERT gene encodes for the reverse transcriptase activity of the telomerase complex and mutations in TERT can lead to dysfunctional telomerase activity resulting in diseases such as dyskeratosis congenita (DKC). Here, we describe a novel TERT mutation at position T1129P leading to DKC with progressive bone marrow (BM) failure in homozygous members of a consanguineous family. BM hematopoietic stem cells (HSCs) of an affected family member were 300-fold reduced associated with a significantly impaired colony forming capacity in vitro and impaired repopulation activity in

mouse xenografts. Recent data in yeast suggested improved cellular checkpoint controls by mTOR inhibition preventing cells with short telomeres or DNA damage from dividing. To evaluate a potential therapeutic option for the patient, we treated her primary skin fibroblasts and BM HSCs with the mTOR inhibitor rapamycin. This led to prolonged survival and decreased levels of senescence in T1129P mutant fibroblasts. In contrast, the impaired HSC function could not be improved by mTOR inhibition, as colony forming capacity and multilineage engraftment potential in xenotransplanted mice remained severely impaired. Thus, rapamycin treatment did not rescue the compromised stem cell function of TERT^{T1129P} mutant patient HSCs and outlines limitations of a potential DKC therapy based on rapamycin.

INTRODUCTION

Telomeres, the protective nucleoprotein structures at chromosome ends, shorten upon each cell division due to the so-called "end-replication problem" [1, 2]. The end-replication problem is compensated for by the reverse transcriptase, telomerase, which is active in germ cells, cancer cells and, to an extent in somatic stem cells [3]. Accelerated telomere shortening leads to the premature replicative senescence of cells and can be caused by mutations of the telomerase components DKC1 (dyskerin), TERC and TERT, among other genes involved in telomere maintenance [4-7]. TERC and TERT represent the RNA and catalytic protein moieties of the telomerase reverse transcriptase, respectively. Mutations affecting the function of these genes may lead to dyskeratosis congenita (DKC), a disease with a highly heterogeneous phenotype [8-11]. Affected patients suffer from a variable combination of skin, nail and mucosal dystrophies, but also life-threatening conditions such as progressive bone marrow failure, pulmonary fibrosis and an increased propensity to develop malignant tumors [12-16]. Telomere loss has been proposed to eliminate cells with a long proliferative history, and in this manner, acts as a tumor suppressor to limit replicative capacity. Telomere attrition also occurs with age and the associated accumulation of senescent cells may contribute to the aging process [13]. In disease states with reduced stem cell replicative reserve, substantially increased stem cell turnover or in the absence of telomerase activity short telomeres accumulate in hematopoietic stem cells [17]. Critically short telomeres are dysfunctional in terms of chromosome end protection and hence upon nucleolytic processing the DNA damage checkpoint is unleashed, thereby driving the onset of replicative senescence [18]. Dysfunctional telomeres are also prone to unscheduled repair events leading to chromosomal rearrangements. Therefore, in the absence of a functional DNA damage checkpoint, chronic telomere shortening could also potentially lead to pathogenic chromosomal instability.

Current treatment for patients affected by dyskeratosis congenita includes the androgen danazol [19-21]. The use of androgens can lead to virilization in female patients and thereby limits its therapeutic range [22, 23].

Stem cell transplantation to cure the progressive bone marrow failure is challenging, and DKC patients have a poor tolerance for conditioning regiments and frequently suffer from life threatening side effects [24-26]. Future therapy options include the utilization of induced pluripotent stem cells that might be beneficial for patients that have defined mutations in telomerase components such as TERC [5].

mTOR is a protein kinase that promotes cell growth in response to nutrient supplies and growth signals, and can be specifically inhibited by rapamycin [27]. As it has been shown that inhibiting the mTOR pathway with rapamycin reduces the rate of cellular senescence onset, we hypothesized that rapamycin might have a therapeutic potential for patients suffering from mutations of the telomerase complex where senescent cells accumulate [28, 29].

In this work we describe a consanguineous Libyan family in which we identify a novel T1129P TERT mutation leading to progressive bone marrow failure in homozygous family members. In order to test our hypothesis that rapamycin may rescue or at least improve the physiology of TERT^{T1129P} patient cells, we analyzed the effect of the mTOR inhibitor rapamycin on growth and senescence of skin fibroblasts and on hematopoietic stem cells using in vitro cultures and xenograft mouse models.

RESULTS

The novel TERT T1129P mutation leads to pathological telomere shortening causing progressive bone marrow failure in homozygous patients

Progressive bone marrow failure including transfusion dependent anemia und thrombocytopenia was first diagnosed in patient II-1 at the age of six years in a consanguineous Libyan family when a blood count was obtained to address symptoms of anemia including weak-

A

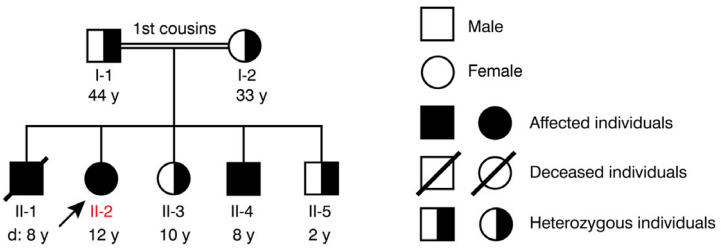

B

Parameter	I-1	I-2	II-2	II-3	II-4	II-5
WBC in n/nl (Normal range)	9.45 (4-10)	7.63 (4-10)	2.16 (4.5-13.0)	9.76 (4.5-13.0)	3.09 (4.5-13.0)	13.9 (5-17.5)
ANC in % (Normal range)	55 (50-80)	60.6 (50-80)	14 (50-80)	55.3 (50-80)	22.7 (50-80)	59 (50-80)
RBC in n/pl (Normal range)	4.9 (4.3-6.1)	3.64 (4-5.2)	2.44 (4.0-5.2)	4.79 (4.0-5.2)	1.71 (4.0-5.2)	4.3 (3.7-5.2)
Hemoglobin in g/dl (Normal range)	15.1 (13-17)	12.1 (12-15)	7.3 * (11.5-15)	12.8 (11.5-15)	6.2 (11.5-15)	11.7 (9.5-13.5)
Platelets in n/nl (Normal range)	181 (150-440)	195 (150-440)	9 (180-530)	280 (180-530)	13 (180-530)	279 (200-480)
MCV in fl (Normal range)	88.4 (83-97)	94.5 (83-97)	81.6 * (69-95)	80.2 (69-95)	106.4 (69-95)	76.3 (74-108)
Reticulocytes in ‰ (Normal range)	14 (5-15)	24.4 (5-15)	1.6 (5-15)	11.4 (5-15)	28.9 (5-15)	8.5 (5-15)

C

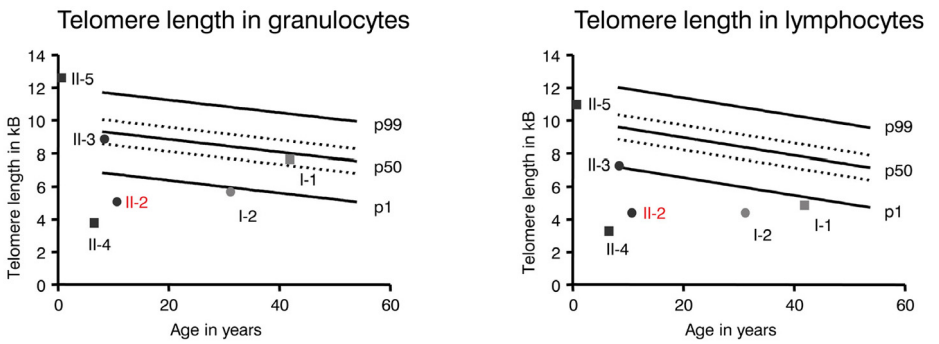

D

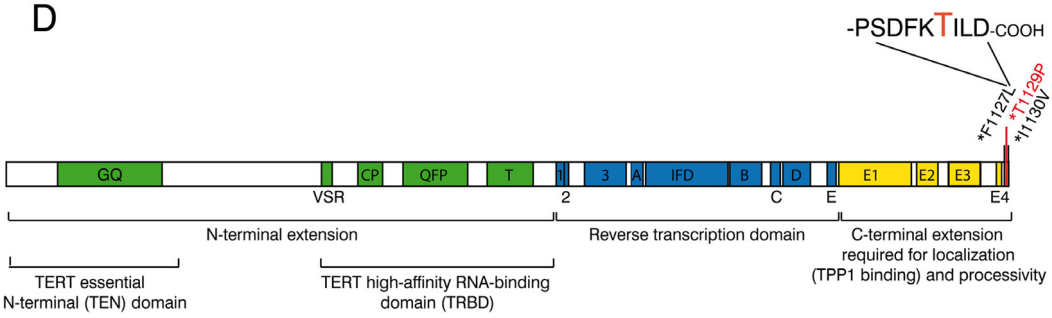

Figure 1.Clinical features and telomere length of the DKC family with the novel T1129P TERT mutation. (**A**) Family tree of the consanguineous Libyan family. Family members affected by dyskeratosis congenita (son II-1 (deceased), daughter II-2, son II-4) are indicated in black. Marked in red: patient II-2 who was analyzed in detail in the following figures. (**B**) Table showing complete blood counts (WBC=white blood cells (n/nl), ANC= absolute neutrophil count (% of WBC), RBC= red blood cells (n/pl), Hb=hemoglobin (g/dl), Plt=platelet count, mean corpuscular volume (MCV in fl) and reticulocytes (‰ of RBC) and the respective age dependent normal values in brackets of the family members I-1, I-2, II-2, II-3, II-4 and II-5 shown in (A). Family members II-2 and II-4 that were diagnosed with dyskeratosis congenita and were homozygous for the $TERT^{T1129P}$ mutation are highlighted with grey color. Indicated with *: Patient II-2 was on a 3-weekly red cell transfusion regimen and had a red cell transfusion of 15 ml/kg erythrocytes 20 days before the sample was taken; patient II-4 had no history of red blood cell or platelet transfusions. (**C**) Telomere lengths of the described family determined in lymphocytes and granulocytes of the peripheral blood. Absolute telomere lengths in kb of lymphocytes and granulocytes of the patient II-2, her affected brother II-4, her siblings II-3, II-5 and her parents I-1 and I-2 are shown in the context of age-dependent percentiles (Females: circle, males: square. Parents: light grey, children: black. Marked in red: patient II-2 who was analyzed in detail). The solid lines represent the respective 1%, 50%, 99% percentile curves. The dashed lines represent the 25% and 75% percentile. (**D**) Schematic representation of the TERT gene with functional domains and known mutations at the C-terminus. Our novel T1129P mutation is depicted in red.

ness and pallor. There was no history of transfusions in the family before. The parents of II-1 were first degree cousins and family studies showed similar thrombocytopenia and anemia in two of their other offspring (II-2 and II-4) (Figure 1 A and B). Normal white blood counts, hemoglobin and platelet counts were observed from the father (I-1), mother (I-2) as well as in the second sister (II-3) and in the third brother (II-5). No family member showed any indication of nail dystrophy or skin alterations.

II-1 died at the age of eight years during conditioning regimen for intended stem cell transplantation that was performed abroad under the suspected diagnosis of aplastic anemia. His aplastic anemia was not diagnosed on a molecular basis and blood samples are no longer available.

The patient II-2 presented at our center at the age of 12 years with progressive bone marrow failure including transfusion dependent anemia and thrombocytopenia, leukopenia (Figure 1B) and hypermenorrhea. Fanconi anemia was excluded as normal results were obtained for the analysis of DNA breakage. Suspected dyskeratosis congenita was confirmed by telomere length analysis in lymphocytes and granulocytes as determined by Flow-FISH (Figure 1C). The telomere lengths in lymphocytes and granulocytes in patients II-2 and II-4 and the mother I-2 corresponded to less than the 1st percentile of age matched controls. Telomere length of the father (I-1) in lymphocytes (right panel) also corresponded to less than the 1st percentile of age-matched controls, whereas it was normal in granulocytes (left panel). The healthy sibling II-3 also displayed a decreased telomere length when compared to age matched controls, although not below the 1st percentile (Figure 1C). Pulmonary function was normal in patient II-2 and not determined in other family members.

Whole exome sequencing and validation by Sanger sequencing revealed a novel homozygous c. 3385 A>C mutation (nucleotide entry NM_198253), resulting in the novel p.Thr1129Pro or T1129P mutation (Figure 1D) of the TERT gene in the 12-year-old patient II-2. No other homozygous mutation was found in the patient. This mutation was absent from public SNP databases (dbSNP, 1000 Genome variant catalogue), conserved and was predicted to be damaging using SIFT and PolyPhen-2 [30, 31]. The unaffected family members were heterozygous carriers of this mutation. The 8-year-old brother II-4 was detected with the same homozygous mutation by Sanger sequencing from peripheral blood.

The T1129P mutated TERT does not show nuclear clustering together with TERC in a ST-cell culture model

The novel T1129P mutation is located at the C-terminus of TERT altering the 4th last amino acid (Figure 1D). This region of normal TERT was shown to bind the telomeric protein TPP1, and has therefore been suggested to be required for the telomeric localization of TERT [32]. To investigate if this novel mutation would influence recruitment of the telomerase complex, we employed a modified "supertelomerase" assay (ST) that used transient, plasmid based expression of the central scaffold protein of the telomerase ribonucleo-protein TERC and hemagglutinin (HA)-tagged TERT in HeLa cells [32-35]. As shown in Figure 2, transfection of N-terminally HA-tagged TERT into HeLa cells resulted in a nucleoplasmic pattern. In line with previous findings, expression of TERC together with HA-TERT resulted in nuclear clusters that have been described as clusters with the telomeres at the chromosomal ends (Figure 2A, compare b with e) [32]. Interestingly, the mutant HA-TERT T1129P protein was detected in the cytoplasm in the absence of co-expressed TERC. When co-expressed with TERC, a nucleoplasmic pattern was observed, but it lacked the typical nuclear clustering of wild type TERT (Figure 2A, compare e to h, k, quantified in B and C) suggesting a failure to be recruited to chromosome ends. Taken together, these results strongly further support the hypothesis that the T1129P mutation impairs the recruitment of TERT to the telomerase complex located at its site of action at the chromosome ends.

mTOR inhibition with rapamycin influences population doublings and senescence of patient skin fibroblast cultures

The proliferative capacity of cells can by quantified by calculating the population doublings that cells undergo during the culturing process as a function of time. Population doublings are defined as the number of times that the cell number is doubled. As telomeres shorten, the proliferative potential decreases. Generally, population doublings can be recorded in skin fibroblast cultures by plating a specific number of cells and then counting those cells after a defined period of growth as described in Material and Methods. Skin fibroblasts represent an easily accessible cell type that can be cultivated over a long time period, and were treated with either 5 nM rapamycin or DMSO as a vehicle control. Fibroblast cultures obtained from the father (I-1) fulfilled criteria of senescence from the beginning, as they did not show population doublings within 4 weeks despite frequent changes of cell culture media (not shown).

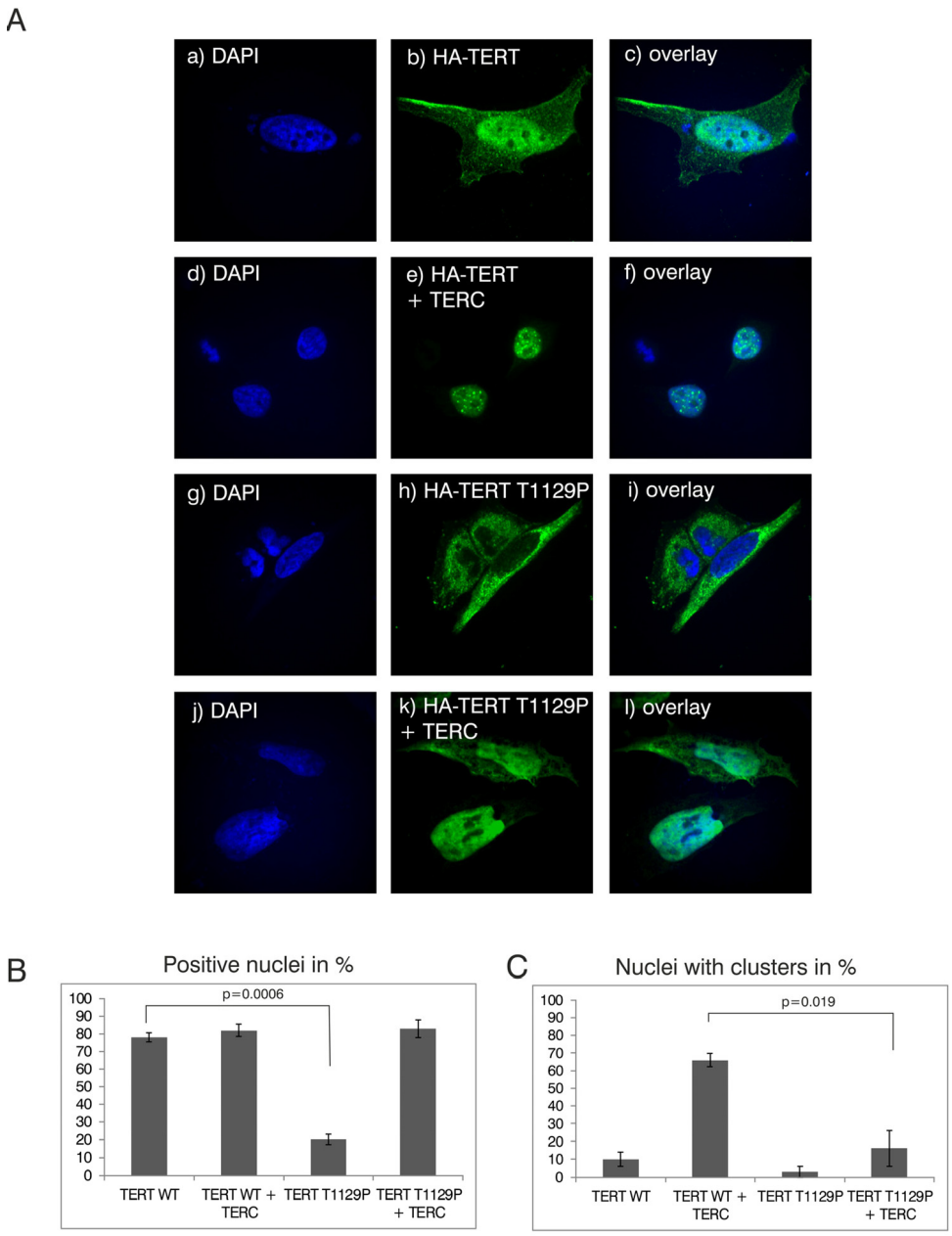

Figure 2. Analysis of nuclear clustering of the TERT T1129P mutation in a cell culture model. (**A**) Representative confocal images of transiently co-transfected HeLa-cells. HA-TERT or HA-TERT T1129P, respectively, harboring 3 HA-tag sequences in frame at the N-terminus were transfected and fixed 48h later. On the indicated pictures e) and k) equal amounts of the TERC minigene was co-transfected together with the respective TERT minigene. The HA-tag was visualized with a mouse monoclonal anti-HA antibody and an anti-mouse secondary antibody linked to Alexa 488 as described in Materials and Methods. The nucleus was visualized by DAPI staining. The panels on the right represent overlays of the TERT wild type or the T1129P mutations, respectively, with the nucleus stained with DAPI. Cells depicted represent the subcellular distribution pattern seen in >90% of the transfected cells. (**B**) and (**C**) Quantification of nuclear accumulation and clustering. For quantification of nuclear accumulation and clustering in the nuclei, 100 cells each from 3 independent transfections have been assessed and counted visually for the presence of nuclear staining and/or nuclear clustering. For statistical analysis a student's unpaired two-tailed t-test was used.

Skin fibroblast cultures of the TERT T1129P homozygous patient II-2 but also from the heterozygous mother I-2 showed impaired population doublings when compared to fibroblasts from a healthy age matched control (Figure 3A). Treatment of the control and mother (I-2) fibroblasts with rapamycin did not influence the proliferative potential measured by population doublings over time (Figure 3A). The fibroblast culture of the patient II-2 did not show a comparable proliferation potential after day 48 and had no vital cells after day 97. In contrast, the rapamycin treated fibroblast culture of patient II-2 still divided (albeit slowly) after day 97 and showed prolonged survival until day 182 (Figure 3A).

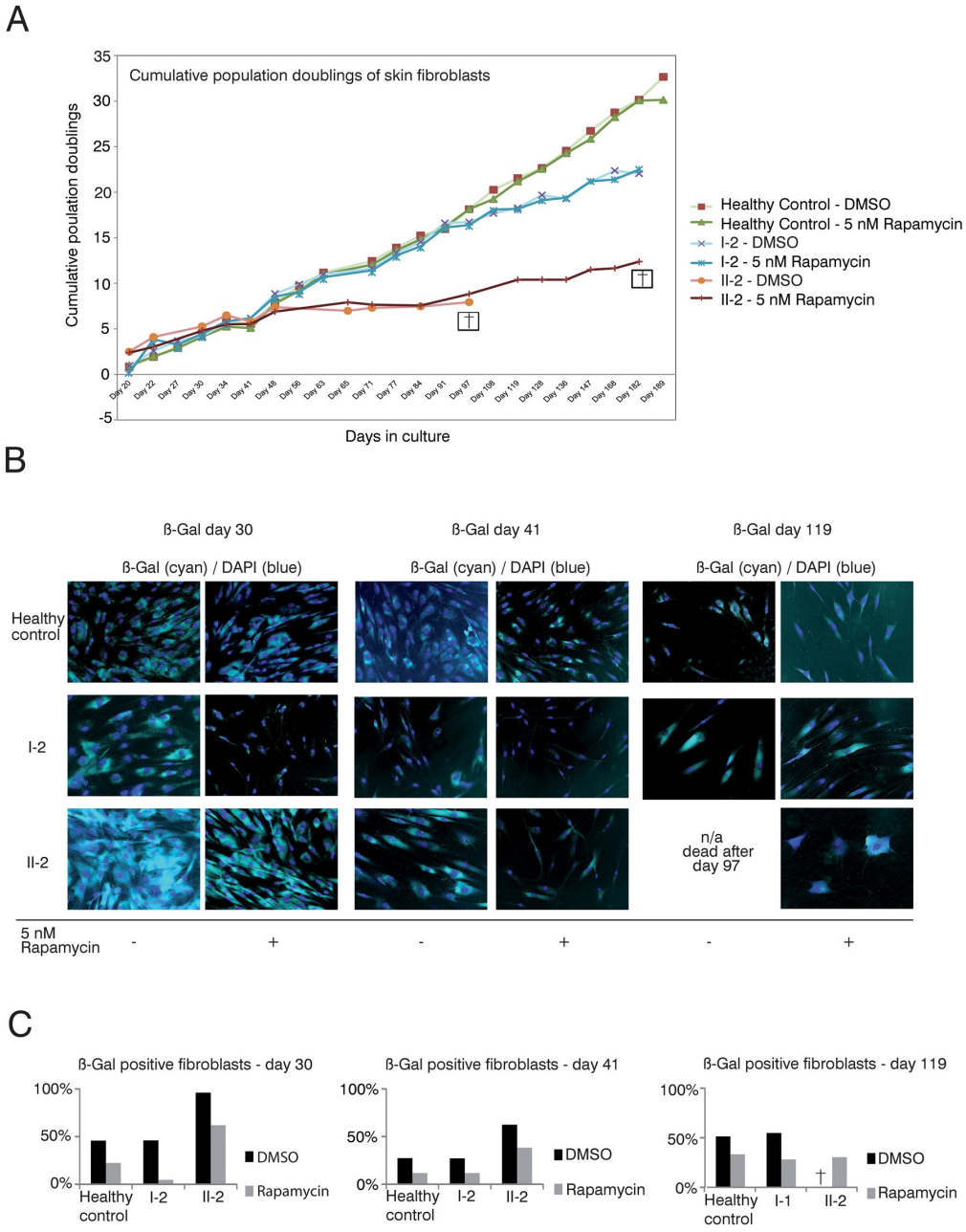

Figure 3. Rapamycin treatment of DKC skin fibroblast cultures. (**A**) Cumulative population doublings of skin fibroblasts. Fibroblast cultures from the mother I-2, the daughter II-2 and a healthy control were trypsinized and viable cells determined by trypan blue staining. Viable cells remained unstained. Population doublings were calculated using the following equation: PD=X + log2(Y/I) where: X = initial PD I = cell inoculum (number of cells plated in the flask) Y = final cell yield (number of cells at the end of the growth period). Cell were defined as dead (indicated with a cross) if no remaining viable cells were detected.

(B) ß-gal senescence assay of skin fibroblasts. Fibroblasts were cultured in DMEM/10% FCS/1%PenStrep containing either 5nM rapamycin dissolved in DMSO or the equal volume of DMSO as negative control (equivalent to a 1:1,000 dilution). For the indicated timepoints, cells were fixed after 24h with 0.1% glutaraldehyde and stained for ß-galactosidase (ß-Gal) at pH 6 as described in Materials and Methods. Nuclei were visualized by staining with DAPI (Sigma-Aldrich), diluted 1:10,000. Coverglasses were embedded in moviol 4-88 (Carl Roth) on slides. Cells were observed at 20-fold magnification and pictures taken at brightfield and fluorescent light with a filter set suitable for DAPI on an Olympus CellR microscope. Depicted overlays of brightfield and fluorescence were merged in ImageJ. Images are representative of the indicated time points. (**C**) Quantification of ß-gal assay. ß-Gal-positive cells were detected at the indicated time points using a programmed plugin for the image editing program ImageJ as described in Materials and Methods. The quantified images were representative of the indicated time points. 200 cells counted by DAPI staining were analyzed for each time point and measurement. The fibroblasts were determined as ß-Gal positive when blue staining in the brightfield reached a defined intensity and surrounding area of the core that was detected in the fluorescence light (Ex 330-385, Em LP420 filter set for DAPI detection).

The limited capacity of cells to divide culminates in senescence, a status that is characterized by decreased viability, enlarged cell size, altered pattern of gene expression and expression of pH dependent beta-galactosidase activity [36-38]. ß-galactosidase activity is present only in senescent cells and is not found in pre-senescent, quiescent or immortal cells [37]. Therefore, we performed ß-galactosidase assays to test if the prolonged survival in the rapamycin treated fibroblast cultures of the patient (II-2) correlated with decreased senescence (Figure 3B and C). We detected decreased senescence in the control fibroblasts, fibroblasts of the mother I-2 and the affected patient II- 2 at day 30 when treated with rapamycin (Figure 3B and C). The same effect was observed at day 41 of this experiment. At day 119 the DMSO treated fibroblast culture of our patient II-2 did not show any vital cells (no viability after day 97). In healthy control fibroblasts and the mother's fibroblasts, the rapamycin treated cultures still showed decreased senescence when compared to the respective DMSO treated cultures (Figure 3B). Taken together, these data reveal a positive correlation between proliferative potential and a decrease of the senescence marker, beta-galactosidase activity, in DC patient cells.

CD34+ HSPCs are reduced more than 300-fold in patient bone marrow

Next, we sought to investigate the effect of rapamycin treatment on hematopoietic stem and progenitor cells (HSPCs), hypothesizing that in line with our previous results with fibroblasts (Figure 3), a prolonged survival of HSPCs could improve the patient's blood counts. If so, rapamycin might offer a therapeutic treatment to reduce transfusion dependence of the affected family members. Patient bone marrow derived HSPCs were characterized and quantified by flow cytometry and functionally characterized in vitro by colony forming unit (CFU) assays as well as in vivo by xeno-transplantation into immunocompromized NOD/SCID/ interleukin 2 receptor γ^{null} (NSG) mice. Rapamycin treatment and control groups were included in all experiments (Figure 4A). As shown in Figure 4B cellularity and HSPC frequency were strongly reduced in the bone marrow of patient II-2. Compared to a healthy female donor the patient had a 4-fold reduced bone marrow mononuclear cell count ($1.53x10^6$/ml vs. $0.4x10^6$/ml) with reduced viability after gradient centrifugation (98.1 percent vs. 84.3 percent viable cells). A dramatic 300-fold reduction was observed in CD34+ HSPCs per ml bone marrow. Only 0.034 percent of all lineage negative cells were CD34+ in the patient II-2 compared to 7.04 percent in the healthy control sample, highlighting a severe HSPC depletion phenotype (Figure 4B and C). Using magnetic bead enrichment for CD34, less than 10,000 CD34+ cells could be isolated from 100 ml bone marrow aspirate, limiting functional studies with these cells.

Impaired clonogenic growth potential of patient II-2 HSPCs in vitro was not improved by rapamycin

To evaluate clonogenicity and lineage differentiation potential of the patient's HSPCs and the influence of rapamycin treatment we performed colony forming unit (CFU) assays (see Figure 4A for experimental design). Plating 3,000 CD34+ cells resulted in approx. 80 colonies per plate in the healthy control. In contrast, the patient's HSPC colony forming potential was significantly reduced, revealing on average only 4 colonies in the DMSO treatment group and 2 colonies in the rapamycin treatment group (Figure 5A). Although colonies treated with rapamycin were reduced in size in both patient and healthy control, this effect was more pronounced in the patient HSPCs (Figure 5B). Furthermore, patient HSPCs showed no long-term self-renewing potential as no colonies were detected anymore in secondary CFU assays, irrespective of rapamycin treatment. In addition to a reduced abundance of HSPCs in the patient's bone marrow, results from the CFU assays indicate a severe functional

impairment including self-renewal potential of mutant progenitors. However, in contrast to our observation in fibroblasts, rapamycin treatment showed no beneficial effect on colony number, size and self-renewal activity.

Xenotransplantation of remaining CD34-negative HSPCs from patient II-2 does not result in multilineage engraftment

Xenotransplantation of human HSPCs into immunocompromized NSG mice is considered the gold standard to evaluate hematopoietic stem cell function. We have recently shown that co-transplantation of mesenchymal stromal cells (MSCs) can enable engraftment of functionally impaired and usually non-transplantable HSPCs derived from Myelodysplastic Syndrome patients [39]. Lacking sufficient amounts of CD34+ HSPCs and to rule out the possibility that the patient's HSPCs are "hidden" within the CD34-negative fraction we co-injected CD34-negative BM MNCs together with healthy human MSCs infra-femorally into sub-lethally irradiated NSG recipient mice. As control, CD34+ healthy HSPCs and MSCs were co-transplanted. In addition, 90-day slow release rapamycin or placebo pellets were implanted subcutaneously. Engraftment of human blood cells was measured by the chimerism for human CD45+ cells 90 days after transplantation. Expression of human CD19 determined lymphoid lineage output, while human CD33 expression was indicative of myeloid differentiation. As expected, healthy HSPCs reconstituted multi-lineage human hematopoiesis in bone marrow (Figure 6A, D), spleen (Figure 6B) and peripheral blood (Figure 6C) of recipient mice. Although not statistically significant, there was a clear trend showing that human CD45+ engraftment was impaired in the rapamycin treatment group in all organs analyzed. In contrast, patient II-2 derived CD34-negative bone marrow MNCs failed to engraft in both rapamycin and placebo treated animals as neither myeloid nor lymphoid cell engraftment was observed.

A

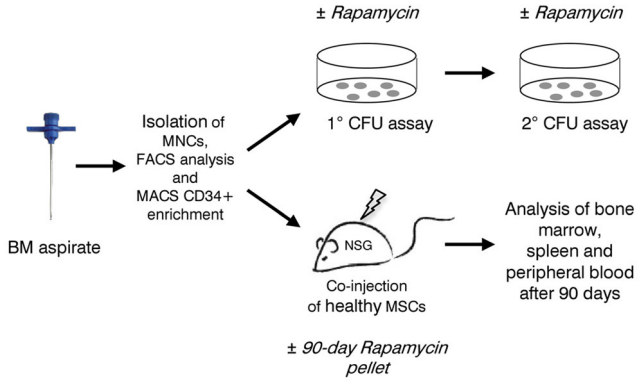

B

	Control	Patient II-2
MNC per ml BM	1.53x10^6	0.4x10^6
Viability (%)	98,1	84,3
CD34+ per ml BM	31900	100

C

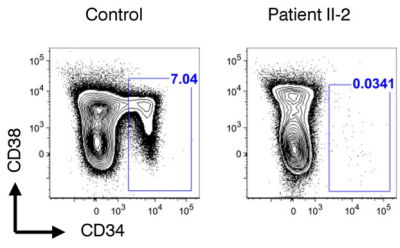

Figure 4. Analysis of patient II-2 bone marrow. (**A**) Experimental setup: Bone marrow mononuclear cells were isolated by gradient centrifugation from patient II-2 and healthy control, analyzed by FACS and either plated in colony forming unit assays (see Figure 5) or transplanted into NSG females (see Figure 6). (**B**) Bone marrow characteristics at time of sampling. (**C**) FACS plots showing CD34 and CD38 levels gated on live, lineage-negative cells. Gates show frequencies of CD34+ cells in percent.

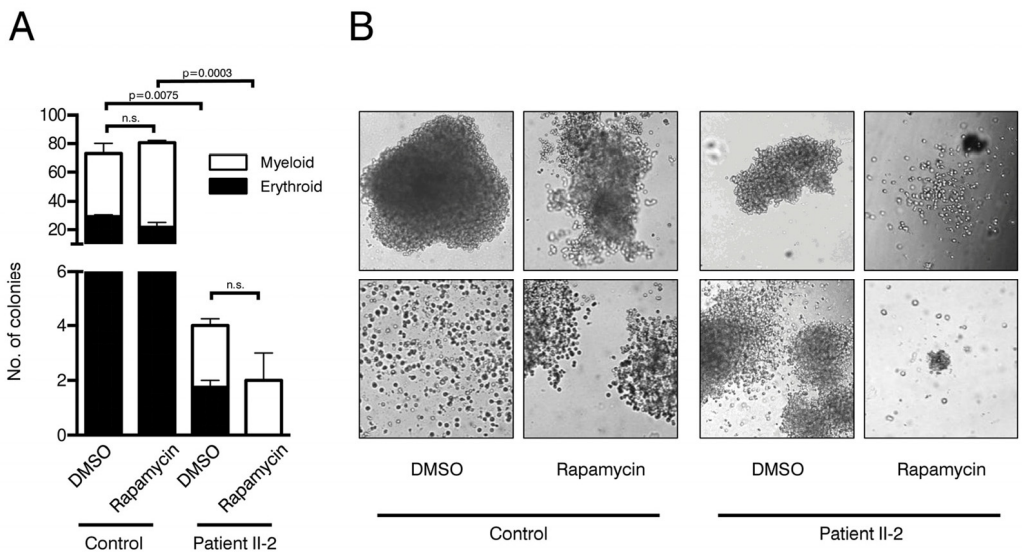

Figure 5. Colony forming unit assays. (**A**) Number of colonies in patient and control CFU assays treated with rapamycin or DMSO. Cells were plated in duplicates. Student's t-test was performed on total number of colonies, n.s. not significant. (**B**) Representative pictures of colonies.

However, CD3+ T cells, which were present in the transplanted CD34-negative cell fraction of patient II-2, expanded over the course of 90 days under placebo treatment leading to a clinically inapparent graft-versus-host disease. Rapamycin almost completely suppressed T cell expansion in the recipient mice, confirming the activity of the rapamycin pellets and being in line with its known mode of action as an immunosuppressive drug (Figure 6A-D).

Taken together, our experiments with bone marrow MNCs from the dyskeratosis congenita patient II-2 revealed a striking reduction in HSPCs associated with a severe functional impairment of stem cell activity that could not be improved by rapamycin treatment.

DISCUSSION

Members of the telomerase complex such as TERC, TERT or DKC1 play fundamental roles in aging processes [4-7]. Mutations in these genes may lead to diseases associated with premature aging such as DKC and cancers. Therefore, a refined knowledge of the effects of these mutations may prove useful for understanding pathways that lead to, or mitigate, long-term health, prevention of cancer and late-stage disease. The novel germline T1129P mutation in the TERT gene identified in a consanguineous Libyan family leads to DKC with progressive bone marrow failure in all homozygous individuals. Patients II-2 and II-4 showed significantly shortened telomeres below the 1st percentile when compared to healthy controls or to heterozygous family members. The pronounced telomere loss for lymphocytes in comparison to granulocytes is consistent with previous findings in healthy individuals as well as in patients with reduced telomere activity [40, 41]. Only homozygous family members showed progressive bone marrow failure. Heterozygous family members showed normal blood results. Heterozygosity of TERC- and most TERT-mutations can lead to haploinsufficiency and to the clinical phenotype of dyskeratosis congenita, although some TERT mutations cause recessive DKC with heterozygous carriers showing normal blood counts [42]. The heterozygous family members described here are phenotypically healthy despite the presence of shortened telomeres indicating a recessive mode of inheritance of the TERT T1129P mutation. This is consistent with the observation that disease severity cannot be predicted by telomere length alone [43]. However, a late onset of clinical symptoms cannot, of course, be ruled out. Strikingly, the phenotype of affected, homozygous family members only showed progressive bone marrow failure with an absence of other DKC related symptoms such as skin or nail dystrophy or pulmonary fibrosis. The localization of the mutation within the gene does not necessarily predict the phenotype, which is highly variable in various muta-

tions described throughout the TERT gene [4]. Our novel autosomal recessive T1129P mutation is in close proximity to the previously described mutations at positions 1127 and 1130 [43, 44]. When comparing the phenotypes and modes of inheritance of these two near-by mutations, it is striking that the mutation F1127L resembles Hoyeraal-Hreidarsson-syndrome and causes autosomal dominant dyskeratosis congenita whereas the somatic I1130V mutation leads to non-severe aplastic anemia [43, 44].

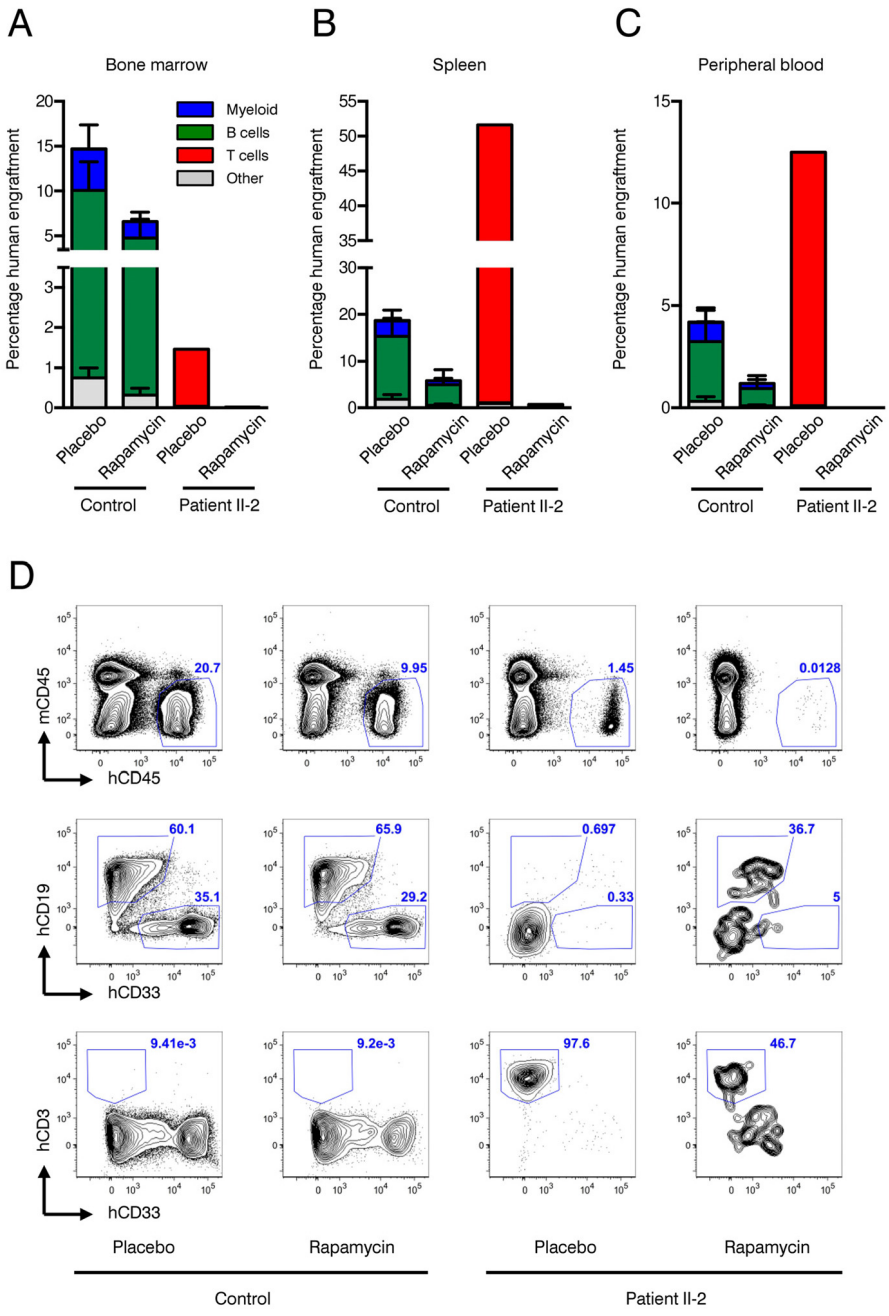

Figure 6. **Xenotransplantation experiments.** (**A**-**C**) Frequencies of human engraftment with respect to lineage differentiation in bone marrow (**A**), spleen (**B**) and peripheral blood (**C**) 90 days after transplantation of patient II-2 or healthy bone marrow. Mice were treated either with rapamycin or placebo. n=2 per condition in healthy donor, n=1 per condition in patient (**D**) Representative FACS plots depicting human (h)CD45 versus mouse (ms)CD45 for blood cell chimerism (upper panel), human (h)CD19 for lymphoid differentiation and human (h)CD33 for myeloid differentiation (middle panel) and human (h)CD3 for T cell expansion. Upper panel is gated on live cells, middle and lower panels are gated on live, hCD45+ cells. Numbers represent percentage of gated events.

It still needs to be elucidated how the T1129P TERT mutation exerts its effect causing aplastic anemia in affected patients. In HeLa cell cultures the T1129P mutated TERT did not efficiently enter the nucleus without co-transfected TERC (Figure 2A and B). Together with the lack of nuclear clustering upon co-transfection with TERC, this indicates an inefficient recruitment of the telomerase complex to telomeres within the nucleus for T1129P mutated TERT. As the postulated binding site of TPP1 is within the C-terminus, binding to TPP1 or other members of the telomerase recruitment complex might be impaired by the novel T1129P mutation. A mutant of the three amino acid sequence F1127/K1128/T1129 has been shown before to display only slightly compromised telomerase catalytic activity in vitro, but its in vivo ability to elongate telomeres was highly compromised [45]. In another study, this mutant was further analyzed for its ability to localize to telomeres and to TPP1. While it did not localize to telomeres, it could still localize with TPP1 in Cajal bodies, even though the association with TPP1 was weaker compared to wild type [32].

As androgens harbor various side effects especially for female patients with DKC including virilization, there is need for substances that are safe and well tolerated antagonizing pre-mature aging processes [22, 39]. mTOR inhibition, by rapamycin, has been demonstrated to extend lifespan in a host of model organisms as well as reduce the onset of cellular senescence in cell culture [46, 47]. Moreover, recent data obtained in yeast suggest that mTOR inhibition by rapamycin can strengthen the DNA damage checkpoint and thereby increase the likelihood that cell division only occurs when damaged chromosomes are repaired [48].

Therefore, rapamycin, a substance well characterized in the clinical setting, might be an attractive target to treat DKC patients as they harbor increased numbers of senescent cells which contain dysfunctional chromosome ends. Before administering rapamycin to the patient, we assessed its effect on skin fibroblasts and on HSPCs – the cells that are most severely affected in our patient. Rapamycin had no effect on enhancing the proliferation of normal skin fibroblasts but did prolong the survival of the fibroblasts from the affected patient II-2 (Figure 3A). In our functional analysis, senescence of skin fibroblasts of patient II-2 was increased, as expected. Rapamycin showed an effect on decreasing cellular senescence in treated skin fibroblast cultures of patient II-2. Strikingly, cellular senescence was also reduced in the fibroblast culture of the mother I-2 and the fibroblasts of the healthy control (Figure 3B and C). As mTOR inhibition regulates cellular pathways that affect senescence and aging, this might show the influence of mTOR on fundamental senescence steps even in healthy cells [47]. All fibroblast cultures showed a higher initial senescence at day 30 when compared to day 41. This can be explained by an increased senescence of the newly plated cells and later a reduced senescence of the increasingly dense cell cultures at day 41 that could have been caused by contact inhibition of geroconversion [49, 50].

Decreased frequency of HSPCs and severe impairment of these cells in functional tests such as colony-forming unit assays and xenotransplantation into immuno-compromized NSG mice highlight a fundamental HSC defect in patient II-2 (Figures 4 and 5).

In contrast to fibroblasts, rapamycin treatment did not improve HSC function in these assays. The fact that rapamycin treatment resulted in a trend towards fewer and smaller colonies argues against a possible improvement of the patient's blood counts by inhibiting mTOR. However, we cannot exclude that long-term rapamycin treatment of CD34+ HSPCs may ultimately lead to restoration of HSC function as CFU assays cover only a few weeks. Due to limited availability of diseased CD34+ HSPCs (only 10,000 CD34+ cells in 100ml bone marrow aspirate) xenotransplantation had to be performed using MNCs not selected for CD34. The data thus exclude the possibility that the patient's HSCs in the diseased BM down-regulated CD34 expression. Even co-transplantation of MSCs, which typically enhance engraftment of stem cells usually not capable of initiating human hematopoiesis in NSG mice, showed no beneficial effect [39].

Interestingly, T cells present in the CD34-negative MNCs expanded in the non-treated xenografts, while the immunosuppressive agent rapamycin blocked their expansion efficiently in the treated animals (Figure 6).

Due to the nature of our biological samples (skin biopsy and bone marrow aspirate from patient II-2) repetitive sampling was not possible or useful.

Previous studies in yeast demonstrated that rapamycin was beneficial for cells with dysfunctional telomeres when cells were given the chance to repair the telomeres and eventually proliferate in the absence of rapamycin [48]. Indeed when telomere dysfunction and rapamycin treatment were chronic, there was an initial lag in growth and only at very late time points the rapamycin treatment appeared to be beneficial (J.K. and B.L unpublished results). In the mouse experiments, rapamycin was constantly released from the pellets. In contrast, rapamycin was added to the fibroblast cultures

at the time of the splitting procedure and a possible degradation of the drug over time might have limited the toxic effects in our fibroblast experiments. Fine-tuning of rapamycin dosage might therefore be required for the anti-senescent effect and to avoid toxic effects [51]. Therefore it may be necessary to re-evaluate the dosage of rapamycin and the effects of cyclic dosing in order to see stronger effects.

The observed difference between fibroblasts and hematopoietic cells might also be explained by the different growth characteristics of the cell types studied: Fibroblasts divide much more slowly than hemato-poietic cells and it is possible that hematopoietic DKC T1129P cells require a stronger therapeutic effect than DKC T1129P fibroblasts for an improvement in survival. This difference of the effect of this mutation in either fibroblast or hematopoietic cells might also be reflected by the most severely affected hematopoiesis of the homozygous TERT T1129P patients, whereas the skin and other epithelial tissues were not clinically affected.

Furthermore, the severity of the telomerase mutation may render cells completely unable to re-elongate telomeres. It should also be considered that continuous presence of rapamycin in our experiment might have had additional toxic effects preventing cell division.

In summary, we report a novel hereditary T1129P TERT mutation that leads to DKC with aplastic anemia that can be attributed to a severe reduction and functional impairment of CD34+ hematopoietic stem cells. Functional analyses to find a therapeutic alternative for this serious condition revealed that rapamycin treatment prolonged survival and decreased levels of cellular senescence in treated skin fibroblasts. However, impaired HSC function could not be restored by rapamycin mediated mTOR inhibition, as colony forming capacity in vitro and multilineage engraftment potential in xenotransplanted mice was unchanged in the presence of rapamycin. Our data argue against a therapeutic use of mTOR inhibitors to treat aplastic anemia in DKC patients with TERT mutations.

MATERIALS AND METHODS

Ethics statement. Investigation has been conducted in accordance with the ethical standards and according to the Declaration of Helsinki and according to national and international guidelines and has been approved by the authors' institutional review board.

Genotype analysis. EDTA-blood samples of the patients and their family were obtained after informed consent had been given. DNA was prepared according to standard protocols (QIAampDNA Blood Mini Kit, Qiagen, Germany). The genebank accession number used was NM_198253 for the cDNA and amino acid sequences.

Telomere length measurement via flow-FISH. Telomere length in lymphocytes and granulocytes from the peripheral blood of our patients was analyzed using flow-FISH as previously described [40, 52, 53]. Briefly, samples were analyzed in triplicates with and without Alexa488-(C3TA2) PNA staining (Panagene, Daejeon, South Korea). Granulocytes, lymphocytes and cow thymocytes were identified based on forward scatter and LDS 751 staining. Cow thymocytes with known telomere length were used as an internal control to calculate telomere length in kilobases. To determine the percentiles, linear regression on 104 blood samples from healthy donors was carried out [54, 55].

Exome capture and Illumina sequencing**.** Exome capture was carried out with the SureSelect Target Enrichment Kit v4 (Agilent, Santa Clara, CA) according to manufacturer's instructions (version 1.7, July, 2014). DNA concentration was determined with the Qubit fluorometer using the BR dsDNA Assay (Qubit 2.0, Invitrogen Life Technologies, Grand Island, NY). 3 µg of genomic DNA was sheared using Covaris S2 instrument (Covaris, Woburn, Mass, USA) to a mean size of 150-200bp. 500 ng of the library was subjected to hybridization with the SureSelect baits for 16 hours at 65 °C. Fragments captured in hybridization were indexed, amplified and sequenced in a paired end 100-bp mode using an Illumina HiSeq2000 deep sequencing instrument (v3 sequencing chemistry; Illumina, San Diego, CA).

Analysis of the whole exome sequencing data. Single nucleotide variant (SNV) calling was performed with the Genome Analysis Toolkit (GATK) and SAMtools mpileup [56, 57]. For GATK, the data were recalibrated with dbSNP v132 and the 1000 Genomes Project Indel release from July 5, 2011 (http://1000genomes.org). Subsequently, SNVs were called by using GATK's Unified Genotyper on the recalibrated data. All GATK calls were annotated for strand bias, low mapping quality, and SNV clusters. The GATK resulting SNV calls were intersected with the SAMtools mpileup SNV calls. All SNVs were intersected with information on gene coding regions by using the Annotation of Genetic Variants framework (ANNOVAR) [58]. By using RefSeq gene annotations, the SNVs were classified as nonsynonymous SNVs affecting protein-coding regions. ANNOVAR was also used to compute the overlap with dbSNP v132 (www.ncbi.nlm.nih.gov/projects/SNP), and

the October 2011 SNV releases of the 1000 Genomes Project (http://1000genomes.org). Additionally the SNVs were filtered using an in-house database, which is based on more than 25 deeply sequenced (>30x coverage) human genomes and which includes sites that are commonly identified as false-positive SNVs by using GATK and SAMtools mpileup. Following these additional filtering steps, candidate SNVs were evaluated computationally to assess the possible effect of an amino acid substitution on the structure and function of the respective protein by using SIFT and PolyPhen-2 [30, 59].

To verify the results obtained by whole exome sequencing, the coding regions of the TERT gene were PCR-amplified and sequenced (GATC Biotech AG, Germany). Primer sequences used for fragment amplification and sequencing are available on request.

Plasmid constructs. The 3xHA-TERT in pCDNA-minigene was kindly provided by Steven Artandi over addgene (pCDNA-3xHA-hTERT, addgene plasmid #51637) [60]. Functionality of this TERT construct with 3xHA at the N-terminus has been previously shown by immortalization of human fibroblasts that lack TERT expression [60].

The 3xHA-TERT T1129P minigene was constructed using the following primers:
forward primer Asc1Tert: CGGGGGCGCGCCCCGCG CGCTCCCCG
reverse primer Pac1Tert: AGACTTAATTAATCAGTC CAGGATGGGCTTGAAGTCTG.

After PCR amplification, the PCR products were digested with AscI and PacI and inserted in an AscI and PacI digested pCDNA vector. The identity of all constructs was confirmed by DNA sequencing (GATC Biotech AG, Germany).

The TERC minigene (pBS U3-hTR-500, addgene plasmid #28170) was kindly provided by Kathleen Collins over addgene [61].

Cell culture and transient transfection. HeLa-cells were grown in Dulbecco's modified Eagle's medium (DMEM) supplemented with 10% FCS and 1% P/S at 37°C and 5% CO_2. Cells were transiently transfected by calcium phosphate precipitation in 6-well plates using 3µg of the test construct DNA as described before [62].

Immunocytochemistry. For immunocytochemical detection of the HA-epitope, transfected cells that had been grown on coverslips in 6-well plates were fixed in 4% paraformaldehyde in phosphate-buffered saline (PBS) for 20min at 4°C and pre-treated with 5% FCS in PBS+/-T (0.1% Triton X-100 in PBS) for 20min at RT to block unspecific antibody binding and to permeabilize the cells. The cells were then incubated with a mouse monoclonal anti-HA antibody (Sigma-Aldrich) at 1:1,000 in 3% FCS/PBS. Immunoreactivity was visualized by a goat anti-mouse secondary antibody conjugated to AlexaFluor488 (CellSignaling) (1.1,000 in 3% FCS/PBS). Before mounting the coverslips upside down in moviol 4-88 (Carl Roth) on slides, cells were washed 3x with PBS and nuclei were visualized by staining with DAPI (4'-6-Diamidino-2-phenylindole, 10mg/ml stock solution, Sigma-Aldrich), diluted 1:10,000 in PBS for 10min at RT.

Microscopy and quantification. Cells were imaged in the 405 and 488nm laser channels (DAPI excitation 405nm, emission 455nm; AlexaFluor excitation 488nm, emission 525nm) using a spinning-disk confocal microscope (Perkin Elmer ERS-6 with a Hamamatsu C9100-50 camera).The system incorporated a Nikon Eclipse TE2000-U inverted microscope using a Nikon 100x objective. Perkin-Elmer Ultraview ERS software and Volocity 6.3 software (Improvision, Lexington, MA) were used for acquisition. Images were subsequently cropped in Adobe Photoshop CS2. Cropped images were imported into Corel Draw X5 for the final figures presented.

For quantification of nuclear accumulation and clustering in the nuclei, 100 cells each from 3 independent transfections have been assessed and counted visually for the presence of nuclear staining and/or nuclear clustering. For statistical analysis a student's unpaired two-sided t-test was used.

Patient data and material. Patient data and samples were acquired and the patient was treated in accordance with the Helsinki Declaration of 1975.

After written consent, the bone marrow sample was taken according to standard procedures as a necessary routine assessment in bone marrow failure patients to determine cellularity and further cytogenetic aberrations.

Skin fibroblasts were obtained by standard procedures from underarm skin under local anesthesia and grown in DMEM (LifeTechnologies) media supplemented with 10% FCS, 1% P/S and 1% fungizone (LifeTechnologies) at 37°C in 5% CO_2.

Determination of population doublings in skin fibroblast cultures. Monolayers were dissociated with trypsin/EDTA and resuspended cells in complete

medium. To check for viability, cells were diluted 1:2 with trypan blue (LifeTechnologies). Viable cells remained unstained. Viability and number were determined using a hemacytometer (improved Neubauer). Population doublings were calculated using the following equation: PD=X + log2(Y/I) where: X = initial PD I = cell inoculum (number of cells plated in the flask) Y = final cell yield (number of cells at the end of the growth period).

Beta-galactosidase (ß-Gal) Staining + DAPI. Fibroblasts were cultured in DMEM/10% FCS/1%PenStrep containing either DMSO (negative control) or 5 nM rapamycin dissolved in DMSO. For several time points cells were semi-confluently seeded on 18mm-coverslips in DMEM/10%FCS/1%PenStrep at 37°C and 5% CO^2. Senescence associated ß-Gal staining was performed according to a modified published protocol [63]. After 24h cells were washed twice with PBS and fixed with 0.1% glutaraldehyde at room temperature for 15 minutes. Following two washing steps with PBS, fibroblasts were stained for ß-galactosidase using a 0.1%ß-Gal / 5 mM Potassium hexacyano-ferrate (II)/5 mM Potassium hexacyano-ferrate (III)/2 mM $MgCl_2$ / 7.4mM Citric Acid / 150 mM NaCl- solution at pH6 for 14-16 hours at 37°C. Nuclei were visualized by staining with DAPI (4'-6-Diamidino-2-phenylindole, 10mg/ml stock solution, Sigma-Aldrich), diluted 1:10,000 in PBS for 20min at RT. Two additional washings with PBS were performed before embedding coverslips upside down in moviol 4-88 (Carl Roth) on slides. Cells were observed at 20-fold magnification on an Olympus CellR microscope and pictures taken at brightfield and fluorescent light (Ex 330-385, Em LP420), respectively. Depicted overlays of brightfield and fluorescence were merged in Fiji.

Quantification of ß-Gal positive cells. The self-written macro Nuclei_PeripheryMeasure was used to count the number of cells with a cytosolic signal above a user-defined threshold within a cell population. As output, the number of criteria-matching cell counts with respect to the total number of cells is provided. The macro works on images or image stacks with at least two channels. In short, the macro takes the nuclear signal (here DAPI) in one channel as reference for individual cells. Segmentation of nuclei is done by intensity thresholding. The corresponding nuclear areas are registered and used to create binary images as masks. In order to measure the cytosolic signal of the second channel (here ß-Gal), dilations are performed on the binary images in a user-defined manner to match cell dimensions. The resulting mask images with intensity values 0 (background) and 1 (foreground) are multiplied with the images of the second channel to select the areas for measurement. For the analysis, the user can specify both a general signal intensity threshold and a minimal number of pixels required above that threshold for positive counts. The software is available as ImageJ macro and can be downloaded from http://www.zmbh.uniheidelberg.de/Central_Services/Imaging_Facility/2D_ImageJ_Macros.html [64]. The following settings were used to define ß-Gal positive cells in the programmed plugin: Find and add nuclei to the ROI manger (yes). Substract background (yes), maximum nuclei radius 80 pixels, minimum nuclei size 300 pixels, maximum nuclei size 4000 pixels, minimum circularity 0, maximum circularity 1. Clear ROI manager (yes). Surrounding analysis: surrounding distance (dilation) 5, threshold to detect intensity: 120, amount of pixels over threshold: 100. For quantification an average number of 200 DAPI stained cells were counted.

FACS analysis, CD34+ magnetic bead enrichment and colony forming unit assays. Bone marrow mononuclear cells were isolated by gradient centrifugation using Histopaque-1077 (Sigma) and labeled with APC-eFluor780-conjugated anti-CD34 (4H11, eBioscience), Alexa-Fluor 700-conjugated anti-CD38 (HIT2, eBioscience), a cocktail of APC-conjugated lineage antibodies consisting of anti-CD4 (RPA-T4), anti-CD8 (RPA-T8), anti-CD11b (ICRF44), anti-CD20 (2H7), anti-CD56 (B159, all BD Biosciences), anti-CD14 (61D3), anti-CD19 (HIB19) and anti-CD235a (HIR2, all eBiocience) and DAPI (Sigma). FACS analysis was performed on LSR Fortessa (BD Biosciences).

CD34+ cells from MNC were isolated using MACS enrichment columns (Miltenyi Biotec) according to the manufacturer's instructions. CD34+ cells were plated in methylcellulose medium (MethoCult H4434; StemCell Technologies) with 5nM rapamycin or DMSO. Colonies were counted after 14 days and pictures were taken with a Nikon Eclipse Ti microscope.

Mouse transplantation and in-vivo rapamycin treatment. Animals were housed under specific pathogen-free conditions at the central animal facility of the German Cancer Research Center (DKFZ). All animal experiments were approved by the Regierungspräsidium Karlsruhe under "Tierversuchsantrag G210/12".

Female NSG mice with 8 weeks of age were sub-lethally irradiated (175 cGy) one day before the cells were injected in the femoral bone marrow cavity. For the healthy control 10^5 CD34+ cells were injected along with 5 $x10^5$ MSCs. For the patient 10^6 CD34-negative MNCs cells were injected along with 5 $x10^5$ MSCs. 90 day slow release implantable pellets (Innovative

Research of America, USA) with 9mg rapamycin/pellet or placebo were implanted subcutaneously on the day of transplantation.

Recipient mice were analyzed 12 weeks post transplantation. Bone marrow cells were labeled with PE-conjugated anti-human CD45 (2D1), APC-eFluor780-conjugated anti-mouse CD45 (30-F11), PE-Cy5-conjugated anti-human CD3 (UCHT1), APC-labeled anti-human CD19 (HIB19), PE-Cy7-conjugated anti-human CD33 (WM-53, all from ebioscience) to assess multilineage human hematopoietic engraftment.

ACKNOWLEDGEMENT

The authors acknowledge the staff at the Nikon Imaging Center at the University of Heidelberg for their assistance and for providing their excellent facility for imaging. We thank Dr. Michaela Socher and A. Rathgeb from the DKFZ Central Animal Facility for excellent mouse husbandry, and the EMBL GeneCore and EMBL IT for technical support.

Funding

C.S. was supported by the Frontier program of the University of Heidelberg. This work was supported by the SFB 1036 of the Deutsche Forschungsgemeinschaft (DFG) and the Forschergruppe NicHem (FOR 2033) of the DFG and by the Dietmar Hopp Stiftung.

Conflict of interest statement

The authors have no relevant conflicts of interest to disclose.

REFERENCES

1. Hug N and Lingner J. Telomere length homeostasis. Chromosoma. 2006; 115:413-425.

2. Lingner J, Cooper JP and Cech TR. Telomerase and DNA end replication: no longer a lagging strand problem? Science. 1995; 269:1533-1534.

3. Shay JW and Wright WE. Telomeres and telomerase in normal and cancer stem cells. FEBS Lett. 2010; 584:3819-3825.

4. Diaz de Leon A, Cronkhite JT, Katzenstein AL, Godwin JD, Raghu G, Glazer CS, Rosenblatt RL, Girod CE, Garrity ER, Xing C and Garcia CK. Telomere lengths, pulmonary fibrosis and telomerase (TERT) mutations. PloS one. 2010; 5:e10680.

5. Batista LF, Pech MF, Zhong FL, Nguyen HN, Xie KT, Zaug AJ, Crary SM, Choi J, Sebastiano V, Cherry A, Giri N, Wernig M, Alter BP, et al. Telomere shortening and loss of self-renewal in dyskeratosis congenita induced pluripotent stem cells. Nature. 2011; 474:399-402.

6. Agarwal S, Loh YH, McLoughlin EM, Huang J, Park IH, Miller JD, Huo H, Okuka M, Dos Reis RM, Loewer S, Ng HH, Keefe DL, Goldman FD, et al. Telomere elongation in induced pluripotent stem cells from dyskeratosis congenita patients. Nature. 2010; 464:292-296.

7. Du HY, Pumbo E, Ivanovich J, An P, Maziarz RT, Reiss UM, Chirnomas D, Shimamura A, Vlachos A, Lipton JM, Goyal RK, Goldman F, Wilson DB, et al. TERC and TERT gene mutations in patients with bone marrow failure and the significance of telomere length measurements. Blood. 2009; 113:309-316.

8. Dokal I. Dyskeratosis congenita in all its forms. British journal of haematology. 2000; 110:768-779.

9. Armanios M and Blackburn EH. The telomere syndromes. Nat Rev Genet. 2012; 13:693-704.

10. Mason PJ and Bessler M. The genetics of dyskeratosis congenita. Cancer Genet. 2011; 204:635-645.

11. Tummala H and Walne AJ. Long tails, short telomeres: Dyskeratosis congenita. Oncotarget. 2015; 6:13856-13857.

12. Calado RT and Young NS. Telomere maintenance and human bone marrow failure. Blood. 2008; 111:4446-4455.

13. Townsley DM, Dumitriu B and Young NS. Bone marrow failure and the telomeropathies. Blood. 2014; 124:2775-2783.

14. Savage SA and Alter BP. The role of telomere biology in bone marrow failure and other disorders. Mechanisms of ageing and development. 2008; 129:35-47.

15. Calado RT. Telomeres and marrow failure. Hematology / the Education Program of the American Society of Hematology American Society of Hematology Education Program. 2009:338-343.

16. Gadalla SM, Cawthon R, Giri N, Alter BP and Savage SA. Telomere length in blood, buccal cells, and fibroblasts from patients with inherited bone marrow failure syndromes. Aging (Albany NY). 2010; 2:867-874.

17. Brummendorf TH and Balabanov S. Telomere length dynamics in normal hematopoiesis and in disease states characterized by increased stem cell turnover. Leukemia. 2006; 20:1706-1716.

18. Karlseder J, Smogorzewska A and de Lange T. Senescence induced by altered telomere state, not telomere loss. Science. 2002; 295:2446-2449.

19. Islam A, Rafiq S, Kirwan M, Walne A, Cavenagh J, Vulliamy T and Dokal I. Haematological recovery in dyskeratosis congenita patients treated with danazol. British journal of haematology. 2013; 162:854-856.

20. Ziegler P, Schrezenmeier H, Akkad J, Brassat U, Vankann L, Panse J, Wilop S, Balabanov S, Schwarz K, Martens UM and Brummendorf TH. Telomere elongation and clinical response to androgen treatment in a patient with aplastic anemia and a heterozygous hTERT gene mutation. Ann Hematol. 2012; 91:1115-1120.

21. Zlateska B, Ciccolini A and Dror Y. Treatment of dyskeratosis congenita-associated pulmonary fibrosis with danazol. Pediatric pulmonology. 2015.

22. Zawar V and Sankalecha C. Facial hirsutism following danazol therapy. Cutis. 2004; 74:301-303.

23. Riedl MA. Critical appraisal of androgen use in hereditary angioedema: a systematic review. Ann Allergy Asthma Immunol. 2015; 114:281-288 e287.

24. Yabe M, Yabe H, Hattori K, Morimoto T, Hinohara T, Takakura I, Shimizu T, Shimamura K, Tang X and Kato S. Fatal interstitial pulmonary disease in a patient with dyskeratosis congenita after allogeneic bone marrow transplantation. Bone marrow transplantation. 1997; 19:389-392.

25. Amarasinghe K, Dalley C, Dokal I, Laurie A, Gupta V and Marsh J. Late death after unrelated-BMT for dyskeratosis congenita following conditioning with alemtuzumab, fludarabine and melphalan. Bone marrow transplantation. 2007; 40:913-914.

26. Giri N, Lee R, Faro A, Huddleston CB, White FV, Alter BP and Savage SA. Lung transplantation for pulmonary fibrosis in dyskeratosis congenita: Case Report and systematic literature review. BMC Blood Disord. 2011; 11:3.

27. Laplante M and Sabatini DM. mTOR signaling in growth control and disease. Cell. 2012; 149:274-293.

28. Demidenko ZN and Blagosklonny MV. Growth stimulation leads to cellular senescence when the cell cycle is blocked. Cell Cycle. 2008; 7:3355-3361.

29. Demidenko ZN, Zubova SG, Bukreeva EI, Pospelov VA, Pospelova TV and Blagosklonny MV. Rapamycin decelerates cellular senescence. Cell Cycle. 2009; 8:1888-1895.

30. Adzhubei IA, Schmidt S, Peshkin L, Ramensky VE, Gerasimova A, Bork P, Kondrashov AS and Sunyaev SR. A method and server for predicting damaging missense mutations. Nature methods. 2010; 7:248-249.

31. Ng PC and Henikoff S. SIFT: Predicting amino acid changes that affect protein function. Nucleic acids research. 2003; 31:3812-3814.

32. Zhong FL, Batista LF, Freund A, Pech MF, Venteicher AS and Artandi SE. TPP1 OB-fold domain controls telomere maintenance by recruiting telomerase to chromosome ends. Cell. 2012; 150:481-494.

33. Abreu E, Aritonovska E, Reichenbach P, Cristofari G, Culp B, Terns RM, Lingner J and Terns MP. TIN2-tethered TPP1 recruits human telomerase to telomeres in vivo. Molecular and cellular biology. 2010; 30:2971-2982.

34. Cristofari G, Adolf E, Reichenbach P, Sikora K, Terns RM, Terns MP and Lingner J. Human telomerase RNA accumulation in Cajal bodies facilitates telomerase recruitment to telomeres and telomere elongation. Molecular cell. 2007; 27:882-889.

35. Cristofari G and Lingner J. Telomere length homeostasis requires that telomerase levels are limiting. The EMBO journal. 2006; 25:565-574.

36. Goldstein S. Replicative senescence: the human fibroblast comes of age. Science. 1990; 249:1129-1133.

37. Dimri GP, Lee X, Basile G, Acosta M, Scott G, Roskelley C, Medrano EE, Linskens M, Rubelj I, Pereira-Smith O and et al. A biomarker that identifies senescent human cells in culture and in aging skin in vivo. Proceedings of the National Academy of Sciences of the United States of America. 1995; 92:9363-9367.

38. Cristofalo VJ, Volker C, Francis MK and Tresini M. Age-dependent modifications of gene expression in human fibroblasts. Critical reviews in eukaryotic gene expression. 1998; 8:43-80.

39. Medyouf H, Mossner M, Jann JC, Nolte F, Raffel S, Herrmann C, Lier A, Eisen C, Nowak V, Zens B, Mudder K, Klein C, Oblander J, et al. Myelodysplastic cells in patients reprogram mesenchymal stromal cells to establish a transplantable stem cell niche disease unit. Cell stem cell. 2014; 14:824-837.

40. Rufer N, Brummendorf TH, Kolvraa S, Bischoff C, Christensen K, Wadsworth L, Schulzer M and Lansdorp PM. Telomere fluorescence measurements in granulocytes and T lymphocyte subsets point to a high turnover of hematopoietic stem cells and memory T cells in early childhood. J Exp Med. 1999; 190:157-167.

41. Aubert G, Baerlocher GM, Vulto I, Poon SS and Lansdorp PM. Collapse of telomere homeostasis in hematopoietic cells caused by heterozygous mutations in telomerase genes. PLoS Genet. 2012; 8:e1002696.

42. Marrone A, Walne A, Tamary H, Masunari Y, Kirwan M, Beswick R, Vulliamy T and Dokal I. Telomerase reverse-transcriptase homozygous mutations in autosomal recessive dyskeratosis congenita and Hoyeraal-Hreidarsson syndrome. Blood. 2007; 110:4198-4205.

43. Vulliamy TJ, Kirwan MJ, Beswick R, Hossain U, Baqai C, Ratcliffe A, Marsh J, Walne A and Dokal I. Differences in disease severity but similar telomere lengths in genetic subgroups of patients with telomerase and shelterin mutations. PloS one. 2011; 6:e24383.

44. Vulliamy TJ, Walne A, Baskaradas A, Mason PJ, Marrone A and Dokal I. Mutations in the reverse transcriptase component of telomerase (TERT) in patients with bone marrow failure. Blood Cells Mol Dis. 2005; 34:257-263.

45. Banik SS, Guo C, Smith AC, Margolis SS, Richardson DA, Tirado CA and Counter CM. C-terminal regions of the human telomerase catalytic subunit essential for in vivo enzyme activity. Molecular and cellular biology. 2002; 22:6234-6246.

46. Blagosklonny MV. Geroconversion: irreversible step to cellular senescence. Cell Cycle. 2014; 13:3628-3635.

47. Komarova EA, Antoch MP, Novototskaya LR, Chernova OB, Paszkiewicz G, Leontieva OV, Blagosklonny MV and Gudkov AV. Rapamycin extends lifespan and delays tumorigenesis in heterozygous p53+/- mice. Aging (Albany NY). 2012; 4:709-714.

48. Klermund J, Bender K and Luke B. High nutrient levels and TORC1 activity reduce cell viability following prolonged telomere dysfunction and cell cycle arrest. Cell Rep. 2014; 9:324-335.

49. Leontieva OV and Blagosklonny MV. Gerosuppression in confluent cells. Aging (Albany NY). 2014; 6:1010-1018.

50. Leontieva OV, Demidenko ZN and Blagosklonny MV. Contact inhibition and high cell density deactivate the mammalian target of rapamycin pathway, thus suppressing the senescence program. Proceedings of the National Academy of Sciences of the United States of America. 2014; 111:8832-8837.

51. Qi H, Su FY, Wan S, Chen Y, Cheng YQ and Liu AJ. The antiaging activity and cerebral protection of rapamycin at micro-doses. CNS Neurosci Ther. 2014; 20:991-998.

52. Beier F, Balabanov S, Buckley T, Dietz K, Hartmann U, Rojewski M, Kanz L, Schrezenmeier H and Brummendorf TH. Accelerated telomere shortening in glycosylphosphatidylinositol (GPI)-negative compared with GPI-positive granulocytes from patients with paroxysmal nocturnal hemoglobinuria (PNH) detected by proaerolysin flow-FISH. Blood. 2005; 106:531-533.

53. Beier F, Masouleh BK, Buesche G, Ventura Ferreira MS, Schneider RK, Ziegler P, Wilop S, Vankann L, Gattermann N, Platzbecker U, Giagounidis A, Götze KS, Nolte F, et al. Telomere dynamics in patients with del (5q) MDS before and under treatment with lenalidomide. Leukemia Research. 2015.

54. Weidner CI, Lin Q, Koch CM, Eisele L, Beier F, Ziegler P, Bauerschlag DO, Jockel KH, Erbel R, Muhleisen TW, Zenke M, Brummendorf TH and Wagner W. Aging of blood can be tracked by DNA methylation changes at just three CpG sites. Genome Biol. 2014; 15:R24.

55. Stepensky P, Rensing-Ehl A, Gather R, Revel-Vilk S, Fischer U, Nabhani S, Beier F, Brummendorf TH, Fuchs S, Zenke S, Firat E, Pessach VM, Borkhardt A, et al. Early-onset Evans syndrome, immunodeficiency, and premature immunosenescence

associated with tripeptidyl-peptidase II deficiency. Blood. 2015; 125:753-761.

56. DePristo MA, Banks E, Poplin R, Garimella KV, Maguire JR, Hartl C, Philippakis AA, del Angel G, Rivas MA, Hanna M, McKenna A, Fennell TJ, Kernytsky AM, et al. A framework for variation discovery and genotyping using next-generation DNA sequencing data. Nature genetics. 2011; 43:491-498.

57. Li H, Handsaker B, Wysoker A, Fennell T, Ruan J, Homer N, Marth G, Abecasis G, Durbin R and Genome Project Data Processing S. The Sequence Alignment/Map format and SAMtools. Bioinformatics. 2009; 25:2078-2079.

58. Wang K, Li M and Hakonarson H. ANNOVAR: functional annotation of genetic variants from high-throughput sequencing data. Nucleic acids research. 2010; 38:e164.

59. Kumar P, Henikoff S and Ng PC. Predicting the effects of coding non-synonymous variants on protein function using the SIFT algorithm. Nature protocols. 2009; 4:1073-1081.

60. Venteicher AS, Meng Z, Mason PJ, Veenstra TD and Artandi SE. Identification of ATPases pontin and reptin as telomerase components essential for holoenzyme assembly. Cell. 2008; 132:945-957.

61. Fu D and Collins K. Distinct biogenesis pathways for human telomerase RNA and H/ACA small nucleolar RNAs. Molecular cell. 2003; 11(5):1361-1372.

62. Stockklausner C, Breit S, Neu-Yilik G, Echner N, Hentze MW, Kulozik AE and Gehring NH. The uORF-containing thrombopoietin mRNA escapes nonsense-mediated decay (NMD). Nucleic acids research. 2006; 34:2355-2363.

63. Debacq-Chainiaux F, Erusalimsky JD, Campisi J and Toussaint O. Protocols to detect senescence-associated beta-galactosidase (SA-betagal) activity, a biomarker of senescent cells in culture and in vivo. Nature protocols. 2009; 4:1798-1806.

64. Schneider CA, Rasband WS and Eliceiri KW. NIH Image to ImageJ: 25 years of image analysis. Nature methods. 2012; 9:671-675.

Research Paper

The p53 tumor suppressor protein protects against chemotherapeutic stress and apoptosis in human medulloblastoma cells

Sarah Waye[1#], Aisha Naeem[1#], Muhammad Umer Choudhry[1#], Erika Parasido[1], Lucas Tricoli[1], Angiela Sivakumar[1], John P. Mikhaiel[1], Venkata Yenugonda[1], Olga C. Rodriguez[1], Sana D. Karam[2], Brian R. Rood[3], Maria Laura Avantaggiati[1*], and Chris Albanese[1,4,*]

[1]Lombardi Comprehensive Cancer Center and Department of Oncology, Georgetown University Medical Center, Washington, DC 20057, USA
[2]Department of Radiation Oncology, University of Colorado, Denver, CO 80208, USA
[3]Center for Cancer and Immunology Research, Children's National Medical Center, Washington, DC 20057, USA
[4]Department of Pathology, Georgetown University Medical Center, Washington, DC 20057, USA
[#]These authors contributed equally
[*]Equal Senior Author Contributions

Key words: p53, apoptosis, autophagy, medulloblastoma, Endonuclease G, BIK, p63, p73
Received: 08/30/15; Accepted: 10/02/15; Published: 10/27/15 DOI: 10.18632/aging.100831
Correspondence to: Chris Albanese, PhD; **E-mail:** albanese@georgetown.edu

Copyright: Waye et al. This is an open-access article distributed under the terms of the Creative Commons Attribution License, which permits unrestricted use, distribution, and reproduction in any medium, provided the original author and source are credited

Abstract: **Medulloblastoma (MB), a primitive neuroectodermal tumor, is the most common malignant childhood brain tumor and remains incurable in about a third of patients. Currently, survivors carry a significant burden of late treatment effects. The p53 tumor suppressor protein plays a crucial role in influencing cell survival in response to cellular stress and while the p53 pathway is considered a key determinant of anti-tumor responses in many tumors, its role in cell survival in MB is much less well defined. Herein, we report that the experimental drug VMY-1-103 acts through induction of a partial DNA damage-like response as well induction of non-survival autophagy. Surprisingly, the genetic or chemical silencing of p53 significantly enhanced the cytotoxic effects of both VMY and the DNA damaging drug, doxorubicin. The inhibition of p53 in the presence of VMY revealed increased late stage apoptosis, increased DNA fragmentation and increased expression of genes involved in apoptosis, including *CAPN12* and *TRPM8, p63, p73, BIK, EndoG, CIDEB, P27^{Kip1} and P21^{cip1}*. These data provide the groundwork for additional studies on VMY as a therapeutic drug and support further investigations into the intriguing possibility that targeting p53 function may be an effective means of enhancing clinical outcomes in MB.**

INTRODUCTION

Medulloblastoma (MB) is a primitive neuroectodermal tumor that arises from granule neuron precursors in the cerebellum or from neural stem cells of the rhombic lip and is the most frequently diagnosed malignant brain tumor in children [1]. Approximately 70% of MB cases occur in children under the age of 10. While less common, MB is also seen in patients between 20 and 44 years of age, with incidences falling off significantly thereafter. A combination of surgery, radiotherapy, and chemotherapy has contributed to improved treatment outcomes, resulting in a 70-80% five-year disease-free patients with medulloblastoma remain significant and recurrence is frequently observed. As with many malignancies, disease recurrence is nearly always fatal, and late mortality remains a serious health issue in long-term MB survivors [2]. Moreover, current therapies result in significant negative impacts on neurological, cognitive and social development, especially in the youngest affected children. Significant efforts are therefore underway to develop more effective and less toxic MB treatments.

The efficacy of many anti-tumor agents relies on their ability to trigger the tumor suppressive activities of p53, which leads to the induction of cell death, frequently via cellular pathways of apoptosis, senescence or mitotic catastrophe. While the activity of the p53 tumor suppressor protein is highly complex [3], its expression is induced by a broad array of cell stressors including DNA-damaging chemotherapeutic drugs and can be an excellent target for therapeutic intervention ([4], see also [3]). Impairment of *p53* signaling by gene mutation or gene silencing/loss has been shown to contribute to the induction, progression and/or recurrence of many tumor types and can confer resistance to tumor therapy. p53 plays unique roles in neural development. For example, p53 has been directly implicated in neurogenesis as well as in neural stem cell self-renewal, neurite outgrowth and axonal regeneration (reviewed in [5]), and acetylation of p53 is required for the induction of neurite outgrowth [6]. Despite this knowledge and that related to the role of p53 in many malignancies, the function of p53 in MB remains under-explored. For example, unlike lung, pancreas and bladder cancers, only a minority of primary MB patients present with p53 mutation or loss, with reported frequencies between 7% [7] and 15% [8]. Interestingly, while the frequency of p53 mutations increases upon recurrence, the percentage of cells with nuclear p53 also increases, rising from 26% at diagnosis to 33% at relapse [8], suggesting that certain mechanisms underlying p53 function may still be intact. Importantly, the MAGIC consortium identified chromosome 17 deletions, where the *p53* locus is located, to be associated with chromothripsis (chromosomal fragmentation) in Group 3 MB [9], while reduced expression of p53 was seen in Group 4 MB [10]. Collectively, these findings highlight the complex and poorly defined role for p53 in human MB, and support the need for mechanistic studies into p53 activity as a possible therapeutic effector protein.

The *in vitro* [11-13] and *in vivo* [14] anti-tumor activities of an experimental CDK inhibitor, VMY-1-103 (VMY), have previously been described by us in both prostate and other solid tumors [11, 13, 15] and in MB [12, 14]. Our previous MB studies established that the extrinsic apoptotic pathway was induced by VMY, as was mitotic catastrophe in a subset of the cells [12]. In the present study, we sought to further define the molecular and genetic mechanisms by which VMY induces MB cell death. Herein, we show in both p53-wild type (D556) and p53-mutant (DAOY) MB cells lines that treatment with VMY resulted in the translocation of p53 into the nucleus, an induction of γH2AX, a decrease in MDM2 protein levels and activation of non-survival macro-autophagy. Interestingly, suppression of p53 function via shRNA knockdown or treatment with the p53 inhibitory compound Pifithrin-α (Pif) [16] resulted in significant increases in cell death following treatment with either VMY or doxorubicin. Gene expression analyses performed on D556 cells treated with VMY and Pif versus VMY alone revealed a significant increase in genes associated with apoptosis and necrosis, including the calcium pathway signaling genes *CAPN12 and TRPM8* suggesting alterations in intracellular calcium signaling may play a role in enhancing cell death. In addition, *p63* and its transcriptional target the pro-apoptotic gene *BIK* were induced, as were *p73* and its target, the caspase-independent intranucleosomal DNase, *Endonuclease-G* (Endo-G) [17].

Given the difficulties in effectively treating MB, especially recurrent disease, targeting p53 in combination with chemotherapy potentially represents a new treatment strategy for medulloblastoma.

RESULTS

Treatment of MB cells induces a durable cytotoxic effect

We have previously reported that VMY induces MB cell death [12, 14]. To test whether VMY's antiproliferative effects were sustained after removal of the compound, colony forming assays were performed. D556 cells were treated with VMY or its parent compound purvalanol B (PVB) for 18 hrs, at which point the media was changed and the cells were allowed to recover in the absence of the drugs until the control plate reached 80% confluency (approximately 3-5 days). VMY treatment resulted in a significant reduction in both the number of colonies (Fig. 1A, B, C) as well as the number of cells per colony (Fig. 1D) versus either DMSO- or PVB- treated D556 cells, which express wild type p53. The DNA damaging drug, doxorubicin (1uM), effectively killed all cells (not shown).

VMY induces a partial DNA damage-like response in DAOY and D556 MB cell lines

Our previous studies established that the induction of cell death in MB cells occurred, at least in part, through the extrinsic apoptotic pathway and mitotic disruption [12, 14]. To further investigate the mechanisms by which VMY impacts cell survival, we interrogated proteins involved in DNA damage response and stress signaling. Time course studies of VMY treatment were performed first in DAOY cells, which express mutant p53 ($p53^{C252F}$). Doxorubicin was used as a positive control for induction of a DNA damage response [18],

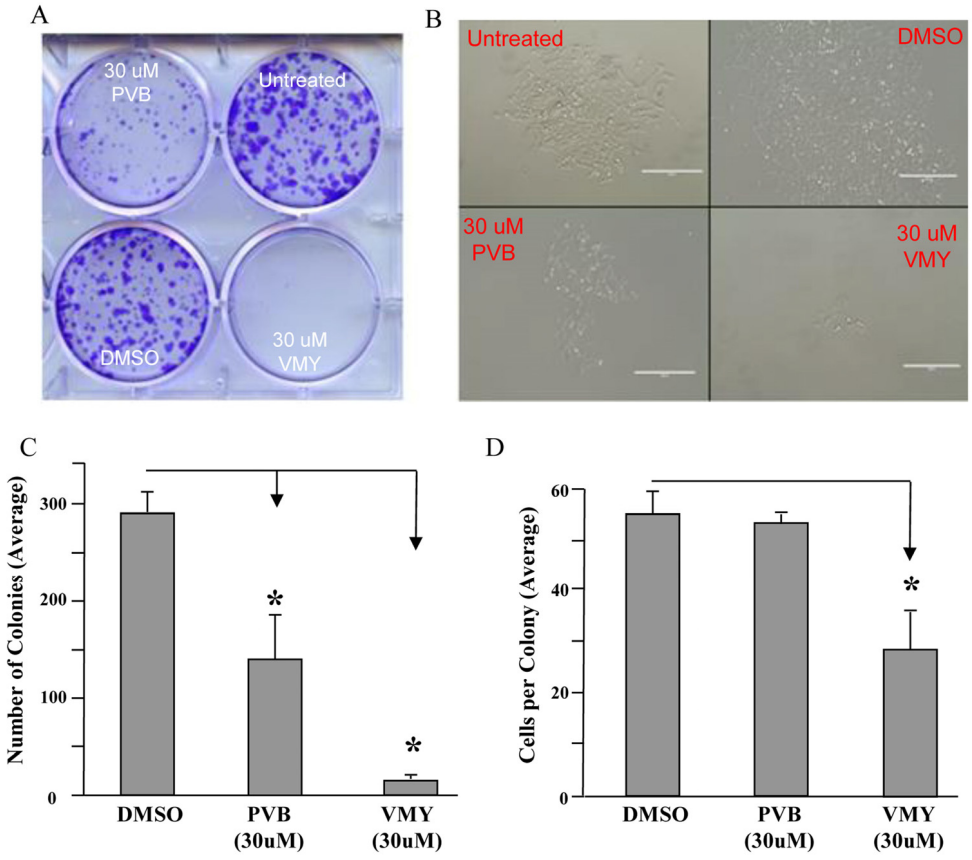

Figure 1. VMY induced cell death. The durability of effects of VMY on cell viability was determined via colony forming assays. 556 cells were treated with DMSO, PVB or VMY for 18 hrs. Fresh media was added and the cells cultured for an additional 3-5 days. (**A**) Cells stained with crystal violet. (**B**) Colonies as visualized by microscopy. (**C**) Quantification of colony number. (**D**) Quantification of cells per colony. The data are shown as average ± standard deviation. PVB; purvalanol B, *; $p<0.05$.

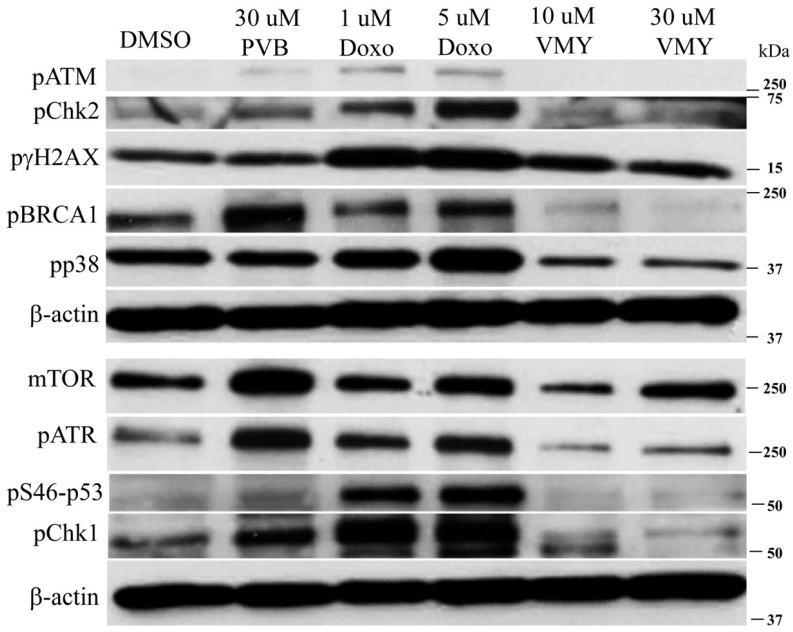

Figure 2. Effects of VMY on stress related proteins. DAOY cells were treated for 18 hrs with DMSO, PVB, VMY or doxorubicin at the concentrations listed and immunoblotting was performed for the proteins shown. β-actin was used as a loading control. PVB; purvalanol B, Doxo; doxorubicin.

and PVB was also tested. Compared to DMSO control, treatment with doxorubicin for 18 hours increased the levels of phosphorylated isoforms of ATM, Chk2, γH2AX, BRCA1 and p38 (Fig. 2) as well as ATR, pS46-p53 and Chk1 (Fig 2). A modest increase in mTOR was also noted. In contrast, the levels of all of these proteins, with the exception of p-γH2AX (Fig 2) and to a lesser extent mTOR, were reduced following treatment with VMY. Interestingly, PVB behaved in a manner similar to doxorubicin despite the fact that PVB is an inefficient inhibitor of MB cell proliferation [12]. In contrast to DAOY cells, the levels of total- and phospho- p38 remained relatively constant in D556 cells and phospho-p38 decreased slightly following 18 hrs of VMY treatment (Fig 3A), however sustained induction of γH2AX was confirmed by western blot and by immunofluorescence in both DAOY and D556 cells (Fig 3A, B).

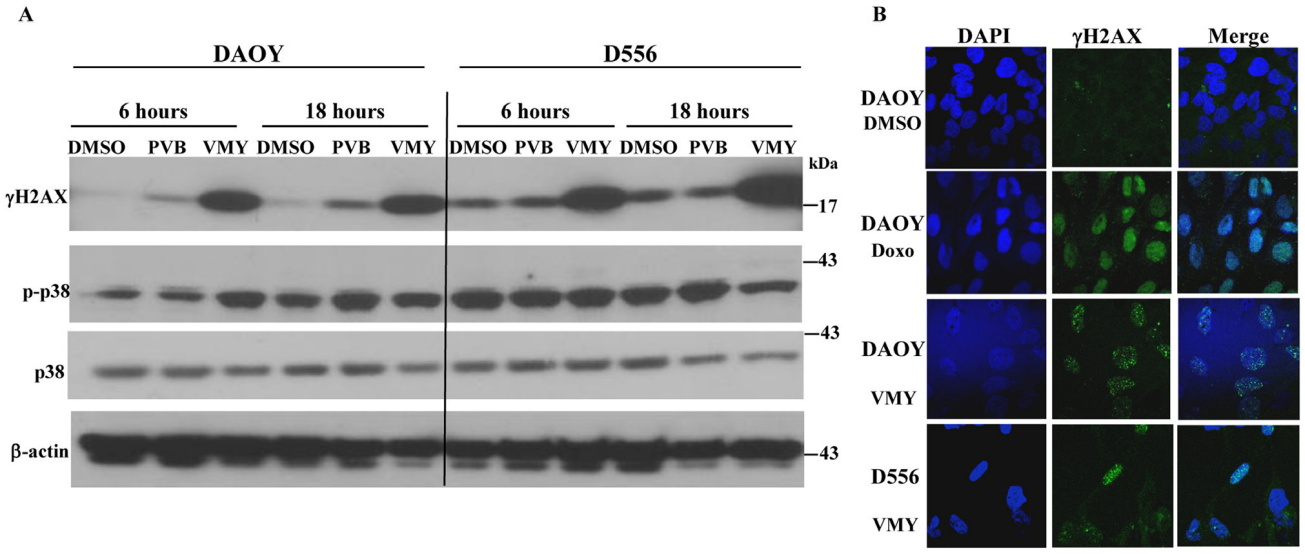

Figure 3. Effects of VMY on stress related proteins in MB cells. DAOY and D556 cells were treated with PVB or VMY. (**A**) Immunoblotting was performed for total and phosphorylated p38 and phosphorylated γ-H2AX following treatment for 6 or 18 hrs. (**B**) Immunofluorescence microscopy for γ-H2AX was performed on DAOY cells treated with 1 uM doxorubicin for 18 hrs and DAOY and D556 cells treated with 10 uM VMY for 18 hrs. DAPI was used to stain the nuclei. PVB; purvalanol B, Doxo; doxorubicin.

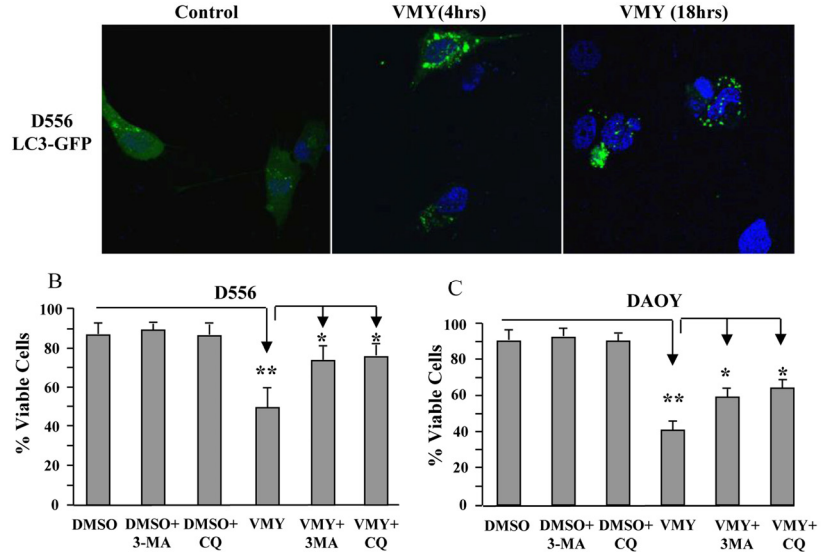

Figure 4. Induction of Autophagy by VMY reduces cell viability. (**A**) D556 cells, transfected with LC3-GFP, were treated with DMSO or VMY for 4 and 18 hrs. Autophagic LC3-GFP puncta were visualized by fluorescence microscopy. Cell nuclei were stained with DAPI. (**B**) D556 and (**C**) DAOY cells were treated with VMY for 18hrs in the presence or absence of 5 uM 3-MA (an inhibitor of early autophagy) or 50 uM chloroquine (an inhibitor of acidification of lysosomes and autophagosomes), and trypan blue viability assays were performed to establish cell viability. The data are shown as the average ± standard deviation of N=3 separate experiments. *; p<0.05, **; p<0.01, 3-MA; 3-methyladenine, CQ; chloroquine.

.

VMY induces autophagy in MB cells

VMY has the ability to block proliferation in prostate cancer cells in part through the induction of catastrophic autophagy [15]. During autophagy, LC3-I (microtubule-associated protein 1 light chain 3) becomes lipidated by the class III phosphoinositide 3-kinase, Vps34, and re-localizes from the microtubules to autophagosomal membranes (reviewed in Kang, et al. [19]). We therefore studied the pattern of subcellular localization of LC3-I in MB cells. D556 cells were transiently transfected with an LC3-GFP expression vector and subjected to fluorescence microscopy as previously described [15]. VMY treatment induced LC3-GFP re-localization and concentration into prototypical autophagic puncta (Fig 4A) with an average of 6 puncta per VMY-treated, LC3-GFP positive cell at 4 hours and 7.8 puncta per cell at 18 hrs, versus an average of 2.3 puncta per cell in control cells (Fig 4A). Our previous data established that inhibition of autophagy protected against VMY-induced cell death in prostate cancer cells [15]. We therefore investigated whether inhibitors of early (3-methyladenine, 3-MA) or late (chloroquine, CQ) autophagy influenced cell survival. Using D556 and DAOY cells, trypan blue dye exclusion assays established that neither 3-MA nor CQ influenced survival in control cells, however significant increases ($p<0.05$, N=3 separate experiments) in cell viability were seen in both cell lines when treated with VMY and the inhibitors (Fig 4B, C).

Regulation of p53 activity is similar in DAOY and D556 MB cell lines

Our earlier investigations into the mechanisms by which VMY reduced overall cell survival in solid tumors clearly established a role for wild type p53 in inducing cell death through both apoptosis and catastrophic autophagy. For example, in adenocarcinoma cell lines with wild type p53, VMY caused a rapid induction of p53 protein levels whereas p53 levels remained constant in cells harboring p53 mutations [15]. Furthermore, the loss of p53 function via deletion, mutation or genetic silencing resulted in a complete loss of VMY-induced cytotoxicity in a variety of cancers, including prostate, breast and pancreas, while re-expression of wild type p53 in PC3 cells or treatment of DU145 cells with PRIMA1 restored VMY-induced autophagy and cell death [11, 15].

We therefore next investigated the effects of VMY on p53 expression in DAOY (p53 C242F mutant [20]) and D556 cells (p53 wild type). Unlike our previous findings in adenocarcinoma cells, p53 levels were high in both cell lines and were not affected by treatment with VMY (Supplemental Fig. 1). Similar results were seen with PVB (Supplemental Fig. 1). The levels of the p53-regulatory protein MDM2 were decreased in both cell lines (Fig 5A) and immunofluorescence microscopy demonstrated that p53 shifted from diffusely cyto-plasmic with some nuclear positivity in control cells to

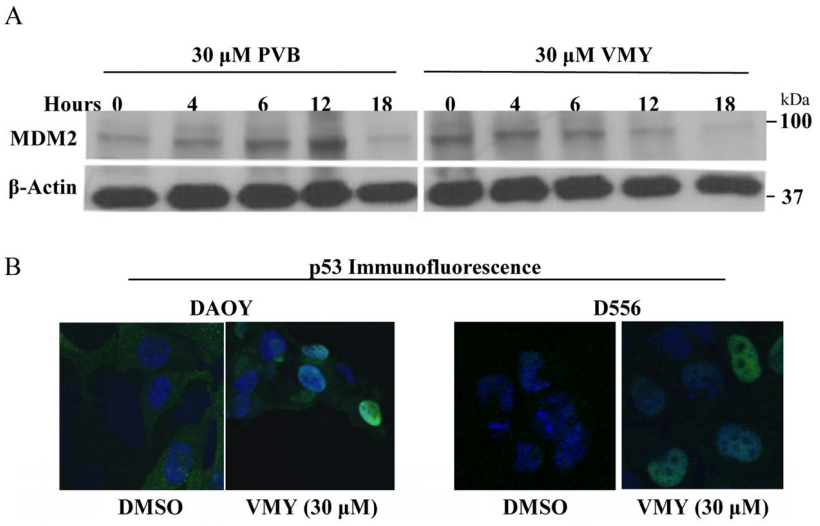

Figure 5. VMY alters the subcellular localization of p53. (**A**) Immunoblotting for MDM2 following exposure of D556 cells to PVB and VMY for the times indicated. β-actin was used as a loading control. (**B**) Immunofluorescence microscopy for p53 subcelluar localization was performed on DAOY (left panels) and D556 (right panels). DAPI was used to stain the nuclei. PVB; purvalanol B.

predominantly nuclear in both cell lines following VMY treatment (Fig 5B). As both the wild type and mutant p53 proteins localize to the nucleus following exposure to VMY, these data suggest that both proteins may retain some functional activity.

The role of p53 in inducing cell death

To determine the role of p53 in regulating MB cell survival in the presence of VMY, p53 was genetically silenced with the previously validated p53 shRNA [15] or chemically inhibited by the p53-inhibitory compound, Pifithrin-α (Pif), which we have used in previous experiments to investigate p53's role in regulating autophagy [16]. The silencing of p53 by shRNA resulted in up to a 68% decrease in p53 protein levels versus pLKO control across all treatment groups in both D556 and DAOY cells (Fig 6A). Surprisingly, both the genetic and chemical silencing of p53 led to significant increases in cell death by VMY as measured by colony forming assay (Fig 6B). Equally surprising was the observation that the loss of p53 failed to protect against cell death by doxorubicin (Fig 6B, C). Dose escalation experiments performed in D556 cells in the presence and absence of Pif established that the heightened chemosensitivity was consistent across a broad range of concentrations (Fig 6D). In addition, experiments performed in DAOY showed that cell-survival declined by 33 percent in VMY-treated cells with p53 shRNA knockdown compared to VMY-treated pLKO control cells (Sup Fig S2).

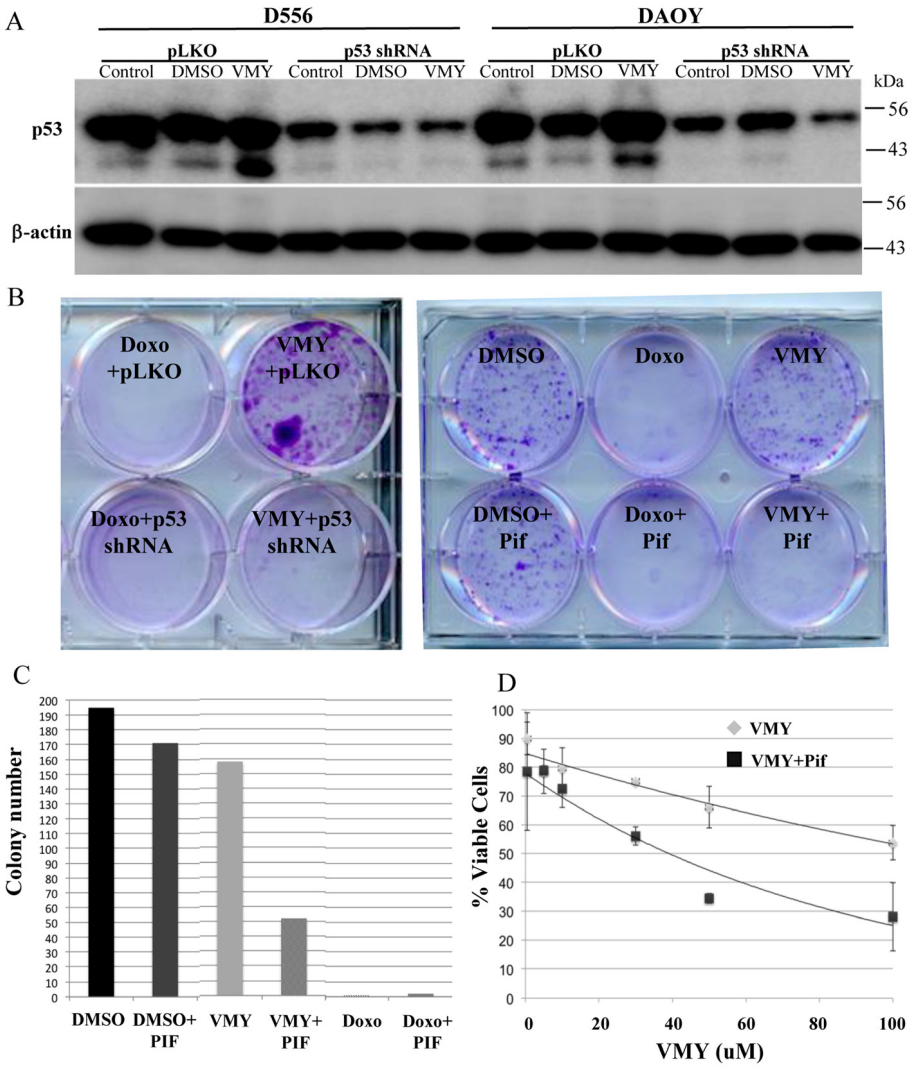

Figure 6. Effects of silencing of p53 on cell survival. (**A**) Genetic silencing of p53. D556 and DAOY cells were infected with p53siRNA or pLKO lentivirus'. The cells were left untreated or exposed for 18 hrs to DMSO or 30uM VMY as indicated, and western blots for p53 and β-actin were run. (**B**) The effects of p53shRNA knockdown (left) and Pifithrin (Pif, right) on cell viability were determined via colony forming assays. D556 cells were treated with DMSO, doxorubicin or VMY for 18 hrs. Fresh media was added and the cells cultured for an addition 3-5 days, followed by staining with crystal violet. (**C**) Quantification of the number of colonies in (**B**). (**D**) Dose response curves of D556 cells treated with VMY at the concentrations shown in the presence and absence of Pifithrin. The data are shown as average ± standard deviation of N=3 separate experiments.

Table 1. Top 25 genes altered in the presence of Pifithrin α plus VMY vs. VMY alone.

Pif + VMY *vs.* VMY			
Up-regulated	**Fold**	**Down-regulated**	**Fold**
EndoG	8.77809E+30	FIGF	-6.10476E+11
CIDEB	1.9687E+12	ANGPT4	-6.017072518
PRSS54	1299.03	GSK3A	-5.35
BIK	19.44	INCA1	-5.18
MAP3K9	18.19	TNFSF14	-4.01
ERBB3	15.17	GDF15	-4.01
BRAT1	7.48	HGF	-3.89
CISH	6.73	BIRC3	-3.41
FADD	6.73	LIF	-2.85
TP63	6.63	NTF3	-2.77
CBX6	6.23	DRD2	-2.75
SRC	5.98	SNCG	-2.67
CBX7	5.98	MAGEA9	-2.67
HDAC4	5.24	ZNF385D	-2.67
RASSF4	4.49	CRIP3	-2.67
TRPM8	4.49	TNFSF15	-2.45
ERBB2	4.06	NAP1L6	-2.45
AKT1	3.84	TENC1	-2.33
UNC5B	3.83	NRCAM	-2.23
TNFRSF10D	3.74	DNAJB7	-2.21
NLRP12-14	3.74	MAGEB2	-2.19
TP73	3.74	PPAPDC2	-2.14
ARHGEF18	3.55	PRSS12	-2.14
TNFRSF25	3.49	CFLAR	-2.07
FASTK	3.48	GADD45A	-2.07

Loss of p53 in the presence of VMY alters calcium, p63 and p73 signaling pathways

In order to more completely define the mechanism underlying the paradoxical effect of p53 silencing, RNAseq next generation sequencing was performed on D556 cells treated with VMY in the presence or absence of Pif. RNA sequence analysis revealed an increase in expression of *calpain 12* in the VMY/Pif treated cells vs. VMY/DMSO control cells (Table 1). In addition, elevated expression of the transient receptor potential channel subfamily (*TRPM8*) gene was seen (Table 1), collectively suggesting that intracellular calcium signaling pathways were affected by p53 silencing. Dysregulation of the calcium signaling pathway downstream of stressors such as excitotoxicity can lead to necrotic cell death in neurons (reviewed in [21, 22]), with one of the hallmarks of necrosis being Endo G induction and intranucleosomal DNA cleavage [22]. As both the pro-apoptosis regulatory genes p63 and p73 were induced by p53 silencing, as were possible downstream targets including Endo-G [23], the pro-apoptotic BH3-protein, BIK (Bcl-2-interacting killer) and CIDEB (cell death-inducing DFFA-like effector B), we assessed levels of late stage apoptosis and necrosis by flow cytometry, by gating for annexin V-positive/propidium iodide (PI)-positive cells. D556 cells were infected with either pLKO or p53shRNA as described above and treated for 18-hours with DMSO, 30uM VMY or 1uM doxorubicin, after which they were analyzed by flow cytometry as previously described [15]. While the annexin$^-$/PI$^+$ fraction of cells was unaffected, the silencing of p53 increased the proportion of annexin V$^+$/PI$^+$ cells following exposure to VMY or doxorubicin

A

	Relative Change (%)			
	Annexin V$^-$/PI$^+$		Annexin V$^+$/PI$^+$	
	PLKO	p53shRNA	PLKO	p53shRNA
DMSO	1	< 1.0	1	7
VMY	1	2.5	1	14
Doxo	1	< 1.0	1	11

B

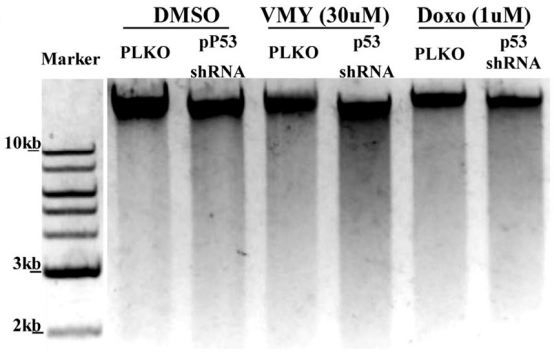

Figure 7. Effects of p53 knockdown on apoptosis and DNA fragmentation in D556 cells. (**A**) The proportion of cells undergoing apoptotic cell death as a result of p53 shRNA knockdown in D556 cells treated for 18 hrs with DMSO, VMY (30uM) or doxorubicin (1uM) as assessed using annexin V and propidium iodide (PI) staining and measured by flow cytometry. Data are shown as percent change in staining versus pLKO-control infected cells. (**B**) D556 cells were infected with pLKO or p53shRNA and treated with DMSO, VMY or doxorubicin for 18hrs. DNA fragmentation of nuclear DNA was assessed by ethidium bromide-agarose gel electrophoresis.

(Fig 7A). Finally, similar effects were seen using agarose gel electrophoresis assays where 18-hour treatment with VMY or doxorubicin plus p53shRNA resulted in enhanced DNA degradation, indicative of necrosis and apoptosis (Fig 7B).

Taken together, these experiments show that p53 protects against drug-induced cell death in medulloblastoma cells and its genetic- or chemical-suppression results in a significant increase in cell sensitivity to VMY and doxorubicin, an experimental and a clinical drug, respectively.

DISCUSSION

Necrosis, apoptosis and autophagy are activated under a variety of cell stress conditions (see references [24, 25] among others), however, little is known about how these complex and partially overlapping mechanisms are induced in medulloblastoma cells. In addition, to date, there have been few publications exploring the effects in medulloblastoma cells of the synthetic modulation of p53 activity during exposure to chemotherapeutic drugs.

We have recently shown in prostate cancer cell lines as well as in primary prostate cancer cells established using our conditional cell reprogramming approach [26, 27], that the induction of p53 by VMY was a prerequisite for inducing both autophagy and apoptosis, and that silencing p53 effectively blocked cell death [15]. Additionally, our earlier studies on VMY's effects on MB established that this experimental drug induced apoptosis and mitotic catastrophe *in vitro* [12]. Furthermore, while our *in vivo* studies showed that 20 mg/kg of VMY administered three times per week for more than four weeks was well tolerated and was effective at treating a mouse model of SHH-driven medulloblastoma [14], a detailed investigation into the mechanism of VMY-induced cell death, and the role that p53 may play had not been explored. We now show that in MB cells, VMY induces the relocalization of p53 into the nucleus, an accumulation of γH2AX, a decrease in MDM2 protein levels and activation of non-survival macro-autophagy. Since the protein levels of key stress-related proteins were reduced by VMY, the possibility existed that components of the CAP-dependent protein translation pathway may be inhibited by VMY. MNK1 is a target of p38 and MAPK and acts to increase CAP-dependent translation through the phosphorylation of the elongation factor eIF4E [28]. 4E-BP1 is a negative regulator of translation and phosphorylation of 4E-BP1 by mTOR inhibits its repressor function. Thus, if VMY negatively regulated CAP-dependent translation, the phosphorylation levels of 4E-BP1 and pMNK1 would be expected to reduce, however VMY increased the levels of these proteins in both D556 and DAOY cells (S.W and C.A, unpublished data). Interestingly, rather than protecting against chemotherapeutic cell killing, the suppression of p53 through shRNA knoc kdown or chemical inhibition by Pifithrin-α resulted in a significant increase in cell death by either VMY or doxorubicin, suggesting that p53 acts as a chemoprotective protein in these primitive neuroectoderm-derived cancer cells.

Regarding its function in the neuroectoderm, p53 performs roles different to those found in other tissues. In the past decade a role for p53 has emerged in neuronal differentiation, axon guidance, neurite outgrowth and axonal regeneration [29, 30]. Analysis of p53-dependent transcriptional activation in normal development *in vivo* by using a lacZ reporter gene under the control of a p53-responsive promoter showed that p53 activity was maximal during neuronal differentiation and clustered in areas that showed little correlation with the apoptosis normally ongoing in the developing nervous system [31, 32]. Furthermore, other studies have shown that approximately one quarter of p53-null mice developed exencephaly due to cellular overgrowth, rather than decreased apoptosis [33, 34].

The dependence of neurite outgrowth and elongation on p53 has also been shown in the developing cerebellum. Gaub et al., 2010 showed that acetylated p53 is required for neurite outgrowth in cerebellar granule cell progenitors. Conversely, the loss of the function acetyl p53 mutant (K-R) inhibits physiological neurite outgrowth in those cells [35]. In cultured rat cerebellar granule cells, Maruoka et al., 2011, showed a p53-mediated neuroprotective effect against glutathione depletion-induced oxidative stress [36].

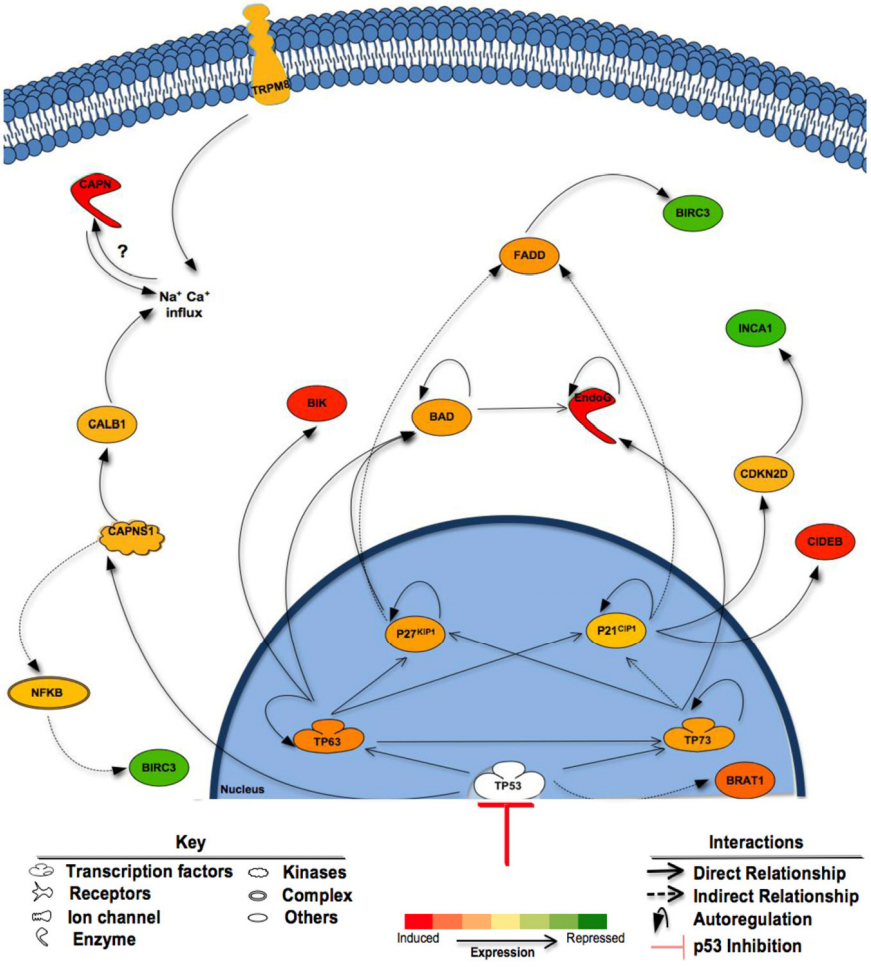

Figure 8. **Proposed mechanisms of enhanced cell death following inhibition of p53**. Shown are the effects of p53 suppression on components of cell death pathways in Pif + VMY *vs.* VMY treated D556 cells. p53 inhibition by Pifithrin resulted in the induction of *p63* and *p73* genes and subsequent enhanced cell death via apoptosis. Induction of the *p63* and *p73* genes leads to the activation of $p21^{CIP1}$ and $p27^{KIP1}$ both of which can indirectly trigger FADD, reducing the expression of BIRC3 (cIAP2). Induction of p73 led to large increases in EndoG and CIDEB expression leading to DNA fragmentation while increased levels of p63 induced apoptosis though BIRC3 and BIK, the latter of which along with TRPM8 can influence intracellular calcium levels. BAD; BCL2-Associated Agonist Of Cell Death, BIK; BCL2-Interacting Killer (Apoptosis-Inducing), BIRC3; baculoviral IAP repeat containing 3 (cIAP2), BRAT1; BRCA1-Associated ATM Activator 1, CAPN; Calpain, CALB1; Calbindin 1, CDKN2D; Cyclin-Dependent Kinase Inhibitor 2D ($p19^{Ink4D}$), CIDEB; Cell Death-Inducing DFFA-Like Effector B, EndoG; Endonuclease G, FADD; Fas-Associated Via Death Domain, INCA1; Inhibitor Of CDK, Cyclin A1 Interacting Protein 1, NF-KappaB; Nuclear Factor Of Kappa Light Polypeptide Gene Enhancer In B-Cells, TRPM8, Transient receptor potential cation channel subfamily M member 8.

Further validation of the role for p53 in neurite outgrowth and neuronal differentiation and maturation comes from studies establishing p53 as a downstream target of neurotrophic receptors. Loss of function experiments of p53 via either gene silencing or dominant negative p53 proteins lacking transactivation capacity have been shown to block NGF-dependent neurite outgrowth and differentiation in PC-12 cells [6, 37]. Another neurotrophic factor, BDNF, has also been shown to stimulate p53 phosphorylation and transcriptional activation in primary cortical neurons [30]. Activation of signaling molecules downstream of NGF or BDNF that are known to induce p53 post-translational modifications and enhance its transcriptional activity has been reported, including ERK1 and ERK2, p38MAPK, JNK1-2 (c-Jun N-terminal kinases 1-2), cytoskeleton remodeling genes, such as GAP-43, the actin-binding protein Coronin 1b and the RAS family member Rab13 [6, 38].

Unresolved however is an actual role for p53 in the biology of human MB. Frequencies of *p53* mutations are low in primary MB but increase significantly in recurrences, and mutant p53 proteins and Myc may collaborate to drive aggressive disease [8]. Additionally, modifications of p53 function are required in *Myc*- [39, 40] but not *Smoothened*- based mouse models to drive MB. The genetic silencing of *p53* in mice with conditional deletion of the *BRCA2-interacting protein* (*BCCIP*) gene also resulted in MB [41]; however the resulting tumor formation was predicated upon the loss of the BCCIP knockdown cassette, which restored BCCIP expression in the neuroectoderm, supporting a role for p53 in neuronal genomic stability. Interestingly, p53 expression levels are lower in group 4 MB, due to the iso-dicentric (17)(p11.2) recombination events frequently seen in this group [10]. However, neither the levels of p53 expression nor its subcellular localization were reported following chemotherapy. It should be noted that etoposide induced p53 activity in D283, MEDI and D458 MB cell lines *in vitro* [42] and the p53 target miR-34a was able to reduce the viability in the p53-impared MB cell line, MEB-Med8a [43], however the effects of silencing of p53 *per se* were not reported. Furthermore, docosahexaenoic acid and etoposide were found to reduce the levels of MDM2 in both p53-mutant DAOY cells as well as in p53-wildtype D283 cells [44] and we also observe decreases in MDM2 with VMY, along with rapid translocation of p53 into the nucleus. Collectively these published studies and our new data suggest that components of the p53 pathway remain intact in a variety of p53-mutant and p53-wild type MB cells.

It was therefore surprising that rather than causing chemotherapeutic resistance, the suppression of p53 function by either shRNA knockdown or Pif sensitized DAOY and D556 cells to both VMY and doxorubicin. Mechanistically, the induction of the *p63* and *p73* and their targeted genes by VMY in the Pif-treated cells was one of the most prominent features (Table 1 and Figure 8). These p53 family-member genes, and their various splice variants, play both similar and distinct roles in development as well as in cancer (reviewed in [45]) and can interact with each other with a high degree of complexity. There is abundant evidence that modulation of p53 function can influence the activity of p63 and p73 (reviewed in [46]) and conversely that p63 and p73 can influence p53 activity in adult neural precursor cells [47]. While the mechanism(s) by which the genetic knockdown or chemical suppression of p53 regulates *p63* and *p73* expression in MB cells has yet to be elucidated, our data suggest that the induction of *p63* and *p73* following p53 suppression fundamentally alters the pro-apoptotic machinery in MB cells (Fig 8). It is also unknown whether the increased sensitivity seen in the cell lines tested extends to a broader array of clinical samples or to the chemo-radiation interventions currently used for treating MB. However as both DAOY and D556 cells show similar sensitivities to p53 functional blockade, the possibility exists that at least a subset of the p53 mutations found in MB patients may not adversely impact p53-targeting regimens. Additional experiments assessing whether the p53 mutant proteins identified in recurrent MB exhibit similar responses to combined p53 suppression and exposure to VMY, doxorubicin or other drugs are clearly warranted.

MATERIALS AND METHODS

Cell lines and cell culture. The human medulloblastoma (MB) cell lines D556 and DAOY were maintained in complete DMEM containing 10% FBS, L-glutamine, and 100 U/ml Penicillin-Streptomycin as previously described [12]. DNA STR fingerprint analyses were performed on both cell lines as a quality control measure. The DAOY data matched the ATCC database for this line, while early and late passage D556 cultures were compared with no significant changes observed and no matches with the available STR database (not shown).

Cell viability and growth. Cell viability was determined using trypan blue dye exclusion and viable and total cell counting using a hemocytometer as previously described [11, 12, 15].

Colony forming assays. A total of 1000 cells were plated in 6 well plates. Cells were allowed to adhere for 24 hrs before treatment, at which point they were

treated with VMY or Doxorubicin for 18 hrs. The media was changed after 18hrs and the plates were incubated in the absence of drug for 3-5 days to reach 80% confluency in the negative control wells. Cells were washed with PBS, fixed with 10% neutral buffered formalin solution for 15-30 minutes and stained with 0.5% (w/v) crystal violet for 30-60 minutes. The crystal violet was aspirated, cells were washed with PBS and dried for one hour before counting.

Flow cytometry. The prostate cells were fixed and stained with 20ug/ml propidium iodide (PI) and 5 U RNase A, and the DNA content and subG1 DNA fragmentation was measured using a FACStar Plus system (Becton-Dickson, Franklin Lakes, NJ) as previously described [11, 12]. Cellular apoptosis was also assessed by APC-Annexin V antibody (Biolegend, San Diego, CA) staining immediately after treatment with VMY and analyzed using FACStar Plus dual laser FACSort system (Becton-Dickson, Franklin Lakes, NJ) as previously described by us [11, 12, 48, 49].

Immunoblotting. Protein extracts were prepared and separated on 4-20% Tris-glycine gels and electro-blotted onto PVDF membranes as previously described [11, 12, 50]. Protein levels were assessed using antibodies against p53 (Millipore, Bellerica, MA #05-224), p-ATM (Cell Signaling, Danvers, MA #5883P), p-Chk2 (Cell Signaling, Danvers, MA #2661P), p-Chk1 (Cell Signaling, Danvers, MA #2348P), p38 (Cell Signaling, Danvers, MA #8690), histone γ-H2AX (Cell Signaling, Danvers, MA #7631), p-histone γH2AX (Cell Signaling, Danvers, MA #9718P), p-BRCA1 (Ser1524) (Cell Signaling, Danvers, MA #9009P), p-P38 MAPK (Cell Signaling, Danvers, MA #9216S), mTOR (Cell Signaling, Danvers, MA #2983), p-ATR (Cell Signaling, Danvers, MA #2853P), p-p53 (Cell Signaling, Danvers, MA #9286P), p-MNK1 (cell signaling, #2111S), p-4E-BP1 (Cell Signaling, Danvers, MA #2855S), MDM2 (Santa Cruz Biotechnology, #sc-965), β-actin (Cell Signaling, Danvers, MA #4967). Densitometry was performed using ImageJ analysis software (NIH, Bethesda, MD) as previously described [11, 12, 50].

Immunofluorescent imaging. Cells were seeded on glass coverslips and treated with DMSO or VMY for 4 or 18 hrs. Cells were washed with PBS and fixed in 10% formalin for 10 min. The coverslips were washed three times with PBS, the cells were permeabilized with 0.1% Triton X-100 and washed three times with PBS. The samples were blocked with 1% BSA for 20 minutes and washed an additional three times in PBS. The cells were exposed to anti-p53 (1:150, Millipore #05-224) or anti-γH2AX (1:150, Cell Signaling #7631) antibodies for 1 hr at room temperature. The slides were washed with PBS an additional three times and stained with the secondary antibody Alexa Fluor goat 488 anti-mouse (1:150, Life Technologies, A-10667) for 30 min at room temperature. Slides were then counter-stained with DAPI for 5 min. The coverslips were mounted onto glass slides with Tris-buffered fluoro-gel (Electron Microscopy Sciences). Confocal microscopy was performed on a Zeiss (Thornwood, NY) LSM510 Meta microscope using a 40x lens.

LC3-GFP. LC3 translocation was detected using the green fluorescent protein (GFP)-fused LC3 construct that was generously donated by Dr Robert Clarke [51]. Briefly, cells were seeded in 6 well plates containing glass coverslips and allowed to attach overnight. The LC3-GFP expression plasmid (14ug) was transfected using Lipofectamine LTX reagent (Life Technologies, Carlsbad, CA #15338-100) as previously described by us [15]. 24 hours after transfection, the cells were treated with VMY or vehicle. After 18 hours, the coverslips with attached cells were stained with DAPI and rinsed 3 times with PBS and the coverslips mounted. Imaging was performed by confocal microscopy as previously described [12, 15].

Autophagy inhibitors. For autophagy inhibition, 3-methyladenine (3-MA) (Sigma-Aldrich, St Louis, MO #M921) was used at 5mM and chloroquine diphosphate (CQ) (Sigma-Aldrich, St Louis, MO #C6628) was used at 50 μM as previously described [15]. Cells were exposed to these inhibitors for 20 minutes prior to treatment with either DMSO or VMY [15].

p53 expression and shRNA knockdown. For lentivirus knockdown experiments, the p53shRNA and pLKO vectors were purchased commercially (Vector Biolabs, Philadelphia, PA, #1854) and used as described by the manufacturer as previously described [15]. Briefly, 293T cells (ATCC, Manassas, VA) were cotransfected with shRNA constructs along with the pHR′8.2ΔR and pCMV-VSV-G helper constructs. After 24 hours, the media was changed and the virus-containing media was harvested after an additional 24 hours of incubation. The MB cells were seeded at 30% confluency and viral infections were performed for 72 hours prior to treatment with VMY or DMSO. Efficiency of the knockdown was monitored by p53 immunoblotting and quantification by ImageJ as previously described [15, 52, 53].

Chemical inhibition of p53. For chemical inhibition of p53, 30uM Pifithrin-α (Sigma-Aldrich, St Louis, MO #P4359) was added one hour prior to treatment with VMY, doxorubicin or DMSO.

DNA fragmentation. D556 cells were infected with pLKO or p53shRNA virus's for 72 hrs prior to treatment with VMY or DMSO. Doxorubicin was used as a positive control. The genomic DNA was isolated after 18 hr treatment with VMY or doxorubicin using the DNeasy blood and tissue kit (Qiagen, MD #69506). 500ng of DNA was run on 1% agarose gel containing ethidium bromide with the electrophoresis carried out at 100V for one hour.

RNAseq and pathway analyses. Total RNA was extracted from D556 cells treated with Pif and VMY as described above using an RNeasy Plus Mini Kit (Qiagen, MD, #74134) and submitted to Otogenetics Corporation (Norcross, GA USA) for RNA-Seq assays. Sequencing was performed on the Illumina HiSeq 2500 (20 million reads, Rapid run, Illumina, CA USA) with chemistry v1.0 and using the 2×106bp paired-end read mode and original chemistry from Illumina according to the manufacturer's instructions. The initial data analysis was started directly on the HiSeq 2500 System during the run. The HiSeq Control Software 2.0.5 in combination with RTA 1.17.20.0 (real time analysis) performed the initial image analysis and base calling. Quality control (QC) was performed using FastQC software. All the samples passed the "Basic Statistics", "Per Base Sequence Quality", "Per Sequence Quality Scores", "Per Base N Content", and "Sequence Length Distribution". No specific filtering was done for the samples. The final FASTQ files comprising the sequence information which was used for all subsequent bioinformatics analyses. Sequences were de-multiplexed according to the 6bp index code with 1 mismatch allowed. After QC, Tophat2 was used for the alignment, and BAM files were obtained. Partek Genomics Suite (6.6 version 6.12.0713 software (Partek Inc.) was utilized to calculate RPKM as normalization, and fold changes were calculated based on the RPKM results. The pathways analysis was performed through the use of QIAGEN's Ingenuity Pathway Analysis (Qiagen, Redwood City, CA).

ACKNOWLEDGEMENTS

Cell cycle analyses were performed in the Lombardi Comprehensive Cancer Center's Flow Cytometry Shared Resource, microscopy was performed in the Lombardi Comprehensive Cancer Center's Microscopy and Imaging Shared Resource, the DNA fingerprint analyses were done through the Lombardi Comprehensive Cancer Center's Tissue Culture Shared Resource and the RNAseq was performed through the Lombardi Comprehensive Cancer Center's Genomics and Epigenomics Shared Resource.

Funding

Funding was provided by; ABCC (Albanese), R01CA193698 (Avantaggiati) and NIH P30 CA51008-18 (Weiner). This work was also supported by the Paul Calabresi Career Development Award for Clinical Oncology (K12, Karam) an American Cancer Society Institutional Grant (Karam) and a Howard Hughes Medical Institute University Grant (Waye). We thank Milton Brown for supplying VMY-1-103.

Conflict of interest statement

Georgetown University has submitted a patent application on VMY-1-103 where V.Y. is an inventor.

REFERENCES

1. Samkari A, White JC and Packer RJ. Medulloblastoma: toward biologically based management. Semin Pediatr Neurol. 2015; 22:6-13.

2. Ning MS, Perkins SM, Dewees T and Shinohara ET. Evidence of high mortality in long term survivors of childhood medulloblastoma. J Neurooncol. 2015;122:321-327.

3. Soussi T and Wiman KG. TP53: an oncogene in disguise. Cell Death Differ. 2015;22:1239-1249.

4. Muller PA and Vousden KH. Mutant p53 in cancer: new functions and therapeutic opportunities. Cancer Cell. 2014; 25:304-317.

5. Quadrato G and Di Giovanni S. Gatekeeper between quiescence and differentiation: p53 in axonal outgrowth and neurogenesis. Int Rev Neurobiol. 2012;105:71-89.

6. Di Giovanni S, Knights CD, Rao M, Yakovlev A, Beers J, Catania J, Avantaggiati ML and Faden AI. The tumor suppressor protein p53 is required for neurite outgrowth and axon regeneration. Embo J. 2006; 25:4084-4096.

7. Pfaff E, Remke M, Sturm D, Benner A, Witt H, Milde T, von Bueren AO, Wittmann A, Schottler A, Jorch N, Graf N, Kulozik AE, Witt O, Scheurlen W, von Deimling A, Rutkowski S, et al. TP53 mutation is frequently associated with CTNNB1 mutation or MYCN amplification and is compatible with long-term survival in medulloblastoma. J Clin Oncol. 2010; 28:5188-5196.

8. Hill RM, Kuijper S, Lindsey JC, Petrie K, Schwalbe EC, Barker K, Boult JK, Williamson D, Ahmad Z, Hallsworth A, Ryan SL, Poon E, Robinson SP, Ruddle R, Raynaud FI, Howell L, et al. Combined MYC and P53 defects emerge at medulloblastoma relapse and define rapidly progressive, therapeutically targetable disease. Cancer Cell. 2015; 27:72-84.

9. Rausch T, Jones DT, Zapatka M, Stutz AM, Zichner T, Weischenfeldt J, Jager N, Remke M, Shih D, Northcott PA, Pfaff E, Tica J, Wang Q, Massimi L, Witt H, Bender S, et al. Genome sequencing of pediatric medulloblastoma links catastrophic DNA rearrangements with TP53 mutations. Cell. 2012;148:59-71.

10. Bien-Willner GA and Mitra RD. Mutation and expression analysis in medulloblastoma yields prognostic variants and a putative mechanism of disease for i17q tumors. Acta Neuropathol Commun. 2014; 2:74.

11. Ringer L, Yenugonda VM, Ghosh A, Divito K, Trabosh V, Patel Y, Brophy A, Grindrod S, Lisanti MP, Rosenthal D, Brown ML, Avantaggiati ML, Rodriguez O and Albanese C. VMY-1-103, a dansylated analog of purvalanol B, induces caspase-3-dependent apoptosis in LNCaP prostate cancer cells. Cancer Biol Ther. 2010; 10:320-325.

12. Ringer L, Sirajuddin P, Heckler M, Ghosh A, Suprynowicz F, Yenugonda VM, Brown ML, Toretsky JA, Uren A, Lee Y, MacDonald TJ, Rodriguez O, Glazer RI, Schlegel R and Albanese C. VMY-1-103 is a novel CDK inhibitor that disrupts chromosome organization and delays metaphase progression in medulloblastoma cells. Cancer Biol Ther. 2011; 12:818-826.

13. Smahi A, Courtois G, Vabres P, Yamaoka S, Solange H, Munnich A, Israël A, Heiss NS, Klauck SKP and Wiemann Sea. Genomic rearrangment in NEMO impairs NF-kB activation and is a cause of incontinentia pigmenti (IP). Nature. 2000; 405:466-472.

14. Sirajuddin P, Das S, Ringer L, Rodriguez O, Sivakumar A, Lee Y, Uren A, Fricke S, Rood B, Ozcan A, Wang SS, Karam S, Yenugonda VM, Salinas P, Petricoin EF, 3rd, Lisanti MP, et al. Quantifying the CDK inhibitor VMY-1-103's activity and tissue levels in an in vivo tumor model by LC-MS/MS and by MRI. Cell Cycle. 2012; 11:3801-3809.

15. Ringer L, Sirajuddin P, Tricoli L, Waye S, Parasido E, Lee RJ, Feldman A, Wu C-L, Dritschilo A, Lynch J, Schlegel R, Rodriguez O, Pestell RG, Avantaggiati ML and Albanese C. The Induction of the p53 Tumor Suppressor Protein Bridges the Apoptotic and Autophagic Signaling Pathways to Regulate Cell Death in Prostate Cancer Cells. Oncotarget. 2014; 5:10678-10691.

16. Garufi A, Pucci D, D'Orazi V, Cirone M, Bossi G, Avantaggiati ML and D'Orazi G. Degradation of mutant p53H175 protein by Zn(II) through autophagy. Cell Death Dis. 2014; 5:e1271.

17. Li LY, Luo X and Wang X. Endonuclease G is an apoptotic DNase when released from mitochondria. Nature. 2001; 412:95-99.

18. Petruccelli LA, Pettersson F, Del Rincon SV, Guilbert C, Licht JD and Miller WH, Jr. Expression of leukemia-associated fusion proteins increases sensitivity to histone deacetylase inhibitor-induced DNA damage and apoptosis. Mol Cancer Ther. 2013; 12:1591-1604.

19. Kang R, Zeh HJ, Lotze MT and Tang D. The Beclin 1 network regulates autophagy and apoptosis. Cell Death Differ. 2011; 18:571-580.

20. Raffel C, Thomas GA, Tishler DM, Lassoff S and Allen JC. Absence of p53 mutations in childhood central nervous system primitive neuroectodermal tumors. Neurosurgery. 1993; 33:301-305; discussion 305-306.

21. Hara MR and Snyder SH. Cell signaling and neuronal death. Annu Rev Pharmacol Toxicol. 2007; 47:117-141.

22. Fujikawa DG. The role of excitotoxic programmed necrosis in acute brain injury. Comput Struct Biotechnol J. 2015; 13:212-221.

23. Kitagawa K and Niikura Y. Caspase-independent mitotic death (CIMD). Cell Cycle. 2008; 7:1001-1005.

24. Galluzzi L, Vitale I, Abrams JM, Alnemri ES, Baehrecke EH, Blagosklonny MV, Dawson TM, Dawson VL, El-Deiry WS, Fulda S, Gottlieb E, Green DR, Hengartner MO, Kepp O, Knight RA, Kumar S, et al. Molecular definitions of cell death subroutines: recommendations of the Nomenclature Committee on Cell Death 2012. Cell Death Differ. 2012; 19:107-120.

25. Klionsky DJ, Abdalla FC, Abeliovich H, Abraham RT, Acevedo-Arozena A, Adeli K, Agholme L, Agnello M, Agostinis P, Aguirre-Ghiso JA, Ahn HJ, Ait-Mohamed O, Ait-Si-Ali S, Akematsu T, Akira S, Al-Younes HM, et al. Guidelines for the use and interpretation of assays for monitoring autophagy. Autophagy. 2012; 8:445-544.

26. Liu X, Ory V, Chapman S, Yuan H, Albanese C, Kallakury B, Timofeeva O, Nealon C, Dalic A, Simic V, Haddad B, Rhim J, Dritschilo A, Riegel A, McBride A and Schlegel R. ROCK inhibitor and feeder cells induce the conditional reprogramming of epithelial cells. American Journal of Pathology. 2012; 180:590-607.

27. Palechor-Ceron N, Suprynowicz FA, Upadhyay G, Dakic A, Minas T, Simic V, Johnson M, Albanese C, Schlegel R and Liu X. Radiation Induces Diffusible Feeder Cell Factor(s) That Cooperate with ROCK Inhibitor to Conditionally Reprogram and Immortalize Epithelial Cells. Am J Pathol. 2013; 183:1862-1870.

28. Bhat M, Robichaud N, Hulea L, Sonenberg N, Pelletier J and Topisirovic I. Targeting the translation machinery in cancer. Nat Rev Drug Discov. 2015; 14:261-278.

29. Arakawa H. p53, apoptosis and axon-guidance molecules. Cell Death Differ. 2005; 12:1057-1065.

30. Tedeschi A and Di Giovanni S. The non-apoptotic role of p53 in neuronal biology: enlightening the dark side of the moon. EMBO Rep. 2009; 10:576-583.

31. Komarova EA, Chernov MV, Franks R, Wang K, Armin G, Zelnick CR, Chin DM, Bacus SS, Stark GR and Gudkov AV. Transgenic mice with p53-responsive lacZ: p53 activity varies dramatically during normal development and determines radiation and drug sensitivity in vivo. Embo J. 1997; 16:1391-1400.

32. Gottlieb E, Haffner R, King A, Asher G, Gruss P, Lonai P and Oren M. Transgenic mouse model for studying the transcriptional activity of the p53 protein: age- and tissue-dependent changes in radiation-induced activation during embryogenesis. Embo J. 1997; 16:1381-1390.

33. Sah VP, Attardi LD, Mulligan GJ, Williams BO, Bronson RT and Jacks T. A subset of p53-deficient embryos exhibit exencephaly. Nat Genet. 1995; 10:175-180.

34. Armstrong JF, Kaufman MH, Harrison DJ and Clarke AR. High-frequency developmental abnormalities in p53-deficient mice. Curr Biol. 1995; 5:931-936.

35. Gaub P, Tedeschi A, Puttagunta R, Nguyen T, Schmandke A and Di Giovanni S. HDAC inhibition promotes neuronal outgrowth and counteracts growth cone collapse through CBP/p300 and P/CAF-dependent p53 acetylation. Cell Death Differ. 2010; 17(9):1392-1408.

36. Maruoka H, Sasaya H, Sugihara K, Shimoke K and Ikeuchi T. Low-molecular-weight compounds having neurotrophic activity in cultured PC12 cells and neurons. J Biochem. 2011; 150:473-475.

37. Knights CD, Catania J, Di Giovanni S, Muratoglu S, Perez R, Swartzbeck A, Quong AA, Zhang X, Beerman T, Pestell RG and Avantaggiati ML. Distinct p53 acetylation cassettes differentially influence gene-expression patterns and cell fate. J Cell Biol. 2006; 173:533-544.

38. Tedeschi A, Nguyen T, Puttagunta R, Gaub P and Di Giovanni S. A p53-CBP/p300 transcription module is required for GAP-43 expression, axon outgrowth, and regeneration. Cell Death Differ. 2009; 16:543-554.

39. Kawauchi D, Robinson G, Uziel T, Gibson P, Rehg J, Gao C, Finkelstein D, Qu C, Pounds S, Ellison DW, Gilbertson RJ and Roussel MF. A mouse model of the most aggressive subgroup of human medulloblastoma. Cancer Cell. 2012; 21:168-180.

40. Pei Y, Moore CE, Wang J, Tewari AK, Eroshkin A, Cho YJ, Witt H, Korshunov A, Read TA, Sun JL, Schmitt EM, Miller CR, Buckley AF, McLendon RE, Westbrook TF, Northcott PA, et al. An animal model of MYC-driven medulloblastoma. Cancer Cell. 2012; 21:155-167.

41. Huang YY, Dai L, Gaines D, Droz-Rosario R, Lu H, Liu J and Shen Z. BCCIP suppresses tumor initiation but is required for tumor progression. Cancer Res. 2013; 73:7122-7133.

42. Meley D, Spiller DG, White MR, McDowell H, Pizer B and See V. p53-mediated delayed NF-kappaB activity enhances etoposide-induced cell death in medulloblastoma. Cell Death Dis. 2010; 1:e41.

43. Fan YN, Meley D, Pizer B and See V. Mir-34a mimics are potential therapeutic agents for p53-mutated and chemo-resistant brain tumour cells. PLoS One. 2014;9:e108514.

44. Wang F, Bhat K, Doucette M, Zhou S, Gu Y, Law B, Liu X, Wong ET, Kang JX, Hsieh TC, Qian SY and Wu E. Docosahexaenoic acid (DHA) sensitizes brain tumor cells to etoposide-induced apoptosis. Curr Mol Med. 2011; 11:503-511.

45. Moll UM and Slade N. p63 and p73: roles in development and tumor formation. Mol Cancer Res. 2004;2:371-386.

46. Pflaum J, Schlosser S and Muller M. p53 Family and Cellular Stress Responses in Cancer. Front Oncol. 2014;4:285.

47. Fatt MP, Cancino GI, Miller FD and Kaplan DR. p63 and p73 coordinate p53 function to determine the balance between survival, cell death, and senescence in adult neural precursor cells. Cell Death Differ. 2014; 21:1546-1559.

48. Albanese C, D'Amico M, Reutens AT, Fu M, Watanabe G, Lee RJ, Kitsis RN, Henglein B, Avantaggiati M, Somasundaram K, Thimmapaya B and Pestell RG. Activation of the *cyclin D1* gene by the E1A-associated protein p300 through AP-1 inhibits cellular apoptosis. J Biol Chem. 1999;274:34186-34195.

49. Albanese C, Wu K, D'Amico M, Jarrett C, Joyce D, Hughes J, Hulit J, Sakamaki T, Fu M, Ben-Ze'ev A, Bromberg JF, Lamberti C, Verma U, Gaynor RB, Byers SW and Pestell RG. IKKalpha Regulates Mitogenic Signaling through Transcriptional Induction of Cyclin D1 via Tcf. Mol Biol Cell. 2003; 14:585-599.

50. Rodriguez OC, Choudhury S, Kolukula V, Vietsch EE, Catania J, Preet A, Reynoso K, Bargonetti J, Wellstein A, Albanese C and Avantaggiati ML. Dietary downregulation of mutant p53 levels via glucose restriction: mechanisms and implications for tumor therapy. Cell Cycle. 2013;11:4436-4446.

51. Schwartz-Roberts JL, Shajahan AN, Cook KL, Warri A, Abu-Asab M and Clarke R. GX15-070 (obatoclax) induces apoptosis and inhibits cathepsin D- and L-mediated autophagosomal lysis in antiestrogen-resistant breast cancer cells. Mol Cancer Ther. 2013; 12:448-459.

52. Perez RE, Knights CD, Sahu G, Catania J, Kolukula VK, Stoler D, Graessmann A, Ogryzko V, Pishvaian M, Albanese C and Avantaggiati ML. Restoration of DNA-binding and growth-suppressive activity of mutant forms of p53 via a PCAF-mediated acetylation pathway. J Cell Physiol. 2010; 225:394-405.

53. Catalina-Rodriguez O, Kolukula VK, Tomita Y, Preet A, Palmieri F, Wellstein A, Byers S, Giaccia AJ, Glasgow E, Albanese C and Avantaggiati ML. The mitochondrial citrate transporter, CIC, is essential for mitochondrial homeostasis. Oncotarget. 2012; 3:1220-1235.

Editorial

Kinase overexpressing cancers responsive to drug withdrawal

DOI: 10.18632/aging.100830

Amit Dipak Amin, Soumya S. Rajan, and Jonathan H. Schatz

Aberrant protein kinase activity promotes tumor survival and proliferation, and targeted kinase inhibitors that halt growth and promote apoptosis demonstrate some cancers are truly kinase addicted. Clinically, this is best exemplified by chronic myeloid leukemia (CML), driven by the fusion kinase BCR-ABL, where tyrosine kinase inhibitor (TKI) therapy can control the disease for years, perhaps indefinitely in many patients. For other cancers, however, the success of kinase inhibition has been more modest. Despite great strides in drug design and delivery, resistance invariably develops, typically limiting median progression free survival (PFS) to a period of months. Development of new-generation inhibitors therefore has focused on increasing potency, overcoming resistance-conferring mutations to the drug target, and hitting parallel signaling pathways that bypass the target altogether. While sequential treatments and/or combination cocktails to circumvent resistance may work in some cases, concerns arise regarding toxicity and cost, prompting exploration of innovative new strategies to prolong PFS. Two recent studies in different cancers propose an alternative with a potential to increase the duration of tumor control by several already approved TKIs.

Approximately 70% anaplastic large cell lymphoma (ALCL) cases are driven by the constitutively activated fusion kinase NPM-ALK [1]. To investigate resistance mechanisms, our laboratory grew patient-derived NPM-ALK-driven cell lines in one of two FDA approved ALK TKIs, crizotinib or ceritinib, at increasing concentrations. Resistance reliably arose due to overexpression of NPM-ALK even if resistance-conferring mutations also began to arise. Strikingly, characterization of resistant phenotypes showed viability of these cells was actually stimulated by – indeed required – continued presence of ALK TKI, as drug withdrawal rapidly induced apoptosis. Concomitantly we observed massive ALK activation, suggesting over-activation provides as much of a fitness deficit as inhibition [2]. These results echo the findings of a prominent study investigating mutant-BRAF inhibition with vemurafenib in melanoma, where resistance also arose due to target overexpression [3]. As in our study, resistant cells underwent apoptosis in response to inhibitor withdrawal. Oncogene over-expression in both reports therefore promoted a dual phenotype of drug resistance and dependence.

Both studies demonstrate potential therapeutic exploitation of the paradoxically toxic response of resistant-dependent cells to drug withdrawal. Xenografted resistant cells in both reports underwent apoptosis leading to tumor regressions upon discontinuation of drug dosing to host animals. After time tumors resumed growth, but sampling showed drug-target expression had returned to baseline – a requirement for their growth without inhibitor. At the same time dependence went away, so did resistance, as re-initiation of inhibitor dosing to host animals led to new rounds of tumor regressions. This suggested cycling of drug through discontinuous dosing could forestall onset of fatal resistance, and was explored in both reports, but especially in the melanoma models [2, 3]. Here both pre-scheduled and individualized intermittent dosing strategies greatly prolonged tumor control compared to continuous drug administration. Patients at risk of developing resistance due to up-regulation of some oncogenes may therefore benefit from intermittent dosing, a strategy carrying both low cost and low toxicity.

A randomized phase 2 trial comparing intermittent vs. continuous inhibitor dosing in melanoma already is enrolling patients (NCT02196181), and one is in planning for ALK+ ALCL. More preclinical assessment, however, also is needed in these and other cancers. Supporting the approach, drug holidays already may be employed to counter toxicity, and some second remissions to the ALK TKI crizotinib have been reported in lung cancer patients whose tumors were previously resistant [4, 5].

Great care must be taken, when determining appropriate timing of drug administration and withdrawal with such strategies, as the onset of resistance may be unpredictable, and drug interruption or re-initiation too early could exacerbate the onset of other resistance pathways [6]. An intriguing alternative, however, is identifying the specific mechanisms by which over-activity of particular oncogenes promote toxicity, and then pharmacologically inducing them as either a direct means of cellular toxicity or to prime the cells for other therapies. Indeed, a recent study showed pharma-cological induction of SYK hyper-activation caused

BCR-ABL+ acute lymphoblastic leukemia (ALL) cell death [7]. Targeted inhibition of several signaling pathway targets downstream failed to rescue resistant cells from NPM-ALK overdose in our systems (unpublished observations), but unbiased approaches are ongoing to determine the mechanisms.

Finally, it is important to keep in mind that intermittent dosing is not a cure and drug cycling eventually will prove futile. Such strategy gives a patient more time, however, delaying the need to change inhibitors, initiate combination cocktails, or a move to traditional therapies like chemotherapy or radiation, all of which may be significantly more toxic. In the ever-expanding arsenal of weapons against cancer, strategies exploiting oncogene overdose appear to hold promise, and in the case of intermittent dosing don't even require development of new drugs.

REFERENCES

1. Pearson JD, et al. J Signal Transduct. 2012; 2012:123253.

2. Amin AD, et al. Cancer research. 2015;75:2916-2927.

3. Das Thakur M, et al. Nature. 2013;494:251-255.

4. Browning ET, et al. Journal of thoracic oncology: official publication of the International Association for the Study of Lung Cancer. 2013; 8:e21.

5. Schrödl K, et al. Respiration; international review of thoracic diseases. 2014; 88:262-264.

6. Foo J, et al. Journal of thoracic oncology: official publication of the International Association for the Study of Lung Cancer. 2012; 7:1583-1593.

7. Chen Z, et al. Nature. 2015; 521:357-361.

Jonathan H. Schatz: Department of Medicine, Division of Hematology-Oncology, Sylvester Comprehensive Cancer Center, University of Miami Miller School of Medicine, Miami, FL, 33136

Correspondence: *Jonathan H. Schatz*
Email: *jschatz@miami.edu*

Keywords: *oncogene overdose, ALK, BRAF, cancer therapeutics*

Received: September 27, 2015
Published: October 22, 2015

Editorial

Sonic Hedgehog in SCLC

DOI: 10.18632/aging.100817

Mikko O. Laukkanen, J Silvio Gutkind, and Maria Domenica Castellone

The Hedgehog (Hh) signal transduction pathway has been discovered as a central regulator of embryonic development, tissue maintenance and repair [1]. Moreover, several recent evidences have highlighted its key function in tumorigenesis [2]. In some familial cancers, such as basal cell carcinoma and medulloblastoma, Hh pathway activation represents the initial tumorigenic event, whereas in other human malignancies, including gastrointestinal, lung, brain, breast and prostate cancers, deregulation of Hh signaling occurs during tumor progression and participates in tumor maintenance. Clinical trials using molecular inhibitors targeting Hh pathway components, in particular the Smo receptor, have often yielded limited clinical benefits unless they are used for the treatment of tumors harboring defined genetic mutations inactivating tumor suppressors (e.g. Ptch receptor) or activating oncogenes (e.g. Smo receptor, Gli transcription factor, Shh ligand) within the Hh pathway. In these specific cases, promising results led to FDA approval of Vismodegig (GDC0449, Genentech), a Smo inhibitor, in the treatment of basal cell carcinoma and medulloblastoma [3]. Notwithstanding, several clinical studies using the same compound in tumors exhibiting Hh overactivity without identified Hh mutations have resulted in discouraging outcome and discontinuation of the trials because of lack of objective response [2]. These unexpected results have been related to drug resistance due to the presence of activating mutations or genetic alterations driving Hh signaling bypassing Smo function. These evidences emphasize the need for further characterization of Hh signaling in tumorigenesis and for a more precise identification of the interaction between Hh and other signaling pathways involved in tumor development and response to therapy.

Small cell lung carcinoma (SCLC) is a very aggressive cancer with extremely poor prognosis, whose genetic events, such as oncogenic driver mutations, have not been defined yet. Classified as neuroendocrine tumors, SCLCs secrete factors of the bombesin (BN)/ Gastrin-Releasing Peptide (GRP) family and express their cognate receptors activating an autocrine loop that increases proliferation and survival [4]. The positivity for this ligand/receptor pair is considered to be a marker of aggressiveness and unfavorable tumor outcome. Recent reports have described the Hh pathway as a key regulator of lung embryogenesis and SCLCs maintenance, although no mutations in Hh signal transduction pathway molecules have been identified, suggesting a ligand-dependent pathway activation [5, 6]. The ligand-dependent activation of Hh signaling can occur in an autocrine manner, where cancer cells express both the ligand and the receptor, or in a paracrine manner, where ligand produced from cancer cells is activating Hh signaling in tumor stroma or vice versa.

To characterize Hh function in SCLC and to evaluate the therapeutic potential of Hh inhibitors in this cancer, we have investigated the possibility of a direct interaction between Hh and BN/GRPR signaling pathways. According to our initial observations, Cyclopamine, an inhibitor of Smo, attenuated BN induced cell proliferation. In support of these data, RNA interference for Sonic Hedgehog (Shh), upstream activator of Smo, reduced BN stimulated growth, matrigel spreading and soft agar colony formation [7]. Surprisingly, when testing the activation of Gli transcription factor upon BN stimulation, we revealed the existence of a direct crosstalk between the two pathways. In order to dissect the signaling molecular events mediating this interaction, we discovered that BN, through its G protein coupled receptor (GRPR) linked to Gαq/Gα12/13 large G proteins, and their downstream target, the Rho small GTPase, was able to stimulate NFkB-mediated transcription of Shh, thus initiating an autocrine signaling loop that links BN/GRPR pathway to production of Shh ligand, and the autocrine Hh signaling activation (Figure 1, left panel) [7].

Our findings, besides shedding new light on the mechanisms of Hh signaling activation in SCLC, may suggest a more general application for other BN/GRPR positive tumors over-expressing Shh pathway, such as pancreatic cancer, neuroblastomas and glioblastomas. Interestingly, use of Hh inhibitors alone in these tumors has not reached positive results that may indicate existence of functional parallel pathways able to counteract the effect of the drug. Moreover, recent re-

ports have highlighted a role for Hh signaling in tumor-stroma interactions, with production of Shh ligand from cancer cells and stimulation of Gli transcription factor in tumor microenvironment (myofibroblasts, endothelial cells, and CSC) [8]. In our study, we have investigated the existence of an autocrine ligand-dependent Hh signaling in SCLC. We certainly believe that it would be interesting to study also the paracrine activation of Hh signaling, which could have the double effect of stimulating proliferation and survival of stroma cells, leading to increased angiogenesis and metastasis and, at the same time, produce growth factors acting on cancer cells to sustain their proliferation, epithelial-to-mesenchymal transition (EMT), dissemination and survival (Figure 1, right panel). Our data connecting BN/GRPR and the Hh signaling pathway may therefore provide valuable knowledge on the complex interaction between tumor cells and cancer microenvironment and may offer the scientific basis for developing novel therapeutic stategies that, by combining different anti-tumor approaches, could be more effective than single agent treatments. In this case, novel co-targeting strategies would target not only cancer cells but also other component of tumor microenvironment. Moreover, simultaneous targeting of BN/GRPR and Hh pathway could help in counteracting mechanisms of cell-autonomous and non-cell autonomous (stroma-dependent) resistance to targeted therapies.

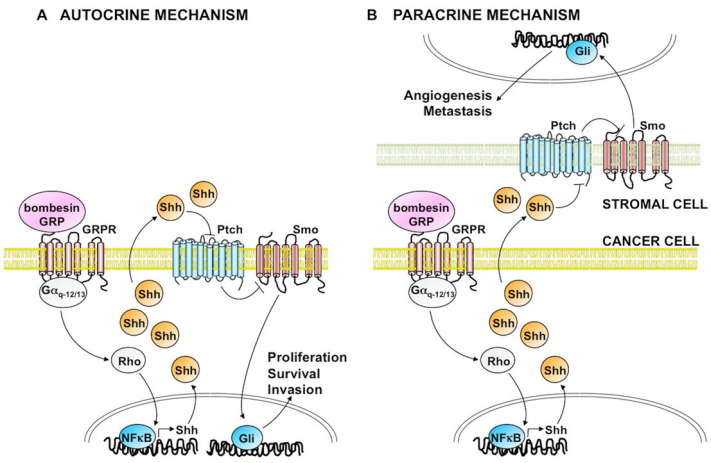

REFERENCES

1. Hahn H, et al. J Biol Chem. 1996; 271: 12125-12128.
2. Amakye D, et al. Nat. Med. 2013; 19: 1410-1422.
3. Gould S.E, et al. Expert Opin. Drug. Discov. 2014; 9: 969-984.
4. Carney DN, et al. Cancer Res. 1987; 47:821-825.
5. Pepicelli CV, et al. Curr Biol. 1998; 8: 1083-1086.
6. Park KS, et al. Nat Med. 2011; 17: 1504-1508.
7. Castellone MD, et al. Oncogene. 2015; 34:1679-1687.
8. Bailey JM,et al. Oncogene. 2009; 28: 3513-3525.

Maria Domenica Castellone: Istituto di Endocrinologia ed Oncologia Sperimentale "G. Salvatore" (IEOS), C.N.R. 80131- Naples; Italy

Correspondence: *Maria Domenica Castellone*
Email: *mcastell@unina.it*

Key words: *Sonic Hedgehog, SCLC, BN/GRPR*
Received: September 9, 2015
Published: September 26, 2015

Research Perspective

ARF: Connecting senescence and innate immunity for clearance

Alper Y. Kearney[1,3], Benedict Anchang[2], Sylvia Plevritis[2], and Dean W. Felsher[1]

[1] Division of Oncology, Departments of Medicine and Pathology, Molecular Imaging Program, Stanford University, Stanford, CA 94305, USA
[2] Department of Radiology, Stanford University, Stanford, CA 94305, USA
[3] Current Address: Genitourinary Medical Oncology, The University of Texas, MD Anderson Cancer Center, Houston, TX 77030, USA

Key words: Myc inactivation, p19arf, innate immunity, senescence
Received: 08/26/15; Accepted: 09/15/15; Published: 09/25/15
Correspondence to: Dean W. Felsher, PhD; **E-mail:** dfelsher@stanford.edu
DOI: 10.18632/aging.100813

Copyright: Kearney et al. This is an open-access article distributed under the terms of the Creative Commons Attribution License, which permits unrestricted use, distribution, and reproduction in any medium, provided the original author and source are credited

Oncogene addiction and MYC

Cancers depend on one or more ubiquitously activated oncogenes to survive and maintain their tumorigenic phenotype. The MYC oncogene is critically important in a variety of hematological malignancies, including Burkitt's lymphoma, acute lymphoblastic leukemia, and multiple myeloma. Cancers' reliance on few oncogenes, aptly termed oncogene addiction, presents an exploitable vulnerability. Indeed, targeted therapies inhibiting key oncogenes in a multitude of cancer types are routinely used in clinic [1]. However, in many cases cancers either do not respond to oncogene inhibition therapies or eventually become resistant following an initial response phase. Resistance to oncogene inhibition therapies and ensuing tumor recurrence are major contributors to cancer-specific mortality.

Experimental model systems of MYC oncogene inactivation in various cancers have revealed molecular mechanisms of oncogene addiction, escape from oncogene dependence resulting in tumor recurrence [2]. Inactivation of the MYC oncogene in mouse models of cancer induces proliferative arrest, apoptosis and/or cellular senescence, as well as the shutdown of angiogenesis; thereby, enabling tumor clearance and sustained tumor regression [3, 4]. However, in some cases, tumors reoccur [5].

Recently, we gained insight into the mechanism of tumor recurrence. We found that when either of two tumor suppressor genes, ARF or p53, is lost or mutated, tumor recurrence rapidly always occurs [6]. We previously reported that p53 loss results in tumor recurrence by maintaining tumor vasculature, despite MYC inactivation, through upregulation of angiogenesis inhibitor TSP1 [3]. Further, we have described that INK4A/ARF loss or RB1 loss results in tumor recurrence through abrogation of cellular senescence. We found distinct mechanisms through which loss of ARF or p53 leads to tumor recurrence in a mouse model of T-ALL [6]. We identified that ARF has a p53-independent effect on the ability of MYC inactivation to elicit expression of genes involved innate immune activation associated with a marked decrease in the recruitment of macrophages.

p53-dependent and p53-independent effects of ARF

We found that ARF loss prevented MYC inactivation from inducing cellular senescence through a p53 independent mechanism [6]. Our observations are consistent with a prior study that ARF regulates cellular senescence in p53-independent manner in melanoma [7]. Further, we found that ARF loss, but not p53 loss, blocked macrophage infiltration into regressing tumors. In contrast, loss of p53 had modest effect on cellular

senescence and no effect on macrophage infiltration, but instead allowed maintenance of tumor vasculature, even in regressing tumors. Thus, the loss of either ARF or p53 enables tumor recurrence, albeit through different mechanisms. Therefore, ARF's effects on angiogenesis are likely to be p53-dependent, while ARF's effects on senescence and innate immune infiltration and activation seem to be p53-independent (Figure 1).

The mechanism through which ARF regulates innate immunity is not clear. Analysis of gene expression revealed a signature of genes involved in innate immunity [6]. ARF, itself, is not thought to be directly a transcription factor, but is known to interact with or regulate transcription factors, such as MYC and p53 [8-10]. We considered ARF may be diminishing MYC's transactivation or transrepression capabilities; however, analysis of MYC target genes did not support this [6].

ARF and immunotherapy

Emerging immunotherapies have intensified interest in the therapeutic role of the innate and adaptive immune system. Biologics targeted at tumor cells for enabling antibody-dependent cell-mediated cytoxicity (ADCC) rely on innate immune system for elimination of cancer cells [11]. Since ARF loss in tumors influences infiltration and activation of innate immune effectors, ARF status may be important to immunotherapies. In particular, this may be relevant for drugs that utilize ADCC, such as anti-ERBB2 antibody trastuzumab and anti-CD20 antibody rituximab.

Cells undergoing senescence secrete factors that bolster the senescent phenotype in both autocrine and paracrine fashion by engaging innate immune system [12]. ARF loss is associated with expression changes in senescence and innate immune system-related genes as well as defects in macrophage infiltration into tumors. Our results are consistent with a previous report that ARF deficiency interferes with macrophage activation, cytokine production, and inflammation [13]. Conceivably, ARF null tumors may present a different secretome profile, which may abrogate SASP-dependent autocrine and paracrine positive feedback loops and elicit incomplete targeting and clearance of tumor cells by immune effectors. We have yet to identify an individual factor that may mediate effects of ARF on innate immune system; however, likely candidates include TGFbeta, IL-1alpha/beta, and NFkB among others. TGFbeta and pro-inflammatory cytokine IL-1 have been previously implicated in the reinforcement and spread of senescence [14, 15]. Transactivation activity of NFkB, common regulator of SASP and innate immunity, is intriguingly altered by ARF [16, 17]; however, whether ARF loss alters SASP and cytokine and chemokine profiles in T-ALL is not known.

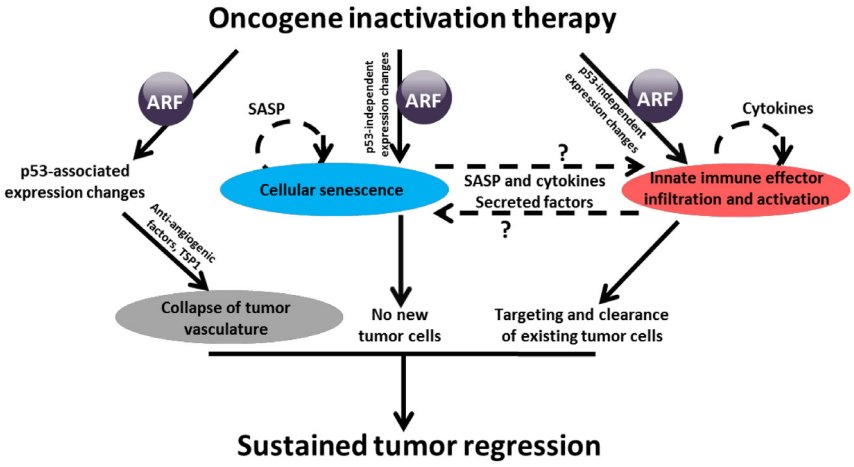

Figure 1. ARF loss interferes with expression of genes associated with senescence and innate immune system. MYC inactivation, in the presence of ARF, triggers gene expression changes in pathways associated with senescence as well as macrophage and innate immune cell activation and infiltration. Microarray analysis revealed that ARF loss precludes these changes, which we propose may be how ARF loss blocks macrophage infiltration. SASP: Senescence-associated secretory phenotype.

Our research has uncovered ARF as a common regulator of senescence and tumor clearance that appears to require the innate immune system. However, there are several questions awaiting answers. First, we have identified innate immune-related gene expression changes due to ARF loss; yet direct causality of these changes in macrophage infiltration into regressing tumors has not been established. Second, the mechanism by which cellular senescence is dependent upon macrophage recruitment is unclear. Third, whether ARF loss in tumors affects other immune infiltrates, such as NK cells, monocytic and granulocytic myeloid cells, or even adaptive immune cells, needs to be investigated. Fourth whether ARF's effect on innate immune-related genes and recruitment of macrophages extends to other types of cancers remains to be determined. Finally, it is of paramount interest whether ARF status may influence efficacy of immunotherapies.

Conflict of interest statement

The authors declare no conflict of interest.

REFERENCES

1. Sharma SV and Settleman J. Oncogene addiction: setting the stage for molecularly targeted cancer therapy. Genes & development. 2007; 21:3214-3231.

2. Felsher DW and Bishop JM. Reversible tumorigenesis by MYC in hematopoietic lineages. Molecular cell. 1999; 4:199-207.

3. Giuriato S, Ryeom S, Fan AC, Bachireddy P, Lynch RC, Rioth MJ, van Riggelen J, Kopelman AM, Passegue E, Tang F, Folkman J and Felsher DW. Sustained regression of tumors upon MYC inactivation requires p53 or thrombospondin-1 to reverse the angiogenic switch. Proceedings of the National Academy of Sciences of the United States of America. 2006; 103:16266-16271.

4. Wu CH, van Riggelen J, Yetil A, Fan AC, Bachireddy P and Felsher DW. Cellular senescence is an important mechanism of tumor regression upon c-Myc inactivation. Proceedings of the National Academy of Sciences of the United States of America. 2007; 104:13028-13033.

5. Karlsson A, Giuriato S, Tang F, Fung-Weier J, Levan G and Felsher DW. Genomically complex lymphomas undergo sustained tumor regression upon MYC inactivation unless they acquire novel chromosomal translocations. Blood. 2003; 101:2797-2803.

6. Yetil A, Anchang B, Gouw AM, Adam SJ, Zabuawala T, Parameswaran R, van Riggelen J, Plevritis S and Felsher DW. p19ARF is a critical mediator of both cellular senescence and an innate immune response associated with MYC inactivation in mouse model of acute leukemia. Oncotarget. 2015; 6:3563-3577.

7. Ha L, Ichikawa T, Anver M, Dickins R, Lowe S, Sharpless NE, Krimpenfort P, Depinho RA, Bennett DC, Sviderskaya EV and Merlino G. ARF functions as a melanoma tumor suppressor by inducing p53-independent senescence. Proceedings of the National Academy of Sciences of the United States of America. 2007; 104:10968-10973.

8. Cleveland JL and Sherr CJ. Antagonism of Myc functions by Arf. Cancer cell. 2004; 6:309-311.

9. Gregory MA, Qi Y and Hann SR. The ARF tumor suppressor: keeping Myc on a leash. Cell cycle. 2005; 4:249-252.

10. Weber JD, Taylor LJ, Roussel MF, Sherr CJ and Bar-Sagi D. Nucleolar Arf sequesters Mdm2 and activates p53. Nature cell biology. 1999; 1:20-26.

11. Scott AM, Wolchok JD and Old LJ. Antibody therapy of cancer. Nature reviews Cancer. 2012; 12:278-287.

12. Krizhanovsky V, Xue W, Zender L, Yon M, Hernando E and Lowe SW. Implications of cellular senescence in tissue damage response, tumor suppression, and stem cell biology. Cold Spring Harbor symposia on quantitative biology. 2008; 73:513-522.

13. Traves PG, Lopez-Fontal R, Luque A and Hortelano S. The tumor suppressor ARF regulates innate immune responses in mice. Journal of immunology. 2011; 187:6527-6538.

14. Tasdemir N and Lowe SW. Senescent cells spread the word: non-cell autonomous propagation of cellular senescence. The EMBO journal. 2013; 32:1975-1976.

15. van Riggelen J, Muller J, Otto T, Beuger V, Yetil A, Choi PS, Kosan C, Moroy T, Felsher DW and Eilers M. The interaction between Myc and Miz1 is required to antagonize TGFbeta-dependent autocrine signaling during lymphoma formation and maintenance. Genes & development. 2010; 24:1281-1294.

16. Chien Y, Scuoppo C, Wang X, Fang X, Balgley B, Bolden JE, Premsrirut P, Luo W, Chicas A, Lee CS, Kogan SC and Lowe SW. Control of the senescence-associated secretory phenotype by NF-kappaB promotes senescence and enhances chemosensitivity. Genes & development. 2011; 25:2125-2136.

17. Rocha S, Garrett MD, Campbell KJ, Schumm K and Perkins ND. Regulation of NF-kappaB and p53 through activation of ATR and Chk1 by the ARF tumour suppressor. The EMBO journal. 2005; 24:1157-1169.

Editorial

Targeting of non-oncogene addiction

DOI: 10.18632/aging.100796

Ana Igea, Jalaj Gupta, and Angel R. Nebreda

Signaling pathways control all phases of tumor development and are critical in cancer therapy as they are largely responsible for the ability of tumor cells to survive or die in response to chemotherapy and radiotherapy. The p38 MAPK signaling pathway is one of the routes that cells use extensively to interpret extracellular signals and orchestrate appropriate responses. This pathway was originally characterized as a key regulator of stress and inflammatory processes, which prompted the development of chemical inhibitors mainly targeting the p38α and p38β family members. These inhibitors were expected to curtail production of inflammatory mediators and be useful for the treatment of inflammatory diseases such as rheumatoid arthritis. Unfortunately, the available information indicates rather disappointing outcomes, sometimes due to toxicity and in other cases for lack of efficacy, notwithstanding that some clinical trial results are not made public [1]. However, recent clinical trials with p38 MAPK inhibitors have given promising results for Chronic Obstructive Pulmonary Disease [2].

Intensive research over the past two decades has provided good evidence for the implication of the p38 MAPK pathway in cellular processes unrelated to stress that are important for normal physiology. It is now clear, for example, that p38 MAPK can regulate the proliferation, differentiation and survival of many cell types. In addition, p38 MAPK signaling has been implicated in several pathologies including cancer. Initial studies performed using cell lines both in culture and in mouse xenografts indicated that this pathway can suppress tumorigenesis. More recent studies have included the use of genetically modified mice to address the role of p38 MAPK signaling in different cell types, showing that this pathway can regulate tumor development at different levels.

Our group has contributed to the study of how the p38 MAPK pathway regulates tumor initiation and progression *in vivo*. Using mouse models, we have shown an important role of p38 MAPK signaling in colon and breast cancer [3, 4]. As reported for other tumor types, we provided evidence that the p38 MAK pathway suppresses tumor initiation in a mouse model of inflammation-associated colon tumorigenesis. Unexpectedly, once the tumor is formed, p38 MAPK signaling contributes to the proliferation and survival of the malignant cells and inhibition of p38 MAPK reduces colon tumor growth [3]. Moreover, genetic and pharmacological experiments indicate that p38 MAPK inhibition cooperates with chemotherapeutic drugs such as cisplatin to kill breast and colon cancer cells in culture and to reduce tumor size *in vivo* in a mouse model of breast cancer [4]. Along the same lines, other groups have shown that inhibition of the p38 MAPK pathway potentiates the anti-tumoral effects of doxorubicin and sorafenib in mouse models of lung and liver cancer, respectively [5, 6]. Taken together, these results strongly suggest that p38 MAPK inhibitors can be potentially exploited for cancer therapy in combination with chemotherapeutic drugs.

The results obtained in mouse models of cancer are promising but any attempt to modulate p38 MAPK activity for therapeutic purposes should be carefully evaluated in preclinical models. This is always an important validation step but in the case of p38 MAK signaling is critical, given the many functions that this pathway can perform depending on the cellular context. We have started to use patient-derived xenografts (PDX) as preclinical models that recapitulate the complexity and heterogeneity of the human tumors. Using PDX models, we have confirmed that pharmacological inhibition of p38 MAPK impairs the growth of colon tumors derived from patients [7]. In line with the possible therapeutic interest that inhibition of p38 MAPK signaling could have for colon cancer treatment, p38 MAPK inhibitors either alone or in combination with other drugs have been used or are currently in clinical trials for different types of cancer (https://clinicaltrials.gov).

It therefore seems that tumor cells may become addicted to p38 MAPK signaling, perhaps to be able to tolerate homeostatic control deficiencies and the kind of permanent stressful conditions in which they have to thrive. Considering that sustained activation of the p38 MAPK pathway in normal cells usually leads to cell cycle arrest and apoptosis, it cannot be considered an oncogenic route. However, the ability of this pathway to perform a variety of functions makes tumor cells to rely on it, illustrating a good example of non-oncogene addiction.

In summary, results obtained by our group and others support that the p38 MAPK pathway could act as an

accessory component of oncogenic networks, which can be potentially exploited in combination therapies to effectively shut down pro-tumorigenic pathways and facilitate tumor cell death. Thus, pharmacological inhibitors of p38 MAPK are worth exploring for cancer therapy and combined with chemotherapeutic drugs could improve current treatments and reduce side effects.

REFERENCES

1. Coulthard LR et al. Trends Mol Med. 2009; 15:369-379.
2. Norman P. Expert Opin Investig Drugs. 2015;24:383-392.
3. Gupta J et al. Cancer Cell. 2014;25:484-500.
4. Pereira L et al. EMBO Mol Med. 2013;5:1759-1774.
5. Morandell S et al. Cell Rep. 2013; 5:868-877.
6. Rudalska R et al. Nature Med.2014; 20:1138-1146.
7. Gupta J et al. Oncotarget. 2015;6:8539-8551.

Angel R. Nebreda: Institute for Research in Biomedicine (IRB Barcelona), 08028 Barcelona, Spain

Correspondence: *Angel R. Nebreda*
Email: *angel.nebreda@irbbarcelona.org*

Received: August 6, 2015
Published: August 18, 2015

Research Paper

Caloric restriction induces heat shock response and inhibits B16F10 cell tumorigenesis both *in vitro* and *in vivo*

Marta G. Novelle[1,3], Ashley Davis[1], Nathan L. Price[1], Ahmed Ali[1], Stefanie Fürer-Galvan[1], Yongqing Zhang[2], Kevin Becker[2], Michel Bernier[1], and Rafael de Cabo[1]

[1]Translational Gerontology Branch, National Institute on Aging, National Institutes of Health, Baltimore, MD 21224, USA
[2]Gene Expression and Genomics Unit, National Institute on Aging, National Institutes of Health, Baltimore, MD 21224, USA
[3]Department of Physiology, CIMUS, University of Santiago de Compostela-Instituto de Investigación Sanitaria, 15782 Santiago de Compostela, Spain; CIBER Fisiopatología de la Obesidad y Nutrición (CIBERobn), 15706 Santiago de Compostela, Spain

Key words: caloric restriction, heat shock, stress response, tumorigenesis, aging
Received: 12/01/14; Accepted: 03/24/15; Published: 04/05/15 DOI: 10.18632/aging.100732
Correspondence to: Rafael de Cabo, PhD; **E-mail:** decabora@grc.nia.nih.gov

Copyright: Novelle et al. This is an open-access article distributed under the terms of the Creative Commons Attribution License, which permits unrestricted use, distribution, and reproduction in any medium, provided the original author and source are credited

Abstract: Caloric restriction (CR) without malnutrition is one of the most consistent strategies for increasing mean and maximal lifespan and delaying the onset of age-associated diseases. Stress resistance is a common trait of many long-lived mutants and life-extending interventions, including CR. Indeed, better protection against heat shock and other genotoxic insults have helped explain the pro-survival properties of CR. In this study, both *in vitro* and *in vivo* responses to heat shock were investigated using two different models of CR. Murine B16F10 melanoma cells treated with serum from CR-fed rats showed lower proliferation, increased tolerance to heat shock and enhanced HSP-70 expression, compared to serum from *ad libitum*-fed animals. Similar effects were observed in B16F10 cells implanted subcutaneously in male C57BL/6 mice subjected to CR. Microarray analysis identified a number of genes and pathways whose expression profile were similar in both models. These results suggest that the use of an *in vitro* model could be a good alternative to study the mechanisms by which CR exerts its anti-tumorigenic effects.

INTRODUCTION

Aging is a complex multifactorial process, whereby organisms undergo major cell degeneration and loss of function. During aging, irreversible and deleterious processes are triggered by accumulation of damaged cellular macromolecules [1, 2]. Several theories have been proposed to explain these processes [3, 4], but the exact molecular mechanisms behind aging remains unknown. Cellular damage may result from oxidative stress, toxic metabolic byproducts, endoplasmic reticulum stress and mitochondrial unfolded protein responses, or exposure to heat stress, among others. Several heat shock proteins (HSP) function as molecular chaperones by preventing misfolding and aggregation of other proteins. This induction of cytoprotective responses promotes longevity [5, 6]; conversely, aging is associated with down-regulation in HSP expression in neuronal tissue, skeletal and cardiac muscle, and the liver [7, 8]. Stimulation of HSP synthesis has been suggested as a viable strategy to counteract the negative effects of aging and eliciting a 'low-grade' stress response may help organisms live longer and improve their survival [9].

More than 8 decades ago, McCay and colleagues observed that severe reduction in calorie intake while maintaining sufficient micronutrient levels for optimum health resulted in lifespan extension [10]. Since then,

numerous studies have reported that lifelong caloric restriction (CR) extends mean and maximum lifespan and delays age-associated diseases in a wide variety of species [11, 12]. Many of the beneficial effects of CR are mediated by altering the expression of several HSPs, notably Hsp70, and the activation of heat shock transcription factor 1 [13-15]. In this context, our group has demonstrated that exposure of HepG2 cells to human serum from CR participants conferred significant cytoprotection against heat stress [7]. Moreover, cells treated with human serum from CR volunteers trigger a transcriptional up-regulation of numerous genes and pathways implicated in stress resistance through activation of the transcription factor NF-E2-related factor (NRF2) [16]. NFR2 plays a key role in maintaining homeostasis during oxidative stress and exposure to carcinogens by coordinately regulating the expression of antioxidants and detoxification enzymes [17] that boost protection against cancer [18].

The anti-tumorigenic properties of CR on spontaneously arising tumors and in experimental cancer models are well-documented [19]. For example, 15 days of 40% CR significantly reduces the growth of brain tumors in mice by reducing angiogenesis and increasing tumor cell apoptosis [20]. The combination of fasting and chemotherapy retards the growth of human breast cancer tumors in mice [21] and delays the progression of pancreatic cancer lesions in a mouse model [22]. The use of the mouse as an experimental tool in cancer research is cumbersome, time-consuming and expensive, and, therefore, has compelled us to explore an alternative approach to study anti-cancer therapies.

In this manuscript we present a new approach to investigate a central mechanism by which CR activates a stress response pathway to combat tumorigenesis. The stress response of murine B16F10 melanoma cells maintained in culture medium supplemented with serum from rats fed CR and *ad libitum* (AL) diet was evaluated and compared to that of mice injected with B16F10 melanoma cells and maintained on either CR or AL. In the latter experimental model, mice were subjected to heat stress followed by the monitoring of a melanoma-specific Hsp70 reporter expression. These results combined with microarray analysis illustrated alteration of a common set of cancer-related genes using in *vitro* and *in vivo* testing.

RESULTS

Growth rate and heat shock response of B16F10 melanoma cells maintained in serum from CR-fed animals

Proliferation of B16F10 melanoma cells was carried out in the presence of serum from rats fed either AL or CR diet. A significant reduction in cell growth was observed following incubation with CR serum as compared to AL serum controls (Fig. 1a). Exposure of B16F10 cells to heat stress (45°C) for 1 h caused a significant difference in survival depending on whether these cells were maintained in CR or AL serum (Fig. 1b). Our observations that CR serum decreased heat-dependent cellular cytotoxicity support previously published results from this laboratory [23].

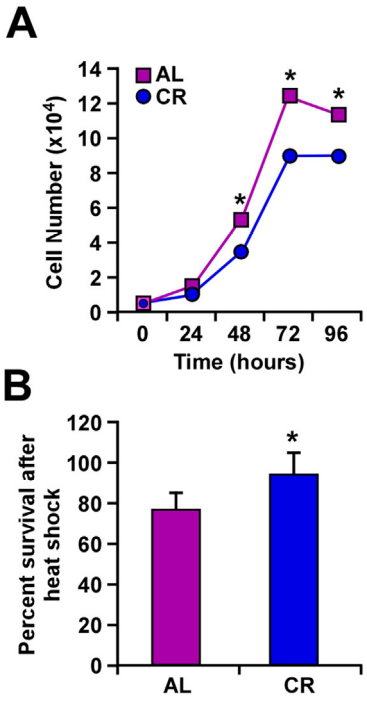

Figure 1. Caloric restriction slows cellular growth and improves response to heat shock. (**A**) B16F10 melanoma cells were maintained in culture with serum from AL- and CR-fed rats over a period of 96 h. The number of cells was counted at 24-h intervals. (**B**) Percent of cells surviving a 1-h treatment at 45°C when maintained in culture with serum from either AL- or CR-fed rats. Data are represented as the mean ± SEM. *, p< 0.05.

Reduction in the number and size of tumors in mice on caloric restriction

To evaluate the effect of CR on tumor growth *in vivo*, mouse B16F10 melanoma cells that were stably transfected with Hsp70-GFP plasmid, were implanted subcutaneously in male C57BL/6 mice fed either a CR or AL diet. A significant decrease in the size and weight of tumors was observed in CR-fed mice along with delayed tumor growth both in the periscapular region and lower back area (Fig. 2).

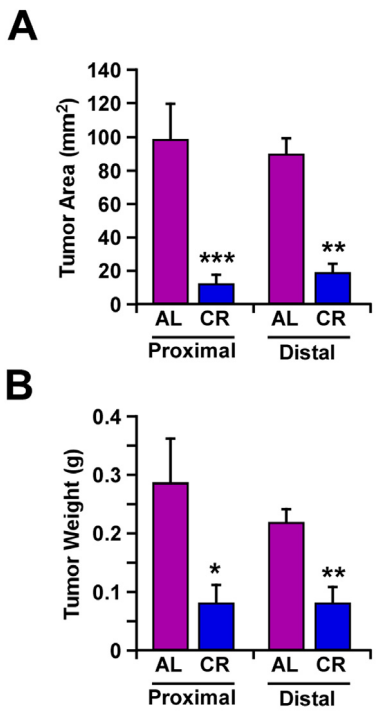

Figure 2. Caloric restriction decreased melanoma tumor growth *in vivo*. In AL- and CR-fed mice, mouse tumor xenografts were formed by implanting B16F10 melanoma cells, at the periscapular region (proximal area) and in the lower back over the hip (distal area). Tumor area (mm^2) (**A**) and individual tumor weight (g) (**B**) were determined after 14 days. Data are represented as the mean ± SEM. n=10/per group. *, p< 0.05, **, p<0.01, *** p<0.001.

Heat stress-mediated induction of Hsp70 expression both in *in vitro* and *in vivo* models

Changes in HSP expression play an important role in the ability of cells to respond to environmental stressors. Earlier work has shown an elevation in Hsp70 expression in B16F10 melanoma cells cultured with serum from CR-fed animals [23]. Here, we compared the effects of CR alone, heat shock alone or the combination 'CR + heat shock' using B16F10 melanoma cells stably expressing GFP-tagged Hsp70 construct under the control of rat *hsp70.1* promoter [24]. The results indicate that the heat-mediated induction of Hsp70 expression was significantly higher when B16F10 cells and tumor-bearing animals were subjected to CR (Fig. 3).

Microarray analysis of B16F10 melanoma cells used in *in vitro* and *in vivo* settings

DNA microarray analysis was performed to compare the global transcriptional effect of CR in B16F10 melanoma cells either grown in culture or implanted in mice. Principal Component Analysis (PCA) revealed inherent *in vivo* and *in vitro* differences that must be taken into account when comparing the impact of CR in gene expression profile. Nevertheless, Venn diagram indicated that both models shared 55 up-regulated and 17 down-regulated transcripts, which were significantly enriched in the CR versus AL pairwise comparisons (Fig. 4a, Supplemental Table 1). Among these shared transcripts, MAP Kinase Interacting Serine/Threonine

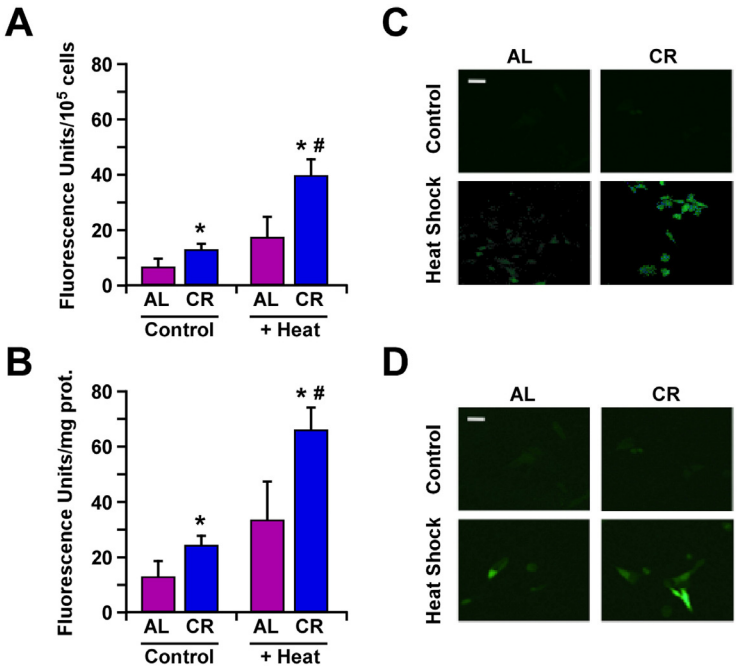

Figure 3. Caloric restriction improves protection against heat shock through increased expression of Hsp70. (**A**) B16F10 melanoma cells stably transfected with a plasmid encoding GFP-tagged Hsp70 construct were maintained in medium supplemented with 10% serum from AL- or CR-fed rats and then subjected or not to heat shock stress for 45 min. Bars represent fluorescence intensity per 10^5 cells. Cell culture experiments were performed as three or more replicates. (**B**) B16F10 tumor xenografts from mice fed either AL or CR diet were subjected to heat shock stress for 45 min and sacrificed after 4h. Bars represent fluorescence intensity per mg of tumor proteins; n=10 per group. Data, obtained by fluorimetery, are represented as the means ± SEM. *, p <0.05 *vs.* AL group; #, p<0.05 *vs.* CR group. (**C**) Images of B16F10 cells and (**D**) tumor cells depicting GFP fluorescence were detected by confocal microscopy. White bar, 20 µm.

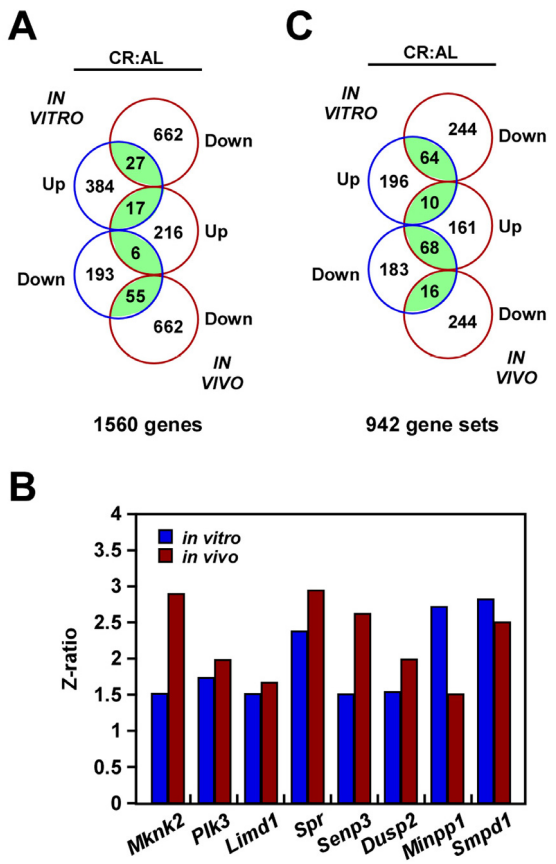

Figure 4. Gene expression profiling in response to caloric restriction. (**A**) Venn diagram showing the overlap of gene **transcripts** with significant change in expression in the CR *versus* AL pairwise comparisons by both B16F10 melanoma cells growing in culture (*in vitro*) and as tumor xenografts (*in vivo*). (**B**) Effect of CR on the expression of a select group of transcripts. (**C**) Venn diagram showing the overlap of gene sets with significant change in expression in the CR *versus* AL pairwise comparisons.

Kinase 2 (*Mknk2*) [25], polo-like kinase 3 (*Plk3*) [26] and LIM Domains Containing 1 (*Limd1*) [27] are implicated in tumorigenesis, whereas *Spr* and *Semp3*, which encode for Sepiapterin Reductase and SUMO1/Sentrin/SMT3 Specific Peptidase 3, are involved in stress response [28, 29]. DUSP2 is an important member of the dual-specificity protein phosphatase subfamily, which is implicated in inflammatory response and reported to be upregulated both with CR and heat shock [30]. Moreover, there is an increased expression of *Minpp1*, which encodes for Multiple Inositol Polyphosphate Phosphatase 1. This phosphatase is induced in response to heat shock, osmotic and oxidative stress conditions, thereby contributing to the regulation of ER stress and apoptosis [31]. Finally, upregulation of *Smpd1* (Sphingomyelin phosphodiesterase 1, also known as ASM) was also observed in both experimental models with CR (Fig. 4b). Its activity is expressed at high levels in cancer cells under the control of an inducible expression of hsp70.1 protein [32]. Using parametric analysis of gene set enrichment, 26 gene sets were identified whose expression levels were significantly altered in the same direction by CR in both experimental models (Fig. 4c, Supplemental Table S2).

DISCUSSION

The aging process involves multiple physiological mechanisms and represents one of the main risk factors for several human pathologies, such as cancer, diabetes, and cardiovascular disease. Dietary CR retards the aging process and age-related disease pathogenesis [33, 34], and many studies have tried to elucidate the exact mechanism(s) by which CR acts (reviewed in [35]). Our work demonstrates that CR significantly decreases tumor cell proliferation, in agreement with previous studies [36, 37], and this phenomenon takes place whether B16F10 melanoma cells were cultured with serum from CR-fed animals or these tumor cells were implanted in CR-fed mice. Moreover, the process of tumorigenesis was significantly decreased in CR-fed animals after heat stress. Hsp70 is one of several heat-shock proteins implicated in the regulation of cancer cell growth. HSPs sustain tumor survival and drive tumor growth [38]; however, induction of Hsp70 family members results in cellular protection against un-favorable environmental conditions, including elevated temperatures, oxidative stress, exposure to heavy metals, proteasome inhibitors, and infection [39]. CR has been previously shown to restore the ability of cells to mount a heat shock response through increase in Hsp70-mediated thermotolerance [40], an observation that was confirmed in the present study. Moreover, B16F10 melanoma cells subjected to heat shock stress showed greater survival when maintained in CR serum as compared to serum from AL-fed animals. It would appear that heat stress and CR acted cooperatively to enhance cell survival, possibly via activation of the deacetylase SIRT1 [40, 41]. It is interesting to note that the combination of heat stress with CR caused a synergistic increase in Hsp70-GFP expression when compared to either condition alone both *in vitro* and *in vivo*.

Microarray results reinforce the idea that despite significant genome-wide gene expression variation between the two experimental models, the expression profile of several transcripts implicated in tumorigenesis and stress response exhibited a comparable pattern,

whether B16F10 melanoma cells were cultured in CR serum or implanted in mice fed a CR diet. Although this *in vitro* model is quite distant from a physiological setting, it displayed a number of molecular pathways similar to the ones observed *in vivo*.

In conclusion, our findings indicate that the impact of CR on the regulation of several pathways implicated in tumorigenesis on an *in vivo* model of heat stress response can be replicated *in vitro* using tumor cells incubated with serum from CR-fed animals. The idea that hormones and nutrients present in serum, whose levels are altered during CR, are involved in homeostasis control mechanisms, including the aging process, has been suggested [7, 16, 23]. These results support the notion that *in vitro* testing may be well suited for the study of molecular aspects of CR that have not been elucidated yet.

MATERIALS AND METHODS

Animals and Dietary Manipulation. The mice were single-housed in duplex caging in a room maintained at a constant temperature (20-22 °C) and humidity (30-70%) in a light:dark 12:12-h schedule, according to established animal protocols and NIH guidelines. Male C57BL/6 mice (3 month old) were fed on a standard purified mouse diet (NIH-31) *ad libitum* (AL; n=10) or maintained on a 40% calorie restriction regimen (CR; n=10) during six weeks. Body weight and food intake was recorded weekly (supplemental figure 1 a, b).

Cell culture. B16F10 melanoma cells (ATCC® CRL-6475™) were purchased from American Type Culture Collection (Manassas, VA); they were cultured in Dulbecco's Modified Essential Medium (DMEM) supplemented with 10% fetal bovine serum and penicillin/streptomycin (Gibco, Gaithersburg, MD) under standard cell culture conditions. Cells were incubated in media with 10% serum from AL- or CR-fed rats (as described previously [23]). Briefly, serum was obtained from overnight fasted, anesthetized 6-month-old male Fisher 344 rats from three different cohorts. The blood collection took place between 7-11:00 a.m. After a 1-h incubation in a water bath at 45°C, cells were trypsinized, washed twice with phosphate-buffered saline (Invitrogen, Grand Island, NY), and then seeded at $1.5x10^5$ cells/well in 96-well plates. Cell proliferation assays were carried out during 96 h by the addition of a tetrazolium salt solution, WST-8, to each well according to the manufacturer's protocol (Dojindo, Indianapolis, IN). The absorbance of the formazan dye formed was measured at 450nm using the Perkin Elmer HTS 7000 Plus BioAssay reader.

Heat shock treatment of B16F10 melanoma xenografts in vivo. One month into the study, mice were injected with $1x10^6$ B16F10 melanoma cells stably transfected with a plasmid containing *GFP* gene linked to rat stress-inducible *hsp70.1* gene promoter [24] in the periscapular region (proximal) and in the lower back over the hip (distal area). After a two-week period, five mice were randomly chosen from each group and placed in a tumor hyperthermia induction chamber (THIC) constructed in our facility. Mice were anesthetized with isoflurane droplets in a closed chamber prior to being placed in the THIC and maintained under anesthesia for the reminder of the experiment. Two membranous tubes filled with pre-warmed water were placed over the proximal (45°C) and distal (27°C) tumors of the anesthetized mice *(supplemental figure 1 c, d)*. The water temperature was maintained throughout the duration of the experiment. After a 45-min heat treatment, the mice recovered for 4 h and then euthanized by cervical dislocation, according to the AAALAC guidelines.

Melanoma tumor growth *in vivo*. Tumor xenografts were formed by implanting murine B16F10 melanoma cells at the periscapular region and in the lower back of AL- and CR-fed mice. Fourteen days later, animals were euthanized and tumors were excised for the determination of the tumor area using a caliper. Tumor weight was also recorded.

GFP fluorescence detection. Experiments were carried out as indicated, using B16F10 melanoma cells stably expressing a plasmid encoding GFP-tagged Hsp70 that were either maintained in culture or used as tumor xenografts in mice. GFP fluorescence was monitored using both a confocal microscope (Axiovert-200, Zeiss LSM 510) to obtain images and a fluorimeter (Perkin-Elmer LS-55 and HTS 7000 Plus BioAssay reader) to accurately quantify GFP expression levels, which were normalized per 10^5 cells (in culture) or mg of tumor proteins.

Microarray analysis. RNA was isolated from B16F10 melanoma cells maintained in culture and as tumor xenografts. For microarray analysis, RNA was processed, reverse transcribed, labeled and hybridized to Mouse 15K cDNA arrays and read on an Illumina BeadArray 500GX reader. Raw data were subjected to Z normalization to ensure compatibility using the formula: z(raw data)=[ln (raw data) – avg(ln(raw data))]/[std dev(ln (raw data))], where ln is natural logarithm, avg is the average over all genes of an array, and std dev is the standard deviation over all genes of an array (Cheadle et al., 2003). The Z ratio (between treatment A and B) is given by z(A)-z(B)/std dev.

Individual genes with Z ratio > 1.5 in both directions, *P* value < 0.05, and false discovery rate > 0.3 were considered significantly changed. All raw data were deposited in the NCBI Gene Expression Omnibus under accession number GSE67430.

Statistical analysis. Statistical analyses were performed using Microsoft Excel software (Microsoft Corp., Redmond, WA). Unpaired t-tests were used for all analyses. Statistical significance was established at $p<0.05$. Data are expressed as means ± standard error of the mean (SEM).

ACKNOWLEDGEMENTS

We would like to thank Dr. Zdzislaw Krawczyk for giving us the plasmid encoding GFP-tagged Hsp70. This work has been supported by the Intramural Research Program of the National Institute on Aging, National Institutes of Health. MGN was supported by CIBER de Fisiopatología de la Obesidad y Nutrición (CIBERobn), an initiative of ISCIII, Spain.

Conflict of interest statement

The authors have no conflict of interests to declare.

REFERENCES

1. Chondrogianni N, Sakellari M, Lefaki M, Papaevgeniou N and Gonos ES. Proteasome Activation Delays Aging in Vitro and in Vivo. Free Radic Biol Med. 2014;71:303-320.

2. López -Otin C, Blasco MA, Partridge L, Serrano M and Kroemer G. The hallmarks of aging. Cell. 2013; 153:1194-1217.

3. Jin K. Modern Biological Theories of Aging. Aging Dis. 2010; 1:72-74.

4. Wiggins J and Bitzer M. Slowing the aging process. Clin Geriatr Med. 2013; 29:721-730.

5. Shore DE, Carr CE and Ruvkun G. Induction of cytoprotective pathways is central to the extension of lifespan conferred by multiple longevity pathways. PLoS Genet. 2012;8:e1002792.

6. Shore DE and Ruvkun G. A cytoprotective perspective on longevity regulation. Trends Cell Biol. 2013; 23:409-420.

7. Allard JS, Heilbronn LK, Smith C, Hunt ND, Ingram DK, Ravussin E and de CR. In vitro cellular adaptations of indicators of longevity in response to treatment with serum collected from humans on calorie restricted diets. PLoS One. 2008;3:e3211.

8. Hall DM, Xu L, Drake VJ, Oberley LW, Oberley TD, Moseley PL and Kregel KC. Aging reduces adaptive capacity and stress protein expression in the liver after heat stress. J Appl Physiol (1985). 2000; 89:749-759.

9. Rattan SI, Fernandes RA, Demirovic D, Dymek B and Lima CF. Heat stress and hormetin-induced hormesis in human cells: effects on aging, wound healing, angiogenesis, and differentiation. Dose Response. 2009; 7:90-103.

10. McCay CM, Crowell MF and Maynard LA. The effect of retarded growth upon the length of life span and upon the ultimate body size. 1935. Nutrition. 1989;5:155-171.

11. McDonald RB and Ramsey JJ. Honoring Clive McCay and 75 years of calorie restriction research. J Nutr. 2010; 140:1205-1210.

12. Mercken EM, Carboneau BA, Krzysik-Walker SM and de Cabo R. Of mice and men: the benefits of caloric restriction, exercise, and mimetics. Ageing Res Rev. 2012; 11:390-398.

13. Brown MK and Naidoo N. The endoplasmic reticulum stress response in aging and age-related diseases. FPHYS. 2012; 3:263.

14. Morimoto RI and Cuervo AM. Proteostasis and the aging proteome in health and disease. J Gerontol A Biol Sci Med Sci. 2014; 69 Suppl 1:S33-38.

15. Sinclair DA. Toward a unified theory of caloric restriction and longevity regulation. Mech Ageing Dev. 2005; 126:987-1002.

16. Omodei D, Licastro D, Salvatore F, Crosby SD and Fontana L. Serum from humans on long-term calorie restriction enhances stress resistance in cell culture. Aging (Albany NY). 2013; 5:599-606.

17. Martin-Montalvo A, Villalba JM, Navas P and de Cabo R. NRF2, cancer and calorie restriction. Oncogene. 2011; 30:505-520.

18. Jaramillo MC and Zhang DD. The emerging role of the Nrf2-Keap1 signaling pathway in cancer. Genes Dev. 2013; 27:2179-2191.

19. Hursting SD, Smith SM, Lashinger LM, Harvey AE and Perkins SN. Calories and carcinogenesis: lessons learned from 30 years of calorie restriction research. Carcinogenesis. 2010; 31:83-89.

20. Mukherjee P, Abate LE and Seyfried TN. Antiangiogenic and proapoptotic effects of dietary restriction on experimental mouse and human brain tumors. Clin Cancer Res. 2004; 10:5622-5629.

21. Lee C, Safdie FM, Raffaghello L, Wei M, Madia F, Parrella E, Hwang D, Cohen P, Bianchi G and Longo VD. Reduced levels of IGF-I mediate differential protection of normal and cancer cells in response to fasting and improve chemotherapeutic index. Cancer Res. 2010; 70:1564-1572.

22. Lanza-Jacoby S, Yan G, Radice G, LePhong C, Baliff J and Hess R. Calorie restriction delays the progression of lesions to pancreatic cancer in the LSL-KrasG12D; Pdx-1/Cre mouse model of pancreatic cancer. Exp Biol Med (Maywood). 2013; 238:787-797.

23. De Cabo R, Fürer-Galban S, Anson RM, Gilman C, Gorospe M and Lane MA. An in vitro model of caloric restriction. Exp Gerontol. 2003; 38:631-639.

24. Wysocka A and Krawczyk Z. Green fluorescent protein as a marker for monitoring activity of stress-inducible hsp70 rat gene promoter. Mol Cell Biochem. 2000; 215:153-156.

25. Ueda T, Sasaki M, Elia AJ, Chio II, Hamada K, Fukunaga R and Mak TW. Combined deficiency for MAP kinase-interacting kinase 1 and 2 (Mnk1 and Mnk2) delays tumor development. PNAS. 2010; 107(32):13984-13990.

26. Strebhardt K. Multifaceted polo-like kinases: drug targets and antitargets for cancer therapy. Nat Rev Drug Discov. 2010; 9:643-660.

27. Sharp TV, Munoz F, Bourboulia D, Presneau N, Darai E, Wang HW, Cannon M, Butcher DN, Nicholson AG, Klein G, Imreh S and Boshoff C. LIM domains-containing protein 1 (LIMD1), a tumor suppressor encoded at chromosome 3p21.3, binds pRB and represses E2F-driven transcription. PNAS. 2004; 101:16531-16536.

28. Rochette L, Lorin J, Zeller M, Guilland JC, Lorgis L, Cottin Y and Vergely C. Nitric oxide synthase inhibition and oxidative

stress in cardiovascular diseases: possible therapeutic targets? Pharmacol Ther. 2013; 140:239-257.
29. Wang Y, Yang J and Yi J. Redox sensing by proteins: oxidative modifications on cysteines and the consequent events. Antioxid Redox Signal. 2012;16:649-657.
30. Lang R, Hammer M and Mages J. DUSP meet immunology: dual specificity MAPK phosphatases in control of the inflammatory response. J Immunol. 2006; 177:7497-7504.
31. Kilaparty SP and Ali N. Changes in expression of Multiple Inositol Polyphosphate Phosphatase1 (Minpp1) under Apoptotic and Cellular Stress Conditions. FASEB J. 2013;27:834.14
32. Zhu H, Yoshimoto T and Yamashima T. Heat shock protein 70.1 (Hsp70.1) affects neuronal cell fate by regulating lysosomal acid sphingomyelinase. J Biol Chem. 2014; 289:27432-27443.
33. Mercken EM, Crosby SD, Lamming DW, JeBailey L, Krzysik-Walker S, Villareal DT, Capri M, Franceschi C, Zhang Y, Becker K, Sabatini DM, de Cabo R and Fontana L. Calorie restriction in humans inhibits the PI3K/AKT pathway and induces a younger transcription profile. Aging Cell. 2013; 12:645-651.
34. Omodei D and Fontana L. Calorie restriction and prevention of age-associated chronic disease. FEBS Lett. 2011; 585:1537-1542.
35. De Cabo R, Carmona-Gutierrez D, Bernier M, Hall MN and Madeo F. The search for antiaging interventions: from elixirs to fasting regimens. Cell. 2014;157:1515-1526.
36. De Lorenzo MS, Baljinnyam E, Vatner DE, Abarzua P, Vatner SF and Rabson AB. Caloric restriction reduces growth of mammary tumors and metastases. Carcinogenesis. 2011; 32:1381-1387.
37. Minor RK, López M, Younts CM, Jones B, Pearson KJ, Anson RM, Dieguez C and de Cabo R. The arcuate nucleus and neuropeptide Y contribute to the antitumorigenic effect of calorie restriction. Aging Cell. 2011; 10:483-492.
38. Daugaard M, Jaattela M and Rohde M. Hsp70-2 is required for tumor cell growth and survival. Cell Cycle. 2005; 4:877-880.
39. Westerheide SD and Morimoto RI. Heat shock response modulators as therapeutic tools for diseases of protein conformation. J Biol Chem. 2005; 280:33097-33100.
40. Raynes R, Leckey BD, Jr., Nguyen K and Westerheide SD. Heat shock and caloric restriction have a synergistic effect on the heat shock response in a sir2.1-dependent manner in Caenorhabditis elegans. J Biol Chem. 2012; 287:29045-29053.
41. Westerheide SD, Anckar J, Stevens SM, Jr., Sistonen L and Morimoto RI. Stress-inducible regulation of heat shock factor 1 by the deacetylase SIRT1. Science. 2009; 323:1063-1066.

Research Paper

Clearance of senescent hepatocytes in a neoplastic-prone microenvironment delays the emergence of hepatocellular carcinoma

Fabio Marongiu*, Maria Paola Serra*, Marcella Sini, Fabrizio Angius, and Ezio Laconi

Department of Biomedical Sciences, Unit of Experimental Medicine, University of Cagliari, 09124 Cagliari, Italy
*These two authors contributed equally to this work.

Key words: cell transplantation, tumor microenvironment, cell senescence, cell competition, liver repopulation, liver carcinogenesis
Received: 11/19/13; Accepted: 1/20/14; Published: 1/23/14 DOI: 10.18632/aging.100631
Correspondence to: Ezio Laconi, MD/PhD; **E-mail:** elaconi@unica.it

Copyright: © Marongiu et al. This is an open-access article distributed under the terms of the Creative Commons Attribution License, which permits unrestricted use, distribution, and reproduction in any medium, provided the original author and source are credited

Abstract: Increasing evidence indicates that carcinogenesis is dependent on the tissue context in which it occurs, implying that the latter can be a target for preventive or therapeutic strategies. We tested the possibility that re-normalizing a senescent, neoplastic-prone tissue microenvironment would exert a modulatory effect on the emergence of neoplastic disease. Rats were exposed to a protocol for the induction of hepatocellular carcinoma (HCC). Using an orthotopic and syngeneic system for cell transplantation, one group of animal was then delivered 8 million normal hepatocytes, via the portal circulation. Hepatocytes transplantation resulted in a prominent decrease in the incidence of both pre-neoplastic and neoplastic lesions. At the end of 1 year 50% of control animals presented with HCC, while no HCC were observed in the transplanted group. Extensive hepatocyte senescence was induced by the carcinogenic protocol in the host liver; however, senescent cells were largely cleared following infusion of normal hepatocytes. Furthermore, levels of Il-6 increased in rats exposed to the carcinogenic protocol, while they returned to near control values in the group receiving hepatocyte transplantation. These results support the concept that strategies aimed at normalizing a neoplastic-prone tissue landscape can modulate progression of neoplastic disease.

INTRODUCTION

Population The role of the microenvironment in the pathogenesis of neoplastic disease is increasingly being appreciated. Starting from the report of Mintz and Illmensee [1], describing the generation of normal genetically mosaic mice from malignant teratocarcinoma cells, several studies have demonstrated that the phenotype of pre-neoplastic and neoplastic cell populations can be profoundly modulated by external cues emanating from the surrounding microenvironment [2-5]. Furthermore, it has been documented that specific gene-expression profiles in non-cancerous tissue are able to predict recurrence and survival in patients with hepatocellular carcinoma (HCC), again pointing to the critical role of the surrounding microenvironment in the natural history of neoplastic disease [6-7]. Along this line, studies from our laboratory have indicated that a growth-constrained/senescent tissue environment is able to generate a powerful driving force for the selective expansion of pre-neoplastic hepatocytes in the liver, leading to their progression to HCC [8]. Exposure to retrorsine (RS), a naturally-occurring pyrrolizidine alkaloid, impairs liver regeneration and induces extensive hepatocyte senescence in rat liver [9-10]. When pre-neoplastic cells isolated from hepatic nodules were transplanted in RS-treated livers, they grew rapidly and evolved into HCC; however, the same cell preparation was unable to expand and progress following injection into untreated, syngeneic normal hosts [8].

These observations provide a rationale for the hypothesis that targeting a neoplastic-prone tissue

landscape may represent a valuable approach to modulate the evolution of carcinogenic process [11-13]. Recently, we have obtained evidence to indicate that orthotopic transplantation of normal hepatocytes in animals previously exposed to a carcinogenic regimen exerts a delaying effect on the growth of early preneoplastic lesions [14]. In the present studies, we have extended this observation and explored the possible biological and molecular mechanisms underlying this phenomenon. Neoplastic process was induced in rat liver through sequential exposure to diethylnitrosamine (DENA) and RS. Normal hepatocytes transplanted following the carcinogenic protocol were able to reduce the incidence of preneoplastic and neoplastic lesions at the end of 1 year. This was associated with clearance of RS-induced senescent hepatocytes by transplanted normal cells.

RESULTS

The induction of hepatocellular carcinoma following exposure to DENA+RS

As already mentioned, naturally occurring pyrrolizidine alkaloids, including RS, are known for their ability to promote the growth of early hepatic nodules in initiated rat liver [15]. However, no studies have been reported to date on the long term effects of these agents in animals previously given a carcinogen. In the present experiments, rats were administered DENA and RS (two single injections, 10 days apart), and they were killed 1 year later. As predicted, multiple pre-neoplastic and neoplastic hepatocellular lesions, ranging in size from a few mm to 2.5 cm in diameter, were observed in all animals exposed to this protocol (figure 1, panel A). Furthermore, histological analysis confirmed the presence of large, advanced hepatocyte nodules in all liver samples in this group, while trabecular HCC was diagnosed in 4 out of 8 rats (figure 1, panel B).

Normal hepatocyte transplantation delays the emergence of HCC induced by DENA+RS

Based on the above findings, we next considered the effect of normal hepatocyte transplantation on the incidence of hepatic nodules and HCC following exposure to DENA+RS. Results are reported figure 2 and table 1. Major differences were already evident upon macroscopic examination. The liver of DENA+RS-treated animals displayed slightly increased stiffness compared to normal, with irregular margins and finely granular surface; however, these changes were largely reversed in rats receiving the infusion of normal cells (figure 2, panels A and B). Most notably, the presence of large nodular lesions and overall tumour burden in the liver were greatly reduced in the latter group (figure 2, panel C); only 2 out of 8 rats in this group had nodules >5mm in diameter; strikingly, in 2 animals no macroscopic lesions were observed. Histological analysis on H&E stained liver samples confirmed and extended these results: overt HCC was found in 4 out of 8 animals given DENA+RS, as mentioned in the preceding paragraphs; however, no HCCs were present in the group receiving normal hepatocyte transplantation following the carcinogenic protocol (table 1). Proliferating hepatocytes were readily observed in hepatic nodules and HCC in animals exposed to DENA+RS, as expected (figure 2, panel D); however, they were fewer in GST 7-7-positive lesions from the group receiving hepatocyte transplantation (figure 2, panel E); in the latter group, areas of repopulated liver displayed scattered BrdU-positive hepatocytes (figure 2, panel F).

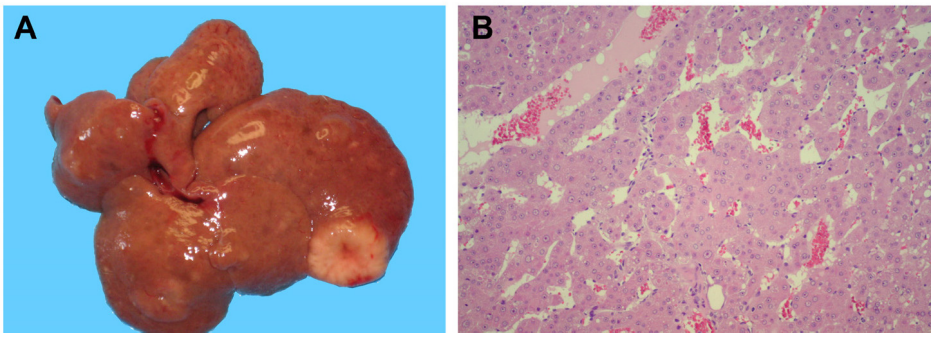

Figure 1. The development of HCC in rats exposed to DENA+RS and killed after one year. Panel (**A**) macroscopic appearance, with withish-grey lesions displaying prominent vasculature; panel (**B**) trabecular HCC with discrete cellular pleomorphism (100x).

Table 1. Incidence of nodules and HCC in the two experimental groups

	Number of animals with:		
	Preneoplastic nodules		HCC
	≤5mm	*>5mm*	
DENA + RS	8/8	7/8	4/8
DENA + RS + Tx	6/8	2/8	0/8
Relative Risk	0.7500	0.2857	0
P value	ns	<0.05	<0.05

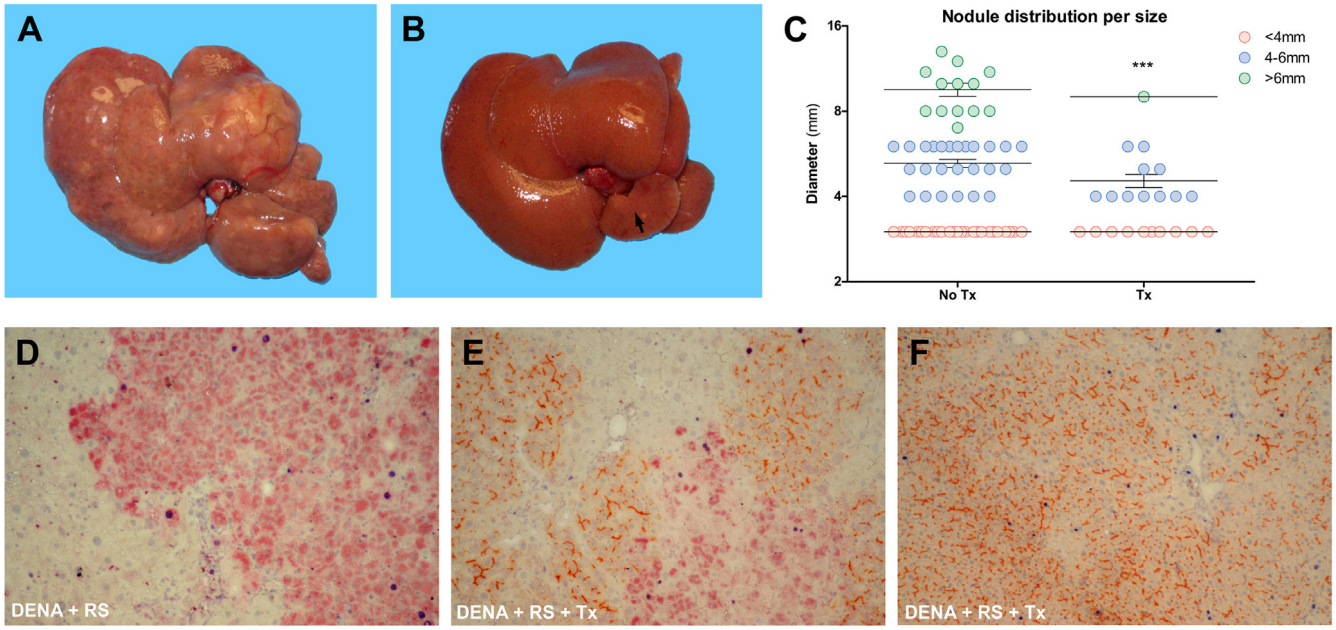

Figure 2. Analysis of liver lesions. Macroscopic appearance of livers from animals exposed to either DENA+RS (panel **A**) or DENA+RS followed by hepatocyte transplantation (panel **B**); both animals were killed 1 year post-treatment. Note the presence of large lesions in panel **A**, while the liver in panel **B** appears normal and shows only one tiny nodule in the caudate lobe. Panel C shows the size distribution of hepatic lesions in both experimental groups; note that the largest lesion found in one animal in DENA+RS-treated group is not included in this plot. ***Significantly different from non-transplanted animals: nodules <4mm, P<0.005; nodules 4-6mm, P<0.001; nodules >6mm, P<0.005. Panels **D-F**: immunohistochemical analysis of liver sections from animals exposed to either DENA+RS (panel **D**) or DENA+RS followed by hepatocyte transplantation (panels **E** and **F**); sections were stained for glutathione-S-transferase 7-7 (GST 7-7, a marker of preneoplastic nodules), BrdU and DPP-IV (orange-rust). Note the presence of BrdU-labelled hepatocytes (dark blue) in GST 7-7-positive lesions (red color, panels **D** and **E**) and in areas of repopulated liver (orange-rust, panel **E** and **F**).

Normal hepatocyte transplantation results in the clearance of DENA+RS-induced senescent hepatocytes

As mentioned in the Introduction, recent findings have indicated that exposure to RS induces extensive hepatocyte senescence in rat liver [10]. Although cell senescence can represent a fail safe mechanism to alt neoplastic progression of altered cells [17], it is now well established that it can also contribute to the emergence of the neoplastic phenotype, possibly through secretion of a host of factors, variably referred to as senescence-associated secretory phenotype (SASP) [18] or senescence-messaging secretome (SMS) [19], and comprising cytokines, growth factors and proteases. Based on this information, it became important to determine the presence of hepatocyte senescence in animals treated with DENA+RS or DENA+RS+Tx. As reported in figure 3, markers related to cell senescence were highly expressed in animals treated with DENA+RS and killed 4 months later; these included the senescence-associated β-galactosidase (SA-β-gal), (panel A); and the phosphorylated form of H2A histone family, member X (γ-H2AX), which is considered as a marker of persistent activation of a DNA damage response and a trigger of cell senescence (panel D). However, both changes were almost completely reversed in animals given DENA+RS followed by hepatocyte transplantation. Transplanted hepatocytes were able to extensively repopulate the host liver; this effect was already prominent at 4 months post-injection (Figure 3, panel C), and persisted after 1 year (data not shown); it was associated with decreased expression of both SA-β-gal and γ-H2AX, which were virtually absent in repopulated areas of the liver and were only detected in residual portions of endogenous parenchyma (figure 3, panels B, C, E, F, G and H).

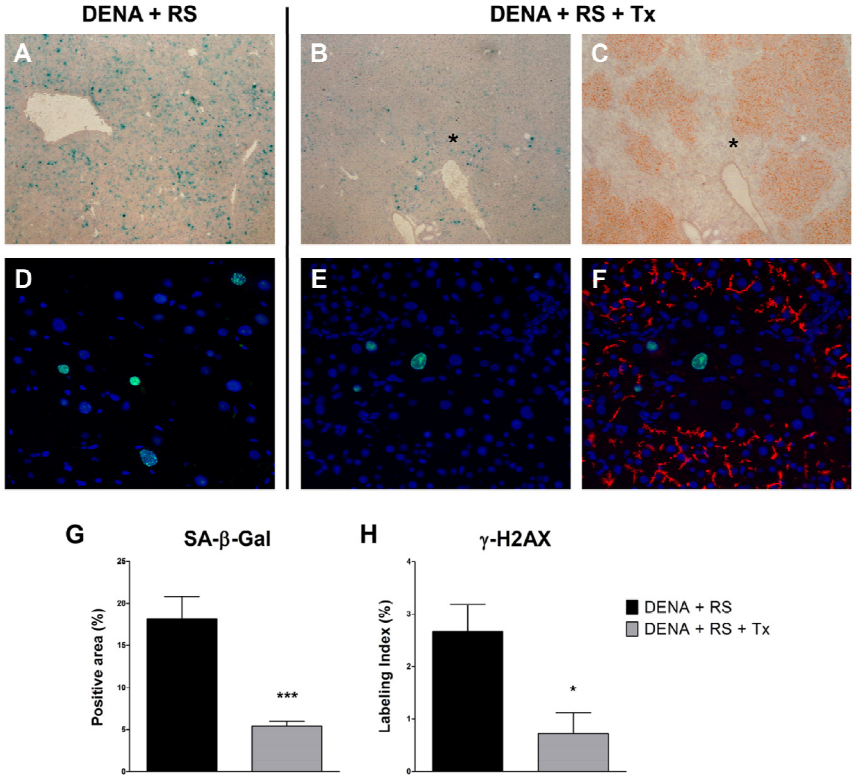

Figure 3. Hepatocyte transplantation reverses the RS-induced senescent phenotype. Expression of SA-β-gal (panels **A**, **B**, **C** and G) and γ-H2AX (panels **D**, **E**, **F** and H), in rat liver exposed to either DENA+RS or DENA+RS followed by normal hepatocyte transplantations. Markers of cell senescence were highly expressed in DENA+RS-treated livers (panels **A**, **D**), while their levels were markedly reduced in animals receiving hepatocyte transplantation (panels **B**, **C**, **E**, **F**). In the latter group, extensive repopulation of the recipient liver was observed (panels **C**, histochemical staining for DPP-IV, orange-rust; panel **F**, immunofluorescence staining for CD26, red); note the residual expression of senescence markers in non-repopulated areas (panel C and F). Panels **A**, **B** and **C**: magnification 40x; panels **D**, **E** and **F**: magnification 200x. Panels **G** and **H**: ***P<0.001; *P<0.05.

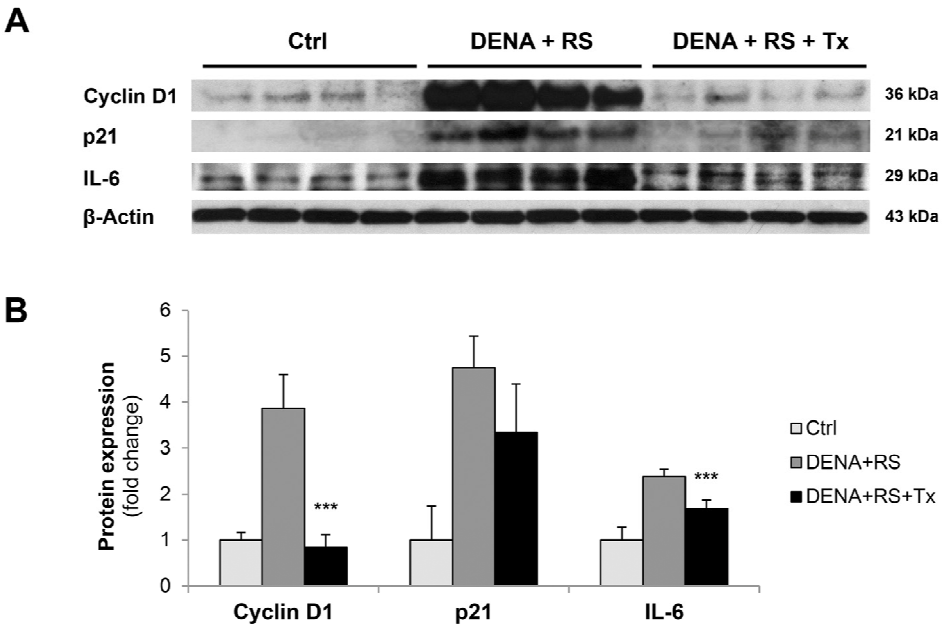

Figure 4. Hepatocyte transplantation reverses the RS-induced senescent phenotype. Expression of cyclin D1, p21 and IL-6 in control rat liver and rat liver exposed to either DENA+RS or DENA+RS followed by normal hepatocyte transplantations. All gene products were highly expressed in DENA+RS-treated livers, while their levels were near control values in animals receiving hepatocyte transplantation (panels **A** and **B**). ***Significantly different from non-transplanted animals: P<0.005.

Hepatocyte transplantation reverses biochemical markers of hepatocyte senescence and SASP

An intriguing interpretation of cell senescence postulates that this unique phenotype emerges when a cell integrates two types of signals: one that reads for growth and one that imposes a block in the replicative cycle [20,21]. For example, DNA damaging agents do not induce senescence in quiescent cells; however, they do so if the presence of persistent DNA damage and cell cycle arrest is coupled with growth promoting stimuli [21]. Under these conditions, cells switch on the senescence program and express markers related to both cell cycle block and growth stimulation. In line with this postulation, both the cyclin-dependent kinase inhibitor, p21, and the positive regulator cyclin D1 were found to be over-expressed in rats exposed to DENA+RS and killed 4 months thereafter (figure 4, panels A and B). Furthermore, a main component of SASP/SMS, namely the pro-inflammatory cytokine IL-6, was also over-expressed in DENA+RS-treated animals. Both findings were in agreement with those reported following exposure to RS alone [10].

Remarkably, these changes were strongly counteracted by transplantation of normal hepatocytes: in fact, the expression of p21, cyclin D1 and IL-6 returned to near-control levels in animals receiving normal cells following exposure to the carcinogenic protocol. (figure 4, panels A and B).

DISCUSSION

The results of these studies indicate that transplantation of normal hepatocytes in a neoplastic-prone liver microenvironment delays the growth of hepatic nodules and the emergence of HCC; furthermore, this effect is associated with clearance of senescent hepatocytes induced by the carcinogenic protocol.

Over a decade ago, we reported that pre-neoplastic hepatocytes grew very rapidly and progressed to HCC upon transplantation into a host liver pre-treated with RS; however, the same cell population was unable to expand following implantation into the liver of a normal, un-treated recipient [8]. Recent studies, aimed at defining the biological and molecular determinants of

the RS-induced effect, revealed the presence of extensive hepatocyte senescence in rat liver exposed to the alkaloid. Based on those findings, it was suggested that cell senescence and the associated SASP/SMS are possibly involved in the induction of the RS-associated neoplastic-prone tissue microenvironment [10]. In fact, it is now widely recognized that the senescence phenotype, while representing a fail-safe mechanism to avoid the risk of malignant transformation in cells harbouring damaged DNA or activated oncogenes [16,17,22,23], can also foster the emergence of premalignant and malignant cells [18,19,24,25], including their acquisition of metastatic potential [26] and resistance to chemotherapy [27,28]. These effects are at least partly mediated by a host of secreted factors, referred to as SASP/SMS and comprising cytokines, growth factors and proteases [18,19]. Among other products, the pro-inflammatory cytokine IL-6 has been attributed a prominent role both as a mediator of SASP effects and in reinforcing the senescence phenotype [24]. Moreover, cell senescence and SASP have been linked to chronic inflammation [29], adding yet another facet to the complex relationship between cancer, aging, and the immune response [30,31]. Interestingly, cell senescence has been reported in association with major risk factors for human neoplasia, including aging, cigarette smoke [32], UV light [33] and liver cirrhosis [34]. Indeed, the presence of hepatocyte senescence has long been documented during the evolution of chronic liver disease [35]. A recent study suggests that parameters related to cell senescence predict progression in non-alcoholic fatty liver disease (NAFLD) [36]. Moreover, a specific role for IL-6, together with TNF, has been proposed in the pathogenesis of liver inflammation and cancer associated with dietary and genetic obesity [37]. Thus, it appears that the tissue microenvironment induced by RS in rat liver, which strongly promotes the neoplastic process, shares intriguing similarities with chronic alterations associated with increased risk of liver cancer in humans.

In the present studies we tested the possibility that normal hepatocyte transplantation would reverse alterations induced by RS in the liver microenvironment, thereby modulating its tumour promoting potential. To this end, animals were sequentially exposed to DENA and RS, followed by two injections of hepatocytes freshly isolated from normal syngenic donors [14]. At end of 1 year, all animals treated with DENA+RS developed large liver tumours, with 50% (4/8) incidence of HCC. By contrast, the number of nodules were greatly reduced in rats receiving normal hepatocyte transplantation; most importantly, no animal in this group showed histological evidence of HCC (figure 2 and Table 1).

The liver of transplanted animals was extensively repopulated by donor-derived cells, resulting in the clearance of DENA+RS-induced senescent hepatocytes. Only residual hepatocyes expressing SA-β-Gal or γ-H2AX were found in these animals, and they were confined to areas of non-repopulated liver (figure 3); furthermore, the expression of cyclin D1, p21 and the SASP-associated cytokine IL-6 were markedly reduced to near control values. In summary, normal hepatocyte transplantation is able to delay DENA+RS-induced carcinogenic process and it is also associated with extensive remodeling of the tissue landscape, consisting in the massive replacement of resident senescent hepatocytes with phenotypically normal cells. It is noteworthy that our results are reminiscent of those reported by the group of the DeGregori in the hematopoietic system: it was observed that transplantation of young, normal bone marrow cells was able to prevent the clonal expansion and leukemogenesis mediated by initiated progenitors in the context of an aged or previously irradiated bone marrow microenvironment [38,39].

In a recent report, Kang et al. described the protective effect of immune-mediated clearance of N-ras-expressing senescent hepatocytes on liver cancer development in mice [40]. The effect was attributed to the putative preneoplastic nature of oncogene-transduced senescent cells, whose removal by a T-cell specific response was therefore considered as directly responsible for the reduced incidence of HCC [40]. While any direct involvement of the immune system was not investigated in our present study, our findings appear difficult to reconcile with the above proposition. In fact, there is no evidence that RS-induced senescent hepatocytes display any direct pre-neoplastic potential [41]; on the other hand, they are able to support the growth of transplanted nodular hepatocytes and their progression to HCC [8]. Thus, it appears that, under the conditions described in our studies, the role of cell senescence is to promote the growth of carcinogen-induced altered cells, possibly through the effect(s) of SASP/SMS components, including IL-6 [42]. Replacement of senescent hepatocytes by normal transplanted cells results in the attenuation of such promoting effect and a delay in the emergence of preneoplastic and neoplastic lesions. Interestingly, a similar paradigm could be applicable to the increased cancer incidence associated with aging [43].

Taken together, these findings reinforce the concept that strategies aimed at preserving and/or re-establishing a normal tissue microenvironment represent an effective approach towards limiting the impact of neoplastic disease. Furthermore, they highlight the role of

senescent cells in fuelling carcinogenesis in a neoplastic-prone tissue landscape.

EXPERIMENTAL PROCEDURES

Animals and treatments. Liver carcinogenesis was induced using a sequential exposure to diethyl-nitrosamine (DENA) and retrorsine (RS) [14]. Male Fischer 344, rats of 4 weeks of age were injected with DENA (160 mg/kg, i.p.), followed by a single dose of RS (30 mg/kg, i.p.), given 10 days after DENA administration. Two weeks later, animals were divided into 2 groups of 12 rats each: group 1 received no further treatment, while group 2 was given two injections of hepatocytes isolated from a normal syngenic donor, containing $4x10^6$ cells each, two weeks apart. Animals from each group were killed at either 4 months (4 rats) or 12 months (the remaining 8 rats) after DENA administration. Starting 24 hours before killing, animals were given 3 injections of 5'-bromo-deoxy-uridine (BrdU, 50 mg/kg, i.p.) every 8 hours. All experiments were approved by the University of Cagliari Ethical Committee for Animal Experimentation; all animals received humane care in accordance with NIH Guidelines for the care and use of animals. Hepatic lesions were microscopically classified according to published criteria [44].

Hepatocyte isolation and transplantation. Hepatocytes for transplantation were isolated from a 6-wk old donor, according to a two-step collagenase perfusion technique [45]. Cell viability, determined by trypan blue exclusion at the end of the isolation procedure, was >90%. Animals were anesthetized and a small incision (about 1 cm) was performed in the upper abdominal wall; hepatocytes, suspended in PBS ($1x10^7$/ml), were then delivered through a branch of the mesenteric veins, using a syringe with a 26-gauge needle. The fate of donor-derived cells in the recipient liver was followed using the F344-dipeptidyl-peptidase type IV (DPP-IV)-deficient model for cell transplantation [46]. Donor hepatocytes were isolated from animals expressing the marker enzyme (DPP-IV-positive), while DPP-IV-deficient rats were used as recipients. Since the Fischer 344 rat is a syngenic strain, no immunosuppression was required for successful cell transplantation.

Histochemical and immunohistochemical methods. After sacrifice, livers were removed and samples were taken from each lobe to be either frozen for cryostat sections or fixed in buffered formalin for standard histological analysis and immunohistochemistry. In animals killed at 12 months, liver lobes were cut into 1-2 mm-thick slices and were macroscopically examined for the presence of hepatic nodules/tumors or any other evident lesion. The extent of liver repopulation in transplanted animals was monitored in cryostat sections stained for DPP-IV expression, using histochemical detection methods. Double staining for BrdU (DAKO, Glostrup, Denmark) and glutathione-S-transferase 7-7 (GST 7-7, Santa Cruz, Santa Cruz, CA) was performed on frozen sections, previously fixed in cold 1% acetic acid/ethyl alcohol and boiled in 0,01M Sodium Citrate, pH 6.0.

Staining for SA-β-gal was performed according to published procedures [47]. Immediately before staining, X-Gal stock solution was prepared by dissolving 20mg/ml X-Gal (Invitrogen, Carlsbed, CA) in dimetylformamide. SA-β-Gal staining solution was prepared as follows: 1 mg/ml of X-Gal stock solution were dissolved in 40 mM citric acid in sodium phosphate, pH 6.0/5 mM potassium ferrocyanide/5 mM potassium ferricyanide/150 mM NaCl/2 mM $MgCl_2$. Frozen sections of 10-µm thickness were fixed for 5' in 4% formaldehyde/0.5% glutaraldehyde at 4°C, washed in PBS and incubated in fresh SA-β-Gal staining solution for 16h at 37°C. Sections were counterstained with Hematoxylin.

Immunofluorescence. Immunoflorescence staining for γ-H2AX and CD26 was performed on frozen sections, following fixation in acetone. Slides were blocked for 30', incubated with primary antibodies (H2AX: Abcam, Cambridge, MA; CD26: BD Pharmigen, San Jose, CA) for 1 h at RT, then incubated with Alexa 488- and Alexa 555-conjugated secondary antibodies (Life Technologies, Carlsbad, CA). Slides were counterstained with DAPI and images were acquired with an IX71 fluorescence microscope with CCD camera (Olympus, Tokyo, Japan).

Western Blot. Liver tissue samples were homogenized in RIPA lysis buffer containing Protease Inhibitors, then centrifuged at 12000 rpm for 30' at 4°C. Protein concentration in supernatants was measured using the BCA method [48]. Samples (20µg protein) were prepared in Laemmli buffer, boiled at 95°C for 5' then loaded into SDS-PAGE precast gels (Biorad, Hercules, CA) and run under denaturing conditions. Proteins were transferred onto nitrocellulose membranes (GE, Fairfield, CT), blocked with 5% non-fat milk for 1 h, then incubated with primary antibodies for Cyclin D1 (Sigma, St. Louis, MO), p21 (Santa Cruz, Santa Cruz, CA) NF-κB, TNF-α, IL-6 and β-Actin (Abcam) overnight at 4°C. Membranes were washed and incubated for 2 h with the appropriate secondary antibody conjugated with HRP. Protein bands were detected using a chemoluminescent substrate (Biorad) and imaged onto Kodak film.

Imaging and Statistical analysis. Relative risk of developing preneoplastic/neoplastic lesions was calculated for both experimental groups, as shown in table 1. Chi-square test was used to evaluate statistical significance. Histological images and western blots were processed for quantification with Image Pro Premier software (Media Cybernetics, Rockville, MD). Results are presented as mean±S.E; two-tailed Student t test was used to evaluate results, with a lowest level of significance of $p<0.05$.

ACKNOWLEDGEMENTS

We thank Mrs. Anna Saba and Mr. Roberto Marras for their technical contribution. Grant Support: this work was supported by AIRC (Italian Association for Cancer Research, grant No. IG 10604) and by Sardinian Regional Government (RAS).

Conflicts of Interest Statement

The authors declare no conflict of interest.

REFERENCES

1. Mintz B, Illmensee K. Normal genetically mosaic mice produced from malignant teratocarcinoma cells. Proc Natl Acad Sci U S A 1975;72:3585-3589.

2. Barcellos-Hoff MH, Ravani SA. Irradiated mammary gland stroma promotes the expression of tumorigenic potential by unirradiated epithelial cells. Cancer Res 2000;60:1254-1260.

3. Laconi E. The evolving concept of tumor microenvironments. Bioessays 2007;29:738-744.

4. Bissell MJ, Hines WC. Why don't we get more cancer? A proposed role of the microenvironment in restraining cancer progression. Nat Med 2011;17:320-329.

5. PM, Kasemeier-Kulesa JC, Teddy JM, Margaryan NV, Seftor EA, Seftor REB, Hendrix MJC. Reprogramming metastatic melanoma cells to assume a neural crest cell-like phenotype in an embryonic microenvironment. Proc Natl Acad Sci U S A 2006;103:3752-3757.

6. Hoshida Y, Villanueva A, Kobayashi M, Peix J, Chiang DY, Camargo A, Gupta S, Moore J, Wrobel MJ, Lerner J, Reich M, Chan JA, Glickman JN, Ikeda K, Hashimoto M, Watanabe G, et al. Gene expression in fixed tissues and outcome in hepatocellular carcinoma. N Engl J Med. 2008; 359:1995-2004.

7. Okamoto M, Utsunomiya T, Wakiyama S, Hashimoto M, Fukuzawa K, Ezaki T, Hanai T, Inoue H, Mori M.Specific gene-expression profiles of noncancerous liver tissue predict the risk for multicentric occurrence of hepatocellular carcinoma in hepatitis C virus-positive patients. Ann Surg Oncol. 2006; 13: 947-54.

8. Laconi S, Pani P, Pillai S, Pasciu D, Sarma DS, Laconi E. A growth-constrained environment drives tumor progression invivo. Proc Natl Acad Sci U S A 2001;98:7806-7811.

9. Laconi S, Curreli F, Diana S, Pasciu D, De Filippo G, Sarma DS, Pani P, Laconi E. Liver regeneration in response to partial hepatectomy in rats treated with retrorsine: a kinetic study. J Hepatol. 1999; 31: 1069-1074

10. Serra MP, Marongiu F, Sini M, Laconi E. Hepatocyte senescence in vivo following preconditioning for liver repopulation. Hepatology 2012;56:760-768.

11. Place AE, Jin Huh S, Polyak K. The microenvironment in breast cancer progression: biology and implications for treatment. Breast Cancer Res. 2011; 13: 227.

12. Correia AL, Bissell MJ (2012) The tumor microenvironment is a dominant force in multidrug resistance. Drug Resist Updat 15: 39-49.

13. Hernandez-Gea V, Toffanin S, Friedman SL, Llovet JM. Role of the Microenvironment in the Pathogenesis and Treatment of Hepatocellular Carcinoma. Gastroenterology 2013;144:512-27.

14. Serra MP, Doratiotto S, Marongiu F, Laconi E. Normal hepatocyte transplantation delays the emergence of chemically-induced pre-neoplastic nodules in rat liver. Cell Transplant. 2012; 21 :671-7

15. Hayes MA, Roberts E, Farber E. Initiation and selection of resistant hepatocyte nodules in rats given the pyrrolizidine alkaloids lasiocarpine and senecionine. Cancer Res. 1985; 45: 3726-3734.

16. Narita M, Lowe SW. Senescence comes of age. Nature Med. 2005; 11: 920–922.

17. Suram A, Kaplunov J, Patel PL, Ruan H, Cerutti A, Boccardi V, Fumagalli M, Di Micco R, Mirani N, Gurung RL, Hande MP, d'Adda di Fagagna F, Herbig U. Oncogene-induced telomere dysfunction enforces cellular senescence in human cancer precursor lesions. EMBO J. 2012;31:2839-2851.

18. Coppé JP, Patil CK, Rodier F, Sun Y, Muñoz DP, Goldstein J, Nelson PS, Desprez PY, Campisi J. Senescence-associated secretory phenotypes reveal cell-nonautonomous functions of oncogenic RAS and the p53 tumor suppressor. PLoS. Biol. 2008; 6: 2853-2868.

19. Kuilman T, Peeper DS. Senescence-messaging secretome: SMS-ing cellular stress. Nat Rev Cancer. 2009; 9: 81-94.

20. Demidenko ZN, Blagosklonny MV. Growth stimulation leads to cellular senescence when the cell cycle is blocked. Cell Cycle. 2008; 7: 3355-3361.

21. Leontieva OV, Natarajan V, Demidenko ZN, Burdelya LG, Gudkov AV, Blagosklonny MV. Hypoxia suppresses conversion from proliferative arrest to cellular senescence. Proc Natl Acad Sci USA. 2008; 109: 13314-13318.

22. Van Nguyen T, Puebla-Osorio N, Pang H, Dujka ME, Zhu C.DNA damage-induced cellular senescence is sufficient to suppress tumorigenesis: a mouse model. J Exp Med. 2007; 204: 1453-1461.

23. Xue W, Zender L, Miething C, Dickins RA, Hernando E, Krizhanovsky V, Cordon-Cardo C, Lowe SW. Senescence and tumour clearance is triggered by p53 restoration in murine liver carcinomas. Nature. 2007;445:656-60

24. Kuilman T, Michaloglou C, Vredeveld LC, Douma S, van Doorn R, Desmet CJ, Aarden LA, Mooi WJ, Peeper DS. Oncogene-induced senescence relayed by an interleukin-dependent inflammatory network. Cell. 2008; 133: 1019-1031.

25. Rodier F, Coppé JP, Patil CK, Hoeijmakers WA, Muñoz DP, Raza SR, Freund A, Campeau E, Davalos AR, Campisi J. Persistent DNA damage signalling triggers senescence-associated inflammatory cytokine secretion. Nat Cell Biol. 2009; 11: 973-979.

26. Angelini PD, Zacarias Fluck MF, Pedersen K, Parra-Palau JL, Guiu M, Bernadó Morales C, Vicario R, Luque-García A, Navalpotro NP, Giralt J, Canals F, Gomis RR, Tabernero J, Baselga J, Villanueva J, Arribas J. Constitutive HER2 signaling promotes breast cancer metastasis through cellular senescence. Cancer Res. 2013; 73: 450-458.

27. Gilbert LA, Hemann MT. DNA damage-mediated induction of a chemoresistant niche. Cell. 2010; 143: 355-366.

28. Sun Y, Campisi J, Higano C, Beer TM, Porter P, Coleman I, True L, Nelson PS. Treatment-induced damage to the tumor microenvironment promotes prostate cancer therapy resistance through WNT16B. Nat Med. 2012; 18: 1359-1368.

29. MM, Weyand CM, Goronzy JJ. Chronic inflammation and aging: DNA damage tips the balance. Curr Opin Immunol. 2012; 24: 488-493.

30. Coussens LM, Zitvogel L, Palucka AK. Neutralizing tumor-promoting chronic inflammation: a magic bullet? Science. 2013; 339: 286-291.

31. Takahashi H, Ogata H, Nishigaki R, Broide DH, Karin M Tobacco smoke promotes lung tumorigenesis by triggering IKKbeta- and JNK1-dependent inflammation. Cancer Cell. 2010; 17:89-97.

32. Tsuji T, Aoshiba K, Nagai A. Cigarette smoke induces senescence in alveolar epithelial cells. Am J Respir Cell Mol Biol. 2004; 31: 643-649.

33. Lewis DA, Yi Q, Travers JB, Spandau DF. UVB-induced senescence in human keratinocytes requires a functional insulin-like growth factor-1 receptor and p53. Mol Biol Cell. 2008; 19: 1346-1353.

34. Wiemann SU, Satyanarayana A, Tsahuridu M, Tillmann HL, Zender L, Klempnauer J, Flemming P, Franco S, Blasco MA, Manns MP, Rudolph KL. Hepatocyte telomere shortening and senescence are general markers of human liver cirrhosis. FASEB J. 2002; 16: 935-942.

35. Paradis V, Youssef N, Dargère D, Bâ N, Bonvoust F, Deschatrette J, Bedossa P. Replicative senescence in normal liver, chronic hepatitis C, and hepatocellular carcinomas. Hum Pathol. 2001; 32: 327-332.

36. Aravinthan A, Scarpini C, Tachtatzis P, Verma S, Penrhyn-Lowe S, Harvey R, Davies SE, Allison M, Coleman N, Alexander G. Hepatocyte senescence predicts progression in non-alcohol-related fatty liver disease J Hepatol. 2013; 58: 549-56.

37. Park EJ, Lee JH, Yu GY, He G, Ali SR, Holzer RG, Osterreicher CH, Takahashi H, Karin M. Dietary and genetic obesity promote liver inflammation and tumorigenesis by enhancing IL-6 and TNF expression. Cell. 2010; 140: 197-208.

38. Marusyk A, Casás-Selves M, Henry CJ, Zaberezhnyy V, Klawitter J, Christians U, DeGregori J. Irradiation alters selection for oncogenic mutations in hematopoietic progenitors.Cancer Res. 2009; 69:7262-7269.

39. Henry CJ, Marusyk A, Zaberezhnyy V, Adane B, DeGregori J.Declining lymphoid progenitor fitness promotes aging-associated leukemogenesis.Proc Natl Acad Sci U S A. 2010; 107:21713-21718.

40. Kang TW, Yevsa T, Woller N, Hoenicke L, Wuestefeld T, Dauch D, Hohmeyer A, Gereke M, Rudalska R, Potapova A, Iken M, Vucur M, Weiss S, Heikenwalder M, Khan S, Gil J, Bruder D, Manns M, Schirmacher P, Tacke F, Ott M, Luedde T, Longerich T, Kubicka S, Zender L. Senescence surveillance of pre-malignant hepatocytes limits liver cancer development. Nature. 2011; 479: 547-551.

41. Laconi S, Montisci S, Doratiotto S, Greco M, Pasciu D, Pillai S, Pani P, Laconi E. Liver repopulation by transplanted hepatocytes and risk of hepatocellular carcinoma. Transplantation. 2006; 82: 1319-1323.

42. Galun E, Axelrod JH. The role of cytokines in liver failure and regeneration: potential new molecular therapies. Biochim Biophys Acta. 2002; 1592: 345-358.

43. Pasciu D, Montisci S, Greco M, Doratiotto S, Pitzalis S, Pani P, Laconi S, Laconi E. Aging is associated with increased clonogenic potential in rat liver in vivo. Aging Cell. 2006; 5: 373-377.

44. Squire RA, Levitt MH. Report of a workshop on classification of specific hepatocellular lesions in rats. Cancer Res. 1975; 35: 3214-3223.

45. Seglen PO. Preparation of isolated rat liver cells. Methods Cell Biol. 1976; 13:29-83.

46. Thompson NL, Hixson DC, Callanan H, Panzica M, Flanagan D, Faris RA, Hong WJ, Hartel-Schenk S, Doyle D. A Fischer rat substrain deficient in dipeptidyl peptidase IV activity makes normal steady-state RNA levels and an altered protein. Use as a liver-cell transplantation model. Biochem J. 1991; 273 (Pt 3): 497-502.

47. Itahana K, Campisi J, Dimri GP. Methods to detect biomarkers of cellular senescence: the senescence-associated beta-galactosidase assay. Methods Mol Biol. 2007; 371: 21-31.

48. Smith PK, Krohn RI, Hermanson GT, Mallia AK, Gartner FH, Provenzano MD, Fujimoto EK, Goeke NM, Olson BJ, Klenk DC. Measurement of protein using bicinchoninic acid. Anal Biochem. 1985; 150:76-85.

Research Paper

Therapeutic and space radiation exposure of mouse brain causes impaired DNA repair response and premature senescence by chronic oxidant production

Shubhankar Suman[1], Olga C. Rodriguez[2], Thomas A. Winters[3], Albert J. Fornace Jr[1, 2, 4], Chris Albanese[2], and Kamal Datta[1,2]

[1] Department of Biochemistry and Molecular & Cell Biology, Georgetown University Medical Center, Washington, DC 20057, USA
[2] Lombardi Comprehensive Cancer Center, Georgetown University, Washington, DC 20057, USA
[3] Nuclear Medicine Department, Warren Grant Magnuson Clinical Center, National Institutes of Health, Bethesda, MD 20892, USA
[4] Center of Excellence In Genomic Medicine Research (CEGMR), King Abdulaziz University, Jeddah, SA

Key words: Radiation, heavy ion radiation, premature aging, senescence, oxidative stress, DNA damage, cerebral cortex, long- term effects
Received: 6/21/13; Accepted: 8/5/13; Published: 8/6/13 DOI: 10.18632/aging.100587
Correspondence to: Kamal Datta, MD; **E-mail:** kd257@georgetown.edu

Copyright: © Suman et al. This is an open-access article distributed under the terms of the Creative Commons Attribution License, which permits unrestricted use, distribution, and reproduction in any medium, provided the original author and source are credited

Abstract: Despite recent epidemiological evidences linking radiation exposure and a number of human ailments including cancer, mechanistic understanding of how radiation inflicts long-term changes in cerebral cortex, which regulates important neuronal functions, remains obscure. The current study dissects molecular events relevant to pathology in cerebral cortex of 6 to 8 weeks old female C57BL/6J mice two and twelve months after exposure to a γ radiation dose (2 Gy) commonly employed in fractionated radiotherapy. For a comparative study, effects of 1.6 Gy heavy ion ^{56}Fe radiation on cerebral cortex were also investigated, which has implications for space exploration. Radiation exposure was associated with increased chronic oxidative stress, oxidative DNA damage, lipid peroxidation, and apoptosis. These results when considered with decreased cortical thickness, activation of cell-cycle arrest pathway, and inhibition of DNA double strand break repair factors led us to conclude to our knowledge for the first time that radiation caused aging-like pathology in cerebral cortical cells and changes after heavy ion radiation were more pronounced than γ radiation.

INTRODUCTION

Radiation exposure to normal brain tissue during therapeutic and diagnostic procedures is unavoidable and radiation has been shown to affect brain function [1-3]. Radiation therapy remains the main mode of treatment for both the primary and secondary brain tumors and fractionated radiation therapy commonly uses a 2 Gy daily dose-fraction [1,4]. Although important advances have been made in the field of radiation therapy to make it more focused, radiation exposure to normal brain tissue is inescapable leading to long-term functional deficit such as cognitive, visual, and motor impairments. Among the diagnostic procedures, computerized tomographic (CT) scan due to its multiple exposure sequences exposes tissues to a higher radiation doses per scan than a single exposure procedures such as x-ray chest. A single head and neck CT scan, depending on age, could expose brain to radiation doses between 20 and 100 mGy and with marked increase in radiation based diagnostic procedures [5-7], the cumulative radiation dose to brain due to repeated exposure could be high enough to raise long-term health concern such as functional decline and cancer [8]. Epidemiological studies in atom bomb survivors have shown increased cancer risk after

exposure to radiation dose between 50 and 200 mGy and exposure at an early age has the highest risk [9]. Cerebral cortex, the outermost layer of the mammalian brain, regulates important functions such as awareness, motor and sensory functions, memory, language, and visual perceptions through its connections to various sub-cortical structures such as the thalamus and basal ganglia. Therefore, any perturbation in cerebral cortical cells caused by radiation exposure would lead to impairment of at least some of these neurological functions compromising quality of life. Studies in mice have shown significant structural alterations of the cerebral cortex eight weeks after exposure to four 5 Gy fractions of γ radiation [1]. However, long-term follow up *in vivo* data on underlying mechanisms of changes in cerebral cortex after exposure to a clinically relevant dose of γ radiation is not available in the literature.

Radiation exposure is intimately linked to the production of reactive oxygen species (ROS) and due to its high oxygen consumption and metabolic rate, the brain is more susceptible to ROS and oxidative stress than other organs [10]. Increased ROS could react with lipids, DNA, and proteins leading to the generation of more reactive species and the establishment of a state of perpetual oxidative stress in cells compromising cerebral cortex function [11,12]. Brain due to its high lipid content is particularly vulnerable to oxidative stress-induced lipid peroxidation, which not only generates lipid-based free radicals but also produces a number of highly reactive aldehydes such as malondialdehyde and 4-hydroxy-2-nonenal (4-HNE). These reactive aldehydes in turn react with cellular proteins to form adducts, which have been implicated in neurodegenerative diseases including Alzheimer's disease [13]. When produced in excess of cellular anti-oxidant capacity, ROS are known to induce, apart from other damages, DNA double stand breaks (DSB), the most lethal form of DNA damage. Experimental evidence indicates that unrepaired DSB could induce cell death, and misrepaired DSB has the potential of causing genomic instability [14,15]. DNA DSB in non-dividing cells is commonly repaired by non-homologous end joining (NHEJ) and aging has been associated with a decline in Ku70, Ku80, and DNAPKcs which are considered major players of the NHEJ pathway [16-22].

Persistent induction of DNA damage due to sustained ROS production results in a perpetual DNA damage response [23,24]. The tumor suppressor gene p53 due to its pivotal role in DNA damage response such as cell cycle arrest, DNA repair, and cell death induction remains an important player in maintenance of cellular homeostasis and genomic integrity after radiation exposure. Upon radiation-induced ROS generation and ensuing DNA damage, p53 is activated leading to alterations in the level of its downstream effectors such as Bax, Bcl2, and p21 resulting in the induction of apoptosis and growth arrest [25]. p53, which is mutated in >50% of human cancers, has also been reported to play important roles in aging and increased p53 activity could usher in premature aging [24,26]. However, cellular senescence and aging is a complex process involving multiple signaling pathways [27-30] and association of the tumor suppressors $p16^{Ink4a}$ and $p19^{Arf}$ with senescence is well documented in literature [31,32].

Radiation injury to the brain has been shown to upregulate intermediate filament proteins such as nestin and glial fibrillary acidic protein (GFAP), which are also reported to be associated with oxidative stress, aging, and neurodegeneration [33,34]. The intermediate filament proteins nestin and vimentin are associated with the developing central nervous system (CNS) and upon terminal differentiation of neural precursor cells to astrocytes and neurons, nestin is no longer expressed and is substituted by GFAP and vimentin [35]. Re-expression of embryonic proteins such as nestin and upregulation of GFAP, which reflects proliferative activation of astroglial cells have been observed in radiation-induced CNS injury and increased cellular stress in brain [12,35-41].

Radiation environment in outer space, compared to that on earth, mostly consists of high-energy protons and heavy ions such as ^{56}Fe, ^{28}Si, ^{16}O, and ^{12}C and associated secondary particle radiation [42-44]. While solar particle events (SPE) with mostly proton radiation are sporadic, the galactic cosmic radiation (GCR) with most of its dose equivalent contributed by heavy ion radiation is ambient is space. Heavy ion radiation with high linear energy transfer (high-LET - deposits more energy per unit volume of tissue compared to low-LET γ radiation prevalent on earth) characteristics is vastly more damaging compared to proton and γ radiation not only due to its densely ionizing primary track but also due to the greater number of highly ionizing secondary delta ray tracks [45-47]. Consequently, from astronauts' health point of view, a major concern for the National Aeronautics and Space Administration (NASA) during long duration space missions is exposure to heavy ion radiation and its consequences on the CNS. Additionally, heavy ion radiation therapy of brain tumors has been shown to inflict subsequent neurological deficits such as cognitive and memory loss that are predicted to be in part due to alterations in cerebral cortex [48-50]. Also, exposure to high-LET neutron radiation has been shown to induce hypoplasia

of the cerebral cortex in the developing mouse brain [51]. While most of the animal studies involving high-LET radiation focused on hippocampus [11,52-58], very few have dealt with cerebral cortex and fewer have reported underlying mechanisms. The current study undertakes long-term follow up investigations of molecular events in cerebral cortex associated with γ radiation exposure and how these events relate to heavy ion radiation exposure. We have shown that there were increased oxidative stress and accelerated senescence signaling after 2 Gy γ radiation. Importantly, we also showed that the effects of oxidative stress and accelerated aging were more pronounced in mice exposed to heavy ions compared to γ radiation.

RESULTS

Persistently raised levels of ROS in cerebral cortical cells after radiation exposure

ROS levels were distinctly increased in freshly isolated cerebral cortical cells two and twelve months after exposure to 1.6 Gy (equitoxic to 2 Gy γ radiation; [59]) of ^{56}Fe radiation compared to shams and 2 Gy γ-irradiated samples. (Figure 1A, B, D, and E). Quantification of flow cytometry data demonstrates a significant increase in ROS levels after ^{56}Fe exposure at both time points relative to control and γ radiation (for 2-month post-radiation: $p<0.008$ compared to control

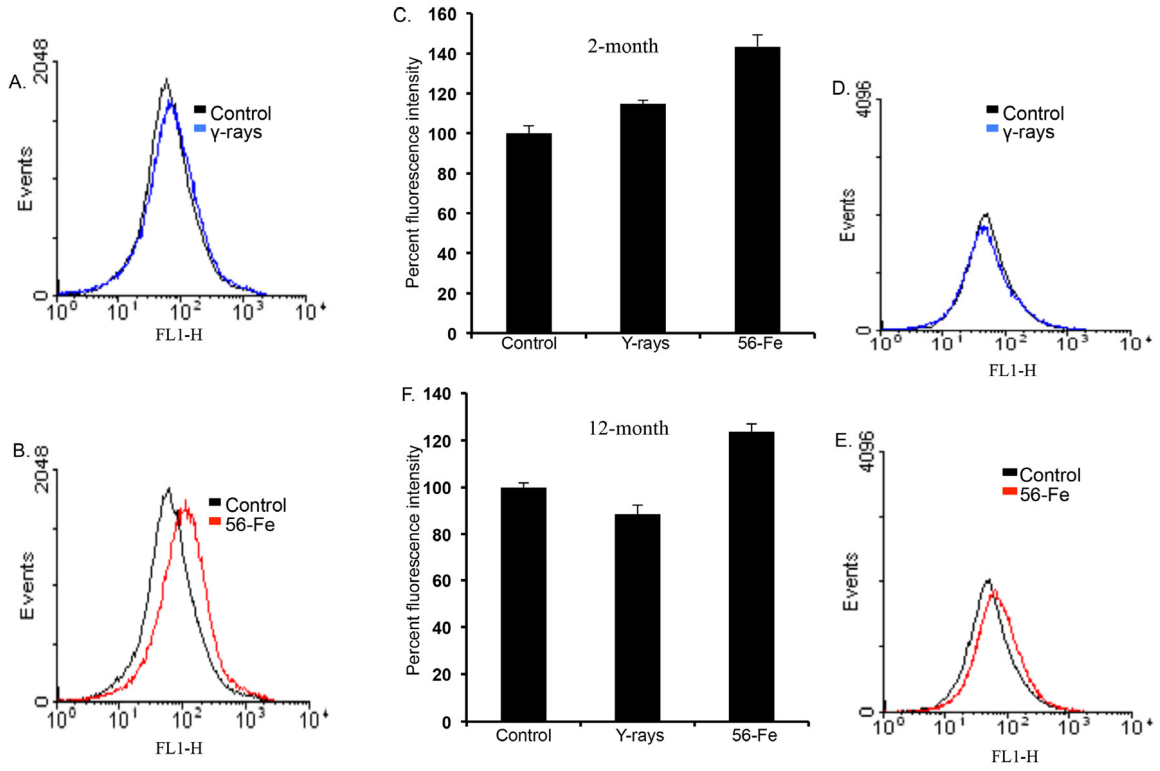

Figure 1. Increased reactive oxygen species (ROS) in cerebral cortical cells after ^{56}Fe radiation. (**A**) Flow cytometry histogram showing ROS level two months after γ radiation. (**B**) Flow cytometry histogram showing ROS level two months after ^{56}Fe radiation. (**C**) Quantification of ROS level two months after radiation presented as mean ± standard error of mean (SEM). (**D**) Flow cytometry histogram showing ROS level twelve months after γ radiation. (**E**) Flow cytometry histogram showing ROS level twelve months after ^{56}Fe radiation. (**F**) Quantification of ROS level twelve months after radiation presented as mean ± SEM.

and $p<0.05$ compared to γ radiation; for 12-month post-radiation: $p<0.04$ compared to control and $p<0.01$ compared to γ radiation; Figure 1C and F). There was a statistically significant increase in ROS levels two month after γ radiation (Figure 1A and C; $p<0.03$ compared to control). We did not observe any detectable alterations in ROS levels in twelve-month post-γ-irradiation groups relative to controls (Figure 1D and F).

Increased lipid peroxidation, oxidative DNA damage and apoptosis after radiation exposure was associated with a decrease in cortical thickness

Persistently elevated levels of 4-HNE indicated by brown coloration visible in the cytoplasm around nuclei both two and twelve months after ^{56}Fe radiation were observed (Figure 2A and C). Although less than ^{56}Fe radiation, we also observed increased 4-HNE levels after γ radiation (Figure 2A and C). Quantification of 4-HNE staining showed significantly more staining in two as well as twelve months post-^{56}Fe irradiation samples relative to γ radiation and controls (for 2-month $p<0.0000001$ compared to control and $p<0.0006$ compared to γ radiation; for 12-month $p<0.00000006$ compared to control and $p<0.000006$ compared to γ radiation; Figure 2B and D). There was also a significant increase in 4-HNE staining two- and twelve-month post-γ-irradiation relative to controls (for 2-month $p<0.00003$ and for 12-month $p<0.02$; Figure 2B and D).

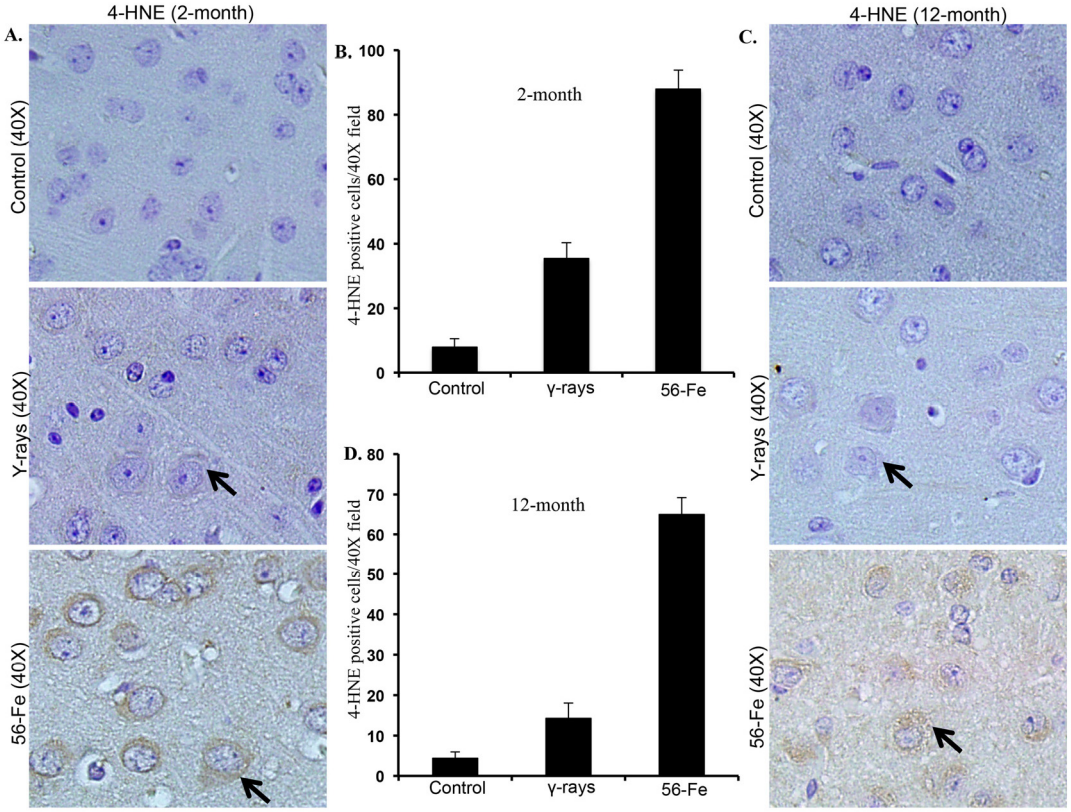

Figure 2. Lipid peroxidation in cerebral cortex was greater after ^{56}Fe radiation. (**A**) Immunohistochemical staining (arrow) of cerebral cortex for 4-hydroxy-2-nonenal (4-HNE) two months after radiation. (**B**) Quantification of 4-HNE staining two months after exposure presented as mean ± SEM. (**C**) Immunohistochemical staining (arrow) for 4-HNE twelve months after radiation. (**D**) Quantification of 4-HNE staining twelve months after radiation presented as mean ± SEM.

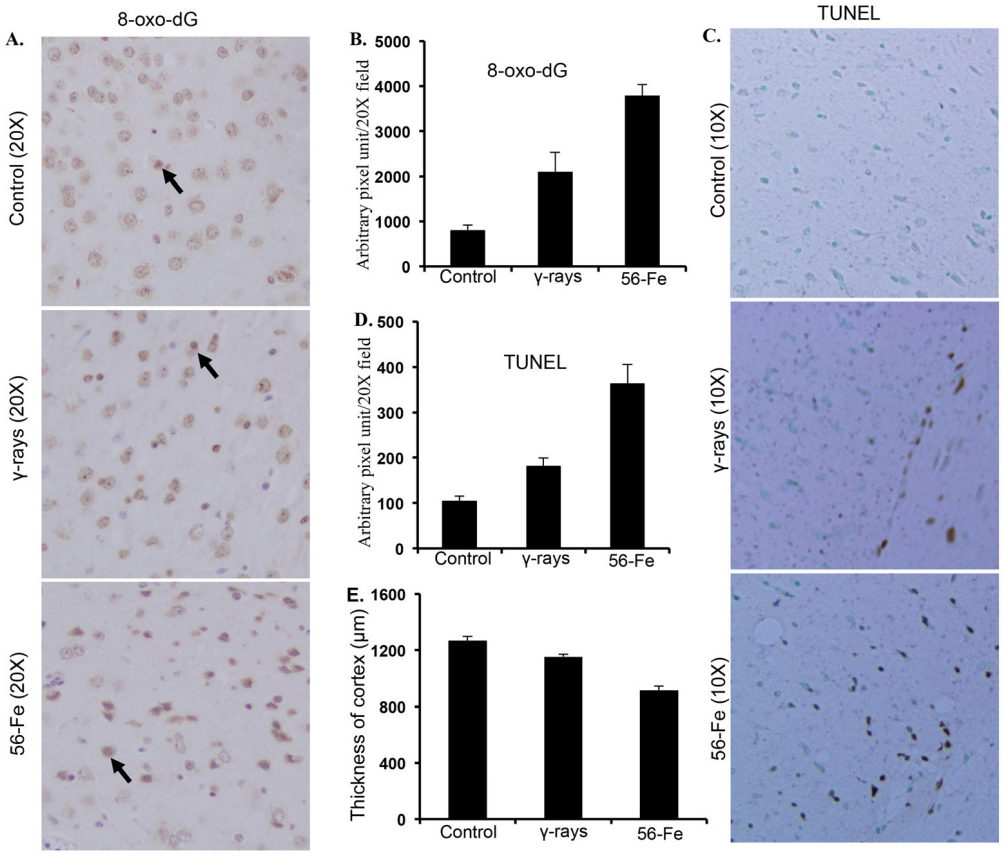

Figure 3. Assessing oxidative DNA damage and cell death in cerebral cortex twelve months after radiation. (**A**) Immunohistochemical staining of cerebral cortex for 8-oxo-dG after exposure to γ and ^{56}Fe radiation. (**B**) Quantification of 8-oxo-dG staining in cerebral cortex presented as mean ± SEM. (**C**) TUNEL staining of cerebral cortex after exposure to γ and ^{56}Fe radiation. (**D**) Quantification of TUNEL staining of cerebral cortex after exposure to γ and ^{56}Fe radiation presented as mean ± SEM. (**E**) Measurement of cerebral cortex thickness in H&E stained histological sections presented as mean ± SEM.

Markedly increased 8-oxo-dG staining in cerebral cortex twelve months after irradiation was observed (Figure 3A). Quantification showed significant difference in 8-oxo-dG staining between γ and ^{56}Fe-irradiated samples (for ^{56}Fe radiation $p<0.0001$ compared to control and $p<0.04$ compared to γ radiation; Figure 3B). Although less than ^{56}Fe radiation, we also observed significantly more 8-oxo-dG staining after γ radiation compared to control ($p<0.001$; Figure 3A and B). TUNEL stain indicating cell death also showed greater number of positive cells twelve months after ^{56}Fe radiation compared to γ radiation and quantification showed significant difference between the two types of radiation (for ^{56}Fe radiation $p<0.0003$ compared to control and $p<0.01$ compared to γ radiation; Figure 3C and D). Small but significant increase in TUNEL positive cells was also observed after γ radiation relative to control ($p<0.01$; Figure 3C. Measurements of cortical thickness showed significantly greater decrease twelve months after exposure to ^{56}Fe radiation relative to control and γ radiation ($p<0.00001$ compared to control and $p<0.0002$ compared to γ radiation; Figure 3E). Cortical thickness twelve months after γ radiation was also decreased which was statistically significant relative to control ($p<0.008$; Figure 3E). Volumetric measurement using magnetic resonance imaging (MRI) also showed decreased brain volume twelve months after radiation exposure (Supplementary figure 1A). While γ radiation showed small but statistically significant decrease in brain volume ($p<0.05$ compared to control), the ^{56}Fe radiation showed greater decrease than γ radiation ($p<0.04$ compared to control and γ radiation; Supplementary materials and methods and Supplementary figure 1A). Physical activity assay performed using a barrier (12" in length and width and 3" in height) showed irradiated mice taking significantly more time to climb the barrier relative to controls and ^{56}Fe irradiated mice needed the most time (for γ radiation $p<0.004$ compared to control and for ^{56}Fe radiation $p<0.01$ compared to control and γ

radiation; Supplementary materials and methods and Supplementary figure 1B). Additionally, γ irradiated mice also showed increased time required climbing the barrier relative to controls ($p<0.02$ compared to control; Supplementary figure 1B).

Exposure to radiation decreased DNA repair proteins and increased DNA damage response and senescence markers in cerebral cortex

Proteins involved in DNA DSB repair, DNA damage response, and senescence were markedly altered two and twelve months after radiation exposure (Figure 4A). Quantitatively, a significant decrease in DNAPKcs level, relative to control and γ radiation, was observed after ^{56}Fe radiation at both the time points (Figure 4B and C). Compared to control, Ku70 levels were significantly decreased two months after γ and ^{56}Fe radiation. However, compared to γ radiation, there was greater decrease in Ku70 levels after ^{56}Fe radiation (Figure 4B and C). Although, compared to control, Ku70 was decreased significantly in both the radiation types, its levels were similar in γ and ^{56}Fe radiation at the twelve-month time point (Figure 4B and C).

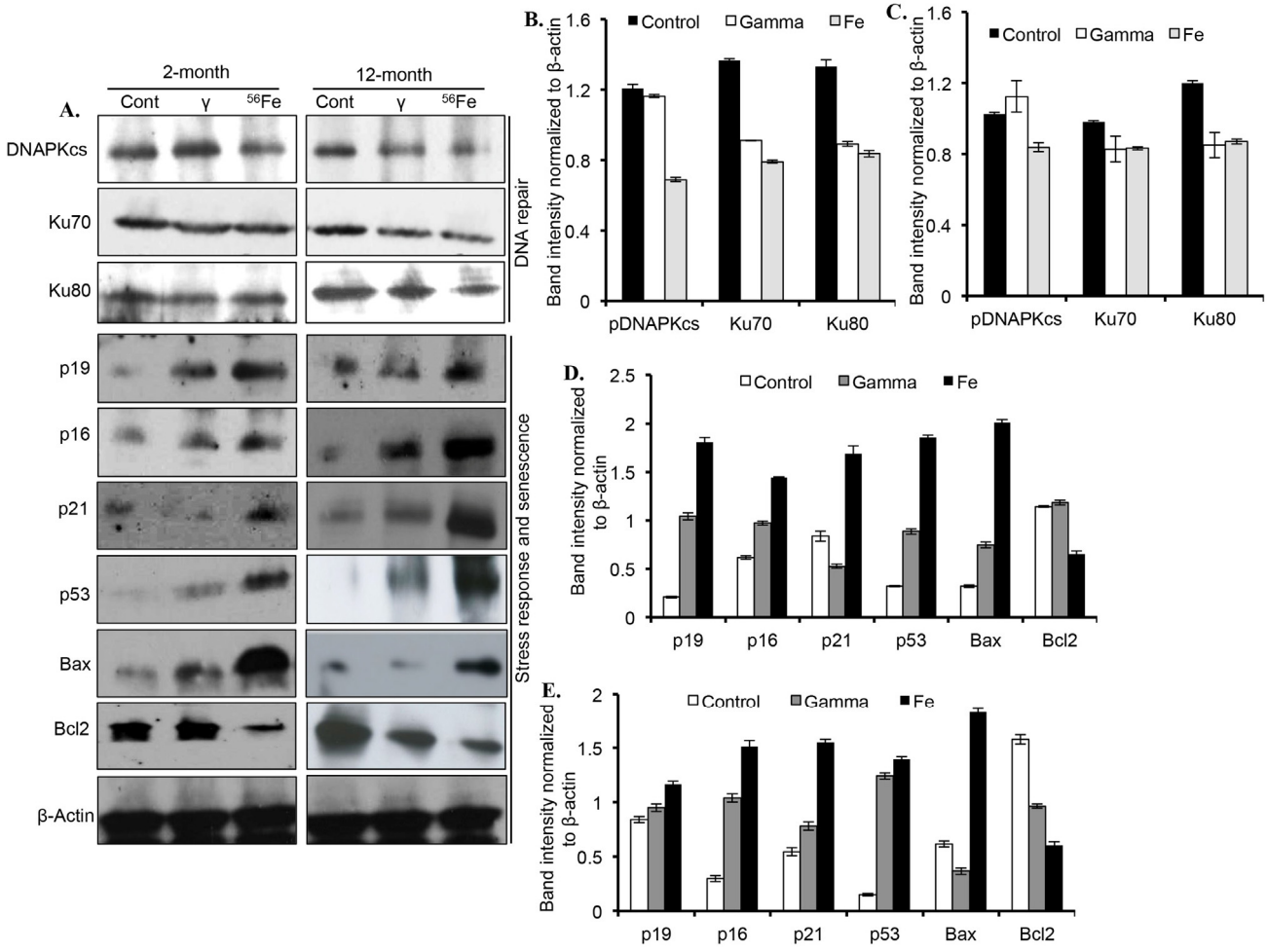

Figure 4. Assessing DNA repair and senescence markers in cerebral cortex. (**A**) Immunoblot images of DNA double strand break repair (Ku70, Ku80, and DNAPKcs), and senescence and DNA damage response (p19, p16, p21, p53, Bax, and Bcl2) proteins two and twelve months after radiation. (**B**) Quantification of Ku70, Ku80, and DNAPKcs two months after radiation. (**C**) Quantification of Ku70, Ku80, and DNAPKcs twelve months after radiation. (**D**) Quantification of p19, p16, p21, p53, Bax, and Bcl2 two months after radiation. (**E**) Quantification of p19, p16, p21, p53, Bax, and Bcl2 twelve months after radiation. Quantification data (panel **B** to **E**) is presented as mean ± SEM.

Compared to controls, the levels of Ku80 were reduced in both the radiation types two and twelve months after exposure. (Figure 4B and C). At both the time points, however, the levels of Ku80 were not different between the two radiation types (Figure 4B and C). While compared to controls the levels of cell-cycle arrest and DNA damage response marker proteins p19, p16, and p53 were noticeably increased two and twelve months after γ radiation, the levels of these proteins after ^{56}Fe radiation showed greater increase than γ radiation (Figure 4D and E). Although p21 is decreased at two months after γ radiation, its level was increased at twelve months post-exposure relative to controls. Bax level was increased at two months but decreased at twelve months after γ radiation. While Bcl2 level two months after γ radiation was similar to control, its level relative to control was lowered at twelve months after γ radiation (Figure 4D and E). However, after ^{56}Fe radiation at both the time points p21 and Bax were increased and Bcl2 was decreased relative to control and γ radiation (Figure 4D and E).

Reactive gliosis was associated with re-expression of nestin and upregulation of GFAP

Stressful stimuli in brain are associated with activation of astroglial cells resulting in re-expression of nestin and upregulation of GFAP [60]. Our observations showed that there was a significant enhancement of nestin staining in the twelve-month post-^{56}Fe radiation exposure samples (for ^{56}Fe radiation $p<0.0007$ compared to control and $p<0.003$ compared to γ radiation; Figure 5A and B). Also, significantly higher expression of GFAP was observed in cerebral cortex twelve months after ^{56}Fe irradiation (for ^{56}Fe radiation $p<0.02$ compared to control and $p<0.05$ compared to γ radiation; Figure 5C and D). Compared to control, statistically significant increase in nestin ($p<0.01$; Figure 5A and B) and GFAP ($p<0.002$; Figure 5C and D) staining was also observed twelve months after γ radiation exposure.

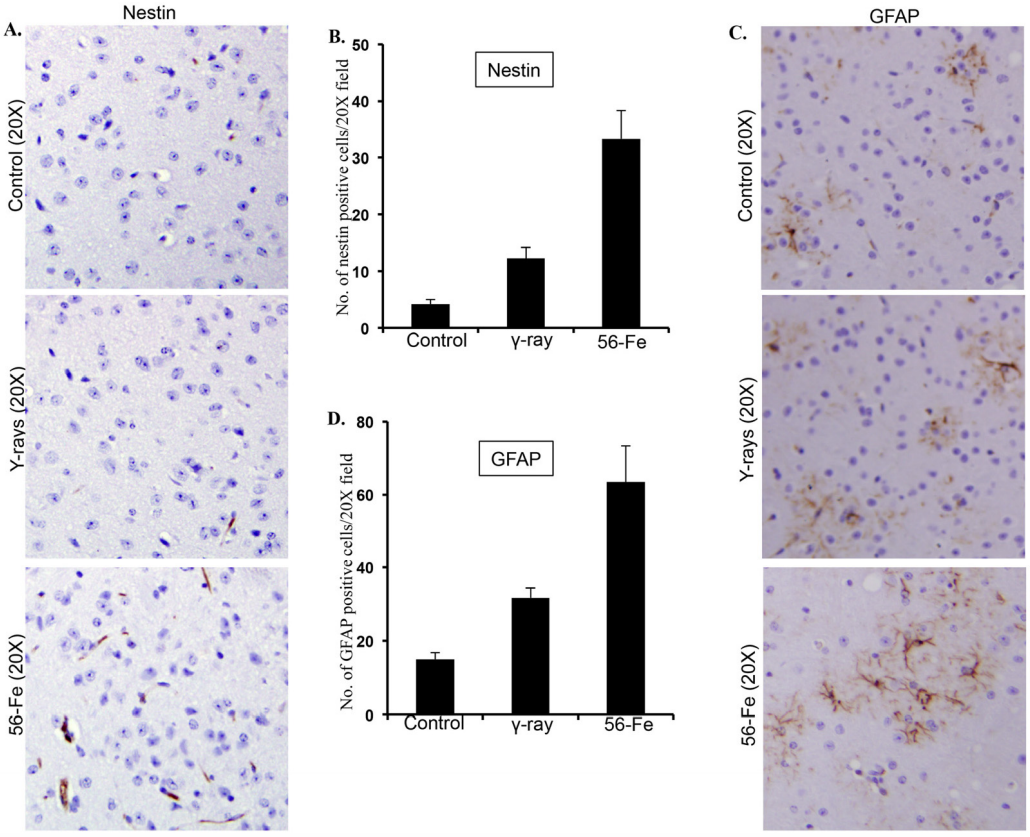

Figure 5. Assessing reactive gliosis twelve months after radiation exposure. (**A**) Comparing immunohistochemical staining of nestin in cerebral cortex after radiation. (**B**) Quantification of nestin staining in cerebral cortex presented as mean ± SEM. (**C**) Comparing immunohistochemical staining of GFAP in cerebral cortex after radiation. (**D**) Quantification of GFAP staining in cerebral cortex presented as mean ± SEM.

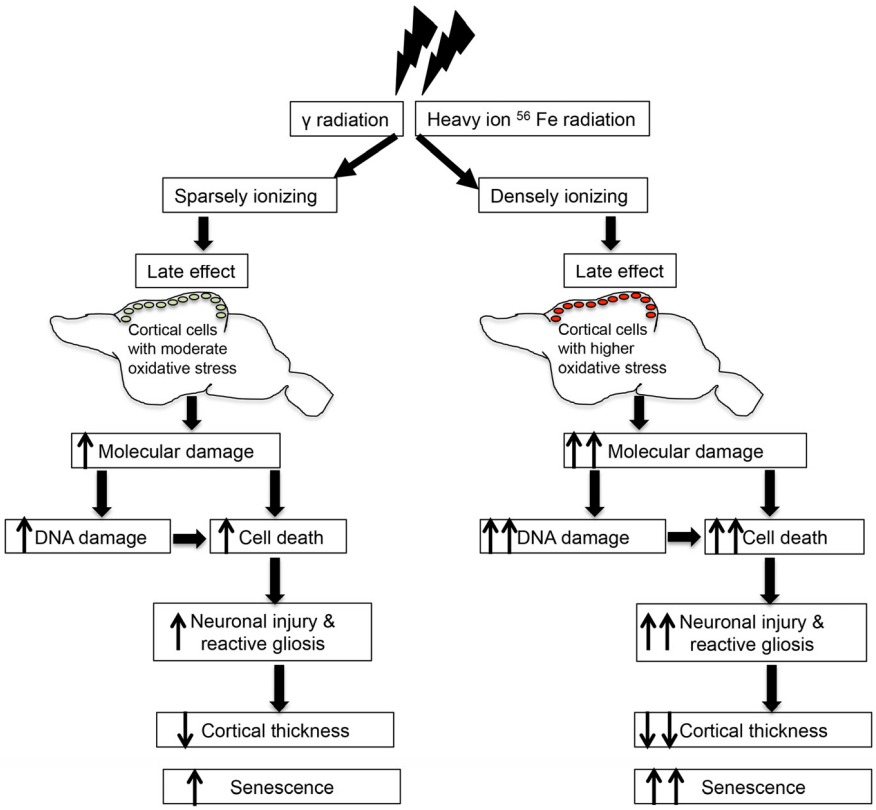

Figure 6. Schematic overview of radiation-induced chronic oxidative stress and accelerated aging.

DISCUSSION

Radiation exposure on one hand has been reported to induce long-term changes in CNS resulting in functional impairments such as motor and sensory disturbances, and learning and memory deficits [61,62] and on the other it has also been associated with risk of initiation and promotion of brain tumor [7,8,63]. However, we still lack a clear mechanistic understanding required to comprehend the persistent molecular events, which unfold in the brain after radiation exposure and has the potential to cause overt neurological deficits or tumor later in life. Importantly, due to its structural makeup and functional demands, the brain is vulnerable to oxidative stress and persistent oxidative stress has been implicated in neuro-degeneration and cancer [64]. Although there are reports relating radiation, both γ and ^{56}Fe, to changes in the cellular redox status in brain, most of the studies are relatively short term [65-68], very few have involved cerebral cortex, and fewer had long-term follow up investigation at the molecular level in the cerebral cortex. Here we demonstrated that, relative to control, there was persistently higher ROS production after γ radiation. We also observed that persistent ROS production was markedly more after ^{56}Fe radiation relative to control and γ irradiation in cerebral cortical cells. While we observed increased lipid peroxidation, DNA damage, and apoptosis along with decreased cortical thickness and brain volume after γ radiation, these effects were more prominent after ^{56}Fe radiation. We also demonstrated that there was increased p21, p19, and p16, and decreased DNA repair proteins in cerebral cortex after radiation exposure suggesting premature senescence.

Radiation-induced damage to biomolecules such as proteins and DNA has mostly been attributed to generation of ROS and consequent oxidative stress, which has been implicated in neurodegeneration, aging, and cancer [64,69-71]. Indeed, oxidative stress associated modifications of biomolecules are known hallmarks of the aging brain [11,72] and it is expected that heavy ion radiation with its propensity to cause

higher oxidative stress and increased damage to biomolecules could accelerate changes in brain commonly associated with aging. Our results of ROS measurement in cerebral cortical cells confirm the notion that heavy ion radiation induces higher oxidative stress relative to γ radiation and are consistent with our earlier results in intestinal epithelial cells [73]. Importantly, chronic oxidative stress leading to sustained DNA damage and continued activation of p53 dependent DNA damage response has been reported to induce chronic elevation of p21 level that could result in continued growth arrest leading to cellular senescence and short life span [24,74,75,75-78]. Indeed, our immunoblot results showed increased p53 and consequent increase in p21 suggesting senescence of cortical cells after radiation exposure. Interestingly, while persistent elevation of p21 is induced by oxidative stress-mediated DNA damage response, its sustained higher level is also known to result in the activation of signaling events promoting mitochondrial perturbation and increased ROS production [79]. Persistent elevation of p53 in γ as well as in ^{56}Fe-irradiated mice also illustrates a state of perpetual DNA damage response (DDR), which is supported not only by elevated p21 but also by alterations of other p53 effectors such as Bax and Bcl2. Our observations of increased Bax and decreased Bcl2 in irradiated mice led us to believe that the balance of pro- and anti-apoptotic factors in cerebral cortex is in favor of cell death. It has been reported that with advancing age there is a gradual decline in normal brain volume and in neurodegenerative diseases a marked cerebral atrophy with decline in cognitive function have been observed [80,81]. Reduction of cortical thickness, a hallmark of degenerative changes, observed after radiation exposure is probably due to cell death (confirmed by our TUNEL assay) mediated by p53-induced alterations of Bax and Bcl2 levels. Taken together our results in this study demonstrated that radiation exposure caused chronic oxidative stress, persistent oxidative DNA damage, and such DNA damages were associated with increased DDR leading to growth arrest as well as cell death in cerebral cortex. Considering the fact that ROS generated immediately after radiation are due to radiolysis of water molecules and are short lived, we believe that the persistent oxidative stress in cerebral cortex observed in our study is due to metabolically regenerated ROS of which mitochondria are the major source [82]. Oxidative stress-associated damage to biomolecules such as oxidative proteins and DNA damage has been implicated in a decline in functional competence of cerebral cortex [11,72,83]. Consequently, our results in cerebral cortex demonstrated a potential risk of developing long-term functional deficit as well as cellular transformation after radiation exposure.

Effects on CNS from heavy ion space radiation exposure due to its higher damaging capacity than γ radiation is a major health concern for astronauts undertaking long duration space missions. Apprehension about acute and long-term heavy ion radiation exposure risks to CNS is primarily due to lack of *in vivo* data in humans and animal models. However, in recent years, substantial work has been published which sheds lights on the effects of heavy ion radiation on different parts of the brain [11,52-58,84,85]. Evidence based on *in vivo* and *in vitro* studies has demonstrated that high-LET radiation adversely alters spatial learning, cognitive, memory, and other CNS faculties [11,54,55,85-88]. Our results also suggest that heavy ion space radiation with higher oxidative stress and greater associated changes has elevated risk of developing neuronal deficit and transformation and will require additional studies.

Radiation-induced persistently increased ROS and DNA damage could lead to sustained cell-cycle arrest potentially leading to senescence [89] and the cell's capability to repair DNA damage including DSB have been reported to decline with advancing age [17,19-21]. Additionally, decreased DSB repair proteins has been associated with enhanced cellular senescence and non-functional DSB repair proteins are known to accelerate organismal aging [16-22]. Our results showing decreased Ku70, Ku80, and DNAPKcs proteins in cerebral cortex, we speculate, is due to sustained higher oxidative stress, which could affect transcription, translation, and stability of repair proteins. Decreased repair proteins leading to reduction in DNA repair, we believe, would accelerate the onset of aging after ^{56}Fe radiation [90]. Additionally, cellular stress has also been reported to consistently upregulate two other well-characterized aging markers, $p19^{Arf}$ and $p16^{Ink4a}$, heralding stress-induced senescence. Importantly, $p19^{Arf}$ is activated in cells under stress including radiation exposure and is associated with the augmentation of p53-dependent DNA damage response through sequestration of MDM2 and thus stabilization of p53 [91]. Indeed, marked upregulation of $p19^{Arf}$ after both γ and ^{56}Fe radiation may have played a prominent role in enhanced p53-dependent DNA damage response in our experimental setting to affect cellular senescence. Although the regulation of $p16^{Ink4a}$, which is a cyclin-dependent kinase inhibitor and is progressively upregulated with advancing age, is not well understood [32], chronic upregulation of both $p19^{Arf}$ as well as $p16^{Ink4a}$ further confirms cellular senescence in cerebral cortex after radiation exposure. Additionally, decreased brain volume in MRI and increased time required to climb the physical barrier after radiation exposure provided further evidence linking premature senescence

and radiation (Supplementary figure 1A and B). However, additional functional studies will be required to relate observed changes in cerebral cortex after radiation to alterations in spatial learning, cognition, memory, and other CNS faculties of the organism.

Radiation-induced cellular damage in brain not only cause enhanced DNA damage response and senescence, but it also triggers repair and remodeling process through a proliferative response known as reactive gliosis [35,36]. Our results are consistent with previous reports relating nestin and GFAP to both γ and heavy ion radiation exposure [36,84]. We demonstrated that these two embryonic proteins showed higher expression in response to both γ and heavy ion radiation exposure suggesting activation of astroglial cells in cerebral cortex. Upregulation of both nestin and GFAP after radiation support a state of reactive gliosis in cerebral cortex. However, reactive gliosis denoted by increased nestin and GFAP does not support regeneration of neurons but instead leads to glial scar formation [36,84], which along with apoptosis may have aggravated shrinkage of cerebral cortex after radiation exposure. Glial scar formation rather than neuronal regeneration is further supported by the upregulation of GFAP that indicates that radiation-induced activation of astroglial proliferative response in cerebral cortex is committed to astrocytosis and subsequent scar tissue formation [84]. Our study has provided evidence that radiation exposure in the mouse brain accelerates the appearance of biological indicators of aging at the molecular level (Figure 6). Knowledge of adverse long-term sequelae of radiation exposure on cerebral cortex will not only allow us to assess risk but will also permit us to design strategies to minimize the effects of radiation on normal tissues.

METHODS

Ethics statement on mice. Six to eight weeks old female C57BL/6J mice were purchased from Jackson Laboratories (Bar Harbor, ME). Mice were housed at the Georgetown University (GU) and Brookhaven National Laboratory (BNL) animal care facilities. Both the facilities are Association for Assessment and Accreditation of Laboratory and Animal Care International (AAALACI)-accredited and all animal procedures were performed as per protocols approved by the Institutional Animal Care and Use Committees (IACUC) at the GU and at the BNL. Mice were housed in groups of five in autoclaved cages and bedding materials in a separate room with 12-h dark and light cycle maintained at 22 °C in 50% humidity. All animals were provided certified rodent diet (LabDiet #5053, Brentwood, MO) with filtered water *ad libitum* and CO_2 asphyxiation was used for euthanasia. Our research followed Guide for the Care and Use of Laboratory Animals, prepared by the Institute of Laboratory Animal Resources, National Research Council, and U.S. National Academy of Sciences. Investigation has been conducted in accordance with the ethical standards and according to the Declaration of Helsinki and according to national and international guidelines and has been approved by the authors' institutional review board.

Radiation. Exposure to heavy ion radiation (^{56}Fe; energy: 1GeV/nucleon; dose rate: 1 Gy/min) was performed at the NASA Space Radiation Laboratory (NSRL) at BNL and ^{137}Cs was used as a source of γ radiation (dose rate: 1 Gy/min) and control mice were sham irradiated. During radiation exposure mice (n=15) were placed in small transparent plastic boxes (3"x1.5"x1.5") with holes for ventilation. Mice were exposed either to 1.6 Gy of ^{56}Fe or to 2 Gy of γ radiation and irradiation experiments was performed three times. The ^{56}Fe radiation dose is equitoxic to γ radiation and was calculated using a relative biological effectiveness (RBE) factor of 1.25 determined earlier [59]. For ^{56}Fe irradiation, the NSRL beam physics team performed the dosimetry, dose rate, and beam uniformity and mice were exposed to constant LET by placing them at the entrance plateau region of the Bregg peak [92-95]. Mice were shipped directly from the vendor to BNL one week prior to radiation and on the day after irradiation all the mice were shipped in a temperature controlled environment to GU for a same day delivery. Mice were followed for up to twelve months, brain surgically removed at two and twelve months post-exposure, washed and cleaned in phosphate buffered saline (PBS), two hemispheres separated in the middle, and one half fixed in 10% buffered formalin. While immersed in sterile PBS, multiple coronal sections of the other half of the brain were made and the cerebral cortex was separated from the rest of the brain under a dissecting scope (MZ6, Leica Microsystem, Wetzlar, Germany) as per protocol described earlier [96]. Cerebral cortex was either used for preparation of cortical single cell suspension for measuring reactive oxygen species (ROS) or flash frozen in liquid N_2 and stored at -80 °C for immunoblots.

Measuring ROS in cerebral cortical cells. Separated cerebral cortex (n=5 mice per group) was mechanically dissociated into single cell suspensions in Hank's balanced salt solution (HBSS) and filtered through a sterile 70 μm nylon mesh (BD Biosciences, Sparks, MD) as per protocol described previously [1,97]. Cells were centrifuged (200xg) for 10 min at room temperature (RT) and supernatant discarded. Cell pellet

was resuspended in 1 ml of PBS at RT. A 2 mM solution of H2DCFDA (Invitrogen, Carlsbad, CA) was freshly prepared in ethanol and 5 µl were added to the cell suspension (final concentration 10 µM) and incubated at 37 °C for 20 min. Cells were centrifuged at 200xg for 5 min, supernatant discarded, and cell pellet resuspended in 500 µl of PBS. Flow cytometric analysis was performed in duplicate using FACSCalibur (BD Biosciences) and acquired data were analyzed using WinMDI v2.8 software.

Immunoblot analysis. Immunoblots were performed using standardized protocol. Flash-frozen cerebral cortical samples isolated two and twelve months after exposure to 2 Gy γ radiation and equitoxic 1.6 Gy of ^{56}Fe radiation were used for immunoblots. Cortical tissues from 5 mice in each group were pooled and homogenized in ice cold lysis buffer (0.5% sodium deoxycholate; 0.5% NP-40; 10mM EDTA in PBS and protease inhibitor cocktail (Sigma, St. Louis, MO)), centrifuged at 12000xg at 4 °C for 15 min, and protein concentration was estimated in the supernatant by the Bradford method. Equal amount proteins with appropriate volume of loading buffer were loaded onto SDS-PAGE. Separated proteins were transferred to polyvinylidene fluoride (PVDF) membrane, treated with 5% non-fat milk in tris-buffered saline with 0.1% Tween (TBST), and exposed to specific primary antibodies for DNAPKcs (Sc-5282; diltion-1:200; Santa Cruz Biotechnology, Santa Cruz, CA), Ku70 (Sc-17789; diltion-1:200; Santa Cruz Biotechnology), Ku80 (Sc-9034; diltion-1:400; Santa Cruz Biotechnology), p53 (Sc-99; diltion-1:500; Santa Cruz Biotechnology), Bax (Sc-7480; diltion-1:250; Santa Cruz Biotechnology), Bcl2 (Sc-7382; diltion-1:250; Santa Cruz Biotechnology), p21 (Sc-6246; diltion-1:500; Santa Cruz Biotechnology), p16 (Sc-1661; diltion-1:200; Santa Cruz Biotechnology), p19 (07-543; diltion-1:200; EMD Millipore, Billerica, MA), and β-actin (Sc-47778; diltion-1:2000; Santa Cruz Biotechnology) and developed by chemiluminescence (Thermo Scientific, Rockford, IL) detection system. Results were recorded by autoradiography, images scanned and displayed. We used ImageJ v1.46 software for densitometric quantification of immunoblot images and band intensity of each protein normalized to β-actin is presented in bar graphs.

Cerebral cortex histology. Twelve months post-irradiation brain samples were fixed in 10% buffered formalin for 72 hours, paraffin embedded, and 4 µm sagittal sections were obtained for further processing. For histologic analysis, slides were stained with hematoxylin and eosin (H&E) using a standard protocol and visualized by bright field microscopy at 4X microscopic magnification. Cortical thickness was measured using a protocol described previously [1]. Briefly, slide images were captured with an Olympus DP70 camera on an Olympus BX61 microscope and the thickness of the cerebral cortex was measured using ImageScope (Aperio Technologies, Vista, CA) software and results expressed in µm. For each study group, sections from seven mice were measured and three sections from each mouse were used. Unstained sections were used for terminal deoxynucleotidyl transferase dUTP nick end labeling (TUNEL) assay and immunohistochemistry.

TUNEL assay. TUNEL assay on brain sections (6 sections from 6 separate mouse from each group) was performed using ApopTag plus peroxidase in situ apoptosis detection kit (Millipore, Billerica, MA) as per manufacturer's instruction. Stained sections were visualized under bright field microscopy at 20X magnification and twelve random fields per group were captured for analysis.

Immunohistochemistry. Anti-8-oxo-dG antibody (clone 2E2; 4354-MC-050) was purchased from Trevigen (Gaithersburg, MD) and immunostaining was performed using recommended protocol. Briefly, following incubation with primary antibody overnight at 4 °C and necessary washing steps, sections were incubated with HRP-conjugated secondary antibody for 30 min at room temperature [73]. Diaminobenzidine (*DAB)* detection system (Invitrogen, Carlsbad, CA) was used to visualize staining. Bright field microscopy was used to capture the images of the cerebral cortex at 10X magnification and twelve images from randomly selected visual fields were captured from each group. For nestin, GFAP, and 4-HNE, immunostaining was performed as per protocol described previously [73,98,99]. Briefly, sections were deparaffinized, antigen retrieval performed, endogenous peroxidase activity quenched, and incubated in blocking buffer (0.1% bovine serum albumin in PBS). Sections were then exposed to anti-nestin (Sc-23927; dilution-1:100; Santa Cruz Biotechnology), anti-GFAP (PA5-16291; dilution-1:150; Thermo Scientific) and anti-4-HNE (Ab-46545; 1:200; Abcam, Cambridge, MA) antibodies for 1.5 hr at RT. Signal detection and color development was performed using SuperPicture™ 3rd Gen IHC detection kit (Cat# 87-9673; Invitrogen) and slides were mounted and visualized under bright field microscopy and twelve images from randomly selected visual fields were captured from each group for quantification. Six slides from six mice in each group were stained for each protein and a representative image from one animal is presented in results.

Data Analysis and statistics. Images were analyzed for TUNEL, 8-oxo-dG, 4-HNE, nestin, and GFAP positive cells using color deconvolution and Image-based Tool for Counting Nuclei (ITCN) plug-ins of ImageJ v1.46 software as per protocol described earlier [73,100,101]. Average number of TUNEL (20X), 8-oxo-dG (20X), nestin (20X), and GFAP (20X) positive nuclei per visual field is presented graphically. Data is presented as mean ± standard error of mean (SEM) and statistical significance between two groups was determined by student's t-test and $p<0.05$ was considered significance.

Supplementary methods

Activity tests. Mice (n=5 mice per study group) were irradiated with 2 Gy γ or 1.6 Gy of ^{56}Fe radiation and twelve months after irradiation each mouse were placed inside a barrier (12" in length and width and 3" in height) and time taken to come out of the barrier was noted in seconds. Results are presented as average time (sec) per mouse relative to sham-irradiated controls.

Mouse brain magnetic resonance imaging (MRI). The MRI was performed on a horizontal Bruker 7T spectrometer with a 20 cm bore run by Paravision 4.0 software as per protocol standardized in the Preclinical Imaging Research Laboratory at the Lombardi Comprehensive Cancer Center at the Georgetown University. Mice (n=3) were anesthetized and anesthesia maintained with 1.5% isoflurane, 30% oxygen and 70% nitrous oxide and animals were placed on a custom-made stereotaxic animal holder equipped with temperature and respiration monitoring and imaged in a 35 mm birdcage radiofrequency coil. The sequence used to assess brain volume was a 3D RARE, matrix: 256x256x256, RARE factor: 8, TR: 500 ms, TE: 7.45 ms, FOV: 3 cm. Volumetric measurement of the brain was determined from MRI stacked images using the Measure Stack plugin tool (developed by Dougherty RF and available at http://www.optinav.com/imagej.html) of the ImageJ v1.46 software as per developer's instruction.

ACKNOWLEDGEMENTS

We are very much thankful to the members of the NASA Space Radiation Laboratory especially to Drs. Peter Guida and Adam Rusek for their excellent support in conducting 56Fe radiation exposures. This study is supported in part by NASA Grant# NNX07AH70G and NNX09AU95G. We also thank the Histopathology and Tissue Shared Resources at the Lombardi Comprehensive Cancer Center at Georgetown University for histology services supported by Award Number P30CA051008 from the National Cancer Institute (NCI). The funders had no role in study design, data collection and analysis, decision to publish, or preparation of the manuscript.

Conflicts of Interest Statement

Authors have no competing financial interest to declare.

REFERENCES

1. Joo KM, Jin J, Kang BG, Lee SJ, Kim KH, Yang H, Lee YA, Cho YJ, Im YS, Lee DS, Lim DH, Kim DH, Um HD, Lee SH, Lee JI, and Nam DH. Trans-differentiation of neural stem cells: a therapeutic mechanism against the radiation induced brain damage. PLoS One. 2012; 7:e25936.

2. Butler JM, Rapp SR, and Shaw EG. Managing the cognitive effects of brain tumor radiation therapy. Curr Treat Options Oncol. 2006; 7:517-523.

3. Gourmelon P, Marquette C, Agay D, Mathieu J, and Clarencon D. Involvement of the central nervous system in radiation-induced multi-organ dysfunction and/or failure. BJR Suppl. 2005; 27:62-68.

4. Jacob R, Gilligan D, Robinson M, and Harmer C. Hyper-fractionated radiotherapy for soft tissue sarcoma: results of the second study of hyper-fractionated radiotherapy. Sarcoma. 1999; 3:157-165.

5. Redberg RF. Cancer risks and radiation exposure from computed tomographic scans: how can we be sure that the benefits outweigh the risks? Arch Intern Med. 2009; 169:2049-2050.

6. Berrington de Gonzalez A, Mahesh M, Kim KP, Bhargavan M, Lewis R, Mettler F, and Land C. Projected cancer risks from computed tomographic scans performed in the United States in 2007. Arch Intern Med. 2009;169:2071-2077.

7. Smith-Bindman R, Lipson J, Marcus R, Kim KP, Mahesh M, Gould R, Berrington de Gonzalez A, and Miglioretti DL. Radiation dose associated with common computed tomography examinations and the associated lifetime attributable risk of cancer. Arch Intern Med. 2009; 169:2078-2086.

8. Brenner DJ, and Hall EJ. Computed tomography--an increasing source of radiation exposure. N Engl J Med. 2007; 357:2277-2284.

9. Pierce DA, Shimizu Y, Preston DL, Vaeth M, and Mabuchi K. Studies of the mortality of atomic bomb survivors. Report 12, Part I. Cancer: 1950-1990. Radiat Res. 1996; 146:1-27.

10. Noseworthy MD, and Bray TM. Effect of oxidative stress on brain damage detected by MRI and in vivo 31P-NMR. Free Radic Biol Med. 1998; 24:942-951.

11. Manda K, Ueno M, and Anzai K. Memory impairment, oxidative damage and apoptosis induced by space radiation: ameliorative potential of alpha-lipoic acid. Behav Brain Res. 2008; 187:387-395.

12. Poulose SM, Bielinski DF, Carrihill-Knoll K, Rabin BM, and Shukitt-Hale B. Exposure to 16O-particle radiation causes aging-like decrements in rats through increased oxidative stress, inflammation and loss of autophagy. Radiat Res. 2011; 176:761-769.

13. Butterfield DA, Reed T, and Sultana R. Roles of 3-nitrotyrosine- and 4-hydroxynonenal-modified brain proteins in

the progression and pathogenesis of Alzheimer's disease. Free Radic Res. 2011; 45:59-72.

14. Datta K, Purkayastha S, Neumann RD, Pastwa E, and Winters TA. Base damage immediately upstream from double-strand break ends is a more severe impediment to nonhomologous end joining than blocked 3'-termini. Radiat Res. 2011; 175:97-112.

15. Khanna KK, and Jackson SP. DNA double-strand breaks: signaling, repair and the cancer connection. Nat Genet. 2001; 27:247-254.

16. Li H, Vogel H, Holcomb VB, Gu Y, and Hasty P. Deletion of Ku70, Ku80, or both causes early aging without substantially increased cancer. Mol Cell Biol. 2007; 27:8205-8214.

17. Canugovi C, Yoon JS, Feldman NH, Croteau DL, Mattson MP, and Bohr VA. Endonuclease VIII-like 1 (NEIL1) promotes short-term spatial memory retention and protects from ischemic stroke-induced brain dysfunction and death in mice. Proc Natl Acad Sci U S A. 2012; 109:14948-14953.

18. Zhao B, Benson EK, Qiao R, Wang X, Kim S, Manfredi JJ, Lee SW, and Aaronson SA. Cellular senescence and organismal ageing in the absence of p21(CIP1/WAF1) in ku80(-/-) mice. EMBO Rep. 2009; 10:71-78.

19. Engels WR, Johnson-Schlitz D, Flores C, White L, and Preston CR. A third link connecting aging with double strand break repair. Cell Cycle. 2007; 6:131-135.

20. Lombard DB, Chua KF, Mostoslavsky R, Franco S, Gostissa M, and Alt FW. DNA repair, genome stability, and aging. Cell. 2005; 120:497-512.

21. Gilchrest BA, and Bohr VA. Aging processes, DNA damage, and repair. FASEB J. 1997; 11:322-330.

22. Rao KS, and Loeb LA. DNA damage and repair in brain: relationship to aging. Mutat Res. 1992; 275:317-329.

23. von Zglinicki T, Saretzki G, Ladhoff J, d'Adda di Fagagna F, and Jackson SP. Human cell senescence as a DNA damage response. Mech Ageing Dev. 2005; 126:111-117.

24. Frontini M, and Proietti-De-Santis L. Interaction between the Cockayne syndrome B and p53 proteins: implications for aging. Aging (Albany NY). 2012; 4:89-97.

25. Liu B, Chen Y, and St Clair DK. ROS and p53: a versatile partnership. Free Radic Biol Med. 2008; 44:1529-1535.

26. O'Neill M, Nunez F, and Melton DW. p53 and a human premature ageing disorder. Mech Ageing Dev. 2003; 124:599-603.

27. Blagosklonny MV. Answering the ultimate question "what is the proximal cause of aging?". Aging (Albany NY). 2012; 4:861-877.

28. Kolosova NG, Vitovtov AO, Muraleva NA, Akulov AE, Stefanova NA, and Blagosklonny MV. Rapamycin suppresses brain aging in senescence-accelerated OXYS rats. Aging (Albany NY). 2013; 5:474-484.

29. Suh Y. Cell signaling in aging and apoptosis. Mech Ageing Dev. 2002; 123:881-890.

30. Greer EL, and Brunet A. Signaling networks in aging. J Cell Sci. 2008; 121:407-412.

31. Wong ES, Le Guezennec X, Demidov ON, Marshall NT, Wang ST, Krishnamurthy J, Sharpless NE, Dunn NR, and Bulavin DV. p38MAPK controls expression of multiple cell cycle inhibitors and islet proliferation with advancing age. Dev Cell. 2009; 17:142-149.

32. Ressler S, Bartkova J, Niederegger H, Bartek J, Scharffetter-Kochanek K, Jansen-Durr P, and Wlaschek M. p16INK4A is a robust in vivo biomarker of cellular aging in human skin. Aging Cell. 2006; 5:379-389.

33. Porchet R, Probst A, Bouras C, Draberova E, Draber P, and Riederer BM. Analysis of glial acidic fibrillary protein in the human entorhinal cortex during aging and in Alzheimer's disease. Proteomics. 2003; 3:1476-1485.

34. Morgan TE, Rozovsky I, Goldsmith SK, Stone DJ, Yoshida T, and Finch CE. Increased transcription of the astrocyte gene GFAP during middle-age is attenuated by food restriction: implications for the role of oxidative stress. Free Radic Biol Med. 1997; 23:524-528.

35. Jin JK, Jeong BH, Na YJ, Kim YS, Carp RI, Wie MB, Moon C, and Shin T. Increased expression of the embryonic intermediate filament, nestin, in the brains of scrapie-infected mice. Neurosci Lett. 2004; 367:254-258.

36. Shi M, Wei LC, Cao R, and Chen LW. Enhancement of nestin protein-immunoreactivity induced by ionizing radiation in the forebrain ependymal regions of rats. Neurosci Res. 2002; 44:475-481.

37. Champagne D, Pearson D, Dea D, Rochford J, and Poirier J. The cholesterol-lowering drug probucol increases apolipoprotein E production in the hippocampus of aged rats: implications for Alzheimer's disease. Neuroscience. 2003; 121:99-110.

38. Chiang CS, McBride WH, and Withers HR. Radiation-induced astrocytic and microglial responses in mouse brain. Radiother Oncol. 1993; 29:60-68.

39. Hwang SY, Jung JS, Kim TH, Lim SJ, Oh ES, Kim JY, Ji KA, Joe EH, Cho KH, and Han IO. Ionizing radiation induces astrocyte gliosis through microglia activation. Neurobiol Dis. 2006; 21:457-467.

40. Rola R, Fishman K, Baure J, Rosi S, Lamborn KR, Obenaus A, Nelson GA, and Fike JR. Hippocampal neurogenesis and neuroinflammation after cranial irradiation with (56)Fe particles. Radiat Res. 2008; 169:626-632.

41. Mao XW, Favre CJ, Fike JR, Kubinova L, Anderson E, Campbell-Beachler M, Jones T, Smith A, Rightnar S, and Nelson GA. High-LET radiation-induced response of microvessels in the Hippocampus. Radiat Res. 2010; 173:486-493.

42. Badhwar GD, and Cucinotta FA. Depth dependence of absorbed dose, dose equivalent and linear energy transfer spectra of galactic and trapped particles in polyethylene and comparison with calculations of models. Radiat Res. 1998; 149:209-218.

43. Cucinotta FA, Wilson JW, Shinn JL, Badavi FF, and Badhwar GD. Effects of target fragmentation on evaluation of LET spectra from space radiations: implications for space radiation protection studies. Radiat Meas. 1996; 26:923-934.

44. Setlow RB. The hazards of space travel. EMBO Rep. 2003; 4:1013-1016.

45. Cucinotta FA, Nikjoo H, and Goodhead DT. The effects of delta rays on the number of particle-track traversals per cell in laboratory and space exposures. Radiat Res. 1998; 150:115-119.

46. Cucinotta FA, Nikjoo H, and Goodhead DT. Applications of amorphous track models in radiation biology. Radiat Environ Biophys. 1999; 38:81-92.

47. Durante M, and Cucinotta FA. Heavy ion carcinogenesis and human space exploration. Nat Rev Cancer. 2008; 8:465-472.

48. Butler RW, and Haser JK. Neurocognitive effects of treatment for childhood cancer. Ment Retard Dev Disabil Res Rev. 2006; 12:184-191.

49. Castro JR, Chen GT, and Blakely EA. Current considerations in heavy charged-particle radiotherapy: a clinical research trial of the University of California Lawrence Berkeley Laboratory, Northern California Oncology Group, and Radiation Therapy Oncology Group. Radiat Res Suppl. 1985; 8:S263-71.

50. Suit H, Goitein M, Munzenrider J, Verhey L, Blitzer P, Gragoudas E, Koehler AM, Urie M, Gentry R, Shipley W, Urano M, Duttenhaver J, and Wagner M. Evaluation of the clinical applicability of proton beams in definitive fractionated radiation therapy. Int J Radiat Oncol Biol Phys. 1982; 8:2199-2205.

51. Ohmachi Y, Ishida Y, Hiraoka T, Hamano T, Fushiki S, and Ogiu T. Postnatal Changes in Mice Exposed In Utero to Fast Neutrons. Journal of Toxicologic Pathology. 2004; 17:63-68.

52. Pecaut MJ, Haerich P, Miller CN, Smith AL, Zendejas ED, and Nelson GA. The effects of low-dose, high-LET radiation exposure on three models of behavior in C57BL/6 mice. Radiat Res. 2004; 162:148-156.

53. Manda K, Ueno M, and Anzai K. Space radiation-induced inhibition of neurogenesis in the hippocampal dentate gyrus and memory impairment in mice: ameliorative potential of the melatonin metabolite, AFMK. J Pineal Res. 2008; 45:430-438.

54. Denisova NA, Shukitt-Hale B, Rabin BM, and Joseph JA. Brain signaling and behavioral responses induced by exposure to (56)Fe-particle radiation. Radiat Res. 2002; 158:725-734.

55. Shukitt-Hale B, Casadesus G, McEwen JJ, Rabin BM, and Joseph JA. Spatial learning and memory deficits induced by exposure to iron-56-particle radiation. Radiat Res. 2000; 154:28-33.

56. Haerich P, Nelson GA, and Pecaut MJ. HZE radiation and dopaminergic modification of startle and prepulse inhibition in mice. Physiol Behav. 2005; 86:103-110.

57. Rola R, Sarkissian V, Obenaus A, Nelson GA, Otsuka S, Limoli CL, and Fike JR. High-LET radiation induces inflammation and persistent changes in markers of hippocampal neurogenesis. Radiat Res. 2005; 164:556-560.

58. Rice OV, Grande AV, Dehktyar N, Bruneus M, Robinson JK, and Gatley SJ. Long-term effects of irradiation with iron-56 particles on the nigrostriatal dopamine system. Radiat Environ Biophys. 2009; 48:215-225.

59. Datta K, Suman S, Trani D, Doiron K, Rotolo JA, Kallakury BV, Kolesnick R, Cole MF, and Fornace AJJ. Accelerated hematopoietic toxicity by high energy (56)Fe radiation. Int J Radiat Biol. 2012; 88:213-222.

60. Eliasson C, Sahlgren C, Berthold CH, Stakeberg J, Celis JE, Betsholtz C, Eriksson JE, and Pekny M. Intermediate filament protein partnership in astrocytes. J Biol Chem. 1999; 274:23996-24006.

61. Monje ML, and Palmer T. Radiation injury and neurogenesis. Curr Opin Neurol. 2003; 16:129-134.

62. DeAngelis LM, Delattre JY, and Posner JB. Radiation-induced dementia in patients cured of brain metastases. Neurology. 1989; 39:789-796.

63. Kleinerman RA. Cancer risks following diagnostic and therapeutic radiation exposure in children. Pediatr Radiol. 2006; 36 Suppl 2:121-125.

64. Waris G, and Ahsan H. Reactive oxygen species: role in the development of cancer and various chronic conditions. J Carcinog. 2006; 5:14.

65. Limoli CL, Giedzinski E, Rola R, Otsuka S, Palmer TD, and Fike JR. Radiation response of neural precursor cells: linking cellular sensitivity to cell cycle checkpoints, apoptosis and oxidative stress. Radiat Res. 2004; 161:17-27.

66. Limoli CL, Giedzinski E, Baure J, Rola R, and Fike JR. Redox changes induced in hippocampal precursor cells by heavy ion irradiation. Radiat Environ Biophys. 2007; 46:167-172.

67. Veeraraghavan J, Natarajan M, Herman TS, and Aravindan N. Low-dose gamma-radiation-induced oxidative stress response in mouse brain and gut: regulation by NFkappaB-MnSOD cross-signaling. Mutat Res. 2011; 718:44-55.

68. Manda K, Anzai K, Kumari S, and Bhatia AL. Melatonin attenuates radiation-induced learning deficit and brain oxidative stress in mice. Acta Neurobiol Exp (Wars). 2007; 67:63-70.

69. Ames BN, Shigenaga MK, and Hagen TM. Oxidants, antioxidants, and the degenerative diseases of aging. Proc Natl Acad Sci U S A. 1993; 90:7915-7922.

70. Datta K, Sinha S, and Chattopadhyay P. Reactive oxygen species in health and disease. Natl Med J India. 2000; 13:304-310.

71. Harman D. Role of free radicals in aging and disease. Ann N Y Acad Sci. 1992; 673:126-141.

72. Balu M, Sangeetha P, Murali G, and Panneerselvam C. Modulatory role of grape seed extract on age-related oxidative DNA damage in central nervous system of rats. Brain Res Bull. 2006; 68:469-473.

73. Datta K, Suman S, Kallakury BV, and Fornace AJJ. Exposure to heavy ion radiation induces persistent oxidative stress in mouse intestine. PLoS One. 2012; 7:e42224.

74. Larsson O. Cellular senescence-an integrated perspective. Cancer Therapy. 2005; 3:495-510.

75. Atadja P, Wong H, Garkavtsev I, Veillette C, and Riabowol K. Increased activity of p53 in senescing fibroblasts. Proc Natl Acad Sci U S A. 1995; 92:8348-8352.

76. Jia L, Li H, and Sun Y. Induction of p21-dependent senescence by an NAE inhibitor, MLN4924, as a mechanism of growth suppression. Neoplasia. 2011; 13:561-569.

77. Kagawa S, Fujiwara T, Kadowaki Y, Fukazawa T, Sok-Joo R, Roth JA, and Tanaka N. Overexpression of the p21 sdi1 gene induces senescence-like state in human cancer cells: implication for senescence-directed molecular therapy for cancer. Cell Death Differ. 1999; 6:765-772.

78. Edwards MG, Anderson RM, Yuan M, Kendziorski CM, Weindruch R, and Prolla TA. Gene expression profiling of aging reveals activation of a p53-mediated transcriptional program. BMC Genomics. 2007; 8:80.

79. Passos JF, Nelson G, Wang C, Richter T, Simillion C, Proctor CJ, Miwa S, Olijslagers S, Hallinan J, Wipat A, Saretzki G, Rudolph KL, Kirkwood TB, and von Zglinicki T. Feedback between p21 and reactive oxygen production is necessary for cell senescence. Mol Syst Biol. 2010; 6:347.

80. Miller AK, Alston RL, and Corsellis JA. Variation with age in the volumes of grey and white matter in the cerebral hemispheres of man: measurements with an image analyser. Neuropathol Appl Neurobiol. 1980; 6:119-132.

81. Mouton PR, Martin LJ, Calhoun ME, Dal Forno G, and Price DL. Cognitive decline strongly correlates with cortical atrophy in Alzheimer's dementia. Neurobiol Aging. 1998; 19:371-377.

82. Kim GJ, Fiskum GM, and Morgan WF. A role for mitochondrial dysfunction in perpetuating radiation-induced genomic instability. Cancer Res. 2006; 66:10377-10383.

83. Campisi J. Senescent cells, tumor suppression, and organismal aging: good citizens, bad neighbors. Cell. 2005; 120:513-522.

84. Cummings P, Obenaus A, Heffron D, and Mandell J. High-energy (HZE) radiation exposure causes delayed exonal

degeneration and astrogliosis in the central nervous system of rats. Gravit Space Biol Bull. 2007; 20:89-90.

85. Tseng B, Giedzinski E, Izadi A, Suarez T, Lan M, Tran K, Acharya M, Nelson G, Raber J, Parihar VK, and Limoli C. Functional consequences of radiation-induced oxidative stress in cultured neural stem cells and the brain exposed to charged particle irradiation. Antioxid Redox Signal. 2013;

86. Rabin BM, Joseph JA, and Shukitt-Hale B. Effects of age and diet on the heavy particle-induced disruption of operant responding produced by a ground-based model for exposure to cosmic rays. Brain Res. 2005; 1036:122-129.

87. Rabin BM, Joseph JA, and Shukitt-Hale B. A longitudinal study of operant responding in rats irradiated when 2 months old. Radiat Res. 2005; 164:552-555.

88. Vlkolinsky R, Titova E, Krucker T, Chi BB, Staufenbiel M, Nelson GA, and Obenaus A. Exposure to 56Fe-particle radiation accelerates electrophysiological alterations in the hippocampus of APP23 transgenic mice. Radiat Res. 2010; 173:342-352.

89. Blagosklonny MV. Cell cycle arrest is not yet senescence, which is not just cell cycle arrest: terminology for TOR-driven aging. Aging (Albany NY). 2012; 4:159-165.

90. Liu GH, Barkho BZ, Ruiz S, Diep D, Qu J et al. Recapitulation of premature ageing with iPSCs from Hutchinson-Gilford progeria syndrome. Nature. 2011; 472:221-225.

91. Ben-Porath I, and Weinberg RA. The signals and pathways activating cellular senescence. Int J Biochem Cell Biol. 2005; 37:961-976.

92. Hamilton SA, Pecaut MJ, Gridley DS, Travis ND, Bandstra ER, Willey JS, Nelson GA, and Bateman TA. A murine model for bone loss from therapeutic and space-relevant sources of radiation. J Appl Physiol. 2006; 101:789-793.

93. Obenaus A, Huang L, Smith A, Favre CJ, Nelson G, and Kendall E. Magnetic resonance imaging and spectroscopy of the rat hippocampus 1 month after exposure to 56Fe-particle radiation. Radiat Res. 2008; 169:149-161.

94. Peng Y, Brown N, Finnon R, Warner CL, Liu X, Genik PC, Callan MA, Ray FA, Borak TB, Badie C, Bouffler SD, Ullrich RL, Bedford JS, and Weil MM. Radiation leukemogenesis in mice: loss of PU.1 on chromosome 2 in CBA and C57BL/6 mice after irradiation with 1 GeV/nucleon 56Fe ions, X rays or gamma rays. Part I. Experimental observations. Radiat Res. 2009; 171:474-483.

95. Tucker JD, Marples B, Ramsey MJ, and Lutze-Mann LH. Persistence of chromosome aberrations in mice acutely exposed to 56Fe+26 ions. Radiat Res. 2004; 161:648-655.

96. Matsumura N, Yoshida N, Ohta A, Miyamoto Y, and Hisatsune T. Neural precursor cells from adult mouse cerebral cortex differentiate into both neurons and oligodendrocytes. Cytotechnology. 2003; 43:19-25.

97. Aguirre A, and Gallo V. Reduced EGFR signaling in progenitor cells of the adult subventricular zone attenuates oligodendrogenesis after demyelination. Neuron Glia Biol. 2007; 3:209-220.

98. Cerbai F, Lana D, Nosi D, Petkova-Kirova P, Zecchi S, Brothers HM, Wenk GL, and Giovannini MG. The neuron-astrocyte-microglia triad in normal brain ageing and in a model of neuroinflammation in the rat hippocampus. PLoS One. 2012; 7:e45250.

99. Poncin S, Van Eeckoudt S, Humblet K, Colin IM, and Gerard AC. Oxidative stress: a required condition for thyroid cell proliferation. Am J Pathol. 2010; 176:1355-1363.

100. Shillingford JM, Piontek KB, Germino GG, and Weimbs T. Rapamycin ameliorates PKD resulting from conditional inactivation of Pkd1. J Am Soc Nephrol. 2010; 21:489-497.

101. Skaland I, Janssen EA, Gudlaugsson E, Klos J, Kjellevold KH, Soiland H, and Baak JP. Phosphohistone H3 expression has much stronger prognostic value than classical prognosticators in invasive lymph node-negative breast cancer patients less than 55 years of age. Mod Pathol. 2007; 20:1307-1315.

SUPPLEMENTARY FIGURE

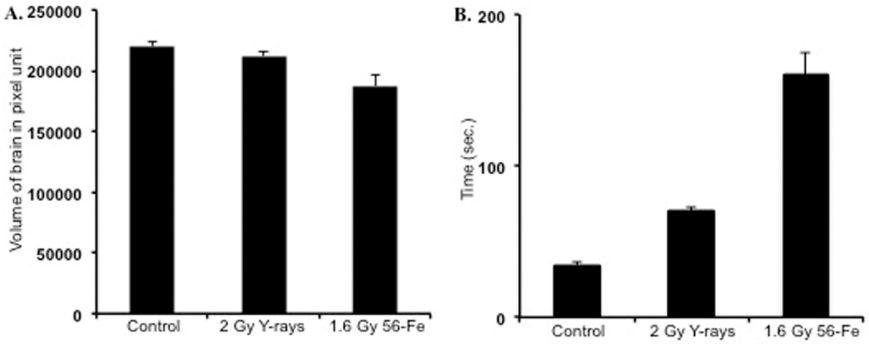

Supplementary Figure 1. Radiation exposure caused decreased brain volume and increased time to cross a barrier. A) Volumetric measurement of brain performed using magnetic resonance imaging (MRI) showed decrease brain volume after radiation exposure. Brain volume was decreased more after ^{56}Fe radiation. B) Activity experiment performed using a physical barrier showed increased time required by the irradiated mice to climb the barrier. ^{56}Fe irradiated mice needed more time to come out of the barrier. Data presented as mean ± SEM.

Research Paper

Rapamycin extends lifespan and delays tumorigenesis in heterozygous p53+/- mice

Elena A. Komarova[1], Marina P. Antoch[2], Liliya R. Novototskaya[1], Olga B. Chernova[3], Geraldine Paszkiewicz[1], Olga V. Leontieva[1], Mikhail V. Blagosklonny[1], and Andrei V. Gudkov[1]

[1] Department of Cell Stress Biology, Roswell Park Cancer Institute, BLSC, L3-312, Buffalo, NY 14263, USA
[2] Department of Molecular & Cellular Biology, Roswell Park Cancer Institute, BLSC, L3-312, Buffalo, NY 14263, USA
[3] Tartis Aging, Inc., Buffalo, NY 14203, USA

Key words: cancer, mutations, DNA damage, aging, mTOR
Received: 8/30/12; Accepted: 10/27/12; Published: 10/29/12 DOI: 10.18632/aging.100498
Correspondence to: Andrei V. Gudkov, PhD; **E-mail:** andrei.gudkov@roswellpark.org and Mikhail V. Blagosklonny, MD/PhD;
E-mail: blagosklonny@oncotarget.com

Copyright: © Komarova et al. This is an open-access article distributed under the terms of the Creative Commons Attribution License, which permits unrestricted use, distribution, and reproduction in any medium, provided the original author and source are credited

Abstract: The TOR (Target of Rapamycin) pathway accelerates cellular and organismal aging. Similar to rapamycin, p53 can inhibit the mTOR pathway in some mammalian cells. Mice lacking one copy of p53 (p53+/- mice) have an increased cancer incidence and a shorter lifespan. We hypothesize that rapamycin can delay cancer in heterozygous p53+/- mice. Here we show that rapamycin (given in a drinking water) extended the mean lifespan of p53+/- mice by 10% and when treatment started early in life (at the age less than 5 months) by 28%. In addition, rapamycin decreased the incidence of spontaneous tumors. This observation may have applications in management of Li-Fraumeni syndrome patients characterized by heterozygous mutations in the *p53* gene.

INTRODUCTION

The mTOR (mammalian Target of Rapamycin) pathway plays a crucial role in the geroconversion from cell cycle arrest to senescence (geroconversion) [1]. Rapamycin suppresses or decelerates geroconversion, maintaining quiescence instead [2-8]. Furthemore, inhibition of the TOR pathway prolongs lifespan in model organisms, including mice [9-13]. In an organism, nutrients activate mTOR [14-16], whereas fasting or calorie restriction deactivates mTOR [17-19]. Calorie restriction slows down aging [20] and postpones tumorigenesis in several animal models [21, 22], including p53-deficient mice [23-25].

Similar to other tumor suppressors, p53 can inhibit mTOR in mammalian cells [26-31]. While causing cell cycle arrest, p53 can suppress geroconversion, thus preventing a senescent phenotype in the arrested cells [30, 31]. Therefore, it is not suprising that p53 inhibits hyper-secretory phenotype, a hallmark of senescence [32] whereas p53-deficiency resulted in pro-inflammatory phenotype [33, 34]. Noteworthy, the activity of p53 is decreased with aging [35]. Lack of one p53-allele (p53+/-) accelerates carcinogenesis and shortens lifespan [36-41]. We propose that rapamycin can decelerate cancer development in p53+/- mice. Here we show experimental evidence supporting this hypothesis.

RESULTS

Rapamycin (approximate dose, 1.5 mg/kg/day) was given in drinking water. 75 mice were divided into two groups: control (n=38) and rapamycin-treated (n=37). The mean lifespan of animals in control group was 373 days and the last 10% of survivals lived as long as 520 days (Fig. 1 A). In rapamycin-treated mice, the mean lifespan was 410 days and lifespan of the last 10% of survivals could not be determined (Fig. 1 A). Mice in both groups were also monitored for tumor development. The data presented in Fig. 1B

demonstrate that carcinogenesis was significantly delayed in rapamycin-treated mice compared to control mice.

Since in our experiments animals started to receive rapamycin at different age, we sought to test whether this affected the outcome of the treatment.

For this, we further subdivided all mice used into two groups: "young" (receiving rapamycin from the age of 5 months or earlier) and "old" (receiving rapamycin starting at 5 months of age or older). Results of the data analysis for the "young" group are shown in Figure 1C and D. The mean lifespan in control group was 373 days, whereas in rapamycin-treated "young" mice the mean lifespan reached 480 days, 3.5 months increase over the control group. Furthermore, 40% of rapamycin-treated "young" mice survived 550 days (Fig. 1C) and by this age developed 2 times less tumors than control mice (Fig. 1D). In the "old" group the difference between control and treated group was blunted (data not shown).

Thus, the life-extending effect of rapamycin is more pronounced when treatment starts earlier in life. In order to confirm that rapamycin administered with drinking water has biological activity in vivo, we measured levels of phosphorylated ribosomal protein S6 (pS6), a marker of the mTOR activity in tissues of control and rapamycin-treated mice. After receiving rapamycin in drinking water for 2 days, mice were sacrificed and the levels of total S6 and pS6 were estimated by Western blot analysis and immuno-cytochemistry (Fig. 2).

As shown in Fig. 2A, levels of pS6 were reduced in the heart, kidney and liver of rapamycin-treated mice. Also, pS6/S6 ratios were lower in rapamycin-treated mice (Fig. S1).

These results were confirmed by immunohistochemical staining showing lower levels of pS6 in tissues of rapamycin-treated mice (Fig. 2B). The variability of pS6 levels among mice may explain the variability of biological effects of rapamycin.

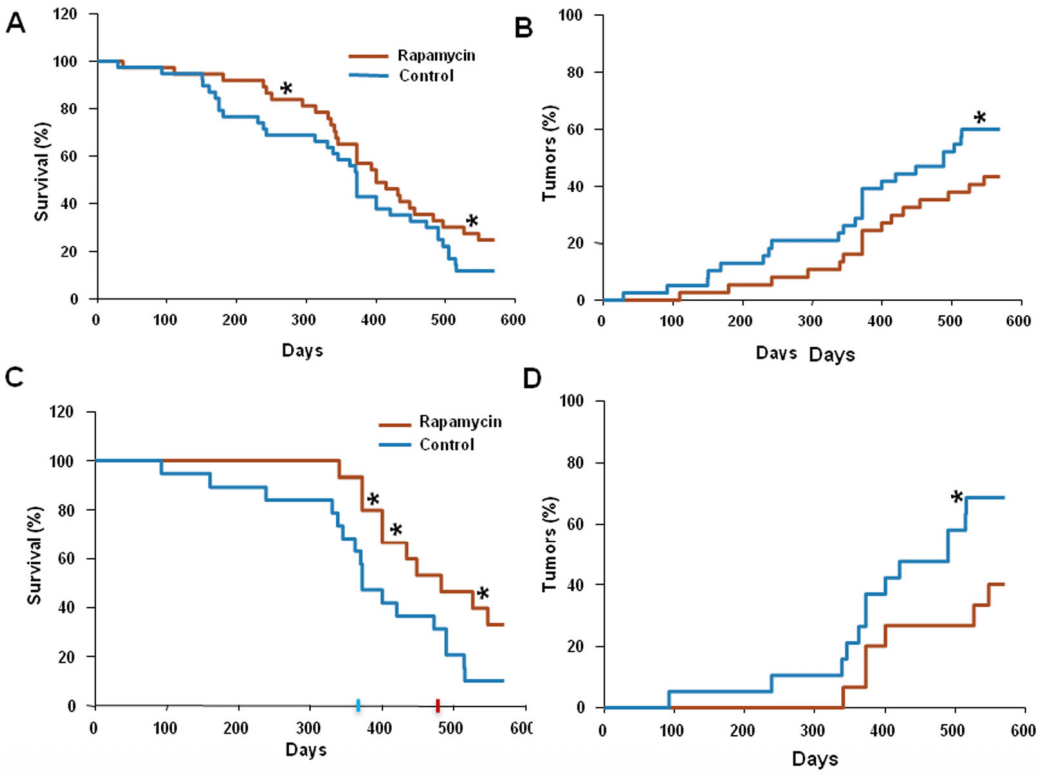

Figure 1. Administration of rapamycin extends lifespan and delays carcinogenesis in p53+/- male mice. (**A**) Kaplan Meier survival curve of rapamycin-treated (red line) and control (blue line) mice. (**B**) Incidence of tumors in rapamycin-treated (red) and control (blue) mice. Animals received rapamycin starting at various ages at 1.5 mg/kg per day in drinking water throughout entire life. * p<0.05. (**C**) Kaplan Meier survival curve of rapamycin-treated (red line) and control (blue line) mice that start receiving rapamycin early in life (<5 months). (**D**) Incidence of tumors in rapamycin-treated (red) and control (blue) mice that start receiving rapamycin early in life (<5 months). * p<0.05 toph

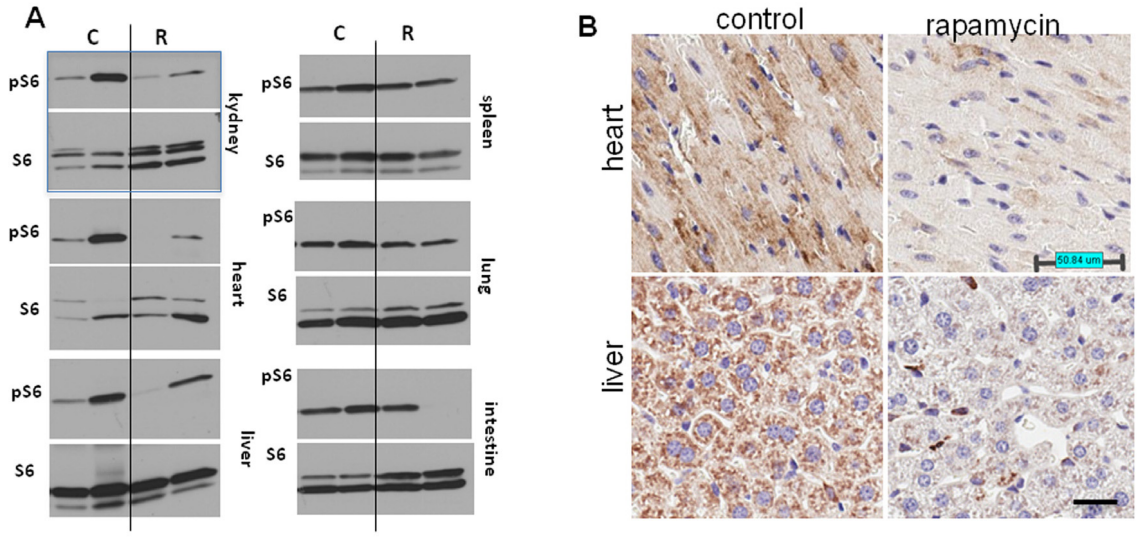

Figure 2. Administration of rapamycin in drinking water inhibits the mTOR pathway in p53+/- male mice. (A) Western blot analysis of whole cell lysates of 6 organs of rapamycin-treated and control mice probed with antibodies specific to S6 and phospho-S6 (Ser240/244). Mice received rapamycin in drinking water for 2 days. (**B**) Immunohistochemistry. pS6 in the heart and the liver. Mice received rapamycin in drinking water for 2 days.

DISCUSSION

Previously it was shown that rapamycin prolongs lifespan in genetically heterogeneous mice [11], [12], inbred mice [42] and Her2-expressing mice [13]. In normal genetically heterogeneous mice, rapamycin extended life span even when its administration was started later in life [11]. Our data in p53+/- mice show that the effect of rapamycin was blunted when treatment started at the age of 5 months or older.

This indicates that the anti-cancer effect of rapamycin is likely to be indirect and is imposed via its systemic effect at the level of an organism rather than through direct inhibition of tumor growth. To further address this question we plan to test the effect of rapamycin on animals with established tumors (by measuring tumor growth) along with evaluating the functional status of mTOR and the ability of rapamycin to suppress it in tumors and normal tissues. As we report here, administration of rapamycin starting early in life increased mean lifespan in p53+/- male mice by 28%. Previous work has demonstrated that the life-extending effects of rapamycin [11, 12] as well as metformin [43, 44], calorie restriction [45] and genetic inhibition of the IGF-I/mTOR/S6K pathway [46, 47] were less pronounced in male mice compared with female mice. Moreover, in some cases, life span extension was achieved in female mice only [43, 47]. Therefore, the observed increase in the median lifespan is dramatic, taking into account that it was achieved in male mice. However, because of low bioavailability of rapamycin, it was given constantly (in drinking water) without interruptions, whereas intermittent schedules may be more appropriate for future clinical developments as cancer-preventive interventions. In fact, a novel formulation of rapamycin (Rapatar) may be given intermittently, which still reveal even more pronounced extension of life span in p53-deficient mice (Comas et al, Aging 2012; this issue).

Our study suggests that rapamycin can be considered for cancer prevention in patients with Li-Fraumeni syndrome. Li-Fraumeni syndrome is an autosomal dominant disorder with a germline p53 mutation [48]. The incidence of cancer in carriers of mutation reaches 50% at the age of 40 and 90% at the age 60. Children of affected parents have an approximate 50% risk of inheriting the familial mutation [48]. Although functional assays have been established allowing for easy genetic testing for TP53 mutation, no effective chemopreventive therapy is currently available. The p53 rescue compounds may hold some promise in the future [48-50]; however these are not clinically approved drugs. In contrast, rapamycin has been used in the clinic for over a decade mostly in renal transplant patients. It was reported that rapamycin significantly decreased cancer incidence in renal transplant patients [51-53].

Our data suggest that rapamycin or its analogs can be considered for cancer prevention in Li-Fraumeni syndrome.

METHODS

Mice. All animal studies were conducted in accordance with the regulations of the Committee of Animal Care and Use at Roswell Park Cancer Institute. The colony of p53-knockout mice on a C57B1/6 background (originally obtained from Jackson Laboratories, Bar Habor, ME) was maintained by crossing p53+/- females with p53-/- males followed by genotyping of the progeny (PCR) as described previously [54]. Heterozygous p53+/- mice were generated by crossing p53-/- males with wild type p53 females. Male mice were kept in polypropelene cages (30x21x10 cm) under standard light/dark regimen (12 hours light : 12 hours darkness) at 22 ± 2 °C, And received standard laboratory chow and water ad libitum.

Rapamycin treatment. Rapamycin (LC Laboratories, USA) was diluted in ethanol at concentration 15 mg/ml. Then the stock was diluted 1:1000 in drinking water. Drinking water was changed every week. Male mice were randomly divided into two groups. Mice of the first group (n=37) were given rapamycin in drinking water (approximately 1.5 mg/kg per day), whereas mice of the second group (n=38) were given tap water without rapamycin and served as control. Once a week all mice were palpated for detection of tumor mass appearance.

Pathomorphological examination. All animals were autopsied. Site, number and size of tumors were checked. All tumors, as well as the tissues and organs with suspected tumor development were excised and fixed in 10% neutral formalin. After the routine histological processing the tissues were embedded into paraffin. 5-7 μm thin histological sections were stained with haematoxylin and eosine and were microscopically examined. Tumors were classified according to International Agency for Research on Cancer recommendations.

Western blot analysis. Tissues were homogenized in Bullet blender using stainless steel 0.5 mm diameter beads (Next Advantage, Inc. NY, USA) and RIPA lysis buffer supplemented with protease and phosphatase inhibitors tablets (Roche Diagnostics, Indianopolis, IN, USA). Lysates were cleared by centrifugation at 4°C at 13000 rpm. Equal amounts of protein were separated on gradient Criterion gels (BioRad) and immunoblotting was performed with rabbit anti-phospho S6 (Ser 240/244) and mouse anti-S6 antibodies from Cell Signaling Biotechnology as described previously [55], [56].

Immunochemistry. Dissected tissue samples were fixed in 10% buffered formalin, embedded into paraffin. 5-7 μm thin histological sections were stained with anti-phospho S6 (Ser240/244) antibody (Cell Signaling) and counterstained with Hematoxylin.

Statistical analyses. The SigmaStat software package was used for analysis. The P values were calculated using Fisher's Exact Test (2-tail). $P<0.05$ was considered as statistically significant.

Conflict of Interest Statement

The authors of this manuscript have no conflict of interests to declare.

REFERENCES

1. Blagosklonny MV. Cell cycle arrest is not yet senescence, which is not just cell cycle arrest: terminology for TOR-driven aging. Aging (Albany NY). 2012; 4:159-165.

2. Demidenko ZN, Zubova SG, Bukreeva EI, Pospelov VA, Pospelova TV, Blagosklonny MV. Rapamycin decelerates cellular senescence. Cell Cycle. 2009; 8:1888-1895.

3. Gan B, Sahin E, Jiang S, Sanchez-Aguilera A, Scott KL, Chin L, Williams DA, Kwiatkowski DJ, DePinho RA. mTORC1-dependent and -independent regulation of stem cell renewal, differentiation, and mobilization. Proc Natl Acad Sci U S A. 2008; 105:19384-19389.

4. Gan B, DePinho RA. mTORC1 signaling governs hematopoietic stem cell quiescence. Cell Cycle. 2009; 8:1003-1006.

5. Chen C, Liu Y, Liu R, Ikenoue T, Guan KL, Zheng P. TSC-mTOR maintains quiescence and function of hematopoietic stem cells by repressing mitochondrial biogenesis and reactive oxygen species. J Exp Med. 2008; 205:2397-2408.

6. Chen C, Liu Y, Zheng P. mTOR regulation and therapeutic rejuvenation of aging hematopoietic stem cells. Sci Signal. 2009; 2: ra75.

7. Adhikari D, Zheng W, Shen Y, Gorre N, Hamalainen T, Cooney AJ, Huhtaniemi I, Lan ZJ, Liu K. Tsc/mTORC1 signaling in oocytes governs the quiescence and activation of primordial follicles. Human Molecular Genet. 2010;19:397-410.

8. Kolesnichenko M, Hong L, Liao R, Vogt PK, Sun P. Attenuation of TORC1 signaling delays replicative and oncogenic RAS-induced senescence. Cell Cycle. 2012; 11:2391-2401.

9. Kapahi P, Zid BM, Harper T, Koslover D, Sapin V, Benzer S. Regulation of lifespan in Drosophila by modulation of genes in the TOR signaling pathway. CurrBiol. 2004; 14: 885-890.

10. Bjedov I, Toivonen JM, Kerr F, Slack C, Jacobson J, Foley A, Partridge L. Mechanisms of life span extension by rapamycin in the fruit fly Drosophila melanogaster. Cell Metab. 2010; 11: 35-46.

11. Harrison DE, Strong R, Sharp ZD, Nelson JF, Astle CM, Flurkey K, Nadon NL, Wilkinson JE, Frenkel K, Carter CS, Pahor M, Javors MA, Fernandezr E, Miller RA. Rapamycin fed late in life extends

lifespan in genetically heterogenous mice. Nature. 2009; 460: 392-396.

12. Miller RA, Harrison DE, Astle CM, Baur JA, Boyd AR, de Cabo R, Fernandez E, Flurkey K, Javors MA, Nelson JF, Orihuela CJ, Pletcher S, Sharp ZD, Sinclair D, Starnes JW, Wilkinson JE et al. Rapamycin, but not resveratrol or simvastatin, extends life span of genetically heterogeneous mice. J Gerontol A Biol Sci Med Sci. 2011; 66: 191-201.

13. Anisimov VN, al. e, Antoch M, Blagosklonny MV. Am J Pathol. 2010: in press.

14. Khamzina L, Veilleux A, Bergeron S, Marette A. Increased activation of the mammalian target of rapamycin pathway in liver and skeletal muscle of obese rats: possible involvement in obesity-linked insulin resistance. Endocrinology. 2005; 146: 1473-1481.

15. Tremblay F, Krebs M, Dombrowski L, Brehm A, Bernroider E, Roth E, Nowotny P, WaldhŠusl W, Marette A, Roden M. Overactivation of S6 kinase 1 as a cause of human insulin resistance during increased amino acid availability. Diabetes. 2005; 54: 2674-2684.

16. Krebs M, Brunmair B, Brehm A, Artwohl M, Szendroedi J, Nowotny P, Roth E, FŸrnsinn C, Promintzer M, Anderwald C, Bischof M, Roden M. The Mammalian target of rapamycin pathway regulates nutrient-sensitive glucose uptake in man. Diabetes. 2007; 56: 1600-1607.

17. Jiang W, Zhu Z, Thompson HJ. Dietary energy restriction modulates the activity of AMP-activated protein kinase, Akt, and mammalian target of rapamycin in mammary carcinomas, mammary gland, and liver. Cancer Res. 2008; 68: 5492-5499.

18. Estep PWr, Warner JB, Bulyk ML. Short-term calorie restriction in male mice feminizes gene expression and alters key regulators of conserved aging regulatory pathways. PLoS One. 2009; 4: e5242.

19. Masternak MM, Panici JA, Bonkowski MS, Hughes LF, Bartke A. Insulin sensitivity as a key mediator of growth hormone actions on longevity. J Gerontol A Biol Sci Med Sci. 2009; 64: 516-521.

20. Wang C, Maddick M, Miwa S, Jurk D, Czapiewski R, Saretzki G, Langie SA, Godschalk RW, Cameron K, von Zglinicki T. Adult-onset, short-term dietary restriction reduces cell senescence in mice. Aging (Albany NY). 2010; 2: 555-566.

21. Dirx MJ, Zeegers MP, Dagnelie PC, van den Bogaard T, van den Brandt PA. Energy restriction and the risk of spontaneous mammary tumors in mice: a meta-analysis. Int J Cancer. 2003; 106: 766-770.

22. Sarkar NH, Fernandes G, Telang NT, Kourides IA, Good RA. Low-calorie diet prevents the development of mammary tumors in C3H mice and reduces circulating prolactin level, murine mammary tumor virus expression, and proliferation of mammary alveolar cells. Proc Natl Acad Sci U S A. 1982; 79: 7758-7762.

23. Berrigan D, Perkins SN, Haines DC, Hursting SD. Adult-onset calorie restriction and fasting delay spontaneous tumorigenesis in p53-deficient mice. Carcinogenesis. 2002; 23: 817-822.

24. Hursting SD, Perkins SN, Phang JM. Calorie restriction delays spontaneous tumorigenesis in p53-knockout transgenic mice. Proc Natl Acad Sci U S A. 1994; 91: 7036-7040.

25. Hursting SD, Perkins SN, Brown CC, Haines DC, Phang JM. Calorie restriction induces a p53-independent delay of spontaneous carcinogenesis in p53-deficient and wild-type mice. Cancer Res. 1997; 57: 2843-2846.

26. Feng Z, Hu W, de Stanchina E, Teresky AK, Jin S, Lowe S, Levine AJ. The regulation of AMPK beta1, TSC2, and PTEN expression by p53: stress, cell and tissue specificity, and the role of these gene products in modulating the IGF-1-AKT-mTOR pathways. Cancer Res. 2007; 67: 3043-3053.

27. Feng Z, Zhang H, Levine AJ, Jin S. The coordinate regulation of the p53 and mTOR pathways in cells. Proc Natl Acad Sci U S A. 2005; 102: 8204-8209.

28. Levine AJ, Feng Z, Mak TW, You H, Jin S. Coordination and communication between the p53 and IGF-1-AKT-TOR signal transduction pathways. Genes Dev. 2006; 20: 267-275.

29. Budanov AV, Karin M. p53 target genes sestrin1 and sestrin2 connect genotoxic stress and mTOR signaling. Cell. 2008; 134: 451-460.

30. Demidenko ZN, Korotchkina LG, Gudkov AV, Blagosklonny MV. Paradoxical suppression of cellular senescence by p53. Proc Natl Acad Sci U S A. 2010; 9660-4: 9660-9664.

31. Korotchkina LG, Leontieva OV, Bukreeva EI, Demidenko ZN, Gudkov AV, Blagosklonny MV. The choice between p53-induced senescence and quiescence is determined in part by the mTOR pathway. Aging (Albany NY). 2010; 2: 344-352.

32. CoppŽ JP, Patil CK, Rodier F, Sun Y, Mu–oz DP, Goldstein J, Nelson PS, Desprez PY, Campisi J. Senescence-associated secretory phenotypes reveal cell-nonautonomous functions of oncogenic RAS and the p53 tumor suppressor. PLoS Biol. 2008; 6: 2853-2868.

33. Komarova EA, Krivokrysenko V, Wang K, Neznanov N, Chernov MV, Komarov PG, Brennan ML, Golovkina TV, Rokhlin OW, Kuprash DV, Nedospasov SA, Hazen SL, Feinstein E, Gudkov AV. p53 is a suppressor of inflammatory response in mice. FASEB J. 2005; 19: 1030-1032.

34. Gudkov AV, Gurova KV, Komarova EA. Inflammation and p53: A Tale of Two Stresses. Genes Cancer. 2011; 2: 503-516.

35. Feng Z, Hu W, Teresky AK, Hernando E, Cordon-Cardo C, Levine AJ. Declining p53 function in the aging process: a possible mechanism for the increased tumor incidence in older populations. Proc Natl Acad Sci U S A. 2007; 104: 16633-16638.

36. Donehower LA, Harvey M, Slagle BL, McArthur MJ, Montgomery CA, Jr., Butel JS, Bradley A. Mice deficient for p53 are developmentally normal but susceptible to spontaneous tumours. Nature. 1992; 356: 215-221.

37. Harvey M, McArthur MJ, Montgomery CA, Jr., Butel JS, Bradley A, Donehower LA. Spontaneous and carcinogen-induced tumorigenesis in p53-deficient mice. Nat Genet. 1993; 5: 225-229.

38. Jacks T, Remington L, Williams BO, Schmitt EM, Halachmi S, Bronson RT, Weinberg RA. Tumor spectrum analysis in p53-mutant mice. Curr Biol. 1994; 4: 1-7.

39. Donehower LA, Harvey M, Vogel H, McArthur MJ, Montgomery CA, Jr., Park SH, Thompson T, Ford RJ, Bradley A. Effects of genetic background on tumorigenesis in p53-deficient mice. Mol Carcinog. 1995; 14: 16-22.

40. Venkatachalam S, Shi YP, Jones SN, Vogel H, Bradley A, Pinkel D, Donehower LA. Retention of wild-type p53 in tumors from p53 heterozygous mice: reduction of p53 dosage can promote cancer formation. Embo J. 1998; 17: 4657-4667.

41. Hinkal G, Parikh N, Donehower LA. Timed somatic deletion of p53 in mice reveals age-associated differences in tumor progression. PLoS One. 2009; 4: e6654.

42. Anisimov VN, Zabezhinski MA, Popovich IG, Piskunova TS, Semenchenko AV, Tyndyk ML, Yurova MN, Rosenfeld SV,

Blagosklonny MV. Rapamycin increases lifespan and inhibits spontaneous tumorigenesis in inbred female mice. Cell Cycle. 2011; 10: 4230-4236.

43. Anisimov VN, Piskunova TS, Popovich IG, Zabezhinski MA, Tyndyk ML, Egormin PA, Yurova MV, Rosenfeld SV, Semenchenko AV, Kovalenko IG, Poroshina TE, Berstein LM. Gender differences in metformin effect on aging, life span and spontaneous tumorigenesis in 129/Sv mice. Aging (Albany NY). 2010; 2: 945-958.

44. Blagosklonny MV. Metformin and sex: Why suppression of aging may be harmful to young male mice. Aging (Albany NY). 2010; 2: 897-899.

45. Turturro A, Duffy P, Hass B, Kodell R, Hart R. Survival characteristics and age-adjusted disease incidences in C57BL/6 mice fed a commonly used cereal-based diet modulated by dietary restriction. J Gerontol A Biol Sci Med Sci. 2002; 57: B379-389.

46. Holzenberger M, Dupont J, Ducos B, Leneuve P, Geloen A, Even PC, Cervera P, Le Bouc Y. IGF-1 receptor regulates lifespan and resistance to oxidative stress in mice. Nature. 2003; 421: 182-187.

47. Selman C, Tullet JM, Wieser D, Irvine E, Lingard SJ, Choudhury AI, Claret M, Al-Qassab H, Carmignac D, Ramadani F, Woods A, Robinson IC, Schuster E, Batterham RL, Kozma SC, Thomas G et al. Ribosomal protein S6 kinase 1 signaling regulates mammalian life span. Science. 2009; 326: 140-144.

48. Upton B, Chu Q, Li BD. Li-Fraumeni syndrome: the genetics and treatment considerations for the sarcoma and associated neoplasms. Surg Oncol Clin N Am. 2009; 18: 145-156, ix.

49. Glazer RI. A new therapeutic basis for treating Li-Fraumeni Syndrome breast tumors expressing mutated TP53. Oncotarget. 2010; 1: 470-471.

50. Herbert BS, Chanoux RA, Liu Y, Baenziger PH, Goswami CP, McClintick JN, Edenberg HJ, Pennington RE, Lipkin SM, Kopelovich L. A molecular signature of normal breast epithelial and stromal cells from Li-Fraumeni syndrome mutation carriers. Oncotarget. 2010; 1: 405-422.

51. Mathew T, Kreis H, Friend P. Two-year incidence of malignancy in sirolimus-treated renal transplant recipients: results from five multicenter studies. Clin Transplant. 2004; 18: 446-449.

52. Campistol JM, Eris J, Oberbauer R, Friend P, Hutchison B, Morales JM, Claesson K, Stallone G, Russ G, Rostaing L, Kreis H, Burke JT, Brault Y, Scarola JA, Neylan JF. Sirolimus Therapy after Early Cyclosporine Withdrawal Reduces the Risk for Cancer in Adult Renal Transplantation. J Am Soc Nephrol. 2006; 17: 581-589.

53. Blagosklonny MV. Prevention of cancer by inhibiting aging. Cancer Biol Ther. 2008; 7: 1520-1524.

54. Leonova KI, Shneyder J, Antoch MP, Toshkov IA, Novototskaya LR, Komarov PG, Komarova EA, Gudkov AV. A small molecule inhibitor of p53 stimulates amplification of hematopoietic stem cells but does not promote tumor development in mice. Cell Cycle. 2010; 9: 1434-1443.

55. Leontieva O, Gudkov A, Blagosklonny M. Weak p53 permits senescence during cell cycle arrest. Cell Cycle. 2010; 9: 4323-4327.

56. Leontieva OV, Blagosklonny MV. DNA damaging agents and p53 do not cause senescence in quiescent cells, while consecutive re-activation of mTOR is associated with conversion to senescence. Aging (Albany NY). 2010; 2: 924-935.

SUPPLEMENTAL FIGURE

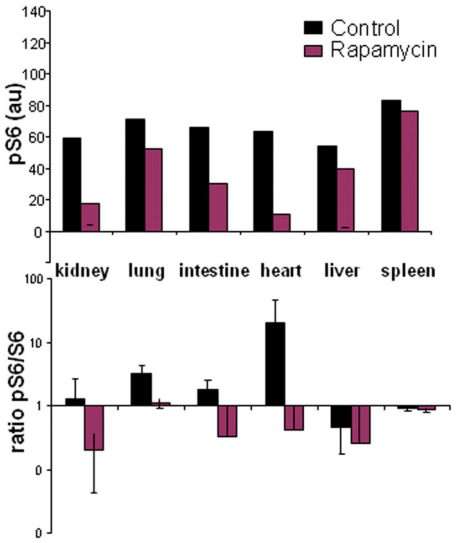

Supplemental Figure S1. Quantitative analysis of data shown in Figure 2A. Top panel - Intensity of phosphorylated S6 (pS6) signal was quantified using ImageJ program (intensity units, IU). Bottom panel – Intensity of pS6 and S6 signals were quantified and the ratio pS6/S6 was calculated.

Research Paper

Reversing the aging stromal phenotype prevents carcinoma initiation

Davina A. Lewis[1], Jeffrey B. Travers[1,2,3], Christiane Machado[1], Ally-Khan Somani[1], and Dan F Spandau[1,5]

[1] Departments of Dermatology, Indiana University School of Medicine, Indianapolis, IN 46202, USA
[2] Pharmacology and Toxicology, Indiana University School of Medicine, Indianapolis, IN 46202, USA
[3] Herman B. Wells Center for Pediatric Research, Indiana University School of Medicine, Indianapolis, IN 46202, USA
[4] Richard L. Roudebush V.A. Medical Center, Indiana University School of Medicine, Indianapolis, IN 46202, USA
[5] Biochemistry & Molecular Biology, Indiana University School of Medicine, Indianapolis, IN 46202, USA

Key words: Senescence, aging, photocarcinogenesis, therapy, UVB
Received: 4/1/11; Accepted: 4/20/11; Published: 4/21/11 DOI: 10.18632/aging.100318
Corresponding author: Dan F Spandau, PhD; **E-mail:** dspanda@iupui.edu

Copyright: © Lewis et al. This is an open-access article distributed under the terms of the Creative Commons Attribution License, which permits unrestricted use, distribution, and reproduction in any medium, provided the original author and source are credited

Abstract: The accumulation of senescent stromal cells in aging tissue changes the local microenvironment from normal to a state similar to chronic inflammation. This inflammatory microenvironment can stimulate the proliferation of epithelial cells containing DNA mutations which can ultimately lead to cancer. Using geriatric skin as a model, we demonstrated that senescent fibroblasts also alter how epithelial keratinocytes respond to genotoxic stress, due to the silencing of IGF-1 expression in geriatric fibroblasts. These data indicate that in addition to promoting epithelial tumor growth, senescent fibroblasts also can promote carcinogenic initiation. We hypothesized that commonly used therapeutic stromal wounding therapies can reduce the percentage of senescent fibroblasts and consequently prevent the formation of keratinocytes proliferating with DNA mutations following acute genotoxic (UVB) stress. Sun-protected skin on the lower back of geriatric human volunteers was wounded by dermabrasion and the skin was allowed to heal for three months. In geriatric skin, we found that dermabrasion wounding decreases the proportion of senescent fibroblasts found in geriatric dermis, increases the expression of IGF-1, and restores the appropriate UVB response to epidermal keratinocytes in geriatric skin. Therefore, dermal rejuvenation therapies may play a significant role in preventing the initiation of skin cancer in geriatric patients.

INTRODUCTION

Cancer is an age-dependent disease in most mammalian species; in humans over 50% of cancers are found in people over 70 years of age [1]. Recently, the accumulation of senescent cells in aging tissues have been shown to acquire a chronic inflammatory phenotype (called SASP, Senescence-Associated Secretory Phenotype) that serves to promote the growth of initiated tumorigenic epithelial cells [2]. Additional reports have demonstrated that in the skin, the accumulation of senescent fibroblasts also increases the susceptibility of epidermal keratinocytes to carcinogenic initiation [3]. Therefore, while investigations into the role of stromal tissue on the initiation and promotion of cancer are in their infancy, they may serve as potential emerging opportunities for interventional and prophylactic therapeutic strategies [4-6]. Our lab is investigating the role of aging in the development of non-melanoma skin cancer (NMSC) as a model for the effect that aging stromal tissue has in controlling carcinogenesis initiation [3, 6-10]. As such, the skin is an excellent model system for these studies; it is accessible, it has a relevant environmental carcinogen (UVB), and it is possible to easily interrogate human disease.

NMSC has the highest incidence rate of all cancers worldwide, including an estimated 2 million newly diagnosed patients in the United States this year alone [11-12]. Although the mortality of NMSC is relatively low compared to other types of cancer, the morbidity

and the cost of treating NMSC is enormous [11, 13]. As NMSC occurs primarily in geriatric individuals, it has been estimated that up to nearly 1% of total Medicare expenses in the United States go towards the treatment of NMSC [13]. Therefore, NMSC is a major burden on our healthcare system [14]. Despite our understanding for decades that sunlight is the main etiologic agent responsible for NMSC (over 90%), the incidence of NMSC continues to rise at an alarming rate [11].

The primary environmental factor that influences the development of skin cancer is exposure to the spectrum of ultraviolet wavelengths found in sunlight. Furthermore, as we age our chances of developing NMSC greatly increases so that at age 65 we have a 50% chance of acquiring a NMSC [15-16]. In fact, 80% of all NMSC are diagnosed in individuals greater than 60 years old [15-16]. While the correlation between aged epidermis and NMSC is apparent, the mechanism responsible for this relationship remains obscure. Early hypotheses describing why the incidence of NMSC increases with age, suggested that excessive sun exposure during adolescence causes mutations in clones of keratinocytes. Subsequently over many decades of genetic selection, these initiated keratinocytes will form detectable tumors [17-18]. However, recent studies have shown that more than 77% of our lifetime sun exposure occurs *after* the age of 18 [19], indicating the vast majority of damaging UVB-irradiation takes place later in life. In fact, more sun exposure occurs after age 59 (26%) than before age 18 (23%) [19]. Recent data from a variety of labs have proposed a modification in the latency theory of carcinogenesis [20-21] based on changes in the effects of stromal cells (i.e. fibroblasts) on epithelial cells in aged individuals [22-23]. This new hypothesis states that the selection of initiated epithelial cells is accelerated in aged tissue due to alterations in gene expression by senescent fibroblasts supporting epithelial cell growth [24-26]. In addition, the aged state of cells may play a greater role in the initiation of carcinogenic DNA mutations than was previously considered [27]. Previously we have shown that the activation of the insulin-like growth factor-1 receptor (IGF-1R) is critical for determining the response of skin keratinocytes to UVB irradiation *in vitro* and *in vivo* [3, 6-10]. If the IGF-1R is functionally inactive *in vitro* at the time of UVB-irradiation, surviving keratinocytes can continue to proliferate with the potential of converting the damaged DNA into initiating carcinogenic mutations [3, 5-6, 10]. Recent data from our laboratories have indicated that similar IGF-1R-dependent UVB responses occur in epidermal keratinocytes *in vivo* [3, 5-6, 10]. Because keratinocytes do not produce IGF-1, the majority of the IGF-1 supplied to the epidermis is produced by dermal fibroblasts. Therefore, any deficiencies in dermal IGF-1 production could have profound effects on the response of epidermal keratinocytes to UVB irradiation. We have demonstrated that such an instance occurs in aged skin, as senescent dermal fibroblasts produce significantly lower levels of IGF-1 than youthful, proliferating fibroblasts [3]**.** Geriatric skin with lower IGF-1 levels responds inappropriately to UVB exposure and results in the production of keratinocytes that can proliferate with DNA damage. Moreover, we demonstrate that therapeutic treatment of geriatric skin can result in increased levels of dermal IGF-1 and protection against acute UVB-mediated formation of keratinocytes proliferating with DNA damage. We hypothesize that the reduced activation of the IGF-1R in aging skin due to silencing of IGF-1 expression in senescent fibroblasts is an important factor in the dramatic increase in NMSC observed in geriatric patients. The incorporation of recent data from our laboratories and these new ideas on the origins of cancer has led us to a new paradigm to explain non-melanoma skin carcinogenesis [3, 5-6, 10]. This new paradigm indicates that the accumulation of senescent fibroblasts in geriatric dermis leads to a silencing of IGF-1 expression in the skin, resulting in a deficient activation of the IGF-1R in epidermal keratinocytes, causing an inappropriate UVB-response in keratinocytes, leading to proliferating keratinocytes containing DNA mutations, and subsequently photocarcinogenesis [3, 5-6]. Therefore, the susceptibility to develop NMSC is dependent on both the exposure of skin to UVB and the biologic age of the skin.

Given our findings that the lack of endogenous IGF-1 [3] in geriatric skin resulted in an inappropriate pro-carcinogenic response to relatively low doses of UVB [3], and that this inappropriate response was reversed by local injections of *exogenous* IGF-1 [3], these studies have examined the ability of dermal wounding to upregulate *endogenous* IGF-1 levels and restore the appropriate UVB response in geriatric skin. We assayed whether ablation of both the epidermis and papillary dermis by dermabrasion could upregulate IGF-1 expression in geriatric skin and restore the appropriate UVB response. The successful development of the prophylactic therapies as described here could have a major impact on how NMSCs can be prevented in susceptible individuals.

RESULTS

Senescent human fibroblasts in vitro contain markers of the DNA damage response

Normal human fibroblasts that are continually cultured

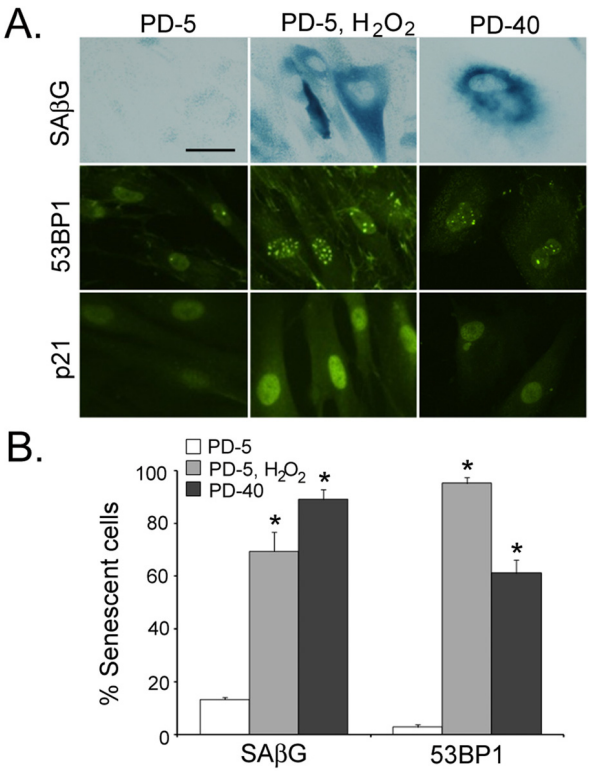

Figure 1. Senescent human fibroblasts contain markers of DNA damage response *in vitro*. (**A**) Low passage neonatal normal human fibroblasts (PD-5), stress-induced senescent fibroblasts (PD-5, H_2O_2), and replicatively senescent fibroblasts (PD-40) were stained for the presence of senescence-associated β-galactosidase activity (blue), with α-53BP1 antibodies (multiple punctate nuclear staining), or α--p21 antibodies (bar = 20 μm). (**B**) The percentage of senescent cells were determined for senescence-associated β-galactosidase and 53BP1 staining. 53BP1-positive cells contained at least four individual fluorescent pin-point spots per nucleus (asterisks indicate significant difference from PD-5 cells, $p<0.001$, two-tailed t-test).

in vitro until they reach replicative senescence have historically been identified by their expression of senescence-associated β-galactosidase [28]. Similarly, replicating fibroblasts treated with DNA-damaging chemotherapeutic drugs or pro-oxidative stressors to induce stress-induced senescence have been assayed for senescence-associated β-galactosidase activity to verify their senescence phenotype [3]. However, because identifying senescent cells using senescence-associated β-galactosidase requires an assay of enzymatic activity, its use in specimens from human tissues is not as effective. Recently, it has been described that markers of a DNA-damage response (DDR) are found in most types of senescent cells, whether induced by replication exhaustion, reactive oxygen species, or oncogene expression [29-32]. To determine the reliability of DDR markers to identify senescent fibroblasts in skin, replicating, stress-induced senescent, and replicative senescent fibroblasts were stained by for the traditional senescence-associated β-galactosidase activity, for the presence of 53BP1, and for the expression of cell cycle inhibitor p21 (Fig.1A). As seen in Fig. 1A, senescent fibroblasts can be identified by nuclei which have greater than four 53BP1-positive foci. When the numbers of senescent fibroblasts were counted in stress-induced senescent and replicatively senescent fibroblasts, the use of either senescent-associated β-galactosidase or 53BP1 foci yielded similar results (Fig. 1B). Therefore, markers of DDR may be useful in identifying senescent fibroblasts *in vivo*.

Senescent fibroblasts accumulate in geriatric dermis in vivo

As we age, the skin becomes altered both phenotypically and biologically. The undulating structure of the dermal-epidermal junction in young skin becomes significantly flattened with age [33-34; Supplemental Fig. 1A]. Both the epidermis and the papillary dermis become atrophied in geriatric skin [33-37; Fig. 2D] and the transcriptome in the geriatric dermis becomes altered, including the relative silencing of the IGF-1 and collagen I genes [3; Fig. 2B]. Additionally, fibroblast morphology transforms from a spindle-shaped cell body and elliptical nucleus to a more rounded cell body and a rounded nucleus [37-38; Supplemental Fig. 1A, white circles]. These morphological changes in fibroblast shape are associated with increasing proportions of senescent fibroblasts in the papillary dermis (Fig. 2C). These senescent fibroblasts can be defined *in vivo* by increased expression of DDR markers (Fig. 2A). Previously, we and others have shown that senescent fibroblasts *in vitro* silence IGF-1 expression [3]. Similarly, intrinsic aging of skin *in vivo* can be characterized by a significantly increased proportion of senescent fibroblasts in the papillary dermis and a corresponding silencing of IGF-1 expression in geriatric dermis.

Dermabrasion restores young adult function in geriatric dermis

Cosmetic dermal rejuvenation techniques have been widely used to stimulate the production of new collagen synthesis by inducing a 'wounding response' in the skin [39-40]. As such, it was of interest to determine if these dermal rejuvenation techniques restored a more youth-

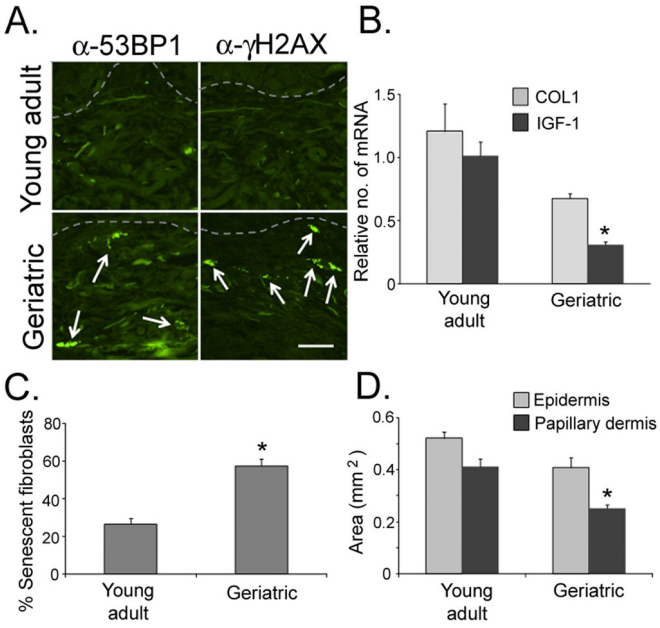

Figure 2. Senescent fibroblasts accumulate in geriatric dermis *in vivo*. Biopsies of sun-protected skin were obtained from six young adult (20-28 years old) and six geriatric (≥65 years old) volunteers. (**A**) Sections of skin were stained with antibodies to 53BP1 and γH2AX. Positive nuclei are indicated by white arrows; dashed line specifies the location of the basement membrane; bar = 25 μm. (**B**) Quantitative PCR analysis of mRNA isolated from skin biopsies, normalized to actin expression. Asterisk indicate statistical significance from young adult values (IGF-1 p=0.005, COL1 p=0.091; two-tailed t-test). (**C**) The number of senescent fibroblasts (based on circular or elliptical nuclear morphology as determined using Nikon Elements Image Analysis software) was counted in the papillary dermis. Asterisk indicates statistical significance from young adult values (p=0.001; two-tailed t-test). (**D**) The area of the epidermis and papillary dermis were calculated from 3mm punch biopsies using Nikon Elements image analysis software. Asterisk indicates statistical significance from young adult values (Epidermis p=0.0577, Papillary dermis p=0.022; two-tailed t-test).

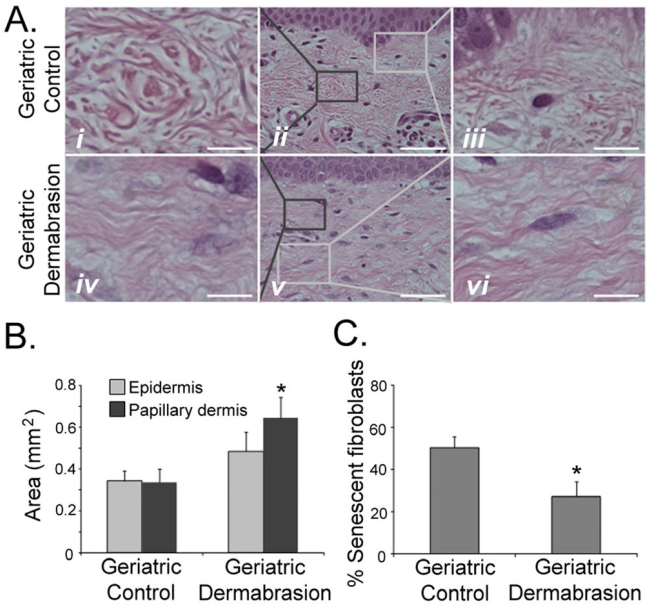

Figure 3. Dermabrasion restores young adult fibroblast function in geriatric dermis. A 5 cm^2 area of sun-protected skin on geriatric (≥65 years old) volunteers was dermabraded. After a healing period of three months, biopsies of untreated and dermabraded skin were obtained. (**A**) Representative H&E sections from untreated and dermabraded geriatric skin. Panels *i* and *iv* are higher magnification images of dark boxes indicated in panels *ii* and *v*. Panels *iii* and *vi* are higher magnification images of light boxes indicated in panels *ii* and *v*. Panels *i* and *iv*, bar=10 μm; panels *ii* and *v*, bar=50 μm; panels *iii* and *vi*, bar=12.5 μm. (**B**) The area of epidermis and papillary dermis were calculated as described in Fig. 2. Asterisk indicates statistical significance from geriatric control values (Epidermis p=0.287, Papillary dermis p=0.013; two-tailed t-test). (**C**) The number of senescent fibroblasts in the papillary dermis was determined as described in Fig. 2. Asterisk indicates statistical significance from control values (p=0.018, two-tailed t-test).

ful phenotype and biology to geriatric skin, and specifically to determine if these techniques could restore the appropriate DNA-damage response found in young skin to UVB-irradiated geriatric skin. Small areas of sun-protected skin on geriatric volunteers were treated by dermabrasion. Biopsies of dermabraded and untreated skin were analyzed after the treated sites were allowed to heal for three months. Consistent with previous reports, dermabraded skin demonstrated increased synthesis of collagen [39-40; Supplemental Fig. 2] and a restoration of the dermal collagen structure similar to that found in young adults (Fig. 3A, panels *i* and *iv*). Dermabasion also reversed the aging-associated atrophy of the papillary dermis (Fig. 2D) by significantly increasing the area of the papillary dermis (Fig. 3B). The thickness of the epidermis was modestly increased by dermabrasion, although this result was not statistically significant (Fig. 3B). Increased thickness of the papillary dermis was accompanied by an increase in fibroblast density in the dermabraded geriatric skin (Fig. 4B; see Supplemental Fig. 3 for example of fibroblast verification) and statistically greater numbers of replicating keratinocytes and fibroblasts (Fig. 4C). The increased proliferative potential of fibroblasts in the dermis corresponded with a decrease in the proportion of dermal senescent fibroblasts (Fig. 3C). The round phenotype of the senescent fibroblast nuclei in control geriatric dermis was replaced with increasing percentages of replicating elliptical fibroblast nuclei

(Fig. 3A, panels *iii* and *vi*). The loss of senescent cells in dermabraded skin can also be observed by assaying for DDR markers. In contrast to the abundant expression of DDR markers in senescent fibroblasts of control geriatric dermis, DDR-positive fibroblasts are not detected in dermabraded geriatric dermis (Fig. 4A).

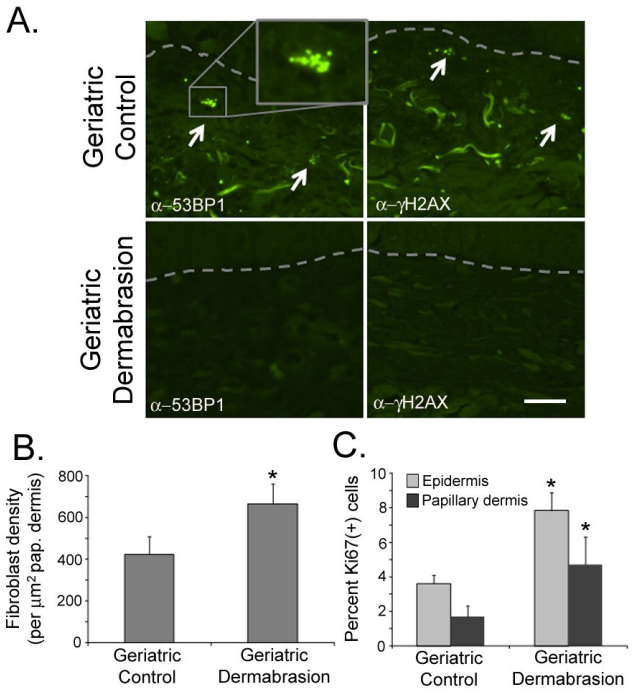

Figure 4. Dermabrasion stimulates fibroblast replication and suppresses senescence in geriatric dermis. (**A**) Skin biopsies described in Fig. 3 were stained with antibodies to 53BP1 and γH2AX. Senescent nuclei are indicated by white arrows, the basement membrane is designated by a dashed grey line, bar=25 μm. (**B**) The density of fibroblasts in the papillary dermis was determined using the Nikon Elements Image Analysis software. Asterisk indicates statistical significance from control values (p=0.0048), two-tailed t-test). (**C**) Sections of biopsies were stained with antibodies to Ki67. The percentage of Ki67(+) fibroblasts in the papillary dermis and the percentage of Ki67(+) keratinocytes in the basal layer of the epidermis were calculated using Nikon Elements image analysis software. Asterisks indicate statistical significance from control values (papillary dermis, p=0.039; epidermis p=0.058, two-tailed t-test).

Our previous data had shown that the silencing of endogenous IGF-1 in geriatric skin resulted in an inappropriate pro-carcinogenenic response to relatively low doses of UVB which could be reversed by local injections of exogenous IGF-1 [3]. Therefore, it was important to determine whether IGF-1 expression was upregulated in geriatric skin treated with dermabrasion.

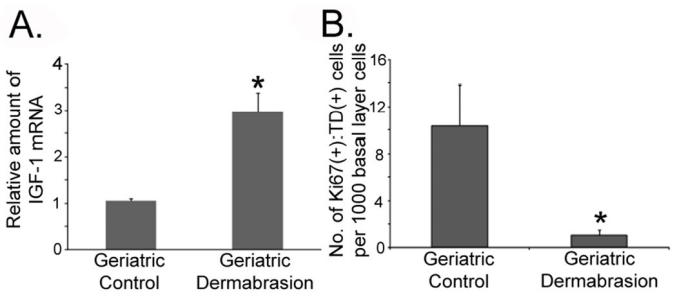

Figure 5. Dermabrasion upregulates IGF-1 expression and restores the appropriate UVB response to geriatric skin. Small areas of dermabraded and untreated skin on geriatric volunteers described in Fig. 2 were irradiated with UVB (dose of 350 J/m^2). Twenty-four hours post-UVB, the irradiated skin was biopsied. (**A**) Total mRNA was isolated and the relative level of IGF-1 expression was determined by quantitative PCR (normalized to actin expression). Asterisk indicates statistically significant differences from control values (p<0.006, two-tailed t-test). (**B**) Sections of biopsies were stained with antibodies to Ki67 and thymine dimers (TD). The number of dual Ki67(+):TD(+) basal keratinocytes were determined for both sets of biopsies. Asterisk indicates statistically significant differences from control values (p<0.05, two-tailed t-test).

At three months following dermabrasion, IGF-1 expression was three-fold higher in treated dermis compared to geriatric controls (Fig. 5A). To assay the UVB-response, small areas of the dermabraded skin and untreated skin on the opposing hip/buttock were irradiated with 350 J/m^2 (one MED) of UVB. Twenty-four hours post-irradiation (the time required to clear TD lesions), the UVB-irradiated areas were biopsied and the basal layer keratinocytes were assayed for co-expression of proliferation (Ki67) markers and UVB-induced DNA damage (TD; see examples of scored keratinocytes in Supplemental Figure 4). Consistent with the ability of dermabrasion to upregulate IGF-1 levels, UVB irradiation of control versus dermabraded skin were similar to our findings using young skin or geriatric skin treated with exogenous IGF-1 (i.e., no keratinocytes proliferating with DNA damage in the dermabraded skin in contrast to significant numbers of Ki67+:TD+ basal keratinocytes in untreated UVB-irradiated skin; Fig. 5B). These findings indicate that dermal rejuvenation upregulates IGF-1 levels and normalizes the UVB response in geriatric skin.

DISCUSSION

We have demonstrated *in vivo* that geriatric skin accumulates increasing proportions of senescent fibroblasts as measured by changes in cellular and

nuclear morphology [3; Fig. 3] as well as the induction of DNA-damage recognition proteins associated with cellular senescence [3; Fig. 3]. Furthermore, we have shown that geriatric skin silences IGF-1 expression [3] leading to deficient activation of the IGF-1R [3] on geriatric epidermal keratinocytes. Therefore, when geriatric skin is irradiated with UVB, a portion of the epidermal keratinocytes respond inappropriately by allowing replication of UVB-damaged DNA and potentially creating 'initiated' tumor cells [3, 5-6]. The role of IGF-1 *in vivo* was confirmed by its ability to correct this inappropriate UVB response in geriatric skin by injection of IGF-1 into the dermis prior to UVB irradiation [3]. Thus, therapies that can restore IGF-1 expression to levels seen in young adult dermis could potentially prevent the initiation of carcinogenesis in geriatric skin. Skin rejuvenation techniques, including dermabrasion, have been widely used to stimulate dermal collagen production and promote a youthful appearance of the skin. We found that dermabrasion of sun-protected geriatric skin decreased the proportion of senescent fibroblasts resulting in increased IGF-1 expression. Most importantly, dermabrasion corrected the inappropriate UVB response normally observed in geriatric skin. These results suggest that dermabrasion of geriatric skin can prophylactically prevent non-melanoma skin carcinogenesis.

It is interesting to note that the use of dermabrasion to prophylactically treat actinic keratosis and NMSC was described over 40 years ago [41]. A number of reports have demonstrated that dermabrasion can reduce the incidence of actinic keratosis and NMSC up to 95% in susceptible individuals for many years after treatment [42-44]. However, the use of dermabrasion has fallen out of favor as a primary method for the prophylaxis of NMSC despite the fact that newer methods of prophylactic therapy, i.e. lasers, topical chemotherapy (5-fluorouracil, imiquimod), have never achieved the same level of effectiveness as dermabrasion [45-49]. In fact, studies of the efficacy of these modalities often use dermabrasion as the gold standard for NMSC prophylaxis [50].

Although the early studies on dermabrasion demonstrated its success in NMSC prophylaxis, the mechanism of how it prevented NMSC was unclear. It was hypothesized (but unproven) that the effectiveness of dermabrasion was due to the removal of previously initiated carcinogenic keratinocytes. However, if this hypothesis was true, other ablative procedures should be just as successful in treating NMSC, but they are not. Our studies suggest a new mechanism by which dermabrasion can prevent NMSC carcinogenesis which focuses on its effect on dermal fibroblasts. The accumulation of senescent fibroblasts in geriatric dermis alters the susceptibility of epidermal keratinocytes to accumulate and fix UVB-induced mutations in their genomes. Furthermore, senescent fibroblasts have been shown to provide an enhanced environment for the growth of carcinogenically initiated epithelial cells via their upregulation of inflammatory cytokines [22-24]. Therefore, the preponderance of senescent fibroblasts in geriatric dermis not only promotes initiating mutations in UVB-exposed keratinocytes but they also promote the expansion of initiated clones of keratinocytes. As demonstrated in these studies, dermabrasion can dramatically reduce the proportion of senescent fibroblasts in treated geriatric dermis. Importantly, the elimination of senescent fibroblasts restores the expression of IGF-1 to normal levels, increases the production of collagen, and prevents the inappropriate UVB response in epidermal keratinocytes. These studies demonstrate an alternative mechanism, other than just removal of initiated keratinocytes, by which dermabrasion can protect geriatric skin from actinic neoplasia.

METHODS

Human subjects. Geriatric volunteers were recruited from patients treated at Indiana University dermatology clinics. These studies were approved by the Indiana University School of Medicine Institutional Review Board and subjects have signed approved consent forms. Specific requirements for inclusion/exclusion from these studies can be found in the Supplemental Materials.

Dermabrasion. Prior to treatment, a region of sun-protected hip/buttock skin was photographed. Next, an approximately 5 x 5 cm area of the subject's lower hip/buttock skin was isolated and anesthetized with xylocaine anesthesia. Under sterile conditions the localized area of skin was then abraded with sterile, coarse (#60) sandpaper down to the mid dermis, with complete removal of all epidermis and superficial dermis. The wounded area was bandaged with moist, occlusive dressings and the volunteer was instructed to change the dressing twice daily until the wound is re-epithelized in 1-2 weeks. Approximately three months later (~Day 90 +/- 7 days) the volunteer returned to the clinic and a localized area 1 x 1 cm of either dermabrasion or untreated normal skin on the opposite hip/buttock was irradiated with dose of 350 J/m^2 of UVB. In Fitzpatrick Skin Types I and II, this dose of UVB is sufficient to cause a minimal erythematous reaction. Permanent marker was used to outline the areas of skin that was irradiated. Twenty-four hours following UVB exposure, photographs were taken of

the skin to document the extent of the UVB reaction. The irradiated skin, as well as unirradiated adjacent skin, was removed by punch biopsy, (4 mm punch biopsies of the UVB-treated skin and 3 mm punch biopsies of unirradiated skin; 4 biopsies per individual).

Human UVB response assay**.** The epidermal response to UVB irradiation was assayed as previously described [3]. Briefly, thin paraffin-embedded sections from unirradiated and UVB-irradiated biopsies were simultaneously stained with antibodies to Ki67 and thymine dimers. Secondary antibodies that specifically detect only one of the primary antibodies are conjugated to the fluorescent dyes AlexaFluor 488 (detecting Ki67, emitting green wavelengths), and AlexaFluor 568 (detecting thymine dimers, emitting red wavelengths). Images were captured sequentially along the entire length of the biopsy specimen (3mm non-irradiated, 4mm irradiated) using a Nikon Eclipse 80i microscope with Intensilight epifluorescence. These images were analyzed by counting the number of keratinocytes in contact with the basement membrane that are Ki67(+), thymine dimer(+), and Ki67(+):thymine dimer(+). These numbers were expressed as a percentage of total basal layer keratinocytes in the biopsy specimen (determined by counting basal layer keratinocytes for each specimen on H&E-stained slides).

Statistical analysis. Statistical analyses were done by two-tailed Student's t test. Statistical significance was defined as $p < 0.05$ unless otherwise noted in the figure legend.

Supplemental Material. Four additional figures and specific protocols for quantitative reverse-transcription PCR, immunofluorescence, growth of human fibroblasts, and senescence-associated β-galactosidase assays can be found in the Supplemental Material.

ACKNOWLEDGEMENTS

We are grateful to Dr. Raymond Konger for his valuable suggestions. This work was supported by grants from the National Institutes of Health (R21CA131901 to DFS; R01HL062996; U19A1070448 to JBT), VA Merit Award (JBT), and a Dermatology Foundation Career Development Award (AKS). The authors have no conflicts of interest in regard to the data presented in this manuscript.

CONFLICT OF INTERESTS STATEMENT

The authors declare no conflicts of interest with the data or ideas presented in this manuscript.

REFERENCES

1. Parkin DM, Bray FI, Devesa SS. Cancer burden in the year 2000. the global picture. Euro J Cancer 2001; 37: S4–S66.

2. Coppe JP, Desprez PY, Krtolica A, Campisi J. The senescence-associated secretory phenotype: the dark side of tumor suppression. Ann Rev Path Mech Dis 2010; 5:99-118.

3. Lewis DA, Travers JB, Somani AK, Spandau DF. The IGF-1/IGF-1R signaling axis in the skin: a new role for the dermis in aging-associated skin cancer. Oncogene 2010; 29: 1475-1485.

4. Anisimov VN. Carcinogenesis and aging 20 years after: escaping horizon. Mech of Ageing Develop 2009; 130: 105-121.

5. Lewis DA, Travers JB, Spandau DF. A new paradigm for the role of aging in the development of skin cancer. J Invest Dermatol 2008; 129:787-791.

6. Lewis DA, Travers JB, Spandau DF. (2010) Aging-associated non-melanoma skin cancer: a role for the dermis. In Textbook of Aging Skin, MA Farage, KW Miller and HI Maibach, eds. (Springer Berlin Heidelberg), pp588-599.

7. Chuang T-Y, Lewis DA, Spandau DF. Decreased incidence of non-melanoma skin cancer in patients with type 2 diabetes mellitus using insulin: a pilot study. Br J Dermatol 2005; 153: 552-557.

8. Kuhn C, Kumar M, Hurwitz SA, Cotton J, Spandau DF. Activation of the insulin-like growth factor-1 receptor promotes the survival of human keratinocytes following ultraviolet B irradiation. Intl J Cancer 1999; 80:431-438.

9. Lewis DA, Spandau DF. UVB-induced activation of NF-κB is regulated by the IGF-1R and dependent on p38 MAPK. J Invest Dermatol 2008; 128:1022-1029.

10. Lewis DA, Yi Q, Travers JB, Spandau DF. UVB-induced senescence in human keratinocytes requires a functional IGF-1R and p53. Mol Biol Cell 2008;19:1346-1353.

11. American Cancer Society. Cancer Facts and Figures 2010. www.cancer.org/downloads/STT/Cancer_Facts_and_Figures_2010.pdf

12. Rogers HW, Weinstock MA, Harris AR, Hinckley MR, Feldman SR, Fleischer AB, et al. Incidence estimate of nonmelanoma skin cancer in the United States, 2006. Arch Dermatol 2010; 146:283-287.

13. Bickers DR, Lim HW, Margolis D, Weinstock MA, Goodman C, Faulkner E, et. al. The burden of skin diseases. J Am Acad Dermatol 2006; 55:490-500.

14. Housman TS, Feldman SR, Williford PM, Fleischer AB, Goldman ND, Acostamadiedo JM, et. al. Skin cancer is among the most costly of all cancers to treat for the Medicare population. J Am Acad Dermatol 2003; 48: 425-429.

15. Kraemer KH. Sunlight and skin cancer: another link revealed. Proc Natl Acad Sci USA 1997; 94:11-14.

16. National Institutes of Health, Sun Protection in Cancer Trends Progress Report – 2009/2010, www.cancer.gov

17. Brash DE, Ziegler A, Jonason AS, Simon JA, Kunala S, Leffell DJ. Sunlight and sunburn in human skin cancer: p53, apoptosis, and tumor progression. J Invest Dermatol Symp Proc 1996; 1: 136-142.

18. Jeffes EWB, Tang EH: Actinic keratosis: current treatment options. Am J Clin Dermatol 2000; 1: 167-179.

19. Godar DE, Urbach F, Gasparro FP, van der Leun JC. UV doses of young adults. Photochem. Photobiol. 2003; 77: 453-457.

20. Vogelstein B, Kinzler KW. Cancer genes and the pathways they control. Nature Med 2004; 10:789-799.

21. Sjoblom T, Jones S, Wood LD, Parsons DW, Lin J, Barber TD, et. al. The consensus coding sequences of human breast and colorectal cancers. Science 2006; 314: 268-274.

22. Krtolica A, Parrinello S, Lockett S, Desprez PY, Campisi J. Senescent fibroblasts promote epithelial cell growth and tumorigenesis: A link between cancer and aging. Proc Natl Acad Sci USA 2001: 98:12072-12077.

23. Parrinello S, Coppe J-P, Krtolica A, Campisi J. Stromal-epithelial interactions in aging and cancer: senescent fibroblasts alter epithelial cell differentiation. J Cell Sci 2005; 118: 485-496.

24. Campisi J. Senescent cells, tumor suppression, and organismal aging: good citizens, bad neighbors. Cell 2005; 120: 513-522.

25. Campisi J. Suppressing cancer: the importance of being senescent. Science 2005; 309:886-887.

26. Dimri GP. What has senescence got to do with cancer? Cancer Cell 2005; 7:505-512.

27. Feng Z, Hu W, Teresky AK, Hernando E, Cordon-Dardo C, Levine AJ. Declining p53 function in the aging process: a possible mechanism for the increased tumor incidence in older populations. Proc Natl Acad Sci USA 2007; 104: 16633-16638.

28. Dimri GP, Lee X, Basile G, Acosta M, Scott G, Roskelly C, et. al. A biomarker that identifies senescent human cells in culture and in aging skin in vivo. Proc Natl Acad Sci USA 1995; 92: 9363-9367.

29. d'Adda di Fagagna, F. Living on a break: cellular senescence as a DNA-damage response. Nat Rev Cancer 2008; 8:512-522.

30. Pospelova TV, Demidenko ZN, Bukreeva EI, Pospelov VA, Gudkov AV, Blagosklonny MV. Pseudo-DNA damage response in senescent cells. Cell Cycle 2009; 8:4112-4118.

31. Seviour EG, Lin SY. The DNA damage response: balancing the scale between cancer and ageing. Aging 2010; 2: 900-907.

32. Redon CE, Nakamura AJ, Martin OA, Parekh PR, Weyemi US, Bonner WM. Recent developments in the use of γ-H2AX as a quantitative DNA double-strand break biomarker. Aging 2011, 3: 168-174.

33. Makrantonaki E, Zouboulis CC. (2010). Pathomechanisms of endogenously aged skin. In Textbook of Aging Skin, MA Farage, KW Miller and HI Maibach, eds. (Springer Berlin Heidelberg), pp 93-99.

34. Ramos-e-Silva M, da Silva Carneiro SC. Elderly skin and its rejuvenation: products and procedures for the aging skin. J Cosmetic Dermatol 2007; 6:40-50.

35. Helmbold P. (2010). Basophilic (actinic) degeneration of the dermis: an easy histological scoring approach in dermal photoaging. In Textbook of Aging Skin, MA Farage, KW Miller and HI Maibach, eds. (Springer Berlin Heidelberg), pp 19-21.

36. Farage MA, Miller KW, Maibach HI. (2010). Degenerative changes in aging skin. In Textbook of Aging Skin, MA Farage, KW Miller and HI Maibach, eds. (Springer Berlin Heidelberg), pp 25-35.

37. Mine S, Fortunel NO, Pageon H, Asselineau D. Aging alters functionally human dermal papillary fibroblasts but not reticular fibroblasts: a view of skin morphogenesis and aging. PLoS ONE 2008; 3: e4066 (1-13).

38. Fisher GJ, Varani J, Voorhees JJ. Looking older: fibroblast collapse and therapeutic implications. Arch Dermatol 2008; 144: 666-672.

39. Lawrence N, Mandy S, Yarborough J, Alt T. History of dermabrasion. Dermatol Surg 2000; 26:95-101.

40. Friedman S, Lippitz J. Chemical peels, dermabrasion, and laser therapy. Dis Mon 2009; 55:223-235.

41. Epstein, E. Planing for precancerous skin: a ten-year evaluation. California Med 1966; 105:26-27.

42. Benedetto AV, Griffin TD, Benedetto EA, Humeniuk HM. Dermabrasion: therapy and prophylaxis of the photoaged face. J Am Acad Dermatol 1992; 27:439-447.

43. Coleman WP, Yarborough JM, Mandy SH. Dermabrasion for prophylaxis and treatment of actinic keratoses. Dermatol Surg 1996; 22: 17-21.

44. Field LM. Dermabrasion and premalignant disease. Dermatol Surg 1997; 23:714.

45. Cooley JE, Casey DL, Kauffman CL. Manual resurfacing and trichloracetic acid for the treatment of patients with widespread actinic damage. Dermatol Surg 1997; 23: 373-379.

46. Hantash BM, Stewart DB, Cooper ZA, Rehmus WE, Koch RJ, Swetter SM. Facial resurfacing for nonmelanoma skin cancer prophylaxis. Arch Dermatol 2006; 142: 976-982.

47. Ostertag JU, Quaedvlieg PJF, Neumann MHAM, Kerkels GA. Recurrence rates and long-term follow-up after laser resurfacing as a treatment for widespread actinic keratoses in the face and on the scalp. Dermatol Surg 2006; 32: 261-267.

48. Halachmi S, Lapidoth M. Lasers in skin cancer prophylaxis. Exp Rev Anticancer Therapy 2008; 8:1713-1715.

49. Love WE, Bernhard JD, Bordeaux JS. Topical imiquimod or fluorouracil therapy for basal and squamous cell carcinoma. Arch Dermatol 2009; 145:1431-1438.

50. Field LM. The superiority of dermabrasion over laser abrasion in the prophylaxis of malignant and premalignant disease. Dermatol Surg 2007; 33:258-259.

SUPPLEMENTAL MATERIAL

Supplemental Experimental Procedures

Quantitative Reverse-Transcriptase PCR. Homogenized tissue from dissected dermal sections was lysed using RNeasy kit (Qiagen) buffers. Cell lysates were then further homogenized using Shredder columns (Qiagen) and RNA isolation continued with RNeasy kit. All of the reagents used for RT and PCR are obtained from SuperArray Biosciences, Frederick, MD. The following were added to a 0.2 ml tube where first a genomic DNA elimination step was performed on 2 μg RNA total volume 10 μl was heated to 42°C for 5 minutes and chilled on ice. Next the reverse transcription cocktail was prepared and 10 μl added to the RNA; 2 μl RT enzyme mix, 4 μl RT buffer, 1 μl primer and external control mix, 3 μl RNase free water. Mixture was heated 42°C for 15 minutes, 95°C for 5 minutes and chilled on ice for experiments, the final volume of cDNA was 20 μl. qRT-PCR is performed using a LightCycler PCR (Roche Scientific, Fishers IN). Quantization of experimental qRT-PCR products was determined by comparison with external control qRT-PCR products from templates of a known copy number. Relative copy numbers of experimental mRNA are then determined following adjustment with actin controls from the same tissue.

Immunofluorescence. Paraffin-embedded sections were deparaffinized, hydrated, and rinsed with tris-buffered saline with tween 20 (TBS) (DAKO, Carpenteria, CA). Antigen retrieval was performed using a water bath at 95°C for 20 minutes with DAKO Target Retrieval buffer. After cooling, the slides are rinsed with TBS, and the slides were then transferred to a clean 100 mm bacterial glass petri dish containing PBS-saturated filter paper under a strip of Parafilm. Primary antibodies (1:50) diluted in 3% BSA in TSB was added to the tissues. The lid was placed on the petri dish and the coverslips incubated for 1 hour at room temperature. The tissues were rinsed in PBS (three 10 minutes washes), and then the appropriate secondary antibody conjugated to the desired fluorochrome was added for 30 minutes at room temperature in the dark. The sections were washed as before, the edges blotted dry, and then mounted with coverslips using Fluoromount G. Antibodies used included: α-53BP1 (Abcam, Cambridge, MA), α-p21 (Cell Signaling, Danvers, MA), α-γH2AX (Millipore, Temecula, CA), α-prolyl-4-hydroxylase (Millipore, Temecula, CA), α-Ki67 (NeoMarkers, Freemont, CA), and α-thymine dimers (Kamiya Biomedical, Seattle, WA).

Senescence-associated β-galactosidase assays. Fibroblasts were washed twice with PBS and fixed with 2% formaldehyde/0.2% glutaraldehyde at room temperature for 10 minutes. After two additional washes with PBS, 2 ml of staining solution (150 mM sodium chloride, 25.2 mM sodium phosphate dibasic, 7.36 mM citric acid, 5 mM potassium ferricyanide, 5 mM potassium ferrocyanide, 2 mM magnesium chloride, 1 ng/ml 5-bromo-4-chloro-3-indolyl-< -D-galactoside, pH 6.0)[25], were added to the cells and they were incubated at 37°C overnight. The cells were again washed with PBS and photographed by bright field microscopy to count blue cells and phase contrast microscopy to count total cells. At least four fields (100X magnification, approximately 200 cells/field) were counted for each plate of cells; at least two plates of cells for each condition (or cell type) were assayed in each experiment.

Isolation and culture of normal human fibroblasts. Excised foreskin tissue was washed with antibiotics, the tissue minced, and individual cells released from the tissue by trypsin digestion (8). Keratinocytes and fibroblasts were separated by differential resistance to treatment with EDTA. Fibroblasts were grown in Dulbecco's Modified Eagles medium containing 10% fetal calf serum. All relevant procedures using human tissue have been approved by the Indiana University School of Medicine Institutional Review Board.

SUPPLEMENTAL FIGURES

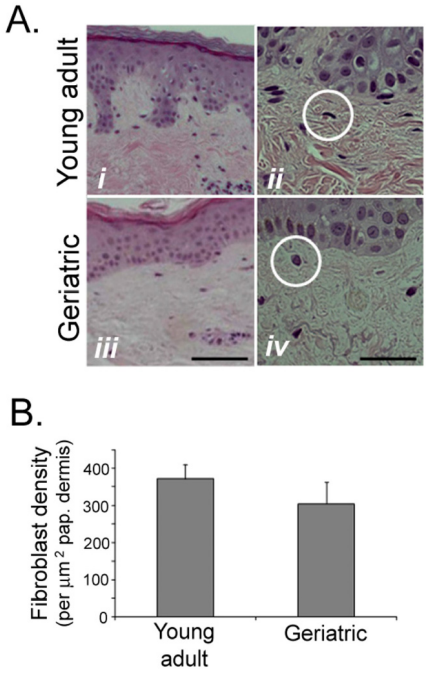

Supplementary Figure 1. Phenotypic changes in geriatric skin. (**A**) H&E sections of the biopsies described in Fig. 2. White circles indicate elliptical nucleus of a replicating fibroblast in panel *ii* and the spherical nucleus of a senescent fibroblast in panel *iv*. Bar=100 μm in panels *i* and *iii*; bar=25 μm in panels *ii* and *iv*. (**B**) The density of fibroblasts was determined in young adult and geriatric skin as described in Fig. 2 (p=0.093; two-tailed t-test).

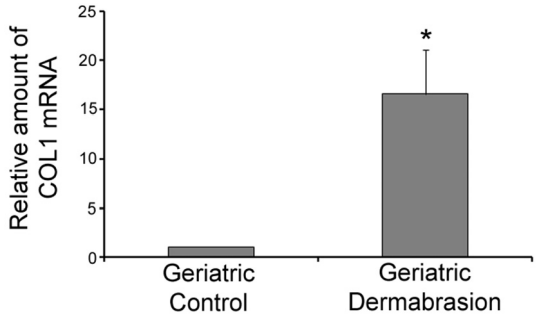

Supplementary Figure 2. Dermabrasion increases collagen expression. Quantitative PCR was conducted on biopsies described in Fig. 2. The relative amount of collagen I mRNA (normalized to actin expression) is shown. Asterisk indicates statistical significance from young adult values (p=0.018,two-tailed t-test).

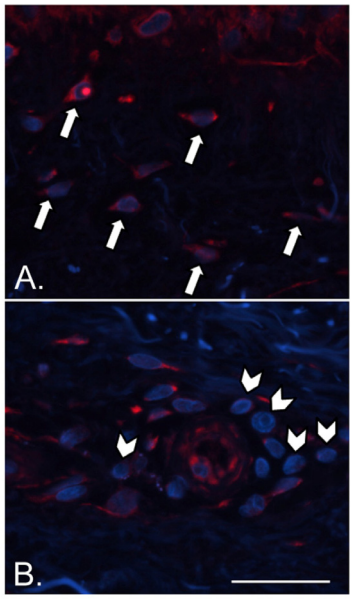

Supplementary Figure 3. Identification of dermal fibroblasts in geriatric dermis. Example of how the identity of fibroblasts was confirmed in the papillary dermis. Sections were stained with antibodies to α-prolyl-4-hydroxylase (red) and DAPI (nuclear-specific stain, blue). Fibroblasts stain positive for α-prolyl-4-hydroxylase and are indicated by arrows in panel **A**. Non-fibroblasts are indicated in panel **B** by chevrons.

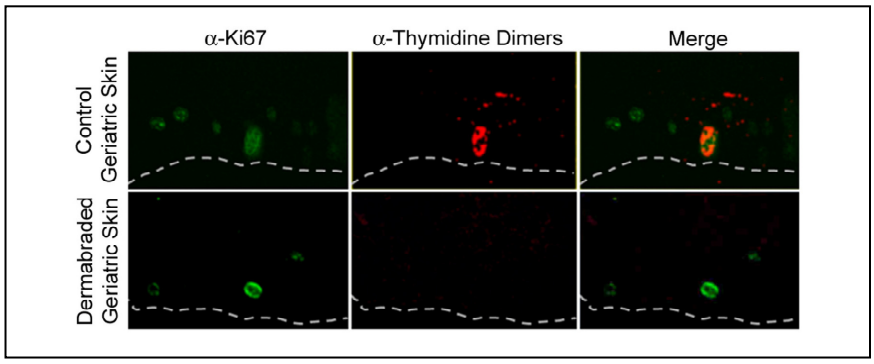

Supplementary Figure 4. Example of the UVB-response assay. Two cm^2 areas on the lower backs of volunteers were irradiated with UVB (350 J/m^2). Twenty-four hours following irradiation, a four mm punch biopsy was obtained from the irradiated skin. Sections of formalin-fixed, paraffin-embedded tissue were stained with both α-Ki67 (staining green) and α-thymine dimer antibodies (staining red). The merged images are shown to the right of the figure. The top series of panels is an example of a cell positive for both Ki67 and thymine dimers (staining yellow, inappropriate UVB response) while the cell indicated in bottom panels is only positive for Ki67 (staining green, appropriate UVB response). The location of the basement membrane is indicated by a grey dashed line. Similar sections were stained with H&E to determine the total number of basal layer keratinocytes in each biopsy.

Research Paper

miR-150-5p suppresses tumor progression by targeting VEGFA in colorectal cancer

Xiaoxiang Chen[1,2], Xueni Xu[1,2], Bei Pan[1], Kaixuan Zeng[1,2], Mu Xu[1], Xiangxiang Liu[1], Bangshun He[1], Yuqin Pan[1], Huiling Sun[1], Shukui Wang[1]

[1]General Clinical Research Center, Nanjing First Hospital, Nanjing Medical University, Nanjing 210006, Jiangsu, China
[2]Medical College, Southeast University, Nanjing 210009, Jiangsu, China

Correspondence to: Shukui Wang; **email:** sk_wang@njmu.edu.cn
Keywords: miR-150-5p, colorectal cancer, VEGFA, Akt/mTOR
Received: May 23, 2018 **Accepted:** November 15, 2018 **Published:** November 26, 2018

Copyright: Chen et al. This is an open-access article distributed under the terms of the Creative Commons Attribution License (CC BY 3.0), which permits unrestricted use, distribution, and reproduction in any medium, provided the original author and source are credited.

ABSTRACT

MicroRNA-150-5p (miR-150-5p) has been implicated in tumor initiation and progression in a variety of cancers. However, its roles in colorectal cancer (CRC) remain largely unknown. In our study, a decreased miR-150-5p expression in CRC tissues was found to be associated with poor overall survival. Moreover, miR-150-5p inhibited CRC cell proliferation, migration, invasion and angiogenesis in vitro and in vivo, and its inhibitory effect could be reversed by transfection of vascular epithelial growth factor A (VEGFA) expression plasmid. Lastly, we demonstrated that miR-150-5p inactivated VEGFA/VEGFR2 and the downstream Akt/mTOR signaling pathway in CRC. Based on these results, we conclude that miR-150-5p may function as a tumor suppressor in CRC, and miR-150-5p/VEGFA axis may be a potential therapeutic target candidate in CRC treatment.

INTRODUCTION

Colorectal cancer (CRC) is one of the most-prevalent malignancies and leading causes of cancer-related death in the world [1]. Much improvement has been made in diagnosis, treatment and understanding of the molecular mechanisms of CRC, but the prognosis for patients with CRC remains poor [2, 3]. Therefore, exploration of the molecular mechanisms involved in the initiation and progression of CRC is urgently needed.

microRNAs (miRNAs), a class of conserved noncoding small RNAs, function as posttranscriptional regulators of gene expression in tumor initiation and progression by binding to the 3'-untranslated region (UTR) of target mRNA [4, 5]. Recent increasing evidence has confirmed that dysregulated miRNAs play key roles in multiple biological processes in CRC [6-8], including cell proliferation, drug resistance, apoptosis, metastasis and angiogenesis and have been identified as potential diagnostic, prognostic and therapeutic biomarkers in CRC diagnosis and treatment.

miR-150-5p, a cancer-related miRNA, has been reported to be aberrantly expressed in various cancers [9, 10]. Zhang Z, et al. [11] have reported that miR-150 is increased in cervical cancer and promotes cell proliferation, migration and invasion by targeting PDCD4. Zhang L, et al. [12] have reported that miR-150 is upregulated in non-small cell lung cancer (NSCLC) cells and significantly associated with survival, and increased expression of miR-150 promotes NSCLC cell proliferation and migration. However, the potential mechanisms of miR-150-5p regulation of CRC progression remain unclear.

In this study, we found that miR-150-5p was obviously downregulated in CRC tissues and negatively correlated with TNM stage, pN stage and overall survival (OS). Furthermore, we identified vascular epithelial growth

factor A (VEGFA), a member of the VEGF family, as a direct target gene of miR-150-5p. We also provided evidence that miR-150-5p inhibited tumor growth, metastasis and angiogenesis in CRC. Lastly, we verified that miR-150-5p suppressed CRC initiation and progression via VEGFA/VEGFR2/Akt/mTOR signaling.

RESULTS

miR-150-5p is downregulated in CRC tissues and cell lines

First, to determine the clinical significance of miR-150-5p in patients with CRC, we used the StarBase database (http://starbase.sysu.edu.cn/) to reveal that miR-150-5p expression was downregulated in CRC tissues compared with normal tissues (Fig. 1A) and the database is accompanied with gene expression data of 32 types of cancers which are derived from 10,882 RNA-seq and 10,546 miRNA-seq data. Then, we measured the miR-150-5p expression in 112 pairs of CRC tissues using qRT-PCR. The results showed that miR-150-5p was significantly downregulated in CRC tissues compared with that in matched adjacent normal tissues (ANTs) (Fig. 1B). In addition, the miR-150-5p expression was markedly downregulated in all CRC cell lines in comparison with coloni epithelial cell (FHC) (Fig. 1C). Next, we examined the potential clinical significance of miR-150-5p in CRC. We used the median miR-150-5p expression as a cut-off value. As shown in Table 1, low miR-150-5p expression was markedly associated with TNM stage (p=0.013) and pM stage (p=0.031).

The Kaplan-Meier survival analysis indicated that CRC patients with low miR-150-5p had an obviously shorter overall survival (OS) (Fig. 1C). Furthermore, the results of univariate and multivariate analyses of potential prognostic factors for overall survival are shown in

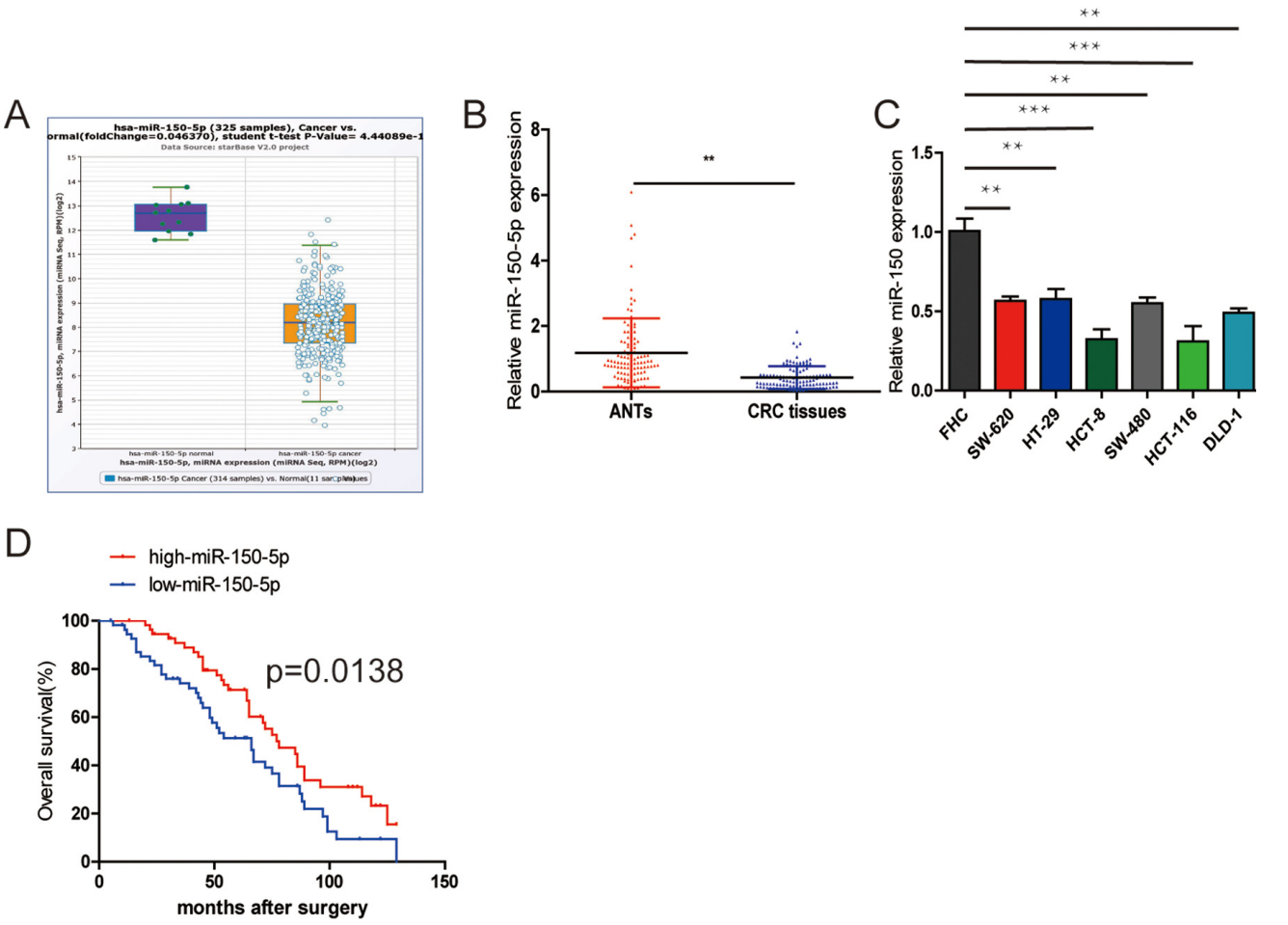

Figure 1. Downregulation of miR-150-5p in CRC and its association with poor OS. (**A**) miR-150-5p was found to be downregulated compared with normal tissues in the Starbase database. (**B**) Quantitative RT-PCR was performed to detect the relative expression of miR-150-5p in CRC tissues compared with ANTs. (**C**) The relative expression of miR-150-5p was assessed in different CRC cell lines and FHC using qRT-PCR. (**D**) Kaplan-Meier survival analysis was employed to detect the correlation between the levels of miR-150-5p expression and overall survival of CRC patients. Data were shown as mean±SD. **p<0.01.

Table 2. The univariate analysis indicated that TNM stage (p=0.001), pN stage (p=0.006), pM stage (p=0.002) and miR-150-5p (p=0.004) were predictors of OS. The multivariate analysis also showed that higher TNM stage (p=0.006), pN stage (p=0.017) and pM stage (p=0.008), as well as lower miR-150-5p (p=0.011), were significantly correlated with poor OS (Table 2). Based on these results, we suggested that miR-150-5p might play a key role in CRC progression.

miR-150-5p inhibits cell proliferation, migration, invasion and angiogenesis in vitro

To determine the biological function of miR-150-5p in CRC, we selected HCT116 and HCT8 cells for transfection of agomiR-150-5p and antagomiR-150-5p or their corresponding negative controls (agomiR-NC and antagomiR-NC). The efficiency of transfection was confirmed by qRT-PCR (Fig. 2A). First, a CCK-8 assay performed to assess CRC cell growth showed that upregulation of miR-150-5p resulted in decreased cell proliferation, while the inhibition of miR-150-5p expression obviously increased cell proliferation in HCT116 and HCT8 cells (Fig. 2B). A colony formation assay further substantiated the role of miR-150-5p in inhibiting the proliferation of CRC cells (Figs. 2C and S1A). Next, wound-healing and transwell invasion assays were performed in HCT116 and HCT8 cells. As shown in Figs. 2D and S1B, 2E and S1C, the migratory and invasive abilities were significantly reduced when miR-150-5p expression was increased, while miR-150-5p downregulation significantly increased cell migration and invasion in HCT116 and HCT8 cells. Additionally, to explore whether miR-150-5p was a key angiogenesis suppressor in CRC, we investigated the influence of miR-150-5p on HUVEC tube formation

Table 1. Correlation between miR-150-5p expression and different clinical characteristics.

Characteristics	n=112	miR-150-5p expression		*P* value
		Low(%)(n= 56)	High(%)(n=56)	
Gender				0.110
Male	74	33	41	
Female	38	23	15	
Age(years)				0.106
<60	36	14	22	
≥60	76	42	34	
Tumor location				0.570
colon	59	31	28	
rectal	53	25	28	
TNM stage				0.013
$\bar{}\alpha$	65	26	39	
β–χ	47	30	17	
Differentiation				0.114
Low	27	10	17	
Moderate	70	37	33	
High	15	9	6	
PN stage				0.819
N0	66	33	33	
N1	31	14	17	
N2	15	9	6	
pM stage				0.031
M0	96	44	52	
M1	16	12	4	
Tumor size				0.701
<5cm	66	34	32	
≥5cm	46	22	24	
CEA				0.115
<10ng/ml	72	32	40	
≥10ng/ml	40	24	16	
CA199				0.088
<10U/ml	51	21	30	
≥10U/ml	61	35	26	

Table 2. Results of the univariate and multivariate analyses of prognostic factors for overall survival in patients with CRC.

Characteristics	Multivariate analysis for OS		Univariate analysis for OS	
	HR(95% CI)	*P*	HR(95% CI)	*P*
Gender(male/female)	—	—	1.158(0.739-1.812)	0.522
Age(<60/≥60)	—	—	0.928(0.618-1.551)	0.928
Tumor location(colon/rectal)	—	—	1.160(0.754-1.785)	0.500
TNM stage(‾α/β–χ)	1.833(1.092-3.019)	0.006	2.073(1.339-3.209)	0.001
Differentiation(low/moderate/high)	—	—	1.322(0.935-1.871)	0.114
PT stage(T1-T2/T3-T4)	—	—	0.674(0.357-1.271)	0.223
PN stage(N0/N1/N2)	1.654(1.104-2.746)	0.017	1.814(1.182-2.785)	0.006
PM stage(M0/M1)	2.745(1.432-5.713)	0.008	2.702(1.451-5.031)	0.002
Tumor size(<5cm/≥5cm)	—	—	0.654(0.420-1.018)	0.060
CEA(<10ng/ml/≥10ng/ml)	—	—	0.775(0.479-1.192)	0.228
CA199(<10U/ml/≥10U/ml)	—	—	0.751(0.488-1.156)	0.193
miR-150-5p(low/high)	1.431(1.091-2.615)	0.011	1.923(1.213-2.918)	0.004

Abbreviations: CI, confidence interval; HR, hazard ratio.

and showed that miR-150-5p upregulation obviously reduced the tube-formation capacity, while silencing miR-150-5p increased the tube-formation ability of HUVECs (Figs. 2F and S1D).

miR-150-5p ameliorates CRC growth, metastasis and angiogenesis in vivo

To evaluate the biological functions of miR-150-5p in vivo, CRC cells were subcutaneously injected into nude mice. First, we investigated the effects of miR-150-5p on the xenograft growth in vivo and found that the volume of tumors injected with agomiR-150-5p was significantly smaller than that with agomiR-NC (Fig. 3A, 3B). Furthermore, to examine the influence that miR-150-5p had on metastasis in vivo, CRC cells were injected into nude mice and agomiR-150-5p or agomiR-NC via the tail vein. After 8 weeks, computed tomography (CT) scanning was used on each mouse, and results revealed that the metastatic lesions in the agomiR-150-5p group were less abundant than that in the agomiR-NC group (Fig. 3C). Following CT scanning, these mice were sacrificed, and hematoxylin-eosin (HE) was employed to stain mouse lungs. Compared with low miR-150-5p-expressing CRC cells, upregulation of miR-150-5p significantly decreased the number of metastatic nodules (Fig. 3C, 3D). We then detected CD31 (a marker for microvessels denoting enhanced angiogenesis) expression using immunohistochemistry (IHC) in xenografts tissues and showed that CD31 expression in the agomiR-150-5p group was significantly lower than those in agomiR-NC group (Fig. 3E).

VEGFA is a direct target gene of miR-150-5p

Many miRNAs have been reported to be dysregulated and exert their functions mainly through their target genes [13, 14]. The PicTarSites, miRandaSites and Tarbase databases were used to search for potential target genes of miR-150-5p. As shown in Fig. 4A, eight potential genes were predicted in all four databases. VEGFA, which was selected as a target gene of miR-150-5p, is closely associated with metastasis and angiogenesis of human cancers. Next, dual-luciferase reporter assays were used to determine whether VEGFA was a direct target gene in CRC cells. The 3'-UTR of VEGFA wild-type (WT-VEGFA-3'UTR), as well as VEGFA mutant type (Mut-VEGFA-3'UTR) were constructed and cloned into pmirGLO luciferase reporter, then cotransfected with agomiR-150-5p or agomiR-NC into HCT116 and 293T cells. Luciferase reporter assay confirmed that miR-150-5p overexpression obviously reduced the luciferase activity of pmirGLO-VEGFA-3'UTR-WT but showed no significant effect on the luciferase activity of pmirGLO-VEGFA-3'UTR-Mut (Fig. 4B). Additionally, qRT-PCR and Western blot analyses showed that both VEGFA mRNA and protein levels are dramatically decreased after miR-150-5p upregulation in HCT116 and HCT8 cells (Fig. 4C, 4D).

VEGFA upregulation could reverse the inhibitory effect caused by miR-150-5p

To investigate whether miR-150-5p suppressed proliferation, migration, invasion, angiogenesis and EMT

process through VEGFA, we cotransfected agomiR-150-5p and pcDNA 3.1-VEGFA or empty vector, and VEGFA upregulation was verified by western blotting (Fig. 5A). Through CCK-8, colony formation, wound-healing, transwell invasion and tube formation assays, we found that ectopic VEGFA expression could partially reverse the suppression of proliferation (Fig. 5B, 5C), migration (Fig. 5D), invasion (Fig. 5E) and angiogenesis (Fig. 5F) caused by miR-150-5p overexpression. These data indicated that VEGFA was not only a direct target gene but also a functional mediator of miR-150-5p in CRC.

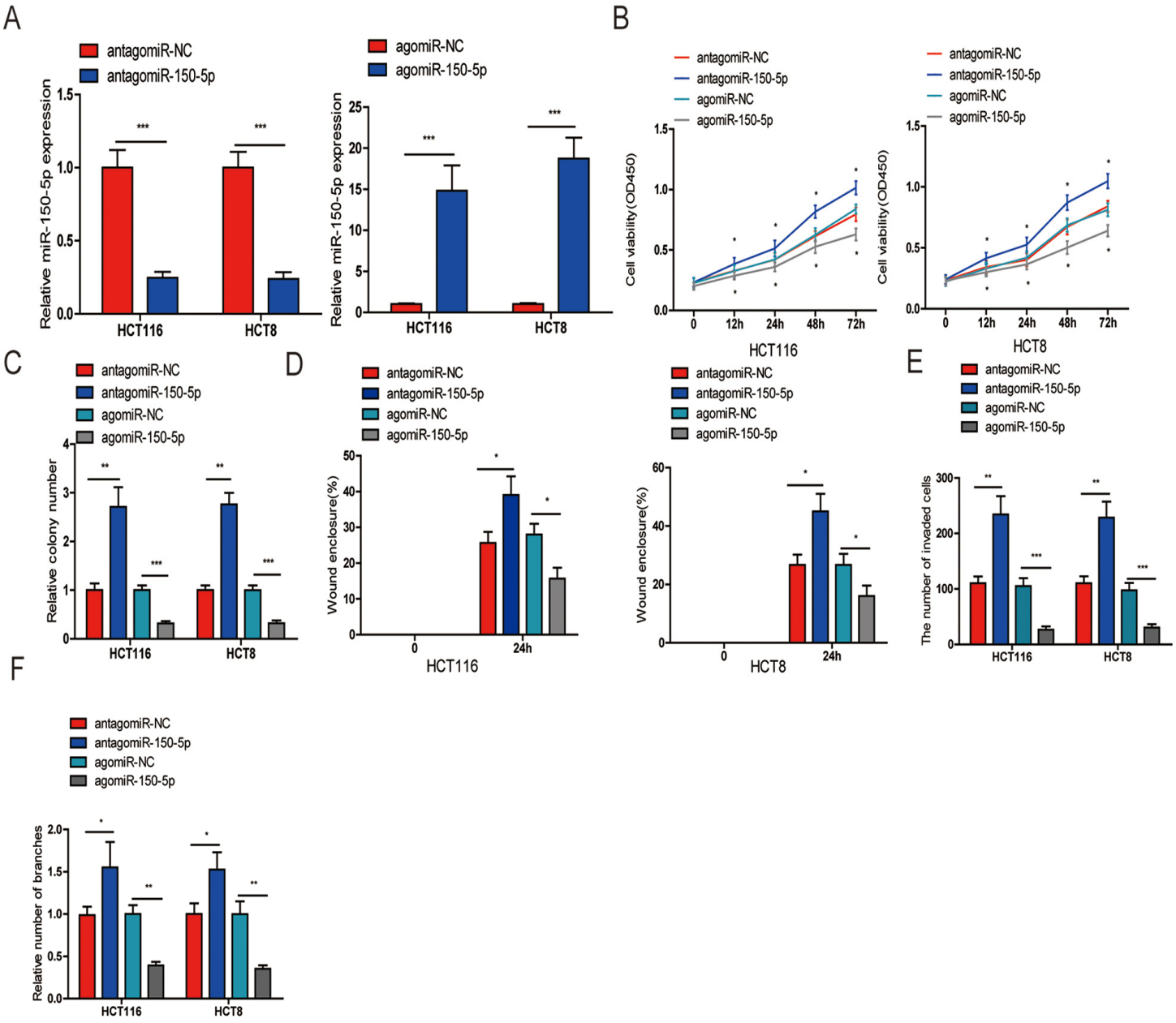

Figure 2. miR-150-5p suppressed CRC cell proliferation, migration, invasion and HUVEC tube formation in vitro. (**A**) qRT-PCR was used to detect the expression of miR-150-5p in CRC cells transfected with antagomiR-150-5p or agomiR-150-5p and their negative control (antagomiR-NC, agomiR-NC). (**B**, **C**) CCK-8 (**B**) and colony formation (**C**) were performed to evaluate the proliferation abilities of CRC cells transfected with antagomiR-150-5p, agomiR-150-5p or negative control (antagomiR-NC, agomiR-NC). (**D**, **E**) Wound-healing (**D**) and transwell (**E**) assays were employed to detect the ability of migration and invasion of antagomiR-150-5p or agomiR-150-5p-transfected CRC cells and their negative control. (**F**) HUVECs were cultured in TCM derived from CRC cells transfected with antagomiR-150-5p or agomiR-150-5p and their negative control in 24-well Matrigel-coated plates. Each bar represents the mean ± SD of three independent experiments. *p<0.05, **p<0.01, ***p<0.001.

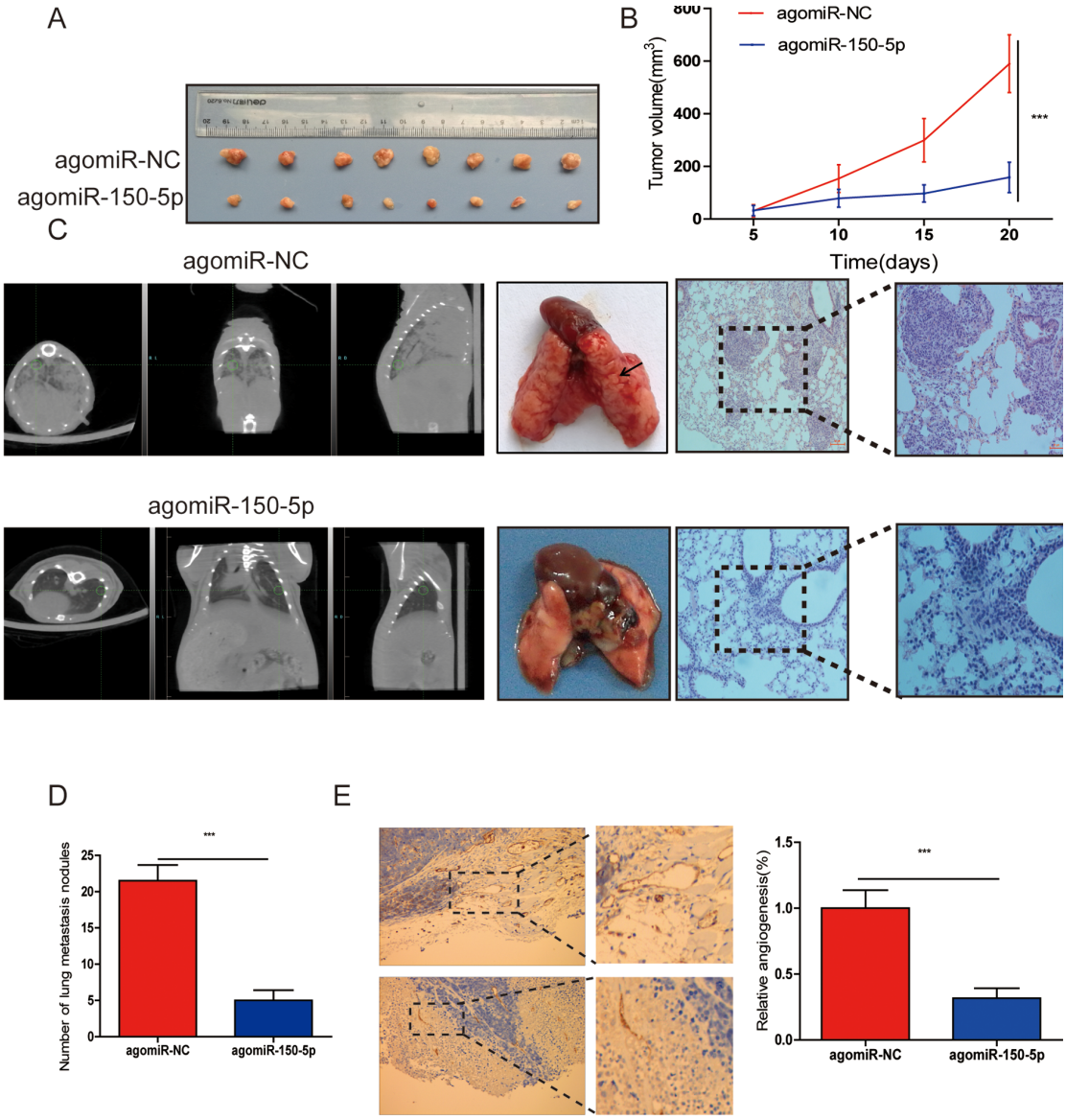

Figure 3. miR-150-5p inhibited tumor growth, metastasis and angiogenesis in vivo. (**A**) Photographs of nude mice and xenograft tumors of CRC cells with miR-150-5p overexpression or not after 20 days of implantation. (**B**) Growth curves of xenografts of CRC cells with or without miR-150-5p overexpression. (**C**) The representative images of lungs from nude mice (left), representative CT scans of lung metastatic foci of the nude mice (middle) and the microscopic images of lung tissue sections stained by hematoxylin and eosin (right). (**D**) A statistical plot of the average number of lung metastases in the tail vein injection. (**E**) These tumor tissues were stained using anti-CD31 antibody, data are shown as the mean ±SD. n=8. ***p<0.001.

The expression of VEGFA is negatively correlated with miR-150-5p

qRT-PCR performed to detect VEGFA mRNA in CRC tissues clearly showed that VEGFA mRNA was overexpressed in CRC tissues compared with matched adjacent normal tissues (ANTs) (Fig. 6A), moreover, we analyzed VEGFA mRNA in CRC tissues at different miR-150-5p levels. The low versus high miR-150-5p levels were defined at the median of miR-150-5p level. The levels of VEGFA mRNA expression in high-miR-150-5p CRC tissues were markedly lower than that in low-miR-150-5p CRC tissues (Fig. 6B). Meanwhile, an obvious negative correlation was found between miR-150-5p and VEGFA mRNA (Fig. 6C).

In addition, IHC was performed to assess the protein expression of VEGFA in CRC tissues, and as shown in Fig. 6D and 6E, the IHC staining intensity indicated that the VEGFA protein expression levels in CRC tissues

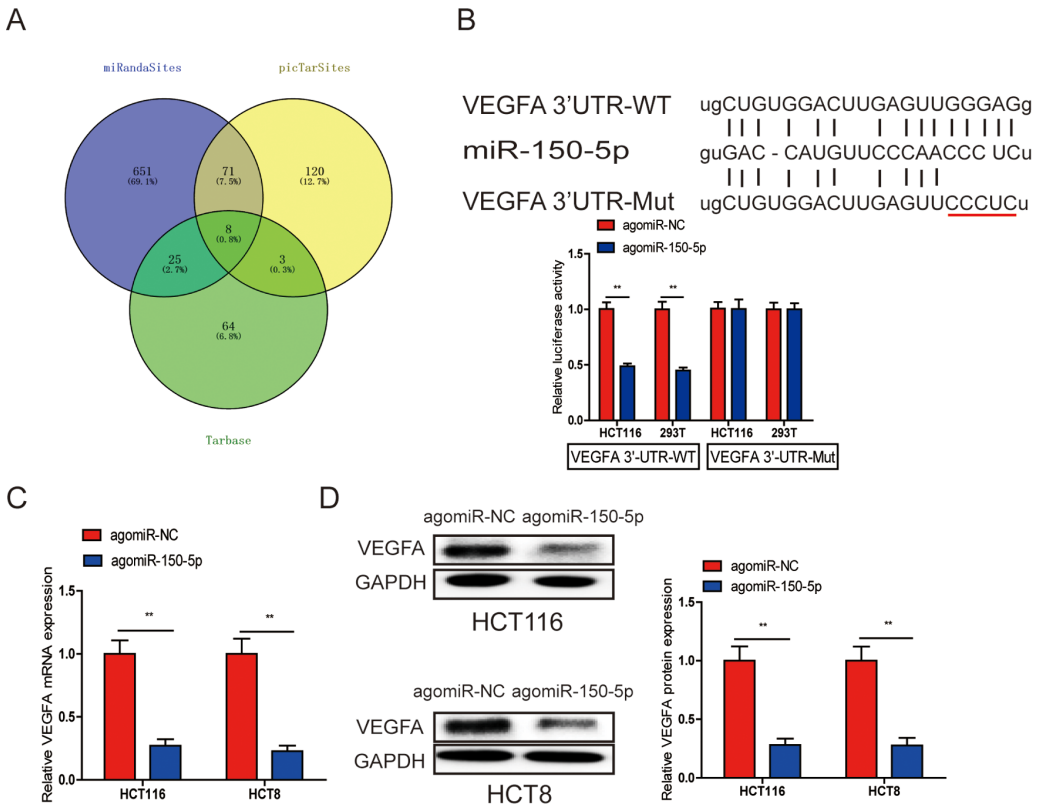

Figure 4. A. VEGFA was a direct target of miR-150-5p in CRC. (**A**) The direct target genes of miR-150-5p were predicted using the PicTarSites, miRandaSites and Tarbase databases. (**B**) Wild-type and mutant VEGFA-3'UTR sequences were cloned into luciferase reporter. Luciferase activity was determined in HCT116 and 293T cells cotransfected with agomiR-150-5p or agomiR-NC and pmirGLO-VEGFA-3'UTR-WT or pmirGLO-VEGFA-3'UTR-Mut. Luciferase activities were normalized to that of renilla luciferase. C, D. qRT-PCR (**C**) and western blot (**D**) analyses showed that both VEGFA mRNA and protein expression levels were dramatically suppressed by agomiR-150-5p in HCT116 and HCT8 cells, GAPDH was used as the internal control. ***p*<0.01.

were obviously higher than in adjacent normal tissues. The VEGFA was relatively upregulated in the low-miR-150-5p expression CRC tissues compared with in high-miR-150-5p CRC tissues (Fig. 6D and 6F); a negative correlation between VEGFA and miR-150-5p was also noted in CRC tissues (Fig. 6G).

VEGFA knockdown significantly inhibits CRC progression

To further verify that miR-150-5p exerts its inhibitory effect via VEGFA, we knocked down VEGFA in HCT116 and HCT8 cells (Fig. 7A) and found that this markedly suppressed CRC cell growth, migration, invasion and HUVEC tube formation (Fig. 7B-7E). These data further proved that miR-150-5p exerted its biological function by inhibiting VEGFA expression.

miR-150-5p inactivates the Akt/mTOR signaling pathway by directly inhibiting VEGFA

Accumulating evidence has shown that VEGFA could bind to its receptor VEGFR2, then activate PI3K and its downstream targets Akt and mTOR, which play crucial roles in cancer progression and survival [15-17]. To further explore whether miR-150-5p inhibited CRC development through VEGFA-mediated Akt/mTOR signaling pathway, we found that miR-150-5p overexpression significantly decreased the level of VEGFA, and then significantly suppressed the phosphorylation of VEGFR2 (p-VEGFR2), Akt (p-Akt) and mTOR (p-mTOR) in HCT116 and HCT8 cells. Next, we treated miR-150-5p in HCT116 and HCT8 cells with VEGFA expression plasmid and found that VEGFA treatment could at least partially increase the expression of p-VEGFR2, p-Akt and p-mTOR (Fig. 8).

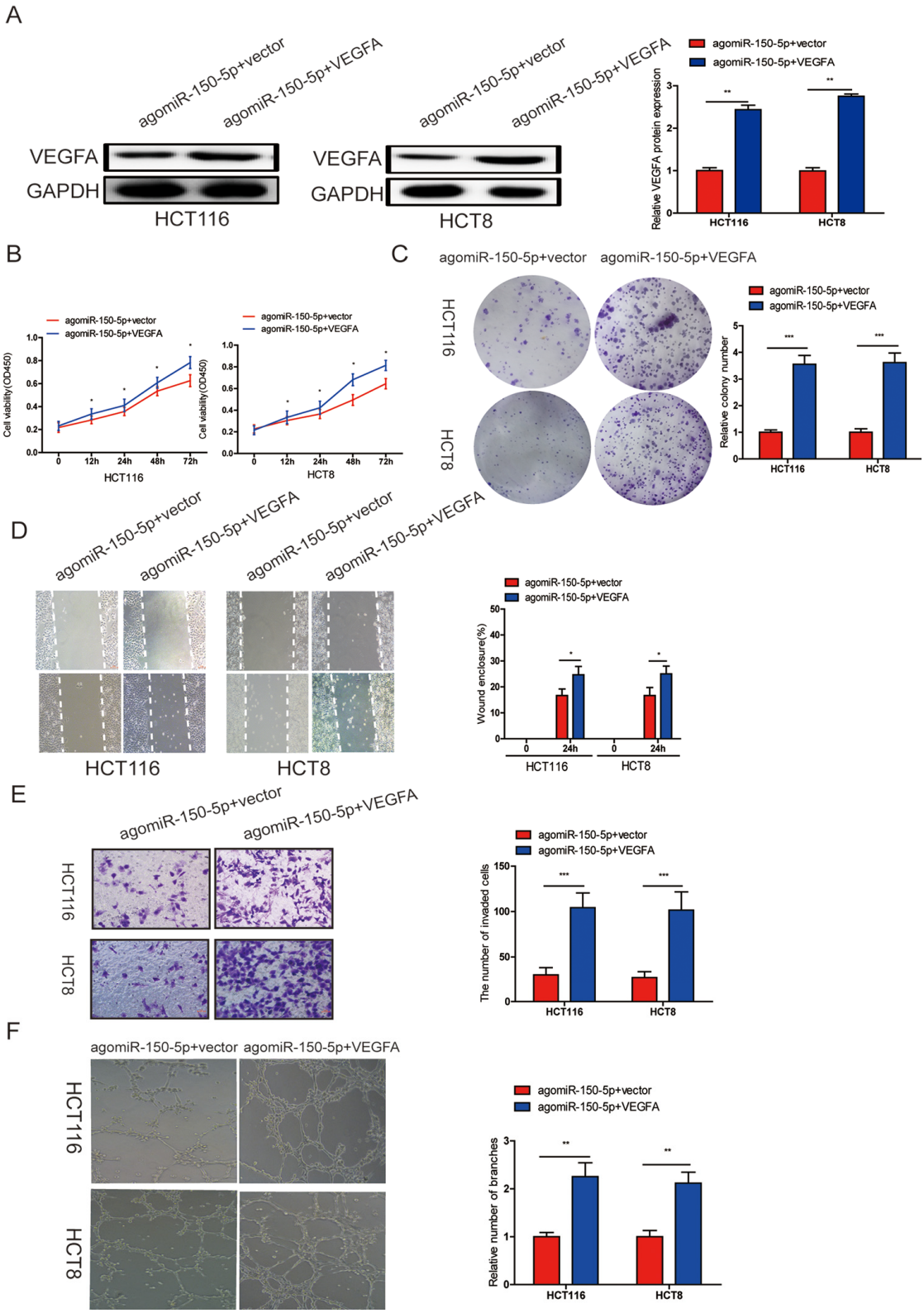

Figure 5. miR-150-5p inhibited CRC progression by targeting VEGFA. (**A**) VEGFA protein expression was determined in HCT116 and HCT8 cells transfected with agomiR-150-5p with VEGFA expression plasmid or empty vector using western blot; GAPDH was used as the internal control. (**B**-**D**) Cell proliferation (**B**, **C**), migration (**D**) and invasion (**E**) were evaluated in HCT116 and HCT8 cells transfected with agomiR-150-5p with VEGFA expression plasmid or empty vector. (**F**) HUVECs were cultured in TCM derived from HCT116 and HCT8 cells transfected with agomiR-150-5p plus VEGFA expression plasmid or empty vector. Data are shown as the mean±SD. *p<0.05, **p<0.01, ***p<0.001.

These results revealed that miR-150-5p exerted its inhibitory function via the VEGFA/VEGFR2/Akt/mTOR signaling pathway.

DISCUSSION

Many studies have demonstrated that dysregulated miRNAs are involved in tumor initiation and progression, including CRC [18]. In our study, we sought to detect an association between miR-150-5p and a clinical outcome in CRC and showed that miR-150-5p was closely associated with TNM stage, distant metastasis and overall survival.

Yushuai Mi, et al. [19] have reported that miR-181a-5p was dysregulated in gastric cancer tissues and cell lines, and high miR-181a-5p expression predicted poor survival in patients with gastric cancer. In our study, we found that miR-150-5p was downregulated in CRC tissues and cell lines. These data indicate that miR-150-5p may play a tumor suppressive role in CRC.

Recently, Mohamed Salem, et al. [20]verified that miR-590-3p promoted ovarian cancer (EOC) growth and metastasis in vitro and vivo. Yuan Gu, et al. [21] reported that miR-191, which has been extensively studied in various types of cancers, suppressed angio-

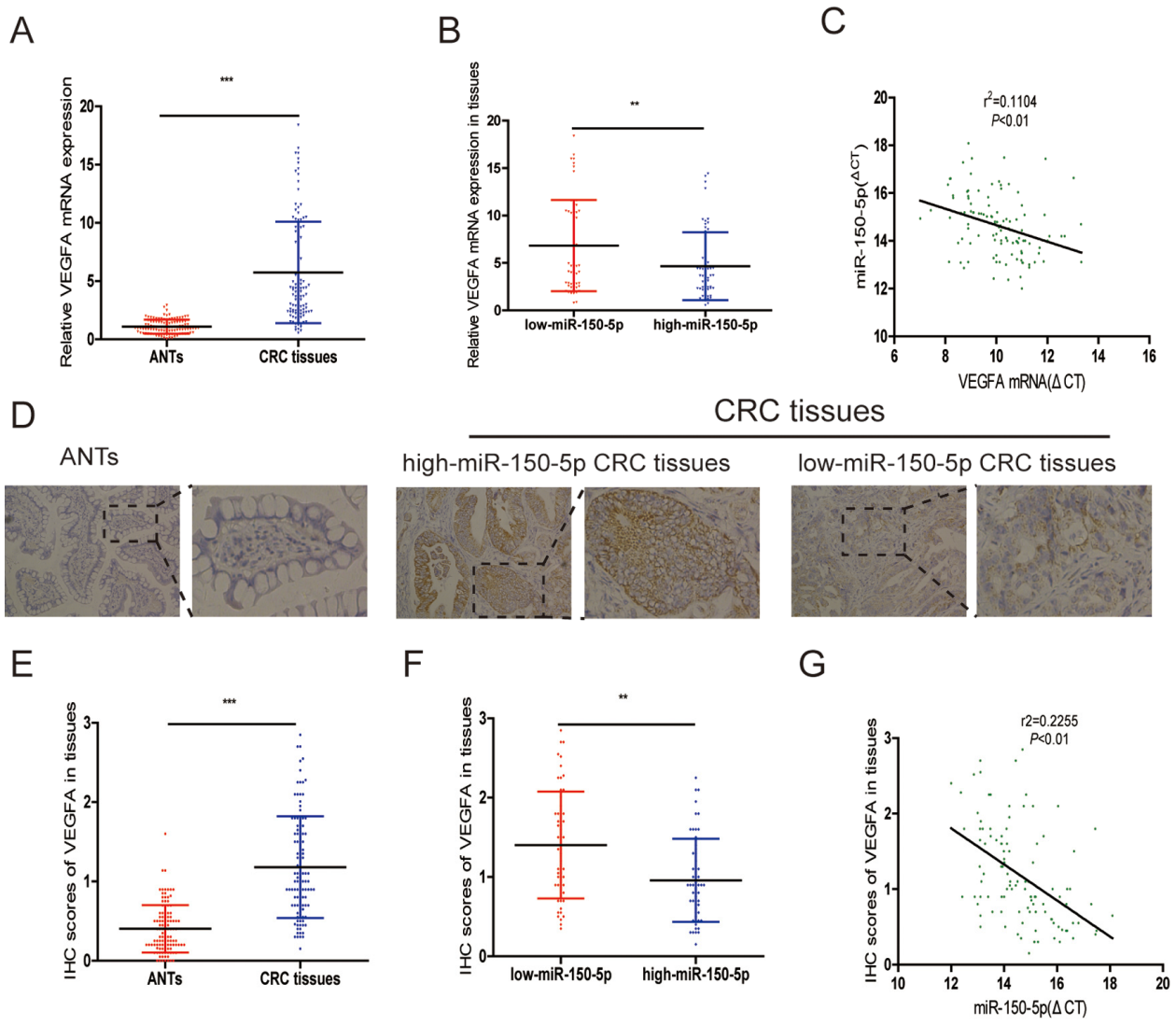

Figure 6. VEGFA was reversely correlated with miR-150-5p in CRC tissues. (**A**) qRT-PCR analysis of VEGFA mRNA expression in CRC tissues and matched adjacent normal tissues. (**B**) Scatterplots of the average VEGFA mRNA expression in patients with low or high expression of miR-150-5p in CRC tissues. (**C**) The correlation between miR-150-5p levels and VEGFA mRNA levels. (**D**) Representative images of IHC in adjacent normal tissues, low or high miR-150-5p CRC tissues. (**E**) The statistical graph showed that the IHC score of VEGFA in CRC tissues was significantly higher than in matched adjacent normal tissues. (**F**) Scatterplots of the average staining scores for VEGFA expression in patients with low or high expression of miR-150-5p. G. The correlation between miR-150-5p levels and VEGFA protein levels. Data were shown as the mean±SD. ***p* <0.01, ****p*<0.001.

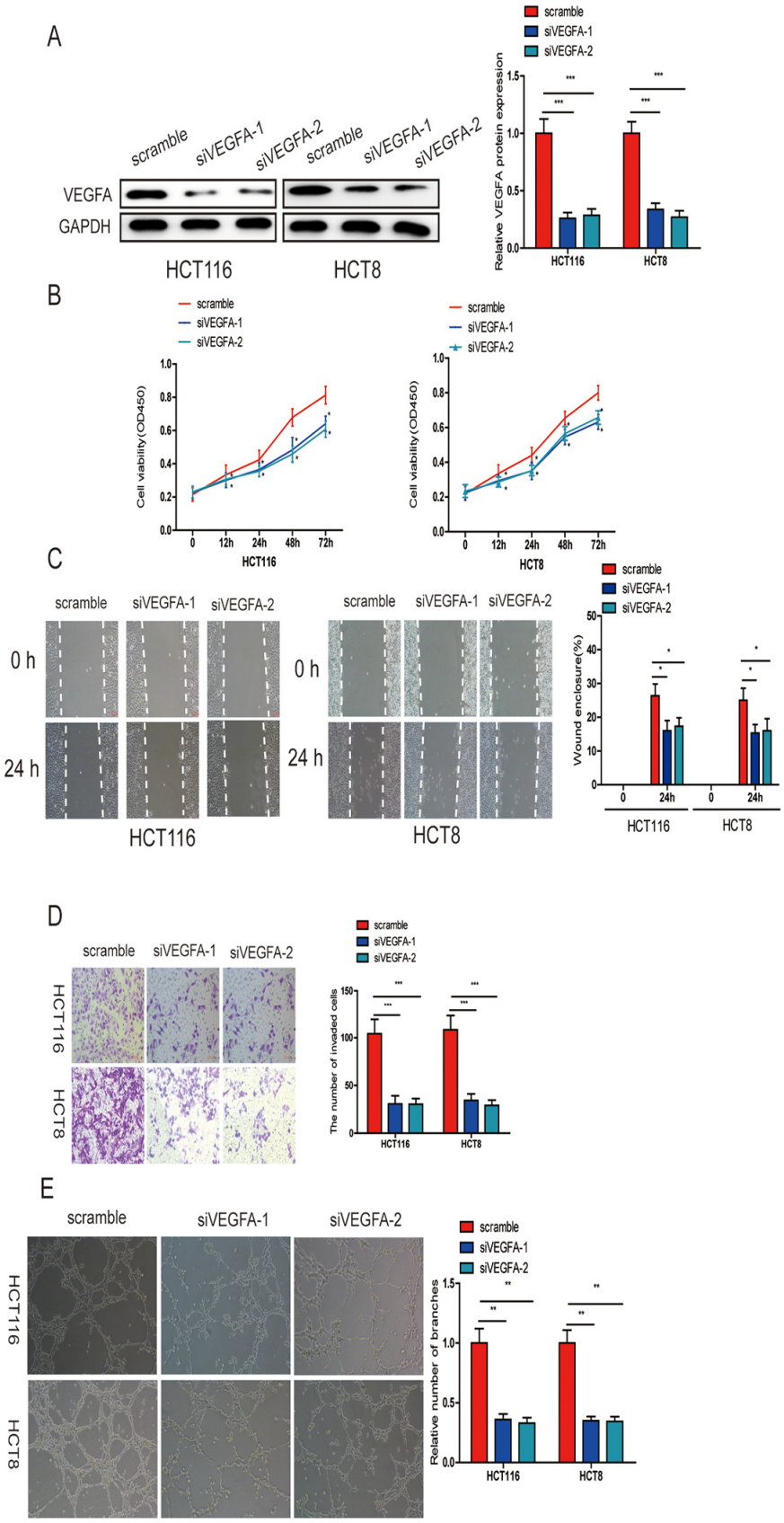

Figure 7. VEGFA knockdown significantly inhibited CRC progression. (**A**) VEGFA expression was downregulated in HCT116 and HCT8 cells transfected with siVEGFA-1 or siVEGFA-2. (**B**) VEGFA knockdown inhibited CRC cell proliferation (**B**), migration (**C**), invasion (**D**) and HUVECs tube formation (**E**). Data are shown as the mean±SD of three independent experiments. **p*<0.05, ***p*<0.01, ****p*<0.001.

genesis by activating NF-κB signaling. Here, we validated that miR-150-5p overexpression inhibited CRC cell proliferation, migration, invasion and angiogenesis in vitro and in vivo, while decreased miR-150-5p promoted CRC progression in vitro.

It is well-accepted that miRNAs exert their function by modulating their target genes by elevating translational repression or mRNA degradation [22, 23]. Wei Kang, et al. [24] have reported that miR-375 inhibited tumor growth in vitro and in vivo, and its targets, YAP1, TEAD4 and CTGF, could partially abolish the tumor-suppressive effect in gastric cancer. Yue Yu, et al. [25] have reported that miR-190 overexpression suppressed EMT and breast cancer progression, and SMAD2, a target of miR-190, could abolish the effects of miR-190 on breast cancer cell EMT and invasion. Herein, using a luciferase reporter assay, we demonstrated that VEGFA was a direct target of miR-150-5p. Moreover, we found that VEGFA upregulation could reverse the inhibitory effect caused by miR-150-5p overexpression, whereas VEGFA knockdown could also inhibit CRC cell growth, migration, invasion and HUVEC tube formation. Additionally, we also showed that the expression of miR-150-5p was reversely correlated with VEGFA expression in CRC tissues. Based on these findings, we could conclude that miR-150-5p exert its biological function by targeting VEGFA in CRC.

Akt and mTOR are both downstream targets of VEGFA. Previous studies have reported that the Akt/mTOR signaling pathway played a critical role in various biological processes of cancers, such as proliferation, metastasis, survival and angiogenesis[26-28].We further examined whether miR-150-5p inhibited tumor initiation and progression by inactivating the VEGFA/VEGFR2/Akt/mTOR signaling pathway, and our data showed that miR-150-5p overexpression could significantly reduce the expression of VEGFA and reduce the activity of VEGFR2 and the downstream Akt/mTOR signaling pathway,

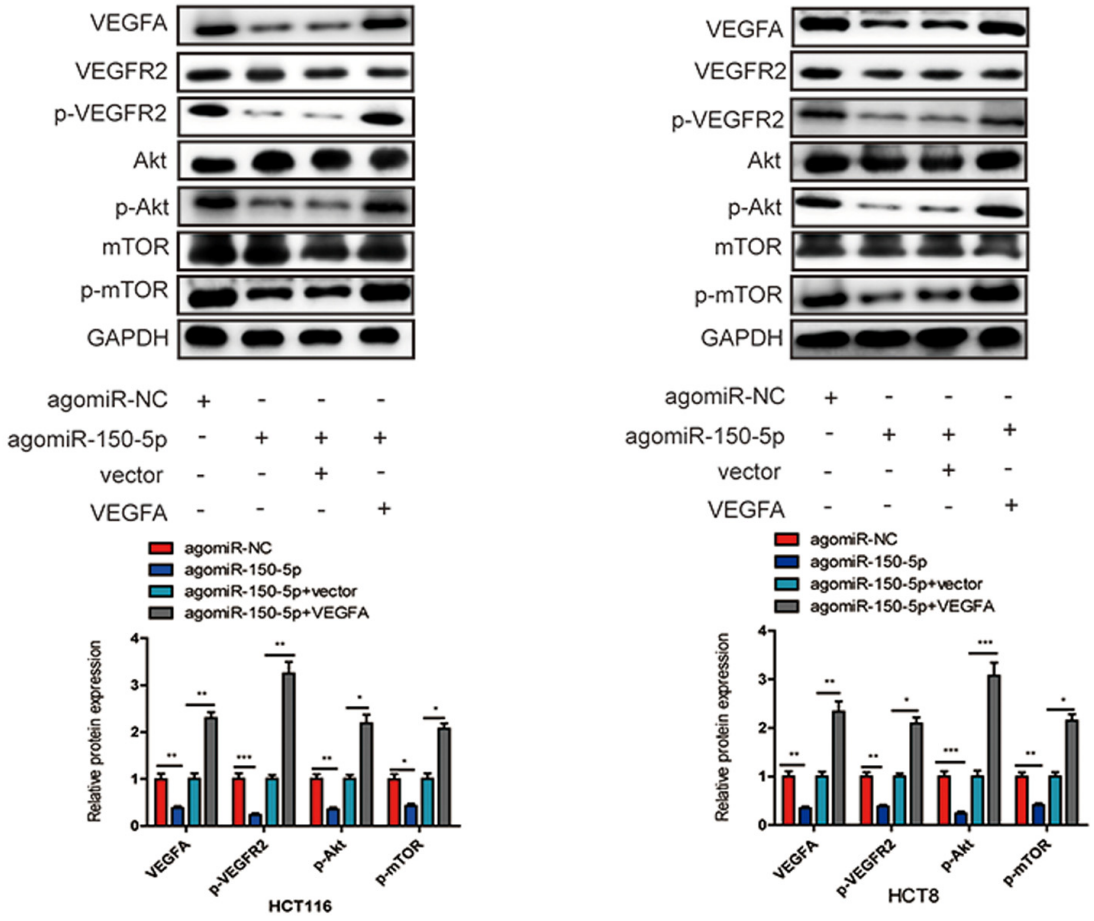

Figure 8. miR-150-5p inhibited VEGFA/VEGFR2/Akt/mTOR signaling pathway in CRC. Western blot was used to measure the expression of VEGFA, VEGFR2, p-VEGFR2, Akt, p-Akt, mTOR, p-mTOR in transfected HCT116 and HCT8 cells. GAPDH was used as a loading control. Data are shown as the mean±SD of three independent experiments. *p<0.05, **p<0.01, ***p<0.001.

In summary, our study demonstrated the pivotal roles of the miR-150-5p-mediated VEGFA/VEGFR2/Akt/mTOR signaling pathway on the tumorigenesis and progression of CRC. This research not only provides a new insight into the mechanism of CRC progression but also highlights miR-150-5p as a potential diagnostic biomarker and therapeutic target of CRC.

MATERIALS AND METHODS

Patient samples

One hundred-twelve fresh CRC tissues and matched adjacent normal tumor tissues were obtained from CRC patients who received radical surgery at Nanjing First Hospital, Nanjing Medical University, between January 2001 and December 2007. The patients who received systemic treatment were excluded. All sample tissues were stored at -80℃ until RNA extraction and embedding in paraffin. Informed consents were obtained from all CRC patients, and this study was approved by the Institutional Review Board of Nanjing First Hospital, Nanjing Medical University. Clinicopathologic characteristics of these patients are listed in Table 1.

Cell culture

The human CRC cell lines including HCT116, HCT8, HT29, SW620, SW480 and DLD-1 and normal colonic epithelial cells (FHC) were obtained from ATCC. These cells were cultured in Dulbecco's Modified Eagle Medium (DMEM, Gibco, USA) with 100 U/ml penicillin, 0.1 mg/ml streptomycin and 10% fetal bovine serum (FBS, Gibco, USA) at 37℃ in 5% CO_2 atmosphere.

Cell transfection

AgomiR-150-5p, antagomiR-150-5p, small interference RNA targeting VEGFA (siVEGFA-1, siVEGFA-2) and their corresponding negative controls (agomiR-NC, antagomiR-NC and scrambled sequence) were obtained from GenePharma (Shanghai, China), and their sequences are listed in Supplementary Materials and methods. pcDNA3.1-VEGFA and empty vector were obtained from GeneCreate (Wuhan, China). Cell transfections were performed using Lipofectamine™ 2000 (Invitrogen, USA) following the manufacturer's protocol.

Cell proliferation assays

Cell proliferation assays were performed using Cell Counting Kit (CCK-8, KeyGEN BioTECH, China) in accordance with the manufacturer's instructions. Approximately 1×10^4 transfected cells were seeded into a 96-well plate. After 12, 24, 48 and 72 h, 10 μl CCK-8 test solution was added into a 96-well plate and incubated for 3 h. The absorbance at 450 nm was measured in a microplate reader (Infinite M200 Pro, Tecan).

Wound-healing assays

HCT116 and HCT8 cells were seeded into 6-well plates and grew to reach 90% confluency. Then, cells were scraped using 200-μl pipette tips, and the wound closure was detected using an inverted microscope (Nikon, Japan) at 100× magnification.

Transwell invasion assays

The cell invasion was evaluated by transwell assay. For this, 3×10^5 cells were cultured in 200 μl of serum-free media in the upper chamber precoated with 100 μl 2% Matrigel (BD Biosciences, USA). The lower chamber was filled with 500 μl of medium containing 10% FBS. After incubation for 36 h, the noninvaded cells were wiped off in the upper chamber with cotton swabs, and the cells in the lower surface were fixed by methanol, then stained with 0.1% crystal violet (Beyotime, China). The invaded cells were counted under inverted microscope (Nikon, Japan) at 200× magnification.

Tube formation assays

HUVECs cells (7×10^5) were suspended in the mixture of tumor-conditioned medium (TCM, 300 μl) and DMEM containing 10% FBS (300 μl), and then plated into a 24-well plate precoated with Matrigel (200 μl per well, BD Biosciences, USA). Tube formation was observed after 6 h incubation at 37℃ and was imaged with a computer-assisted inverted microscope (Nikon, Japan), the number of tube branches was counted using Image J software.

Dual-luciferase reporter assays

The 293T and HCT116 cells were cotransfected with pmirGLO-VEGFA-3'UTR-WT and pmirGLO-VEGFA-3'UTR-Mut reporter plasmids and agomiR-NC and agomiR-150-5p. Twenty-four hours after transfection, dual-luciferase reporter assay (Promega, Madison, WI, USA) was performed to measure the relative luciferase activity normalized to renilla luciferase activity.

Western blot

The total proteins were extracted from cells with RIPA lysis buffer mixed with phenylmethyl sulfonylfluoride (PMSF), protein inhibitors and phosphatase inhibitors

(KeyGEN BioTECH, China). Equal amounts of proteins were separated with 10% SDS-PAGE gel and transferred to polyvinylidene difluoride (PVDF) membranes (Millipore, USA). The membranes were blocked with 5% bovine serum albumin (BSA) for 1.5 h and then incubated with primary antibodies: rabbit polyclonal anti-VEGFA (1:1000, ab46154, abcam, UK), anti-VEGFR2 (1:1000, ab39256, abcam, UK), anti-phospho(Y1175)-VEGFR2 (1:1000, ab194806, abcam, UK), anti-Akt (#9272, Cell Signaling Technology, USA), anti-phospho (Ser473)-Akt (1:2000, #4060, Cell Signaling Technology, USA), anti-mTOR (1:1000, ab2732, abcam, UK), anti-phospho(S2448)-mTOR (1:1000, ab84400 abcam, UK) and rabbit anti-GAPDH (1:10000, ab9485, abcam, UK). Proteins were then detected by enhanced chemiluminescence system (ECL) reagent (KeyGEN BioTECH, China) after incubation with secondary antibodies for 1 h at room temperature.

RNA isolation and quantitative RT-PCR

TRIzol reagent (Invitrogen, USA) was used to extract total RNA in accordance with manufacturer's instructions. MiR-150-5p expression was detected by a Hairpin-it^{TM} microRNA and U6 snRNA normalization RT-PCR quantitation kit (Genepharma, China). For VEGFA mRNA, complementary DNA (cDNA) was synthesized using PrimeScript^{TM} reagent kit with gDNA Eraser (Takara, Dalian, China) and qRT-PCR was analyzed using SYBR Premix Ex Taq kit (Takara, Dalian, China). The relative expression of miRNA or mRNA was analyzed using the $2^{-\Delta\Delta CT}$ method. All results were normalized to GAPDH or U6 gene. The primers for VEGFA and GAPDH mRNA are listed below.

Immunohistochemistry

The CRC tissues, adjacent normal tissues and xenograft tissues were collected, paraffin-embedded and cut into 4-μm-thick sections. Sections were incubated with rabbit anti-VEGFA and anti- CD31 antibodies at 4℃ overnight, followed by incubation with secondary antibodies. The sections were visualized under an inverted microscope (Nikon, Japan) at 200× or 400× magnification. The staining intensity was scored by two independent pathologists into the following four categories: no staining=0, weak staining=1, moderate staining=2 and strong staining=3. The stain-positive tissues were scored into four grades: 0 (0%), 1 (1-33%), 2 (34%-66%), and 3 (67%-100%). The final ICH score was calculated by multiplying the percentage of positive cells by the intensity score.

In vivo experiments

All animal experiments were approved by the Animal Care Committee of Nanjing First Hospital, Nanjing Medial University (acceptance No. SYXK 20160006). For xenografted tumor model, 1×10^7 CRC cells in 0.2 ml PBS were subcutaneously injected into BABL/c nude mice, which were randomly divided into two group (n=8 per group). After tumor formation (day 6), 2 nmol agomiR-150-5p or agomiR-NC were injected into tumors, and the injections were performed 7 times at an interval of 2 days between each injection (day 6, 8, 10, 12, 14, 16, 18). The mice were sacrificed 2 days after their last injection, and the tumor volumes were calculated with the following equation:

$V=0.5 \times (\text{length} \times \text{width}^2)$

For metastasis experiments, 2×10^6 cells in 0.2 ml PBS were injected into the tail vein of nude mice which were randomly divided into two groups (n=8 per group). After 8 weeks of injection, computed tomography (CT) scans were performed to detect the lung metastasis in mice. After CT scans, mice were sacrificed, and their lungs were removed and stained by hematoxylin and eosin (HE) Staining.

Statistical analysis

All experiments were performed more than three times. The data are expressed as the mean ± SD and analyzed by SPSS 22.0 software. The Student's t-test and one-way analysis of variance (ANOVA) were performed to detect the differences between groups. Pearson's, Mann-Whitney U-test or $\chi2$-test was used to analyze the relationship between miR-150-5p expression and clinicopathological features. The Kaplan-Meier method was applied to assess overall survival (OS). The survival curves were compared with log-rank test. The follow-up time was censored if the patient was lost` during follow-up. Cox proportional hazards model was used to perform multivariate analysis and calculate the 95% confidence interval (95% CI). A statistically significant difference was considered at $P < 0.05$.

Table 3. The primers for VEGFA and GAPDH mRNA.

VEGFA	Forward: 5'-TGGCTCACTGGCTTGCTCTA-3'
	Reverse: 5'-ATCCAACTGCACCGTCACAG-3'
GAPDH	Forward: 5'-GGTGGTCTCCTCTGACTTCAA-3'
	Reverse: 5'-GTTGCTGTAGCCAAATTCGTTGT-3'

CONFLICTS OF INTEREST

The authors declare no conflicts of interest.

FUNDING

This project was supported by grants from the National Nature Science Foundation of of Nanjing Medicine (ZDX16001ZDX16001); Innovation team of Jiangsu provincial health-strengthening engineering by science and education (CXTDB2017008) to SKW. Jiangsu Youth Medical Talents Training Project to B.H (QNRC2016066) and Y.P (QNRC2016074); Nanjing Medical Science and Technique Development Foundation to BSH (No. JQX13003).

REFERENCES

1. Siegel R, Desantis C, Jemal A. Colorectal cancer statistics, 2014. CA Cancer J Clin. 2014; 64:104–17. https://doi.org/10.3322/caac.21220

2. Haggar FA, Boushey RP. Colorectal cancer epidemiology: incidence, mortality, survival, and risk factors. Clin Colon Rectal Surg. 2009; 22:191–97. https://doi.org/10.1055/s-0029-1242458

3. Kubokura N, Takahashi-Yanaga F, Arioka M, Yoshihara T, Igawa K, Tomooka K, Morimoto S, Nakatsu Y, Tsuzuki T, Nakabeppu Y, Matsumoto T, Kitazono T, Sasaguri T. Differentiation-inducing factor-3 inhibits intestinal tumor growth in vitro and in vivo. J Pharmacol Sci. 2015; 127:446–55. https://doi.org/10.1016/j.jphs.2015.03.005

4. Garzon R, Calin GA, Croce CM. MicroRNAs in Cancer. Annu Rev Med. 2009; 60:167–79. https://doi.org/10.1146/annurev.med.59.053006.104707

5. Bartel DP. MicroRNAs: genomics, biogenesis, mechanism, and function. Cell. 2004; 116:281–97. https://doi.org/10.1016/S0092-8674(04)00045-5

6. Ohtsuka M, Ling H, Doki Y, Mori M, Calin GA. MicroRNA Processing and Human Cancer. J Clin Med. 2015; 4:1651–67. https://doi.org/10.3390/jcm4081651

7. Brennecke J, Hipfner DR, Stark A, Russell RB, Cohen SM. bantam encodes a developmentally regulated microRNA that controls cell proliferation and regulates the proapoptotic gene hid in Drosophila. Cell. 2003; 113:25–36. https://doi.org/10.1016/S0092-8674(03)00231-9

8. Zhang G, Chen L, Khan AA, Li B, Gu B, Lin F, Su X, Yan J. miRNA-124-3p/neuropilin-1(NRP-1) axis plays an important role in mediating glioblastoma growth and angiogenesis. Int J Cancer. 2018; 143:635–44; https://doi.org/10.1002/ijc.31329

9. Lu W, Zhang H, Niu Y, Wu Y, Sun W, Li H, Kong J, Ding K, Shen HM, Wu H, Xia D, Wu Y. Long non-coding RNA linc00673 regulated non-small cell lung cancer proliferation, migration, invasion and epithelial mesenchymal transition by sponging miR-150-5p. Mol Cancer. 2017; 16:118. https://doi.org/10.1186/s12943-017-0685-9

10. Suetsugu T, Koshizuka K, Seki N, Mizuno K, Okato A, Arai T, Misono S, Uchida A, Kumamoto T, Inoue H. Downregulation of matrix metalloproteinase 14 by the antitumor miRNA, miR-150-5p, inhibits the aggressiveness of lung squamous cell carcinoma cells. Int J Oncol. 2018; 52:913–24. https://doi.org/10.3892/ijo.2017.4232

11. Zhang Z, Wang J, Li J, Wang X, Song W. MicroRNA-150 promotes cell proliferation, migration, and invasion of cervical cancer through targeting PDCD4. Biomed Pharmacother. 2018; 97:511–17. https://doi.org/10.1016/j.biopha.2017.09.143

12. Zhang L, Lin J, Ye Y, Oba T, Gentile E, Lian J, Wang J, Zhao Y, Gu J, Wistuba II, Roth JA, Ji L, Wu X. Serum MicroRNA-150 Predicts Prognosis for Early-Stage Non-Small Cell Lung Cancer and Promotes Tumor Cell Proliferation by Targeting Tumor Suppressor Gene SRCIN1. Clin Pharmacol Ther. 2017; 103:1061-73. https://doi.org/10.1002/cpt.870

13. Xiao J, Lv D, Zhou J, Bei Y, Chen T, Hu M, Zhou Q, Fu S, Huang Q. Therapeutic Inhibition of miR-4260 Suppresses Colorectal Cancer via Targeting MCC and SMAD4. Theranostics. 2017; 7:1901–13. https://doi.org/10.7150/thno.19168

14. Wang X, Yu M, Zhao K, He M, Ge W, Sun Y, Wang Y, Sun H, Hu Y. Upregulation of MiR-205 under hypoxia promotes epithelial-mesenchymal transition by targeting ASPP2. Cell Death Dis. 2016; 7:e2517. https://doi.org/10.1038/cddis.2016.412

15. Claesson-Welsh L, Welsh M. VEGFA and tumour angiogenesis. J Intern Med. 2013; 273:114–27. https://doi.org/10.1111/joim.12019

16. Trinh XB, Tjalma WA, Vermeulen PB, Van den Eynden G, Van der Auwera I, Van Laere SJ, Helleman J, Berns EM, Dirix LY, van Dam PA. The VEGF pathway and the AKT/mTOR/p70S6K1 signalling pathway in human epithelial ovarian cancer. Br J Cancer. 2009; 100:971–78. https://doi.org/10.1038/sj.bjc.6604921

17. Massari F, Ciccarese C, Santoni M, Brunelli M, Piva F, Modena A, Bimbatti D, Fantinel E, Santini D, Cheng L, Cascinu S, Montironi R, Tortora G. Metabolic alterations in renal cell carcinoma. Cancer Treat Rev. 2015; 41:767–76.

https://doi.org/10.1016/j.ctrv.2015.07.002

18. Li J, Zou K, Yu L, Zhao W, Lu Y, Mao J, Wang B, Wang L, Fan S, Song B, Li L. MicroRNA-140 Inhibits the Epithelial-Mesenchymal Transition and Metastasis in Colorectal Cancer. Mol Ther Nucleic Acids. 2018; 10:426–37. https://doi.org/10.1016/j.omtn.2017.12.022

19. Mi Y, Zhang D, Jiang W, Weng J, Zhou C, Huang K, Tang H, Yu Y, Liu X, Cui W, Zhang M, Sun X, Zhou Z, et al. miR-181a-5p promotes the progression of gastric cancer via RASSF6-mediated MAPK signalling activation. Cancer Lett. 2017; 389:11–22. https://doi.org/10.1016/j.canlet.2016.12.033

20. Salem M, O'Brien JA, Bernaudo S, Shawer H, Ye G, Brkić J, Amleh A, Vanderhyden BC, Refky B, Yang BB, Krylov SN, Peng C. miRNA-590-3p promotes ovarian cancer growth and metastasis via a novel FOXA2-versican pathway. Cancer Res. 2018; 78:4175–90; https://doi.org/10.1158/0008-5472.CAN-17-3014

21. Gu Y, Ampofo E, Menger MD, Laschke MW. miR-191 suppresses angiogenesis by activation of NF-κB signaling. FASEB J. 2017; 31:3321–33. https://doi.org/10.1096/fj.201601263R

22. Bagga S, Bracht J, Hunter S, Massirer K, Holtz J, Eachus R, Pasquinelli AE. Regulation by let-7 and lin-4 miRNAs results in target mRNA degradation. Cell. 2005; 122:553–63. https://doi.org/10.1016/j.cell.2005.07.031

23. Bartel DP. MicroRNAs: target recognition and regulatory functions. Cell. 2009; 136:215–33. https://doi.org/10.1016/j.cell.2009.01.002

24. Kang W, Huang T, Zhou Y, Zhang J, Lung RW, Tong JH, Chan AW, Zhang B, Wong CC, Wu F, Dong Y, Wang S, Yang W, et al. miR-375 is involved in Hippo pathway by targeting YAP1/TEAD4-CTGF axis in gastric carcinogenesis. Cell Death Dis. 2018; 9:92. https://doi.org/10.1038/s41419-017-0134-0

25. Yu Y, Luo W, Yang ZJ, Chi JR, Li YR, Ding Y, Ge J, Wang X, Cao XC. miR-190 suppresses breast cancer metastasis by regulation of TGF-β-induced epithelial-mesenchymal transition. Mol Cancer. 2018; 17:70. https://doi.org/10.1186/s12943-018-0818-9

26. Trinh XB, Tjalma WA, Vermeulen PB, Van den Eynden G, Van der Auwera I, Van Laere SJ, Helleman J, Berns EM, Dirix LY, van Dam PA. The VEGF pathway and the AKT/mTOR/p70S6K1 signalling pathway in human epithelial ovarian cancer. Br J Cancer. 2009; 100:971–78. https://doi.org/10.1038/sj.bjc.6604921

27. Bauer TM, Patel MR, Infante JR. Targeting PI3 kinase in cancer. Pharmacol Ther. 2015; 146:53–60. https://doi.org/10.1016/j.pharmthera.2014.09.006

28. Ma XM, Blenis J. Molecular mechanisms of mTOR-mediated translational control. Nat Rev Mol Cell Biol. 2009; 10:307–18. https://doi.org/10.1038/nrm2672

SUPPLEMENTARY MATERIAL

SUPPLEMENTARY FIGURE

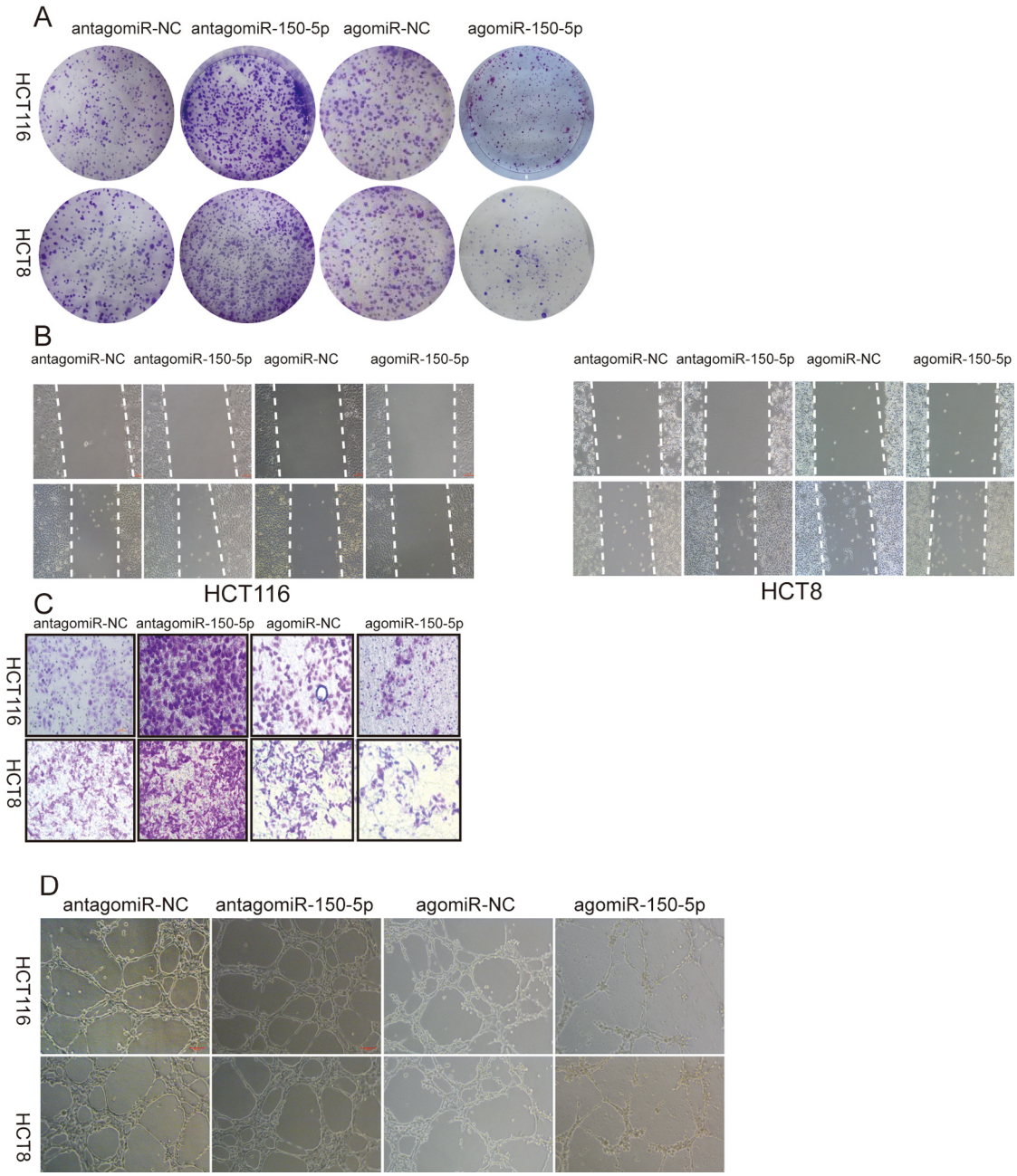

Figure S1. (**A**-**D**) Representive amages of colony formation(A), wound healing(B, ×40), transwell (**C**, ×200) and tube formation (**D**, ×100) in antagomiR-NC group, antagomiR-150-5p group, agomiR-NC group and agomiR-150-5p group.

The sequence of scramble, siVEGFA-1, siVEGFA-2, agomiR-150-5p, agomiR-NC

scramble	5′-UUCUCCGAACGUGUCACGUTT-3′
	5′-ACGUGACACGUUCGGAGAATT-3′
siVEGFA-1	5′-CCGAAACCAUGAACUUUCUTT-3′
	5′-AGAAAGUUCAUGGUUUCGGTT-3′
siVEGFA-2	5’- GCGGCGUCGCACUGAAACUTT-3’
	5’- AGUUUCAGUGCGACGCCGCTT-3’
agomiR-150-5p	5’-UCUCCCAACCCUUGUACCAGUG-3’
	5’-CUGGUACAAGGGUUGGGAGAUU-3’
agomiR-NC	5’-UUCUCCGAACGUGUCACGUTT-3’
	5’-ACGUGACACGUUCGGAGAATT-3’
antagomiR-150-5p	5’-CACUGGUACAAGGGUUGGGAGA-3’
antagomiR-NC	5’-CAGUACUUUUGUGUAGUACAA-3’

antagomiR-150-5p and antagomiR-NC

Research Paper

Naringin targets Zeb1 to suppress osteosarcoma cell proliferation and metastasis

He Ming[1], Qiu Chuang[1], Wang Jiashi[1], Li Bin[1], Wang Guangbin[1], Ji Xianglu[1]

[1]Department of Orthopedic Surgery, Shengjing Hospital of China Medical University, Heping District, Shenyang 110004, People's Republic of China

Correspondence to: Ji Xianglu; **email:** jixiangludor@163.com
Keywords: naringin, osteosarcoma, Zeb1, proliferation, metastasis
Received: July 10, 2018 **Accepted:** December 6, 2018 **Published:** December 22, 2018

Copyright: Ming et al. This is an open-access article distributed under the terms of the Creative Commons Attribution License (CC BY 3.0), which permits unrestricted use, distribution, and reproduction in any medium, provided the original author and source are credited.

ABSTRACT

Naringin, a citrus bioflavonoid, has anti-inflammatory actions and cardio- and neuroprotective effects. In addition, naringin exhibits multiple antitumor actions in several cancer types, including osteosarcoma, the most common type of bone cancer. Here, we show that naringin inhibits proliferation and invasion and induces apoptosis in human osteosarcoma cells by inhibiting zinc finger E-box binding homeobox 1 (Zeb1), a transcriptional repressor of epithelial differentiation involved in tumor metastasis. Our expression analyses confirm that Zeb1 is highly expressed in osteosarcoma specimens and cell lines. The effects of naringin, which included downregulation of Cyclin D1, MMP2, and bcl-2, where reproduced by siRNA-mediated Zeb1 silencing, whereas Zeb1 overexpression increased proliferation, migration, and Cyclin D1, MMP2, and bcl-2 levels. In addition, naringin administration reduced tumor nodule formation and attenuated the expression of the above proteins in the livers of mice injected with MG63 osteosarcoma cells. Our study provides preclinical evidence for the potential therapeutic application of naringin in the treatment of osteosarcoma.

INTRODUCTION

Although adjuvant chemotherapy has improved osteosarcoma survival rate in recent years, development of multidrug resistance severely impacts prognosis and restricts success of curative attempts [1-3]. Therefore, new and effective drugs to treat osteosarcoma are clearly needed.

Naringin, a bioflavonoid abundant in grapefruit and other citrus, has multiple biological activities. It possesses sedative, antifungal, antispasmodic, and analgesic properties, and provides cardioprotective, neuroprotective, and anticancer effects [4]. In addition, naringin has been demonstrated to inhibit inflammatory responses, prevent bone degeneration, and exert anabolic effects on bone cells [5, 6]. Naringin promotes the expression of β-catenin and increase Ser552 phosphorylation on β-catenin in UMR-106 osteosarcoma cells. This led to activation of lymphoid enhancer factor (LEF)/T-cell factor (TCF) transcription factors to stimulate bone development [7]. Naringin abrogates osteoclastogenesis and bone resorption by inhibiting RANKL-induced NF-κB and ERK activation [8] , and demonstrated therapeutic potential to attenuate polymethylmethacrylate-induced osteoclastogenesis and osteolysis. There is substantial evidence supporting a role for naringin as an anticancer agent. Studies also indicated that naringin could reduce the release of inflammatory factors and inhibit the growth of W256 carcinosarcoma in rats [4, 9, 10]. Moreover, growth arrest and apoptosis were common effects of naringin in several *in vitro* and *in vivo* studies conducted on breast, cervical, ovarian, bladder, hepatic, skin, colorectal, and gastric cancer cells [11, 12].

Zeb1 (zinc finger E-box binding homeobox 1) is a transcription factor that represses epithelial differentia-

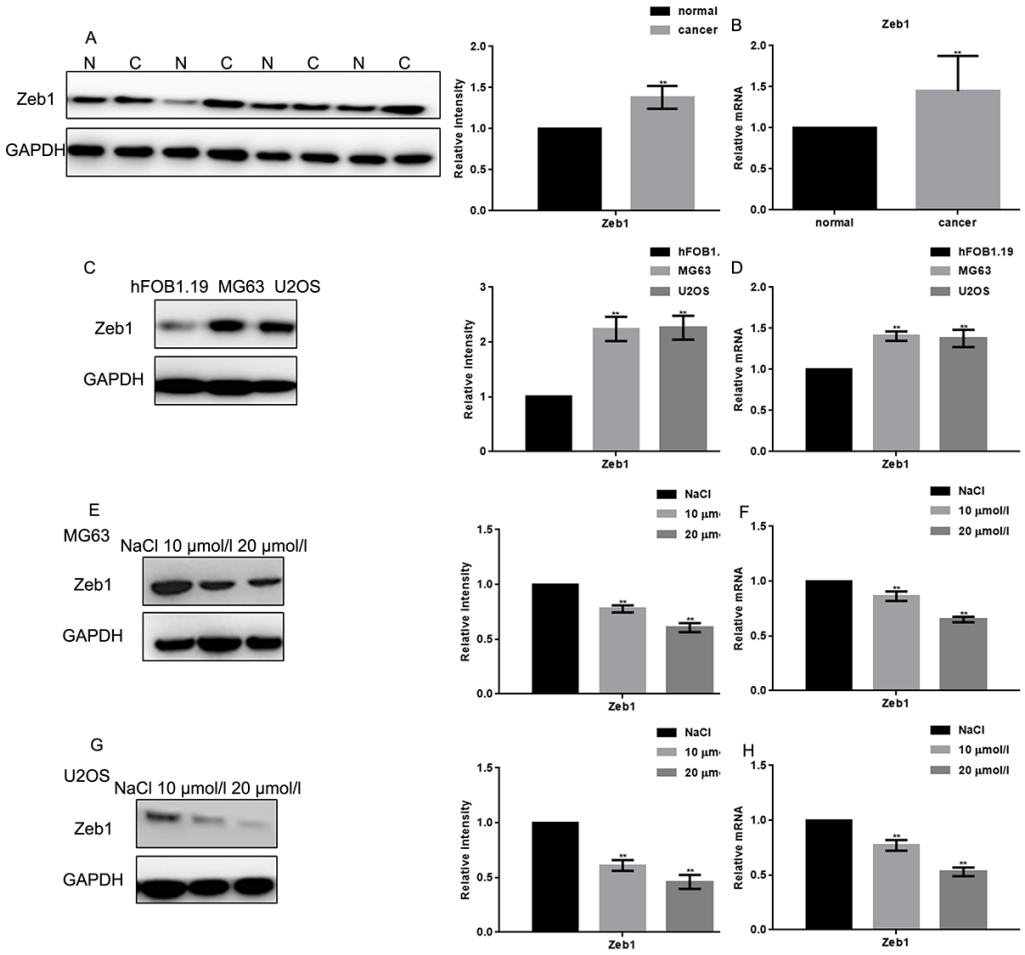

Figure 1: Naringin inhibits the expression of Zeb1 in osteosarcoma cells. (**A, B**) Zeb1 expression in 30 human osteosarcoma specimens and their adjacent normal tissue counterparts was detected by Western blot and real-time PCR. ***P* < 0.05, vs normal tissues. (**C, D**) Zeb1 expression in MG63, U2OS and hFOB1.19 cells, detected by Western blot and real-time PCR. ***P* < 0.05, vs hFOB1.19 cells. (**E-H**) Zeb1 expression detected by Western blot and real-time PCR in MG63 and U2OS cells treated with NaCl or indicated concentrations of naringin for 24 h. ***P* < 0.05, compared with NaCl.

tion and promotes a mesenchymal phenotype [13]. Zeb1 is upregulated in several cancers, where it influences cell motility, cell cycle, and survival, and is an important contributor to tumor invasion and metastasis [14, 15].

Studies have shown that Zeb1 can override the G1 checkpoint directly, by stimulating Cyclin D1 expression, and indirectly, by regulating the Wnt signaling pathway [16, 17]. Zeb1 was shown to promote the progression of lung cancer by increasing the expression of MMP2, a member of the matrix metalloproteinases family that play an important role in cell migration and facilitate invasion and metastasis of tumor cells [18, 19]. Zeb1 has also been shown to be upregulated in osteosarcoma, and to contribute to its development [20, 21].

Using human osteosarcoma cell lines as experimental model, in the present study we provide *in vitro* and *in vivo* evidence that naringin suppresses proliferation and metastasis of osteosarcoma cells by inhibiting the expression of Zeb1. Our findings highlight the potential of naringin, a safe and natural flavonoid, for osteosarcoma therapy.

RESULTS

Naringin inhibits the expression of Zeb1 in osteosarcoma cells

The expression of Zeb1 in human osteosarcoma samples was assessed by Western blot and real-time PCR (Figs. 1A, B). Both assays showed that Zeb1 was overexpressed in most samples, although heterogeneity

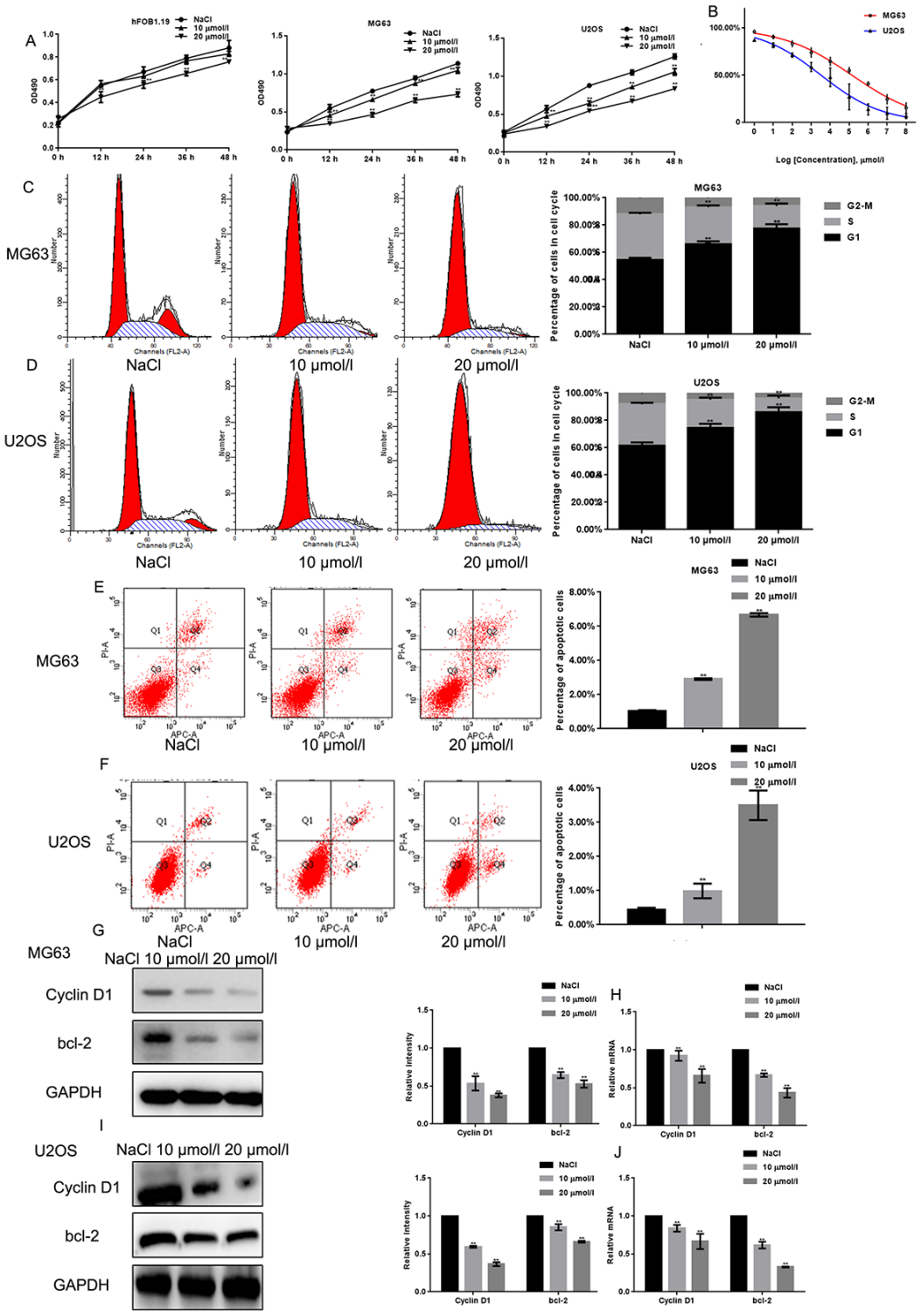

Figure 2: Naringin inhibits the proliferation of osteosarcoma cells. (**A**) Results of MTT proliferation assays in hFOB1.19, MG63, and U2OS cells cultured with various concentrations of naringin for different times. Results represent the mean ± SD of three experiments done in triplicate. ***P* < 0.05, compared with NaCl. (**B**) Proliferation inhibition rates induced by naringin on MG63 and U2OS cells. IC_{50} values were calculated through linear regression. (**C, D**) Flow cytometric analysis of cell cycle distribution in MG63 and U2OS cells pre-incubated with or without naringin for 24 h and stained with PI. The experiment was repeated three times. ***P* < 0.05, compared with NaCl. (**E, F**) Flow cytometric assay of apoptosis in MG63 and U2OS cells pre-incubated with or without naringin for 24 h and stained with Annexin V-FITC/PI. The experiment was repeated three times. ***P* < 0.05, compared with NaCl. (**G-J**) Expression of Cyclin D1 and bcl-2 detected by Western blot and real-time PCR in MG63 and U2OS cells treated with NaCl or naringin for 24 h. ***P* < 0.05, compared with NaCl.

was evident. In cultured cells, both Western blot and real-time PCR showed much stronger Zeb1 expression in osteosarcoma MG63 and U2OS cells than in control hFOB1.19 osteoblasts (Figs. 1C, D). Upon exposure to naringin (10 or 20 μmol/L) for 24 h, Zeb1 protein and mRNA levels were dramatically decreased, in dose-dependent manner, in both osteosarcoma cell lines (Figs. 1 E-H).

Naringin inhibits proliferation and induces apoptosis in osteosarcoma cells

The MTT assay revealed that naringin treatment inhibited the proliferation of MG63 and U2OS cells in a concentration dependent manner (Fig. 2A). The inhibitory effect of naringin on the proliferation of hFOB1.19 was only obvious when the concentration of naringin was 20 μmol/L. The IC50 of naringin on MG63 and U2OS cells at 24 h was ~50 μmol/L and ~30 μmol/L, respectively (Fig. 2B). Next, we used flow cytometry to evaluate cell cycle staging in PI-stained MG63 and U2OS cells previously exposed to various concentrations of naringin for 24 h. Naringin induced a dose-dependent increase in the percentage of cells in G_1 phase, and decreased the number of cells in S phase, compared to control (Figs. 2C, D). To assess whether naringin can promote apoptosis, flow cytometry was used in Annexin-V-FITC-stained osteosarcoma cells. Results showed a dose-dependent increase in apoptotic cells treated with naringin (Figs. 2E, F). In line with these antiproliferative and pro-apoptotic effects, both Western blot and real-time PCR assays showed that exposure to 10 or 20 μmol/L naringin for 24 h dramatically decreased the expression of Cyclin D1 and bcl-2 (Figs. 2G-J).

Naringin inhibits migration of osteosarcoma cells

The effects of naringin on osteosarcoma cell migration and invasion was assessed using Transwell assays in the absence or presence, respectively, of Matrigel. Results showed that naringin exposure (10 or 20 μmol/L for 24 h) significantly decreased both migration and invasion of MG63 and U2OS cells in a dose-dependent manner (Figs. 3A-D). These effects were consistent with a decrease in MMP2 expression, detected in both cell lines in Western blot, real-time PCR, and zymography gel assays (Figs. 3E-H).

Naringin suppresses osteosarcoma cell proliferation and migration by inhibiting Zeb1

To test the hypothesis that naringin exerts antiproliferative and anti-invasive effects by inhibiting Zeb1, its effects were tested in MG63 cells transfected with a plasmid encoding Zeb1 (Zeb1 overexpression) or an empty vector backbone (control). Conversely, siRNAs were introduced to downregulate Zeb1 (si-Zeb1), and to serve as non-targeted, negative control (si-NC). MTT assays showed that proliferation was stimulated by Zeb1 overexpression, and decreased to control inhibition levels by naringin (20 μmol/L) (Fig. 4A). On the other hand, Zeb1 suppression, although partial, decreased cell proliferation, and naringin induced no further inhibition in these cells. (Fig. 4B). We next examined whether migration was affected in Zeb1-overexpressing and Zeb1-suppressed cells. Transwell assay results indicated that Zeb1 overexpression enhances the migration of MG63 cells, while Zeb1 silencing recapitulates the inhibitory effect of naringin on control cells (Figs. 4C, D). Finally, we analyzed the effects of Zeb1 overexpression and downregulation on Cyclin D1, MMP2, and bcl-2 expression. The results showed that expression of these proteins increased upon Zeb1 upregulation (Figs. 4 E-F). Meanwhile, Zeb1 silencing lowered protein expression to levels like those observed in naringin-treated control cells (Figs. 4 G-H).

Naringin inhibits the invasion of MG63 cells *in vivo*

To examine the effect of naringin on osteosarcoma cell tumorigenesis *in vivo*, MG63 cells were injected into nude mice via the tail vein. After daily administration of naringin (5 or 10 mg/kg) or 0.9% NaCl for 16 days, mice were sacrificed and lung tissues processed for microscopic histological analysis. Results showed that naringin significantly prevented lung degeneration and reduced the incidence of metastatic nodules (Fig. 5A). Moreover, Western blots (Fig. 5B) and real-time PCR assays (Fig. 5C) showed that the expression of Zeb1, Cyclin D1, MMP2, and bcl-2 was decreased in the livers of mice treated with naringin.

DISCUSSION

Naringin, a flavonoid present in citrus fruits, has HMG-CoA reductase inhibitor activity, and at low (nM) doses increases osteogenic activities in an osteoblast cell model *in vitro* [22]. Moreover, naringin-induced osteogenic differentiation has been recently described in bone marrow stromal cells and stem cells[23].On the other hand, naringin has been shown to inhibit cell proliferation and promote cell apoptosis in breast cancer, cervical cancer, melanoma, and bladder cancer cells [24]. Thus, we speculated that naringin may have therapeutic effect on osteosarcoma as well.

In this study, we tested the hypothesis that naringin has anticancer actions through inhibition of Zeb1, a zinc finger homeodomain transcription factor implicated in invasiveness and metastasis development in several

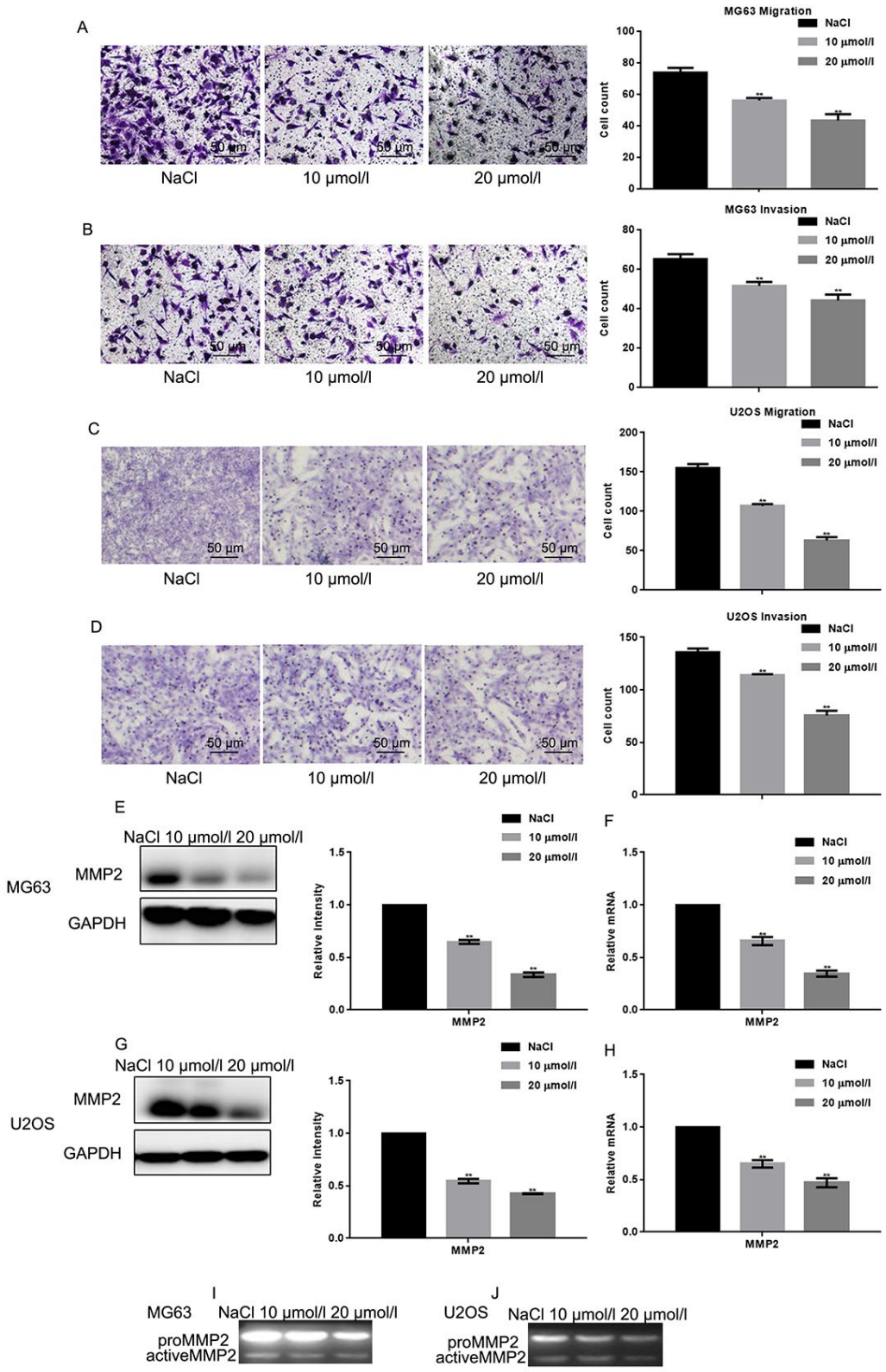

Figure 3: Naringin inhibits migration and invasion of osteosarcoma cells. (**A-D**) Migration and invasion were studied, respectively, using Transwell assays with or without Matrigel, in naringin-treated MG63 and U2OS cells. Cell count results represent the mean ± SD of three experiments. ***P* < 0.05, compared with NaCl. (**E-H**) MMP2 expression by Werstern blot and real-time PCR in MG63 and U2OS cells treated with NaCl or naringin for 24 h. ***P* < 0.05, compared with NaCl. (**I, J**) Zymography gel assay showing the inhibitory effect of naringin on MMP2 activity in MG63 and U2OS cells.

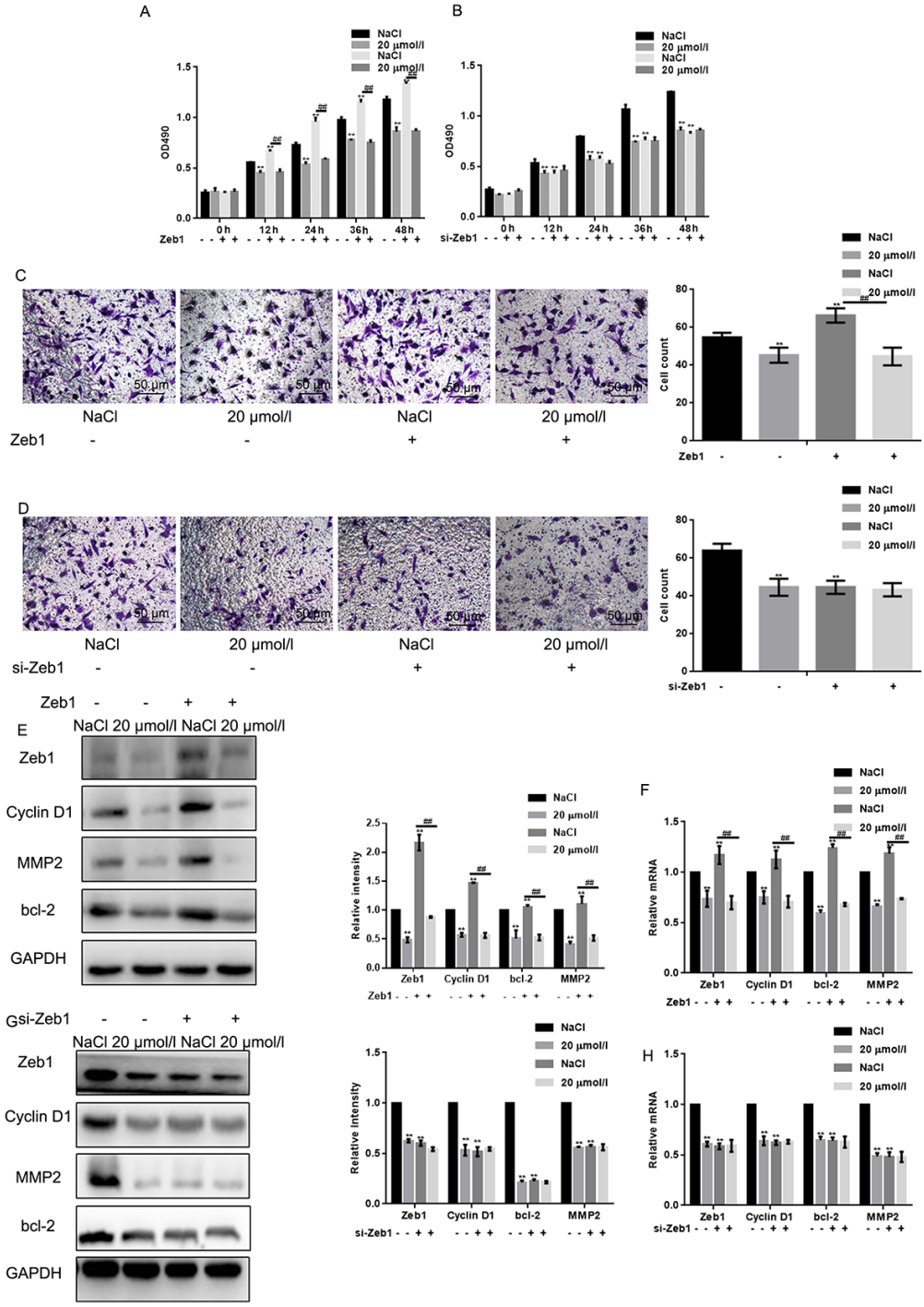

Figure 4: Naringin suppresses osteosarcoma cell proliferation and migration by inhibiting Zeb1. (**A**) MTT proliferation assay of MG63 cells expressing a control vector or Zeb1. Cells were incubated with 20 μmol/L of naringin or NaCl and assayed at the indicated times. Results represent the mean ± SD of three experiments done in triplicate. ***P* < 0.05, compared with NaCl. ## *P* < 0.05, compared with Zeb1 overexpressed group. (**B**) MTT proliferation assay of MG63 cells transfected with si-Zeb1 (Zeb1 silencing) or si-NC (negative control). Cells were treated with 20 μmol/L of naringin or NaCl and assayed at the indicated times. Results represent the mean ± SD of three experiments done in triplicate. ***P* < 0.05, compared with NaCl. (**C**) Results of Transwell migration assays (without Matrigel) performed in MG63 cells expressing control vectors or Zeb1. Cells were treated with 20 μmol/l of naringin or NaCl. ***P* < 0.05, compared with NaCl; ## *P* < 0.05, compared with Zeb1 overexpressed group. (**D**) Results of Transwell migration assays (without Matrigel) performed in MG63 cells transfected with si-Zeb1 (Zeb1 silencing) or si-NC (negative control). Cells were treated with 20 μmol/l of naringin or NaCl. ***P* < 0.05, compared with NaCl. (**E, F**) Western blot and real-time PCR assay results for Zeb1, Cyclin D1, bcl-2, and MMP2 expression in MG63 cells expressing Zeb1 or empty vector. Cells were incubated with 20 μmol/l of naringin or NaCl (control). ***P* < 0.05, compared with NaCl; ## *P* < 0.05, compared with Zeb1 overexpressed group. (**G, H**) Western blot and real-time PCR assay results for Zeb1, Cyclin D1, bcl-2, and MMP2 expression in MG63 cells transfected with si-Zeb1 or si-NC. Cells were treated with 20 μmol/l of naringin or NaCl. ***P* < 0.05, compared with NaCl.

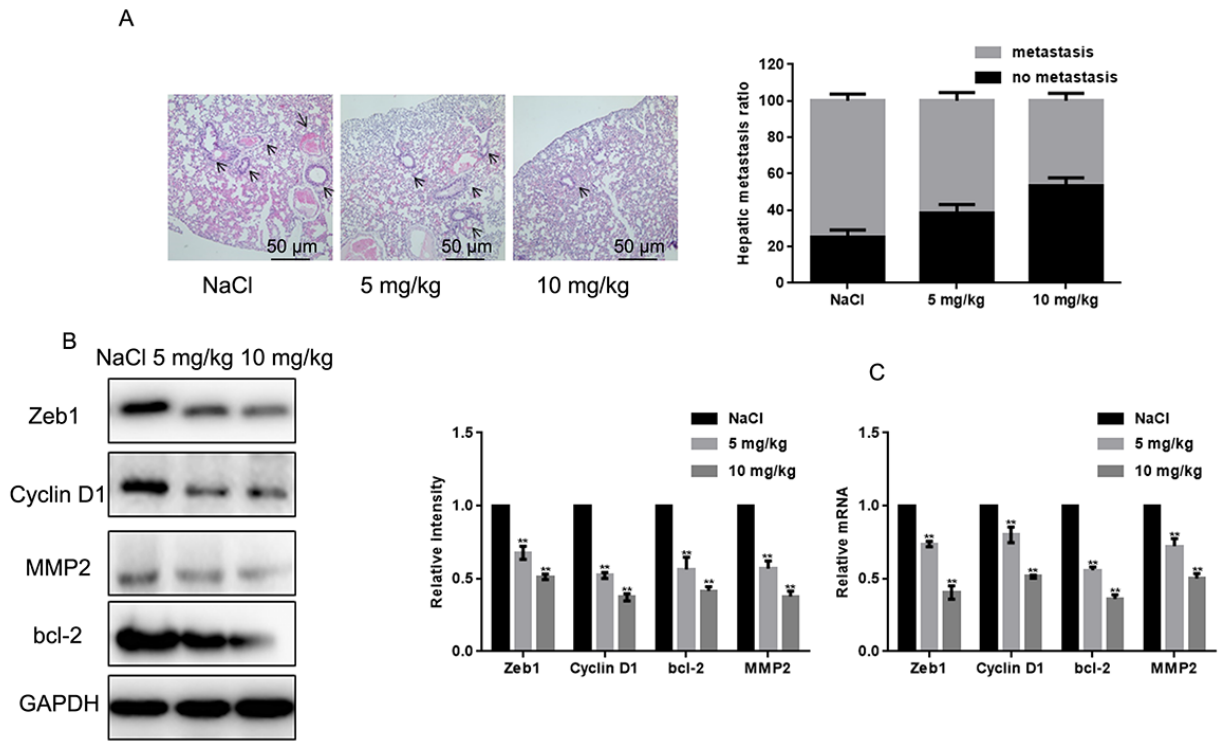

Figure 5: Naringin inhibits lung invasion by MG63 cells *in vivo*. (**A**) Representative images of lung histopathology (H&E staining; 400×) from mice injected with MG63 cells and treated daily with two different doses of naringin or NaCl (control) for 16 days. (**B, C**) Zeb1, Cyclin D1, bcl-2, and MMP2 expression in liver tumor samples, detected by Western blot (B) and real-time PCR (C). $^{**}P < 0.05$, compared with NaCl-treated controls.

tumor types, including osteosarcoma and lung cancer [25-27]. We first confirmed high Zeb1 expression in human specimens and in human MG63 and U2OS osteosarcoma cell lines. In these cells, naringin dose-dependently inhibited the expression of Zeb1, reduced proliferation by arresting the cell cycle in the G1 phase, and promoted apoptosis. In contrast, naringin had weaker effects on normal osteoblasts. The induction of apoptosis by naringin correlated with a decrease in anti-apoptotic bcl-2 protein expression; the latter was also observed in a study evaluating naringin's effects in an ovarian cancer mouse model [12]. Naringin-mediated apoptosis has been documented in cervical cancer cells, in two studies that implicated NF-κB/COX-2-caspase-1 pathway repression [9] and expression of caspases, p53, Bax, and Fas death receptor [28] respectively.

Our results also showed that both naringin exposure and Zeb1 silencing significantly suppressed osteosarcoma cell migration in Transwell assays. This is consistent with the down-regulation of MMP2, observed under both conditions, and the stimulation of MMP2 expression seen instead after ectopic expression of Zeb1 in these cells. These effects may be related to a well-known role of Zeb1 in promoting metastasis through epithelial-to-mesenchymal transition (EMT), although more research is needed to clarify the mechanisms at play in osteosarcoma [29].

Importantly, we demonstrated that naringin's effects *in vitro* correlated with antimetastatic actions *in vivo*, as its administration to nude mice injected with osteosarcoma MG63 cells attenuated the formation of tumor nodules in the liver. In summary, our data showed that naringin inhibits the malignant phenotype of osteosarcoma cells by inhibiting the expression of Zeb1 and Zeb1-associated proteins such as Cyclin D1 and MMP2. The present findings support the potential of naringin as a novel therapeutic strategy for osteosarcoma.

MATERIALS AND METHODS

Drugs and reagents

Naringin, 3-(4,5-dimethyl-2-thiazolyl)-2,5-diphenyl-2-H-tetrazolium bromide (MTT), propidium iodide (PI), and Trypan Blue were purchased from Beyotime Biotechnology (Shanghai, China). Fetal bovine serum (FBS), Dulbecco's modified Eagle's medium (DMEM), Lipofectamine 2000, and TRIzol were obtained from

Invitrogen (Carlsbad, CA, USA). RT-PCR kits were obtained from Promega (Beijing, China). SYBR Premix Ex Taq reagents were obtained from TaKaRa (Dalia, China). Anti-Zeb1, anti-cyclin D1, anti-bcl-2, anti-MMP2, and anti-GAPDH antibodies were purchased from Santa Cruz Biotechnology (Dallas, TX, USA). HRP-conjugated secondary antibody, BCA protein assay kit, and enhanced chemiluminescence (ECL) solution were purchased from Beyotime Biotechnology. All experiments were completed in the Central Laboratory of our hospital.

Human samples

Tissue samples were obtained from patients undergoing surgery at Shengjing Hospital of China Medical University (Table 1). The original histopathologic reports were obtained from each case, and the diagnosis of osteosarcoma was confirmed. Part of the excised tissue was embedded in paraffin, and part of the sample was snap-frozen at −80°C. Clinical samples were collected after written informed consent was obtained, and the study was approved by the Ethics Committee at the Academic Medical Center of Shengjing Hospital of China Medical University.

Table 1. Patient information.

Group		N	Percent
Sex	Male	13	65%
	Female	7	35%
Age	<20	12	60%
	>20	8	40%
History	Yes	1	5%
	No	19	95%
Site of primary disease	Tibia	11	55%
	Femur	7	35%
	Humerus	2	10%
TNM	I	9	45%
	II	7	35%
	III	5	25%

Cell culture

Human osteosarcoma MG63 and U2OS cells, and human hFOB1.19 osteoblasts (SV40-transfected), used as control, were supplied by the Cell Pool Bank of China (Guangzhou, China). The cells were cultured in DMEM supplemented with 10% FBS at 37°C under an atmosphere of 5% CO_2 and 95% air.

Cell viability assay

The MTT assay was employed to assess cell viability. Cells were cultured in 96-well plates at a concentration of 1×10^4 cells/ml and incubated with 10 or 20 μmol/L naringin for 12, 24, 36, or 48h. At those time intervals, 0.01 ml of MTT solution (5 mg/ml) was added to each well. After a 4 h incubation at 37 °C, medium was replaced by 0.15 ml DMSO. After 15 min incubation at 37 °C, optical densities (490 nm) were measured.

Cell cycle assay

Cells were incubated with 10 or 20 μmol/L naringin for 24 h and fixed in 75% ethanol at 4°C overnight. After resuspension in 10 μg/ml PI, cell cycle stages were determined using a FACS Vantage flow cytometer using CellQuest (Becton Dickinson and Co., San Jose, CA, USA).

Apoptosis assay

Cells were incubated with 10 or 20 μmol/L naringin for 24 h, washed twice with cold PBS, and stained with 5 μl ANNEXIN-V-FITC/10 μl PI for 15 min. After addition of 400 μl binding buffer to each tube, the apoptosis rate was measured by flow cytometry within 1 h.

Transwell migration assay

Transwell assays were performed using a modified Boyden chamber with Nuclepore polycarbonate membranes. After 24 h treatment with 10 or 20 μmol/L naringin, 1×10^5 cells in 100 μl FBS-free DMEM were placed in the upper part of the chamber with or without Matrigel, whereas the lower compartment was filled with 600 μl DMEM containing 10% FBS. After 8 h incubation at 37°C, the invading cells on the lower surface of the filter were fixed, stained with Trypan Blue, and counted under high-power magnification (400×).

Zymography

Cells were cultured in 12-well plates and treated with 10 or 20 μmol/L naringin. After 24 h, media was changed into DMEM containing 5% FBS (the source of proMMP2). After another 24 h, the media were harvested, cleared by centrifugation at 12,000 rpm for 10 min, and subjected to analysis by SDS-PAGE impregnated with 1 mg/ml gelatin. The gels were incubated at 37°C overnight, stained with Coomassie Blue, destained, and then scanned.

Transfection

To stably overexpress and silence Zeb1, cells were transfected with a pcDNA3.1 vector encoding Zeb1, and with a Zeb1-targeted siRNA, respectively (Shanghai GeneChem Company, Shanghai, China). An empty pcDNA3.1 vector and a non-targeted siRNA were transfected as respective controls, and cells were

Table 2: Primers for RT-PCR.

Name	Forward primer (5'->3')	Reverse primer (5'->3')
Zeb1 (NM_001323643.1)	GCACAACCAAGTGCAGAAG	CATTTGCAGATTGAGGCTG
Cyclin D1 (NM_053056.2)	CCGAGGAGCTGCTGCAAATGGAGCT	TGAAATCGTGCGGGGTCATTGCGGC
MMP2 (NM_004530.5)	CGCATCTGGGGCTTTAAACAT	TCAGCACAAACAGGTTGCAG
GAPDH (NM_002046.6)	GAAGGCTGGGGCTCATTTG	AGGGGCCATCCACAGTCTTC

selected with puromycin (1.5 μg/mL). Lipofectamine 2000 was used for cell transfection according to the manufacturer's protocols. We extracted protein and total RNA at 24 h after transfection.

Real-time PCR

Total RNA was extracted after the indicated treatments (24 h) using TRIzol according to the manufacturer's protocol. Cells or tissues were lysed by 0.2 mL chloroform and centrifuged (12,000 × g at 4°C for 15 min). The supernatant was then treated with 0.5mL isopropanol and centrifuged (12,000 × g at 4°C for 10 min). The RNA pellet was dissolved in 1 mL 75% ethanol, centrifuged (7,500 × g at 4°C for 5 min), and the supernatant discarded. After resuspension in DEPC water, 1 μg of RNA was reverse transcribed to cDNA using a RT-PCR kit. Real-time PCR was performed using an Mx 3000P real-time PCR system (Applied Biosystems, Shanghai, China) and SYBR Premix Ex Taq as a DNA-specific fluorescent dye. PCR was carried out for 40 cycles of 95°C for 10 s and 60°C for 30 s. Primer sequences for detection of mRNA expression were synthesized (Table 2). All the reactions were repeated at least three times. Gene expression levels were calculated relative to the housekeeping gene GAPDH using Stratagene Mx 3000P software.

Western blot

Tissues (homogenized by grinding) and treated cells were lysed with lysis solution at 4°C for 30 min, followed by centrifugation (12,000 × g at 4°C for 15 min). From each sample, 20 μg of protein was fractionated by 10% sodium dodecyl sulphate-polyacrylamide gel electrophoresis (SDS-PAGE) and transferred onto polyvinylidene difluoride (PVDF) membranes (Amersham, Beijing, China). After blocking with 5% nonfat dry milk in TBST for 1 h at room temperature, proteins were probed with specific antibodies against Zeb1, Cyclin D1, or MMP2. To assure equal loading, gels were stripped and reprobed with an anti-GAPDH antibody. Following incubation with HRP-conjugated secondary antibodies, signals were detected by chemiluminescence. All the reactions were repeated at least three times.

***In vivo* experiments**

Five- to six-week-old female, athymic nude BALB/c mice (Vital River Laboratory Animal Technology Co. Ltd., Shanghai, China) were split into three groups of six and received tail vein injections containing 2×10^6 MG63 cells in 0.1 ml saline. The following day, and once a day thereafter, the mice were given intravenous injections of naringin (5 or 10 mg/kg) or 0.9% NaCl (control). On day 16 following tumor cell injection, liver samples were collected for histological examination.

All experimental procedures involving animals were conducted in accordance with the Guide for the Care and Use of Laboratory Animals (NIH publication no. 80-23, revised 1996) and followed institutional ethical guidelines. The study was approved by the Ethics Committee at the Academic Medical Center of Shengjing Hospital of China Medical University.

Histopathology

Lung specimens were fixed with 4% paraformaldehyde. Serial sections were cut using a microtome and affixed onto positively charged slides. Tissues were deparaffinized and rehydrated through graded xylene and alcohol. The sections were lightly counterstained with hematoxylin–eosin, dehydrated through an ethanol series, cleared in xylene and mounted. Stained sections were viewed using a light microscope (400×).

Statistical analysis

All data are presented as the mean ± SD. Statistical significance between two groups of data was evaluated by Student's t test (two-tailed) using GraphPad Prism

software (GraphPad, Inc., La Jolla, CA, USA). $P < 0.05$ was considered significant.

Ethics statement and consent to participate

Research involving human subjects, human material, or human data has been performed in accordance with the Declaration of Helsinki and was approved by the Research Ethics Committee of Shengjing Hospital (R20160965).

Compliance with ethical standards

For the use of clinical materials for research purposes, written consent and approval from patients were obtained from the Shengjing Hospital of China Medical University. Patient consent was obtained in writing according to institutional regulations.

Consent to publish

We have obtained consent to publish from the participants to report individual patient data.

AUTHOR CONTRIBUTIONS

Ming He: conceived of the study and carried out molecular studies. Qiu Chuang: carried out molecular studies. Wang Jiashi: participated in the design of the study and performed statistical analysis. Li Bin: participated in the study design and coordination and helped to draft the manuscript. Wang Guangbin: conceived the study. Ji Xianglu: helped to draft the manuscript.

ACKNOWLEDGMENTS

All personnel who have contributed to this article are in the list of authors.

CONFLICTS OF INTEREST

The authors declare no conflicts of interest.

REFERENCES

1. Degnan AJ, Chung CY, Shah AJ. Quantitative diffusion-weighted magnetic resonance imaging assessment of chemotherapy treatment response of pediatric osteosarcoma and Ewing sarcoma malignant bone tumors. Clin Imaging. 2018; 47:9–13. https://doi.org/10.1016/j.clinimag.2017.08.003

2. Shi J, Fu Q, Yang P, Liu H, Ji L, Wang K. Downregulation of microRNA-15a-3p is correlated with clinical outcome and negatively regulates cancer proliferation and migration in human osteosarcoma. J Cell Biochem. 2018; 119:1215–22. https://doi.org/10.1002/jcb.26294

3. Davis JC, Daw NC, Navid F, Billups CA, Wu J, Bahrami A, Jenkins JJ, Snyder SE, Reddick WE, Santana VM, McCarville MB, Guo J, Shulkin BL. (18)F-FDG uptake during early adjuvant chemotherapy predicts histologic response in pediatric and young adult patients with osteosarcoma. J Nucl Med. 2018; 59:25–30. https://doi.org/10.2967/jnumed.117.190595

4. Raha S, Yumnam S, Hong GE, Lee HJ, Saralamma VV, Park HS, Heo JD, Lee SJ, Kim EH, Kim JA, Kim GS. Naringin induces autophagy-mediated growth inhibition by downregulating the PI3K/Akt/mTOR cascade via activation of MAPK pathways in AGS cancer cells. Int J Oncol. 2015; 47:1061–69. https://doi.org/10.3892/ijo.2015.3095

5. Yin FM, Xiao LB, Zhang Y. [Research progress on Drynaria fortunei naringin on inflammation and bone activity]. Zhongguo Gu Shang. 2015; 28:182–86.

6. Chen R, Qi QL, Wang MT, Li QY. Therapeutic potential of naringin: an overview. Pharm Biol. 2016; 54:3203–10. https://doi.org/10.1080/13880209.2016.1216131

7. Wang D, Ma W, Wang F, Dong J, Wang D, Sun B, Wang B. Stimulation of Wnt/β-Catenin Signaling to Improve Bone Development by Naringin via Interacting with AMPK and Akt. Cell Physiol Biochem. 2015; 36:1563–76. https://doi.org/10.1159/000430319

8. Ang ES, Yang X, Chen H, Liu Q, Zheng MH, Xu J. Naringin abrogates osteoclastogenesis and bone resorption via the inhibition of RANKL-induced NF-κB and ERK activation. FEBS Lett. 2011; 585:2755–62. https://doi.org/10.1016/j.febslet.2011.07.046

9. Zeng L, Zhen Y, Chen Y, Zou L, Zhang Y, Hu F, Feng J, Shen J, Wei B. Naringin inhibits growth and induces apoptosis by a mechanism dependent on reduced activation of NF κB/COX 2 caspase-1 pathway in HeLa cervical cancer cells. Int J Oncol. 2014; 45:1929–36. https://doi.org/10.3892/ijo.2014.2617

10. Kawaguchi K, Kikuchi S, Hasegawa H, Maruyama H, Morita H, Kumazawa Y. Suppression of lipopolysaccharide-induced tumor necrosis factor-release and liver injury in mice by naringin. Eur J Pharmacol. 1999; 368:245–50. https://doi.org/10.1016/S0014-2999(98)00867-X

11. Guo B, Zhang Y, Hui Q, Wang H, Tao K. Naringin suppresses the metabolism of A375 cells by inhibiting the phosphorylation of c-Src. Tumour Biol.

2016; 37:3841–50. https://doi.org/10.1007/s13277-015-4235-z

12. Cai L, Wu H, Tu C, Wen X, Zhou B. Naringin inhibits ovarian tumor growth by promoting apoptosis: An in vivo study. Oncol Lett. 2018; 16:59–64.

13. Aigner K, Dampier B, Descovich L, Mikula M, Sultan A, Schreiber M, Mikulits W, Brabletz T, Strand D, Obrist P, Sommergruber W, Schweifer N, Wernitznig A, et al. The transcription factor ZEB1 (deltaEF1) promotes tumour cell dedifferentiation by repressing master regulators of epithelial polarity. Oncogene. 2007; 26:6979–88. https://doi.org/10.1038/sj.onc.1210508

14. Browne G, Sayan AE, Tulchinsky E. ZEB proteins link cell motility with cell cycle control and cell survival in cancer. Cell Cycle. 2010; 9:886–91. https://doi.org/10.4161/cc.9.5.10839

15. Caramel J, Ligier M, Puisieux A. Pleiotropic Roles for ZEB1 in Cancer. Cancer Res. 2018; 78:30–35. https://doi.org/10.1158/0008-5472.CAN-17-2476

16. Wang M, He SF, Liu LL, Sun XX, Yang F, Ge Q, Wong WK, Meng JY. Potential role of ZEB1 as a DNA repair regulator in colorectal cancer cells revealed by cancer-associated promoter profiling. Oncol Rep. 2017; 38:1941–48. https://doi.org/10.3892/or.2017.5888

17. Hanrahan K, O'Neill A, Prencipe M, Bugler J, Murphy L, Fabre A, Puhr M, Culig Z, Murphy K, Watson RW. The role of epithelial-mesenchymal transition drivers ZEB1 and ZEB2 in mediating docetaxel-resistant prostate cancer. Mol Oncol. 2017; 11:251–65. https://doi.org/10.1002/1878-0261.12030

18. Bae GY, Choi SJ, Lee JS, Jo J, Lee J, Kim J, Cha HJ. Loss of E-cadherin activates EGFR-MEK/ERK signaling, which promotes invasion via the ZEB1/MMP2 axis in non-small cell lung cancer. Oncotarget. 2013; 4:2512–22. https://doi.org/10.18632/oncotarget.1463

19. Shan Y, Zhang L, Bao Y, Li B, He C, Gao M, Feng X, Xu W, Zhang X, Wang S. Epithelial-mesenchymal transition, a novel target of sulforaphane via COX-2/MMP2, 9/Snail, ZEB1 and miR-200c/ZEB1 pathways in human bladder cancer cells. J Nutr Biochem. 2013; 24:1062–69. https://doi.org/10.1016/j.jnutbio.2012.08.004

20. Wang H, Xing D, Ren D, Feng W, Chen Y, Zhao Z, Xiao Z, Peng Z. MicroRNA 643 regulates the expression of ZEB1 and inhibits tumorigenesis in osteosarcoma. Mol Med Rep. 2017; 16:5157–64. https://doi.org/10.3892/mmr.2017.7273

21. Yi L, Liu M, Tang Z. MicroRNA 130a inhibits growth and metastasis of osteosarcoma cells by directly targeting ZEB1. Mol Med Rep. 2017; 16:3606–12. https://doi.org/10.3892/mmr.2017.6968

22. Li H, Yang B, Huang J, Xiang T, Yin X, Wan J, Luo F, Zhang L, Li H, Ren G. Naringin inhibits growth potential of human triple-negative breast cancer cells by targeting β-catenin signaling pathway. Toxicol Lett. 2013; 220:219–28. https://doi.org/10.1016/j.toxlet.2013.05.006

23. Wang H, Li C, Li J, Zhu Y, Jia Y, Zhang Y, Zhang X, Li W, Cui L, Li W, Liu Y. Naringin enhances osteogenic differentiation through the activation of ERK signaling in human bone marrow mesenchymal stem cells. Iran J Basic Med Sci. 2017; 20:408–14.

24. Wong RW, Rabie AB. Effect of naringin on bone cells. J Orthop Res. 2006; 24:2045–50. https://doi.org/10.1002/jor.20279

25. Zhang X, Zhang Z, Zhang Q, Zhang Q, Sun P, Xiang R, Ren G, Yang S. ZEB1 confers chemotherapeutic resistance to breast cancer by activating ATM. Cell Death Dis. 2018; 9:57. https://doi.org/10.1038/s41419-017-0087-3

26. Yu P, Shen X, Yang W, Zhang Y, Liu C, Huang T. ZEB1 stimulates breast cancer growth by up-regulating hTERT expression. Biochem Biophys Res Commun. 2018; 495:2505–11. https://doi.org/10.1016/j.bbrc.2017.12.139

27. Langer EM, Kendsersky ND, Daniel CJ, Kuziel GM, Pelz C, Murphy KM, Capecchi MR, Sears RC. ZEB1-repressed microRNAs inhibit autocrine signaling that promotes vascular mimicry of breast cancer cells. Oncogene. 2018; 37:1005–19. https://doi.org/10.1038/onc.2017.356

28. Ramesh E, Alshatwi AA. Naringin induces death receptor and mitochondria-mediated apoptosis in human cervical cancer (SiHa) cells. Food Chem Toxicol. 2013; 51:97–105. https://doi.org/10.1016/j.fct.2012.07.033

29. Liu Y, El-Naggar S, Darling DS, Higashi Y, Dean DC. Zeb1 links epithelial-mesenchymal transition and cellular senescence. Development. 2008; 135:579–88. https://doi.org/10.1242/dev.007047

Research Paper

Long noncoding RNA B3GALT5-AS1 suppresses colon cancer liver metastasis via repressing microRNA-203

Liang Wang[1,*], Zhewei Wei[1,*], Kaiming Wu[1], Weigang Dai[1], Changhua Zhang[1], Jianjun Peng[1], Yulong He[1]

[1]Department of Gastrointestinal Surgery, The First Affiliated Hospital, Sun Yat-sen University, Guangzhou 510080, China
*Equal contribution

Correspondence to: Yulong He; **email:** yulong_he123@163.com
Keywords: long noncoding RNA, colon cancer, liver metastasis, microRNA, epithelial-to-mesenchymal transition
Received: August 28, 2018 **Accepted:** October 27, 2018 **Published:** December 10, 2018

Copyright: Wang et al. This is an open-access article distributed under the terms of the Creative Commons Attribution License (CC BY 3.0), which permits unrestricted use, distribution, and reproduction in any medium, provided the original author and source are credited.

ABSTRACT

Long noncoding RNAs (lncRNAs) are implicated in various cancers, including colon cancer. Liver metastasis is the main cause of colon cancer-related death. However, the roles of lncRNAs in colon cancer liver metastasis are still largely unclear. In this study, we identified a novel lncRNA B3GALT5-AS1, which is reduced in colon cancer tissues and further reduced in colon cancer liver metastasis tissues. Reduced expression of B3GALT5-AS1 is associated with liver metastasis and poor outcome of colon cancer patients. Gain-of-function and loss-of-function assays revealed that B3GALT5-AS1 inhibited proliferation but promoted migration and invasion of colon cancer cells. Further investigation revealed that B3GALT5-AS1 directly bound to the promoter of *miRNA-203*, repressed *miR-203* expression, upregulated miR-203 targets ZEB2 and SNAI2, and induced epithelial-to-mesenchymal transition (EMT). *In vivo* study revealed that B3GALT5-AS1 suppressed colon cancer liver metastasis via its binding on *miR-203* promoter and the repression of miR-203. miR-203 is increased and epithelial phenotype is preferred in colon cancer liver metastasis tissues. Collectively, our data revealed the suppressive roles of B3GALT5-AS1/miR-203/EMT regulation axis in colon cancer liver metastasis. Our data suggested that the activating B3GALT5-AS1/miR-203/EMT axis may be potential therapeutic strategy for colon cancer liver metastasis.

INTRODUCTION

Colon cancer is one of the most prevalent malignancies and causes of cancer-related deaths worldwide [1]. Distant metastasis, especially liver metastasis accounts for the major cause of deaths of colon cancer patients [2]. Most colon cancer patients with liver metastasis are not suitable for surgery [3]. In addition, there is a lack of effective treatments for colon cancer patients with liver metastasis [4]. Thus, the prognoses of colon cancers with liver metastases are very poor with a 5-year survival rate of 10-15% [5]. Therefore, further revealing critical molecular mechanisms driving colon cancer liver metastasis and developing more effective therapies for colon cancers with liver metastasis are urgently needed.

Colon cancer liver metastasis is a complex and multistep process [6]. Many molecules are contradictorily involved in this process [7, 8]. The detailed molecular mechanisms mediating the process are largely unclear [9]. Epithelial-to-mesenchymal transition (EMT) plays critical roles during the process of colon liver metastasis [10, 11]. EMT permits the migration and invasion of various tumor cells, which is beneficial for the early invasion of primary cancers

[12]. EMT may also discount proliferative capacity of cancer cells [13]. In the distant metastatic locations, disseminated cancer cells require mesenchymal-to-epithelial transition (MET), a reverse process of EMT, to settle and growth [7]. MET enables metastatic cancer cells to acquire epithelial phenotype and colonize in distant organs [14-16]. Epithelial marker E-cadherin is reported to be elevated in lymph node metastases and distant metastases relative to primary tumors [17]. Therefore, identifying critical EMT-MET regulators during colon cancer liver metastasis cascade are beneficial for appropriate therapy of colon cancer liver metastasis.

Genomic and transcriptomic sequencings have demonstrated that although 70% of human genome transcribe RNA molecules, only about 2% of human genome encode proteins [18]. Therefore, most of human transcriptome are non-coding RNAs [19]. Many of these non-coding RNAs have critical regulatory roles in cancers [20]. Long noncoding RNA (lncRNA) is a class of RNA transcript with limited protein coding ability and greater than 200 nucleotides in length [21]. Accumulating evidences displayed that lncRNAs are commonly deregulated in many pathological states and have important roles during various pathophysiological processes [22-27]. As to colon cancer, several lncRNAs are revealed to regulate colon cancer cells proliferation, apoptosis, migration, invasion, chemoresistance, and so on, such as lncRNA N-BLR, GAS5, HNF1A-AS1, CRNDE, LINC01133 [28-32]. However, the roles of lncRNAs in EMT and liver metastasis of colon cancer are largely unclear.

microRNA (miRNA) is another class of non-coding RNA transcript with 20-25 nucleotides in length [33]. Similarly, miRNAs are reported to have important regulatory roles during various pathophysiological processes [34-38]. Several miRNAs are well-known EMT regulators through repressing EMT-inducing transcription factors [39, 40]. miR-200 family have been reported to inhibit EMT by directly repressing ZEB1 and ZEB2 [39, 41-43]. miR-203 has been reported to inhibit EMT via repressing ZEB2 and SNAI2 [44, 45]. However, miR-203 has different roles in different cancers [40, 46-49]. miR-203 is revealed to exert tumor suppressive roles in prostate, lung, nasopharyngeal, and colorectal cancer [50-52]. However, miR-203 is also revealed to be increased in colorectal cancer tissues compared with adjacent normal mucosa [46]. Furthermore, miR-203 is also revealed to be upregulated in colorectal cancer liver metastasis tissues compared with primary colorectal cancer tissues [46]. Meta-analysis indicated that the upregulation of miR-203 indicted worse prognosis in colorectal cancer [49]. These controversial results suggested that more investigations of the expression and roles of miR-203 in EMT and liver metastasis of colon cancer are needed.

In this study, using public available RNA-seq dataset of colon cancer [53], we identified that lncRNA B3GALT5-AS1 is reduced in colon cancer tissues, and further reduced in colon cancer liver metastasis tissues. In clinical specimens, we further confirmed the expression pattern of B3GALT5-AS1 in colon cancer and liver metastasis. Furthermore, we confirmed the negative correlation between miR-203 and B3GALT5-AS1 expression pattern in colon cancer liver metastasis. In addition, biological roles of B3GALT5-AS1 and miR-203 in EMT and liver metastasis of colon cancer were explored using gain-of-function and loss-of-function experiments.

RESULTS

B3GALT5-AS1 is reduced in colon cancer and further reduced in liver metastasis tissues

Analyzing the RNA-seq dataset from GSE50760 which containing 18 normal colonic epithelium, 18 primary colorectal cancers, and 18 metastasized cancers in liver, we noted that lncRNA B3GALT5-AS1 (C21orf88) is reduced in primary colorectal cancers compared with normal colonic epithelium and is further reduced in metastasized cancers in liver (Fig. 1A). To further explore B3GALT5-AS1 expression pattern in human colon cancer, we collected 64 pairs of primary colon cancer tissues and corresponding adjacent colonic epithelium tissues. Through searching the National Center for Biotechnology Information (NCBI), we found two transcript variants of B3GALT5-AS1. qRT-PCR results displayed that transcript variant 2 (NCBI Reference Sequence: NR_026543.1) is the main transcript of B3GALT5-AS1 in both normal colon tissues and colon cancer tissues (Figure S1). Furthermore, transcript variant 2 is reduced in colon cancer, and while transcript variant 1 doesn't have significant difference between colon cancer and normal colonic epithelium tissues (Figure S1). Therefore, we focused our attention on transcript variant 2 of B3GALT5-AS1.

The expression of B3GALT5-AS1 in 64 pairs of primary colon cancer tissues and corresponding normal colonic epithelium tissues was measured via qRT-PCR. As displayed in Fig. 1B, B3GALT5-AS1 is markedly reduced in primary colon cancer tissues compared with colonic epithelium tissues. Analyses of the association between the expression of B3GALT5-AS1 and clinicopathologic features of colon cancers displayed that lower B3GALT5-AS1 expression is correlated with larger tumor size, distant metastasis, and advanced

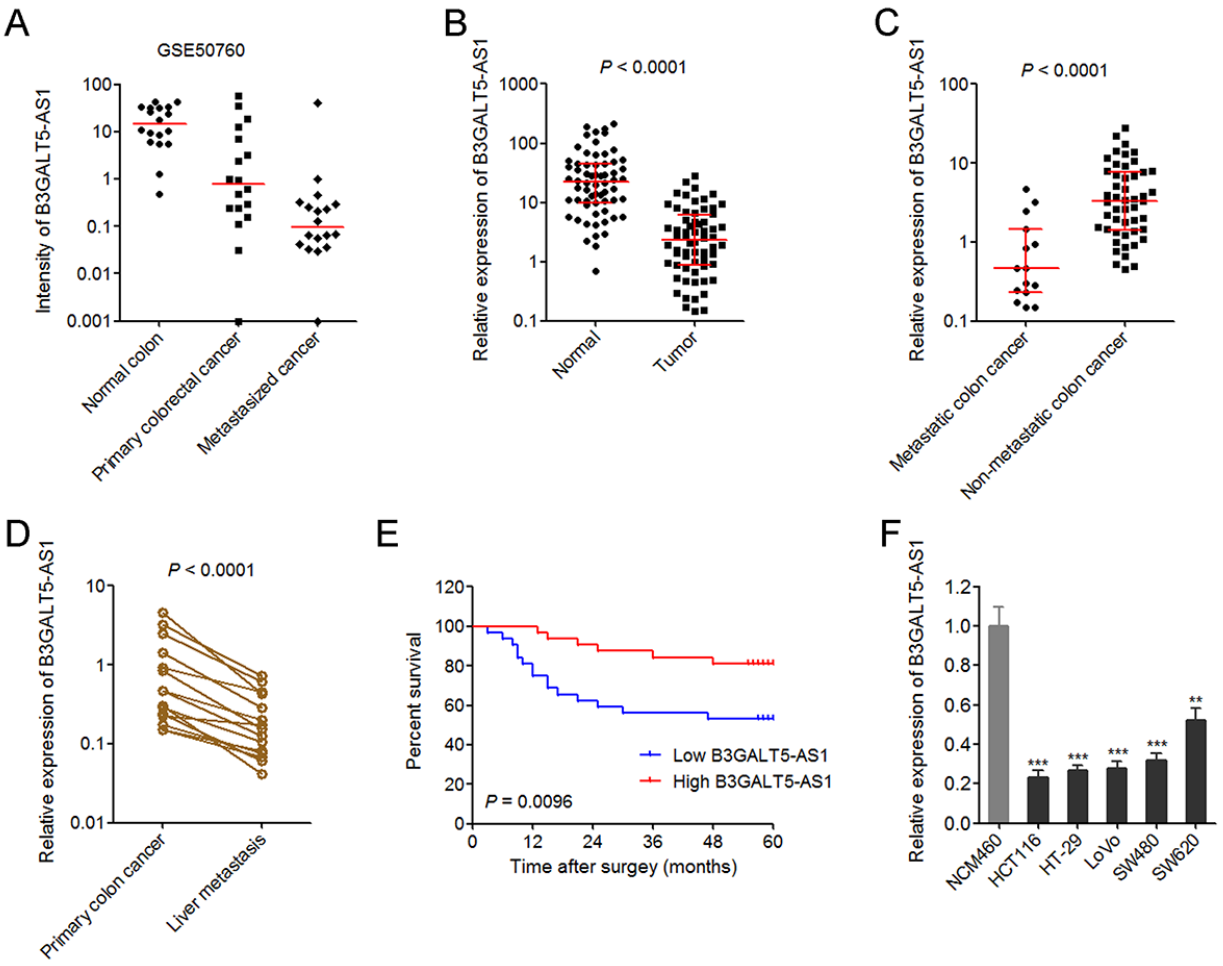

Figure 1. The expression pattern of B3GALT5-AS1 in colon cancer and its association with prognosis. (**A**) The expression intensity of B3GALT5-AS1 in 18 pairs of normal colonic epithelium, primary colorectal cancers, and metastasized cancers in liver from GSE50760. (**B**) The expression of B3GALT5-AS1 in 64 pairs of primary colon cancer tissues and adjacent colonic epithelium tissues was detected using qRT-PCR. $P < 0.0001$, Wilcoxon signed-rank test. (**C**) The expression of B3GALT5-AS1 in 15 colon cancer tissues with metastasis and 49 colon cancer tissues without metastasis. $P < 0.0001$, Mann-Whitney test. (**D**) The expression of B3GALT5-AS1 in 15 pairs of primary colon cancer tissues and corresponding liver metastasis tissues was measured using qRT-PCR. $P < 0.0001$, Wilcoxon signed-rank test. (**E**) Kaplan-Meier survival analysis of the correlation between B3GALT5-AS1 expression level and overall survival of 64 colon cancer patients. The median expression level of B3GALT5-AS1 was used as cut-off. $P = 0.0096$, Log-rank test. (**F**) The expression of B3GALT5-AS1 in normal colonic epithelial cell line NCM460 and colon cancer cell lines HCT116, HT-29, LoVo, SW480 and SW620 was measured using qRT-PCR. Results are displayed as mean ± s.d. of three independent experiments. $^{**}P < 0.01$, $^{***}P < 0.001$, Student's *t*-test.

AJCC stages (Table 1). To confirm the association between B3GALT5-AS1 expression and distant metastasis, we re-analyzed the expression of B3GALT5-AS1 in colon cancer tissues with (n = 15) or without (n = 49) metastasis. The results displayed that B3GALT5-AS1 is significantly reduced in primary colon cancer tissues with metastasis compared with that without metastasis (Fig. 1C). For these 15 colon cancers with metastasis, we collected their corresponding liver metastasis tissues. The expression of B3GALT5-AS1 in these 15 pairs of primary colon cancer tissues and corresponding liver metastasis tissues was measured via qRT-PCR. As displayed in Fig. 1D, B3GALT5-AS1 is markedly reduced in liver metastasis tissues compared with primary colon cancer tissues. Kaplan-Meier survival analysis of these 64 colon cancer patients displayed that colon cancer patients with lower B3GALT5-AS1 expression had worse survival than those with higher B3GALT5-AS1 expression (Fig. 1E). Moreover, the expression of B3GALT5-AS1 in normal colonic epithelial cell line NCM460 and colon cancer cell lines HCT116, HT-29, LoVo, SW480 and SW620 was measured by qRT-PCR. As displayed in Fig. 1F, B3GALT5-AS1 was also significantly reduced in colon

Table 1. Correlation between B3GALT5-AS1 expression and clinicopathologic features of colon cancers.

Features	N of cases	B3GALT5-AS1		*P*-value
		Low	High	
Total	64	32	32	
Age (years)				0.316
>65	34	19	15	
≤65	30	13	17	
Gender				0.802
Male	31	15	16	
Female	33	17	16	
Location				0.802
Right	35	17	18	
Left	29	15	14	
Tumor size (cm)				**0.002**
>3	36	24	12	
≤3	28	8	20	
Depth of invasion				0.757
T1	2	1	1	
T2	9	6	3	
T3	25	12	13	
T4	28	13	15	
Lymph node metastasis				0.523
N0	25	12	13	
N1	22	13	9	
N2	17	7	10	
Distant metastasis				**0.008**
M0	49	20	29	
M1	15	12	3	
AJCC stage				**0.043**
I	8	4	4	
II	17	8	9	
III	24	8	16	
IV	15	12	3	

The median expression level of B3GALT5-AS1 was used as cut-off.
P-value was acquired by Pearson chi-square tests.

cancer cell lines compared with normal colonic epithelial cell line. These data suggested that B3GALT5-AS1 is reduced in colon cancer and further reduced in liver metastasis tissues. Low expression of B3GALT5-AS1 indicts poor outcome of colon cancers.

B3GALT5-AS1 suppresses colon cancer cell proliferation

To explore the effects of B3GALT5-AS1, we stably overexpressed B3GALT5-AS1 in HCT116 cells by transfecting B3GALT5-AS1 overexpression plasmid (Fig. 2A), and stably knocked-down B3GALT5-AS1 in SW620 cells by transfecting two independent shRNAs against B3GALT5-AS1 (Fig. 2B). Glo cell viability assays displayed that B3GALT5-AS1 overexpression markedly reduced cell viability, and while B3GALT5-AS1 knockdown significantly upregulated cell viability of colon cancer cells (Fig. 2C, D). EdU incorporation assays further displayed that enhanced expression of B3GALT5-AS1 markedly suppressed cell proliferation, and while B3GALT5-AS1 knockdown markedly promoted proliferation of colon cancer cells (Fig. 2E, F). Due to B3GALT5-AS1 is high expressed in normal colonic epithelial cell line NCM460, we further determined the effects of B3GALT5-AS1 knockdown on NCM460 cell viability and cell proliferation using Glo cell viability assay and EdU incorporation assay. As displayed in Figure S2A-C, transient knockdown of B3GALT5-AS1 also promoted NCM460 cell proliferation. Collectively, these data suggested that B3GALT5-AS1 suppresses cell viability and cell proliferation of colon cancer and colonic epithelial cells.

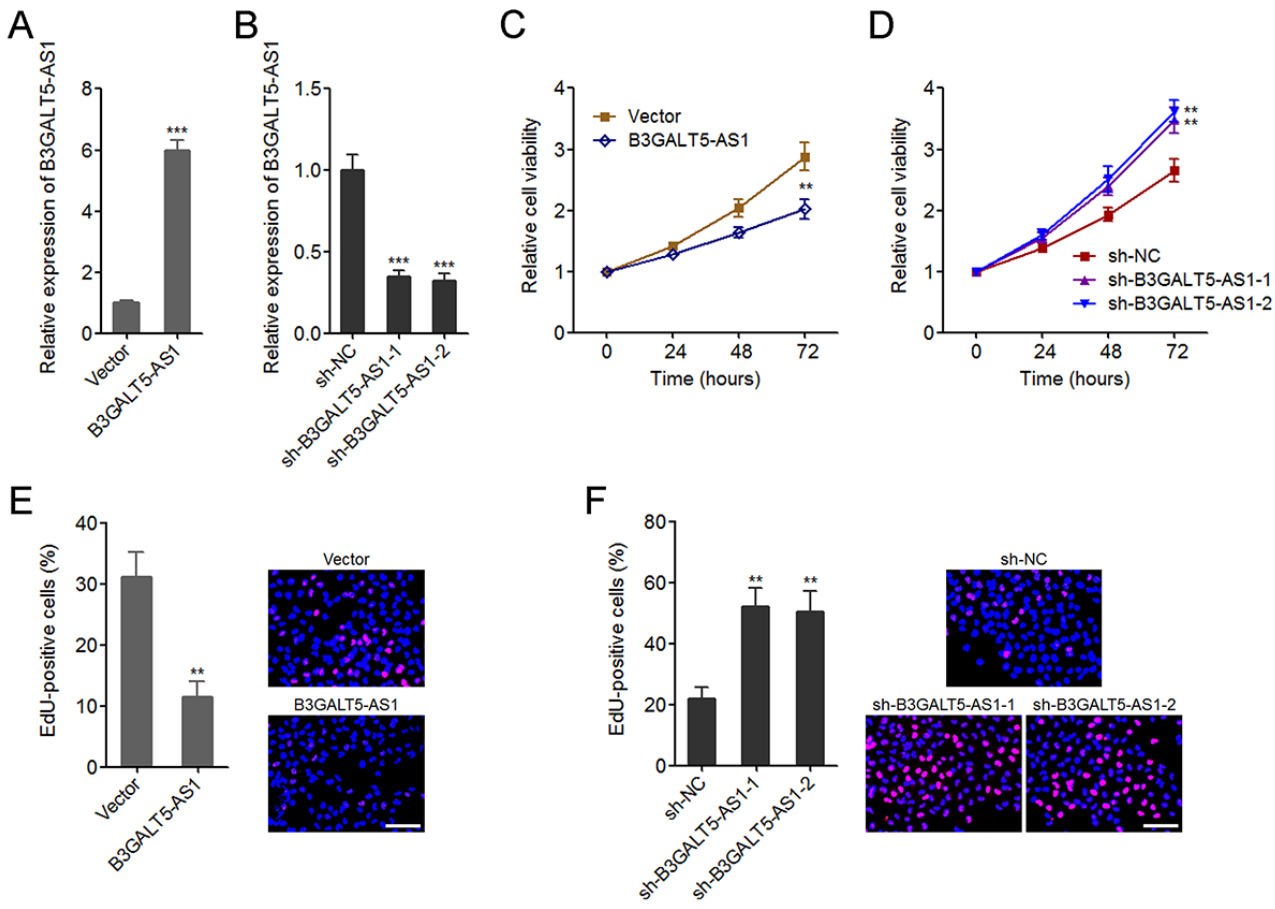

Figure 2. B3GALT5-AS1 suppressed colon cancer cell proliferation. (**A**) The expression of B3GALT5-AS1 in B3GALT5-AS1 stably overexpressed and control HCT116 cells was detected using qRT-PCR. (**B**) The expression of B3GALT5-AS1 in B3GALT5-AS1 stably depleted and control SW620 cells was detected using qRT-PCR. (**C**) Cell viability of B3GALT5-AS1 stably overexpressed and control HCT116 cells was detected using Glo cell viability assay. (**D**) Cell viability of B3GALT5-AS1 stably depleted and control SW620 cells was detected using Glo cell viability assay. (**E**) Cell proliferation of B3GALT5-AS1 stably overexpressed and control HCT116 cells was detected using EdU incorporation assay. The red color indicts EdU-positive cells. Scale bars = 100 μm. (**F**) Cell proliferation of B3GALT5-AS1 stably depleted and control SW620 cells was detected using EdU incorporation assay. The red color indicts EdU-positive cells. Scale bars = 100 μm. Results are displayed as mean ± s.d. of three independent experiments. $^{**}P < 0.01$, $^{***}P < 0.001$, Student's *t*-test.

B3GALT5-AS1 promotes colon cancer cell migration, invasion and EMT

We then further explored the roles of B3GALT5-AS1 in migration and invasion of colon cancer cells. Transwell migration assays displayed that B3GALT5-AS1 overexpression promoted cell migration, and while B3GALT5-AS1 knockdown inhibited cell migration of colon cancer cells (Fig. 3A, B). Transwell invasion assays displayed that enhanced expression of B3GALT5-AS1 promoted invasion, and while B3GALT5-AS1 knockdown repressed invasion of colon cancer cells (Fig. 3C, D). Similarly, B3GALT5-AS1 knockdown also repressed migration and invasion of NCM460 cells (Figure S2D, E). The opposing effects of B3GALT5-AS1 on cell proliferation and migration, invasion implied that EMT may mediate the roles of B3GALT5-AS1 in colon cancer. Thus, we further explored the roles of B3GALT5-AS1 in EMT of colon cancer cells. The results displayed that B3GALT5-AS1 overexpression reduced the expression of epithelial marker E-cadherin and increased mesenchymal marker N-cadherin (Fig. 3E, F), suggesting that B3GALT5-AS1 overexpression induced EMT of colon cancer cells. B3GALT5-AS1 knockdown upregulated the expression of E-cadherin and downregulated N-cadherin (Fig. 3G, H), suggesting that B3GALT5-AS1 knockdown repressed EMT of colon cancer cells. Similarly, B3GALT5-AS1 knockdown also repressed EMT of NCM460 cells (Figure S2F). These data demonstrated that B3GALT5-AS1 promotes migration, invasion and EMT of colon cancer and colonic epithelial cells.

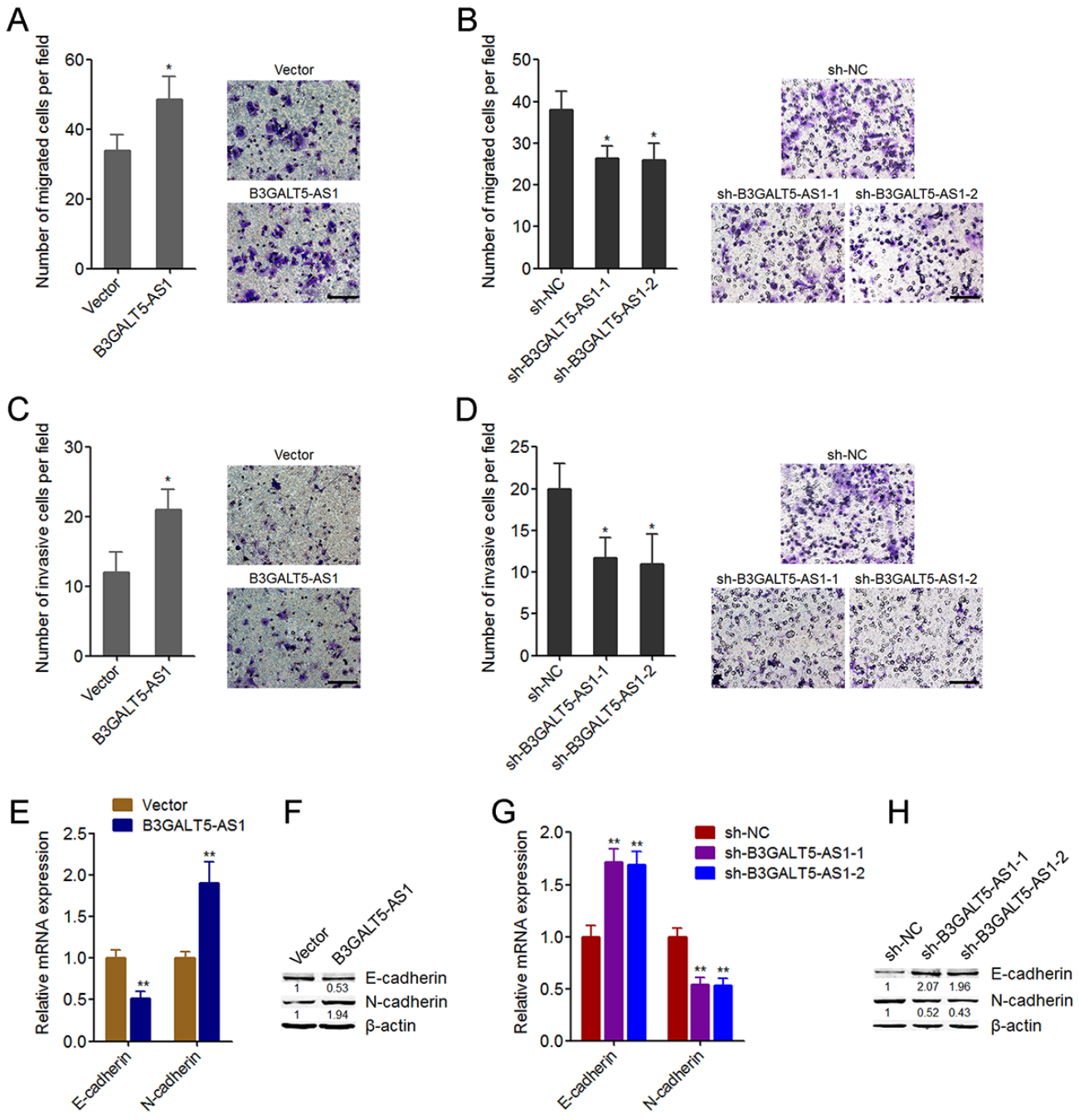

Figure 3. B3GALT5-AS1 promoted migration, invasion, and EMT of colon cancer cells. (**A**) Cell migration of B3GALT5-AS1 stably overexpressed and control HCT116 cells was detected using transwell migration assay. Scale bars = 100 μm. (**B**) Cell migration of B3GALT5-AS1 stably depleted and control SW620 cells was detected using transwell migration assay. Scale bars = 100 μm. (**C**) Cell invasion of B3GALT5-AS1 stably overexpressed and control HCT116 cells was detected using transwell invasion assay. Scale bars = 100 μm. (**D**) Cell invasion of B3GALT5-AS1 stably depleted and control SW620 cells was detected using transwell invasion assay. Scale bars = 100 μm. (**E**) E-cadherin and N-cadherin mRNA levels in B3GALT5-AS1 stably overexpressed and control HCT116 cells were detected using qRT-PCR. (**F**) E-cadherin and N-cadherin protein levels in B3GALT5-AS1 stably overexpressed and control HCT116 cells were detected using western blot. (**G**) E-cadherin and N-cadherin mRNA levels in B3GALT5-AS1 stably depleted and control SW620 cells were detected using qRT-PCR. (**H**) E-cadherin and N-cadherin protein levels in B3GALT5-AS1 stably depleted and control SW620 cells were detected using western blot. Results are displayed as mean ± s.d. of three independent experiments. **P* < 0.05, ***P* < 0.01, Student's *t*-test.

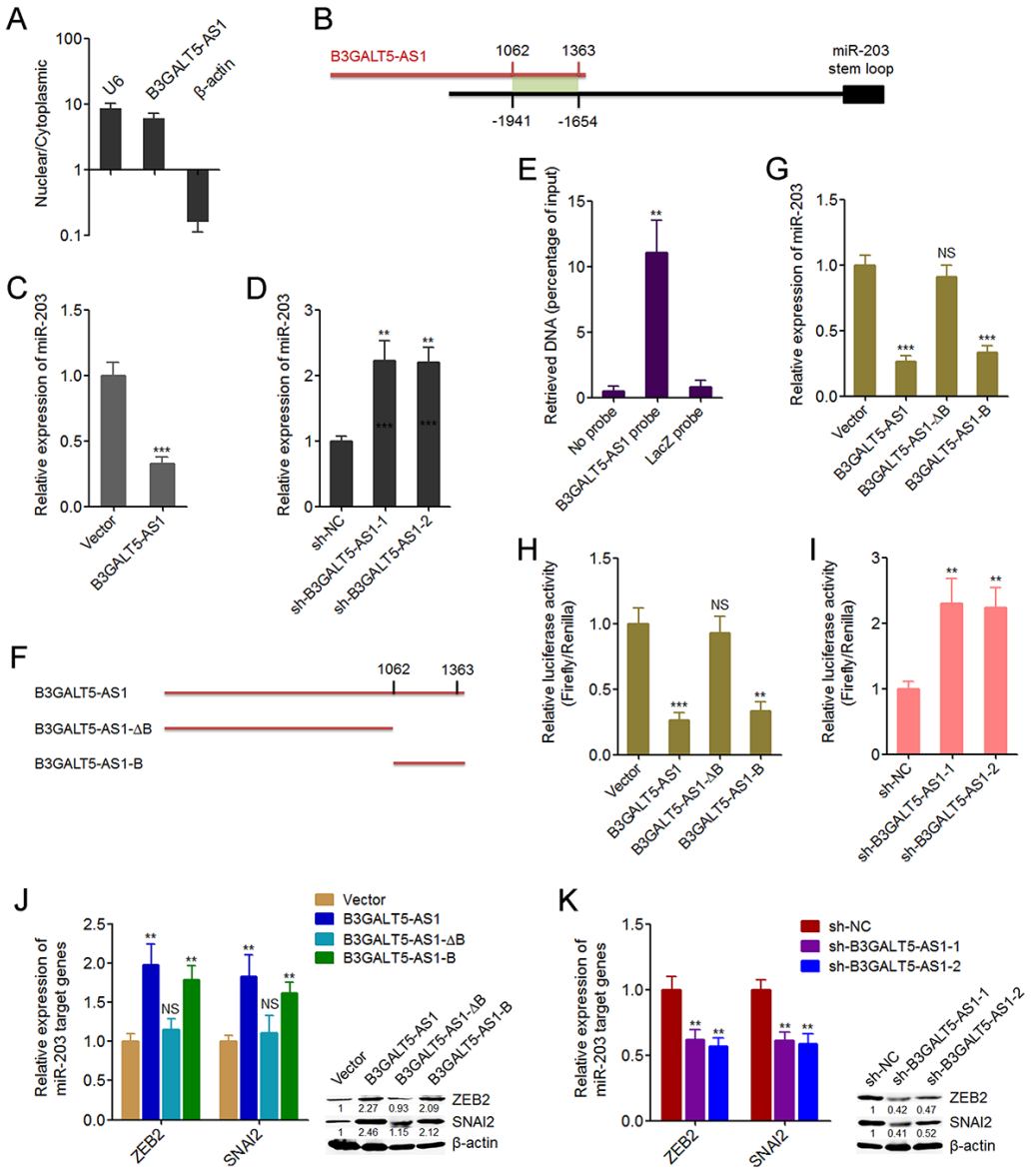

Figure 4. B3GALT5-AS1 bound to the promoter of *miR-203* and repressed the expression of miR-203. (**A**) The subcellular distribution of B3GALT5-AS1 in the cytoplasmic and nuclear fractions of HCT116 cells was evaluated using cytoplasmic and nuclear RNA isolation followed by qRT-PCR.β-actin and U6 were used as cytoplasmic and nuclear controls, respectively. (**B**) Schematic outline of the predicted interaction sites between B3GALT5-AS1 and the promoter of *miR-203*. (**C**) The expression of miR-203 in B3GALT5-AS1 stably overexpressed and control HCT116 cells was detected using qRT-PCR. (**D**) The expression of miR-203 in B3GALT5-AS1 stably depleted and control SW620 cells was detected using qRT-PCR. (**E**) ChIRP assays in HCT116 cells were carried out with anti-sense probe sets specific for B3GALT5-AS1 or LacZ (negative control). The enriched DNA was measured using qRT-PCR with specific primers against *miR-203* promoter. (**F**) Schematic outline of the constructed different depletion transcripts of B3GALT5-AS1. (**G**) After transient transfections of the different B3GALT5-AS1 expressing plasmids into HCT116 cells, miR-203 expression was measured using qRT-PCR. (**H**) After transient co-transfection of the firefly luciferase reporter containing the promoter of *miR-203*, renilla luciferase expression plasmid pRL-TK, and the different B3GALT5-AS1 expression plasmids into HCT116 cells, luciferase activities were detected using dual luciferase reporter assays. Results are displayed as the relative ratio of firefly luciferase activity to renilla luciferase activity. (**I**) After transient co-transfection of the firefly luciferase reporter containing the promoter of *miR-203* and pRL-TK into B3GALT5-AS1 stably depleted and control SW620 cells, luciferase activities were measured by dual luciferase reporter assays. Results are shown as the relative ratio of firefly luciferase activity to renilla luciferase activity. (**J**) After transient transfections of the different B3GALT5-AS1 expressing plasmids into HCT116 cells, the expression of ZEB2 and SNAI2 was detected using qRT-PCR and western blot. (**K**) The expression of ZEB2 and SNAI2 in B3GALT5-AS1 stably depleted and control SW620 cells was detected using qRT-PCR and western blot. Data are displayed as mean ± s.d. of three independent experiments. ***P* < 0.01, ****P* < 0.001, NS, not significant, Student's *t*-test.

B3GALT5-AS1 directly binds the promoter of *miR-203* and represses the expression of *miR-203*

To investigate the underpinning mechanism mediating the roles of B3GALT5-AS1 in colon cancer, we first confirmed the subcellular distribution of B3GALT5-AS1 in colon cancer cells using cytoplasmic and nuclear RNA purification. As displayed in Fig. 4A, B3GALT5-AS1 was dominantly localized in the nucleus. Several miRNAs are reported to be involved in EMT [11]. miR-203, miR-200 family (including miR-200a, miR-200b, miR-200c, miR-141, miR-429), miR-34a, miR-9 are reported to inhibit EMT [11, 44]. miR-29a is reported to promote EMT. Therefore, we predicted the potential roles of B3GALT5-AS1 on these miRNAs via searching the potential binding sites of B3GALT5-AS1 on the promoters of these miRNAs using Basic Local Alignment Search Tool (BLAST) (https://blast.ncbi.nlm.nih.gov/Blast.cgi). As displayed in Figure S3, the promoter of *miR-203* has the strongest binding potential with B3GALT5-AS1. The predicted interaction region covers 1062-1363 nucleotides of B3GALT5-AS1 (Fig. 4B). Then, we investigated whether B3GALT5-AS1 regulates miR-203 expression in colon cancer cells. qRT-PCR results displayed that B3GALT5-AS1 overexpression significantly suppressed miR-203 expression, and while depletion of B3GALT5-AS1 markedly upregulated miR-203 expression (Fig. 4C, D). ChIRP assays displayed that *miR-203* promoter was specifically enriched by B3GALT5-AS1 antisense probe sets (Fig. 4E). Next, we expressed the truncated B3GALT5-AS1 fragments with or without the binding sites, which encode 1062-1363 nucleotides or 1-1061 nucleotides of B3GALT5-AS1, respectively (Fig. 4F). Transient transfections of the full-length or truncated B3GALT5-AS1 expression plasmids into HCT116 cells revealed that the depletion of the binding sites abolished the repressive roles of B3GALT5-AS1 on miR-203 expression, and while only the binding sites of B3GALT5-AS1 could sufficiently repress miR-203 expression (Fig. 4G). These results suggested that the binding region is responsible for the effects of B3GALT5-AS1 on miR-203. To further investigate whether B3GALT5-AS1 regulates the promoter activity of *miR-203*, we cloned *miR-203* promoter containing the binding region into luciferase reporter. Dual luciferase reporter assays displayed that B3GALT5-AS1 overexpression significantly downregulated the promoter activity of *miR-203*, which was abolished by the depletion of binding sites of B3GALT5-AS1, and while only the binding sites of B3GALT5-AS1 could sufficiently downregulated *miR-203* promoter activity (Fig. 4H). Conversely, B3GALT5-AS1 knockdown significantly upregulated *miR-203* promoter activity (Fig. 4I). miR-203 is reported to inhibit EMT via repressing the expression of EMT-inducing transcription factor ZEB2 and SNAI2 [44, 45]. Therefore, we further investigate the roles of B3GALT5-AS1 on miR-203 targets ZEB2 and SNAI2. Transient transfections of the different B3GALT5-AS1 expression plasmids into HCT116 cells demonstrated that B3GALT5-AS1 overexpression upregulated ZEB2 and SNAI2, which were abolished by the depletion of binding sites of B3GALT5-AS1, and while only the binding sites of B3GALT5-AS1 could sufficiently upregulated ZEB2 and SNAI2 (Fig. 4J). Conversely, B3GALT5-AS1 knockdown downregulated ZEB2 and SNAI2 (Fig. 4K). All these results suggested that B3GALT5-AS1 inhibited miR-203 and upregulated miR-203 targets ZEB2 and SNAI2 via interacting with *miR-203* promoter.

miR-203 is increased in colon cancer and further increased in liver metastasis

To explore whether the regulation of miR-203 and EMT by B3GALT5-AS1 exists *in vivo*, we measured miR-203 expression in the same 64 pairs of primary colon cancer tissues and corresponding adjacent colonic epithelium tissues used in Fig. 1B. As displayed in Fig. 5A, miR-203 was markedly upregulated in colon cancer tissues compared with colonic epithelium tissues. Analyses of the correlation between the expression of B3GALT5-AS1 and miR-203 in these 64 colon cancer tissues displayed that the expression of miR-203 was inversely correlated with that of B3GALT5-AS1 in colon cancer tissues (Fig. 5B). miR-203 expression in 15 pairs of primary colon cancer tissues and corresponding liver metastasis tissues used in Fig. 1D was also detected. As displayed in Fig. 5C, miR-203 was significantly upregulated in liver metastasis tissues compared with primary colon cancer tissues. In addition, the expressions of ZEB2 and SNAI2 were measured in the same 15 pairs of primary colon cancer tissues and corresponding liver metastasis tissues. The results displayed that ZEB2 and SNAI2 were both downregulated in liver metastasis tissues compared with primary colon cancer tissues (Fig. 5D, E). The expression of EMT markers E-cadherin and N-cadherin were also measured in these paired primary colon cancer tissues and liver metastasis tissues. As displayed in Fig. 5F, G, E-cadherin was upregulated and while N-cadherin was downregulated in liver metastasis tissues compared with primary colon cancer tissues. These data suggested that miR-203 is increased in colon cancer and further increased in liver metastasis tissues, which is inversely associated with B3GALT5-AS1. ZEB2 and SNAI2 were reduced, and epithelial feature was preferred in liver metastasis tissues.

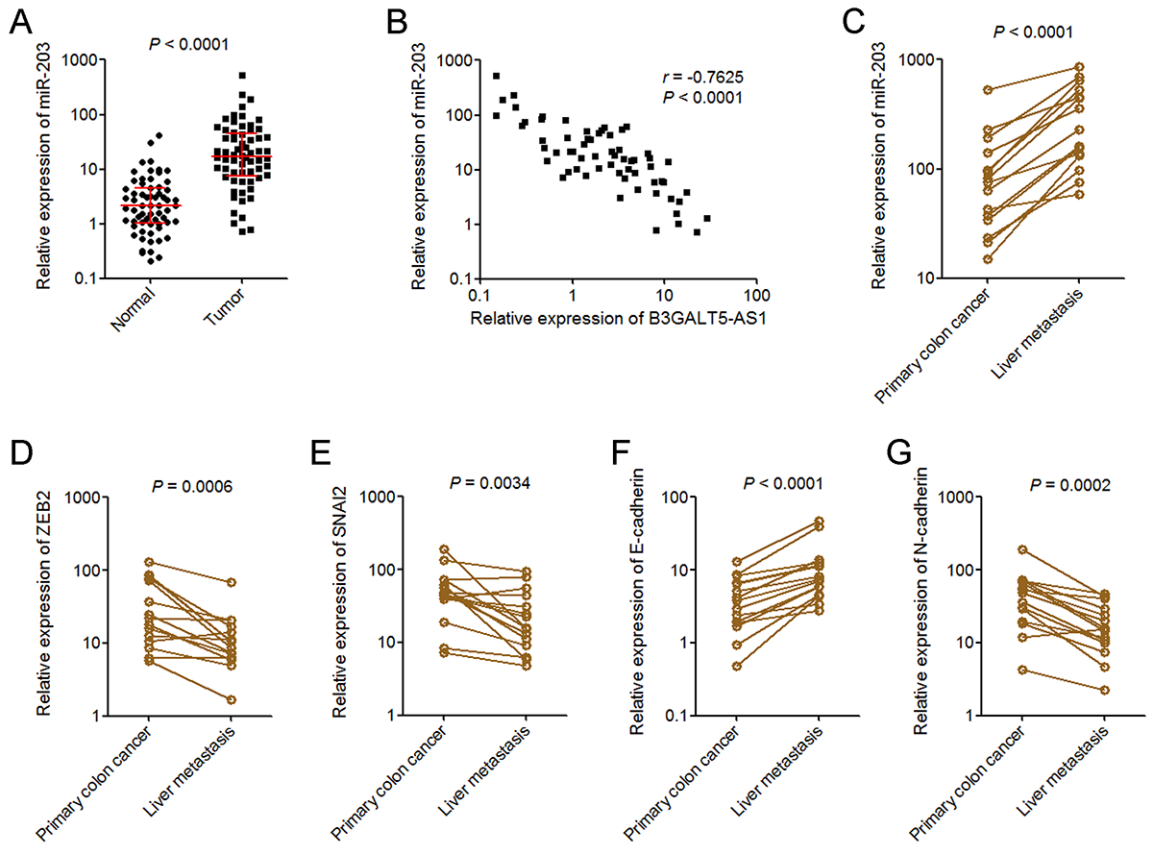

Figure 5. miR-203 expression pattern in colon cancer. (**A**) miR-203expression in 64 pairs of primary colon cancer tissues and adjacent colonic epithelium tissues was measured by qRT-PCR. $P < 0.0001$, Wilcoxon signed-rank test. (**B**) The correlation between B3GALT5-AS1 and miR-203 expression level in colon cancer tissues. $n = 64$, $r = -0.7625$, $P < 0.0001$, Pearson's correlation analysis. (**C**) The expression of miR-203 in 15 pairs of primary colon cancer tissues and corresponding liver metastasis tissues was measured using qRT-PCR. $P < 0.0001$, Wilcoxon signed-rank test. (**D**) The expression of ZEB2 in 15 pairs of primary colon cancer tissues and corresponding liver metastasis tissues was measured using qRT-PCR. $P = 0.0006$, Wilcoxon signed-rank test. (**E**) The expression of SNAI2 in 15 pairs of primary colon cancer tissues and corresponding liver metastasis tissues was measured using qRT-PCR. $P = 0.0034$, Wilcoxon signed-rank test. (**F**) The expression of E-cadherin in 15 pairs of primary colon cancer tissues and corresponding liver metastasis tissues was measured using qRT-PCR. $P < 0.0001$, Wilcoxon signed-rank test. (**G**) The expression of N-cadherin in 15 pairs of primary colon cancer tissues and corresponding liver metastasis tissues was measured using qRT-PCR. $P = 0.0002$, Wilcoxon signed-rank test.

B3GALT5-AS1 suppresses colon cancer liver metastasis

Next, we explored whether B3GALT5-AS1 have effects on colon cancer liver metastasis. The binding sites depleted B3GALT5-AS1 was stably overexpressed in HCT116 cells with a similar overexpression level to B3GALT5-AS1 full length overexpression clone (Fig. 6A). B3GALT5-AS1 stably overexpressed and control HCT116 cells were injected through the spleen to establish liver metastasis model in nude mice. The results displayed that ectopic expression of B3GALT5-AS1 decreased the amount of liver metastatic foci, which was abolished by the depletion of binding sites (Fig. 6B). The expressions of B3GALT5-AS1 and miR-203 were measured in the liver metastatic foci formed by these different HCT116 clones. The results confirmed the overexpression of B3GALT5-AS1 and the downregulation of miR-203 in the liver metastatic foci formed by B3GALT5-AS1 stably overexpressed cells (Fig. 6C). Depletion of the binding sites abolished the effects of B3GALT5-AS1 on miR-203 *in vivo* (Fig. 6C). Proliferation marker Ki67 immunohistochemical staining of the liver metastatic foci displayed that B3GALT5-AS1 overexpression decreased the proportion of Ki67-positive cells, which was abolished by the depletion of binding sites (Fig. 6D). The expressions of ZEB2 and SNAI2 were measured in the liver metastatic foci, and the results displayed that ZEB2 and SNAI2 were upregulated in the liver

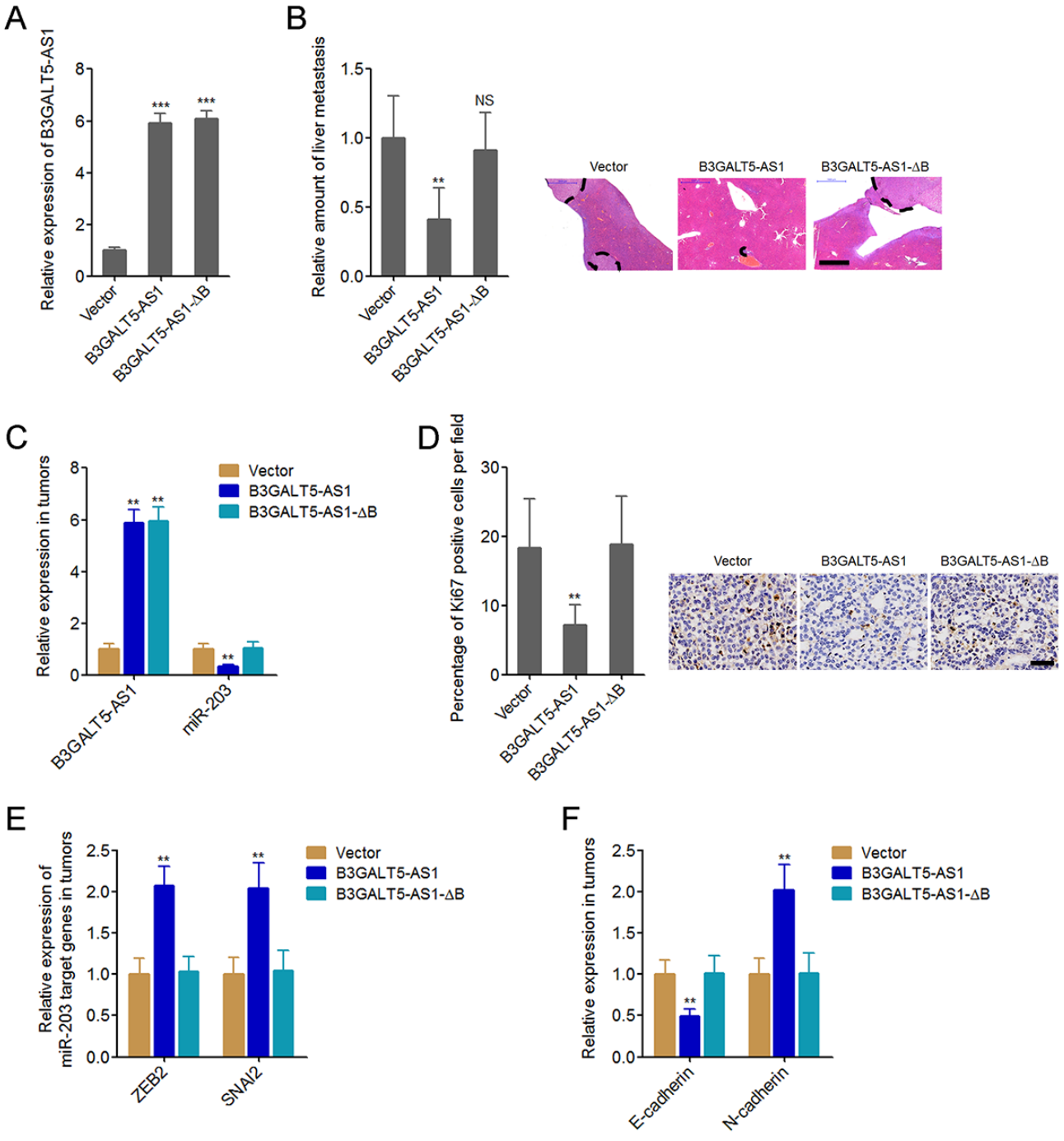

Figure 6. B3GALT5-AS1 inhibited colon cancer liver metastasis. (**A**) B3GALT5-AS1 expression in different B3GALT5-AS1 stably overexpressed HCT116 cells clones was measured using qRT-PCR. Data are displayed as mean ± s.d. of three independent experiments. ***$P < 0.001$, Student's *t*-test. (**B**) Indicated B3GALT5-AS1 stably overexpressed HCT116 cells were intra-splenic injected to establish liver metastasis. The amount of liver metastatic foci was assessed at the 42th day after intra-splenic injection using HE staining. Scale bars = 1000 μm. (**C**) The expression of B3GALT5-AS1 and miR-203 in liver metastatic foci formed by these indicated B3GALT5-AS1 stably overexpressed HCT116 cells was detected using qRT-PCR. (**D**) Immunohistochemical staining of Ki67 in liver metastatic foci formed by these indicated B3GALT5-AS1 stably overexpressed HCT116 cells. Scale bars = 50 μm. (**E**) The expression of ZEB2 and SNAI2 in liver metastatic foci formed by these indicated B3GALT5-AS1 stably overexpressed HCT116 cells was measured using qRT-PCR. (**F**) The expression of E-cadherin and N-cadherin in liver metastatic foci formed by these indicated B3GALT5-AS1 stably overexpressed HCT116 cells was detected using qRT-PCR. For **B**-**F**, data are displayed as mean ± s.d. of six mice in each group. **$P < 0.01$, NS, not significant, Mann-Whitney test.

metastatic foci formed by B3GALT5-AS1 stably overexpressed cells, which were abolished by the depletion of binding sites of B3GALT5-AS1 (Fig. 6E). The expression of EMT markers E-cadherin and N-cadherin were also measured in the liver metastatic foci. The results displayed that E-cadherin was downregulated and while N-cadherin was upregulated in the liver metastatic foci formed by B3GALT5-AS1 stably overexpressed cells, which were also abolished by the depletion of binding sites of B3GALT5-AS1 (Fig. 6F). All these results suggested that B3GALT5-AS1 inhibited miR-203, upregulated ZEB2 and SNAI2, induced EMT, and suppressed colon cancer liver metastasis *in vivo*.

Depletion of B3GALT5-AS1 promotes colon cancer liver metastasis in a miR-203-dependent manner

To further investigate whether the inhibition of miR-203 mediates the roles of B3GALT5-AS1 in colon cancer liver metastasis, we stably inhibited miR-203 expression in B3GALT5-AS1 stably depleted SW620 cells (Fig. 7A). The constructed cell clones were injected through the spleen to establish liver metastasis model in nude mice. The results displayed that B3GALT5-AS1 knockdown increased the amount of liver metastatic foci, which was attenuated by the inhibition of miR-203 (Fig. 7B). The expressions of B3GALT5-AS1 and miR-203 were measured in the liver metastatic foci formed by these stable clones. The results confirmed the downregulation of B3GALT5-AS1 and the upregulation of miR-203 in liver metastatic foci formed by B3GALT5-AS1 stably depleted cells, and also the inversion of miR-203 in the liver metastatic foci formed by B3GALT5-AS1 and miR-203 concurrently depleted cells (Fig. 7C). Proliferation marker Ki67 immunohistochemical staining of the liver metastatic foci displayed that B3GALT5-AS1 knockdown increased the proportion of Ki67-positive cells, which was attenuated by the inhibition of miR-203 (Fig. 7D). The expressions of ZEB2 and SNAI2 were measured in the liver metastatic foci, and the results displayed that ZEB2 and SNAI2 were downregulated in the liver metastatic foci formed by B3GALT5-AS1 stably depleted cells, which were abolished by the inhibition of miR-203 (Fig. 7E). The expression of EMT markers E-cadherin and N-cadherin were also measured in the liver metastatic foci. The results displayed that E-cadherin was upregulated and while N-cadherin was downregulated in the liver metastatic foci formed by B3GALT5-AS1 stably depleted cells, which were also abolished by the inhibition of miR-203 (Fig. 7F). All these results demonstrated that B3GALT5-AS1 knockdown increased miR-203, downregulated ZEB2 and SNAI2, and inhibited EMT *in vivo*. These data also suggested that B3GALT5-AS1 knockdown promoted colon cancer liver metastasis at least partially via the upregulation of miR-203.

DISCUSSION

Distant metastasis, particular liver metastasis, is the major cause of colon cancer-related death [4]. However, the critical molecular mechanisms underpinning colon cancer liver metastasis are largely unknown. In the present study, we found a novel regulation axis in the process of colon cancer liver metastasis, which is the induction of EMT by lncRNA B3GALT5-AS1 via repressing miR-203. Our data revealed that B3GALT5-AS1 directly binds to the promoter of *miR-203*, represses *miR-203* expression, upregulates miR-203 targets ZEB2 and SNAI2, induces EMT, and finally suppresses colon cancer liver metastasis. Consistent with the suppressive roles of B3GALT5-AS1/miR-203/ZEB2-SNAI2/EMT in colon cancer liver metastasis, B3GALT5-AS1 is reduced, miR-203 is increased, ZEB2 and SNAI2 are reduced, epithelial marker E-cadherin is increased, mesenchymal marker N-cadherin is reduced in liver metastasis tissues compared with primary colon cancer tissues.

In the liver metastatic foci, the metastasized colon cancer cells undergo MET and regain epithelial phenotype to permit their settlement and proliferation [54]. Our data support this theory. Our *in vivo* liver metastasis assays demonstrated that overexpression of B3GALT5-AS1 induced mesenchymal phenotype of liver metastasized colon cancer cells and inhibited liver metastasis of colon cancer. Depletion of B3GALT5-AS1 induced epithelial phenotype of liver metastasized colon cancer cells and promoted liver metastasis of colon cancer. Therefore, the opposing roles of EMT in early invasion and late settlement of colon cancer liver metastasis processes imply that disease stage-specific therapies are warranted.

Mechanistically, we identified a long interaction region with about 300 nucleotides between the last 300 nucleotides of B3GALT5-AS1 and the promoter of *miR-203*. ChIRP assays revealed the physical binding between B3GALT5-AS1 and the promoter of *miR-203*. Dual luciferase reporter assays and depletion mapping assays revealed that B3GALT5-AS1 inhibited the promoter activity of *miR-203*, which was dependent on the interaction region. Consistently, B3GALT5-AS1 repressed miR-203 expression both *in vitro* and in liver metastasized colon cancer cells *in vivo*, which were also dependent on the interaction region. The inverse correlation between B3GALT5-AS1 and miR-203 expression in colon cancer tissues supported the negative regulation of miR-203 by B3GALT5-AS1.

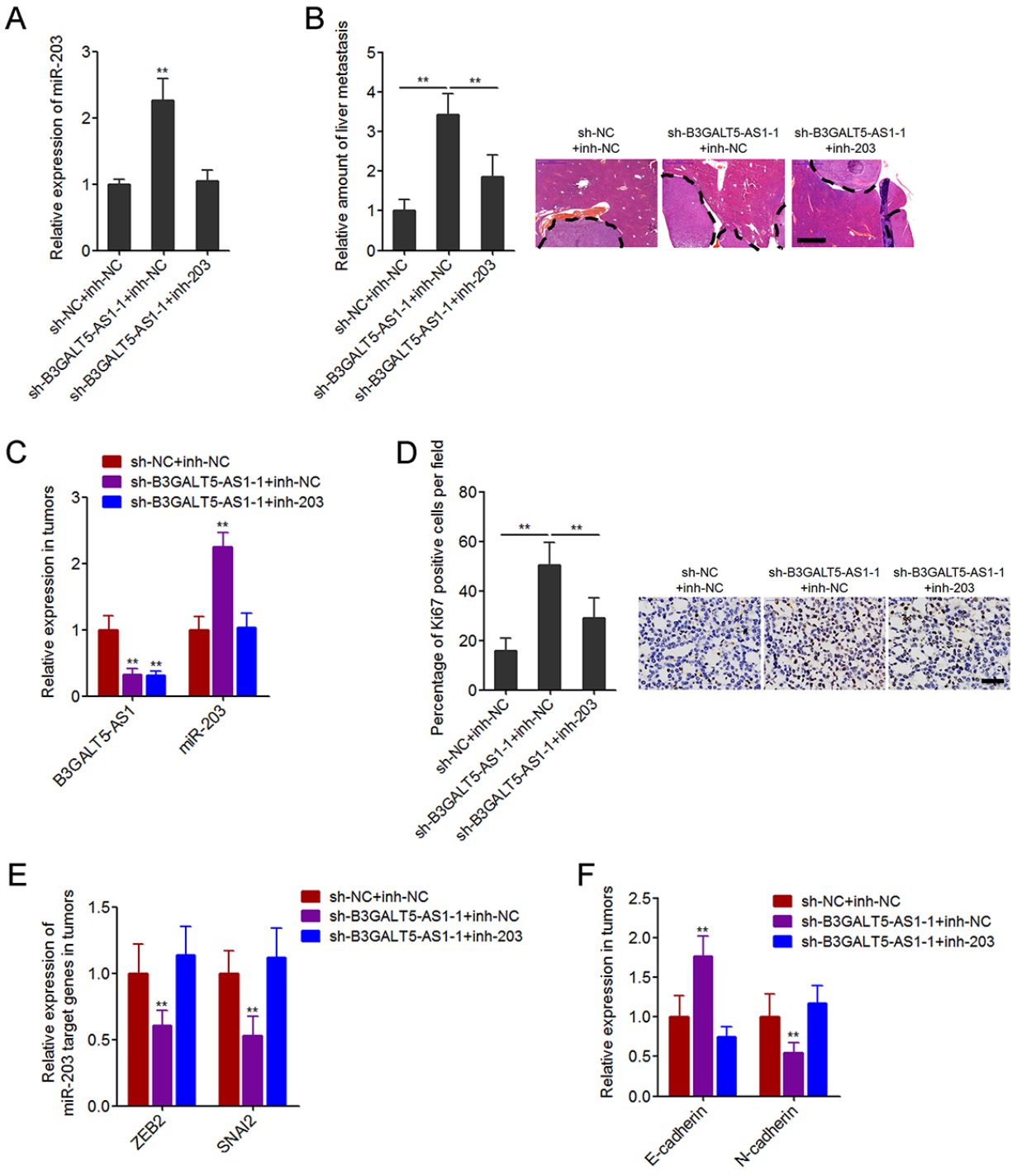

Figure 7. Depletion of B3GALT5-AS1 promoted colon cancer liver metastasis in a miR-203-dependent manner. (**A**) miR-203 expression in B3GALT5-AS1 and miR-203 concurrently depleted and control SW620 cells was measured using qRT-PCR. Data are displayed as mean ± s.d. of three independent experiments. ***P* < 0.01, Student's *t*-test. (**B**) B3GALT5-AS1 and miR-203 concurrently depleted and control SW620 cells were intra-splenic injected to establish liver metastasis. The amount of liver metastatic foci was detected at the 42th day after intra-splenic injection using HE staining. Scale bars = 1000 μm. (**C**) The expression of B3GALT5-AS1 and miR-203 in liver metastatic foci formed by B3GALT5-AS1 and miR-203 concurrently depleted and control SW620 cells was detected using qRT-PCR. (**D**) Immunohistochemical staining of Ki67 in liver metastatic foci formed by B3GALT5-AS1 and miR-203 concurrently depleted and control SW620 cells. Scale bars = 50 μm. (**E**) The expression of ZEB2 and SNAI2 in liver metastatic foci formed by B3GALT5-AS1 and miR-203 concurrently depleted and control SW620 cells was measured using qRT-PCR. (**F**) The expression of E-cadherin and N-cadherin in liver metastatic foci formed by B3GALT5-AS1 and miR-203 concurrently depleted and control SW620 cells was detected using qRT-PCR. For **B**-**F**, data are displayed as mean ± s.d. of six mice in each group. ***P* < 0.01, Mann-Whitney test.

Furthermore, *in vivo* functional assays revealed that inhibition of miR-203 attenuated the pro-metastatic roles of B3GALT5-AS1 depletion in colon cancer liver metastasis. Except for miR-203, other EMT regulators may also be B3GALT5-AS1 downstream targets, which need further investigation. Excluding EMT, other mechanisms may also mediate the roles of B3GALT5-AS1 in colon cancer cell proliferation, which also need further investigation. Nonetheless, our results suggested that the negative regulation of miR-203 and positive regulation of EMT by B3GALT5-AS1 at least partially mediated the roles of B3GALT5-AS1 in colon cancer liver metastasis.

In summary, we demonstrated that lncRNA B3GALT5-AS1 is reduced in colon cancer tissues, and further reduced in colon cancer liver metastasis tissues. Low expression of B3GALT5-AS1 indicts poor outcome of colon cancer patients. B3GALT5-AS1 inhibits proliferation, promotes migration and invasion, induces EMT, and inhibits liver metastasis of colon cancer cells via repressing miR-203. Our data suggested that B3GALT5-AS1/miR-203/EMT axis may be potential therapeutic target for colon cancer liver metastasis.

MATERIALS AND METHODS

Patient and tissue specimens

Sixty-four pairs of primary colon cancer tissues and adjacent normal colonic epithelium tissues, and 15 colon cancer liver metastasis tissues were collected from colon cancer patients with written informed consent who received surgical resection at The First Affiliated Hospital, Sun Yat-sen University (Guangzhou, China). These tissue samples were diagnosed with pathological examination. All resected tissues were immediately snap-frozen in liquid nitrogen and stored at -80 °C until use. The Research Review Board of The First Affiliated Hospital, Sun Yat-sen University reviewed and approved this study.

Cell culture

The human normal colonic epithelial cell line NCM460 and colon cancer cell lines HCT116, HT-29, LoVo, SW480 and SW620 were acquired from the Institute of Biochemistry and Cell Biology of the Chinese Academy of Sciences (Shanghai, China). NCM460 was maintained in Dulbecco's Modified Eagle's Medium (Gibco, Grand Island, NY, USA). HCT116 and HT-29 were cultured in McCoy's 5A Medium (Sigma-Aldrich, Saint Louis, MO, USA). LoVo was cultured in Ham's F-12K Medium (Invitrogen, Carlsbad, CA, USA). SW480 and SW620 were maintained in L-15 Medium (Gibco). These cells were maintained in the above described medium added with 10% fetal bovine serum (Gibco) at 37°C in a humidified incubator with 5% CO_2.

RNA isolation and quantitative real-time PCR (qRT-PCR)

Total RNA was isolated from indicated tissues and cells with TRIzol Regent (Invitrogen) according to the manufacturer's instruction. The isolated RNA was deal with DNase I (Takara, Dalian, China) to get rid of genomic DNA. Next, reverse transcription was carried out using the RNA and the M-MLV Reverse Transcriptase (Invitrogen) following the manufacturer's instruction. Quantitative real-time PCR (qRT-PCR) assays were performed using SYBR® Premix Ex Taq™ II (Takara) on ABI StepOnePlus Real-Time PCR System (Applied Biosystems, Foster City, CA, USA) following the manufacturers' protocols. β-actin was employed as an endogenous control for the quantitation of mRNAs and lncRNAs. Primers' sequences were as follows: for transcript variant 1 of B3GALT5-AS1, 5'-ATTTCACGGATGAGACGAC-3' (forward) and 5'-CCTTGAGAGACGAAGCAC-3' (reverse); for transcript variant 2 of B3GALT5-AS1, 5'-TCACGGATGAGACGACTC-3' (forward) and 5'-AAGGCTTCCAAACACGAAAA-3' (reverse); for E-cadherin, 5'-GCCCCATCAGGCCTCCGTTT-3' (forward) and 5'-ACCTTGCCTTCTTTGTCTTTGTTGGA-3' (reverse); for N-cadherin, 5'-TGGACCATCACTCGGCTTA-3' (forward) and 5'-ACACTGGCAAACCTTCACG-3' (reverse); for ZEB2, 5'-TGAGGATGACGGTATTGC-3' (forward) and 5'-ATCTCGTTGTTGTGCCAG-3' (reverse); for SNAI2, 5'-GGCAAGGCGTTTTCCAG-3' (forward) and 5'-CAGCCAGATTCCTCATGTTT-3' (reverse); and for β-actin, 5'-GGGAAATCGTGCGTGACATTAAG-3' (forward) and 5'-TGTGTTGGCGTACAGGTCTTTG-3' (reverse). For miRNAs quantitation, qRT-PCR was carried out as above described with TaqMan microRNA assays following the manufacturer's instruction (Applied Biosystems). U6 served as an endogenous control for the quantitation of miRNAs. The quantitation of RNA was calculated with the comparative Ct method.

Western blot

Total proteins were isolated from tissues or cells using RIPA buffer (Beyotime, Shanghai, China). Identical quantity of protein samples were separated using sodium dodecyl sulfate-polyacrylamide gel electrophoresis (SDS-PAGE). Then, proteins were transferred to nitrocellulose filter membrane (Millipore, Bedford, MA, USA). Next, the membranes were blocked with 5% bovine serum albumin, followed by being incubated with primary antibodies against β-actin

(Sigma-Aldrich), E-cadherin (Abcam, Hong Kong, China), or N-cadherin (Abcam). After three washes using TBS buffer, the membranes were incubated with IRdye 700-conjugated goat anti-mouse IgG or IRdye800-conjugated goat anti-rabbit IgG (Li-Cor, Lincoln, NE, USA). Last, immunoreactive bands were detected using an Odyssey infrared scanner (Li-Cor).

Plasmids construction

For construction of different B3GALT5-AS1 overexpression plasmids, B3GALT5-AS1 full-length nucleotides, 1-1061 nucleotides of B3GALT5-AS1, and 1062-1363 nucleotides of B3GALT5-AS1 were PCR amplified with Thermo Scientific Phusion Flash High-Fidelity PCR Master Mix (Thermo-Fisher Scientific, Waltham, MA, USA). Then, the PCR products were subcloned into the Hind III and Xba I, Hind III and BamH I, or BamH I and Xba I sites of the pcDNA3.1 plasmid (Invitrogen), termed as pcDNA3.1-B3GALT5-AS1, pcDNA3.1-B3GALT5-AS1-ΔB, pcDNA3.1-B3GALT5-AS1-B, respectively. The PCR primers' sequences are as follows: for pcDNA3.1-B3GALT5-AS1, 5'-CCCAAGCTTGACGCGGCGGGCGGCTCC-3' (forward) and 5'-GCTCTAGAAATTTTACTTTTTTTGGAGACAGGG-3' (reverse); for pcDNA3.1-B3GALT5-AS1-ΔB, 5'-CCCAAGCTTGACGCGGCGGGCGGCTCC-3' (forward) and 5'-CGGGATCCTATGGAGGTTCTGTTTGCTTCTGCA-3' (reverse); for pcDNA3.1-B3GALT5-AS1-B, 5'-CGGGATCCAAATGTAATGATGTCTTGTGCC-3' (forward) and 5'-GCTCTAGAAATTTTACTTTTTTTGGAGACAGGG-3' (reverse). Empty plasmid pcDNA3.1 was employed as negative control. Two pairs of cDNA oligonucleotides suppressing B3GALT5-AS1 expression were inserted into the SuperSilencing shRNA expression plasmid pGPU6/Neo (GenePharma, Shanghai, China), named sh-B3GALT5-AS1-1 and sh-B3GALT5-AS1-2. The target sites are 5'-GCAAGACAGCGCATTGATTGG-3' and 5'-GCATAAGAGAGACCAACTTGG-3', respectively. A scrambled shRNA was employed as negative control and named sh-NC. The promoter of *miR-203* containing the predicted B3GALT5-AS1 binding sites was PCR amplified using the Thermo Scientific Phusion Flash High-Fidelity PCR Master Mix and subcloned into the Kpn I and Hind III sites of firefly luciferase reporter pGL3-Basic plasmid (Promega, Madison, WI, USA), named pGL3-miR203-pro. The PCR primers' sequences are as follows: 5'-GGGGTACCTCCTCTCCATCACGACTACT-3' (forward) and 5'-CCCAAGCTTGTTTCTGCTTCTCAGACCCT-3' (reverse).

Stable cell lines construction

For construction of B3GALT5-AS1 stably overexpressed HCT116 cells, pcDNA3.1-B3GALT5-AS1, pcDNA3.1-B3GALT5-AS1-ΔB, or pcDNA3.1 was transfected into HCT116 cells with Lipofectamine 3000 (Invitrogen) following the manufacturer's protocols. Next, the cells were selected with neomycin for four weeks. For construction of B3GALT5-AS1 stably depleted SW620 cells, sh-B3GALT5-AS1-1, sh-B3GALT5-AS1-2, or sh-NC was transfected into SW620 cells with Lipofectamine 3000 (Invitrogen). Next, the cells were selected with neomycin for four weeks. Recombinant lentiviruses containing miR-203 inhibitor or the control were purchased from GenePharma (Shanghai, China). B3GALT5-AS1 stably depleted SW620 cells were transfected with 2×10^6 transducing units of miR-203 inhibition lentiviruses and selected with puromycin for four weeks. The stably cell lines were identified by qRT-PCR.

Cell proliferation assay

Cell proliferation was assessed by Glo cell viability assay and Ethynyl deoxyuridine (EdU) incorporation assay. For Glo cell viability assay, 2,000 colon cancer cells per-well were plated into 96-well plates and maintained for indicated time. At the end of the incubation period, luminescence values were measured with the CellTiter-Glo® Luminescent Cell Viability Assay (Promega) following the manufacturer's protocol. EdU incorporation assay was carried out using the EdU kit (Roche, Mannheim, Germany) following the manufacturer's instruction. The results were collected with the Zeiss fluorescence photomicroscope (Carl Zeiss, Oberkochen, Germany) and measured via counting at least ten random fields.

Cell migration and invasion assays

Cell migration and invasion were evaluated by transwell assays. For transwell migration assay, 40,000 indicated colon cancer cells resuspended in serum-free medium with 1 μg/ml Mitomycin C to repress cell proliferation were seeded into the upper chambers of transwell inserts (Millipore). Medium supplemented with 10% FBS was added to the lower chambers. After incubation for 24 hours, colon cancer cells remaining on the upper membranes were fully removed. The colon cancer cells migrated through the membranes were fixed in methanol, stained using 0.1% crystal violet, and imaged with the Zeiss fluorescence photomicroscope (Carl Zeiss). The results were measured via counting at least ten random fields. Transwell invasion assay was performed with the Cell Invasion Assay Kit from CHEMICON (Millipore) according to the

manufacturer's protocol. The results were analyzed as transwell migration assay.

Purification of cytoplasmic and nuclear RNA

Cytoplasmic and nuclear RNA was purified with Cytoplasmic & Nuclear RNA Purification Kit (Norgen, Belmont, CA, USA) following the manufacturer's protocol. The purified RNA was measured using qRT-PCR.

Chromatin isolation by RNA purification (ChIRP)

ChIRP was carried out using Magna ChIRP RNA Interactome Kit (Millipore) following the manufacturer's protocol. Anti-sense DNA probes specific for B3GALT5-AS1 were synthesized by Biosearch Technologies. Probes sequences are as follows: 1, 5'-aaactcaaagaaccggcctc-3'; 2, 5'-ggcatctggggtttgagaag-3'; 3, 5'-ttgcatgactttggctcatt-3'; 4, 5'-taagtattgctccagcattc-3'; 5, 5'-gaagatagcctctctgacag-3'; 6, 5'-atacctcttttgacagagct-3'; 7, 5'-ccacctcaaaggatgatcaa-3'; 8, 5'-ttctgcaccttggtctaatc-3'. ChIRP enriched DNA was measured by qRT-PCR to assess *miR-203* promoter enrichment. Primers' sequences were as follows: 5'-ACTGGGAAGATGGAGGTTG-3' (forward) and 5'-GATGGAAGTGGGCATAGGG-3' (reverse).

Dual luciferase reporter assay

The constructed firefly luciferase reporter pGL3-miR203-pro was cotransfected with renilla luciferase expression vector pRL-TK into indicated SW620 cells. The different B3GALT5-AS1 expression plasmids were cotransfected with pGL3-miR203-pro and pRL-TK into HCT116 cells. Forty-eight hours after transfection, the luciferase activity was detected by Dual-Luciferase® Reporter Assay System (Promega) following the manufacturer's protocols.

Animal study

To establish *in vivo* liver metastasis model, 2×10^6 indicted colon cancer cells in 100 μL phosphate buffered saline were intra-splenic injected into 6-week old nude mice acquired from Laboratory Animal Center of Sun Yat-sen University (Guangzhou, China). The mice were housed in a temperature and light controlled pathogen-free animal facility with free access to food and water to being allowed to grow for 6 weeks. Then the mice were sacrificed and the livers were resected. The resected livers were fixed in formalin, paraffin embedded, deparaffinized, rehydrated, and antigen retrieved. The amount of liver metastatic foci was counted via hematoxylin-eosin (HE) staining. The sections were incubated with primary antibody specific for Ki67 (Abcam) and horseradish peroxidase-conjugated secondary antibody (Beyotime, Shanghai, China), followed by being visualized with 3, 3-diaminobenzidine. The animal care and use committee of The First Affiliated Hospital, Sun Yat-sen University reviewed and approved the experimental protocols concerning the handling of mice.

Statistical analysis

Statistical analyses were performed using GraphPad Prism Software (GraphPad Software, La Jolla, CA, USA). Student's *t*-test, Wilcoxon signed-rank test, Mann-Whitney test, Pearson chi-square test, Pearson's correlation analysis, or Log-rank test was carried out as indicated. *P*-values < 0.05 were considered as statistically significant.

Abbreviations

lncRNAs, long noncoding RNAs; miR-203, microRNA-203; EMT, epithelial-to-mesenchymal transition; MET, mesenchymal-to-epithelial transition; miRNA, microRNA; qRT-PCR, quantitative real-time PCR; SDS-PAGE, sodium dodecyl sulfate-polyacrylamide gel electrophoresis; EdU, Ethynyl deoxyuridine; ChIRP, chromatin isolation by RNA purification; HE, hematoxylin-eosin.

AUTHOR CONTRIBUTIONS

YH, LW, and ZW conceived the study; LW, ZW, KW, WD, CZ, and JP carried out the experiments; YH, LW, and ZW collected and analyzed the data. YH and LW wrote the manuscript. All authors read and approved the final manuscript.

CONFLICTS OF INTEREST

All authors declare no conflict of interest.

REFERENCES

1. Torre LA, Bray F, Siegel RL, Ferlay J, Lortet-Tieulent J, Jemal A. Global cancer statistics, 2012. CA Cancer J Clin. 2015; 65:87–108. https://doi.org/10.3322/caac.21262

2. Geng L, Chaudhuri A, Talmon G, Wisecarver JL, Are C, Brattain M, Wang J. MicroRNA-192 suppresses liver metastasis of colon cancer. Oncogene. 2014; 33:5332–40. https://doi.org/10.1038/onc.2013.478

3. Akgül Ö, Çetinkaya E, Ersöz Ş, Tez M. Role of surgery in colorectal cancer liver metastases. World J Gastroenterol. 2014; 20:6113–22.

https://doi.org/10.3748/wjg.v20.i20.6113

4. Manfredi S, Lepage C, Hatem C, Coatmeur O, Faivre J, Bouvier AM. Epidemiology and management of liver metastases from colorectal cancer. Ann Surg. 2006; 244:254–59. https://doi.org/10.1097/01.sla.0000217629.94941.cf

5. Landreau P, Drouillard A, Launoy G, Ortega-Deballon P, Jooste V, Lepage C, Faivre J, Facy O, Bouvier AM. Incidence and survival in late liver metastases of colorectal cancer. J Gastroenterol Hepatol. 2015; 30:82–85. https://doi.org/10.1111/jgh.12685

6. Urosevic J, Garcia-Albéniz X, Planet E, Real S, Céspedes MV, Guiu M, Fernandez E, Bellmunt A, Gawrzak S, Pavlovic M, Mangues R, Dolado I, Barriga FM, et al. Colon cancer cells colonize the lung from established liver metastases through p38 MAPK signalling and PTHLH. Nat Cell Biol. 2014; 16:685–94. https://doi.org/10.1038/ncb2977

7. Polyak K, Weinberg RA. Transitions between epithelial and mesenchymal states: acquisition of malignant and stem cell traits. Nat Rev Cancer. 2009; 9:265–73. https://doi.org/10.1038/nrc2620

8. Rokavec M, Horst D, Hermeking H. Cellular model of colon cancer progression reveals signatures of mRNAs, miRNA, lncRNAs, and epigenetic modifications associated with metastasis. Cancer Res. 2017; 77:1854–67. https://doi.org/10.1158/0008-5472.CAN-16-3236

9. Mehlen P, Puisieux A. Metastasis: a question of life or death. Nat Rev Cancer. 2006; 6:449–58. https://doi.org/10.1038/nrc1886

10. Spaderna S, Schmalhofer O, Hlubek F, Berx G, Eger A, Merkel S, Jung A, Kirchner T, Brabletz T. A transient, EMT-linked loss of basement membranes indicates metastasis and poor survival in colorectal cancer. Gastroenterology. 2006; 131:830–40. https://doi.org/10.1053/j.gastro.2006.06.016

11. Vu T, Datta PK. Regulation of EMT in colorectal cancer: a culprit in metastasis. Cancers (Basel). 2017; 9:E171. https://doi.org/10.3390/cancers9120171

12. Yuan JH, Yang F, Wang F, Ma JZ, Guo YJ, Tao QF, Liu F, Pan W, Wang TT, Zhou CC, Wang SB, Wang YZ, Yang Y, et al. A long noncoding RNA activated by TGF-β promotes the invasion-metastasis cascade in hepatocellular carcinoma. Cancer Cell. 2014; 25:666–81. https://doi.org/10.1016/j.ccr.2014.03.010

13. Ocaña OH, Córcoles R, Fabra A, Moreno-Bueno G, Acloque H, Vega S, Barrallo-Gimeno A, Cano A, Nieto MA. Metastatic colonization requires the repression of the epithelial-mesenchymal transition inducer Prrx1. Cancer Cell. 2012; 22:709–24. https://doi.org/10.1016/j.ccr.2012.10.012

14. Zhang W, Zhou P, Meng A, Zhang R, Zhou Y. Down-regulating Myoferlin inhibits the vasculogenic mimicry of melanoma via decreasing MMP-2 and inducing mesenchymal-to-epithelial transition. J Cell Mol Med. 2018; 22:1743–54. https://doi.org/10.1111/jcmm.13455

15. Kahlert UD, Joseph JV, Kruyt FA. EMT- and MET-related processes in nonepithelial tumors: importance for disease progression, prognosis, and therapeutic opportunities. Mol Oncol. 2017; 11:860–77. https://doi.org/10.1002/1878-0261.12085

16. Korpal M, Ell BJ, Buffa FM, Ibrahim T, Blanco MA, Celià-Terrassa T, Mercatali L, Khan Z, Goodarzi H, Hua Y, Wei Y, Hu G, Garcia BA, et al. Direct targeting of Sec23a by miR-200s influences cancer cell secretome and promotes metastatic colonization. Nat Med. 2011; 17:1101–08. https://doi.org/10.1038/nm.2401

17. Jeschke U, Mylonas I, Kuhn C, Shabani N, Kunert-Keil C, Schindlbeck C, Gerber B, Friese K. Expression of E-cadherin in human ductal breast cancer carcinoma in situ, invasive carcinomas, their lymph node metastases, their distant metastases, carcinomas with recurrence and in recurrence. Anticancer Res. 2007; 27:1969–74.

18. Iyer MK, Niknafs YS, Malik R, Singhal U, Sahu A, Hosono Y, Barrette TR, Prensner JR, Evans JR, Zhao S, Poliakov A, Cao X, Dhanasekaran SM, et al. The landscape of long noncoding RNAs in the human transcriptome. Nat Genet. 2015; 47:199–208. https://doi.org/10.1038/ng.3192

19. Yan X, Hu Z, Feng Y, Hu X, Yuan J, Zhao SD, Zhang Y, Yang L, Shan W, He Q, Fan L, Kandalaft LE, Tanyi JL, et al. Comprehensive genomic characterization of long non-coding RNAs across human cancers. Cancer Cell. 2015; 28:529–40. https://doi.org/10.1016/j.ccell.2015.09.006

20. Schmitt AM, Chang HY. Long noncoding RNAs in cancer pathways. Cancer Cell. 2016; 29:452–63. https://doi.org/10.1016/j.ccell.2016.03.010

21. Ponting CP, Oliver PL, Reik W. Evolution and functions of long noncoding RNAs. Cell. 2009; 136:629–41. https://doi.org/10.1016/j.cell.2009.02.006

22. Lin A, Hu Q, Li C, Xing Z, Ma G, Wang C, Li J, Ye Y, Yao J, Liang K, Wang S, Park PK, Marks JR, et al. The LINK-A lncRNA interacts with PtdIns(3,4,5)P3 to

hyperactivate AKT and confer resistance to AKT inhibitors. Nat Cell Biol. 2017; 19:238–51. https://doi.org/10.1038/ncb3473

23. Lin A, Li C, Xing Z, Hu Q, Liang K, Han L, Wang C, Hawke DH, Wang S, Zhang Y, Wei Y, Ma G, Park PK, et al. The LINK-A lncRNA activates normoxic HIF1α signalling in triple-negative breast cancer. Nat Cell Biol. 2016; 18:213–24. https://doi.org/10.1038/ncb3295

24. Grelet S, Link LA, Howley B, Obellianne C, Palanisamy V, Gangaraju VK, Diehl JA, Howe PH. A regulated PNUTS mRNA to lncRNA splice switch mediates EMT and tumour progression. Nat Cell Biol. 2017; 19:1105–15. https://doi.org/10.1038/ncb3595

25. Yuan JH, Liu XN, Wang TT, Pan W, Tao QF, Zhou WP, Wang F, Sun SH. The MBNL3 splicing factor promotes hepatocellular carcinoma by increasing PXN expression through the alternative splicing of lncRNA-PXN-AS1. Nat Cell Biol. 2017; 19:820–32. https://doi.org/10.1038/ncb3538

26. Kaur P, Tan JR, Karolina DS, Sepramaniam S, Armugam A, Wong PT, Jeyaseelan K. A long non-coding RNA, BC048612 and a microRNA, miR-203 coordinate the gene expression of neuronal growth regulator 1 (NEGR1) adhesion protein. Biochim Biophys Acta. 2016; 1863:533-43. https://doi.org/10.1016/j.bbamcr.2015.12.012

27. Ellis BC, Graham LD, Molloy PL. CRNDE, a long non-coding RNA responsive to insulin/IGF signaling, regulates genes involved in central metabolism. Biochim Biophys Acta. 2014; 1843:372-86. https://doi.org/10.1016/j.bbamcr.2013.10.016

28. Rigoutsos I, Lee SK, Nam SY, Anfossi S, Pasculli B, Pichler M, Jing Y, Rodriguez-Aguayo C, Telonis AG, Rossi S, Ivan C, Catela Ivkovic T, Fabris L, et al. N-BLR, a primate-specific non-coding transcript leads to colorectal cancer invasion and migration. Genome Biol. 2017; 18:98. https://doi.org/10.1186/s13059-017-1224-0

29. Fang C, Qiu S, Sun F, Li W, Wang Z, Yue B, Wu X, Yan D. Long non-coding RNA HNF1A-AS1 mediated repression of miR-34a/SIRT1/p53 feedback loop promotes the metastatic progression of colon cancer by functioning as a competing endogenous RNA. Cancer Lett. 2017; 410:50–62. https://doi.org/10.1016/j.canlet.2017.09.012

30. Han P, Li JW, Zhang BM, Lv JC, Li YM, Gu XY, Yu ZW, Jia YH, Bai XF, Li L, Liu YL, Cui BB. The lncRNA CRNDE promotes colorectal cancer cell proliferation and chemoresistance via miR-181a-5p-mediated regulation of Wnt/β-catenin signaling. Mol Cancer. 2017; 16:9. https://doi.org/10.1186/s12943-017-0583-1

31. Kong J, Sun W, Li C, Wan L, Wang S, Wu Y, Xu E, Zhang H, Lai M. Long non-coding RNA LINC01133 inhibits epithelial-mesenchymal transition and metastasis in colorectal cancer by interacting with SRSF6. Cancer Lett. 2016; 380:476–84. https://doi.org/10.1016/j.canlet.2016.07.015

32. Pickard MR, Mourtada-Maarabouni M, Williams GT. Long non-coding RNA GAS5 regulates apoptosis in prostate cancer cell lines. Biochim Biophys Acta. 2013; 1832:1613-23. https://doi.org/10.1016/j.bbadis.2013.05.005

33. Ge Y, Zhang L, Nikolova M, Reva B, Fuchs E. Strand-specific in vivo screen of cancer-associated miRNAs unveils a role for miR-21(∗) in SCC progression. Nat Cell Biol. 2016; 18:111–21. https://doi.org/10.1038/ncb3275

34. Jeong JH, Cheol Kang Y, Piao Y, Kang S, Pak YK. miR-24-mediated knockdown of H2AX damages mitochondria and the insulin signaling pathway. Exp Mol Med. 2017; 49:e313. https://doi.org/10.1038/emm.2016.174

35. Cho YM, Kim TM, Hun Kim D, Hee Kim D, Jeong SW, Kwon OJ. miR-148a is a downstream effector of X-box-binding protein 1 that silences Wnt10b during adipogenesis of 3T3-L1 cells. Exp Mol Med. 2016; 48:e226. https://doi.org/10.1038/emm.2016.3

36. Yuan JH, Yang F, Chen BF, Lu Z, Huo XS, Zhou WP, Wang F, Sun SH. The histone deacetylase 4/SP1/microrna-200a regulatory network contributes to aberrant histone acetylation in hepatocellular carcinoma. Hepatology. 2011; 54:2025–35. https://doi.org/10.1002/hep.24606

37. Werner TV, Hart M, Nickels R, Kim YJ, Menger MD, Bohle RM, Keller A, Ludwig N, Meese E. MiR-34a-3p alters proliferation and apoptosis of meningioma cells in vitro and is directly targeting SMAD4, FRAT1 and BCL2. Aging (Albany NY). 2017; 9:932–54. https://doi.org/10.18632/aging.101201

38. Penolazzi L, Lambertini E, Bergamin LS, Roncada T, De Bonis P, Cavallo M, Piva R. MicroRNA-221 silencing attenuates the degenerated phenotype of intervertebral disc cells. Aging (Albany NY). 2018; 10:2001–15. https://doi.org/10.18632/aging.101525

39. Gregory PA, Bert AG, Paterson EL, Barry SC, Tsykin A, Farshid G, Vadas MA, Khew-Goodall Y, Goodall GJ. The miR-200 family and miR-205 regulate epithelial to mesenchymal transition by targeting ZEB1 and SIP1. Nat Cell Biol. 2008; 10:593–601. https://doi.org/10.1038/ncb1722

40. Zhao G, Guo Y, Chen Z, Wang Y, Yang C, Dudas A, Du Z, Liu W, Zou Y, Szabo E, Lee SC, Sims M, Gu W, et al. miR-203 functions as a tumor suppressor by inhibiting epithelial to mesenchymal transition in ovarian cancer. J Cancer Sci Ther. 2015; 7:34–43. 10.4172/1948-5956.1000322

41. Brabletz S, Brabletz T. The ZEB/miR-200 feedback loop--a motor of cellular plasticity in development and cancer? EMBO Rep. 2010; 11:670–77. https://doi.org/10.1038/embor.2010.117

42. Renthal NE, Chen CC, Williams KC, Gerard RD, Prange-Kiel J, Mendelson CR. miR-200 family and targets, ZEB1 and ZEB2, modulate uterine quiescence and contractility during pregnancy and labor. Proc Natl Acad Sci USA. 2010; 107:20828–33. https://doi.org/10.1073/pnas.1008301107

43. Wang G, Guo X, Hong W, Liu Q, Wei T, Lu C, Gao L, Ye D, Zhou Y, Chen J, Wang J, Wu M, Liu H, Kang J. Critical regulation of miR-200/ZEB2 pathway in Oct4/Sox2-induced mesenchymal-to-epithelial transition and induced pluripotent stem cell generation. Proc Natl Acad Sci USA. 2013; 110:2858–63. https://doi.org/10.1073/pnas.1212769110

44. Duan X, Fu Z, Gao L, Zhou J, Deng X, Luo X, Fang W, Luo R. Direct interaction between miR-203 and ZEB2 suppresses epithelial-mesenchymal transition signaling and reduces lung adenocarcinoma chemoresistance. Acta Biochim Biophys Sin (Shanghai). 2016; 48:1042–49. https://doi.org/10.1093/abbs/gmw099

45. Qu Y, Li WC, Hellem MR, Rostad K, Popa M, McCormack E, Oyan AM, Kalland KH, Ke XS. MiR-182 and miR-203 induce mesenchymal to epithelial transition and self-sufficiency of growth signals via repressing SNAI2 in prostate cells. Int J Cancer. 2013; 133:544–55. https://doi.org/10.1002/ijc.28056

46. Hur K, Toiyama Y, Okugawa Y, Ide S, Imaoka H, Boland CR, Goel A. Circulating microRNA-203 predicts prognosis and metastasis in human colorectal cancer. Gut. 2017; 66:654–65. https://doi.org/10.1136/gutjnl-2014-308737

47. Zhang A, Lakshmanan J, Motameni A, Harbrecht BG. MicroRNA-203 suppresses proliferation in liver cancer associated with PIK3CA, p38 MAPK, c-Jun, and GSK3 signaling. Mol Cell Biochem. 2017; 441:89–98. https://doi.org/10.1007/s11010-017-3176-9

48. Wan D, Shen S, Fu S, Preston B, Brandon C, He S, Shen C, Wu J, Wang S, Xie W, Chen B, Liya A, Guo Y, et al. miR-203 suppresses the proliferation and metastasis of hepatocellular carcinoma by targeting oncogene ADAM9 and oncogenic long non-coding RNA HULC. Anticancer Agents Med Chem. 2016; 16:414–23. https://doi.org/10.2174/1871520615666150716105955

49. Shao Y, Gu W, Ning Z, Song X, Pei H, Jiang J. Evaluating the Prognostic Value of microRNA-203 in Solid Tumors Based on a Meta-Analysis and the Cancer Genome Atlas (TCGA) Datasets. Cell Physiol Biochem. 2017; 41:1468–80. https://doi.org/10.1159/000470649

50. Saini S, Majid S, Yamamura S, Tabatabai L, Suh SO, Shahryari V, Chen Y, Deng G, Tanaka Y, Dahiya R. Regulatory Role of mir-203 in Prostate Cancer Progression and Metastasis. Clin Cancer Res. 2011; 17:5287–98. https://doi.org/10.1158/1078-0432.CCR-10-2619

51. Funamizu N, Lacy CR, Kamada M, Yanaga K, Manome Y. MicroRNA-203 induces apoptosis by upregulating Puma expression in colon and lung cancer cells. Int J Oncol. 2015; 47:1981–88. https://doi.org/10.3892/ijo.2015.3178

52. Jiang Q, Zhou Y, Yang H, Li L, Deng X, Cheng C, Xie Y, Luo X, Fang W, Liu Z. A directly negative interaction of miR-203 and ZEB2 modulates tumor stemness and chemotherapy resistance in nasopharyngeal carcinoma. Oncotarget. 2016; 7:67288–301. https://doi.org/10.18632/oncotarget.11691

53. Kim SK, Kim SY, Kim JH, Roh SA, Cho DH, Kim YS, Kim JC. A nineteen gene-based risk score classifier predicts prognosis of colorectal cancer patients. Mol Oncol. 2014; 8:1653–66. https://doi.org/10.1016/j.molonc.2014.06.016

54. Hur K, Toiyama Y, Takahashi M, Balaguer F, Nagasaka T, Koike J, Hemmi H, Koi M, Boland CR, Goel A. MicroRNA-200c modulates epithelial-to-mesenchymal transition (EMT) in human colorectal cancer metastasis. Gut. 2013; 62:1315–26. https://doi.org/10.1136/gutjnl-2011-301846

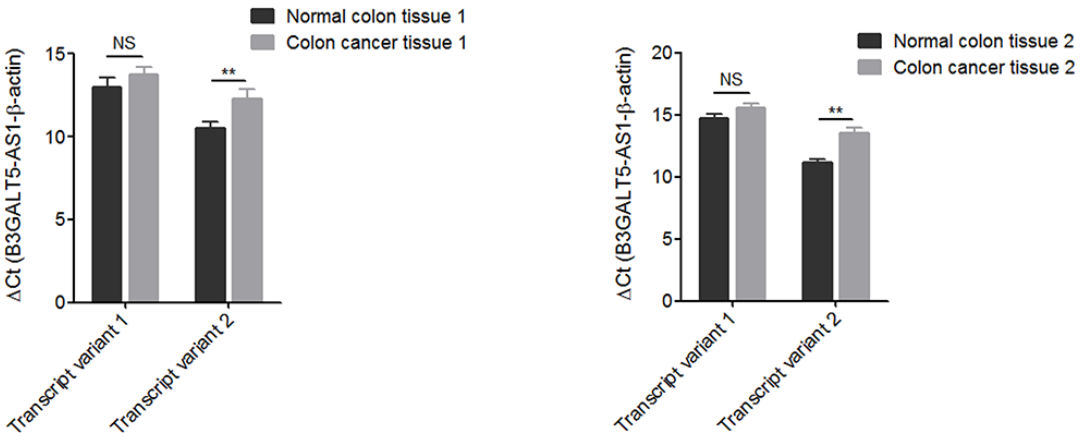

Figure S1. The expression of transcript variants of B3GALT5-AS1 in colon cancer. The expression of B3GALT5-AS1 in 2 pairs of primary colon cancer tissues and adjacent normal colonic epithelium tissues was measured using qRT-PCR. Data are displayed as mean ± s.d. of three independent experiments. ***P* < 0.01, NS, not significant, Student's *t*-test.

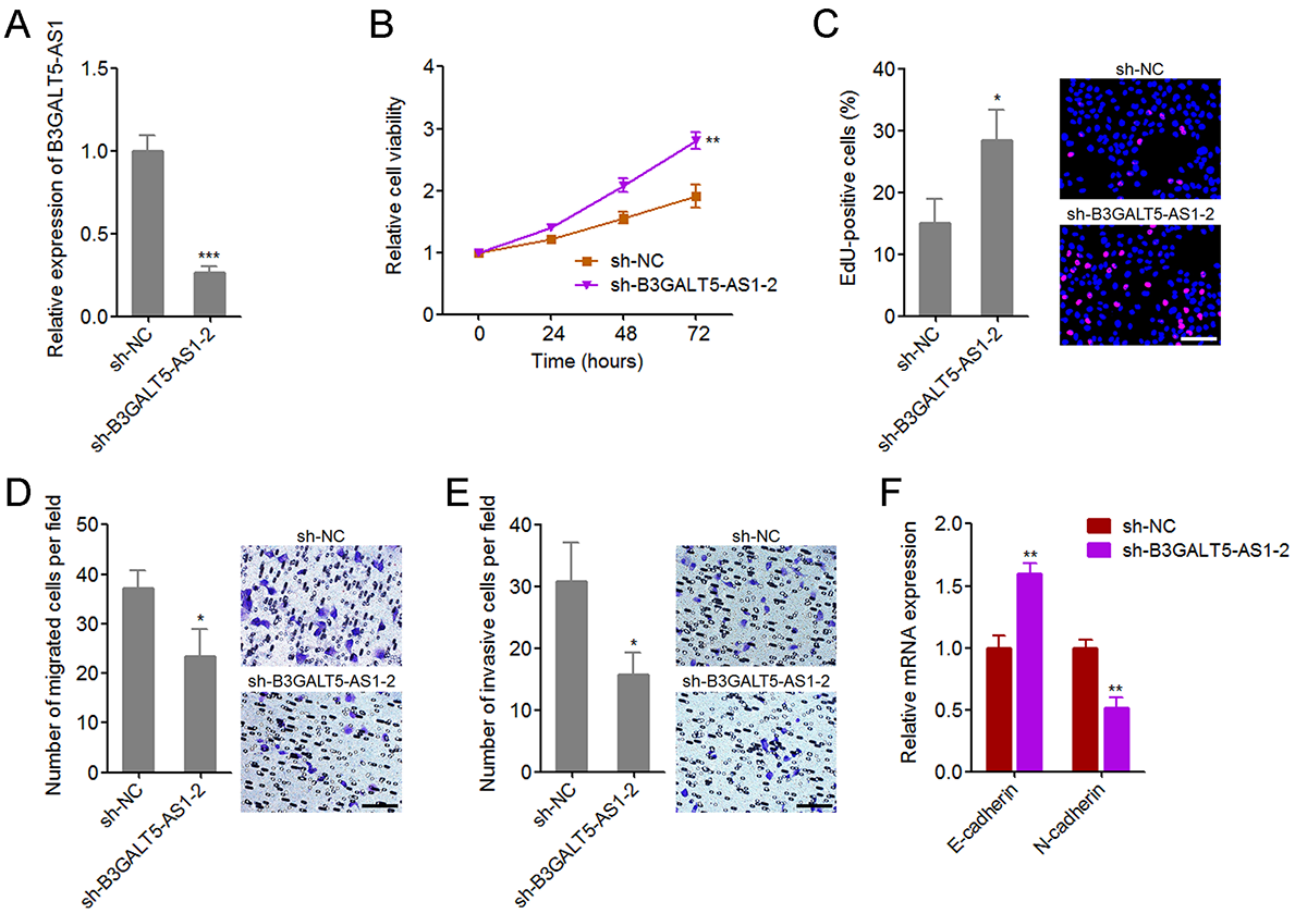

Figure S2. Knockdown of B3GALT5-AS1 promoted proliferation and suppressed migration, invasion, and EMT of NCM460 cells. (**A**) After transient transfection of B3GALT5-AS1 specific or control shRNA into NCM460 cells, the expression of B3GALT5-AS1 was detected using qRT-PCR. (**B**) After transient transfection of B3GALT5-AS1 specific or control shRNA into NCM460 cells, cell viability was detected using Glo cell viability assay. (**C**) After transient transfection of B3GALT5-AS1 specific or control shRNA into NCM460 cells, cell proliferation was detected using EdU incorporation assay. The red color indicts EdU-positive cells. Scale bars = 100 μm. (**D**) After transient transfection of B3GALT5-AS1 specific or control shRNA into NCM460 cells, cell migration was detected using transwell migration assay. Scale bars = 100 μm. (**E**) After transient transfection of B3GALT5-AS1 specific or control shRNA into NCM460 cells, cell invasion was detected using transwell invasion assay. Scale bars = 100 μm. (**F**) After transient transfection of B3GALT5-AS1 specific or control shRNA into NCM460 cells, the expression of E-cadherin and N-cadherin was detected using qRT-PCR. Data are displayed as mean ± s.d. of three independent experiments. **P* < 0.05, ***P* < 0.01, ****P* < 0.001, Student's *t*-test.

A

Promoter of miRNAs	Predicted expect
miR-203	1e-30
miR-34a	5e-20
miR-200b/200a/429	0.32
miR-200c/141	0.097
miR-9	0.003
miR-29a	0.041

B

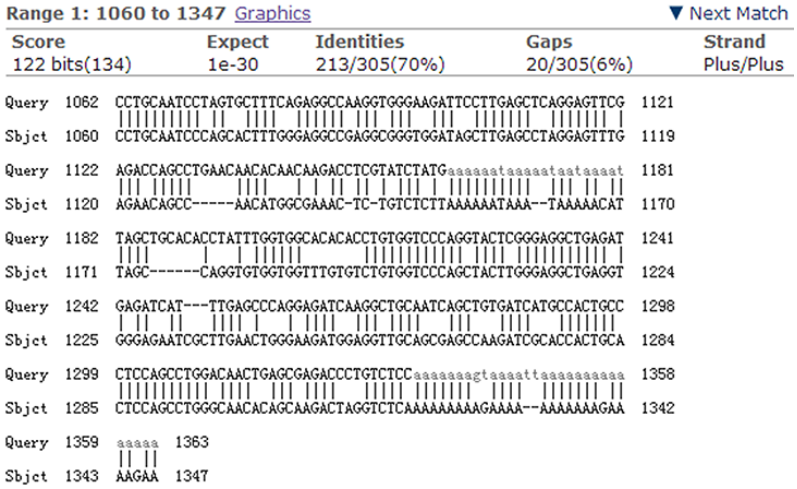

Figure S3. The binding potential between B3GALT5-AS1 and promoters of miRNAs involved in EMT. (**A**) The binding potential between B3GALT5-AS1 and promoters of miRNAs was predicted by Basic Local Alignment Search Tool (BLAST) (https://blast.ncbi.nlm.nih.gov/Blast.cgi). (**B**) Schematic outline of the predicted interaction sites between B3GALT5-AS1 (query) and the promoter of *miR-203* (subject).

Research Paper

A four-methylated mRNA signature-based risk score system predicts survival in patients with hepatocellular carcinoma

Yu Wang[1], Zhiping Ruan[1], Sizhe Yu[1],Tao Tian[1], Xuan Liang[1], Li Jing[1], Wenyuan Li[1], Xiao Wang[1], LCL Xiang[1], F.X. Claret[2], Kejun Nan[1],Hui Guo[1]

[1]Department of Medical Oncology, The First Affiliated Hospital of Xi'an Jiaotong University, Xi'an, Shaanxi, PR China
[2]Department of Systems Biology, The University of Texas MD Anderson Cancer Center, Houston, TX 77030, USA

Correspondence to: Hui Guo; **email:** guohuihappy97@163.com
Keywords: score system, nomogram, prognosis, methylation, hepatocellular carcinoma
Received: September 16, 2018 **Accepted:** December 19, 2018 **Published:** January 10, 2019

Copyright: Wang et al. This is an open-access article distributed under the terms of the Creative Commons Attribution License (CC BY 3.0), which permits unrestricted use, distribution, and reproduction in any medium, provided the original author and source are credited.

ABSTRACT

Evidence suggests that altered DNA methylation plays a causative role in the pathogenesis of various cancers, including hepatocellular carcinoma (HCC). Thus, methylated differently expressed genes (MDEGs) could potentially serve as biomarkers and therapeutic targets in HCC. In the present study, screening four genomics profiling datasets (GSE62232, GSE84402, GSE73003 and GSE57956) enabled us to identify a total of 148 MDEGs. A signature was then established based on the top four MDEGs (BRCA1, CAD, CDC20 and RBM8A). Taking clinical variables into consideration, we constructed a risk score system consisting of the four-MDEG signature and the patients' clinical features, which was predictive of prognosis in HCC. The prognostic value of the HCC risk score system was confirmed using TCGA HCC samples. The scores were then used to construct a nomogram, performance of which was evaluated using Harrel's concordance index (C-index) and a calibration curve. The signature-based nomogram for prediction of overall survival in HCC patients exhibited good performance and was superior to traditional staging systems (C-index: 0.676 vs 0.629, P< 0.05). We have thus established a novel risk score system that is predictive of prognosis and is a potentially useful guide for personalized treatment of HCC patients.

INTRODUCTION

Hepatocellular carcinoma (HCC) is the fifth most common cancer in China, where it is estimated to have killed 140 million people [1]. The leading cause of HCC is chronic infection with a hepatitis virus, alcohol abuse, exposure aflatoxin, tobacco smoking and diabetes [2]. Although there are a large number of studies examining HCC formation and progression, the precise mechanism underlying its pathogenesis remains unclear [3]. Moreover, the rate of early diagnosis of HCC is low; most patients are diagnosed with advanced disease. TNM stage at diagnosis is still regarded as the best predictor of survival [4]. However, because HCC is a highly heterogeneous malignancy, the prognoses of patients with the same stage disease may differ due to inherent clinical and molecular diversities [5]. Therefore, new valid and reliable prognostic and predictive biomarkers are needed to improve risk prediction and offer better information for guiding personalized therapy.

Alterations in epigenetic modifications such as DNA methylation, histone acetylation and RNA interference are important heritable contributory factors in tumor development [6]. For example, altered DNA methylation is thought to contribute to the pathogenesis of a variety of cancers, including HCC [7]. However,

multiple studies indicate that a variety of genes are aberrantly hyper- or hypomethylated in HCC [8], but a comprehensive profile of the pathways within the interaction network remains to be elucidated. Several genes encoding epigenetic regulatory proteins, including EZH2 and HBV, have been shown to be involved in hepatocellular malignancy [9-10]. In addition, evidence now suggests that methylated mRNA may be a valid predictor of HCC [11]. But to the best of our knowledge, there are no prior studies examining methylated differentially expressed genes (MDEGs) on a genome-wide scale and focusing on predicting prognosis in HCC. In the present study, therefore, we comprehensively analyzed high-dimensional data from the Gene Expression Omnibus (GEO) and The Cancer Genome Atlas (TCGA) to build a novel MDEG-based risk score system that is predictive of prognosis and could potentially guide personalized therapy for HCC patients.

RESULTS

Identification and enrichment analysis of MDEGs in HCC

The flowchart for this study is shown in Figure 1. GSE62232, GSE84402, GSE73003 and GSE57956 comprised the training cohort downloaded from the GEO database. The mRNA expression datasets GSE62232 and GSE84402 were calculated using the limma package in R (v 3.5.1). GSE62232 included 81 HCC and 10 normal liver samples, while, GSE84402 included 14 paired HCC and non-tumor samples (Affymetrix Human Genome U133 plus 2.0 platform). The GEO2R online analysis tool was used to calculate the datasets for the methylation difference profiles GSE73003 and GSE57956. The GSE73003 series consisted of 20 paired HCC and non-tumor samples, while GSE57956 consisted of 59 paired HCC and non-tumor samples (Illumina Human Methylation27 BeadChip). With cut-off criteria of $P < 0.05$ and $|\log2FC| > 1$, a total of 130 hypomethylation-high expression genes were detected by overlapping 3476 hypomethylated genes (4869 in GSE57956, 3748 in GSE73003) and 1945 upregulated genes (3972 in GSE62232, 3213 in GSE84402). Similarly, 18 hypermethylation-high expression genes were detected by overlapping 1689 hypermethylated genes (2651 in GSE67956, 1881 in GSE73003) and 338 downregulated genes (583 in GSE62232, 745 in GSE73003) (Figure 2A). To confirm that the P value and $|\log2FC|$ conform to logic using a different test, a representative volcano plot was constructed for GSE84402 (Figure 2B).

To obtain a deeper understanding of MDEGs, enrichment analysis with the Database for Annotation,

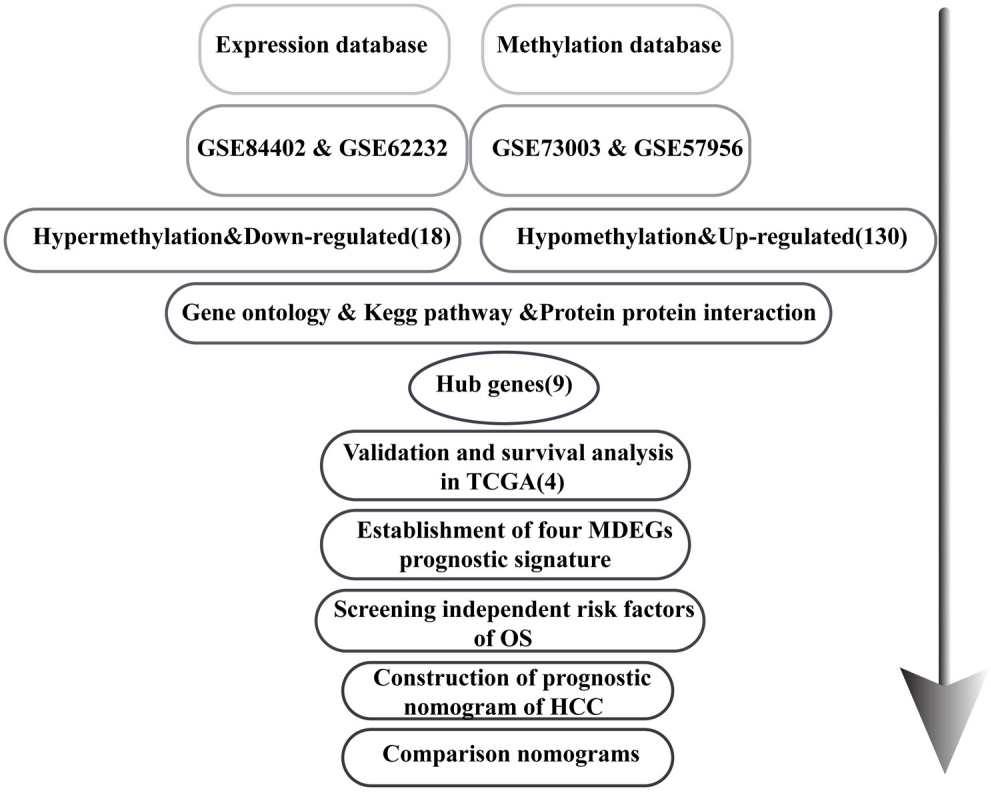

Figure 1. Flowchart of the study.

Visualization and Integrated Discovery (DAVID, https://david.ncifcrf.gov/) was used to elucidate biological function. The top significant terms emerging form the gene oncology enrichment analysis are shown in Figure 2C. MDEGs were enriched in "biological processes of cellular response to DNA damage stimulus," "liver development," "viral process," "angiogenesis," and "cell cycle." Regarding molecular function, MDEGs showed enrichment in "protein binding," "ATP binding," "enzyme binding," and "protein kinase activity." Enrichment of cell com-ponents was mostly "nucleus region," which suggests MDEGs may play an important role in transcription in HCC. Kyoto Encyclopedia of Genes and Genomes (KEGG) analysis suggested that MDEGs were sig-nificantly enrichened in pathways in "cancer," "leukocyte transendothelial migration," and "chemokine signaling pathway." (Figure 2D).

Identification of hub MDEGs and their clinical value in HCC

To identify the connections among MDEGs, a protein-protein interaction (PPI) network for MDEGs was constructed using STRING protein databases (Figure 3A). The top hub genes were CDC20, CDKN3, GNAI1, RBM8A, BRCA1, CAD, ACLY, MMP9, and MAPK1 based on a combined score >0.7 and connection numbers >8. To verify the hub genes, 371 HCC and 50 non-tumor samples were downloaded from TCGA as a validation cohort. Within this group, the expression and methylation values of most hub genes were consistent with the training group, with the exception of MMP9 (Figure 3B, C). We then further investigated the association between gene methylation and expression. The results showed a mild or moderate negative correlation,

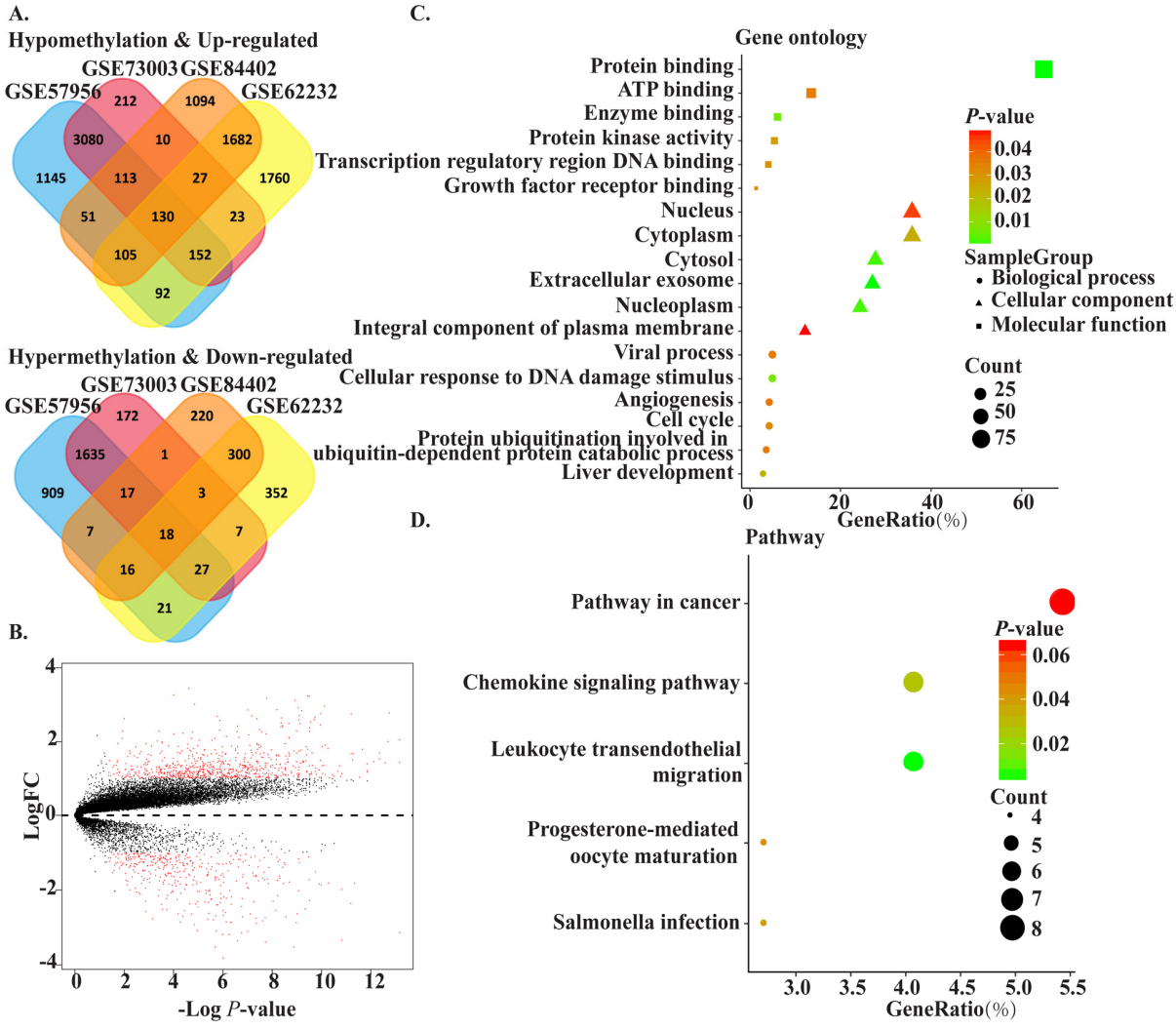

Figure 2. The methylated-differentially expressed genes identification and function. (**A**) Venn of methylated-differentially expressed genes in gene expression datasets (GSE62232, GSE84402) and gene methylation datasets (GSE73003, GSE57956). (**B**) The volcano plot of GSE84402. Log2 (FC) vs. -log10 (p value) for differentially expressed mRNA. Red dot represents significant mRNA (log2|FC|>1, P<0.05). (**C**) The significant enriched gene ontology of MDEGs. (**D**) The significant enriched KEGG pathways of MDEGs.

which suggests methylation leads to decreased gene expression (Figure 3D-E). Expression of CDC20, CDKN3, GNAI1, RBM8A, BRCA1, and CAD showed a significant negative correlation with expression ($p<0.05$), whereas expression of ACLY, MMP9 and MAPK1 showed no correlation or was positively correlated. And results also were verified in MethHC, a database of DNA Methylation and gene expression in Human Cancer (http://methhc.mbc.nctu.edu.tw/php/index.php) (Supplementary Figure 1).

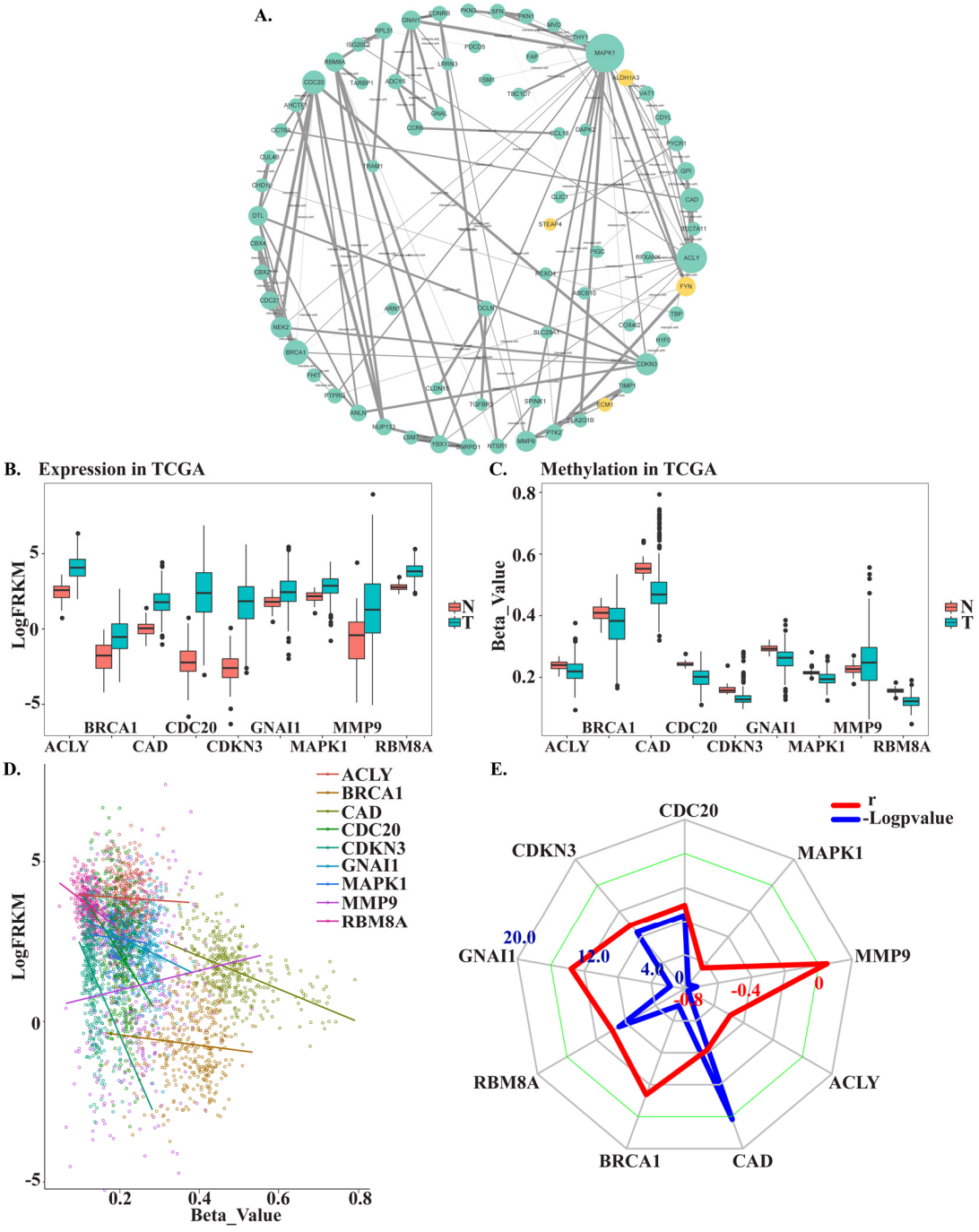

Figure 3. Screening and verifying hub MDEGs. (**A**) Protein-protein interaction network of MDEGs. Green dot represents hypo methylation-high expression gene. Yellow dot represents hyper methylation- low expression. The size of dot was decided by the connection degree of gene and the width of line between genes was decided by connectivity between two genes. (**B**) Expression of hub genes in TCGA. (**C**) Methylation of hub genes in TCGA. Beta-Value represents ratio of methylation. T represents tumor tissue, N represents normal tissue. (**D**) Correlation of expression and methylation of hub genes. (**E**) Radar map of hub genes correlation. Red line represents r and blue line represents - Logpvalue.

To identify hub MDEGs with potential prognostic value, we used the Kaplan-Meier method with the Log-rank test to evaluate the relation between expression of the aforementioned genes and the patients' overall survival (OS). Details of the clinical characteristics are presented in Supplementary Table 1. We found that OS was negatively related to expression of CDC20, RBM8A, BRCA1 and CAD, but had no relation with CDKN3 or GNAI1. Ultimately, the top four hub MDEGs were identified: CDC20, RBM8A, BRCA1 and CAD. To further confirm the results, we verified the four hub genes in Gene Expression Profiling Interactive Analysis (GEPIA, http://gepia.cancer-pku.cn/) (Supplementary Figure 2). Receiver operating characteristic curve (ROC) analysis showed that all four of these genes have high sensitivity and specificity, which suggests high diagnostic value for distinguishing HCC patients from healthy individuals (Figure 4E). These four MDEGs may thus be useful as biomarkers for early diagnosis of HCC.

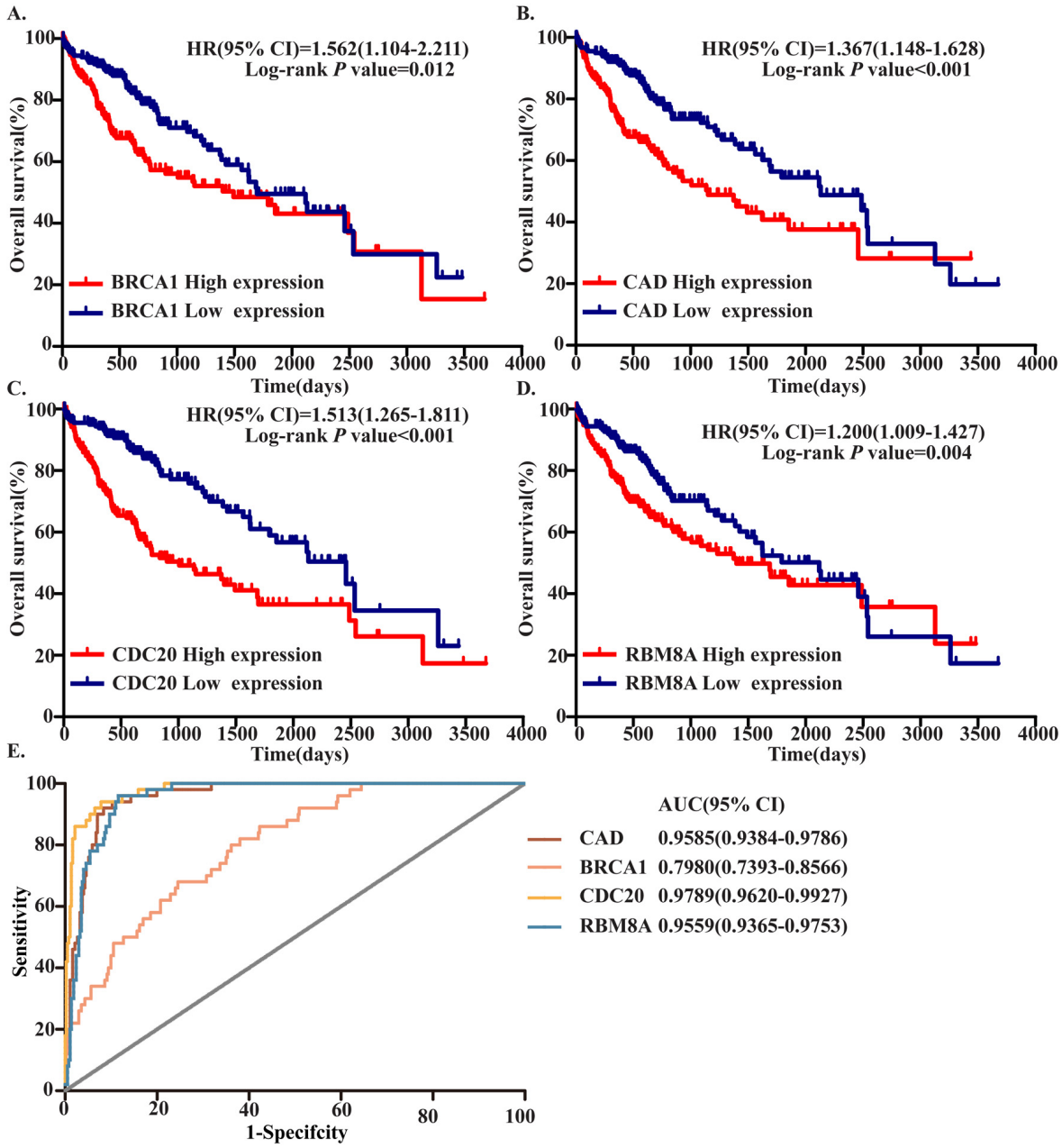

Figure 4. Four hub MDEGs were associated with overall survival in HCC patients by using Kaplan-Meier curve and Log-rank test. The patients were stratified into high expression group and low expression group according to median expression of each mRNA. (**A**) BRCA1; (**B**) CAD; (**C**) CDC20; (**D**) RBM8A. (**E**) ROC curves of the 4 hub MDEGs in HCC. The X axis shows false positive rate, presented as "1-Specifcity". The Y axis indicates true positive rate, shown as "Sensitivity".

Prognostic value of a four-MDEG signature risk score in HCC

To assess the prognostic value of CDC20, RBM8A, BRCA1 and CAD, we constructed a prognostic signature by integrating the expression of these four MDEGs using a regression coefficient. We then calculated a risk score for each patient and ranked them based on increasing score, after which patients were classified into a high-risk (n = 179) or a low risk (n = 179) group based on the median risk score. The risk score distribution, survival status, and expression profile of the four prognostic MDEGs are shown in Figure 5A. OS and progression-free survival (PFS) rates among patients were 60.7% and 53.3%, respectively, in the high-risk group, as compared to 69.2% and 67.2% in the low-risk group (Figure 5B, C). The hazard ratio (HR) of high-risk group versus low-risk group was 1.515 for OS (P = 0.001, 95% confidence interval (CI) = 0.8075-2.222) and 2.559 for PFS (P < 0.001, 95%CI = 1.891-3.227). Thus, patients in the high-risk group had significantly poorer OS and PFS than patients in the low-risk group (Figure 5D, E).

A ROC analysis of the predictive efficiency of the four-MDEG signature suggested it had good performance with respect to both death and progression prediction (Figure 5F). Taking into consideration the patients' clinical features, including age, gender, clinical stage, T stage, grade, adjacent hepatic tissue inflammation, and HCC risk factors (virus infection, alcohol abuse, non-alcoholic fatty liver disease, hemochromatosis, alpha-1 antitrypsin deficiency), univariate and multivariate Cox regression analysis were used to assess the signature

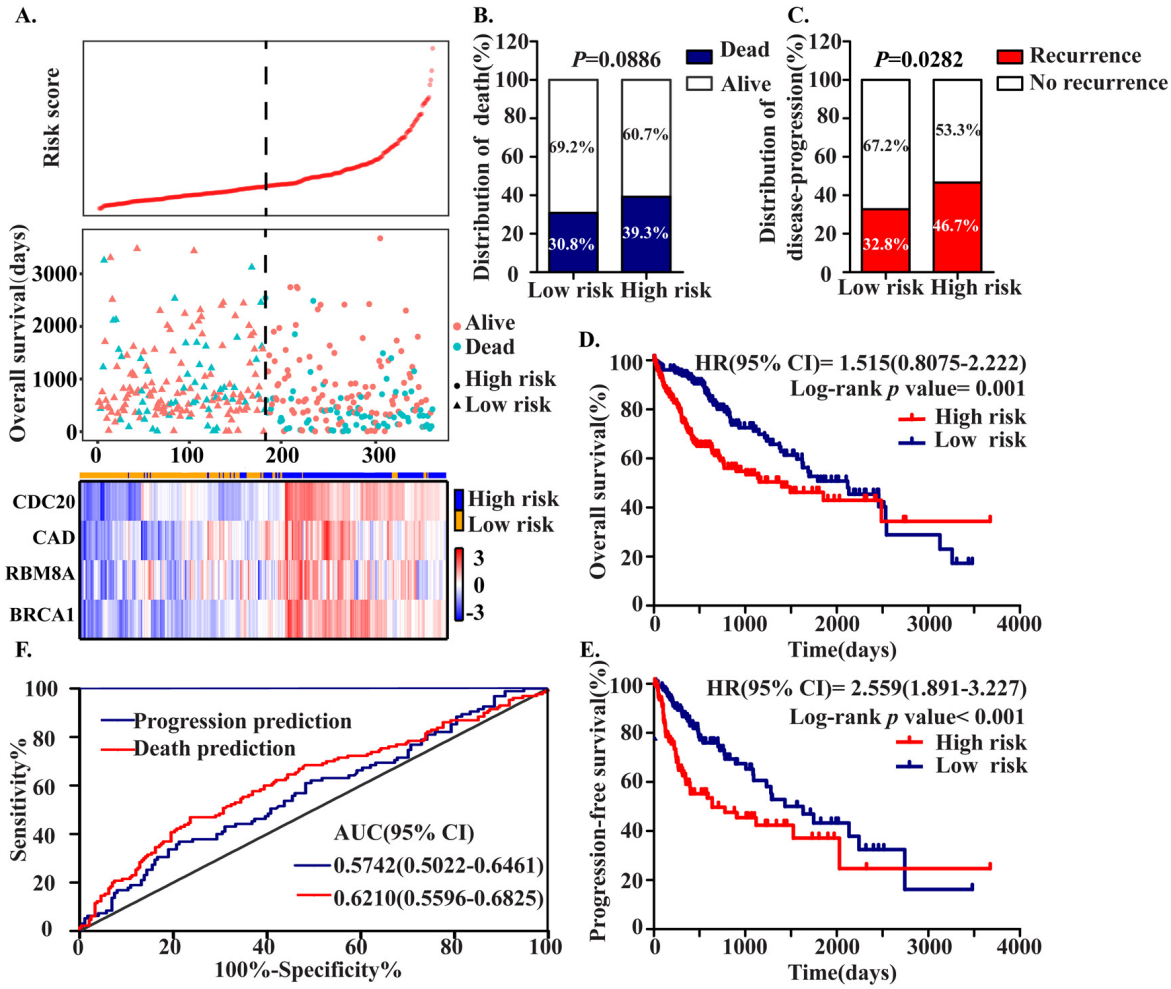

Figure 5. Construction of the Four MDEGs signature of HCC. The patients were stratified into high risk group and low risk group based on median of risk score. (**A**) Risk score distribution of HCC patients, Survival status of each patient and Expression heatmap of the four hub MDEGs corresponding to each sample above. Red: high expression; Blue: low expression. (**B**, **C**) The distribution of death (**B**) and disease-progression (**C**) in high and low risk group. (**D**, **E**) Kaplan-Meier estimates of the overall survival (**D**) and progression-free survival (**E**) time of patients using the four MDEGs signature based risk score. (**F**) The ROC curve of the four MDEGs signature.

(high-risk vs. low-risk) with respect to OS. In the univariate analysis, clinical stage (HR = 2.229, $P < 0.001$), T stage (HR = 2.534, $P < 0.001$), HCC risk factors (HR = 0.631, $P = 0.011$), fibrosis (HR = 0.542, $P = 0.002$) and the four-MDEG signature (HR = 4.467, $P < 0.001$) were all significantly associated with OS in HCC patients. To integrate all independent risk factors affecting OS for construction of a HCC prognostic nomogram, significant clinicopathological factors from the univariate analyses were entered into multivariate COX regression analyses. The results indicated that the four-MDEG signature (HR = 2.022, P < 0.001) was a significant independent factor of OS, as were T stage (H = 2.149, $P < 0.001$) and HCC risk factors (HR = 0.651, $P = 0.019$) (Table 1).

Establishment of a nomogram for OS prediction in HCC

To provide a clinically associated quantitative method that could be used to predict the probabilities of 3- and 5-year OS in HCC, a prognostic nomogram was established in which the score integrated the three independent prognostic factors, T stage, HCC risk factors and the four-MDEG signature (Figure 6A). Harrel's concordance index (C-index) for OS prediction was 0.676. The calibration curves for the nomogram for the 3- and 5- year OS rates showed good agreement between the prediction and the actual observation (Figure 6B). Each patient for whom there was complete clinical information about T stage, HCC risk factors, and the four-MDEG signature would obtain a Nomo-score reflecting total points. Using the Nomo-score, patients were divided into three risk groups based on the tertiles, which had cut-off values of 28.50 and 44.60. From KM analysis of the TCGA dataset, significant differences were observed between the high-, intermediate- and low-risk groups (P = 0.0003) (Figure 6C).

Comparison of predictive accuracy between the nomogram and a single independent factor

The TNM stage system is regarded as the best predictor of survival. Moreover, we found that T stage was an independent prognostic factor for OS in HCC. The predictive power of the nomogram for HCC prognosis

Table 1. Univariate/multivariate COX regression analyses of clinicopathologic factors associated with OS.

Variables	Univariate analysis		Multivariate analysis	
	HR(95%CI)	*P*	HR(95%CI)	*P*
Age(≥65 vs. < 65)	1.265(0.893-1.791)	0.235		
Gender(Male vs. Female)	0.817(0.573-1.164)	0.262		
Clinical stage(III +IV vs. I+II)	2.229(1.559-3.188)	<0.001*		
Grade(G3+G4 vs. G1+G2)	1.113(0.774-1.601)	0.564		
T stage(T3+T4 vs.T1+T2)	2.534(1.783-3.601)	<0.001*	2.149(1.499-3.081)	<0.001*
AFP(<25ng/ml vs. >=25ng/ml)	1.002(0.697-1.442)	0.991		
Adjacent hepatic tissue inflammation(Yes vs. No)	0.699(0.468-1.044)	0.699		
Fibrosis(Yes vs. No)	0.542(0.366-0.803)	0.002*		
Child-Pugh(A vs. B+C)	1.141(0.578-2.251)	0.703		
BMI(>=25 vs <25)	0.733(0.515-1.043)	0.084		
Family history(Yes vs. No)	1.225(0.858-1.748)	0.264		
HCC risk factors(Yes vs. No)	0.631(0.443-0.898)	0.011*	0.651(0.454-0.933)	0.019*
Four MDEGs signature (high risk vs. low risk)	4.467(1.995-10.002)	<0.001*	2.022(1.486-2.753)	<0.001*

Abbreviations: OS, overall survival; HR, hazard ratio; 95% CI, 95% confidence interval.
*Statistically significant; AFP, Alpha-fetoprotein; BMI, body mass index.

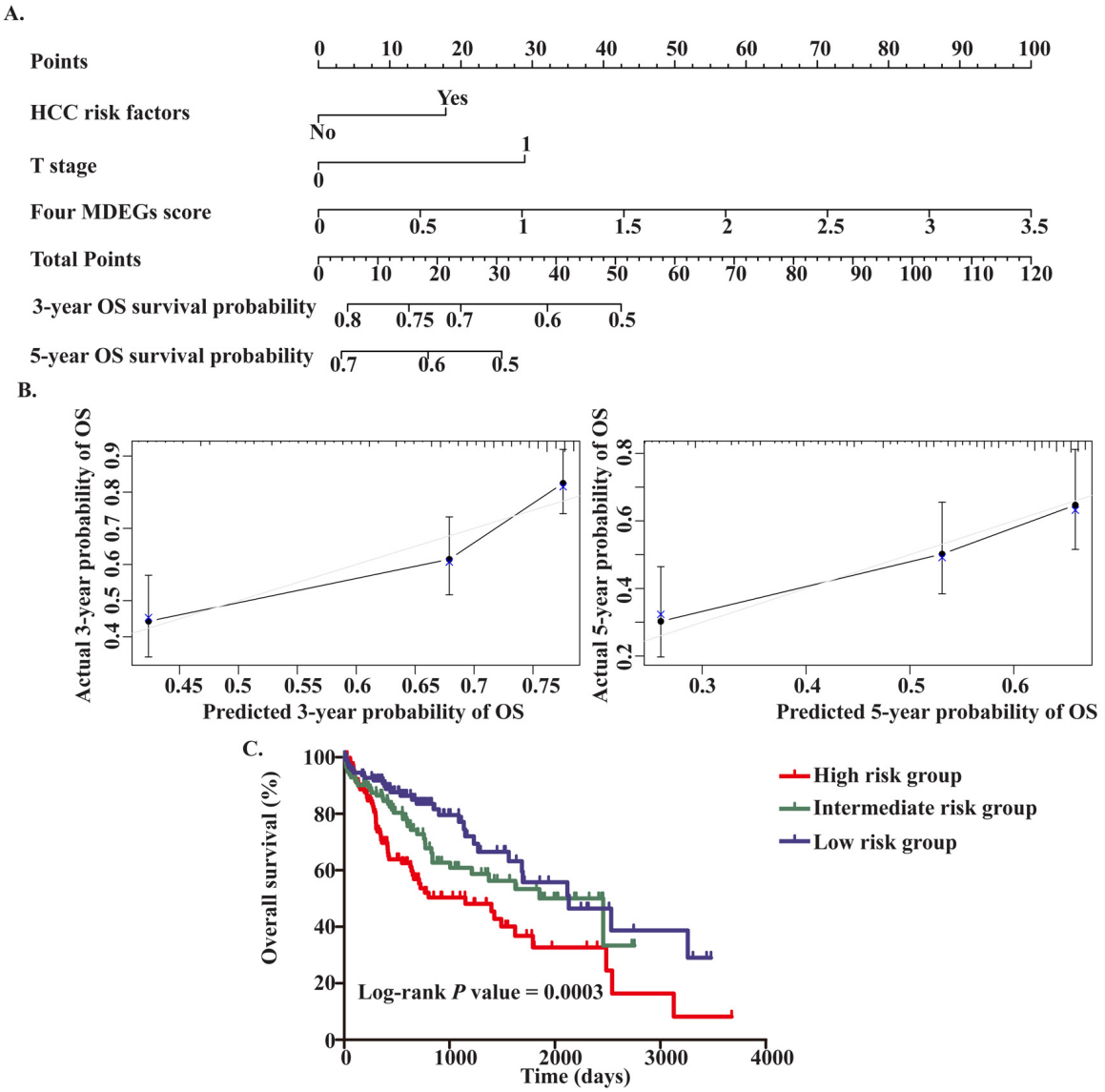

Figure 6. Establishment of the OS nomogram for HCC patients. (**A**) Nomogram for predicting OS of HCC. There are three components in this nomogram: the four MDEGs score, HCC risk factor and T stage. Each of them generates points according to the line drawn upward. And the total points of the three components of an individual patient lie on "Total Points" axis which corresponds to the probability of 3-year and 5-year OS rate plotted on the two axes below. (**B**) Calibration plots of the nomogram for predicting OS rate at 3 year (Left) and 5 years (Right). The predicted and the actual probabilities of OS were plotted on the x- and y-axis, respectively. (**C**) Kaplan-Meier curves of three risk subgroups stratified by the total points the nomogram gives.

was compared with that of T stage. The C-index for OS prediction based on T stage was 0.629, which was significantly lower than the C-index for the nomogram (0.676, P<0.05). This suggests our nomogram is a more accurate predictor of OS in HCC than conventional staging systems and is potentially valuable for predicting survival of HCC patients.

DISCUSSION

A valid and accurate molecule-based method for identifying patients who have a poor prognosis is urgently needed to optimize their individual therapy. Therefore, effective and credible biomarkers and genetic signatures that can serve as prognostic predictors and treatment targets are critically needed for HCC. In the last decade, methylation has come to be recognized as an important epigenetic regulator of gene expression in eukaryotes, and it is now well established that methylation, especially DNA methylation, is crucially involved in multiple cancers, including HCC [12, 13]. Nishida showed that alterations in DNA methylation are a common feature of hepatocarcinogenesis [14]. Although some studies have identified

MDEGs in HCC [15, 16], their predictive value for HCC patients has not been systematically investigated until now. To our knowledge, this is the first study to develop a MDEG-based risk score that is predictive of prognosis in HCC.

We used methylation and expression microarrays with GEO databases to screen for MDEGs and were able to obtain a set of MDEGs through in *silico* analysis. Enrichment analysis of the MDEGs suggested they were involved in key biological processes, including DNA damage, viral processes, angiogenesis, and cell cycling. Given that hepatitis virus is a main cause of HCC, the presence of DNA damage due to integration of the virus genome into the host DNA is reasonable [17]. Also reasonable is the involvement of angiogenesis, since HCC is a highly vascular tumor. In addition, KEGG enrichments suggested that significantly enriched pathways include chemokine signaling pathways, which suggests that inflammation and immunity are critical factors in the pathogenesis, progression and metastasis of HCC [18]. Chemokine signaling reportedly influences HCC invasion and/or metastasis through effects on the tumor microenvironment [19, 20]. Evidence indicates, for example, that chemokines such as CCL5, CCL7, CXCL8 act via CCRs on myeloid-derived suppressor cells (MDSCs) to form an inhibitory tumor microenvironment that promotes tumor pathogenesis, progression and resistance [21-23].

Based on PPI analysis, we identified nine hub genes, which were verified and analyzed in a validation cohort from TCGA. Four of these hub genes, which were significantly associated with OS of HCC patients, were ultimately selected. Earlier research has consistently demonstrated that upregulation of BRCA1, CDC20, RBM8A and CAD promotes progression, invasion, metastasis and chemoresistance in HCC [24-27]. While the efficacy of any single marker is limited, a multiple-marker signature could have greater diagnostic and prognostic value. We therefore constructed a four-MDEG signature that was an independent prognostic factor for HCC patients. This signature was predictive of both OS and PFS. If applied, relatively minor examination using our risk score system could help identify high- and low-risk HCC patients and provide useful information that could aid in selecting a therapeutic strategy.

To increase the accuracy of the prediction of prognosis, both genetic and clinically-related variables were integrated into the nomogram. Ultimately, the OS nomogram included the four-MDEG signature, T stage and HCC risk factors. The nomogram for HCC performed well when used to predict OS, and its predictive ability was verified using a C-index and a calibration curve. Indeed, the nomogram provides greater predictive accuracy for OS than traditional systems. As regards the prognostic signature or nomogram, if we are able to put it into clinical practice in the future, we anticipate being able to identify patients at high-risk of cancer-related death before treatment, and recommend a more aggressive therapeutic strategies with dynamic surveillance. However, there are limitations to our study. First, whether the prognostic signature or nomogram can be applied to patients must be confirmed in larger groups of HCC patients. Second, the molecular mechanism of the four MDEGs in HCC remains to be explored further.

In summary, we have developed a novel four-MDEG expression-based risk score system for objectively and accurately predicting survival and prognosis in HCC patients. In addition, the MDEG signature could also shed new light on the role of methylation in the pathogenesis and progression of HCC, which may provide information helpful for selection of therapeutic strategies. The four MDEGs could potentially serve as biomarkers and therapeutic targets for dynamic surveillance and treatment of HCC patients.

MATERIALS AND METHODS

Data processing

The raw data and clinical information were download from the GEO (https://www.ncbi.nlm.nih.gov/geo/) and TCGA (https://cancergenome.nih.gov/). Gene methyltion profiling of the GSE73003 and GSE57956 datasets was conducted using the GPL8490 platform (Illumina Human Methylation27 BeadChip), which included 27,578 highly informative CpG sites and more than 14476 genes (http://www.illumina.com/pages.ilmn?ID=243). Gene expression profiling of the GSE84402 and GSE62232 datasets was conducted using the GPL570 platform (Affymetrix Human Genome U133 plus 2.0 Array), which included 54675 unique probes and tested more than 23517 genes (http://www.affymetrix.com/support/technical/byproduct.affx?product=hg-u133-plus). The GSE73003 series consisted of 20 paired HCC and non-tumor samples. The GSE57956 series consisted of 59 paired HCC and non-tumor samples. The GSE84402 series included 14 paired HCC and non-tumor samples. And the GSE62232 series included 81 HCC and 10 normal liver samples. From TCGA, we downloaded 371 HCC and 50 non-tumor samples. The mRNA-seq data were preprocessed and submitted for analysis as the upper quantile normalized FPKM values. GEO2R was used to screen for genes differentially methylated between tumor and non-tumor samples. The differentially

expressed genes were identified using the limma package in R. Values of P<0.05 and |FC|≥1 were considered significant. Finally, hypomethylation-high expression genes were detected by overlapping hypomethylated and upregulated genes; similarly, hypermethylation-low expression genes were detected by overlapping hypermethylated and downregulated genes.

Functional and pathway enrichment analysis

Functional annotations in MDEGs were done using The Database for Annotation, Visualization and Integrated Discovery (DAVID; https://david.ncifcrf.gov/), which enriched gene oncology and pathways. Gene oncology involved three categories: cellular components, molecular function, and biological processes. Pathway enrichment was carried out using the Kyoto Encyclopedia of Genes and Genomes (KEGG, https://www.kegg.jp/), which contains information about genomes, biological pathways, diseases, and chemical substances. The criterion for significant enrichment of biological processes and pathways was $P = 0.05$.

Hub MDEG screening and verification

STRING protein databases (https://string-db.org/) were used to evaluate interactive relationships among the MDEGs. We used Cytoscape software to construct a network based on the STRING results. Combined scores >0.7 and connection numbers >8 were deemed to indicate hub genes. To confirm the results, the hub MDEGs were validated in TCGA. The Pearson correlation test was used to assess the relationship between hub gene methylation and expression in HCC.

Formulation of MDEG signatures and association of signatures and clinical features

ROC curve analysis was used to evaluate the diagnostic effectiveness of hub MDEGs. The prognostic value of hub MDEGs were evaluated using the Kaplan-Meier method with the Log-rank test. Hub MDEGs related to OS were considered to be prognostic. Using the combination of weighted MDEG expression values, independent hub MDEG biomarkers were integrated into a MDEG signature using a risk scoring method as shown in the following equation: Risk Score (patient) = $\sum_{i=1}^{n} \frac{expression(mRNAi)}{median} * coefficient(mRNAi)$. Here, Risk Score (patient) is a MDEG signature risk score for a HCC patient. In addition, *mRNAi* represents the *i*th prognostic mRNA, while expression (*mRNAi*) is the expression value of *mRNAi* for the patient. *Coefficient (mRNAi)* is the regression coefficient of *mRNAi*, which represents the contribution of *mRNAi* to the prognostic risk score. Based on the risk score, patients can be assigned to a high-risk or low-risk group. Subsequently, a risk score system was constructed, and the median risk score was regarded as the cutoff point. HCC patients were then divided into high- and low-risk groups. Kaplan-Meier survival curves were calculated to compare survival and recurrence risk between the high- and low-risk groups.

Statistical analysis

To identify independent predictors of OS in HCC, univariate Cox regression analysis was performed to evaluate the prognostic value of signatures with a threshold value of 0.2. Multivariate Cox regression analyses were conducted using Forward LR. Hazard ratios (HRs) and 95% confidence intervals (CIs) were computed based on the Cox regression analysis. A nomogram was constructed based on the results of the multivariate Cox regression analyses using rms version 3.5.1 (http://www.r-project.org/). The performance of the nomogram was assessed using Harrel's concordance index (C-index) and comparing the predicted and actual probabilities for OS. Bootstraps with 1,000 resamples were used for these activities. Comparisons between the nomogram and other staging systems were made using the rcorrp.cens package in Hmisc and were evaluated using the C-index. Each patient received the total points from the nomogram (Nomo-score). KM curve analysis was performed to evaluate the performance of the nomogram by dividing patients into high-, intermediate- and low-risk groups using tertiles of the Nomo-scores as cut-off points. Values of $P < 0.05$ were considered significant. Statistical analysis was performed using the IBM SPSS Statistics software program version 22.0 (IBM Corp., NY, USA).

Abbreviations

MDEG: methylated differently expressed gene; HCC: hepatocellular carcinoma; OS: overall survival; PFS: progression-free survival; HR: hazard ratio; CI: confidence interval; KM curve: Kaplan-Meier curve.

AUTHOR CONTRIBUTIONS

Hui Guo and Yu Wang designed the research and performed analysis; Zhiping Ruan, Sizhe Yu, Tao Tian and Xuan Liang collected and analyzed data and constructed figures; Li Jing, Wenyuan Li, Xiao Wang, LCL Xiang performed statistical analyses; F.X. Claret and Kejun Nan guided experiments; Hui Guo and Yu Wang drafted and revised the manuscript.

ACKNOWLEDGEMENTS

This work benefited from the Gene Expression Omnibus (GEO) database and the Cancer Genome Atlas

(TCGA) database. We were grateful to the access to the resources and the efforts of the staff to expand and improve the two databases.

CONFLICTS OF INTEREST

The authors declare that there are no financial or other relationships that might lead to a conflict of interest of the present article.

FUNDING

This study was supported in part by grant 81672432 from the National Natural Science Foundation of China (to H.G).

REFERENCES

1. Siegel RL, Miller KD, Jemal A. Cancer Statistics, 2017. CA Cancer J Clin. 2017; 67:7–30. https://doi.org/10.3322/caac.21387

2. Forner A, Llovet JM, Bruix J. Hepatocellular carcinoma. Lancet. 2012; 379:1245–55. https://doi.org/10.1016/S0140-6736(11)61347-0

3. Guo H, Jing L, Cheng Y, Atsaves V, Lv Y, Wu T, Su R, Zhang Y, Zhang R, Liu W, Rassidakis GZ, Wei Y, Nan K, Claret FX. Down-regulation of the cyclin-dependent kinase inhibitor p57 is mediated by Jab1/Csn5 in hepatocarcinogenesis. Hepatology. 2016; 63:898–913. https://doi.org/10.1002/hep.28372

4. Amin MB, Greene FL, Edge SB, Compton CC, Gershenwald JE, Brookland RK, Meyer L, Gress DM, Byrd DR, Winchester DP. The Eighth Edition AJCC Cancer Staging Manual: Continuing to build a bridge from a population-based to a more "personalized" approach to cancer staging. CA Cancer J Clin. 2017; 67:93-99. https://doi.org/10.3322/caac.21388

5. Bruix J, Gores GJ, Mazzaferro V. Hepatocellular carcinoma: clinical frontiers and perspectives. Gut. 2014; 63:844–55. https://doi.org/10.1136/gutjnl-2013-306627

6. Chen Z, Li S, Subramaniam S, Shyy JY, Chien S. Epigenetic Regulation: A New Frontier for Biomedical Engineers. Annu Rev Biomed Eng. 2017; 19:195–219. https://doi.org/10.1146/annurev-bioeng-071516-044720

7. Nordlund J, Syvänen AC. Epigenetics in pediatric acute lymphoblastic leukemia. Semin Cancer Biol. 2018; 51:129–38. https://doi.org/10.1016/j.semcancer.2017.09.001

8. Sang L, Wang XM, Xu DY, Zhao WJ. Bioinformatics analysis of aberrantly methylated-differentially expressed genes and pathways in hepatocellular carcinoma. World J Gastroenterol. 2018; 24:2605–16. https://doi.org/10.3748/wjg.v24.i24.2605

9. Cai MY, Tong ZT, Zheng F, Liao YJ, Wang Y, Rao HL, Chen YC, Wu QL, Liu YH, Guan XY, Lin MC, Zeng YX, Kung HF, Xie D. EZH2 protein: a promising immunomarker for the detection of hepatocellular carcinomas in liver needle biopsies. Gut. 2011; 60:967–76. https://doi.org/10.1136/gut.2010.231993

10. Lee SM, Lee YG, Bae JB, Choi JK, Tayama C, Hata K, Yun Y, Seong JK, Kim YJ. HBx induces hypomethylation of distal intragenic CpG islands required for active expression of developmental regulators. Proc Natl Acad Sci USA. 2014; 111:9555–60. https://doi.org/10.1073/pnas.1400604111

11. Xu RH, Wei W, Krawczyk M, Wang W, Luo H, Flagg K, Yi S, Shi W, Quan Q, Li K, Zheng L, Zhang H, Caughey BA, et al. Circulating tumour DNA methylation markers for diagnosis and prognosis of hepatocellular carcinoma. Nat Mater. 2017; 16:1155–61. https://doi.org/10.1038/nmat4997

12. Casadevall D, Kilian AY, Bellmunt J. The prognostic role of epigenetic dysregulation in bladder cancer: A systematic review. Cancer Treat Rev. 2017; 61:82–93. https://doi.org/10.1016/j.ctrv.2017.10.004

13. Hlady RA, Sathyanarayan A, Thompson JJ, Zhou D, Wu Q, Pham K, Lee JH, Liu C, Robertson KD. Integrating the Epigenome to Identify Drivers of Hepatocellular Carcinoma. Hepatology. 2019. https://doi.org/10.1002/hep.30211

14. Nishida N, Nishimura T, Nakai T, Chishina H, Arizumi T, Takita M, Kitai S, Yada N, Hagiwara S, Inoue T, Minami Y, Ueshima K, Sakurai T, Kudo M. Genome-wide profiling of DNA methylation and tumor progression in human hepatocellular carcinoma. Dig Dis. 2014; 32:658–63. https://doi.org/10.1159/000367982

15. Sun XJ, Wang MC, Zhang FH, Kong X. An integrated analysis of genome-wide DNA methylation and gene expression data in hepatocellular carcinoma. FEBS Open Bio. 2018; 8:1093–103. https://doi.org/10.1002/2211-5463.12433

16. Liu S, Miao C, Liu J, Wang CC, Lu XJ. Four differentially methylated gene pairs to predict the prognosis for early stage hepatocellular carcinoma patients. J Cell Physiol. 2018; 233:6583–90. https://doi.org/10.1002/jcp.26256

17. Lee WY, Bachtiar M, Choo CC, Lee CG. Comprehensive review of Hepatitis B Virus-associated hepatocellular carcinoma research through text mining and big data analytics. Biol Rev Camb Philos Soc. 2018. https://doi.org/10.1111/brv.12457

18. Yu S, Wang Y, Jing L, Claret FX, Li Q, Tian T, Liang X,

Ruan Z, Jiang L, Yao Y, Nan K, Lv Y, Guo H. Autophagy in the “inflammation-carcinogenesis” pathway of liver and HCC immunotherapy. Cancer Lett. 2017; 411:82–89. https://doi.org/10.1016/j.canlet.2017.09.049

19. Zhu Y, Gao XM, Yang J, Xu D, Zhang Y, Lu M, Zhang Z, Sheng YY, Li JH, Yu XX, Zheng Y, Dong QZ, Qin LX. C-C chemokine receptor type 1 mediates osteopontin-promoted metastasis in hepatocellular carcinoma. Cancer Sci. 2018; 109:710–23. https://doi.org/10.1111/cas.13487

20. Liu J, Chen S, Wang W, Ning BF, Chen F, Shen W, Ding J, Chen W, Xie WF, Zhang X. Cancer-associated fibroblasts promote hepatocellular carcinoma metastasis through chemokine-activated hedgehog and TGF-β pathways. Cancer Lett. 2016; 379:49–59. https://doi.org/10.1016/j.canlet.2016.05.022

21. Thakur A, Schalk D, Tomaszewski E, Kondadasula SV, Yano H, Sarkar FH, Lum LG. Microenvironment generated during EGFR targeted killing of pancreatic tumor cells by ATC inhibits myeloid-derived suppressor cells through COX2 and PGE2 dependent pathway. J Transl Med. 2013; 11:35. https://doi.org/10.1186/1479-5876-11-35

22. Qin Y, Vasilatos SN, Chen L, Wu H, Cao Z, Fu Y, Huang M, Vlad AM, Lu B, Oesterreich S, Davidson NE, Huang Y. Inhibition of histone lysine-specific demethylase 1 elicits breast tumor immunity and enhances antitumor efficacy of immune checkpoint blockade. Oncogene. 2018. https://doi.org/10.1038/s41388-018-0451-5. Epub ahead of print.

23. Kumar D, Xu ML. Microenvironment Cell Contribution to Lymphoma Immunity. Front Oncol. 2018; 8:288. https://doi.org/10.3389/fonc.2018.00288

24. Liao Y, Yuan S, Chen X, Zhu P, Li J, Qin L, Liao W. Up-regulation of BRCA1-associated RING Domain 1 Promotes Hepatocellular Carcinoma Progression by Targeting Akt Signaling. Sci Rep. 2017; 7:7649. https://doi.org/10.1038/s41598-017-07962-7

25. Cui X, Li X, Li J, Wang X, Sun W, Cheng Z, Ding J, Wang H. inFRank: a ranking-based identification of influential genes in biological networks. Oncotarget. 2017; 8:43810–21. https://doi.org/10.18632/oncotarget.11878

26. Liang R, Lin Y, Ye JZ, Yan XX, Liu ZH, Li YQ, Luo XL, Ye HH. High expression of RBM8A predicts poor patient prognosis and promotes tumor progression in hepatocellular carcinoma. Oncol Rep. 2017; 37:2167–76. https://doi.org/10.3892/or.2017.5457

27. Zhai X, Zhu H, Wang W, Zhang S, Zhang Y, Mao G. Abnormal expression of EMT-related proteins, S100A4, vimentin and E-cadherin, is correlated with clinicopathological features and prognosis in HCC. Med Oncol. 2014; 31:970. https://doi.org/10.1007/s12032-014-0970-z

SUPPLEMENTARY MATERIAL

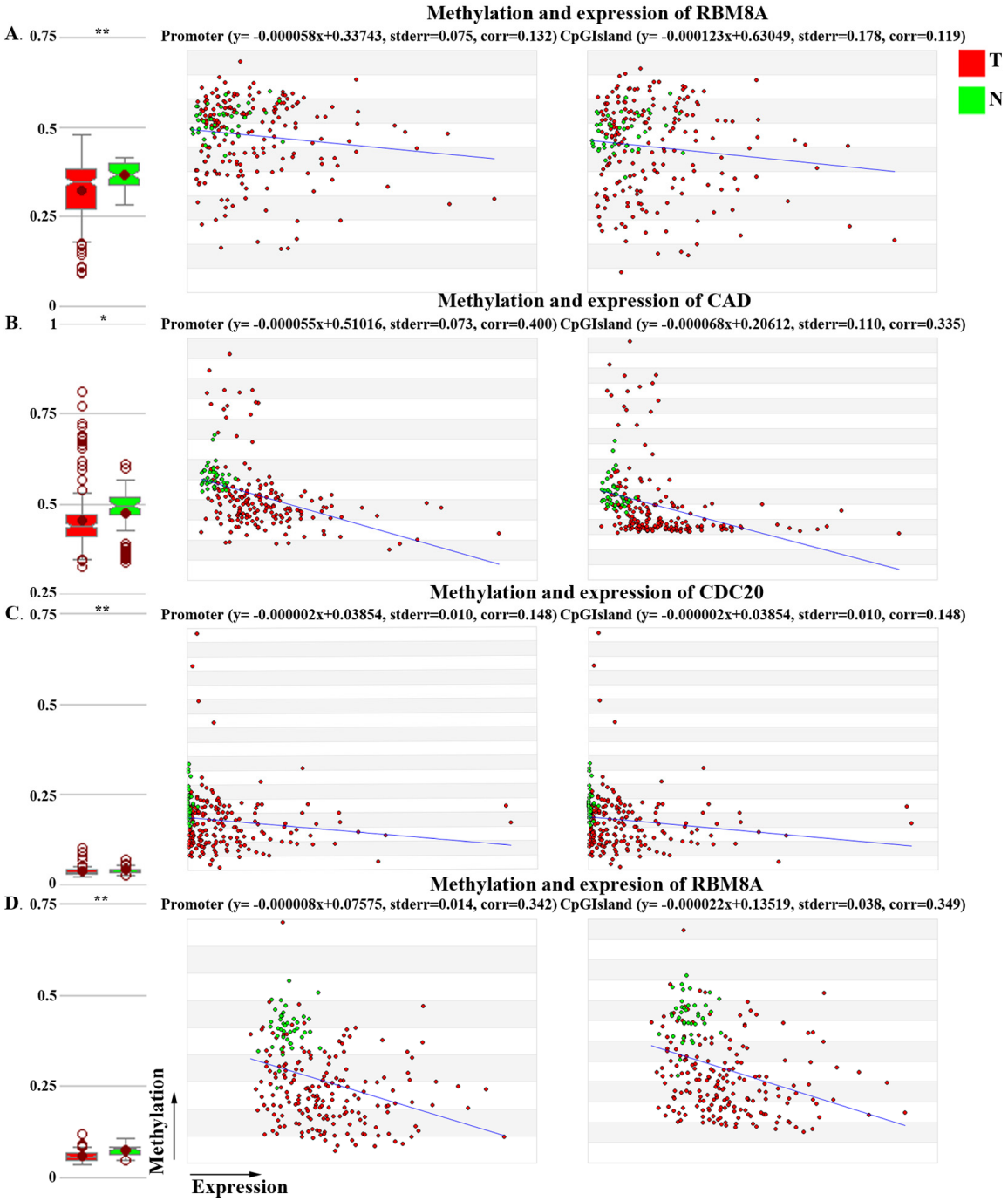

Supplementary Figure 1. Methylation and correlation with expression of the four hub genes. (**A**) BRCA1 (**B**) CAD (**C**) CDC20 (**D**) RBM8A Red dot represents tumor sample; green dot represents normal sample. Horizontal axis is expression and vertical axis is methylation. *: P<0.05; **: P<0.005.

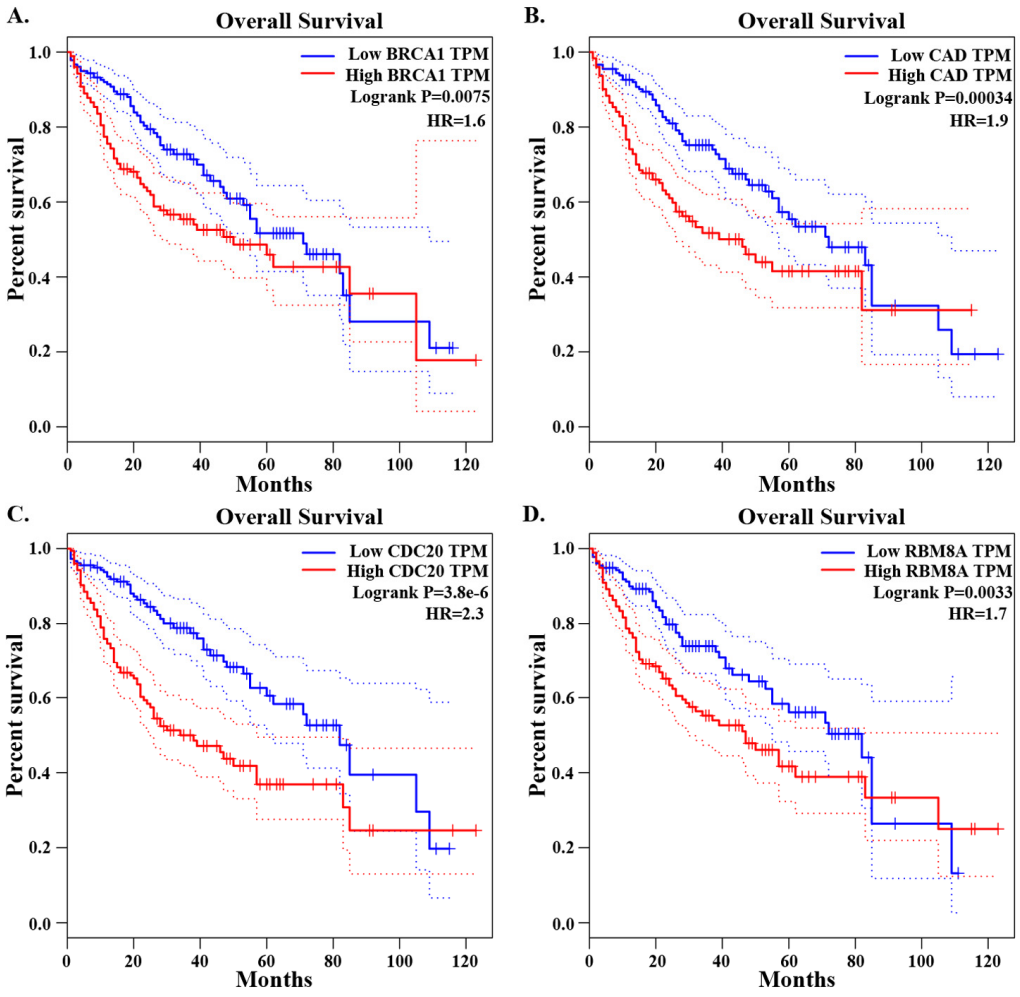

Supplementary Figure 2. Relation between expression of the four hub genes and OS. (**A**) BRCA1 (**B**) CAD (**C**) CDC20 (**D**) RBM8A.

SUPPLEMENTARY TABLE

Please browse the link in Full Text version to find the data of **Supplementary Table 1. The clinical characteristics of TCGA.**

Research Paper

MicroRNA-141 suppresses growth and metastatic potential of head and neck squamous cell carcinoma

Zhiguo Zhao[1], Dan Gao[2], Tie Ma[1], Liping Zhang[1]

[1]Department of Oral and Maxillofacial Surgery, Shengjing Hospital of China Medical University, Shenyang, P.R.China
[2]Department of Clinical Laboratory, Shengjing Hospital of China Medical University, Shenyang, P.R.China

Correspondence to: Liping Zhang; **email:** zhanglipingcmu@163.com
Keywords: EGFR, HNSCC, miR-141, growth, metastasis
Received: September 12, 2018 **Accepted:** January 21, 2019 **Published:** February 8, 2019

Copyright: Zhao et al. This is an open-access article distributed under the terms of the Creative Commons Attribution License (CC BY 3.0), which permits unrestricted use, distribution, and reproduction in any medium, provided the original author and source are credited.

ABSTRACT

MicroRNAs (miRNAs) serve as regulatory factors in both healthy tissue and various cancers. Here, we used an miRNA microarray to screen for miRNAs differentially expressed between HNSCC and adjacent epithelial tissue. Among these, levels of miR-141 were significantly reduced in HNSCC tissues. Expression levels of epidermal growth factor receptor (EGFR) were enhanced in tissues with low miR-141 expression but were reduced by miR-141 overexpression, and there was a significant negative correlation between EGFR and miR-141 levels in HNSCC tissues ($P < 0.01$). Luciferase assays confirmed that miR-141 targeted EGFR mRNA. *In vitro*, miR-141 inhibited the proliferation and migration of Cal-27 and FaDu HNSCC cells with corresponding decreases in CDK4 and MMP2. miR-141 also enhanced the incidence of apoptosis among the cells with a corresponding decrease in bcl-2. In BALB/c mice injected with FaDu HNSCC cells, miR-141 mitigated hepatic metastasis and inhibited expression of EGFR, CDK4, bcl-2 and MMP2. These results suggest that miR-141 functions as a tumor suppressor in HNSCC and that it suppresses tumor growth and metastasis by suppressing EGFR signaling. MiR-141 thus appears to be a potentially useful therapeutic target in the treatment of HNSCC.

INTRODUCTION

Head and neck squamous cell carcinoma (HNSCC) is the sixth most common type of human cancer, with more than 70% of patients suffering with recurrent or metastatic disease [1]. There is thus an urgent need for effective therapeutic regimens to treat HNSCC.

MiRNAs play fundamental roles in normal physiological and pathological processes, including cancer. miRNAs may affect the progression of cancer through their post-transcriptional regulation on genes [2]. For example, miR-141 is reportedly downregulated in several cancers, including hepatocellular carcinoma and gastric, colorectal, bladder and ovarian cancers [3-5]. However, the role of miR-141 in HNSCC remains unclear.

Epidermal growth factor receptor (EGFR) is a widely distributed cell surface receptor involved in the physiological processes of cell growth and differentiation as well as in cancer metastasis. More than 90% of HNSCCs exhibit upregulated EGFR expression [6, 7]. Identification of key factors that inhibit EGFR expression may improve the treatment of HNSCC. In the present study, therefore, we examined the effects of miR-141 on EGFR expression in HNSCC cells. We also analyzed the effects of miR-141 on proliferation, apoptosis and migration of HNSCC cells *in vivo* and *in vitro*. Our findings suggest miR-141 acts

as a tumor suppressor by targeting EGFR expression in HNSCC cells.

RESULTS

Identification of miRNAs differentially expression in HNSCC

A miRNA microarray was used to screen for abnormal expression of miRNAs in 30 samples of paired HNSCC and normal tissues. We found that twelve miRNAs are downregulated and six are upregulated in HSCC tissues (Table 1). Among these, levels of miR-141 were significantly reduced in HNSCC tissues. Further analysis revealed that levels of miR-141 expression are lower in HNSCC tissues than adjacent normal tissues and that the decrease correlated with the occurrence and development of HNSCC (Table 2, Fig. 1A, B).

EGFR is a direct target of miR-141

EGFR is highly expressed in HNSCC tissues (Fig. 1C). Moreover, patients showing higher EGFR expression had shorter survival times than those with lower EGFR expression (Fig. 1D). Levels of miR-141 expression correlated negatively with EGFR expression in HNSCC (Fig. 1E). MiRDB analysis showed that miR-141 bound the 3'-UTR of EGFR via (Fig. 2A). Luciferase assays showed that when FaDu and Cal-27 cells were cotransfected with EGFR and miR-141, luciferase activity was suppressed. By contrast, no suppression was detected when EGFR-mut or miR-141 antisense was transfected into the cells (Fig. 2B). Consistent with the luciferase activity, we observed that EGFR mRNA and protein expression was relatively high, while miR-141 expression was relatively low, in HNSCC cells (Fig. 2C, D). In addition, expression of miR-141 mimic in these cells

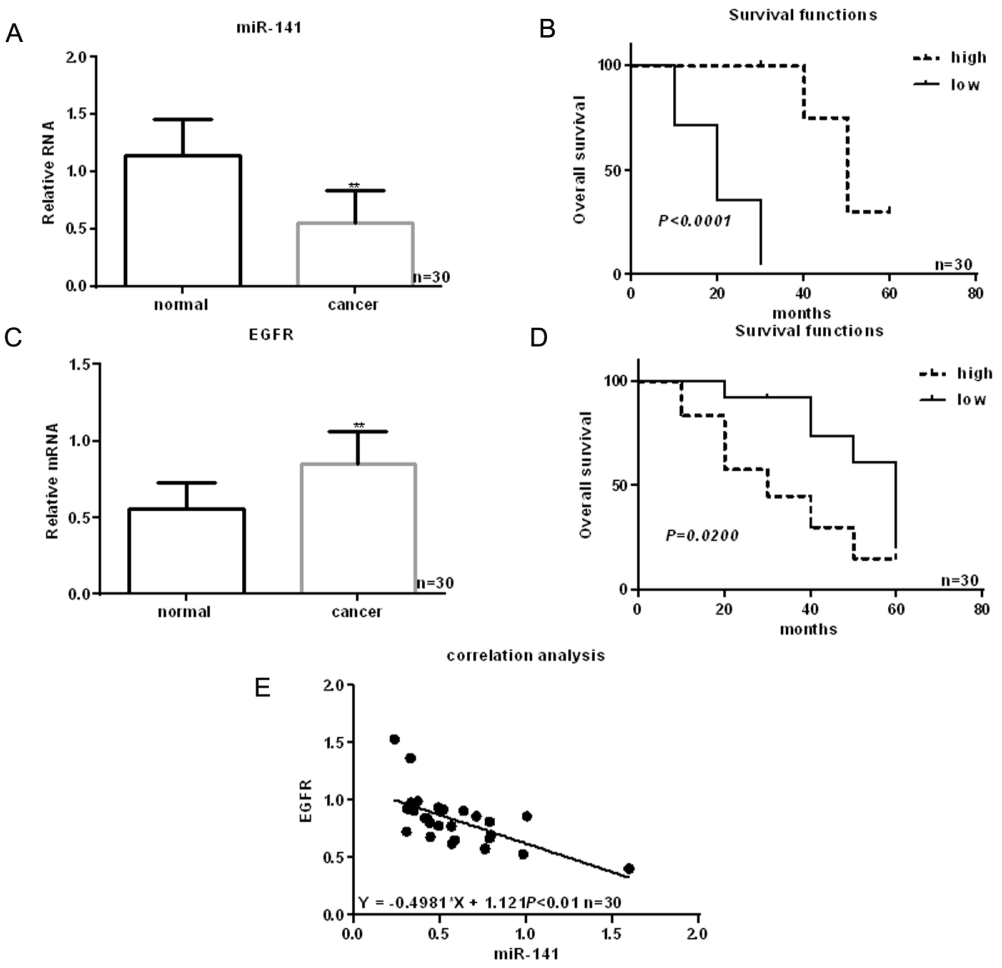

Figure 1. Identification of miRNAs differentially expressed in HNSCC. (**A**) Expression of miR-141 in HNSCC tissues and adjacent normal tissues detected using real time PCR. (**B**) Relationship between miR-141 and survival in HNSCC patients. (**C**) Expression of EGFR in HNSCC tissues and adjacent normal tissues detected using real time PCR. (**D**) Relationship between EGFR and survival in HNSCC patients. (**E**) Correlation between expression levels of miR-141 and EGFR in HNSCC. ** *P*< 0.05 vs. adjacent tissues.

Table 1. Differentially expressed miRNAs in HNSCCs.

miRNA	Fold change (HNSCC/adjacent tissues)	Trend
miR-106b-5p	31.37	Down
miR-141-3p	63.25	Down
miR-142-3p	11.42	Down
miR-149-3p	13.25	Down
miR-150-5p	27.37	Up
miR-191-5p	9.62	Up
miR-195-5p	12.10	Down
miR-21-5p	25.62	Up
miR-28-3p	14.12	Down
miR-30b-3p	39.42	Down
miR-3689c	9.64	Up
miR-425-5p	8.12	Down
miR-4728-5p	10.04	Down
miR-4779	12.94	Up
miR-541-3p	34.72	Down
miR-548g-3p	22.73	Up
miR-574-3p	39.64	Down
miR-590-5p	41.37	Down

Table 2. Relationship between miR-141 and HNSCCs.

Variables	Description	No. of patient	miR-141 expression		χ^2	*P*
			Low	High		
Gender	Male	18	10	8	0.13	0.71
	Female	12	9	3		
Age(years)	<40	14	8	6	0.43	0.51
	≥40	16	11	5		
Family history	No	24	13	11	4.34	0.04
	Yes	6	6	0		
TNM grade	IIA	14	5	9	8.87	0.01
	IIB	13	11	2		
	III	3	3	0		

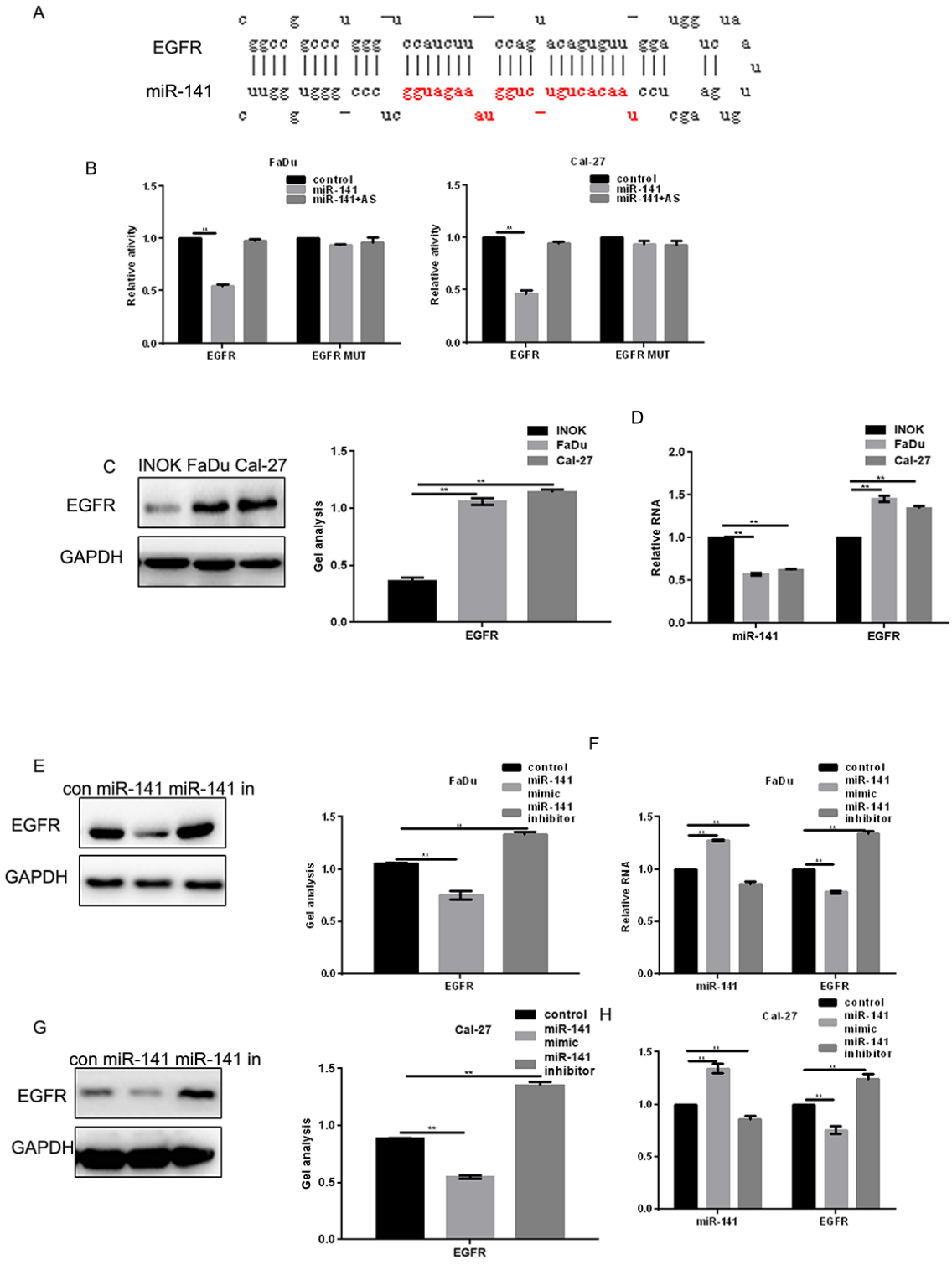

Figure 2. EGFR is a direct target of miR-141. (**A**) Prediction of miR-141 binding sites in the EGFR 3'-UTR. (**B**) Interaction between miR-141 and the EGFR 3'-UTR in FaDu and Cal-27 cells tested in luciferase assays. AS, antisense. (**C**) Western blots showing expression of EGFR in INOK, FaDu and Cal-27 cells. (**D**) Western blots showing expression of miR-141 and EGFR in INOK, FaDu and Cal-27 cells. (**E, F**) Western blot and real-time PCR showing co-expression of EGFR in FaDu cells with miR-141 mimic or inhibitor. (**G, H**) Western blot and real-time PCR showing co-expression of EGFR in Cal-27 with miR-141 mimic or inhibitor. Bars depict the mean ± SD. ** *P*< 0.05 vs. INOK cells (C, D) or control (E, F).

decreased expression of EGFR, while an miR-141 inhibitor enhanced EGFR expression (Fig. 2E-H).

miR-141 inhibits HNSCC cell proliferation

MTT assays showed that an miR-141 mimic inhibited proliferation of HNSCC cells, while an miR-141 inhibitor promoted their proliferation (Fig. 3A). EGFR is known to increase cell proliferation by enhancing expression of CDK4 [8]. We found that miR-141 mimic suppressed CDK4 expression, while an miR-141 inhibitor had the opposite effect (Fig. 3B-E).

miR-141 promotes HNSCC apoptosis

AV-PI assays showed that transfection of miR-141 mimic promoted apoptosis of FaDu and Cal-27 cells as compared to control (Fig. 4A, B). Western blotting and real-time PCR showed that this may reflect an inhibitory effect of miR-141 on expression of bcl-2 (Fig. 4C-F), a downstream EGFR effector [9].

miR-141 inhibits HNSCC metastasis

Transwell assays were used to assess the effect of miR-141 on FaDu and Cal-27 cell migration. The results indicated that miR-141 overexpression reduced the number of migrating cells, and miR-141 inhibition had the opposite effect (Fig. 5A-D). Western blot and real-time PCR showed that matrix metalloproteinase 2 (MMP2), an enzyme involved in breaking down extracellular matrix and known to be positively regulated by EGFR [10], was significantly downregulated by miR-141 (Fig. 5E-H).

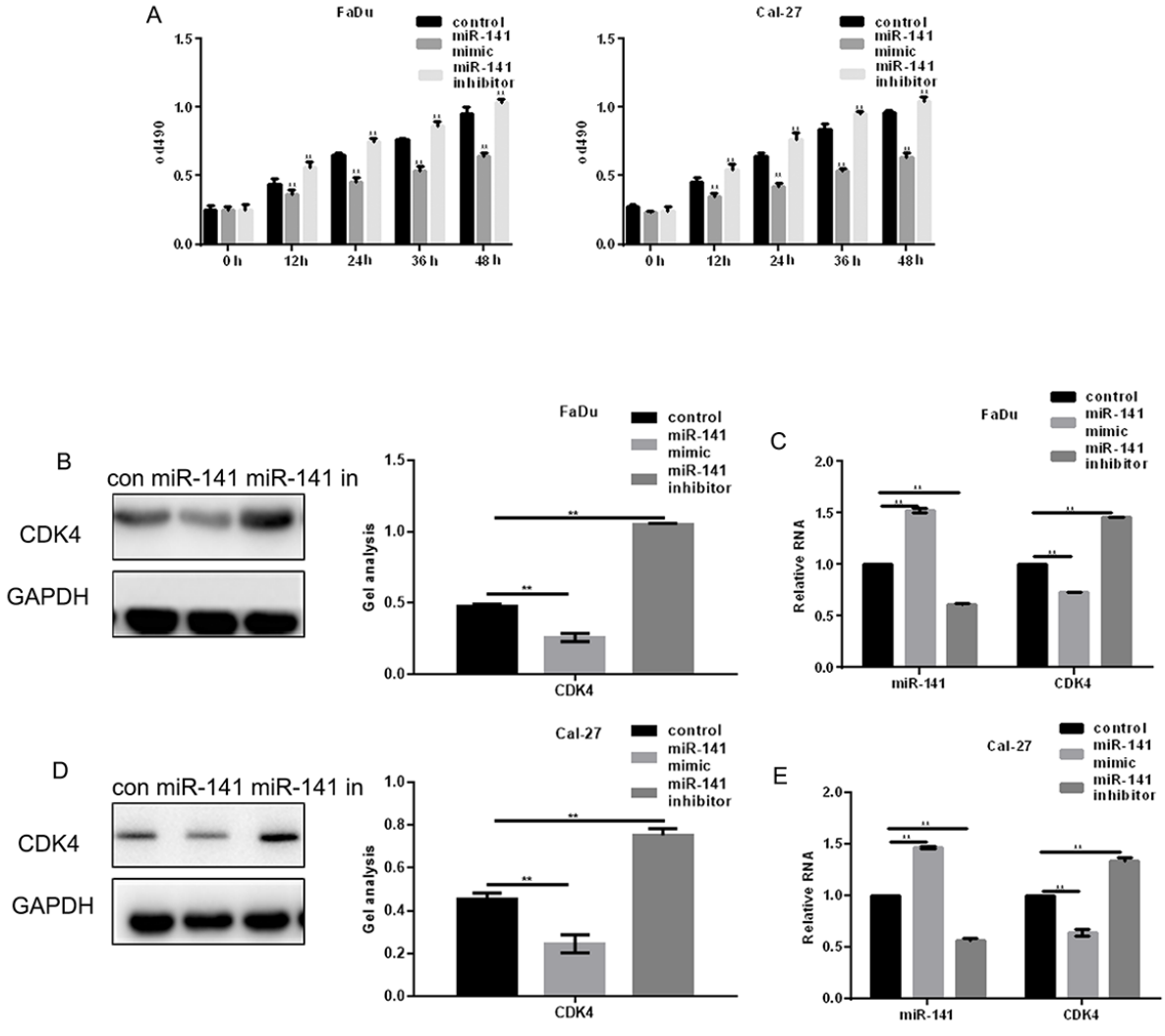

Figure 3. MiR-141 inhibits HNSCC cell proliferation. (**A**) MTT assays showing the effect of miR-141 mimic and inhibitor on FaDu and Cal-27 cell proliferation. (**B-E**) Western blots and real-time PCR were used to detect the expression of CDK4 in FaDu and Cal-27 cells expressing miR-141 mimic or inhibitor. Bars depict the mean ± SD. ** *P*< 0.05 vs. control.

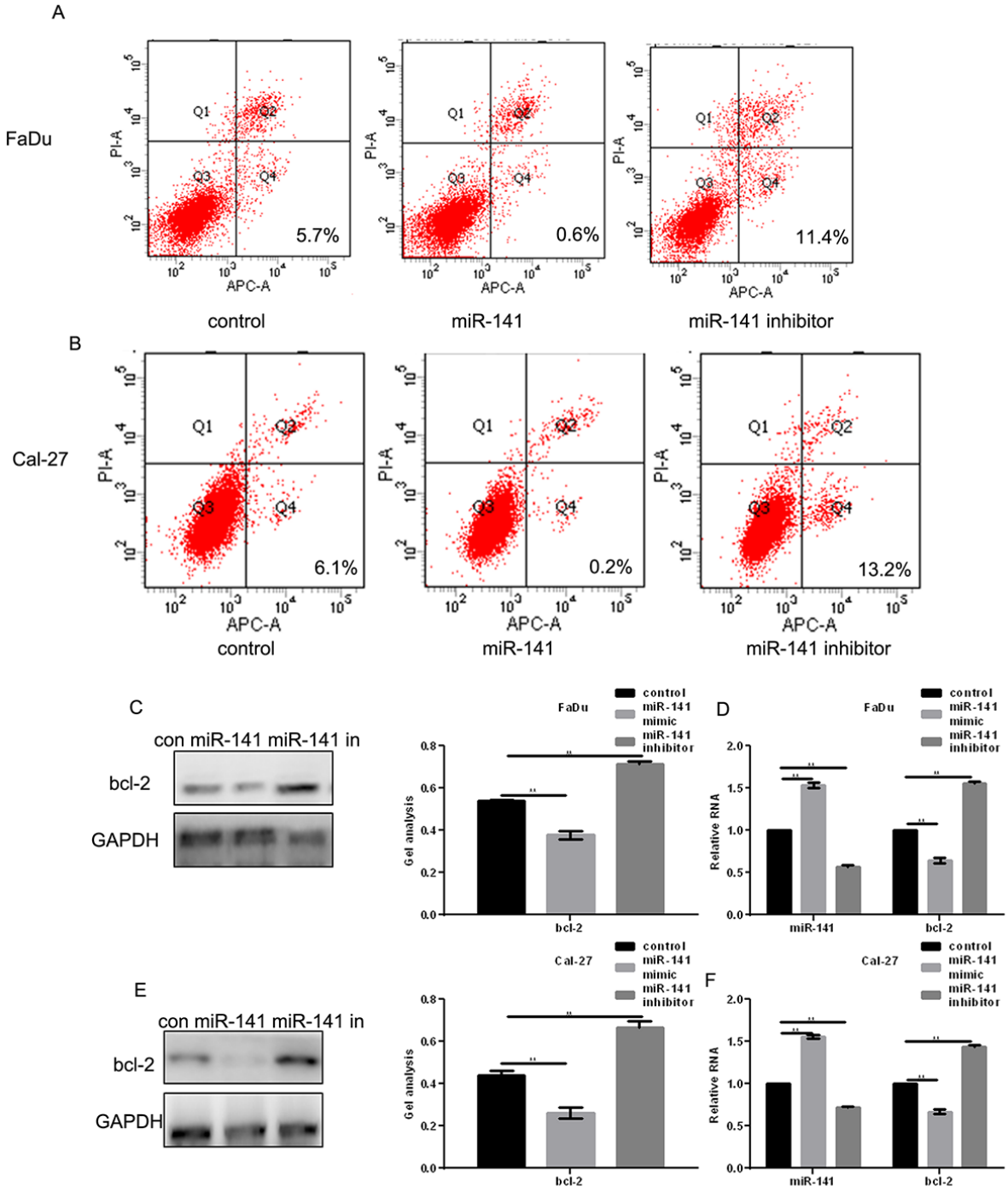

Figure 4. MiR-141 promotes HNSCC apoptosis. (**A, B**) Flow cytometry AV-PI assays showing the effect of miR-141 on FaDu and Cal-27 cell apoptosis. (**C-F**) Western blots and real-time PCR showing the effect of miR-141 mimic and inhibitor on bcl-2 expression in FaDu and Cal-27 cells. Bars depict the mean ± SD. *** P*< 0.05 vs. control.

miR-141 inhibits FaDu cell invasion *in vivo*

FaDu cells stably expressing control or miR-141 agomir were injected into BALB/c nude mice via the tail vein to examine the effect of miR-141 on cell invasiveness *in vivo*. Hematoxylin-eosin staining of liver tissues showed that miR-141 inhibited the hepatic metastatic activity of FaDu cells (Fig 6A, B). We also found that overexpression of miR-141 can downregulate the expression of EGFR, CDK4, bcl-2 and MMP2 *in vivo*

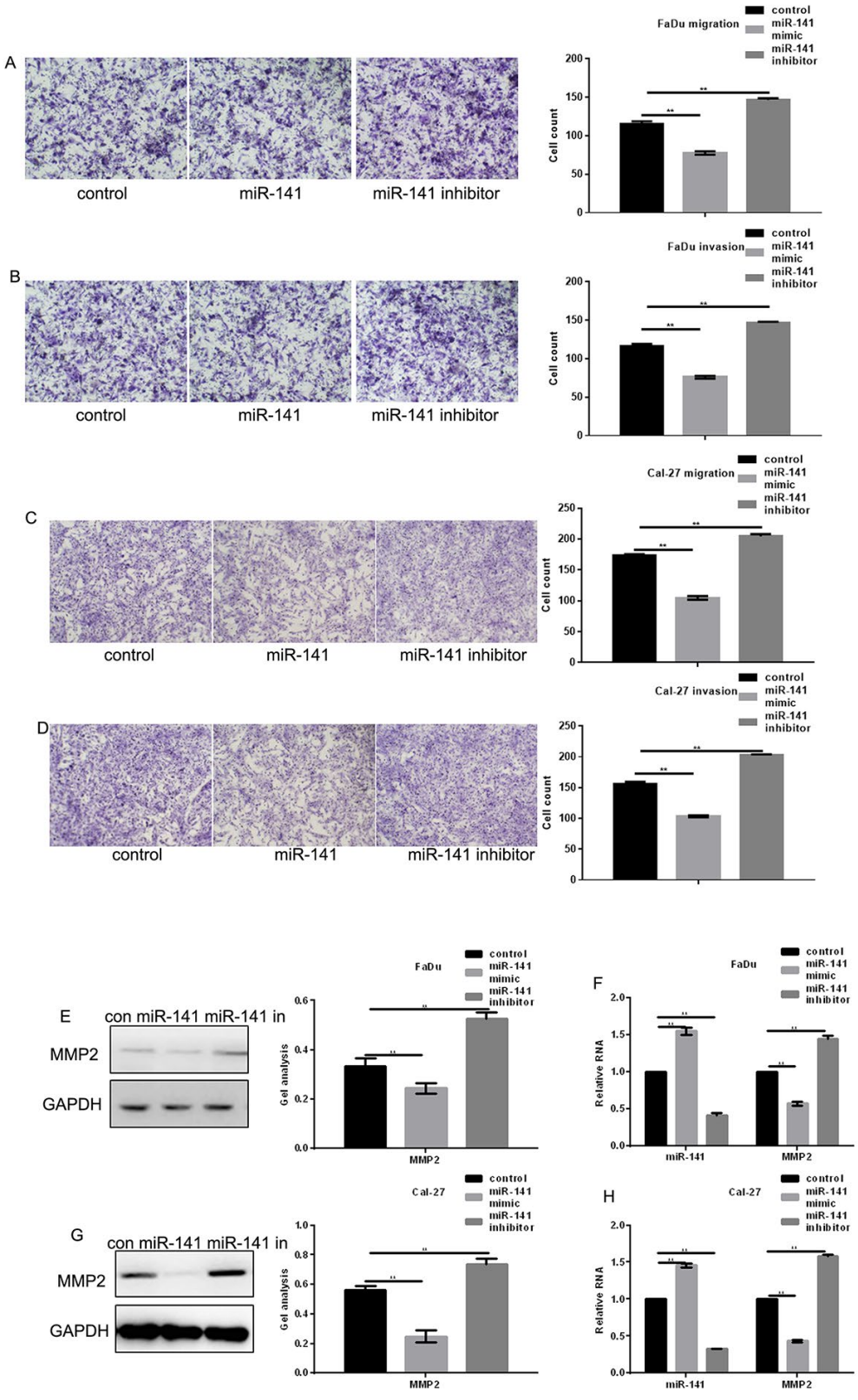

Figure 5. MiR-141 inhibits HNSCC metastasis. (**A-D**) Transwell assays with and without Matrigel showing the effect of miR-141 on FaDu and Cal-27 cell migration and invasion. Left panels: representative images of migrated cells under the indicated conditions. Right panels: Group data showing counts of migrated cells. Bars depict the mean ± SD of three experiments. (**E-H**) Western blots and real-time PCR the effect of miR-141 mimic and inhibitor on MMP2 expression in FaDu and Cal-27 cells. Bars depict the mean ± SD. ** *P*< 0.05 vs. control.

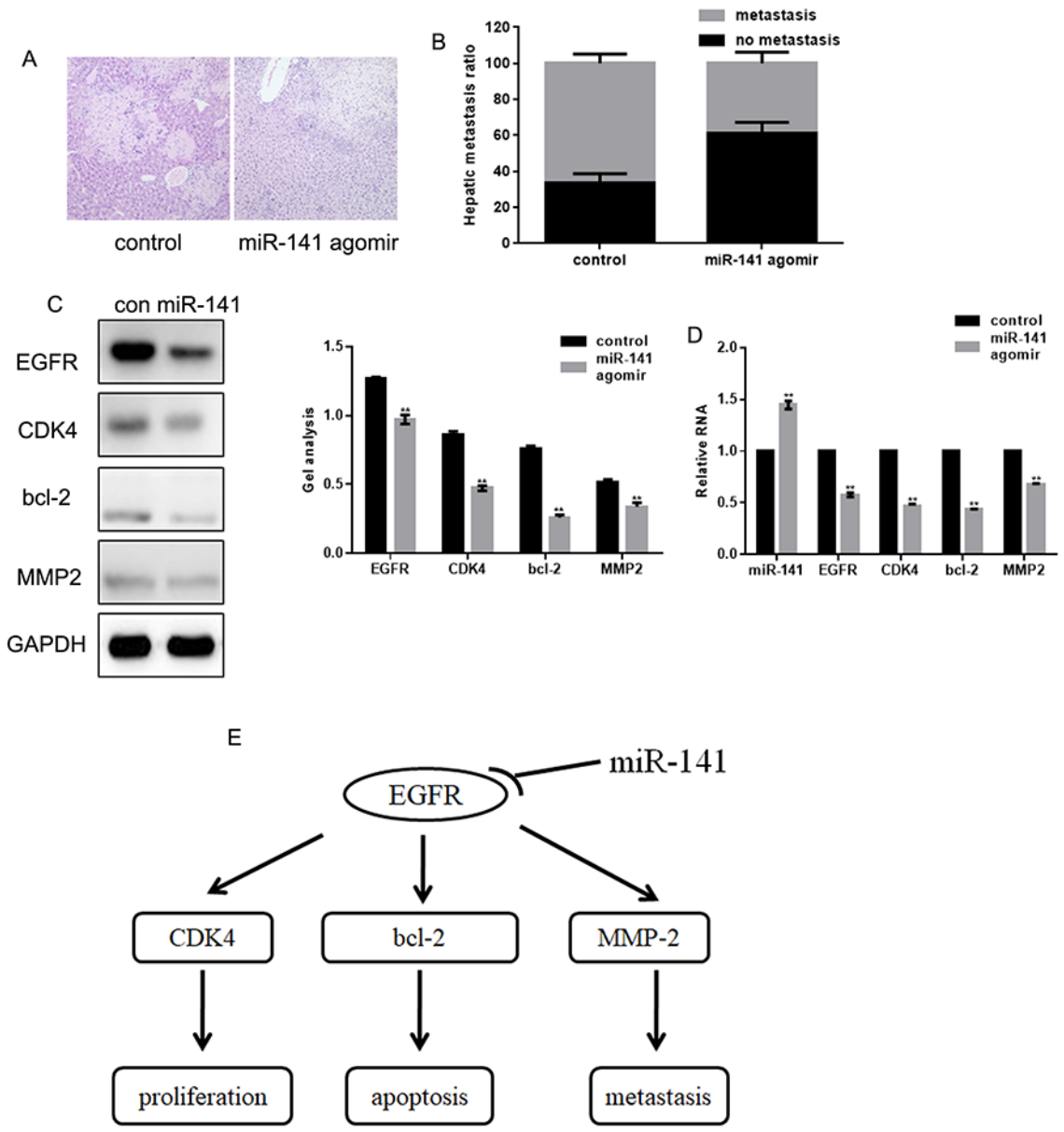

Figure 6. MiR-141 inhibits FaDu cell invasion *in vivo*. (**A**) Livers were dissected and stained with hematoxylin and eosin. (**B**) Bar graph showing the effect of miR-141 on the relative levels of hepatic metastasis. (**C, D**) Western blots and real-time PCR showing the effect of miR-141 on expression of EGFR, CDK4, bcl-2 and MMP2 in tissues. Bars depict the mean ± SD. ** *P*< 0.05 vs. control.

(Fig 6C, D). These findings suggest that by suppressing EGFR, miR-141 inhibits the growth and metastasis of HNSCC (Fig 6E).

DISCUSSION

In many tumors, levels of miR-141 expression are lower than in healthy tissue, and its increased expression can inhibit tumor progression [11]. For example, miR-141 has been shown to inhibit the development of gastric, prostate, colorectal and liver cancers by inhibiting cell proliferation and metastasis and promoting cell apoptosis [12-14]. In our study, we found that miR-141 was weakly expressed in HNSCC tissues and that higher expression of miR-141 improves patients' survival time.

EGFR plays important roles in angiogenesis and in the migration, proliferation and apoptosis of tumor cells [15]. In the present study, we demonstrated that EGFR

is highly expressed in HNSCC tissues and that miR-141 targeted and bound to EGFR. As a result, overexpression of miR-141 can inhibit the EGFR expression at both the protein and mRNA level.

We also found that overexpression of miR-141 inhibits HNSCC cell proliferation by inhibiting the CDK4 expression and promotes HNSCC cell apoptosis by inhibiting bcl-2. In addition, miR-141 inhibited HNSCC cell migration and invasion by inhibiting expression of MMP2. Because CDK4, bcl-2, and MMP2 are all regulated by EGFR [16, 17] and do not bind miR-141 (predicted by miRDB), we suggest the inhibitory effect of miRNA-141 on the HNSCC cell growth and metastasis reflects, at least in part, its targeting of EGFR. We also demonstrated that miR-141 agomir inhibits HNSCC metastasis *in vivo* and that miR-141 also inhibits expression of EGFR, CDK4, bcl-2 and MMP2 *in vivo*.

In summary, our results suggest that miR-141 functions as a tumor suppressor in HNSCC and that it suppresses tumor growth and metastasis by suppressing EGFR signaling. MiR-141 thus appears to be a potentially useful therapeutic target in the treatment of HNSCC.
Conclusion

MiR-141 functions as a tumor suppressor in HNSCC and that it suppresses tumor growth and metastasis by suppressing EGFR signaling.

MATERIALS AND METHODS

Samples

Thirty samples of fresh primary HNSCC and the adjacent normal epithelial tissues were obtained during surgery at Shengjing Hospital of China Medical University between 2011-2017. These included tongue SCC (56.67%, 17), oropharynx SCC (33.33%, 10), mouth floor SCC (6.67%, 2) and buccal mucosa SCC (3.33%, 1). None of the patients were treated with chemotherapy before the operation. The average age of the patients was 42.78 years (range: 29 to 63 years), and 18 of the patients were male. This study was approved by the Research Ethics Committee of Shengjing Hospital of China Medical University, and all patients provided written informed consent.

MicroRNA microarray analysis

Total RNA was extracted from tissues using a miRNA isolation kit (Takara, Japan) according to the manufacturer's protocol. MicroRNA microarray analysis was carried out by Huibai Biotechnology (Shenyang, China). Differentially expressed miRNAs were identified using a Moderated t-test, with the Benjamini-Hochberg correction (adjusted $P<0.05$ and fold change >2).

Cell lines and cell cultures

The FaDu (human pharynx SCC) and Cal-27 (human tongue SCC) HNSCC cell lines and immortalized normal oral keratinocytes (INOKs) were purchased from the cell bank of the Chinese Academy of Sciences (Beijing, China). Cells were cultured in DMEM medium (Invitrogen, Beijing, China) supplemented with 10% fetal bovine serum (FBS) (Gibco, Beijing, China) at 37°C in an atmosphere of 95% air/5% carbon dioxide.

Real-time PCR

Total RNA was extracted from tissues and cells using a Trizol kit (Takara, Japan), after which cDNA was obtained using a TaqMan® reverse transcription kit (Ribobio, China). The real-time PCR protocol entailed incubation at 95°C for 10 min, followed by 40 cycles at 95°C for 15 s and 60°C for 1 min. U6 and GAPDH were used as internal controls. A stem-loop RT-PCR assay was used to detect expression of miRNAs, as described previously [18, 19]. Primer sequences are listed in Table 3.

Western blotting

Total proteins were isolated from the cells using RIPA buffer. Thirty-microgram aliquots of protein were boiled for 5 min, separated by sodium dodecyl sulfate-polyacrylamide gel electrophoresis, and transferred to polyvinylidene fluoride membranes (Bio-Rad Laboratories, Tianjin, China). After incubation in blocking solution for 2 h at room temperature, the membranes were incubated with primary antibodies overnight at 4°C. Membranes were probed with anti-EGFR (1:500), anti-CDK4 (1:500), anti-bcl-2 (1:500), anti-MMP2 (1:500), anti-GAPDH (1:1000), HRP-conjugated anti-mouse (1:5000) and anti-rabbit (1:5000) (Santa Cruz Biotechnology, Texas, USA). GAPDH was used as a loading control.

Luciferase assays

The EGFR and EGFR-mut (the miR-141 binding site was mutated) 3'-UTR were cloned into the pMIR-REPORTTM vector (Ambion, China). For reporter assays, 1×10^4 cells were plated in a 96-well plate. After 24 h, the cells were cotransfected with miR-141 mimic, antisense or control (Ribobio, Guangzhou, China) plus 100 ng of EGFR or EGFR-MUT using Higene. Lysates were collected 48 h after transfection, and luciferase

Table 3. Primer sequences.

Name	Forward primer (5'->3')	Reverse primer (5'->3')
miR-141	ACACTCAGGTAGAAATG	ATTGTGACACCGAGTAC
U6	CTCGCTTCGGCAGCACA	ACGCTTCACGAATTTGC
h-EGFR	GACAGGCCACCTCGTCG	TGCGTGAGCTTGTTACTCGT
h-CDK4	CACTCTAACACTGTCTGG	ACATCGTTACCGAGAGTA
h-bcl-2	TTCTTTGAGTTCGGTGGGGTC	TGCATATTTGTTTGGGGCAGG
h-MMP2	CGCATCTGGGGCTTTAAACAT	CCATTAGCGCCTCCATCGTA
h-GAPDH	GACAGTCAGCCGCATCTTCT	GCGCCCAATACGACCAAATC
m-EGFR	GGCTATCTGACAGAGGTCGC	CTCTCACGGATTACCGCTCC
m-CDK4	TGATGCGCCAGTTTCTAAGAGG	GGTCGGCTTCAGAGTTTC
m-Bcl-2	TGCGTGAAGGCTTGAGATGT	TCCCCCTTTCCTAGACCCAG
m-MMP2	GCACACCAGGTGAAGGATGT	AAACGAGCGAAGGGCATACA
m-GAPDH	CAGGTTGTCTCCTGCGACTT	TATGGGGGTCTGGGATGGAA

All the reactions were carried out as described previously [20].

activity was assessed using a Dual Luciferase Reporter Assay System (Promega, USA).

MTT assays

Cells were plated into a 96-well plate at a density of 1,000 cells per well. After 24 h, the cells were transfected with the miR-141 mimic, miR-141 inhibitor or control. Cell proliferation was analyzed after 0, 12, 24 and 48 h using MTT assays (Beyotime Biotechnology, Tianjin, China) according to the manufacturer's protocol, measuring absorbance at 490 nm. All assays were performed in triplicate wells, and experiments were independently performed at least three times.

Transwell assays

After cells were transfected with the miR-141 mimic, miR-141 inhibitor or control, 1×10^5 cells in serum-free medium were seeded to the upper chamber of Transwell plates left bare or coated with Matrigel. After 8 h, cells on the lower side of the chamber were fixed and stained with 0.4% trypan blue (Beyotime Biotechnology, Tianjin, China) and counted under a microscope.

Annexin V-FITC/PI (propidium iodide) assays

Cells were seeded into 6-well plates to a density of 8,000 cells/well and incubated for 24 h. The cells were then transfected with miR-141 mimic, miR-141 inhibitor or control. After an additional 24 h, cellular apoptosis was analyzed using an AV-PI assay (Beyotime Biotechnology, Tianjin, China) according with the manufacturer's protocol. Suspended cells were incubated with AV-PI for 5 min at room temperature. Apoptosis was then assessed using flow cytometry in at least three independent experiments.

Nude mouse experiment

FaDu cells infected with control or miR-141 agomir were used for *in vivo* liver metastasis assays. Five- to six-week-old female, athymic nude BALB/c mice (animal experiment center, Wuhan University, China) were injected via the tail vein with 1×10^6 cells

suspended in 1 ml of saline. Six weeks after the injection, liver samples were collected for histological examination. All procedures were conducted in accordance with the Guide for the Care and Use of Laboratory Animals (NIH publication no. 80-23, revised 1996) and the institutional ethical guidelines of Shengjing Hospital of China Medical University.

Histopathology

Liver specimens were fixed with 4% paraformaldehyde and cut into serial sections (2 μm). The sections were then deparaffinized in xylene, rehydrated through a descending graded ethanol series, and stained with hematoxylin and eosin. The stained sections were dehydrated through an ascending graded ethanol series and mounted on slides. The pathological changes were observed under a light microscope.

Bioinformatic and statistical analyses

MiRDB (http://www.mirdb.org/) was used to predict the target genes of miR-141. All statistical analyses were performed using SPSS 13.0 software (SPSS Inc., Chicago, IL, USA). All data are presented as the mean ± standard deviation. Groups were compared using two tailed Student's t-test and one-way ANOVA. Values of $P < 0.05$ were considered statistically significant.

Ethics approval and consent to participate

Research involving human subjects, human material, or human data, was performed in accordance with the Declaration of Helsinki and was approved by the Research Ethics Committee of Shengjing Hospital of China Medical University (R20141121).

Consent for publication

Written informed consent for the publication of all manuscript details was obtained from Shengjing Hospital of China Medical University.

AUTHOR CONTRIBUTIONS

Zhiguo Zhao conceived the study and carried out the molecular studies. X carried out molecular studies. Dan Gao participated in the design of the study and performed the statistical analysis. Tie Ma participated in the study design and coordination and helped to draft the manuscript. Liping Zhang conceived the studied and draft the manuscript.

ACKNOWLEDGMENTS

All personnel who have contributed to this article are in the list of authors.

CONFLICTS OF INTEREST

The authors declare no conflict of interest.

REFERENCES

1. Swick AD, Prabakaran PJ, Miller MC, Javaid AM, Fisher MM, Sampene E, Ong IM, Hu R, Iida M, Nickel KP, Bruce JY, Wheeler DL, Kimple RJ. Cotargeting mTORC and EGFR signaling as a therapeutic strategy in HNSCC. Mol Cancer Ther. 2017; 16:1257–68. https://doi.org/10.1158/1535-7163.MCT-17-0115

2. Fu WF, Chen WB, Dai L, Yang GP, Jiang ZY, Pan L, Zhao J, Chen G. Inhibition of miR-141 reverses cisplatin resistance in non-small cell lung cancer cells via upregulation of programmed cell death protein 4. Eur Rev Med Pharmacol Sci. 2016; 20:2565–72.

3. Xu S, Ge J, Zhang Z, Zhou W. miR-141 inhibits prostatic cancer cell proliferation and migration, and induces cell apoptosis via targeting of RUNX1. Oncol Rep. 2018; 39:1454–60. https://doi.org/10.3892/or.2018.6209

4. Wang H, Li H, Zhang L, Yang D. Overexpression of MEG3 sensitizes colorectal cancer cells to oxaliplatin through regulation of miR-141/PDCD4 axis. Biomed Pharmacother. 2018; 106:1607–15. https://doi.org/10.1016/j.biopha.2018.07.131

5. Sha M, Lin M, Wang J, Ye J, Xu J, Xu N, Huang J. Long non-coding RNA MIAT promotes gastric cancer growth and metastasis through regulation of miR-141/DDX5 pathway. J Exp Clin Cancer Res. 2018; 37:58. https://doi.org/10.1186/s13046-018-0725-3

6. Schuettler D, Piontek G, Wirth M, Haller B, Reiter R, Brockhoff G, Pickhard A. Selective inhibition of EGFR downstream signaling reverses the irradiation-enhanced migration of HNSCC cells. Am J Cancer Res. 2015; 5:2660–72.

7. Argiris A. EGFR inhibition for recurrent or metastatic HNSCC. Lancet Oncol. 2015; 16:488–89. https://doi.org/10.1016/S1470-2045(15)70178-6

8. Xu G, Li JY. CDK4, CDK6, cyclin D1, p16(INK4a) and EGFR expression in glioblastoma with a primitive neuronal component. J Neurooncol. 2018; 136:445–52. https://doi.org/10.1007/s11060-017-2674-7

9. Bourouba M, Benyelles-Boufennara A, Terki N, Baraka-Kerboua E, Bouzid K, Touil-Boukoffa C. Epidermal growth factor receptor (EGFR) abundance correlates with p53 and Bcl-2 accumulation and patient age in a small cohort of North African nasopharyngeal carcinoma patients. Eur Cytokine Netw. 2011; 22:38–44. https://doi.org/10.1684/ecn.2011.0270

10. Kang DY, Sp N, Kim DH, Joung YH, Lee HG, Park YM, Yang YM. Salidroside inhibits migration, invasion and angiogenesis of MDA MB 231 TNBC cells by regulating EGFR/Jak2/STAT3 signaling via MMP2. Int J Oncol. 2018; 53:877–85.

11. Li X, Tian Z, Jin H, Xu J, Hua X, Yan H, Liufu H, Wang J, Li J, Zhu J, Huang H, Huang C. Decreased c-Myc mRNA stability via miR-141-3p/AUF1 axis is crucial for p63alpha inhibition of Cyclin D1 transcription and bladder cancer cell tumorigenicity. Mol Cell Biol. 2018; 38:e00273-18. https://doi.org/10.1128/MCB.00273-18

12. Zhu SH, He XC, Wang L. Correlation analysis of miR-200b, miR-200c, and miR-141 with liver metastases in colorectal cancer patients. Eur Rev Med Pharmacol Sci. 2017; 21:2357–63.

13. Ye Y, Li SL, Ma YY, Diao YJ, Yang L, Su MQ, Li Z, Ji Y, Wang J, Lei L, Fan WX, Li LX, Xu Y, Hao XK. Exosomal miR-141-3p regulates osteoblast activity to promote the osteoblastic metastasis of prostate cancer. Oncotarget. 2017; 8:94834–49. https://doi.org/10.18632/oncotarget.22014

14. Long ZH, Bai ZG, Song JN, Zheng Z, Li J, Zhang J, Cai J, Yao HW, Wang J, Yang YC, Yin J, Zhang ZT. miR-141 inhibits proliferation and migration of colorectal cancer SW480 cells. Anticancer Res. 2017; 37:4345–52. https://doi.org/10.21873/anticanres.11828

15. Fernández-Mateos J, Seijas-Tamayo R, Mesía R, Taberna M, Pastor Borgoñón M, Pérez-Ruiz E, Adansa Klain JC, Vázquez Fernández S, Del Barco Morillo E, Lozano A, González Sarmiento R, Cruz-Hernández JJ, et al, and Spanish Head and Neck Cancer Cooperative Group (TTCC). Epidermal growth factor receptor (EGFR) pathway polymorphisms as predictive markers of cetuximab toxicity in locally advanced head and neck squamous cell carcinoma (HNSCC) in a Spanish population. Oral Oncol. 2016; 63:38–43. https://doi.org/10.1016/j.oraloncology.2016.10.006

16. Wiechec E, Hansson KT, Alexandersson L, Jönsson JI, Roberg K. Hypoxia mediates differential response to anti-EGFR Therapy in HNSCC cells. Int J Mol Sci. 2017; 18:E943. https://doi.org/10.3390/ijms18050943

17. Rüddel J, Wennekes VE, Meissner W, Werner JA, Mandic R. EGF-dependent induction of BCL-xL and p21CIP1/WAF1 is highly variable in HNSCC cells--implications for EGFR-targeted therapies. Anticancer Res. 2010; 30:4579–85.

18. Feng J, Wang K, Liu X, Chen S, Chen J. The quantification of tomato microRNAs response to viral infection by stem-loop real-time RT-PCR. Gene. 2009; 437:14–21. https://doi.org/10.1016/j.gene.2009.01.017

19. Chen C, Ridzon DA, Broomer AJ, Zhou Z, Lee DH, Nguyen JT, Barbisin M, Xu NL, Mahuvakar VR, Andersen MR, Lao KQ, Livak KJ, Guegler KJ. Real-time quantification of microRNAs by stem-loop RT-PCR. Nucleic Acids Res. 2005; 33:e179. https://doi.org/10.1093/nar/gni178

20. Pfaffl MW. A new mathematical model for relative quantification in real-time RT-PCR. Nucleic Acids Res. 2001; 29:e45. https://doi.org/10.1093/nar/29.9.e45